Emergent Properties in Exoplanetary Systems

by

Juliette Becker

A dissertation submitted in partial fulfillment
of the requirements for the degree of
Doctor of Philosophy
(Astronomy and Astrophysics)
in The University of Michigan
2019

Doctoral Committee:

Professor Fred Adams, Chair
Professor Nuria Calvet
Professor David Gerdes
Professor Michael Meyer
Professor Emily Rauscher

Juliette C. Becker

jcbecker@umich.edu

ORCID iD: 0000-0002-7733-4522

For Michael

ACKNOWLEDGEMENTS

I would first like to thank my advisor, Fred Adams, for the best guidance over the past four and a half years. I am grateful to have had such a wonderful PhD advisor. I hope that someday I can understand physics as deeply as Fred does! Fred, it has been a joy to work with you during my PhD, and I am truly grateful to have an advisor as supportive (both scientifically and personally) as you.

I would also like to thank Konstantin Batygin, who introduced me to both exoplanets and theory when I was a Caltech undergraduate and he was a Caltech graduate student and has been a constant source of support and inspiration ever since. I am looking forward to working with you again once I start my job at Caltech, Konstantin!

I would like to thank Andrew Vanderburg, whose support, encouragement, and advice began before I even applied to graduate schools and has continued to the current day. Andrew, I would not be the scientist I am today with your friendship, and I look forward to many more years of writing great papers together.

I would also like to thank Tali Khain: we have been working together for around three years now, and in that time we have both grown into much stronger scientists. It has been a joy to work with you, and improve ourselves side by side. Thank you, Tali, for also being such a wonderful friend!

I would like to thank Joey Rodriguez, one of my favorite people to write a paper with. Joey: I strive to be as positive an influence on the astronomical community and my collaborators as you are.

I would like to also thank David Gerdes, my second mentor at the University of Michigan.

I have grown a lot from being part of your lab group and working with you has made my PhD experience much richer.

I would also like to thank the whole UM TNO group: Larissa Markwardt, Stephanie Hamilton, Kyle Franson, Ed Lin, Kevin Napier (and Tali, Dave and Fred). You are all a lot of fun; between all of your encouragement for me to take up 3D printing as a hobby, buy a chocolate fountain, stare at DS9 frames for hours on end, become an amateur encyclopedia contributor, remake Moana, and give our friends nicknames, I'm somewhat surprised this thesis even got done at all.

I would also like to thank the important friends who have made my PhD a lot of fun: I would like to thank Clara Eng (we will eventually write that paper together!), whose advice has not been wrong yet. I would like to thank Ellen Price for her friendship, constant companionship (mostly via GChat, since we live in different states), and her great advice about computational methods. I would like to thank Alison Ponce, a great friend who has accidentally taught me to make my papers and figures more interesting! I would like to also thank Iryna Butsky, who always reminds me to look on the bright side.... luminosity! (I couldn't resist... Iryna, thanks also for teaching me ChaNGa, and for being my compatriot in Python since 2012. When we're both tenured profs, we WILL make our jokes catch on, and maybe come up with some even 'better' ones).

I would also like to thank my other astronomy friends, collaborators, and mentors, whose help and advice have been invaluable over the past several years: Sarah Ballard, Marta Bryan, Dan Fabrycky, Jesse Golden-Marx, Stephanie Hamilton, John Johnson, Heather Knutson, Gongjie Li, Larissa Markwardt, Erin May, Sarah Millholland, Ben Montet, Tim Morton, Phil Muirhead, Sam Quinn. Science wouldn't be as fun as it is without wonderful people like you to work with!

I would like to thank my thesis committee, Fred Adams, Nuria Calvet, David Gerdes, Michael Meyer, and Emily Rauscher, for their years of feedback and support.

I would also like to thank the other supportive faculty at the University of Michigan who

have made my time here an enriching and enjoyable experience: Eric Bell, Joel Bregman, Chuck Cowley, Elena Gallo, Sally Oey. I would particularly like to thank Jon Miller for his continued guidance and support: I hope that I will be as helpful to future students as you have been to me.

This thesis would not have been possible without the help of many people. I would like to offer additional thanks to the numerous other scientists not listed above with whom I have authored papers over the course of my PhD. I would like to thank Bill Moore, who was my first physics teacher despite the fact he taught statistics.

Most importantly, I would like to thank all of my family.

First, I would like to thank my soon-to-be parents-in-law, Bob and Dianne Dieterle, for their support and advice throughout the years. Thanks also to Sarah Dieterle, who has proofread many of my applications and papers throughout the years, from the NSF GRFP application in 2013 to my postdoc applications this past fall! Thank you for your enthusiastic support and for giving me such a wonderful introduction to the University of Michigan when I first visited in 2014.

My penultimate thanks is to my parents, Jeff and Jere Becker, who have supported me and listened to me talk incessantly about the contents of this thesis for the past several years. I am so grateful to have you both in my life, and that you have always supported me in what I have chosen to do. Thank you for bringing me so many hot chocolates over the years while I typed away at papers and finally this thesis. Thank you for the baseball games, the Starbucks trips, the Saw Mill lunches; thank you both for spending countless hours attending everything I find important, from my track meets to my research talks.

Finally, I would like to thank Michael Dieterle, my other half, who has spent countless hours talking to me about my research, suggested (often successful) solutions when I've been stuck, helped me debug code ("Have you checked your oscillating wave functions?"), prevented me (once) from throwing my laptop into a pond in my frustration, and always filled my life with joy. This thesis was originally entitled "Dynamically Constraining the Un-

seen Properties of Exoplanets." The connection to emergent properties and the subsequent grounding in more than a hundred years of systems analysis in science was Michael's idea: as always, thank you for both inspiring and helping me to do and become better. Michael, thank you for being part of my life, and I look forward to this coming August 9th, after which we will take the next step in our lives together as husband and wife.

TABLE OF CONTENTS

LIST OF FIGURES

Figure

LIST OF TABLES

Table

ABSTRACT

As the number of known exoplanets approaches four thousand, the fundamental tactic of the field must shift from reductionist analyses of individual planets to systems-level coherent analyses of entire planetary systems. The major contribution of this thesis is to make explicit the study of emergent properties in exoplanetary systems, and the ways that emergent properties can be forward-modeled and reverse-engineered to better understand the unseen components in exoplanetary systems. In both cases, the (known) relationship between the independent properties of the constituent parts of the system and the resultant emergent properties is leveraged to provide a better understanding of the system as a whole and constrain unknown properties for future analysis.

The specific contributions of this thesis are as follows. First, in Chapter II, I present the forward modeling of system stability from the measured properties of multi-planet systems discovered by Kepler. In Chapter III, I constrain the presence of additional unseen companions in these same systems by utilizing the observed emergent properties of each system. In Chapter IV, I present the discovery of two additional planets in the WASP-47 system, constrain their masses using two independent methods (transit timing variations and radial velocities) and then utilize dynamical models to measure the unseen properties of the system. In Chapter V, I make population-level inferences about non-transiting companions to hot Jupiters orbiting cool stars using the dynamics of the emergent interactions in the systems. In Chapter VI, I present the discovery of five planets in the HIP 41378 system, three of which have ambiguous orbital periods, and utilize a combination of supplementary observations and dynamics to constrain the orbital periods, creating a road-map for future similar analysis in K2/TESS systems. In Chapter VII, I present the discovery of four vali-

dated planets and two additional candidates in the K2-266 system, which exhibit an unusual geometry, and propose a novel mechanism for creating system geometries of these types. In Chapter VIII, I use numerical simulations to explore how emergent properties of Kuiper Belt Objects in our own solar system may be reproduced in the presence of Planet Nine, a proposed new member of the solar system. In Chapter IX, I present the discovery of a new Kuiper Belt Object, the first of a new class of high-inclination, long-orbital-period objects, whose current-day inclination cannot be explained in our existing picture of the solar system. The final goal of the work in this thesis is to enable a better understanding of the census of exoplanets in the galaxy. In Chapter X, I both describe the impacts so far of the work described in this thesis and summarize avenues of future work.

CHAPTER I

Emergent Properties with a Focus on Astronomy

1.1 Emergence

The overarching goal of this thesis is to study the interplay between entire planetary systems and their constituent, individual components. This thesis focuses on the dynamical properties and long term evolution of this class of systems, properties which cannot be accurately modeled until the entire system is considered coherently. Before embarking upon the specifics of this dynamical exploration, it is useful to briefly consider the history of emergence.

The connection between the individual self and the universal whole is one of the fundamental questions underpinning religion and philosophy. Marcus Aurelius, the stoic philosopher and Roman emperor, wrote in his *Meditations* (Antoninus, 161 - 180 A.D.):

> Ever consider this Universe as one living being, with one material substance and one spirit. Observe how all things are referred to the one intelligence of this being; how all things act on one impulse; how all things are concurrent causes of all others; and how all things are connected and intertwined.
>
> - Marcus Aurelius, *Meditations*, Book 4, Section 40

The concept that 'all things are connected and intertwined' is a tenant of stoic philosophy: it serves partially to remind stoics of the humanity of others, that all people are connected,

and to enable compassion and virtuous action. It also serves as justification for the state of the world and the existence of suffering: despite hardship, life and its actions have meaning and purpose, as one individual's actions affect not only others in the world but also all of the universe. For physicists, this quote also reminds us not to neglect the off-diagonal terms in our eigenmatrices.

This aspect of natural interconnectedness must be considered when studying any reasonably complex system. For such complex systems, independent analyses of isolated components does not construct an accurate picture of the entire system. The concept of the whole being more than the sum of its parts is commonly termed 'emergence', with the properties that the whole gains that the parts did not have being called 'emergent properties'. This concept stands in contrast to reductionism, a philosophy which attempts to understand complex systems by reducing them to their parts. A reductionist would think that one can understand a system by considering its simplest components, while studying the emergent properties necessitates considering the entire system coherently.

In his 1843 book *A System of Logic*, British philosopher John Stuart Mill described in depth the concept of emergence as it applies to life science, explaining that separate models of many aspects of an organism's behavior cannot merely be summed together to describe its full action (Mill, 1843):

> 'To whatever degree we might imagine our knowledge of the properties of the several ingredients of a living body to be extended and perfected, it is certain that no mere summing up of the separate actions of those elements will ever amount to the action of the living body itself.' - John Stuart Mill, *A System of Logic*

Indeed, the example of a living organism is perhaps the most illustrative example of emergence: if mammalian cytokines are studied *in vitro*, in isolation of the host cells with which they interact, minimal useful information could be gained: perhaps the physical structure of the molecule, its chemical properties, or its response to temperature and acidity. Studied *in*

vitro but in the presence of immune cells and a pathogen, some novel reactions can become clear: such as immune cell activation leading to pathogen destruction and removal. However, even this cannot inform the entire picture, as many inflammatory molecules also modify and signal host cells to initiate repair after an injury. Only once studied in a model organism can all of these complex interactions be seen at once.

Particularly when the interplay between aspects of a system becomes complex (as it does in the mammalian immune system), a system may reveal emergent properties that could not have been predicted by modeling the constituent parts independently. Concrete examples of this arise in many fields, demonstrating the importance of a systems-level approach to studying complex phenomena. Before we turn our attention to the subject of this thesis (the study and use of emergent properties in exoplanetary systems), we will first take a brief survey through emergent properties as studied and applied in other fields to provide the context for the use of the concept in planetary astrophysics.

1.1.1 Emergence in nature and ecology

In ecology, individual study of species or organisms often falls short in describing how they exist together in nature, both as single-species populations and as multi-species ecosystems. One remarkable example of this effect is *Ection* army ants, which construct bridges with their bodies to navigate unfavorable geometry (Reid et al., 2015). A complete study of a single ant (even including gene sequencing, behavior tests, microbiome analysis, etc) would not reveal this behavior, as each ant is fully autonomous and functions independently without its cohort. Only when an entire colony of ants is studied does this emergent property of their problem-solving behavior become evident.

Similarly, other animal species become more than the sum of their parts when traveling as a population: Cucker & Smale (2007) models a flock of migrating birds, whose flight pattern and speed become uniform but cannot be predicted by studying any individual bird (even in the same environment), by explicitly defining the variables which emerge as a result

of group interactions. Population dynamics in fish are evident when gazing upon a school of fish coherently swimming together, but cannot be derived from studying any single fish (or even any two fish, Parrish et al., 2002). Even the pseudo-fluid dynamics of automobile traffic jams requires a study of the entire population of commuters (Li et al., 2007), rather than study of the car and its mechanical capabilities. Group dynamics in nature illustrate that emergent properties can only be observed once a group is assembled and that the group inherits properties not belonging individually to any of its members.

On a larger scale, the entire evolutionary process serves as an emergent property. Macroevolution, defined as evolutionary change on a scale larger than a single species, occurs due to interactions between species, the species and its environment, and other factors that only become evident when the entire ecosystem is studied. The complex interplay between species populations, especially when groups of predators and prey are introduced, is commonly modeled (to first order) as a system of differential equations, with coefficients representing the birth rates and death rates due to nature, hazards, and various predators, or in a generalized model (Anderson et al., 1981; Mena-Lorcat & Hethcote, 1992; Yeakel et al., 2011). These models have been used to great success to understand and predict the evolution of population levels and also to describe food webs (Polis, 1991; Mccann & Hastings, 1997). However, one difficulty in constructing these models resides in the fact that for a complete understanding of the system, all species must be modeled and the interaction coefficients must be known. In many ecosystems (such as the ocean), we have a yet incomplete mapping of the species which exist, making such modeling incomplete. In this case, the reductionist approach falls short: even an analysis of the dynamics of a single species cannot be derived without consideration of the feedback effects resulting from the larger systems and its emergent properties (Ulanowicz, 1997). Similarly, the exact interplay between species is often difficult to quantify (ex: Angerbjorn et al., 1999) and can change depending on the presence of other species or environmental factors, resulting in theoretical models often failing to match the real data (Polis, 1991) unless they are tuned properly (Kratina et al., 2012).

As a final example: there is nothing about the rabbit that made immediately clear the danger it posed to the Australian ecosystem until it was placed into said ecosystem (Lees & Bell, 2008). The invasive prey species destabilized the ecosystem, harming many indigenous species. The full impact of many invasive species is not felt until years later and in most cases cannot be easily predicted due to the complex interplay between environmental factors. Even efforts to fix the problem were met with the same difficulties of modeling the impact of changes in the ecosystem: for example, a series of viruses were introduced to attempt to cull the rabbit population in Australia, starting with the myxoma virus in the 1950s (Kerr, 2012). Though the myxoma virus was intended to decrease the rabbit population in Australia, it resulted instead in an increase in the overall rabbit population (Dwyer et al., 1990) due to the unexpected complex interplay between population levels and relative predation across species. Eventually, years later, the accidental release of a different virus in 1995 successfully culled the rabbit population, resulting in the re-emergence of previously threatened species (Pedler et al., 2016). The entire dynamics of the rabbit population cannot be modeled without including not only the strains of virus released and the natural predators, but also other prey species and even environmental factors (James et al., 2011). This example highlights the need for systems-level analysis, lest the emergent properties that mediate the population dynamics are ignored.

1.1.2 Emergence in microbiology and medicine

The case for considering emergent properties is perhaps more cogent when considering life. Synaptic plasticity is an emergent property of the human brain: when a large number of individual synapses are networked together, they form structures which play important roles in memory and learning. Individual neurons or even small networks cannot reproduce the full capability of the human brain, meaning that to study the brain neuroscientists must model the entire neural network instead of just isolated components (ex: Post & Weiss, 1997). Brain recovery after a stroke depends on the interplay between damaged neurons and

the ability of the brain to regain lost connections; synaptic plasticity is one of the emergent properties studied in an effort to increase stroke recovery (Bernhardt et al., 2016). Individual neuron health does less to predict stroke recovery than the plasticity of the entire network.

Tissue morphogenesis involves the coherent migration of groups of cells, which requires coordination between the cells in order to maintain tissue integrity (Londono et al., 2014), a process which only occurs when cells are able to communicate and signal. In general, the consideration of emergent proprieties is a necessity for medical research (Finzer, 2017), as the human disease and targeted therapies are so complex that their full effects cannot be studied except *in vivo*. Clinical trials require human subjects because there is no simple model that can reproduce the emergent properties relevant to patient outcomes.

Even animal testing can be justified by the necessity of studying the emergent properties of a living system. In Barr-Sinoussi & Montagutelli (2015), the authors argue for the use of animal test subjects in medical and biological research by describing the necessity of animal models as a consequence of our need to understand the entire system coherently:

> 'Humans and other mammals are very complex organisms in which organs achieve distinct physiological functions in a highly integrated and regulated fashion. Relationships involve a complex network of hormones, circulating factors and cells and cross-talk between cells in all the compartments.... Scientists are very far from being able to predict the functioning of a complex organism from the study of separate cells, tissues and organs. Therefore, despite arguments put forward by [animal rights activists], studies on animals cannot be fully replaced by *in vitro* methods, and it is still a long way before they can.'

Without animal models, the authors argue, we do not currently have the capabilities to study the interplay between different aspects of the physiology of a living organism (be it mice or humans). Animal models are often used to construct and study the emergent properties that would occur in the human system.

1.1.3 Modeling emergence mathematically

The mathematical definition of emergence used in Cucker & Smale (2007), for example, is when a number of individuals reach a consensus without external forcing. In this case, the emergent property is the variable which cannot be defined until the components are assembled into a whole. In Almond et al. (2013), authors attempt to model a binary square network, deriving the emergent properties of the system admittance and conductance from the circuit structure. They find that with a combination of spectral and averaging techniques, the behavior can be predicted and matched to experimental results.

The systems in which emergent properties can be modeled most effectively are the simplest systems with the lowest numbers of important variables. This is why Almond et al. (2013) can model emergent properties (such as system impedance) in circuits to good fidelity, and biologists can do pretty well at modelling predator-prey population dynamics (as long as all species are known), but the pathogen-human interaction is so much harder to model because of the large number of distinct cell types and natural bacterial colonizing bacterial in humans.

With a deep enough understanding of the physics behind a system, it would be possible to model these emergent properties or even work backwards to solve for unknown variables using Monte Carlo techniques and matching a model to observations. This is a point we will return to in Section 1.3; but first, we turn to the more general topic of how exoplanets have been discovered over the past 25 years.

1.2 Limitations of Exoplanet Discovery Methods

For a thesis about exoplanetary systems, some knowledge about the abundance and types of exoplanets that exist is needed. The first exoplanet ever discovered orbited pulsar PSR 1257+12 (Wolszczan & Frail, 1992). Though significant, it was difficult to draw too many conclusions about exoplanets from this initial discovery, which orbited a dead star. The

first exoplanet discovery around a main sequence star, that of the hot Jupiter 51 Peg b, announced in Mayor & Queloz (1995), was a paradigm shift. Previous to this point, Jupiters were expected to reside past the ice line in systems (excluding the remarkable prediction of Struve, 1952). A Jupiter orbiting ~ 0.05 AU from its host star upended previous assumptions of planet formation, and begged the question: 'What other types of planets are out there?' In 2000, a planet first discovered via radial velocities, HD 209458 b, was found to also be transiting Charbonneau et al. (2000a). Since those first significant discoveries, the number of known exoplanets and the number of methods used to find them have both increased, allowing the discovery of different classes of exoplanets. The thousands of planets which have been found via recent surveys and methods have enabled the more thorough description of exoplanet classes.

As of February 7, 2019, there were 3912 confirmed exoplanets, with a few thousand additional known candidates (as measured by the NASA Exoplanet Archive; Akeson et al., 2013a), which are plotted in Figure 1.1. We use in this section the set of 'confirmed' exoplanets as designated by IPAC, although the standards for being a confirmed planet differ by discovery method, as we will discuss. It is expected that some of the planets presented here as confirmed are actually false positives (caused by other astrophysical signals such as stellar rotation masquerading as planets, ex: Vanderburg et al., 2016a).

Transit and radial velocity discoveries always yield a measure of the radius or mass (in the form of $M \sin i$). In an effort to include all known planets on this plot, where accurate measured masses were not available, masses were extrapolated from the radii measurements using the following procedure: for planets with radii in the range $r_p = 1.5 - 4R_\oplus$, we use the Wolfgang relationship from Wolfgang et al. (2016), which gives a probabilistic mass-radius conversion function for planets from the Kepler sample (where the Kepler sample is all exoplanets discovered by the transiting planet hunting mission Kepler, Borucki et al. 2010). For planets smaller than $r_p = 1.5R_\oplus$, we use the relation from Weiss & Marcy (2014a). For planets larger than the upper limit, we use a characteristic gas giant density generated by a

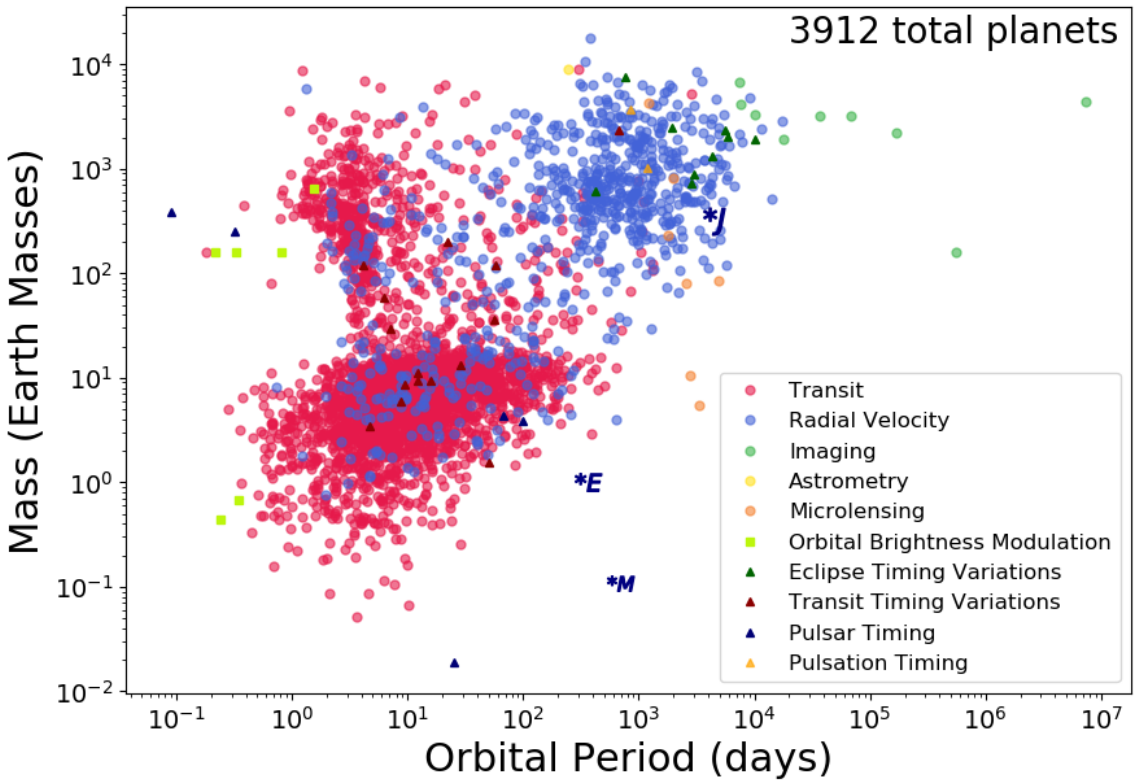

Figure 1.1 Orbital Periods and Masses of Discovered Exoplanets. A diagram of all planets discovered so far, and the methods by which they were discovered. For comparison to our own solar system, Mars, Earth, and Jupiter are denoted by their initials. This population of planets plotted here includes all those classified as validated planets by the NASA Exoplanet Archive (Akeson et al., 2013a) as of February 12, 2019.

Gaussian draw from the observed gas giant densities (as done in Vanderburg et al., 2016b). The relationships used are plotted in Figure 1.2.

Note that an updated version of the Wolfgang relation, a non-parametric approach which uses Bernstein polynomials, is available in (Ning et al., 2018), and will likely be published soon. If only $M \sin i$ values are available for a given planet, we assume that the inclination is edge-on and use that value of $M \sin i$ for plotting purposes. When neither an accurately measured mass nor radius was available, an estimate for the mass was chosen from the recent literature. The cases in which this was done span several methods of discovery. The direct imaging detections and sources of their mass estimates are Fomalhaut b (Kalas et al., 2008), HR 8799 e (Wang et al., 2018), LkCa 15 b and c (Sallum et al., 2015), β Pictoris b (Chilcote

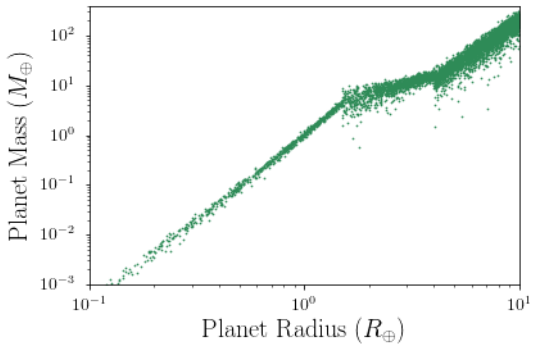

Figure 1.2 Estimated Mass-Radius Relation. The radius to mass conversion used when planetary masses have not been measured. For many of the transiting planets in the Kepler sample, the host stars are too faint for masses to be measured using radial velocity, requiring an extrapolation any time masses are needed (for example, for secular theory or numerical N-body simulations).

et al. 2017, with an updated estimate available in Snellen & Brown 2018), Kepler-37 e was detected via transit timing variations, and we use an estimate of its mass from Hadden & Lithwick (2014). One of the three systems discovered via orbital brightness modulation, KIC 10001893, was plotted with mass estimates drawn from Silvotti et al. (2014). The set of known planets is clearly subject to some biases, as evident from a cursory glance at the distribution of planets discovered thus far: the different discovery methods populate very different regions of the plot, for instance we see transit-discovered planets populating shorter orbital periods, radial velocity discoveries residing at longer periods and larger masses, and direct imaging detections taking up the longest orbital periods.

In the remainder of this section, we list the methods by which exoplanets have been discovered so far (all those represented on Figure 1.1), and the limitations of each method.

1.2.1 Methods Using Light Curves

When studying an astrophysical object, the amount of light received from an object is one of the most useful pieces of information that we can use to derive the properties of that object. When we measure the amount of light coming from the source at different points in time, we can construct a time-series that describes how the brightness of the source changes over a period of time. Many astrophysical sources have brightnesses that change drastically over short periods of time: for example, a supernova explosion results in a rapid brightening and then a subsequent decrease in brightness over a longer period of time (ex: Fox et al., 2015). More common, however, are sources that remain roughly the same level of brightness

over time, and most main sequence stars fit into this category. In either case, a time-series of the changing brightness of a source is called a light curve. For any particular astrophysical object, theoretical predictions can be compared to observed light curves to learn more about an object's specific properties.

Although stars are relatively constant in their brightness compared to more variable astrophysical sources, even main sequence stars do not reside at an exactly constant luminosity level. Over the pre-main-sequence lifetime of a star, its luminosity will slowly decline at rates too small to detect over our observational baselines (see the models of Baraffe et al., 2015, for luminosity evolution by spectral type of star). Once descended to the main sequence, stars will exhibit slightly increasing luminosities. Magnetic activity cycles (leading to the birth, evolution, and death of star spots) may also modulate the luminosity of the star (Basri et al., 2011; Roettenbacher & Kane, 2017) on shorter timescales. Brightness modulations also occur due to star spots periodically crossing across the limb of the star as the star rotates (ex: Roettenbacher et al., 2013), which occurs over much shorter and easily measurable timescales, with the exact rate depending on the stellar rotation rate (Slettebak et al., 1975; Fekel, 1997).

Variability in a stellar light curve can also be caused by objects passing in front of the star as measured from our line of sight. The 'dippers', a source type found in the Kepler data set characterized by large non periodic decreases in stellar flux, exhibit regions of decreased brightness when a circumstellar disk is present (Bodman et al., 2017; Rodriguez et al., 2017d).

By studying the light curves of main sequence stars, we can learn more about the qualities of the stars themselves, such as their variability timescales or the rotation rates, and more about the presence of additional objects near the star. In this section, we describe the ways that light curves can be used to discover planets.

1.2.1.1 Transits

The vast majority of planets known as of 2019 came from the over 100 million light curves produced by transit surveys, including among others Kepler, KELT, WASP, and HATNet. The transit method functions via favorable geometry: a planet passing in front of a star can be observed from Earth if its orbit takes it through our line of sight to the star. In this case, the light observed from the star decreases as the planet blocks some fraction of the light. The fractional flux blocked is

$$\delta F = (\pi r_p^2)/(\pi r_*^2), \tag{1.1}$$

where δF is the fractional decrease in light observed during a transit event, r_p is the planet's radius, and r_* is the star's radius. This ratio is commonly simplified as r_p^2/r_*^2. Typical depths of transit include 0.0084% for earth-like planets transiting sun-like stars, and 1% for Jupiter-sized planets transiting sun-like stars: clearly, it is much easier to detect exoplanets with larger radii.

The depth of transit does not depend on the distance that the planet orbits from its host star (also called the semi-major axis, a), for the reason that a is very small compared to the distance from Earth to the distant planet-hosting star. As such, transiting planets are essentially projected on the plane of the sky, which is why the Equation 1.1 is the ratio of the projected areas of the planet and star, rather than a more complex expression using the ratio of volumes of the spheres they represent.

The distance that a planet orbits from its host star does change its transit probability. The geometric likelihood ratio that a planet will transit increases the closer the planet is to its host star, for the reason that a larger fraction of randomly distributed inclinations result in orbital trajectories passing in front of the star's projected surface. When you consider an ensemble of planets with isotropically distributed orbital inclinations, the geometric

likelihood of transit P_{tr} can be written as (Kipping, 2014):

$$P_{tr} = \frac{R_* + r_p}{a} \frac{1 + e \sin \omega}{1 - e^2} \tag{1.2}$$

where again a is semimajor axis, e is eccentricity, and ω is the argument of periapsis of the planet. For circular planets and planets that are small compared to their host stars, this simplifies to the commonly used expression

$$P_{tr} = \frac{R_*}{a}. \tag{1.3}$$

This expression does not explicitly depend on the inclination, but inherent in its functional form is the effect of orbital inclination on likelihood of transit. The orbital inclinations that are small enough to allow a planet to be detected also decrease in amplitude the further away you get from the star. In Figure 1.3, we show the orbital inclinations of the orbits that are observable for three different masses of host star, and superimpose the (estimated) orbital inclinations for the set of planets discovered with transits for which these observations exist. We assume the longitude of ascending node is identical for all planets. This demonstrates that the parameter space in which planets can be discovered with the transit method is increasingly narrow at larger orbital period, explaining the functional form of Equation 1.3. To discover a planet via transits, it is generally accepted that three or more transits need to be observed for a planet to be a validated detection. What this means is a orbital baseline will ideally be a total of three times as long as the orbital period of the planet.

Another important aspect of transit surveys is the baseline of the observations. A longer baseline of observation allows more transits to be observed for a given planet, and similarly a shorter orbital period (smaller a) allows a larger number of transits to be observed for a given baseline. This is a very important effect given that most of planets discovered via transit come from the Kepler mission. The Kepler mission functioned from 2009 until 2013, and during this time it observed a 100 square degree section of sky continuously (Borucki

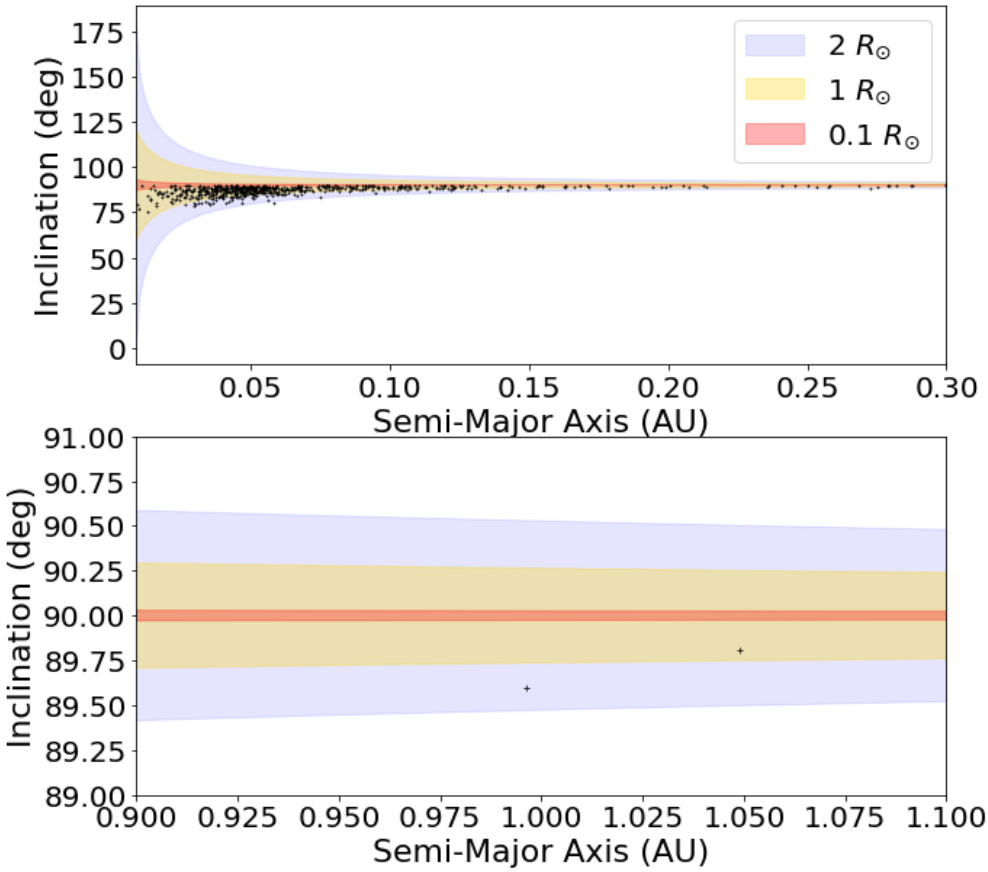

Figure 1.3 Range of Transiting Inclination by Orbital Radius. For semi-major axis in the range where planets tend to be discovered by Kepler, the range of inclinations that allow a transiting geometry for three different spectral types of stars. Here we plot with shaded regions the orbital inclinations that allow a planet to transit for three different types of host stars, assuming identical geometries otherwise. Top panel: the inner part of the system, where the largest number of planets were found with Kepler. Bottom panel: the area around 1 AU (where Earth is found), where the range of allowable inclinations is very narrow. In both panels, we show planet inclinations as crosses. Note that by definition, observed inclinations are reported as less than 90 degrees, but the true value may be either above or below the 90 degree plane.

Planet Type Studied	Occurrence Rate[1]	Ref.
2-4 $R_\oplus$ around GK-stars planets w/ P $<$ 50 days	0.13 $\pm$ 0.008	H12
4-8 $R_\oplus$ around GK-stars planets w/ P $<$ 50 days	0.023 $\pm$ 0.003	H12
8-32 $R_\oplus$ planets around GK-stars w/ P $<$ 50 days	0.013 $\pm$ 0.002	H12
1-2 $R_\oplus$ planets around GK-stars with 200 $<$ P $<$ 400 days	$5.7^{+1.7}_{-2.2}\%$	P13
FGK-stars with 0.8-1.25 $R_\oplus$ planets w/ P $<$ 85 days	16.5% $\pm$ 3.6%	F13
0.5-4 $R_\oplus$ around M-dwarf w/ P $<$ 50 days	$0.90^{+0.04}_{-0.04}$	DC13
0.5-4 $R_\oplus$ around M-dwarf w/ P $<$ 50 days	$0.51^{+0.06}_{-0.05}$	DC13
1-1.5 $R_\oplus$ around M-dwarf w/ P $<$ 50 days	$0.56^{+0.06}_{-0.05}$	DC15
1.5-2 $R_\oplus$ around M-dwarf w/ P $<$ 50 days	$0.46^{+0.07}_{-0.05}$	DC15
Compact multiple around mid M-dwarf w/ P $<$ 10 days	$21\%^{+7\%}_{-5\%}$	M15

Table 1.1 Various Estimates of the Occurrence Rate of Exoplanets. [1]: when occurrence rate is given in decimal form, it refers to the number of planes per star; when given as a percentage, authors computed the percentage of host stars that host at least one planet / system of the specified type. The full references are as follows: H12, Howard et al. (2012a); P13, Petigura et al. (2013a); F13, Fressin et al. (2013a); DC13, Dressing & Charbonneau (2013a); DC15, Dressing & Charbonneau (2015); M15, Muirhead et al. (2015).

et al., 2010). The results of the survey was a continuous and long observational baseline which allowed the discovery of planets with orbital periods up to about a year, including many multi-planet systems (Torres et al., 2011; Steffen & Farr, 2013; Rowe et al., 2014; Steffen & Hwang, 2015).

Altogether, transits are an incredibly powerful technique that allows the measurement of both the orbital radius and physical radius of the planet. Transits are more effective at discovering planets at shorter orbital periods, and they are more effective at finding bigger planets around smaller stars. Transits do not by default give any information about the mass of the planet - planet-planet interactions are required for masses to be derivable (see Section 1.2.1.4).

Despite these limitations, an extremely large number planets have been found by the Kepler mission using this method. Since the biases for this method are very well known, these discoveries have been used to great success to estimate the occurrence rate of planets in the galaxy (Petigura et al., 2013c; Dressing et al., 2015a). The results of these surveys are summarized in Table 1.1.

From these studies, the current expectation is that there is (to an order of magnitude) one planet per star in the regime we can currently measure. One important factor to note of these studies is that they give estimates only for planets with orbital periods sufficiently short that the Kepler sample allows the full occurrence rate to be derived; since there is evidence that the planet occurrence rate changes by semi-major axis (Mulders et al., 2015), these rates cannot be easily extrapolated. As such, the more exact qualities and quantities of planets that exist outside this range, as well as what type of stars are most likely to host what types of planets and what types of system architectures, are still largely open questions.

1.2.1.2 Microlensing

Microlensing can be applied to discover planets at extremely large distances from the earth. In order to observe a microlensing event, a particularly favorable geometry must occur: a foreground object must pass in front of a bright background source, and then the light from the bright source in the background is gravitationally focused around the foreground object. This results in an increase of the apparent brightness of the background source, followed by a return to normal flux. During a microlensing event, the background star's brightness can be increased by several orders of magnitude for as long as the foreground star remains in a position between the Earth and the bright background source. If the foreground star hosts a planet, then instead of a smooth increase and then decrease in flux for the background star, there may be a spike somewhere in the light curve. By analyzing the exact shape of the spike in the light curve, the planet to star mass ratio and projected separation can be recovered.

Microlensing is more sensitive to planets that have orbital periods near the Einstein ring, which tends to be 1-8 AU for typical geometries, a very different parameter space than is probed by transits. However, microlensing events are extremely difficult to predict. To do so accurately would require complete knowledge of the relative spatial velocities of our all stars near us, as well as the distant background sources. Because of our lack of knowledge of

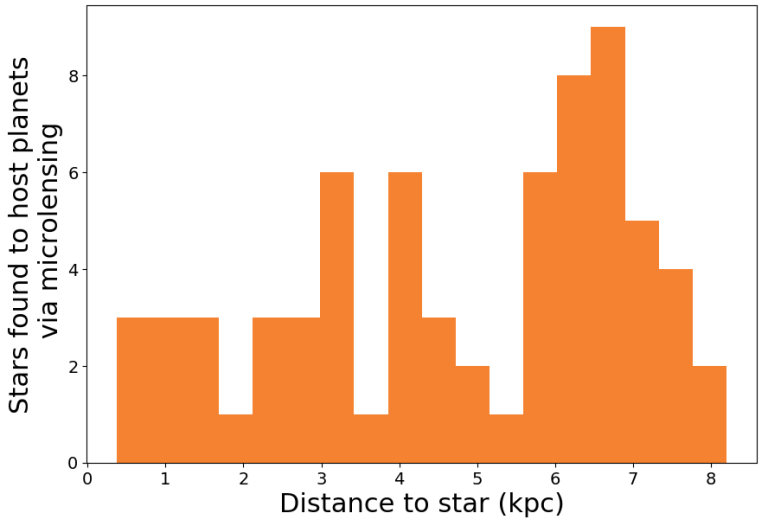

Figure 1.4 Distances to Planets Discovered with Gravitational Microlensing. A histogram of distance to host star for all stars found to be hosting planets using the gravitational microlensing method. Microlensing allows the discovery of planets around stars much more distant than is typically possible with other discovery methods. Data retrieved February 12, 2018.

these populations, targeted microlensing studies are not possible. Instead, the best way to find microlensing events is massive surveys of the entire sky. Because these events are low probability, once the initial, single microlensing observation has been made, it is generally not possible to re-observe the (potentially planet-hosting) foreground star.

Figure 1.4 shows a histogram of the distances from Earth for stars found to host planets via microlensing for stars whose distances have been measured. Gravitational microlensing can discover planets around stars at distances on scales of several kpc (Bennett et al., 2015), much further than is typically possible with other exoplanet discovery methods.

OGLE, the Optical Gravitational Lensing Experiment (Udalski et al., 1994), has found some planets using this technique (ex: Udalski et al., 2005), including some small planets at larger orbital radii (Beaulieu et al., 2006) and even multi-planet systems (Gaudi et al., 2008; Han et al., 2013). OGLE points a 1.3 meter telescope at a single field, waiting for gravitational microlensing events to occur. When one does occur, they utilize a large number of additional telescopes to follow the event and get an accurate light curve.

Microlensing is plagued by difficulties of false positives, and it is difficult to determine which planets are false positives because of the difficulty of following-up on planet candidates once the microlensing event has ended. There is also often degeneracy in the solutions for planet properties (Gaudi et al., 1998; Shin et al., 2019), particularly in multi-planet systems. However, microlensing does have the remarkable ability to constrain the occurrence rates of free-floating planets (Ma et al., 2016; Peña Ramírez et al., 2016; Henderson & Shvartzvald, 2016), which is not possible via the other methods listed here. WFIRST is a promising future mission which will attempt to discover more planets via this method, and it is expected to discover roughly 1400 bound exoplanets (Penny et al., 2018).

1.2.1.3 Orbital Brightness Modulation

Orbital brightness modulation, also called Doppler beaming (Loeb & Gaudi, 2003), measured the roughly sinusoidal variation of a star's brightness due to the periodic radial velocity of a star caused by a nearby planet's orbit. This is the same concept used to discover planets via radial velocity, but the stellar radial velocity is measured via brightness changed instead of directly through spectra. A star's motion through space will decrease or increase its flux F by an amount $\delta F = 4v_{\perp}/c$, when $v_{\perp}$ is the velocity of the source perpendicular to the observer and c is the speed of light. In theory, a visual inspection of a light curve would show a sinusoidal variation in stellar brightness on the orbital period of the planet. In reality, the signal is too small to be easily evident, so instead Fourier analyses and the like are commonly used, where the light curve is transformed into a power spectrum. The high-frequency end of this power spectrum is useful for asteroseimology, and the low-frequency end can in theory hold evidence of planet signals.

Three systems of planets of varying reliability have been detected using this method, and are plotted in Figure 1.1. These systems are Kepler-70 (also known as KIC 05807616), KIC 10001893, and Kepler-76 (KIC 4570949). Since there have been to date so few detections made via orbital brightness modulation (Doppler beaming), we will discuss them all.

A discovery using this method was announced in (Charpinet et al., 2011) around Kepler target KIC 05807616 (later named Kepler-70). However, the existence of the planets around Kepler-70 in particular has been hotly contested: Krzesinski (2015) used a larger set of Kepler data than was used in the original discovery paper, and found that the low-frequency signals used as evidence of planets were actually spurious. Although these planets are still included in the NASA Exoplanets Archive, they are likely not real.

Subsequently, KIC 10001893 is a pulsating B-type sub-dwarf observed by Kepler, and Silvotti et al. (2014) attempted to take advantage of the baseline afforded by continuous Kepler observations to study the asteroseismological properties of the star. This analysis showed signals in the low-frequency part of the spectrum, which the authors attribute to planets. The candidate planets around KIC 10001893 have not been confirmed by any further work, and Krzesinski (2015) suggests that the planets should be revisited in a manner similar to what they did for Kepler-70, as the KIC 10001893 'planet signals' might be plagued by similar issues to those of Kepler-70.

The final discovery via orbital brightness modulation, Kepler-76 b, announced in (Faigler et al., 2013), was a bit different than the planets around Kepler-70 and KIC 10001893: Kepler-76 b was first identified as an eclipsing binary, and Faigler et al. (2013) subsequently studied the brightness modulations and found evidence of a 2 M_{jup} planet, which they then confirmed with radial velocities. Kepler-76 b is thus the only secure discovery of a planet with orbital brightness modulation. The biases in orbital brightness modulation are extreme: since the signal drops off as the orbital period of the planet increases and the mass decreases, this method is extremely biased towards close and large exoplanets.

1.2.1.4 Transit Timing Variations

In a system with only one exoplanet, or where multiple planets are not gravitationally interacting with each other, their orbital periods should be constant over time. However, when systems become sufficiently tightly packed, the gravitational interactions between the

planets may cause periodic accelerations and deaccelerations whenever planet-planet interactions occur. Whenever this occurs, there will be some slight modulation of the observed orbital period for the planet. By observing the deviations from the expected time of transit for a single planet, additional planets that may be gravitationally perturbing the observed planet can be discovered. The method of using observed variations in the time of transit to infer the presence of additional planets in the system is called transit timing variations (TTVs).

It is important to note that for extremely short-period exoplanets, TTVs can also be caused by stellar activity or magnetic variations in the surface of the star. In this case, the period of the variation signal will be extremely short (the length of the periodic variation signal is commonly called the superperiod - stellar variability generally results in shorter superperiods than planet-induced TTVs do). The existence of TTVs can also make it difficult to determine the true orbital period of a planet from a short baseline of data. In the original Kepler mission this was not too much of a problem, because the three years of observational baseline generally allowed the recovery of multiple superperiods for tightly packed systems in which TTVs might occur. For missions with shorter baselines, such as K2 or TESS, this effect can be dangerous and occlude measurement of the 'true' orbital period.

TTVs can also be used to measure the masses of exoplanets. When two exoplanets that both transit are observed to have anti-correlated TTVs, the amplitude of those variations can be used to extract the planetary masses. The first system to be found to exhibit TTVs was Kepler-9 (Holman et al., 2010), which was also the first multi-transiting system. TTVs can also be used to deduce the presence of additional non-transiting companions, which was done for the first time in the Kepler-19 system (Ballard et al., 2011). The specific techniques and an application of this method will be discussed in Chapter IV.

1.2.1.5 Eclipse Timing Variations

Eclipse timing variations is a well known method of finding exoplanets, specifically circumbinary ones. Circumbinary exoplanets are those that orbit a binary star system. As opposed to a 'transit', a phrase generally used to describe a smaller planet crossing in front of a larger star, 'eclipse' generally refers to the larger body being in the front: eclipse timing, then, refers to the deviations in star-in-front-of-star events (eclipses) compared to the expected values. Every planetary system revolves around the system barycenter (see Section 1.2.2). In the case of a binary star system, the barycenter of the system will change significantly over time. In an isolated binary system, these changes will be periodic, leading to a light curve in which the flux depends primarily on exactly where in their orbits each component of the binary reside. If one star passes in front of the other along our line of sight, then we can also measure the eclipse times in the light curve.

Just like for transit timing variations, the presence of an additional component in the system (a third star, a planet, or many planets) can cause deviations from perfectly periodic eclipses. Although other set-ups, such as redistribution of angular momentum in a short period binary (Applegate, 1992), can cause the orbital period of the binary to change over time, potentially mimicking the effect of a planet. Since the eclipsing binaries tend to have very short orbital periods, this effect can be relevant, but the timescale tends to be long compared to the orbits of detectable planets (in MXB 1658-298 b, both effects are visible simultaneously: Jain et al., 2017).

The Kepler sample was ripe with thousands of eclipsing binaries (Slawson et al., 2011), but only a few (ex: Kepler-451, Baran et al., 2015) have been discovered to host exoplanets, with ETVs being a less favorable discovery method. The more famous circumbinary planets Kepler-16 b (Doyle et al., 2011), Kepler 34 b and Kepler 35 b Welsh et al. (2012), Kepler-47 b and c (Orosz et al., 2012a), and Kepler-413 b (Kostov et al., 2014) were not discovered via ETVs, but instead via transits. The rest of the thousands of eclipsing binaries in the Kepler data may also host planets, but their geometries were not sufficiently favorable to

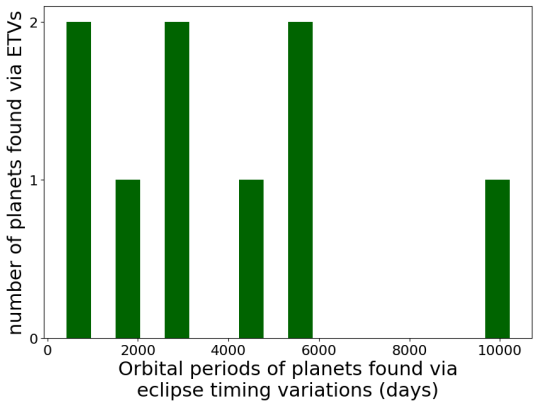

Figure 1.5 Orbital Periods of ETV Detections. The orbital periods for the nine planets detected via eclipse timing variations. The orbital period of the binary is much shorter in most cases, usually being less than a day. In comparison, these planets have longer orbital periods compared to exoplanets discovered using most other methods.

allow detection of a signal in the Kepler data. Gong & Ji (2017) suggests that the high incidence rate of *transiting* circumbinary planets indicates that such planets form at high rates in the plane of the binary's orbit.

1.2.1.6 Pulsation Timing

Stars which change radius slightly over time in an effort to maintain equilibrium will exhibit pulsations (Gautschy & Saio, 1996). Some stars, such as those on the instability strip of the HR diagram (Cepheids), will have large, regular, easily measurable pulses. Other stars, such as the sun, will pulse in non-regular manners: they can be studied asteroseismically with a high-precision light curve to understand the modes propagating through their interiors, but the pulses may not arrive regularly.

For stars that do pulse periodically, such as A-type variable stars, the presence of a planet can cause slight deviations from perfect periodicity in the pulse. The planet parameters can be derived from the semi-amplitude of the time-travel delays due to the planet's affect. Similar in form to the the radial velocity semi-amplitude K (Equation 1.9), the semi-amplitude of the time-travel delays can be written as (Sowicka et al., 2017; Hermes, 2018):

$$K_{pulsation} = \frac{a}{c}\frac{m_p}{M}\sin i \tag{1.4}$$

where the units of this amplitude are time, and a is the semi-major axis of the planet's orbit,

m_p the planetary mass, M the stellar mass, i the orbital inclination, the orbit is assumed to be circular, and c is the speed of light. Murphy et al. (2016) announced the discovery of a planet 12 times as massive as Jupiter via this method, and stellar companions (i.e., Handler et al., 2002) have also been detected in this way.

It is important to note that the discovery in Silvotti et al. (2014), while around a pulsating star, was found via a Fourier analysis of the light curve (orbital brightness modulation) and a direct extraction from that spectrum of additional low-frequency signals (taken to be planets), rather than deviations in pulse timing as used in Murphy et al. (2016), although Murphy et al. (2016) did use a Fourier spectrum to determine the dominant modes of oscillation. Both of these methods are promising for finding planets around pulsating (and even post-main-sequence) stars.

1.2.1.7 Pulsar Timing

The first-ever discovery of an exoplanet was announced in (Wolszczan & Frail, 1992) and was discovered via pulsar timing. The planet orbited the pulsar PSR 1257+12, and was extremely low mass and had a very short orbital period. Pulsars are rapidly rotating neutron-degenerate stars (Goldreich & Julian, 1969; Sturrock, 1971; Shapiro & Teukolsky, 1983) which appear to emit pulses according to their rotation rate as their magnetic poles periodically line up with Earth's line of sight (Cheng et al., 1986; Maeder & Meynet, 2000; Kramer et al., 2006). Pulsar timing is similar in its mechanism to TTVs, ETVs, and pulsation timing: normally, the pulses of a pulsar are regular in timing as the rotation rate of the pulsar is constant, the same way that transits and eclipses are expected to be perfectly periodic. However, if a planet is present, its gravitational influence can lead to the pulses' timing deviating slightly from perfect periodicity, and the exact manner in which this occurs can be used to predict the properties of the planet.

1.2.2 Methods Using Stellar Reflex Motion

Another fundamental way to find planets around stars is to study their physical motion through space over time. All stars in the galaxy are moving in some fashion; the Milky Way galaxy itself has complex density and velocity substructures, which contribute to the bulk motions of stars through the disk. On a smaller scale, when stars reach a close physical proximity to other stars or clusters, they may interact, leading to local scattering motions on shorter timescales (Laughlin & Adams, 2000; Boley et al., 2012; Li & Adams, 2015a). These factors contribute to each star having a preferential direction of motion through space at each point in time, although the direction and magnitude will change with time. Over short timescales, this can be measured as a linear trend in a star's position relative to the solar system.

Over even shorter timescales, the motions within a gravitationally bound system can lead to small variations of stars' velocities through space: although it is common to colloquially say that 'planets orbit stars', a more accurate description is that all objects in a gravitationally bound system orbit the barycenter (center of mass) of the system. Then, the overall velocity of a star is a sum of its bulk motion through the galaxy plus the instantaneous perturbations due to objects with which it is gravitationally bound, such as planets or other stars.

Perturbations in stellar velocity due to the influence of gravitationally bound companions will occur over relatively short timescales. In the solar system, the orbital dynamics of bound objects are dominated by the sun until they reach about 1,000 AU - 2,000 AU, at which the galactic tide starts to significantly affect their dynamics (Bannister et al., 2017), and eventually (closer to 10,000 AU) objects may become unbound from the solar system.

The amplitude of the reflex motion of a star due to a planet in a bound orbit can be written as follows:

$$V = (m_p/M)v_p \tag{1.5}$$

where v_p is the reflex velocity amplitude for the planet, V the solar reflex velocity amplitude, m_p the planetary mass, and M the stellar mass. This expression was derived assuming a one planet system, but the general concept remains the same even when applied to systems with larger multiplicities: all objects are in orbit around the center of mass of the system. Massive planets, or planets with particularly short orbital periods, can cause the physical location of the system barycenter to change over time, causing a larger stellar reflex velocity.

In any case, sufficiently large or close-in planets will cause the star to move in physical space with an amplitude and periodicity that depends on the masses and orbital periods of its planets. Depending on the orbital parameters of extra bodies in the system, this signal might be measurable. There are several methods of detecting exoplanets that take advantage of this fact.

1.2.2.1 Radial Velocities

In Section 1.2.1, we discussed the ways that a measure of the star's brightness over time (the light curve) can tell us about objects (including planets) orbiting the star. Another technique that can be used to study stars is spectroscopy. In spectroscopy, the amount of light coming from a star at different wavelengths is measured, and different wavelengths of light correspond to different energies of photon via the expression:

$$E = hc/\lambda_{emit} \tag{1.6}$$

where h is the Planck constant, c the speed of light, and λ_{emit} the wavelength of the emitted (or absorbed, as the case may be) photon. For example, an x-ray photon is extremely high energy and low wavelength. If we were to look at how bright in the x-ray a human being was, they would not appear very bright, because humans do not emit significant amounts of x-ray radiation. However, if we were to study an active galactic nuclei (AGN), which is an extremely high-energy astrophysical source, it would have a high level of of x-ray emission.

In contrast, a human would be dim in the x-ray, but bright if studied in infrared wavelengths. Different objects, both astrophysical and human-like, have emission profiles that depend on the properties of the object (commonly characterized as the effective temperature of the object). In conjunction, because atoms are quantized, electrons can transition between only particular energy states according to the expression:

$$\lambda_{emit} = \frac{1}{RZ^2}\left(n_1^{-2} - n_2^{-2}\right)^{-1} \tag{1.7}$$

where λ_{emit} remains the true wavelength of the photon, R is the Rydberg constant, Z is the atomic number of the atom under consideration, and n_1 and n_2 denote the two energy levels between which the atom is transitioning. The exact value of λ is the exact wavelength at which the photon will be emitted.

In stars, what one expects to see when looking in different wavelengths is well-studied and a strict function of the size of the star. A stellar spectrum might include both emission and absorption lines, which both result from the transitions of electrons between energy levels in atoms as described above, or from the transitions between (vibrational, rotational) energy levels in molecules. For absorption, features occur at particular wavelengths defined by Equation 1.7, which correspond to where atoms and molecules can absorb energy. Stars have a large number of absorption lines in their spectra because atoms in the stellar photosphere absorb part of the continuum of light coming from the hotter center of the star. Depending on the atoms present in the star's photosphere, the absorption lines that can be seen will vary. For example, a star with lots of calcium in its photosphere will have spectral features at the wavelengths corresponding to the solutions to Equation 1.7 for calcium, which will be a distinct and finite set of observable lines. For a star the mass of the Sun, the absorption lines present will be the same as those present in a spectrum of the Sun: hydrogen, oxygen, carbon, iron, etc. For stars much more massive than the sun, metallic absorption lines will not be present, as the photosphere will be too hot for metals to generally remain unionized,

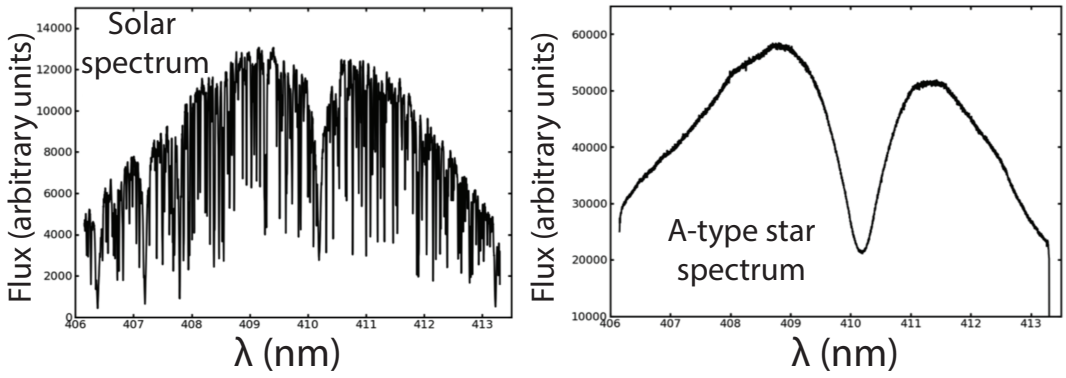

Figure 1.6 Comparison of Spectra for the Sun and HR 6827. Stars of different masses exhibit very different spectra at the same wavelengths, and the species present in the stellar photosphere vary widely by stellar mass. Here, an illustrative comparison centered on the 410.1 nm Balmer line. Spectra taken from Becker et al. (2015a). Left panel: one HIRES echelle order of the Solar spectrum measured by observing reflected sunlight from the asteroid Vesta. This spectrum is representative of those of low-mass stars observed by the CPS program. Right panel: the same HIRES order, this time showing an observation of an A-type star, HR 6827. This rapidly rotating star has hundreds of times fewer spectral features than are seen in the Solar spectrum.

and instead hydrogen absorption features will be most prominent (Struve, 1931). In Figure 1.6, we plot the difference in spectra observed for two stars: the sun, and rapidly rotating A-type star HR 6827. In each of these two spectra, the 410.1 nm Balmer line is present and obvious. In the sun, there are additionally a large number of additional absorption features.

The final piece of the radial velocity puzzle is the effect of stellar motion on observations of these spectral lines. When observing real stars, the spectral features may occur at different wavelengths than expected, which is due to the motion of the star in the direction along our line of sight. If the star moves along our line of sight, its absorption features will be subject to a spectroscopic Doppler shift, the sign dependent upon the direction of motion. The speed of the star is related to the wavelength of the light emitted and observed as follows:

$$\frac{\lambda_{obs} - \lambda_{emit}}{\lambda_{emit}} = (v_{\perp}/c) \tag{1.8}$$

when λ_{emit} is the 'true' wavelength of a spectral line, at which it was emitted, λ_{obs} is wave-

length of the same feature as observed, $v_\perp$ the radial velocity of the source, and finally c again is the speed of light.

The next step of discovering planets via radial velocities is to convert the measured amplitude of the stellar velocity's curve into planet properties. First published in Paddock (1913), the equation for the semi-amplitude of a radial velocity curve as it depends on the parameters of the star and planet is:

$$K = \left(\frac{2\pi G}{P}\right)^{1/3} \frac{m_p}{(M+m_p)^{2/3}} \frac{\sin i}{\sqrt{1-e^2}} \tag{1.9}$$

where G is the gravitational constant, P the orbital period, m_p the planetary mass, M the stellar mass, i is the inclination of the planet's orbit (oriented such that 90 degrees denotes an edge-on orbit relative to the plane of the sky), and e the planetary eccentricity. With this expression, the amplitude of a radial velocity signal can be converted to an $m_p \sin i$ and an orbital period of the planet causing the signal.

No matter the spectral type of the star, the Doppler technique can be combined with our knowledge of what that star's spectrum should look like (that is, at what wavelengths the spectral lines should reside) to get this additional information about the star's velocity in physical space. This method has been extremely efficient at discovering (and confirming) planets, with to-date 727 confirmed planets being discovered in this way.

1.2.3 Methods Using Images

1.2.3.1 Astrometry

Astrometry is a planet discovery method very similar to the radial velocity method, except that instead of measuring a star's motion along our line of sight from Earth, we measure the star's motion perpendicular to our line of sight. Instead of using spectra to derive a star's instantaneous radial velocity, astrometry uses images taken over a long time baseline and measures the star's motion on the plane of the sky.

Astrometry is similar in spirit to the way Kuiper Belt Objects are discovered: if multiple images taken at different points in time show evidence that an object's relative position (after correcting for any systematic effects due to the changing position of the observer) is moving, then its orbit can be reconstructed. For Kuiper Belt Objects, this means one can directly detect the orbit of the object. For stars, this means one can model what extra components in the system must be present in order to reproduce the observed periodic signal.

To date, the only 'planet' discovery via astrometry is DENIS-P J082303.1-491201 b, which may be either an exoplanet or a brown dwarf (Sahlmann et al., 2013). The Gaia mission will acquire astrometry over an extended baseline on a large number of stars, perhaps enabling a new set of astrometric analyses on a large number of stars.

1.2.3.2 Direct Imaging

In direct imaging, planets are detected by blocking out the light from their host star and directly measuring either the reflected starlight or thermal emission from the planet itself. To discover planets via this method requires high-contrast imaging capabilities.

Fomalhaut b, discovered via direct imaging in 2008 using HST data (Kalas et al., 2008) and subsequently studied in depth by other groups, is a good example of the unique type of planet that can be discovered via direct imaging: its estimated orbital radius of 115 AU makes it one of the most distant planets discovered. In Figure 1.1, a cursory glance shows that direct imaging exclusively discovers planets at the largest orbital periods. However, for Fomalhaut b, the nature of its discovery method makes its planetary mass uncertain. In Figure 1.1, we use the current estimate of 0.5 M_{jup}, but competing theories give vastly different planetary mass estimates: the discovery paper, Kalas et al. (2008), placed an upper limit on its mass of 3 M_{jup}, and other works give vastly different values, including recent results that doubt Fomalhaut b is a planet at all (Janson et al., 2012) and others which in contrast confirm its planetary nature (Currie et al., 2012).

The HR 87999 system is a perfect example of the potential power of direct imaging. The

first three known planets orbiting this young star were announced in Marois et al. (2008). A fourth planet was discovered in (Marois et al., 2010). Modern analysis, such as Wang et al. (2018), utilize the power of a decades-long observational baseline to map the orbits of these long-period planets. From a coherent analysis of all the data, accurate mass measurements can be extracted for all planets, giving rare insight to the outer region of a planetary system.

With only visual clues provided by single epoch direct imaging to discriminate between competing hypotheses, it is difficult to determine the correct answer. If images are taken repeatedly over a long baseline, then information about the orbits of objects can be used to derive masses (as done for HR 8799 in Wang et al., 2018) and information about the variability of signals can be used to confirm the planetary nature of companions.

Going forwards, the increased capabilities of direct imaging (as well as increased baselines allowing the study of planetary motion) will allow better studies of the outer regimes of planetary systems. As this happens, direct imaging will grow to have more in common with the methods utilizing stellar motion, as the motion of planets can be detected in successive high-contrast images of a system (as has been done for HR 8799). Proposed direct imaging missions such as the Habitable Exoplanet Imaging Mission (HabEx) and the Large Ultra-Violet Optical Infra Red (LUVOIR) Surveyor will allow the study of new parameter spaces in exoplanetary systems (Kopparapu et al., 2018), and allow us to fill in some of the occurrence rate estimates missed by transit missions such as Kepler.

1.3 Emergence as Applied in Exoplanet Systems

One large problem facing modern exoplanetary astrophysics is how planets form (Morbidelli & Raymond, 2016; Armitage, 2018). Despite the remarkable advances that have been made in exoplanet detection over the past 25 years, we still do not understand the processes by which planets and planetary systems form and assemble themselves, including even our own solar system (Pfalzner et al., 2015).

One complicating factor is our incomplete knowledge of the systems that form our basis

for understanding planet formation outside the solar system: when the observed systems are used as constraints on the potential mechanisms of planet formation, the observational biases, which manifest strongly in the distributions of exoplanet properties, must be accounted for.

One solution has been to attempt to reconstruct occurrence rates of planets of particular types by modeling the specific biases inherent in each population. As described in the previous section, the objects that we can discover in any exoplanet system are limited by the observational biases of each method. For example, planets discovered via the transit method will tend to have shorter orbital periods and will be by necessity confined to a few degrees of the central plane, meaning that large longer-period planets will mostly remain undiscovered due to their low transit probabilities. In contrast, planets discovered via the radial velocity method will tend to be larger in mass, resulting in discoveries of the tightly packed systems of super-Earths that appear so common from the Kepler data to be very unlikely. To attempt to estimate the planetary occurrence rate of any type of planet is a difficult task: the bias and detection efficiency of a survey must be characterized exactly, which requires a large survey of uniformly collected data. Such a sample is difficult to collect, but one exists in the Kepler data. Kepler observed the same 100 square degree patch of sky for roughly four years from 2009 to 2013 (Howell et al., 2014a; Christiansen et al., 2013), resulting in a continuous, long-baseline study of more than 500,000 stars, a population large enough from which to derive statistics. Using the well-defined detection efficiency (Christiansen et al., 2015) and detection probabilities for the Kepler sample, many groups calculated occurrence rates of various types of planets in short orbital periods, which is the population that Kepler was the most sensitive to detect (Fressin et al., 2013a; Petigura et al., 2013a; Howard et al., 2012a; Dressing & Charbonneau, 2013a; Burke et al., 2015; Dressing & Charbonneau, 2015). The results of these studies are summarized in Table 1.1. The end result was a rough estimate of the occurrence rates of planets in the galaxy, which taught us that the order of magnitude estimate is on the order of at least one planet per star.

However, as useful as these bulk estimates are, in order to start placing further constraints

on planet formation more detail is required, both on individual systems and bulk population abundances. The transit data from Kepler only describes the inner-most region of each system: the region of our solar system where no planets reside. Even combining Kepler transit data with follow-up radial velocity data yields an incomplete measure of what resides where in parameter space: the radial velocity signal falls off as orbital period increases, so extremely long-period planets (particularly Earth-size or Neptune-size ones) would need to be found via another method entirely (direct imaging, for example).

This poses a difficulty when what we really want to study is the emergent properties of these exoplanetary systems. To understand planet formation, and understand how any particular system is assembled, we need to know about all the components of the system. For example, if all Kepler tightly packed compact systems are accompanied by massive outer companions, this has very different implications for their formation mechanisms than if they are always lonely (Batygin et al., 2016a).

If all hot Jupiters are lonely and lack nearby planetary companions, then either those companions do not form (indicating strong constraints on the initial conditions in the disk), or they are destabilized during the migration of the giant planet. In contrast, if these companions do exist, their occurrence rates can help us constrain what fraction of hot Jupiters form via destabilizing mechanisms versus dynamically quiet ones.

The reason that it matters if we have incomplete pictures of these populations is that in exoplanetary systems, the factors that we care about for determining the long-term dynamics of a system are emergent properties which depend on the objects in the system.

The properties we measure from data are the current orbits of the objects. However, these change over time. To provide insights about how systems formed and migrated, it is often necessary to integrate/extrapolate backwards to the system's history. For example, a system could have formed *in situ* (where we observe it to be now), formed in a disk then migrated inwards due to disk torques, or formed in a disk and been subject to scattering interactions after the disk dissipates. The dissipation of the disk generally occurs fairly early

in the star's life: estimates vary from widely accepted estimates of 3-6 Myr (Hernández et al., 2007) to more controversial estimates of 10 Myr or longer (Pfalzner et al., 2014).

Modeling of exoplanet systems is commonly done by necessity with the assumption that the objects observed are the only objects present in the system (ex: Fressin et al., 2012; Becker et al., 2015b; Gillon et al., 2016). However, this assumption is not always true, as subsequent observations often find planets that were missed at first (ex: Marois et al., 2010; Buchhave et al., 2016; Gillon et al., 2017).

When we only know about part of the system and attempt to derive inferences about planet formation as a whole from the system's existence, we are likely to make mistakes and draw incorrect conclusions because we are using incomplete data. There are two solutions to this problem: first, we could discover all planets in the system by using complementary discovery methods, and put off any theoretical analysis until those system pictures are complete. Second, when constructing our theoretical models from the existing data, we can account for the incompleteness in our observations by using dynamical techniques and statistical methods to supplement the data that we do have.

In the next section, the test case of K2-266 will demonstrate how the important emergent properties of exoplanetary systems can change depending on our knowledge of the system and subsequently be used to constrain the system properties beyond what is possible with the initial observational data.

1.3.1 Emergence: the Test Case of K2-266

K2-266 is a system which hosts at least four and possibly six planets (Rodriguez et al., 2018c). The observed orbital configuration of these planets is fairly tightly packed, leading to significant planet-planet interactions. The unique orbital geometry of this system, shown in Figure 1.7, is that of an inner planet highly misaligned (by 14 degrees) relative to the outer five planets.

The Kepler data set is full of tightly packed systems of planets (Lissauer et al., 2012a),

but these generally have inclination distributions with widths of 1.4 degrees (Fabrycky et al., 2014a) or so. In comparison, the inclination of K2-266 b seems unusual, which is suggestive towards how these systems form: it might seem that systems like K2266 are fundamentally different from the typical Kepler system of tightly packed inner planets (called STIPs), and thus is evidence of different formation pathways for these systems. However, K2-266 bs transit was grazing, and the only reason the planet was found at all was its extremely short orbital period allowed its discovery. As such, it is possible that more Kepler STIPs - maybe even *all* of them! - host such planets which were not discovered due to unfavorable geometry. This question - is K2-266 totally typical, or totally atypical? - encapsulates the difficulties of making insights towards planet formation using limited, observationally biased data. Since we do not know what the fundamental populations and abundances of exoplanets are, we cannot fully correct for these observational biases, meaning that drawing correct conclusions about planet formation is difficult.

This is similar to modeling predator-prey dynamics in nature: a differential model may describe well the dynamics of a population, until the discovery of a previously unseen species suggests that the previously measured interaction coefficients must be wrong. For example: say a first model found that the lions are eating ten zebra per year each, and it suggested that the system was in equilibrium; however, once crocodiles are discovered to live in the population as well (and also will be eating zebras), where exactly the prey is coming from to feed them all becomes unclear. Kepler STIPs can be produced via disk migration (Boley & Ford, 2013) or in situ (Hansen & Murray, 2012), but if we find that the apparently dynamically quiet systems are more active than thought, and they actually commonly have misaligned inner planets as well (rather than K2-266 being just a weird outlier), we have to return to the drawing board and look for the mechanism that can produce these planets while also constructing the observed STIPs (and also look for that hidden trove of zebras). As such, constructing complete pictures of the components that are, can be, and are not in an exoplanetary system is imperative for future efforts to use these systems to make insights

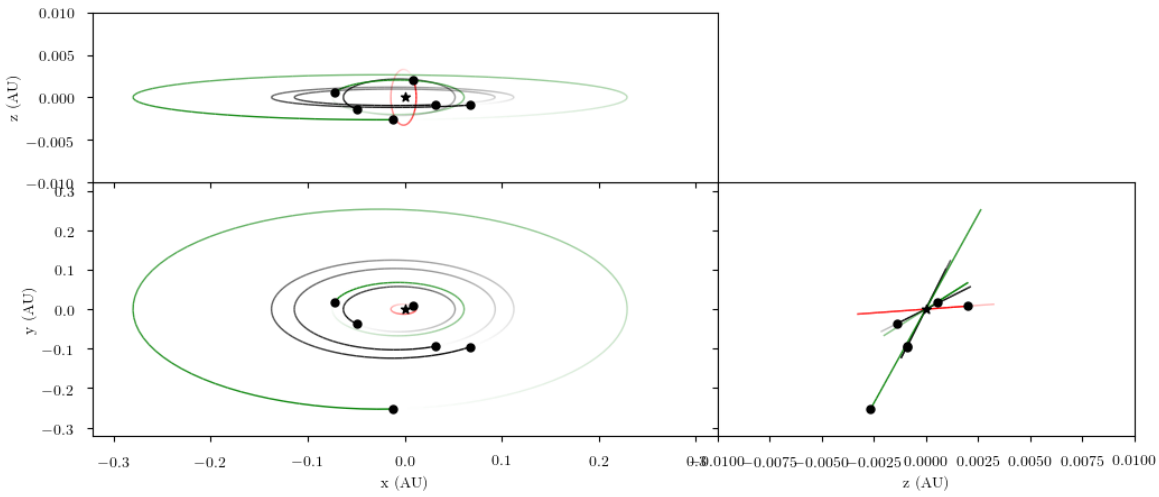

Figure 1.7 System Geometry of K2-266 Six-Planet System. System geometry (Rodriguez et al., 2018c) projected along various axes. The black and red lines denote validated planets, while the green lines denote candidates. The red line denotes the innermost planet, ultra-short-period planet K2-266 b, whose orbit is inclined by roughly 14 degrees relative to the other planets in the system. Plot created using Rebound N-body integration package's plotting tools (Rein & Tamayo, 2015a).

towards planet formation.

In Figure 1.8, we plot the difference in evolution computed using secular Laplace-Lagrange theory (an orbit-averaging analytic technique described in detail in Chapter II, which derives the equations of motion for individual planets as they depend on a matrix of the secular eigenmodes of the system) when off-diagonal matrix terms (those that mediate the interactions between the planets) are included versus ignored. To construct these secular evolution curves, we draw a posterior from the EXOFAST fit results from Rodriguez et al. (2018c), excepting the inclination of K2-266 b (the ultra-short period planet), whose inclination we drew from a Rayleigh distribution with a width of 1.4 degrees. A summary of the approximate orbital periods and masses of the planets in this system are given in Table 1.2 for reference; the complete table is available in Rodriguez et al. (2018c). We assume that the observed six planets are the 'true' six planets in the system, and that there are no undiscovered planets in the system (this is likely a faulty assumption, but beyond the scope of this introduction to address).

Planet:	**b**	**K2-266.02**	**c**	**d**	**e**	**K2-266.06**
Period (days)	0.658524	6.1002	7.8140	14.69700	19.4820	56.682
Radius ($r_\odot$)	3.3	0.646	0.705	2.93	2.73	0.90
Mass ($m_\odot$)	11.3	0.209	0.29	9.4	8.3	0.70
Inclination i (deg)	75.32	87.84	88.28	89.46	89.45	89.40
Eccentricity e	–	0.051	0.042	0.047	0.043	0.31

Table 1.2 A Summary of the Relevant Orbital Elements for Planets in the K2-266 System. The approximate median values of the orbital parameters for the planets in the K2-266 system. In secular evolutions, starting inclinations were drawn from above or below the midplane of the star with equal chance. Errors on measured values can be found in Rodriguez et al. (2018c).

In the left panel, we set off-diagonal terms to zero, evolving the dynamics of each planet only under the effect of its own and the star's gravity. Unsurprisingly, the system evolves forward in time at constant inclinations, as no perturbative forces change the orbits of the planets over time. In the right panel, we plot system evolution under the effect of the full interaction matrix, where planet-planet interactions are modeled. Then, the planetary inclinations oscillate with time due to those planet-planet forces.

The secular inclination evolution of the planets is only evident when the planets are considered together: this is an example of an emergent property of the system, as it only becomes evident once all bodies in the system are considered together (rather than considered individually and then the independent models added together). We note that for the system evolutions plotted in Figure 1.8, we use only secular theory, which treats each planetary orbit as a smeared ring of mass (rather than as particles). The full N-body dynamics will be even more complex, but even the secular example makes evident the importance of considering the interactions between planets in order to measure the emergent property of their long-term dynamical evolution.

So, it is clear that the full modeling of system dynamics is imperative to studying the evolution of a planetary system, as emergent properties can only be observed once the system is considered in totality. However, the additional difficultly in modeling emergent properties

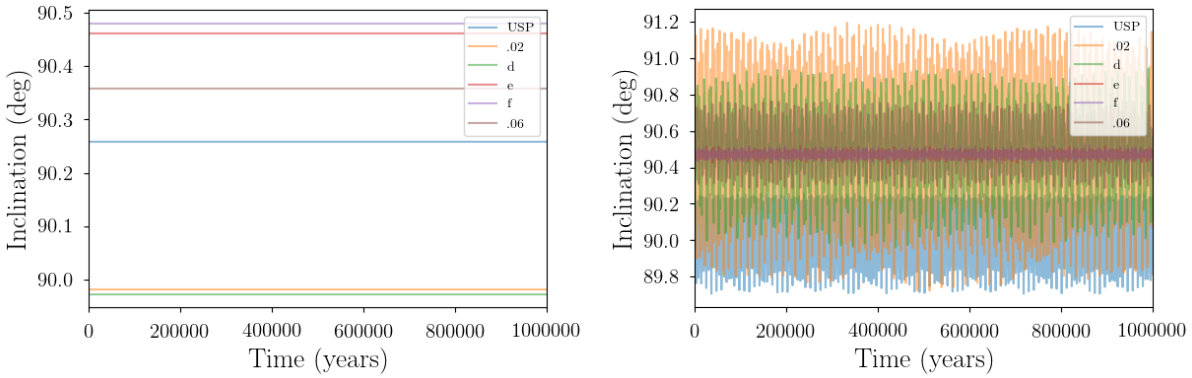

Figure 1.8 The Effect of the Off-Diagonal Interaction Terms in the Secular Eigenmatrix. Comparison of the evolution of the six candidate planets in K2-266 from their initial state after the disk dissipates, plotting both when planet-planet interactions are (right panel) and are not (left panel) considered. 'USP' denotes the ultra short period planet K2-266 b, while the other more typical planets are labeled with the designations from the discovery paper Rodriguez et al. (2018c).

occurs due to the issues discussed in Section 1.2: due to observational bias and the limited capabilities of the methods by which we discover exoplanets, many planetary systems studied will be incomplete. What we think is a single-planet system may actually host three planets at varying inclinations; what we see as a six planet system may actually be a nine planet system; what we see as a hot Jupiter with a vastly exterior companion may actually have several smaller undetectable planets in between the two. As such, it is important to know how our understanding of a system changes if we only know about some of the planets that reside in the system.

In Figure 1.9, we demonstrate the effect that incomplete observations can have on the derived emergent properties of the system. We plot two secular integrations of the system, using the same methods and parameters as before but with different starting assumptions. In the left panel, we plot the system if all planets were known, highlighting the evolution of K2-266 d in red. In the right panel, we pretend that we had only discovered the inner three planets, but again plot the evolution of K2-266 d in red. Note that the scales on the two plots are the same, but the amplitude and period of K2-266 d's evolution are very different.

When only the inner three planets are 'known', the more massive ultra-short period

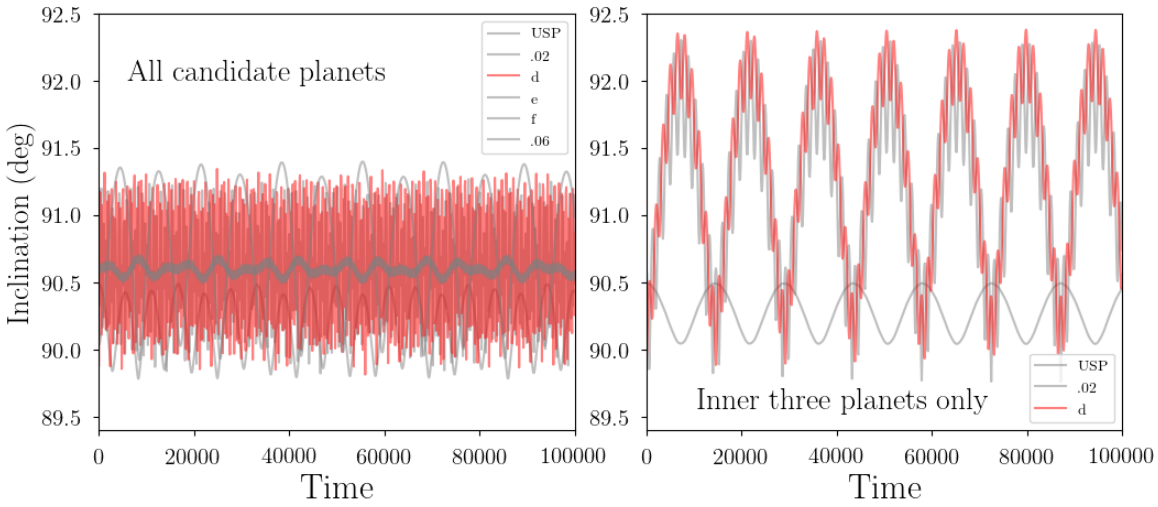

Figure 1.9 Effect of Including Inter-Planet Interactions on Secular Evolution. Two panels showing the computed secular evolution of the K2-266 system if all (left panel) or just the inner three (right panel) known planets are present. In red is K2-266 d, which has an orbital period of roughly 7 days (in comparison to its inner neighbor's 6-day period, and its outer neighbor's 14-day period).

planet (whose inclination here has again been decreased, and is not the true observed value) tugs around planets .02 and d, leading to a higher amplitude of their inclination evolution over time. When the outer three planets are also included in the model, the outer disk of five planets becomes coupled and shares the evolution in angular momentum direction between all five members instead of only between two.

Just between these two cases, it is clear that with only three planets known, the dynamics of the system would appear very different than they do with all six planets known. As a complicating factor, two of the planets in this system (.02 and .06) are only candidates rather than validated planets.

It is clear from the K2-266 test case that which and how many planets are included in the model can change drastically our understanding of the system. This is very dangerous, and what I refer to in this thesis as the 'reductionist trap' - when we accidentally model a system incompletely because we only know about some of the planets due to observational bias, we inadvertently ignore the important emergent properties of the system.

1.4 Solving Astrophysical Mysteries with Observations and Dynamics

The goal of this thesis is to use emergent properities to better understand exoplanetary systems. Unlike medicine, in which the 'system' - the human body - is so complex that it really cannot be modeled except through empirical methods, exoplanets have a huge advantage in that the important aspects of the system can be turned into a mathematical model fairly easily. Using numerical simulations (ex: Chambers, 1999a), the force equation can be integrated to give exact solutions for evolution of planets over time (recent suites of numerical simulations have been used to study planetary dynamics in, for example, Becker & Batygin, 2013; Khain et al., 2018a; Puranam & Batygin, 2018). Similarly, approximate solutions can be constructed using dynamical methods such as secular theory (Murray & Dermott, 1999), which allows an easier but slightly less accurate solution to the orbital evolution of planets over time (recent applications in the literature of secular theory include Michtchenko & Malhotra, 2004; Van Laerhoven & Greenberg, 2012; Saillenfest et al., 2017a; Li et al., 2018).

The main impact of how easy it is to construct a model for exoplanet interactions is that emergent properties can be used in two ways: first, to forward model the system, and derive an expected emergent property from the fundamental parameters of its constituent pieces; second, to take an observed emergent property and reverse engineer the required planet properties that allow the measured emergent property to exist in the system. In both cases, the (known) relationship between the independent properties of the constituent parts of the system and the resultant emergent properties is leveraged to provide a better understanding of the system as a whole and constrain unknown properties for future analysis.

1.4.0.1 Forward modeling

The term 'forward modeling' refers to taking known parameters and using them to produce a model of subsequent evolution. An example of this would be taking the observed planets and orbital elements of a multi-planet system, then unfold the dynamics forward using dynamical simulations to evaluate the changes of the planets' orbits over time. Once a complete enough picture of the system is assembled - one that measured the locations and physical parameters of all bodies significantly affecting the evolution of the system - these evolution predictions can be used to model future behavior of the system, or it can be used to extract the past dynamical evolution of the system. This is useful towards making conclusions about how a system may have formed, because you can construct a range of possible histories for the system. For example, with a well-studied system, its past evolution could be constrained to be dynamically quiet to the extent that it must have formed via disk migration instead of another more dynamically active pathway. The caveat here is that for forward modeling to work, the current state of the system must be well-known, or at least a careful accounting of the possible parameters must exist for any components that are not known. With an incomplete picture of a multi-planet system, the computed evolution may be incorrect, if any significant modes of oscillations are unknown or measured incorrectly.

An example of this is the Kepler multi-planet systems, which will be discussed in depth in Chapter II of this thesis. If the systems exist as they are currently observed and there are no outer perturbers or additional unseen planets present, then a numerically computed model of the current system will yield an accurate measure of its past evolution. For the Kepler compact multi-planet systems, this may suggest either a lack of migration (*in situ* formation) or a slow adiabatic migration through the disk. However, if additional external companions exist in these systems, then the models constructed using currently measured parameters may not be correct, depending on if the possible perturbers are decoupled from the inner system. We show an example of what this might look like in Chapter III.

In order for numerical and secular models to be used correctly for determining how

systems form, we must have very complete pictures of what is present in each system. These pictures can be constructed by combining observations from multiple sources (for example, transit data to understand the inner system plus radial velocity data to understand the exterior system; see Chapter IV). However, when combining observations, we must also be aware of what regimes in the system are not being studied, because planets that contribute significantly to the dynamics of the system may hide in these undetectable regimes.

The emergent properties of a system, which depend on planet-planet interactions and cannot be modeled correctly if not all components are known, do not emerge in their entirety until a complete observational picture of the system has been constructed. This limitation occludes the use of observationally incomplete systems for making insights towards planet formation.

In Chapter II of this thesis, we use forward modeling to derive emergent properties (transit duration variations, or how the time a planet takes to cross the face of the star changes over time, and system stability) of systems from the measured properties of their planets.

1.4.0.2 Reverse modeling

From measured emergent properties, the fundamental and independent properties of planetary systems can be determined by working backwards. Just as the constituent properties of planets that make up a system can be used to compute the evolution of the system over time, the reverse can also be done: starting with some observable evolving property, such as the transit timing variations of an observable planet, it is possible to construct a model for what else must be present in the system to cause that signal.

Such reverse modeling of emerging properties requires a very deep understanding of how constituent factors of the system interact to create these emergent properties. In planetary astronomy, unlike in molecular biology, we do have complete models that describe the evolution of factors we care about. Unlike the human body, which is extremely complex,

interactions between planets in exoplanet systems are actually very simple. The evolving orbits of stars and planets are mediated mainly by Newton's laws, and can be described by $F = m(d^2r/dt^2)$. The most basic and reproducible way to model properties of exoplanet systems is numerical simulations, which utilize Newton's simple equations to incrementally evolve a systems forward in time by repeatedly computing forces between particles, moving them according to their computed velocities, and repeating the process. These simulations - called N-body simulations for the fact they can model any number N of bodies - can model to good fidelity the evolution of a planetary system (as long as all relevant particles are included in the simulation). The true limitation with N-body simulations is computing power: although it may be easy to model an eight planet system orbiting a single star, it is much more difficult and computationally unfeasible to include the asteroid belt, comprised of more than hundreds of thousands of asteroids, as individual particles in that same simulation. For that reason, time saving techniques such as smooth particle hydrodynamics simulations to study gas, dust, or planetesimal disks and analytical techniques such as secular Laplace-Lagrange theory are commonly used to construct these models instead.

These techniques, among others, can be used to derive the inferred properties of planetary systems from a measured emergent property. One important thing to keep in mind is that the technique used (be it N-body simulations or a simple secular model) must accurately account for all important parameters influencing the evolution of the system. For example, when studying an old planetary system where the gas disk has disbursed, it may be reasonable to neglect planeteismals and other smaller bodies in the system and use N-body simulations. When studying a young system, however, this may not be a reasonable assumption and full hydrodynamic simulations might need to be used.

The primary use of reverse modeling of emergent properties in this thesis is to derive the properties of systems, including both the planetary properties and the system-wide limits on orbital architecture. In Chapter III, we describe how the existence of a compact multi-planet system (and its implicitly derived emergent property of dynamical stability) can be

used to make inferences about the presence of planets in the exterior regions of the system. In Chapter IV, we describe how a measured emergent property (in this case, a TTV time series) can be used to derive the planetary parameters that would not be derivable from the transit shape alone. In Chapter VI, we describe how the interplay between independent and emergent properties can be used to better understand the components of a system, using the HIP 41378 as a test case.

1.4.1 In This Thesis

Nobel Prize-winning physicist Robert Laughlin wrote in his book *A Different Universe: Reinventing Physics from the Bottom Down*:

> 'I think a good case can be made that science has now moved from an Age of Reductionism to an Age of Emergence, a time when the search for ultimate causes of things shifts from the behavior of parts to the behavior of the collective.'
> - Robert Laughlin

Though the reductionist approach is more traditionally associated with string theorists and particle physicists, it is easy in the study of exoplanets to accidentally fall into a reductionist trap: every time we assume all parameters of a system are known, we inadvertently condense a complex system to a much more simple but incomplete subset of its true dynamics.

The severe observational bias brought by our exoplanet discovery methods prevents the construction of a full census of the types of planets existing in the galaxy. However, this bias is not the problem, as to some extent occurrence rates can be corrected: the true problem is the difficulty of measuring the correlations in planet occurrence, which in turn makes it difficult to draw conclusions about the full architectures of systems that exist and their relative abundances.

This thesis attempts to make explicit the study of emergent properties in exoplanetary systems and emphasize the importance of such system-level analyses moving forward. We utilize information gained from reductionist methods (which study individual properties in

isolation to the rest of the system) to populate a systems-based model and study the emergent properties of the system, which in turn enable a deeper understanding of its components and dynamics. This process bolsters the information derivable from observational studies, enabling a better understanding of the census of exoplanets in the galaxy.

In Chapter II, we begin with a dynamical exploration of the effectiveness of dynamical mechanisms in exciting orbital inclination within the multi-planet exoplanetary systems discovered by Kepler. We also provide constraints and predictions for the expected transit duration variations (TDVs) for each planet under consideration. In Chapter III, we consider perturbations due to possible additional outer planets in a subset of the Kepler multi-planet systems considered in the previous chapter. We use the fact that the discovered compact systems sometimes contain multiple transiting planets with aligned orbital angular momentum vectors which are tightly aligned with each other to place constraints on possible additional (non-transiting) planets in these systems. In Chapter IV, we use data from the K2 mission to show that WASP-47, a previously known hot Jupiter host, also hosts two additional transiting planets: a Neptune-sized outer planet and a super-Earth inner companion. We study the masses of these planets using transit timing variations and radial velocity observations. When combined with new stellar parameters and reanalyzed transit photometry, our mass measurements both place strong constraints on the compositions of the two small planets and allow a precise dynamical analysis, which we use to constrain the orbital inclination of WASP-47 c, the outer Jovian planet, and make insights towards the likely formation history of this particular system. In Chapter V, we consider the dynamics of hot Jupiter-hosting systems orbiting cool stars, and find that the orbits of most moderately wide planetary companions must be well aligned with the orbits of the hot Jupiters and the spins of the host stars. In Chapter VI, we present the discovery of a five planet system transiting a bright (V = 8.9, K = 7.7) star called HIP 41378. We show that these estimates for the orbital periods can be made more precise by taking into account dynamical stability considerations, and then consider the system in the updated context of new data not available at the time

we first announced the discovery of the five planets. In the additional data, the ambiguous-period, long-period planets HIP 41378 d and HIP 41378 f both transit again, yielding a set of discrete possible orbital periods for these two planets. We identify the most probable orbital periods for these two planets using our knowledge of the planets' transit durations, the host star's properties, the system's dynamics, and data from the ground-based HATNet, KELT, and WASP transit surveys. In Chapter VII, we describe our discovery of a compact multi-planet system orbiting the K-type star K2-266. We identify up to six possible planets orbiting K2-266 and validated four of these planets. The system has mutual misalignment between the innermost planet and the rest of the system. We additionally provide a dynamical mechanism that can explain the observed rare system geometry in the K2-266 system. Then, we turn briefly away from planets around other stars and examine the properties of objects in the furthest reaches of our own solar system. In Chapter VIII, we demonstrate the effect of proposed solar system member Planet Nine on the known extreme Trans-Neptunian Objects (TNOs), and study how the observed properties of these Kuiper Belt Objects may be reproduced in the presence of Planet Nine. In Chapter IX, we present the discovery of a new Kuiper Belt Object, 2015 BP_{519}, which is to date the most extreme (defined by the reduced Kozai action) TNO in our solar system, and has the highest orbital inclination out of all long-orbital-period TNOs. Finally, in Chapter X we end with a summary of the results of this work and its significance in the study of exoplanets moving forwards.

CHAPTER II

Oscillations of Relative Inclination Angles in Compact Extrasolar Planetary Systems

Results in this chapter were published in: ***Becker, J. C.**, & Adams, F. C. 2016. Oscillations of Relative Inclination Angles in Compact Extrasolar Planetary Systems. Monthly Notices of the Royal Astronomical Society, 455, 2980* and are presented here with minor revisions.

2.1 Abstract

The Kepler Mission has detected dozens of compact planetary systems with more than four transiting planets. This sample provides a collection of close-packed planetary systems with relatively little spread in the inclination angles of the inferred orbits. A large fraction of the observational sample contains limited multiplicity, begging the question whether there is a true diversity of multi-transiting systems, or if some systems merely possess high mutual inclinations, allowing them to appear as single-transiting systems in a transit-based survey. This chapter begins an exploration of the effectiveness of dynamical mechanisms in exciting orbital inclination within exoplanetary systems of this class. For these tightly packed systems, we determine that the orbital inclination angles are not spread out appreciably through self-excitation. In contrast, the two Kepler multi-planet systems with additional non-transiting planets are susceptible to oscillations of their inclination angles, which means their currently observed configurations could be due to planet-planet interactions alone. We also provide constraints and predictions for the expected transit duration variations (TDVs) for each planet. In these multi-planet compact Kepler systems, oscillations of their incli-

nation angles are remarkably hard to excite; as a result, they tend to remain continually mutually transiting (CMT-stable). We study this issue further by augmenting the planet masses and determining the enhancement factor required for oscillations to move the systems out of transit. The oscillations of inclination found here inform the recently suggested dichotomy in the sample of solar systems observed by Kepler.

2.2 Introduction

The Kepler mission has discovered a large number of compact extrasolar systems containing multiple planets that can be observed in transit (Lissauer et al., 2012a; Batalha et al., 2010). Roughly forty of these such systems have four or more planets. The inventory of these four-plus planet systems includes mostly super-Earth sized planets, which have radii $R_P = 2 - 5R_\oplus$ and orbital periods in the range 1 – 100 d. Moreover, the orbital periods of the planets within a given system are regularly spaced (roughly logarithmically uniform in period or semimajor axis). Because all of the planets were observable by Kepler at their times of discovery, these systems have an additional stringent dynamical constraint: they must have retained a relatively narrow spread in their orbital inclination angles. On the other hand, orbital inclination can often be excited in close-packed planetary systems. The goal of this chapter is thus to explore the oscillations of orbital inclination within solar systems of this class. Excitation of inclination can be driven by a variety of mechanims, incluing unseen additional companions, perturbations from stellar encounters in clusters (Adams & Laughlin, 2001; Li & Adams, 2015b), and self-excitation through interactions among the observed planets. This chapter focuses on this latter mechanism.

Slight deviations from true coplanarity in these systems (e.g., as observationally supported in Rowe et al. 2014; Lissauer et al. 2011a; and others) allow for the possibility of oscillations in the inclination angles of the planetary orbits, e.g., due to secular interactions between the planets (see also Van Laerhoven & Greenberg, 2012). If such oscillations were common, and had sufficient amplitude, then not all members of a solar system could be seen in transit at every epoch. As a result, multi-planet systems would display evidence for "missing" planets, i.e., exceptions to the (roughly) logarithmically even spacing of orbits that are often observed. The ubiquity of this

class of exoplanetary systems places strong constraints on both their architectures and dynamical histories. We note that the inclination angle oscillations for Jupiter and Saturn in our own solar system are large enough to periodically move the orbits out of a mutually transiting configuration.

Statistical analyses of the Kepler system architectures suggest that there could exist two distinct populations of planetary systems (Ballard & Johnson, 2016a; Morton & Winn, 2014a), namely, a population with single-transiting planets and an additional population of multi-planet systems. The existence of these two distinct populations could be explained by either two true distributions of solar systems (e.g., created by two different formation histories) or a single distribution in which some systems exhibit a high degree of scatter in orbital inclination angles. Excitation of inclination in nearly coplanar systems could shift some planets out of a transiting configuration, thereby leading to the population of single-transit systems. In this case, the single-transit systems would be a subset of the multi-transiting group rather than a distinct population.

This chapter explores possible oscillations of the inclination angles in compact extrasolar systems. The measured planetary radii $R_P = 2-5R_\oplus$ imply planetary masses $M_P = 4-30M_\oplus$, where we use a conversion law based primarily on the probabilistic mass-radius relationship derived in Wolfgang et al. (2016):

$$\frac{M}{M_\oplus} \sim \text{Normal}\left(\mu = 2.7\left(\frac{\text{R}}{\text{R}_\oplus}\right)^{1.3}, \sigma = 1.9\right) \tag{2.1}$$

where M refers to the mass of a body, R its radius, and this expression represents a $r^{1.3}$ scaling law with a normal distribution of scatter due to potential planetary composition variation. The Wolfgang relationship describes the a distribution of the potential masses for planets in the range $R_P = 1.5 - 4R_\oplus$. Since a small number of planets in our sample lie outside these bounds, we supplement the Wolfgang relation in two ways: for planets with radii $R_P < 1.5R_\oplus$, we supplement with the rocky relation from Weiss & Marcy (2014b); for planets with radii $R_P > 4R_\oplus$, we determine starting density using the Wolfgang relation, then add a scatter and choose a radius anomaly to account for varying core masses and inflation due to thermal effects (Laughlin et al., 2011). Of the 208 planets in our sample, only 9 fall above the regime described by the Wolfgang relation.

With relatively large masses and close proximity, planet-planet interactions can be significant.

On the other hand, these planetary systems orbit relatively old stars (with ages of $\sim 1-6$ Gyr, weighted toward the lower end of this range; see Walkowicz & Basri 2013), so that they are expected to be dynamically stable over ∼Gyr time scales. These systems are also generally non-resonant. These considerations — significant interactions coupled with long-term stability and non-resonance — suggest that the planetary systems are subject to secular interactions (Murray & Dermott, 1999). In the present context, we are interested in secular oscillations of the inclination angles of the orbits. If such oscillations have sufficient amplitudes, the resulting spread of inclinations angles in the system will sometimes be large enough that not all of the planets can be seen in transit. When observed in such a configuration, the system will appear to have gaps in the regular spacing of planetary orbits that these systems usually exhibit. The goal of this chapter is to understand the amplitude of self-excitation of inclination angle oscillations and provide limits on transit duration variations, an observable with amplitude directly related to inclination evolution over time, for observed Kepler systems with no unseen companions. This analysis will allow future observations of transit durations for these systems to inform the presence of massive outer companions in these systems.

We note that spreads in the inclination angles can be produced by a variety of astronomical processes. This work will focus on secular oscillations of the inclination angles by the compact solar system planets themselves (with semi-major axes $a > 0.5$ AU). Future work will focus on the effect of possible additional bodies in the outer part of the solar system (where $a \approx 5-30$ AU), roughly analogous to the giant planets in our outer Solar System.

We stress that oscillations of inclination angles are not rare. Within our Solar System, for example, the orbital inclinations of Jupiter and Saturn oscillate with a period of about 51,000 years and an amplitude of about 1° (see Figure 7.1 in Murray & Dermott 1999). The inclination angles of the two orbits coincide every half period (25,500 years), so that an observer oriented in that plane would see both planets in transit at that epoch. However, the amplitude of the oscillation is sufficient to move both planets out of transit for an appreciable fraction of the secular cycle.

This chapter focuses on the case of self-excitation of inclination angles for Kepler systems with four or more planets, where the secular dynamics of such systems are considered in Section 3. An analysis of the observed compact, mutually transiting systems is presented in Section 2.4.1, which

shows that the systems are consistently mutually transiting over time. An orbital architecture that is continually mutually transiting is denoted here as CMT-stable (which should not be confused with dynamical stability). We consider a generalized class of systems in Section 3.2, and study compact systems which have been discovered to host an additional non-transiting planet in Section 3.3 (where these systems are shown to be more active). We also compare these results with numerical simulations in Section 2.4.4. Section 2.5 presents observables for the compact Kepler systems discovered to date; specifically, the transit durations are predicted to vary and the magnitude of these variations are determined. In Section 2.6, we study the stability of the observed Kepler systems by considering how the predicted oscillation amplitudes would vary if planet masses are scaled upward: the systems are found to be remarkably dynamically stable. The chapter concludes, in Section 2.7, with a summary of our results and a discussion of their implications, as well as a statement on our plans for future work.

2.3 Secular Theory for Inclination Angles

To evaluate the behavior of mutual inclination for these isolated systems, we apply Laplace–Langrange secular theory (Murray & Dermott, 1999). This formalism allows the use of the long-period terms of the disturbing function to describe orbital motion over many secular periods.

2.3.1 Review of the Theory

We expand to second order in inclination and eccentricity, and first order in mass. With this expansion, inclination and eccentricity are decoupled, so we can write the disturbing function as a function of inclination alone:

$$\mathcal{R}_j^{(\mathrm{sec})} = n_j a_j^2 \left[\frac{1}{2} B_{jj} I_j^2 + \sum_{k=1}^{N} \left(B_{jk} I_j I_k \cos\left(\Omega_j - \Omega_k\right) \right) \right], \tag{2.2}$$

where j is the planet number, n is the mean anomaly, I is the inclination, ω is argument of pericenter, and Ω is the longitude of the ascending node. The coefficients B_{ij} are defined by

$$B_{jj} = -n_j \left[\frac{1}{4} \sum \frac{m_k}{M_c + m_j} \alpha_{jk} \bar{\alpha}_{jk} b^{(1)}_{3/2}(\alpha_{jk}) \right], \tag{2.3}$$

and

$$B_{jk} = n_j \left[\frac{1}{4} \frac{m_k}{M_c + m_j} \alpha_{jk} \bar{\alpha}_{jk} b^{(1)}_{3/2}(\alpha_{jk}) \right], \tag{2.4}$$

where R_c is the stellar radius, m_k indicates the mass of the kth planet, M_c denotes the mass of the central star, α_{jk} denotes the semi-major axis ratio a_j/a_k, and $\bar{\alpha}_{jk}$ denotes the semi-major axis ratio $a_j/a_k < 1$. The quantities $b^{(1)}_{3/2}$ is the Laplace coefficient, which is defined by

$$b^{(1)}_{3/2} = \frac{1}{\pi} \int_0^{2\pi} \frac{\cos\psi \; d\psi}{(1 - 2\alpha\cos\psi + \alpha^2)^{3/2}}, \tag{2.5}$$

(as given in Murray & Dermott 1999). All of the coefficients B_{jk} can be considered as frequencies that describe the interaction between each pair of planets, and are elements of the matrix denoted as **B**. This application of secular theory allows us to evaluate the problem analytically, but neglects higher-order terms. In this formulation, the only terms in the disturbing function are those that do not depend on the mean longitudes, as we assume that the short-period terms average out over long timescales. The coefficient matrix **B** describes inclination evolution. Solving for the matrix elements of **B** allow us to determine the time evolution of inclination.

The matrix **B** defines an eigenvalue problem (Murray & Dermott, 1999), where the eigenvalues describe the interaction frequencies between any pair of planets. The eigenfrequencies of this matrix, denoted here as f_i, along with the eigenvectors $\mathcal{I}_{jk}$, can be used to describe the time evolution of the system. Given the matrix **B**, we can solve for the eigenvalues and eigenvectors using standard methods. With these quantities specified, we also need the initial conditions to specify the full solution for the time evolution of the inclination angles I_j and the angles Ω_j. It is convenient to transform the dependent variables according to

$$p_j = I_j \sin\Omega_j \qquad \text{and} \qquad q_j = I_j \sin\Omega_j, \tag{2.6}$$

so that the solutions take the form

$$p_j(t) = \sum_{k=1}^{N} I_{jk} \sin(f_k t + \gamma_k) \tag{2.7}$$

and

$$q_j(t) = \sum_{k=1}^{N} I_{jk} \cos(f_k t + \gamma_k) \,, \tag{2.8}$$

where the phases γ_k, along with the overall amplitudes, are determined by the initial conditions. The quantities I_{jk} are eigenvectors, where we use the standard (but awkward) notation such that the first index j specifies the planet number and hence the components of the eigenvector and the second index k runs over the different eigenvectors. It is also useful to define normalized eigenvectors $\mathcal{I}_{jk}$ and corresponding scaling factors T_k such that

$$I_{jk} = T_k \mathcal{I}_{jk} \,. \tag{2.9}$$

The initial conditions then specify the scaling factors through the expressions

$$p_j(t=0) = \sum_{k=1}^{N} T_k \mathcal{I}_{jk} \sin\gamma_k \tag{2.10}$$

and

$$q_j(t=0) = \sum_{k=1}^{N} T_k \mathcal{I}_{jk} \cos\gamma_k \,. \tag{2.11}$$

The scaled eigenvectors I_{jk} (which conform to the system's boundary conditions), the eigenvalues f_k, and the phases γ_k are sufficient to specify the time evolution of the orbital inclination of each body in the system, i.e.,

$$I_j(t) = \sqrt{[p_j(t)]^2 + [q_j(t)]^2} \,, \tag{2.12}$$

where the solutions $p_j(t)$ and $q_j(t)$ are given by equations (5.6) and (5.7). Implicit in this solution is the linear dependance on the interaction coefficients (the matrix elements given by equations [5.3]). From this solution, we note that the inclination evolution has a linear dependance on mass ratio and a second order dependence on the semi-major axis ratio between the planet in question and each planet exterior to its orbit.

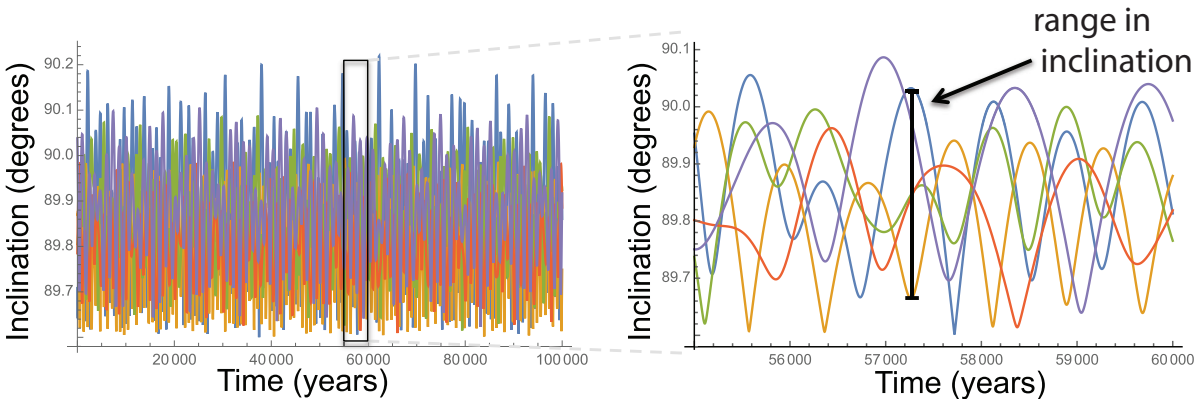

Figure 2.1 Illustrative Evolution of Kepler-256's Orbital Inclination. Plotted here are the inclination evolutions of five roughly coplanar planets, with initial conditions drawn from the priors of Kepler-256. Although the inclinations of the planets generally stay within a plane, there is also instantaneous variation, which manifests as a range in the inclinations of plane of planets. This variation may lead planets to be knocked out of a transiting configuration. The mutual inclination, shown on the right panel, changes as planets precess, meaning that the width of the plane containing all the planets oscillates over time.

2.4 Inclination Oscillations due to Self-Excitation

The compact Kepler systems with four or more planets are tightly packed systems with minimal mutual inclinations. From this population, it appears that planets in multi-transiting systems generally have non-null values of mutual impact parameter, and subsequently inclination (Rowe et al., 2014). Systems with non-null mutual inclinations exhibit non-parallel angular momentum vectors, allowing the possibility of excitation in inclination and other orbital elements. To test the magnitude of these excitations, we take the population of all Kepler systems with four or more transiting planets as examples of compact, multi-body, transiting systems. We obtain our data from the NASA Exoplanet Archive[1], updating system parameters when newer values have been found (such as in the case of Kepler-296; Barclay et al., 2015a).

There are observational biases inherent in the Kepler systems, as a photometric transit survey is by definition more likely to find systems with low mutual inclinations and aligned argument of pericenters (Ragozzine & Holman, 2010). The Kepler multi-planet systems are likely more aligned and more compact in inclination plane width than an 'average' system, but the sample found by Kepler is representative of the type of system we would expect to see from photometric transit

[1]http://exoplanetarchive.ipac.caltech.edu

surveys such as Kepler (Borucki et al., 2010), K2 (Howell et al., 2014a), and TESS (Ricker et al., 2015). It is not currently clear, however, whether the Kepler multi-planet systems that we do see in transit are CMT-stable or if we are catching them at a lucky moment in which all planets appear to be in transit. This differentiation is important because the former possibility describes a much less dynamically active system than the latter. To test the stability against exciting planets out of the transiting plane, we used the secular theory described in Section 2.3 to numerically evolve each system in the Kepler multi-planet sample for several secular periods. This procedure results in a measure of the spread in impact parameter $\Delta b(t)$ (see below). We also compute the probability that the system is mutually transiting, marginalized over all trials and realizations in our simulations. If $\Delta b(t) < 2$ for an entire secular period and the probability of all planets transiting simultaneously for a random time-step in a random realization of the system is high ($P(\text{transit}) > 0.85$) then the system is said to be CMT-stable in a transiting configuration. Note that the condition of being CMT-stable against oscillating planets out of transit is much more confining that being dynamically stable against planet ejection. For a given Kepler system, we can use a Monte Carlo analysis to evaluate $\Delta b(t)$ not just once, but many times, with starting orbital elements for each realization selected from observationally motivated priors. For parameters that have been measured (for transiting systems, the radius of the planet r_p and the semi-major axis a_p, and sometimes the inclination I_p or eccentricity e_p), we draw each planet's orbital element from a normal distribution with mean and standard deviation determined from observations. For orbital elements not measured, we draw a value from priors summarized in Table 2.1.

Observationally measured inclinations have been fit from photometric light curves, and for these planets there is a degeneracy between angles over 90 degrees and under 90 degrees. The literature reports inclination angles as < 90 degrees, so when we use a literature measurement, we choose a value not only from that planet's measured posterior but also choose its orbit to fall above or below the midplane of the star with equal probability. For planets without measured inclinations, we choose a plane width from a Rayleigh distribution with width 1.5 degrees (Fabrycky et al., 2014b), subject to the constraint that all planets must be transiting. This choice of distribution follows work done by Fabrycky & Winn (2009); Lissauer et al. (2012a); Fang & Margot (2012); Ballard & Johnson (2016a). In these recent works, Rayleigh distributions with varying widths are used to

Orbital Element Distributions

Parameter	Prior
ω	uniform on $(0°, 360°)$
Ω	uniform on $(0°, 360°)$
e	uniform on $(0, 0.1)$
I	Rayleigh distribution with width $\sigma = 1.5$ degrees

Table 2.1 Priors on Unconstrained Orbital Elements. When orbital elements have not been measured observationally, we draw their values randomly from the prior distributions summarized in this table.

describe the size of the plane containing the planets. The value we use here, 1.5 degrees, is within the range suggested by the work of Fabrycky et al. (2014b).

We note that the argument of the ascending node is not necessarily independent of the value of inclination angle as assumed here. As planetary systems evolve to attain nonzero inclination angles, modeled here by a Rayleigh distribution, the nodes will evolve into some other distribution, which should be characterized in future work.

Once we have the initial conditions for each Kepler system, we can evolve orbits as according to the secular theory described in Section 2.3. This must be done individually for each realization of initial conditions for each system.

2.4.1 Evaluating the Secular Behavior of the Compact, Multi-Planet Kepler Systems

A tightly packed, roughly coplanar system of planets will trade angular momentum as the system evolves (while keeping the total angular momentum vector of the system constant). The magnitude of this exchange determines the magnitude of the variations in orbital elements of each body. Equation 5.11 describes the inclination evolution for each body in a system. Once the inclination solutions for each planet in a system have been found using equation 5.11, a comparison between them (see Figure 2.1, which illustrates how the mutual inclination can change over time) yields a measure of the mutual inclination between all planets in the system. This mutual inclination describes the width of the plane containing all the planets.

As the condition for transiting is more rigorous than approximate coplanarity (even as planets'

inclinations vary in concert, the planets with larger orbital separations are more likely to cease transiting), we remove the dependence on orbital and stellar properties by working in terms of impact parameter, b, which is defined as:

$$b_j = \frac{a_j}{R_*} \cos(I_j) \tag{2.13}$$

where j is planet number, a is the semi major axis, R_* the radius of the central star, and I the inclination. When $-1 < b_j < 1$, planet j will transit. Using the analytic expression for inclination evolution (Equation 5.11), we can describe the long-term behavior of not only individual planets but the range of their respective impact parameters. The process of extracting the mutual impact parameter Δb is shown in Figure 2.2.

Using this technique, we explored the evolution of orbits for the entire initial condition parameter space for each Kepler multi-planet system. For a given system, we conducted 4000 Monte Carlo trials for each Kepler system, resulting in 4000 realizations of $\Delta b(t)$, with different initial conditions drawn from the observational priors, supplemented with the values in Table 2.1. This sample can be used to calculate the mean range of the impact parameter over time for the Kepler system, as well as the width of the plane of planets in impact-parameter space.

We repeated this process of 4000 Monte Carlo trials for each for the 43 systems in our sample of multi-planet Kepler systems, resulting in a measure of the inclination evolution behavior for each system. Figure 2.3 visualizes the results of these trials, where each point represents the mean mutual impact parameter for a different Kepler system. Mean mutual impact parameter is the typical width of the plane containing all planets in the system, and must be smaller than the diameter of the star for all planets to transit. An impact parameter plane width of $\Delta b = 2$, marked on the plot, is the upper limit for all planets in the plane to be transiting.

For each point in Figure 2.3, the height of the point as compared to the transit limit ($\delta b = 2$) corresponds to the width of the plane containing all the planets. The scatter (represented by error bars) corresponds to the width of the distribution due to the variations between realizations. For all systems, the projected plane containing the planets is much smaller than the diameter of the star, which means we would expect to see all the planets in transit at for the majority of the secular

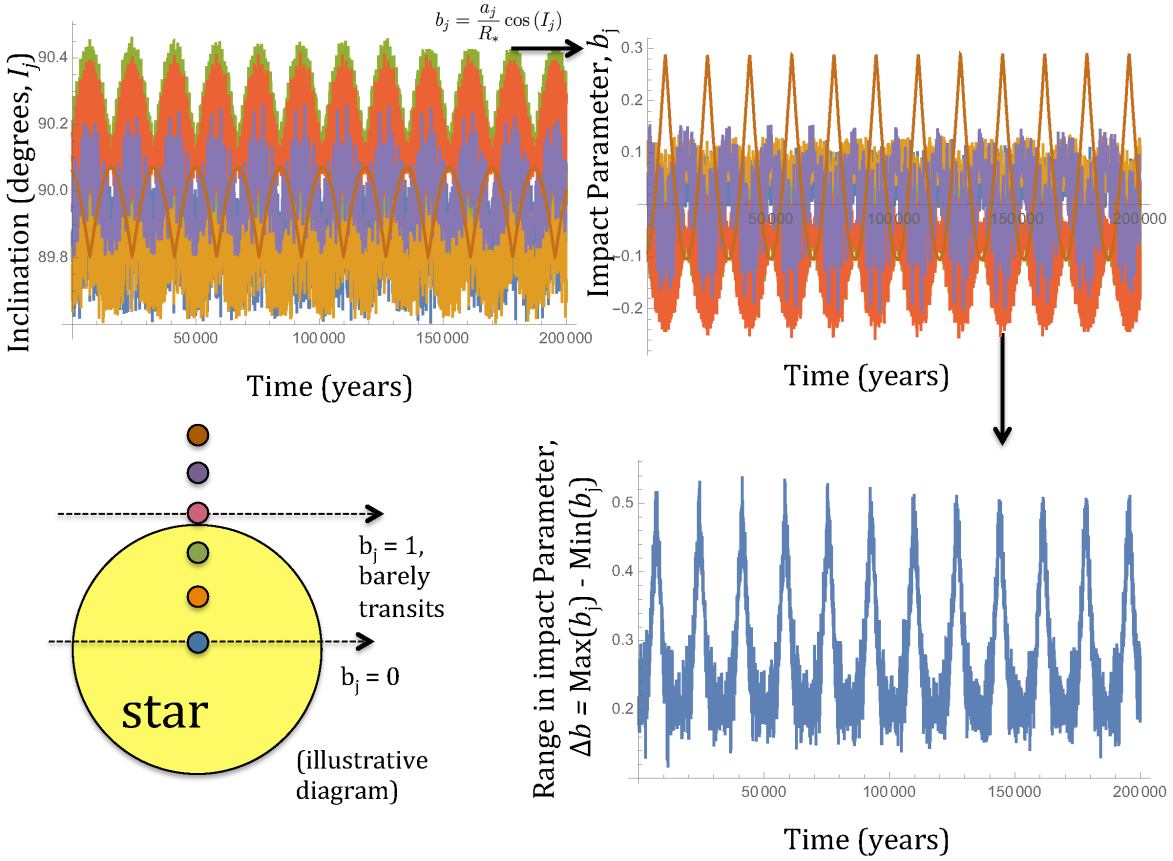

Figure 2.2 The Meaning of the Mutual Impact Parameter. The parameterization of mutual impact parameter, as illustrated by test case Kepler-11. First, a plot of inclination for all bodies in a system (upper left) is generated by solving equation 5.11 with the initial parameters of the system as boundary conditions. The semi-major axis dependency is removed using equation 2.13, and the result, impact parameter over time for each planet, is shown (upper right). The inclinations attained by each planet result in vastly different impact parameters due to the differences in semi-major axis. Planets closer to the star can attain more inclination with less effect on their impact parameter. Finally, the range between impact parameters is calculated (lower right) as was done for mutual inclination in Figure 1. The result is a measure of the range of the mutual impact parameter over time, $\Delta b(t)$. As long as this width describes a plane that lies entirely within the limbs of the star, the planets will be CMT-stable.

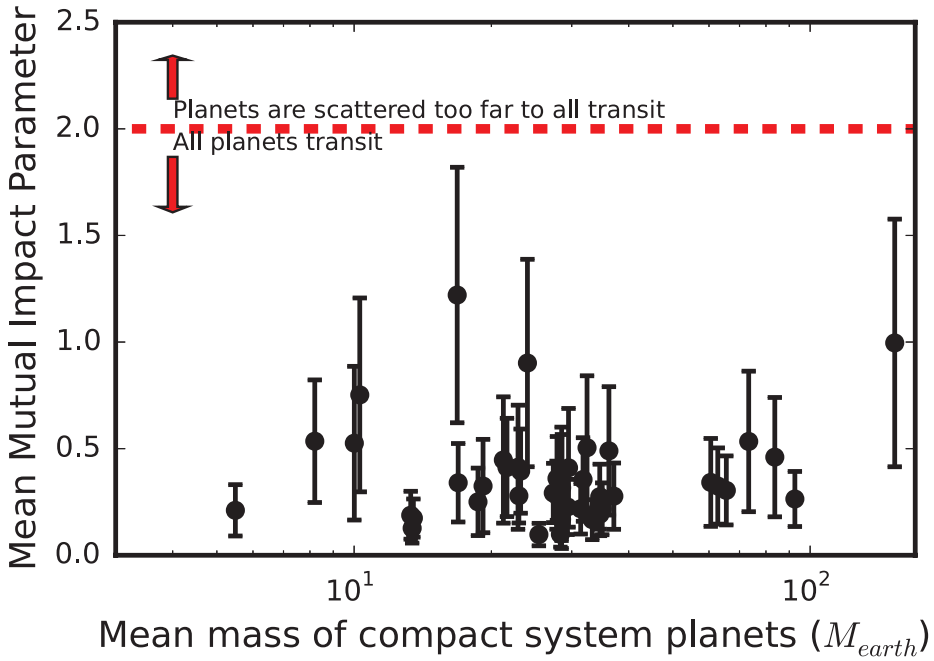

Figure 2.3 Mean Mutual Impact Parameter for True Kepler Systems. For each multi-planet *Kepler* system, the parameters of the system were sampled 4000 times and evolved forward in time. The resulting inclination angles for the planetary orbits were converted to a mutual impact parameter (see text). The mean and scatter of these values are plotted here for each system as a function of the total mass of the transiting planets, given in earth masses. The dotted horizontal line indicates the level above which it is not possible to observe all the planets in transit.

history of the system.

This parameterization represents the average behavior of each system over time. The plane width demonstrates how much range in impact parameter is normal for each architecture of system. However, we care about the transiting behavior of each system with respect to a single line of sight: that of the observer (Kepler) who originally identified the planets as mutually transiting. For example, it would be possible for a system's impact parameter range to be small enough for it to be possible for all planets to transit, but for the plane to be situated in such a location that only some planets transit. To understand how likely this is to happen, we plot in Figure 2.4 the mutual transit probability for each observed system as blue circular points. This probability is defined as the probability that a random time-step from a random realization, chosen from the sample of all 4000 realizations considered in the construction of Figure 2.3, will have all planets transiting along the line of sight to Earth. A probability of 1 would mean that the planets never left a transiting configuration in any time-step in any of our simulations, while a probability of 0 means that the system was never mutually transiting in any time-step in any realization.

Figure 2.4 shows that for the observed Kepler systems, all planets are expected to be transiting more than 85% of the time. Indeed, for most systems the probability of mutual transit is even closer to 100%. This demonstrates that not only do we expect the Kepler multi-planet systems to have plane widths small enough to potentially be transiting (Figure 2.3), the majority of the time they should maintain these transiting configurations with respect to our line of sight (Figure 2.4).

From an analysis of the results in Figure 2.3 and Figure 2.4, it appears that while Kepler systems do excite mutual inclinations due to their dynamical interactions with each other (as their mutual impact parameters do change over time), the magnitude of these interactions are small enough that although an initially non-null mutual inclination exists, it remains, through the process of secular evolution, smaller than the threshold necessary for planets to not be observed in transit. From this, we can state that the observed Kepler systems are generally CMT-stable.

The Kepler systems with four or more planets do not exhibit sensitivity to self-excitation of inclination due to dynamic interactions between the inner, roughly coplanar planets. This result indicates that self-excitation (in the mode considered here) is not a dominant mechanism in knocking planets out a transiting plane and thereby creating tightly-packed systems in which only some

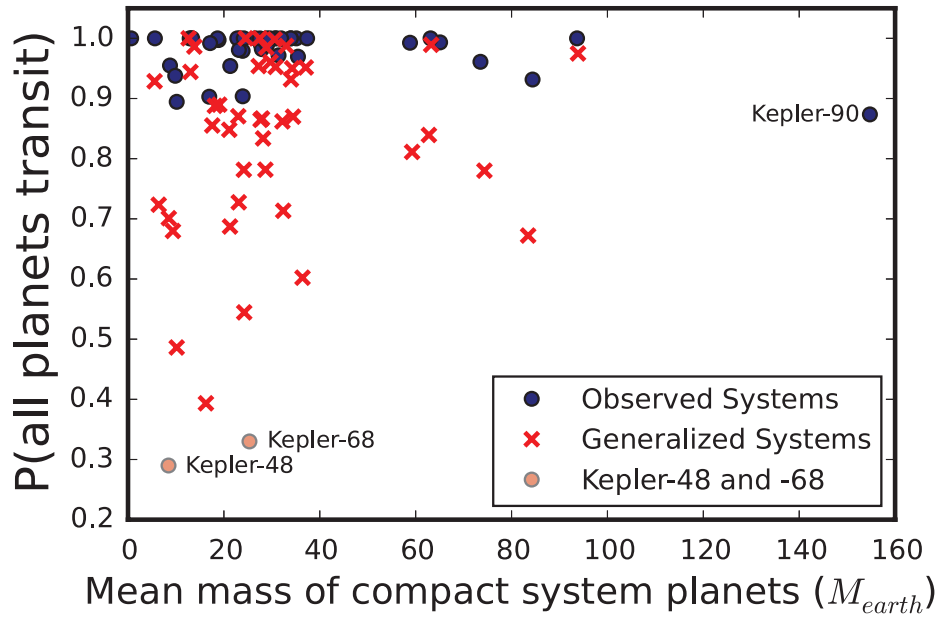

Figure 2.4 Computed Probabilities that all Planets Transit. For all realizations considered in Sections, 2.4.1, 2.4.2, and 2.4.3, we plot as circles the probability that a randomly chosen time-step from a randomly chosen realization will have all planets transiting along the line of sight to Earth. For the observed Kepler systems, all systems are mutually transiting more than 85% of the time. This result indicates that statistically the observed Kepler systems are seen in transit an overwhelming majority of the time. The generalized systems, plotted as crosses, are mutually transiting a much lower fraction of the time, as are Kepler-48 and -68, the observed currently non transiting systems.

planets transit.

It it important to note that the analysis of these observed Kepler system is limited by several factors: the measured mutual inclinations will be artificially low compared random systems drawn from the true distribution of planetary architectures, as these are systems with narrow enough ranges in inclination to be discovered in transit in the first place; the impact parameters of observed systems are likely artificially low due to the signal-to-noise bias against higher impact parameters; the deviation between measured planetary arguments of pericenter will also be artificially low (Ragozzine & Holman, 2010). These systems are not a representative sample of the true distribution of systems. As a result, the analysis presented here for the observed Kepler systems is not an analysis of the underlying planet population, but only of this particular class of heretofore discovered systems.

2.4.2 Inclination Oscillations in Generalized Kepler Systems

The Kepler systems that we see are observationally biased in that they likely have unusually low mutual inclinations and aligned arguments of pericenter (Ragozzine & Holman, 2010). As we have shown in Section 2.4.1, the observed Kepler systems are remarkably CMT-stable in their transiting configurations. We are not simply lucky to see these systems in transit, merely viewing them at an opportune time: instead, we are seeing systems that will likely be consistently transiting over many secular timescales. The Kepler systems are indeed a special class of system. It would also be interesting to compare their behavior with that of generalized Kepler systems, with a wider range of starting orbital parameters.

To construct these systems, we repeat the following process for each Kepler system in our sample:

- Generate a compact planetary system based on the target Kepler system. To do this, we draw each orbital parameter from an inflated distribution, treating measured 3σ errors as the width of our prior from which to draw orbital parameters. We convert radii to masses using the extended Wolfgang relation.

- We evaluate the system for dynamical stability using the Hill-radii criteria outlined in Fabrycky et al. (2014b). We compute the separation between two orbits (Δ) in terms of their Hill radii:

$$\Delta = (a_{out} - a_{in})/R_H \tag{2.14}$$

  when the mutual Hill radius is given by:

$$R_H = \left(\frac{M_{in} + M_{out}}{3M_*}\right)^{1/3} (a_{out} - a_{in})/2 \tag{2.15}$$

  and for a system to be considered dynamically stable, $\Delta > 2\sqrt{3}$ and for each pair of planets, $\Delta_{in} + \Delta_{out} > 18$ (Fabrycky et al., 2014b).

- If the system is dynamically stable according to these Hill arguments, we evolve the system

and repeat the process for another set of starting parameters.

Once this process is completed for each Kepler system, we have a sample of analog Kepler systems, which are based on the observed systems but no longer exactly the systems that we observe. This sample allows us to compute the mean mutual impact parameter over time, just as we did for the observed Kepler systems in the previous section.

The result is shown in Figure 2.5, which shows the same statistic plotted in Figure 2.3 computed from the generalized Kepler systems. For these generalized systems, the range of the impact parameter over time is higher, suggesting that the Kepler systems we observe are a particularly CMT-stable subset of the dynamically possible compact systems that could exist. Figure 2.4 shows as red crosses the mutual transit probability (over all time-steps and all realizations) for these generalized systems, demonstrating that the generalized systems spend significant amounts of time in non-mutually transiting configurations, as their plane widths imply they should.

2.4.3 Inclination Oscillations in Systems with Non-transiting Planets

Long-term RV followup to systems with transiting planets has not only found masses for Kepler planets, but has also resulted in the characterization of additional, non-transiting companions to some transiting systems (Marcy et al., 2014). Additionally, transit-timing variation analysis (Agol et al., 2005a; Holman & Murray, 2005) has both confirmed masses of planets and provided additional candidate planets (Cochran et al., 2011; Hadden & Lithwick, 2014). The current state of these systems provides insight to their dynamical history: assuming that systems form from roughly coplanar protoplanetary disks, something in the evolution of these systems has resulted in sufficiently large spread in inclinations to prevent all planets from being seen in transit.

As shown in Section 2.4.1, the observed multi-transiting Kepler systems are CMT-stable against self-perturbation (mutual inclinations excited by dynamical interactions between the transiting planets). Furthermore, the generalized Kepler systems are more likely than not to be seen in mutual transit. For multi-planet systems with some planets transiting and additional non-transiting companions, something in the dynamical history of the systems has resulted in misalignment in inclination between the planets. This effect could be explained in one of many ways: it could be due to a difference in formation mechanism between the purely multi-transiting systems and the

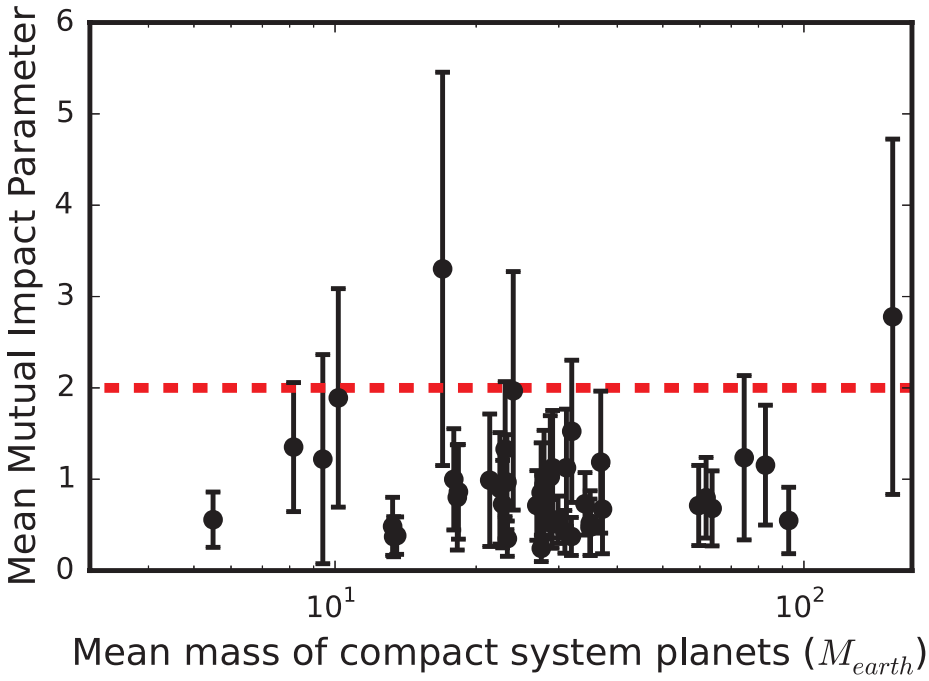

Figure 2.5 Mean Mutual Impact Parameter for Generalized Kepler Systems. For the generalized multi-planet *Kepler* systems, the parameters of the system were sampled 4000 times and evolved forward in time, just as in Figure 2.3. The resulting inclination angles for the planetary orbits were converted to a mutual impact parameter (see text). The mean and scatter of these values are plotted here for each system as a function of the total mass of the transiting planets, given in earth masses. The dotted horizontal line indicates the level above which it is not possible to observe all the planets in transit.

systems with some planets outside the transiting plane; it could be due to some other perturbation, such as an as-yet undiscovered stellar or massive planetary companion (a possibility beyond the scope of this chapter); or finally, it could be due to the effect of self-excitation between all (known) planets in the system. Our analysis probes this final possibility, which would apply if all discovered planets (both those that are currently transiting and those that are currently non-transiting) in a system had started out roughly coplanar, in a potentially transiting configuration, and then through secular interactions some planets had been perturbed out of the transiting plane.

We can test this explanation for the currently observed misalignment of Kepler systems that have been discovered to have multiple transiting planets and additional, non-transiting companions using the same method that was used to evaluate the transit stability of the most tightly packed Kepler systems in Section 2.4. Two examples of systems of this architecture are Kepler-48 and Kepler-68. By starting the planets of these systems in transiting configuration, we force the starting conditions to be a roughly coplanar disk containing all the planets.

Kepler-48 (Steffen et al., 2013a; Marcy et al., 2014) is a four planet system with three inner transiting planets and one non-transiting companion at more than 1 AU (a minimum mass 657 $M_{\oplus}$ companion with a period of roughly a 980 day period). Kepler-68 (Gilliland et al., 2013) is a three planet system with two transiting planets and one non-transiting planet, also outside of 1 AU (with a minimum mass of 0.95 M_{jup} companion in roughly a 580 day period).

To evaluate the transit stability of Kepler-48 and Kepler-68, we performed the same Monte Carlo evolution described in Section 2.4.1, with all orbital parameters drawn from observationally constrained priors except inclination. Though the true orbital inclination of the outer planets in the Kepler-48 and Kepler-68 systems is not known, we choose the orbital inclinations for the giant outer planets in each system by drawing a mutual inclination plane width from a Rayleigh distribution with a width of 1.5 degrees (from Fabrycky et al., 2014b, which suggested a Rayleigh distribution width between 1.0 degrees and 2.2 degrees). We constrain this choice of plane width such that the planets all start out mutually transiting, to mimic the starting conditions of the compact Kepler systems. With these starting conditions, we are probing what would happen to the observability of these systems over time, if they did start on feasibly observable architectures.

Through 4000 trials, Kepler-48 and Kepler-68 exhibited significantly more range in their mutual

impact parameters than the other compact Kepler systems. Figure 2.6 plots the behavior of Kepler-48 and Kepler-68 overlaid on the previous result for the compact Kepler systems. Kepler-68's mean mutual impact parameter is well above the limit for a mutually transiting system, while Kepler-48 spends about 60% of its orbits in a transiting configuration (marginalized over starting parameters).

We treat Kepler-48 and Kepler-68 as isolated systems. In other words, in our experiments, the only perturbation available to excite oscillations in inclination is that of the interactions between known bodies in each system. Thus, by generating the mean mutual impact parameter over one secular period for these systems after they start in a transiting configuration, we can make a statement about the amplitude of self-excitation in these compact systems. As shown in Figure 2.6, both Kepler-48 and Kepler-68 would be expected to develop significant mutual inclinations that prevent all planets from being seen in transit purely through excite self-excitations of inclination. Figure 2.4 shows as salmon points the mutual transit probability for these two systems, confirming that it is unlikely that the magnitude of the secular interactions would allow these two planets to be seen in transit.

This result indicates that even if these systems were to begin their secular evolution in a roughly coplanar configuration, they would be expected to self-excite sufficient oscillations to produce the current orbital state (where not all planets transit - we do not have sufficient limits on the observed inclinations to make a stronger comparison). Kepler-48 and Kepler-68 are examples of systems that 'make sense' dynamically: it is not required to add additional effects (such as a perturbing companion or stellar flyby) to their systems to explain their current non-transiting nature. It is important to note that the outer planets in these two systems are significantly external to the standard compact systems described in Section 2.4.1, which generally fell within 0.5 AU of their host star. Kepler-48 and -68 have outer companions at roughly 1.4 and 1.8 AU, respectively. It is possible that part of the reason for the activity of these systems is the lower transit probability of these outer companions, but the presence of Kepler-90 (which has an outer companion semi-major axis of roughly 1 AU) in the CMT-stable sample indicates that external companions do not ensure non-transiting configurations.

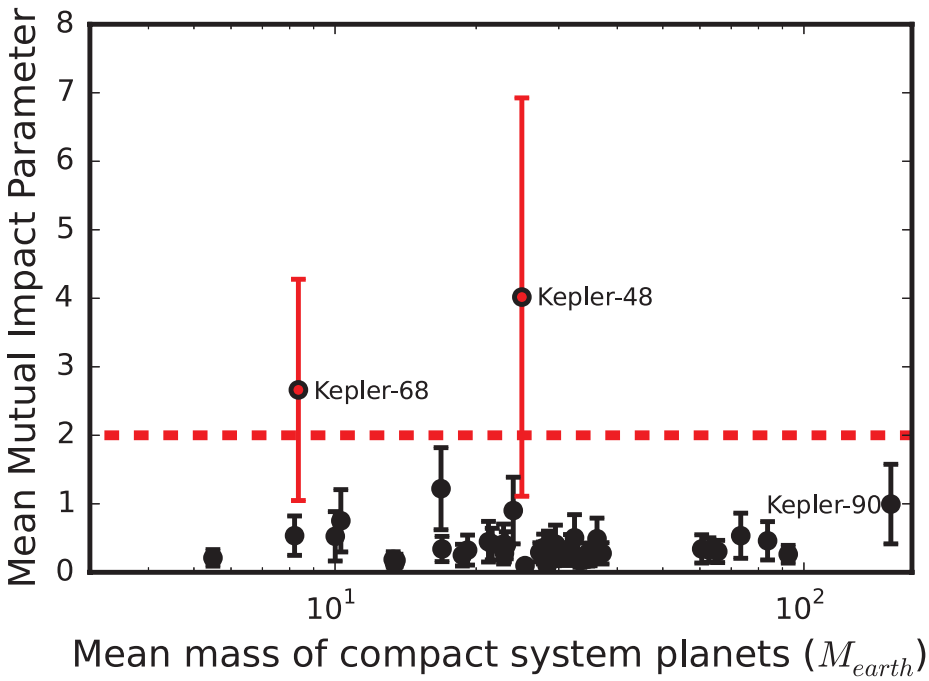

Figure 2.6 Comparison of Kepler Systems With and Without Non-Transiting Companions. Kepler systems in which all discovered planets are transiting are plotted as black points (they correspond to the same data presented in Figure 2.3), while Kepler systems where additional non-transiting planets have been discovered are plotted as red points. Kepler-48, marked (Steffen et al., 2013a; Marcy et al., 2014) is a four planet system with three inner transiting planets and one non-transiting companion outside of 1 AU. Kepler-68 (Gilliland et al., 2013), marked, is a three planet system with two transiting planets within 0.1 AU and one additional non-transiting planet at 1.4 AU.

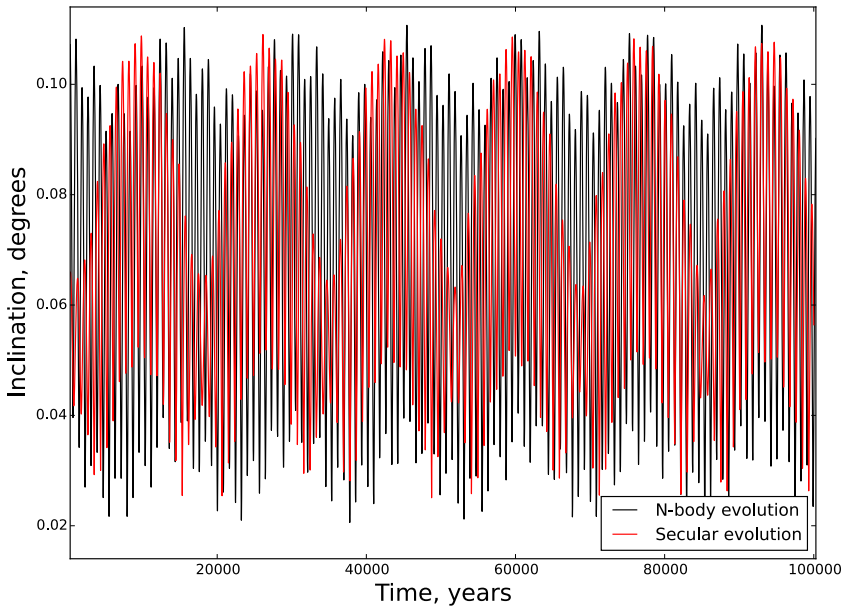

Figure 2.7 Comparison between Secular Theory and Numerical Simulations for Kepler-341 b. An illustrative realization of Kelper-341b, with the result from the numerical N-body code `Mercury6` plotted in black and the secular theory evolution plotted in red.

2.4.4 Comparison to Numerical Integrations

The discussion thus far has considered inclination oscillations as described by second-order Laplace-Lagrange theory. Although the amplitudes of the oscillations are small, so that the second order theory is expected to be accurate, in this section we compare the results to numerical simulations. These latter calculations, by definition, include interactions to all orders.

For these compact systems, eccentricity and inclination are generally low, but to evaluate the error inherent in our second-order expansion, we evolved each compact system using hybrid symplectic and Bulirsch-Stoer integrator `Mercury6` (Chambers 1999). The numerical integrator should provide the effectively 'right' answer, and significant deviations between the second-order theory and numerical results would indicate that second order secular theory is insufficient to describe the evolution of the orbital architectures. We compared 400 numerical N-body realizations with 400 secular evolutions (see the visualization of one realization of the comparison in Figure 2.7) to compute the deviations plotted in Figure 2.8, which describe the mean deviation, in degrees,

between secular theory and the numerical results. This comparison yielded a standard deviation of the difference in inclination angle obtained using secular theory and numerical results; this value was found to be less than 0.01 degrees.

For our use of second order second theory to be adequate for further analysis, we would want this variation between the numerical result and secular result to be much smaller than the threshold for significant inclination (which can cause a planet to become non-transiting). The planet in our sample with the largest semi-major axis and largest number of planets in the system, Kepler-11g, orbits a star with a radius $R_* = 0.0053$ AU. This planet would need to attain an inclination of 0.65 degrees out of the plane of the other planets to no longer transit. Planets with semi-major axes less than this value would need an even larger range of inclinations to be no longer seen as mutually transiting. Given that the typical deviation between the `Mercury6` numerical results and secular theory is less than 0.01 degrees, the match between secular theory and N-body numerics is good enough to use the second order secular theory for these compact systems.

We additionally note that although there is variation in the period of secular effects between numerical and second-order secular theory (Veras & Ford, 2012), this does not affect our result, as we are concerned with the amplitude rather than period of inclination oscillations, and these amplitudes are well-predicted to a reasonable precision. If we were concerned with the exact period of secular effects, second-order Laplace-Lagrange theory would not always be sufficient.

Finally, for completeness we note that the standard deviation of the residuals between the secular and numerical results is not the only measure of the difference (e.g., one could use the difference between the *ranges* of inclination angles instead). In this case, however, the differences between the two approaches is small: The differences would have to be nearly 100 times larger in order to change our main conclusion, i.e., that the Kepler compact systems remain CMT-stable.

2.5 Transit Duration Variations

Oscillations of the orbital inclination angles, as described in secular theory through equation 5.11, result in planets taking different paths across the face of the star as a function of time. These changing chords, in turn, result in the duration of the planetary transit varying with inclination

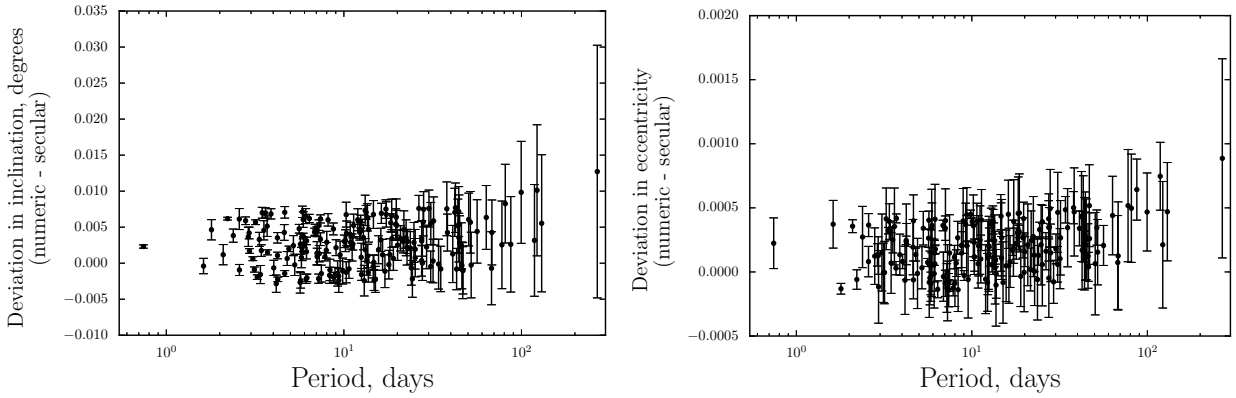

Figure 2.8 The Measured Deviation between Numerical and Secular Results. A residuals plot of (*top panel*) the deviation in inclination over several secular periods for each planet in our sample and (*bottom panel*) the deviation in eccentricity for the sample sample of realizations. The averaged deviation in inclination between the numerical and secular methods is generally below 0.01 degrees for all planets. We do not want to use fractional residuals here because inclination is plane invariant, so 0 degrees and 90 degrees are different only by convention. To take a fractional value imputes some importance to the frame of reference we use.

and hence with time. For the case of vanishing eccentricity, we can write τ_T, the time from first to fourth contact (the transit duration) for a single transit analytically (see Seager et al. 2007), in the form

$$\tau_T(t) = \frac{P}{\pi} \arcsin \Theta \tag{2.16}$$

where we have defined the effective angle

$$\Theta \equiv \frac{R_*}{a} \left[\frac{(1 + r_p/R_*)^2 - (a/R_* \cos^2 i)}{1 - \cos^2 i} \right]^{1/2} , \tag{2.17}$$

where P is the period of the planet, a is its semi-major axis, R_* the radius of the central star, r_p is the radius of the planet, and i is the inclination of the plane; note that the inclination angle is a function of the time t at which the duration is evaluated (so that the duration will also be a function of time). We also assume that orbital elements are effectively constant during a single transit, but that variations occur from transit to transit. Substituting equation 5.11 into this expression then yields a measure of the transit duration, τ, at any point during a planet's secular evolution. The second order secular theory used in this work computes motions with the evolution of inclination decoupled from that of eccentricity, so the null eccentricity approximation for extracting transit

durations from our derived transit parameters is sufficient. A product of our stability study of the Kepler systems is time series of $I(t)$ and subsequently $\Delta b(t)$. From these expressions, we can compute the times series $\tau_T(t)$, evaluated at each transit epoch for each planet in a system.

Thus far, observational study of secular TDVs has been limited by two main factors: (1) the signature of TDVs caused by even massive planets is generally small due to small yearly changes in inclination and eccentricity, and (2) to find TDVs to good precision, the cadence of photometric measurements must be high enough such that durations can be extracted from individual transits. Through TTVs can been used to determine dynamical quantities of multi-planet systems with good success (Agol et al., 2005a; Holman & Murray, 2005), TDVs in multi-planet systems are generally as much as several order of magnitude smaller in amplitude (see, for example, Figure 4 in Nesvorný et al., 2013, which demonstrates the difference in amplitude between a TTV and TDV signal for one system). However, there has been recent success measuring the amplitude of planetary TDVs (Maciejewski et al., 2013). Since transit duration depends on the chord a planet takes across its star in our line of sight and oscillating inclination can directly change this chord, secular interactions exciting inclinations will also lead to potentially observable transit duration variations.

Transit duration variations are thought to be one of the few (but currently feasible) promising ways to find moons around extrasolar planets (Kipping, 2009), as the perturbing effect of a moon would alter both the time of center transit and the duration of said transit for a transiting planet. Secular TDVs can also be used to constrain the oblateness of the central body, which has been done observationally for the KOI-13 system (Szabó et al., 2012). In this context, the stellar oblateness leads to precession of the orbital elements and thereby mimics the effects of secular interactions among multiple planets (see equation 5.2, which depends on the stellar oblateness J_2). In order for TDVs to be a useful method to detect exomoons or measure stellar oblateness, the amplitude due to these effects must be large compared to the intrinsic variation which we determine here. We also note that TDVs are now being compiled from the Kepler data (Mazeh et al., 2015), with more data expected in the near future. The time series $\tau_T(t)$ yields two useful measures: first, it yields the transit duration variation rate, which can be parameterized as $\delta\tau_{T,t}$, the change in duration per unit time (in Table 1, we parameterize this as as a variation per year. For example: a TDV of 1 sec yr^{-1} would mean that over one year, the expected duration would change by one second,

regardless of when or how frequently the transits occur). Second, it yields the duration variation per orbit, $\delta\tau_{T,n}$, which can be directly compared to the magnitude of other effects that can also cause TDVs. Both of these measures provide useful constraints on the properties of the system: the yearly TDVs provide approximate limits for the signal due to secular interactions between planets only. The duration variation per orbit allows for a fit to a series of durations over time, where:

$$\tau_T(t) = \tau_T(0) + \delta\tau_{T,n}\ n \tag{2.18}$$

where n is the number of orbits observed. If this is done, then variation accumulates as $(\Delta\tau_T) = \delta\tau_{T,n}\ n$ when $(\Delta\tau_T)$ is the total change in duration over an extended baseline of time. In this case, when the time series contains N independent measurements, the precision in fitting $\delta\tau_{T,n}$, as given in Equation 2.18, is increased. The uncertainty scales like $\sigma \propto N^{-3/2}$, with one factor of N^{-1} being due to the number of observed transits, a factor of $N^{-1/2}$ being due to the independent nature of these observations (as used in Pl & Kocsis, 2008). In this way, a large number of transit duration measurements can better constrain the TDV per orbit than would be possible looking at yearly drift alone using two widely separated transits (see Figure 3 in Szabó et al., 2012, which is the first example of observed long-period TDVs of the type we would see for secular interactions considered in this work).

The effect of secular interactions between planets in a multi-planet system can occlude observations of other parameters traced by transit durations (such as the presence of exomoons or solar oblateness), but it can also provide evidence for additional planets in the system, as non-transiting planets contribute to the duration variations even if they are not directly observable.

In Table 2, we present expected yearly TDVs for each planet considered in this work. These values are also presented in histograms in Figure 2.9. Though these values are small because the yearly change in inclination for each planet is very small, they provide limits for the kind of TDVs expected in the observed Kepler multi-planet systems without the presence of a perturber. The presence of a perturbing secondary in any of these systems would lead to transit durations outside the expected range. For example, circumbinary planets can exhibit TDVs on the order of hours (such as for Kepler-47, as in Welsh et al., 2014). For exomoons, the TDV amplitude is expected

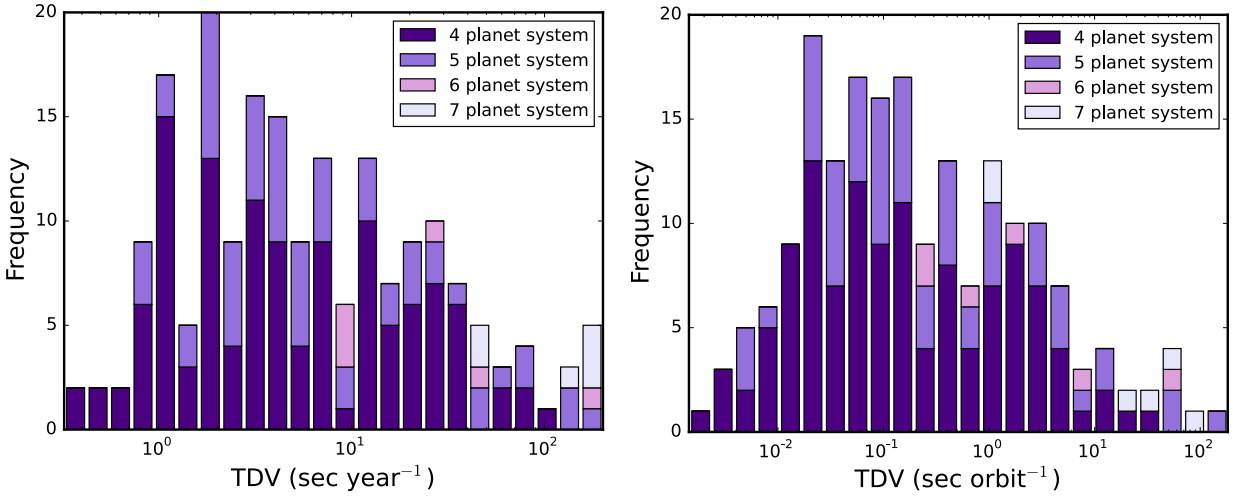

Figure 2.9 Transit Duration Variation Amplitudes for Kepler Multis. A histogram of the derived annual TDV values in this work, for Kepler systems with four or more coplanar planets. Data is presented in (*upper panel*) TDV year^{-1} and (*lower panel*) TDV orbit^{-1}. The bulk of the transit duration variations range from 0.01 to 10 seconds per orbit. The data visualized here is also given in Table 2. This histogram includes only compact mutually transiting systems with four or more planets (Kepler-37, -48, and -68 are not included).

to scale with $M_s a_s^{-1/2}$, when s denotes a satellite (Kipping, 2009). This amplitude is typically on the order of tens of seconds, being 13.7 seconds for the Earth-Moon system (Kipping, 2011). In comparison, typical values for the secular interactions within a compact system are a bit smaller (being typically between $10^{-2} - 10^{1}$ seconds per orbit).

Significant deviation in transit durations above these predicted values would suggest the presence of an additional effect (perturbing planet, extreme solar oblateness, exomoon, etc.) in the system. The range of transit duration variations summarized in Figure 2.9 thus serves as a baseline of the expected TDV distribution for tightly packed, coplanar, multi-planet systems.

2.6 Planetary Mass Constraints

The observed current coplanarity of the Kepler multi-planet systems is a stringent constraint on the planets' orbital properties. For most of the planets in the Kepler system, the ratio R_p/R_* is well-known. Combined with a value of the stellar radius (determined from either spectroscopy or interferometry), this value yields a measure of the planetary radius.

To perform a dynamical analysis, these measured radii must be converted to mass. Although some Kepler planets have masses measured via long-term radial velocity surveys (Marcy et al., 2014), the population of four-plus planet systems generally do not have measured masses due to the difficultly of measuring masses for small planets in multi-planet systems. Much recent work has been conducted aimed at finding a mass-radius relationship for exoplanets (Wolfgang et al., 2016; Weiss & Marcy, 2014b; Rogers, 2015a). When testing the CMT-stability of the compact Kepler systems, we use a supplemented version of the Wolfgang relation (Wolfgang et al., 2016). This relation introduces a large amount of scatter in density for planets that could be gaseous or rocky, which is useful for exploring the entire extent of parameter space in which the real planets could be living. However, another question that the apparent relative CMT-stability of the Kepler systems engenders is the effect of systematic mass enhancement (which could be due to an incorrect measurement of the stellar radius, as in Muirhead et al., 2012, in which the correction of such a misconception can be found). To test the effect of such systematic radius errors, we will inflate the masses of the constituent planets in the Kepler compact systems and examine the dynamical and CMT-stability of the systems.

For this experiment, we make a different choice in converting radii to masses: we use conversion law $M_P = M_\oplus (R_P/R_\oplus)^{2.1}$ inferred from results of the Kepler mission (Lissauer et al., 2012a). Using this relation removes the scatter due to composition, enabling a qualitative study of the general stability status of the Kepler multi-planet systems, without noise from differing compositions between trials.

Determining the effect of planetary mass enhancement with respect to roughly estimated values would help determine if the parameter space of CMT-stable systems (which we have shown includes all the systems in our sample) changes if the planetary masses are systematically underestimated. To determine the extent of this parameter space, we evaluate the dynamical stability of the Kepler systems with varying mass enhancement factors, which places constraints on the maximum ratio by which the masses can be enhanced without losing the currently observing transiting configuration of the systems.

To evaluate the effect of having larger planets in each system, we performed 40 numerical simulations of each system using `Mercury6` for each mass enhancement factor. The integration

time for each system was 10^6 dynamical times. This full treatment accounts for effects ignored in the secular theory such as the coupling of eccentricity and inclination, and instabilities due to orbit crossing or other effects. A mass enhancement factor describes the factor by which we increase all planetary masses within a single system. Although we alter the masses of the planets, we do not alter starting semi-major axes. The systems for each enhancement factor were created using observationally constrained orbital parameters supplemented with orbital parameters drawn from the standard priors (see Table 2.4). When a system remains CMT-stable for the entire time, this means that it is observable in transit and the system as a whole does not go dynamically unstable (e.g., by ejecting a planet).

There are two potential causes of instability in these systems. First, increased inclination oscillations can cause a some planets in a system to lie outside a mutual line of sight, even as a system remains dynamically stable. For the purposes of our analysis, we consider this to be an CMT-unstable system. Second, true dynamical instability (in the form of ejected/star-consumed planets or orbit crossing) also results in an CMT-unstable system. When either of these criteria (large inclination oscillations or true dynamical instability) is met for a certain mass enhancement factor, we categorize that system as unstable.

We parameterize the dynamical fullness of a system in terms of the surface density of a disk consisting of the mass of its constituent planets spread over an annulus with an inner radius equal to the semi-major axis of the most interior planet, and an outer radius equal to the semi-major axis of the most exterior planet:

$$\Sigma = \frac{\sum_{i=1}^{i=n} m_i}{\pi(a_n^2 - a_1^2)} \tag{2.19}$$

where n is the number of planets in a system, a is the semi-major axis, m is the planetary mass, and i denotes the planet number.

In Figure 2.10, we plot the mass enhancement factor required to make a system CMT-unstable against the the surface density of the planet annuli. This plot is essentially a comparison of the dynamical fullness of the system (surface density) to the stability against excitation (mass enhancement factor required to knock a system out of transit). The observed result appears to intuitively support that a higher surface density of material leads to a less CMT-stable system (for

which a lower mass enhancement factor can excited oscillations out of the plane). The large scatter of the data could also be explained by the existence of two distinct populations (one containing the disks where planet surface density is below 200 $M_{\oplus}$/ AU^2, and another where the density is above 200 $M_{\oplus}$/ AU^2, where the former are significantly less sensitive to mass enhancement).

For many systems with a surface density $\Sigma > 200$ $M_{\oplus}$/ AU^2, hot or warm Jupiter-like planets would be CMT-stable even in a multiple-planet system. This finding suggests that Jovian-size planets can exist in tightly-packed multi-planet systems with semi-major axis similar to those of the discovered Kepler systems (although this result holds only for Myr timescales, as discussed below).

The mass enhancement factor required to render the systems CMT-unstable may seem higher than expected. On one hand, the integrations are carried out for only 10^6 dynamical times, which generally works out to be a few million years, which is short compared to the system ages. The critical enhancement factor appropriate for the ages of the systems are thus lower, but we assume here that the short-time values provide a good relative measure of stability. On the other hand, these systems are in CMT-stable configurations, even though their surface densities are much larger than that of out solar system (the analogous value for our solar system is 0.49 $M_{\oplus}$/ AU^2). For comparison, we note that the GJ 876 system (one of the most dynamically active systems discovered to date) has a surface density $\Sigma = 2750$ $M_{\oplus}$/ AU^{-2}, which is much larger than the systems considered here.

2.7 Conclusions

This chapter has explored the dynamics of compact solar systems undergoing oscillations in their orbital inclination angles. If such oscillations occur with sufficient amplitude, then not all of the planets in a multi-planet system are expected to transit at a given epoch. By comparing the conditions required for the excitation of inclination angles with the observed properties of compact multi-planet systems, we can put constraints on their dynamical history. In this work, we have provided measures of $\Delta b(t)$, the spread in impact parameters, and characterized the potential dynamical history of compact extrasolar systems. We have also utilized our method to test the

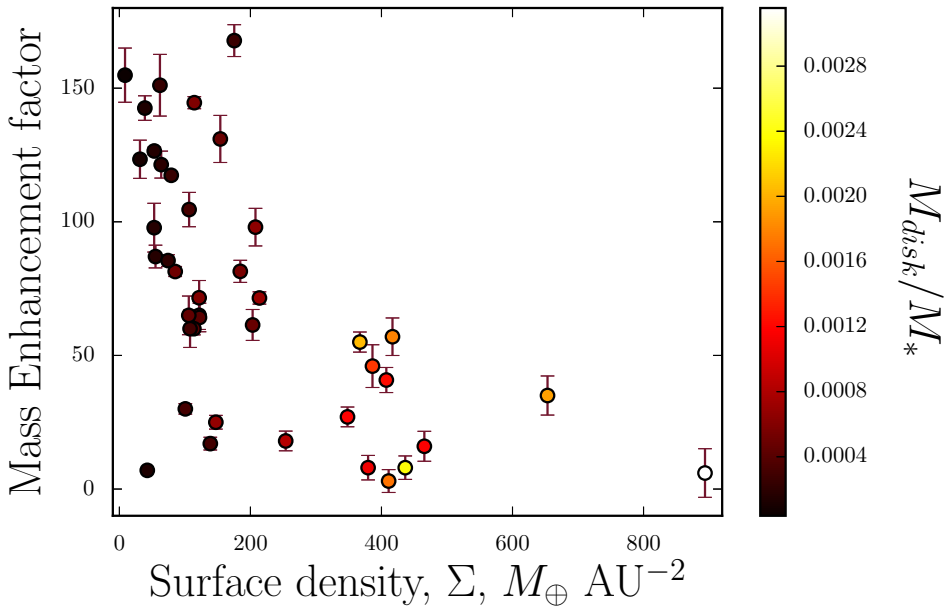

Figure 2.10 Mass Enhancement Factor Required to Destabilize System. The mass enhancement factor required to knock a system out of a CMT-stable transiting configuration, plotted by the surface density of the annulus containing all the planets (which is defined in Equation 2.19). The points are shaded based on the ratio of the total planet mass to stellar mass (M_{disk}/M_*). The shape of the trend can be explained two ways. It could be explained by the existence of two distinct populations (one containing the disks where planet surface density is below 200 $M_\oplus$/ AU^2, and another where the density is above 200 $M_\oplus$/ AU^2, where the former are significantly less sensitive to mass enhancement), or it could be explained as a monotonic (but high-scatter) decreasing trend with surface density.

dynamical and CMT-stability of a small sample of systems with additional non-transiting planets. From our derived $\Delta b(t)$, we have extracted subsequently the expected TDVs for observed systems in the case that these systems have no additional non-transiting companions. Finally, we have explored the effect of enhancing the mass of planets in these tightly packed systems, with an aim at determining how robustly the transit stability holds as planetary masses increase.

We have done this analysis by examining the multi-planet Kepler systems with the greatest number of transiting planets and analyzing their long-term stability, using a combination of secular (Sections 2.4, 2.4.3, and 2.5) and numerical techniques (Sections 2.4.4 and 2.6). Using the Kepler systems with the greatest number of transiting planets as our sample, we derived $\Delta b(t)$ for each planet using Monte Carlo techniques to marginalize over potential values of present orbital elements. We have determined that the compact Kepler systems are CMT-stable against being excited into non-mutually-transiting configurations.

Compact solar systems could have configurations that allow for a significant spread in the orbital inclinations through secular interactions between the constituent planets (Section 2.4). However, for the types of architectures observed in the Kepler sample of multi-planet systems, the expected range of inclination angles is almost always small. As shown in Figure 3, the typical spread in the mean mutual impact parameter is typically less than ~ 0.5, whereas impact parameters greater than 2 are required for planets to move out of transit. This result can also be expressed in terms of inclination angles: self-excitation generally produces $\Delta i < 0.5$ deg, whereas angles of $1 - 2$ deg are required to compromise transit in these compact systems. As a result, for most of the systems discovered by the Kepler mission, the self-excitation of inclination angle oscillations is generally not large enough to prevent planets from being observed in transit.

We have also tested the behavior of generalized Kepler systems. For these generalizations, we drew orbital parameters for each system from expanded but observationally inspired posteriors, then tested the dynamical stability. For dynamically stable analogs, we proceeded with the analysis used for the observed Kepler systems. We found that the generalized systems are experience significantly more action in mutual impact parameter excitation, resulting in these systems being on average less CMT-stable than the observed Kepler systems. The observed Kepler systems are remarkably CMT-stable, even compared to their analogs.

Our derived result that self-excitation of inclination angle oscillations is generally not large enough to prevent planets from being observed in transit holds for the Kepler systems, but not their analogs; even then, it has an important exception. We have also considered another type of Kepler system that contains 2 or 3 transiting planets and an additional planet not seen in transit (where the additional body was discovered by radial velocity follow-up). Kepler 48 and Kepler 68 are examples of this type of system. These systems are CMT-unstable to significant oscillations in inclination angle, so that the expected spread in inclination angle is generally large enough to move planets out of transit. We found this result by secularly evolving these systems after starting them in a nearly coplanar configuration. Even starting roughly coplanar, the magnitude of these systems' self-excitation is large enough that not all planets can be seen in transit simultaneously for most of each system's orbital history. This finding indicates that the current Kepler systems with non-transiting companions could have started roughly coplanar and subsequently had some of their planets excited out of the plane via dynamical interactions between the planets that we know about. Specifically, it is not necessary to introduce additional bodies into these systems to recreate the currently observed architectures.

We have focused on the secular interactions of compact systems of planets, and derived observables corresponding to the current known properties of these systems. These observables, the transit duration variations for Kepler systems with the observationally determined properties, are given in Table 2. Implicit in the motivation behind the calculation of these TDVs is the idea that there could be additional bodies in the systems we are considering, leading to true TDVs deviating from those that we have found here. An additional massive companion or an exomoon, for example, could cause transit duration variations with a larger amplitude than those derived in this work. If future observations of TDVs in these systems are vastly different than expected, it could potentially be evidence for either an exomoon or additional, exterior, non-transiting bodies in these compact systems.

We have also explored the effect of planetary mass enhancement in these systems. The stability of systems is related to how much the constituent planets' masses must be enhanced to result in a system that will no longer mutually transit. Generally, systems with higher effective surface density (calculated by spreading the mass of discovered planets within an annulus with inner and outer

radii equal to the inner and outer planet's orbital radii) do not allow mass enhancement factors as high as those with lower surface density. This result suggests that dynamically 'full' systems would not be mutually transiting if they hosted Jovian-mass planets. However, some systems with lower surface densities would be CMT-stable in a transiting configuration even with Jovian-mass planets (at least over time scales of ~ 10 Myr), indicating that it might be possible to see multi-transiting compact systems with Jovian-mass planets if they existed. The stability boundaries – over longer time scales – should be explored further in future work.

Spreads in the inclination angles in compact systems can be produced by a variety of astronomical processes, in addition to those considered in this work. Excitation by the compact solar system planets themselves (with semi-major axes $a < 0.5$ AU) is not generally a significant effect, but we have not (yet) calculated the effect caused by possible additional bodies in the outer part of the solar system (where $a \approx 5 - 30$ AU). Since planet formation is a relatively efficient process, the additional giant planets, not seen in transit by Kepler, are not only possible but likely. The orbits of these outer planets can be endowed with high inclination angles through a variety of dynamical mechanisms. For example, most solar systems form within clusters, and inclinations can be excited through dynamical interactions between solar systems and other cluster members (Adams & Laughlin, 2001; Adams, 2010; Li & Adams, 2015b). In addition, a range of inclination angles can be realized through the formation of planets in warped disks. The observed angular momentum vectors in star-forming cores do not point in the same direction as a function of radius (Goodman & Weare, 2010a; Caselli et al., 2002). This heterogeneity can lead to differences in angular momentum vector of the disk plane as a function of radius (for disks produced through collapse of the cores), which in turn will influence the inclination angles of forming planets (see also Spalding et al., 2014a). These various mechanisms can lead to inclined, massive, outer secondaries to the compact systems that we have considered in this work. The presence of such secondaries would alter the stability of these systems, and this effect could be evident in the TDVs. Additionally, it is possible that a system of planets would have only some planets mutually transiting, instead of the condition of all planets in a system transiting that we have considered in this work. For example, although we see four planets in a system discovered by Kepler, it is possible that another short-period companions exists in such a system, resulting in our picture of the system being incomplete. Extensions on our

calculation that account for this possibility could potentially be explored by using techniques such as the semi-analytical code CORBITS (Brakensiek & Ragozzine, 2015).

In summary, we have determined that self-excitation is not usually a dominant mechanism in exciting mutual inclination in tightly packed, multi-planet systems. Self-excitation does operate in some solar system architectures, where Kepler-48 and Kepler-68 are prime examples. Subsequent analysis of the effect of perturbing secondaries and stellar fly-bys in a dense cluster environment will complete the picture of how and when mutual inclinations are excited in exoplanetary systems.

Transit Duration Variations for Kepler Compact Systems

Planet	Orbital Period, days	$\tau_{T,n}$, TDV (s yr^{-1})	$\tau_{T,t}$, TDV (s orbit^{-1})
Kepler 11	10.3039	9.322660729	0.263177435
Kepler 11	13.0241	8.478858911	0.302546593
Kepler 11	22.6845	27.49182915	1.708598352
Kepler 11	31.9996	9.333648315	0.818282226
Kepler 11	46.6888	47.07565441	6.021659764
Kepler 11	118.3807	195.5615046	63.42659673
Kepler 20	3.6961219	1.914759018	0.019389542
Kepler 20	6.098493	9.46333942	0.158115368
Kepler 20	10.854092	4.0055073	0.119112725
Kepler 20	19.57706	50.15850045	2.690290337
Kepler 20	77.61184	73.36444964	15.59986281
Kepler 24	4.244384	0.743325382	0.008643722
Kepler 24	8.1453	1.056218584	0.023570458
Kepler 24	12.3335	1.232153241	0.041634964
Kepler 24	18.998355	3.605506001	0.187667625
Kepler 26	3.543919	1.859049714	0.018050196
Kepler 26	12.2829	3.710922038	0.124879135
Kepler 26	17.2513	6.100397395	0.28832818
Kepler 26	46.827915	37.7182322	4.839085401
Kepler 32	0.74296	2.028539272	0.004129106
Kepler 32	2.896	0.980507587	0.007779589
Kepler 32	5.90124	1.7046195	0.027559914
Kepler 32	8.7522	3.609925168	0.08656106
Kepler 32	22.7802	5.932320689	0.370245073
Kepler 33	5.66793	4.848962172	0.075297474
Kepler 33	13.17562	5.861904438	0.211600617
Kepler 33	21.77596	2.870395649	0.171248276
Kepler 33	31.7844	10.62434609	0.925173879
Kepler 33	41.02902	10.88222417	1.223252036
Kepler 49	2.576549	1.222377872	0.008628812
Kepler 49	7.2037945	2.229154696	0.043995541
Kepler 49	10.9129343	3.964566165	0.118534384
Kepler 49	18.596108	16.67313555	0.84946693
Kepler 55	2.211099	0.74535018	0.004515186
Kepler 55	4.617534	2.075484138	0.026256489
Kepler 55	10.198545	7.323822446	0.204636528
Kepler 55	27.9481449	7.955549215	0.609158472
Kepler 55	42.1516418	23.59027592	2.724298248

Transit Duration Variations for Kepler Compact Systems (continued)

Planet	Orbital Period, days	$\tau_{T,n}$, TDV (s yr^{-1})	$\tau_{T,t}$, TDV (s orbit^{-1})
Kepler 62	5.714932	6.558019889	0.102681199
Kepler 62	12.4417	10.787751	0.367720443
Kepler 62	18.16406	7.847335247	0.390519091
Kepler 62	122.3874	126.4774292	42.40888689
Kepler 62	267.291	200.7871286	147.0372394
Kepler 79	13.4845	12.8033798	0.473005959
Kepler 79	27.4029	28.46032201	2.136699611
Kepler 79	52.0902	20.63076067	2.944275204
Kepler 79	81.0659	89.08814913	19.78633147
Kepler 80	3.072186	2.130009061	0.017928175
Kepler 80	4.645387	1.943170254	0.024730898
Kepler 80	7.053	1.714628021	0.03313225
Kepler 80	9.522	1.971262692	0.051425653
Kepler 82	2.382961	0.965129741	0.006301004
Kepler 82	5.902206	2.222408585	0.035937297
Kepler 82	26.444	17.76864363	1.287326061
Kepler 82	51.538	10.89753388	1.538731784
Kepler 84	4.224537	4.439153917	0.051379096
Kepler 84	8.726	2.002291695	0.047868486
Kepler 84	12.883	3.658674592	0.129136177
Kepler 84	27.434389	10.50305215	0.789437858
Kepler 84	44.552169	29.82330904	3.640255081
Kepler 85	8.306	1.592408413	0.036237108
Kepler 85	12.513	2.059758945	0.070613051
Kepler 85	17.91323	15.62065426	0.766620199
Kepler 85	25.216751	26.0037509	1.796520854
Kepler 90	7.008151	44.64259007	0.857156198
Kepler 90	8.719375	51.72347308	1.235606461
Kepler 90	59.73667	122.8193078	20.10086701
Kepler 90	91.93913	163.2018666	41.10859624
Kepler 90	124.9144	196.2255593	67.15451508
Kepler 90	210.60697	160.6239691	92.6808971
Kepler 90	331.60059	200.873026	182.492093
Kepler 102	5.28696	21.67804261	0.314002587
Kepler 102	7.07142	5.624323905	0.108964265
Kepler 102	10.3117	3.349150204	0.094617622
Kepler 102	16.1457	0.736673755	0.032586612
Kepler 102	27.4536	42.68179251	3.210325641

Transit Duration Variations for Kepler Compact Systems (continued)

Planet	Orbital Period, days	$\tau_{T,n}$, TDV (s yr^{-1})	$\tau_{T,t}$, TDV (s orbit^{-1})
Kepler 106	6.16486	3.817466082	0.064477107
Kepler 106	13.5708	7.56602341	0.281306823
Kepler 106	23.9802	35.33153826	2.321253024
Kepler 106	43.8445	18.90988445	2.271491586
Kepler 107	3.179997	0.746863983	0.006506918
Kepler 107	4.901425	0.979622681	0.013154924
Kepler 107	7.958203	4.806241849	0.104791913
Kepler 107	14.749049	1.19795885	0.048407545
Kepler 122	5.766193	3.958098992	0.062529213
Kepler 122	12.465988	0.796688261	0.027209606
Kepler 122	21.587475	24.6377173	1.457167415
Kepler 122	37.993273	64.29884982	6.692941794
Kepler 150	3.428054	1.867968128	0.017543824
Kepler 150	7.381998	1.135021003	0.022955405
Kepler 150	12.56093	4.078868983	0.140368186
Kepler 150	30.826557	18.32964457	1.548054337
Kepler 169	3.250619	2.003755495	0.017845057
Kepler 169	6.195469	3.473185364	0.058953458
Kepler 169	8.348125	4.542706201	0.103898847
Kepler 169	13.767102	4.044452569	0.152549017
Kepler 169	87.090195	21.57958002	5.148958444
Kepler 172	2.940309	0.46849388	0.003774019
Kepler 172	6.388996	0.965003916	0.016891524
Kepler 172	14.627119	3.850997739	0.154326033
Kepler 172	35.118736	8.863030127	0.852762781
Kepler 186	3.8867907	2.174369234	0.023154296
Kepler 186	7.267302	2.671048208	0.053181682
Kepler 186	13.342996	5.6398171	0.206170019
Kepler 186	22.407704	21.23861165	1.303858968
Kepler 186	129.9441	127.2638103	45.30734602
Kepler 197	5.599308	1.746693303	0.026795271
Kepler 197	10.349695	1.664512376	0.047197796
Kepler 197	15.677563	2.946426313	0.126555573
Kepler 197	25.209715	19.27829892	1.331508004
Kepler 208	4.22864	0.327987695	0.003799841
Kepler 208	7.466623	1.085357765	0.022202623
Kepler 208	11.131786	2.145926971	0.065446575
Kepler 208	16.259458	1.939023031	0.086376612

Transit Duration Variations for Kepler Compact Systems (continued)

Planet	Orbital Period, days	$\tau_{T,n}$, TDV (s yr^{-1})	$\tau_{T,t}$, TDV (s orbit^{-1})
Kepler 215	9.360672	5.214125094	0.133719767
Kepler 215	14.667108	7.140540403	0.286934458
Kepler 215	30.864423	13.54786835	1.145608602
Kepler 215	68.16101	73.36673268	13.70068658
Kepler 220	4.159807	1.08595549	0.012376343
Kepler 220	9.034199	0.726348102	0.017978009
Kepler 220	28.122397	31.65200923	2.438713341
Kepler 220	45.902733	28.54622634	3.589999468
Kepler 221	2.795906	1.622302263	0.012426862
Kepler 221	5.690586	1.258209005	0.019616292
Kepler 221	10.04156	3.116385606	0.085735269
Kepler 221	18.369917	7.160429778	0.360373975
Kepler 223	7.384108	6.794688993	0.1374595
Kepler 223	9.848183	4.741440907	0.12793035
Kepler 223	14.788759	3.494873231	0.141602296
Kepler 223	19.721734	11.9376658	0.645017725
Kepler 224	3.132924	1.856809099	0.015937649
Kepler 224	5.925003	0.971515147	0.015770494
Kepler 224	11.349393	3.646370338	0.113381068
Kepler 224	18.643577	13.12338292	0.67032
Kepler 235	3.340222	0.564712568	0.00516785
Kepler 235	7.824904	7.345399102	0.15747135
Kepler 235	20.060548	6.816955222	0.374662623
Kepler 235	46.183669	39.50423791	4.998494925
Kepler 238	2.090876	0.884749492	0.005068223
Kepler 238	6.155557	2.172310058	0.036635009
Kepler 238	13.233549	3.287882421	0.119206447
Kepler 238	23.654	1.177061595	0.076280041
Kepler 238	50.447	39.55458755	5.466877474
Kepler 251	4.790936	3.555780556	0.04667265
Kepler 251	16.514043	6.199763248	0.2805018
Kepler 251	30.133001	10.65335888	0.879500476
Kepler 251	99.640161	96.79454965	26.4236288
Kepler 256	1.620493	0.323635851	0.001436848
Kepler 256	3.38802	0.427493436	0.003968099
Kepler 256	5.839172	0.884567462	0.014151073
Kepler 256	10.681572	2.074977703	0.060723353

Transit Duration Variations for Kepler Compact Systems (continued)

Planet	Orbital Period, days	$\tau_{T,n}$, TDV (s yr^{-1})	$\tau_{T,t}$, TDV (s orbit^{-1})
Kepler 265	6.846262	3.529407786	0.066200686
Kepler 265	17.028937	6.886638378	0.32129351
Kepler 265	43.130617	31.42320459	3.713156719
Kepler 265	67.831024	60.40531736	11.22562885
Kepler 282	9.220524	15.78120361	0.398660183
Kepler 282	13.638723	20.28678008	0.758043217
Kepler 282	24.806	25.75148128	1.750112999
Kepler 282	44.347	26.5277244	3.223082175
Kepler 286	1.796302	0.713292306	0.003510379
Kepler 286	3.468095	1.26801456	0.012048205
Kepler 286	5.914323	3.526176454	0.05713684
Kepler 286	29.221289	13.69225381	1.09617892
Kepler 296	5.841648	2.228023946	0.035658443
Kepler 296	10.21457	15.68127047	0.438842287
Kepler 296	19.850242	16.85583517	0.916691527
Kepler 296	34.14204	64.98518257	6.078703295
Kepler 296	63.336	82.07825957	14.24248945
Kepler 299	2.927128	1.224694325	0.009821471
Kepler 299	6.885875	1.810056081	0.034147452
Kepler 299	15.054786	12.26546764	0.505901344
Kepler 299	38.285489	27.25944274	2.859290672
Kepler 306	4.646186	3.606915153	0.045913421
Kepler 306	7.240193	3.698312183	0.073360257
Kepler 306	17.326644	10.59158411	0.502785225
Kepler 306	44.840975	39.39149661	4.839323602
Kepler 338	9.341	3.640821013	0.093175093
Kepler 338	13.726976	3.068493345	0.115400369
Kepler 338	24.310856	7.040320215	0.468921126
Kepler 338	44.431014	13.81305425	1.681446594

Transit Duration Variations for Kepler Compact Systems (continued)

Planet	Orbital Period, days	$\tau_{T,n}$, TDV (s yr^{-1})	$\tau_{T,t}$, TDV (s orbit^{-1})
Kepler 341	5.195528	1.217989712	0.017337259
Kepler 341	8.01041	1.039299363	0.022808806
Kepler 341	27.666313	22.75719988	1.724952917
Kepler 341	42.473269	12.26030004	1.426671292
Kepler 402	4.028751	1.081566673	0.01193798
Kepler 402	6.124821	0.917643194	0.015398357
Kepler 402	8.921099	3.453650264	0.084411934
Kepler 402	11.242861	2.886419391	0.088908526
Kepler 444	3.6001053	2.256350153	0.022255063
Kepler 444	4.5458841	1.40080575	0.017446303
Kepler 444	6.189392	1.916669517	0.032501422
Kepler 444	7.743493	2.784776198	0.059079164
Kepler 444	9.740486	1.368811474	0.036528463

Table 2.2 Transit Duration Variations for Kepler Multi-Planet Systems. Predicted values of the transit duration variations (TDVs) for the current sample of Kepler compact systems containing only the planets that have been discovered so far. Duration variations are presented both per orbit as well as per year to machine precision. True errors are typically on the order of 1% of reported values, but are not reported for brevity.

CHAPTER III

Effects of Unseen Additional Planetary Perturbers on Compact Extrasolar Planetary Systems

Results in this chapter were published in: ***Becker, J. C.***, *& Adams, F. C. 2017. Effects of Unseen Additional Planetary Perturbers on Compact Extrasolar Planetary Systems. Monthly Notices of the Royal Astronomical Society, 468, 549* and are presented here with minor revisions.

3.1 Abstract

Motivated by the large number of compact extrasolar planetary systems discovered by the Kepler Mission, this chapter considers perturbations due to possible additional outer planets. The discovered compact systems sometimes contain multiple transiting planets, so that their orbital angular momentum vectors are tightly aligned. Since planetary orbits are susceptible to forced oscillations of their inclination angles, the highly aligned nature of these systems places constraints on possible additional (non-transiting) planets. If planets in the outer regions of these solar systems have sufficiently large mass or sufficiently small semi-major axis, they will induce the compact inner orbits to oscillate in and out of a transiting configuration. This chapter considers the dynamics of the compact systems discovered to host five or more planets. In order to not perturb these systems out of a continually, mutually transiting state, additional planetary companions must generally have periastron $p > 10$ AU. Specific constraints are found for each of the 18 planetary systems considered, which are obtained by marginalising over other orbital parameters using three different choices of priors for the companion properties (a uniform prior, a transit-inspired prior, and an non-

transiting disk prior). A separate ensemble of numerical experiments shows that these compact systems generally cannot contain Jupiter-analogs without disrupting the observed orbits. We also consider how these constraints depend on system properties and find that the surface density of the planetary system is one of the most important variables. Finally, we provide specific results for two systems, WASP-47 and Kepler-20, for which this analysis provides interesting constraints.

3.2 Introduction

In this chapter, we examine the effect of outer perturbing companions on compact systems of closely-packed planets (specifically, a subset of the multi-planet systems discovered by the Kepler spacecraft). This chapter considers the effects of including hypothetical companions into the observed systems, with a focus on whether or not the entire system of planets remains in a mutually transiting configuration. The analysis thus considers the secular, dynamical, and transit stability of the systems, but does not provide any constraints on the long-term dynamical fate of the system or its formation history.

Our knowledge of high planetary multiplicity systems originates largely from the Kepler mission (Borucki et al., 2010; Batalha et al., 2010). The Kepler mission has enabled population-level progress such as constraining the size distribution of exoplanets (Howard et al., 2012a; Fressin et al., 2013a), searching for and determining the abundance of rocky habitable exoplanets (Dressing et al., 2015a; Petigura et al., 2015; Burke et al., 2015), defining a transition zone between rocky and gaseous planets (Rogers, 2015a), and much more additional work that was impossible before the era of large-scale transit surveys. One particularly interesting sub-population that has been found is a collection of high-multiplicity systems. More than forty planetary systems were found by the original Kepler mission to have four or more transiting planets, and more such systems continue to be found by the K2 mission (Vanderburg et al., 2016b).

Although the Kepler mission found many short-period planets, long-period planets are harder to find. Their transits are much less frequent and their radial velocity signals are smaller than for planets closer to the star. Finding long-period companions to existing Kepler systems with any number of known planets can be approached from two directions: observational searches and

theoretical constraints. Observational searches that have met with success at finding potential long-period companions include re-analysing legacy data (Wang et al., 2015b; Foreman-Mackey et al., 2016; Uehara et al., 2016), conducting follow-up radial velocity searches (Knutson et al., 2014b) or searching using adaptive optics (Adams et al., 2013; Ziegler et al., 2016; Baranec et al., 2016).

Theoretical searches, in contrast, can inform on what populations of unseen planets could exist in principle. These studies can be either analytic or numerical. The analytic approach is by necessity limited in scope, as analytically tractable equations cannot encapsulate the full behaviour of a complex planetary system. As an example, Lai (2016) generalised the secular approximation for the behaviour of systems with more than two planets, and found that perturbing companions can indeed excite the inclinations of the orbits in the inner systems.

In general, the secular approximation is an efficient, time-saving technique (see also Batygin et al. 2011, Van Laerhoven & Greenberg 2012, Spalding & Batygin 2015, and many additional recent papers) which is often applied to this problem. However, to evaluate the effects of massive, outer perturbers on an inner compact system, one must use full N-body numerical simulations. Multi-planet systems are often highly chaotic, so that many realisations of the systems must be considered to fully evaluate their dynamics. The numerical approach can thus test specific systems and determine probabilities of varying potential outcomes. Huang et al. (2017) used N-body experiments to test the stability of super-Earth systems in the presence of a companion exterior to 1 AU, and determined that a majority of super-Earth systems are destabilised by the presence of such a perturbing companion. Mustill et al. (2016a) performed a complementary set of numerical experiments, but found the same destabilising effect (albeit at a lower rate).

In this work, our goal is to test not only the stability of observed Kepler multi-planet systems, but also to map their transiting behaviour. Petrovich et al. (2014) found that for systems where tightly packed inner planets have significant eccentricities or inclinations, the excitation of those orbital elements must occur before the planets attain their tightly packed configurations. This finding suggests that a tightly packed system with all of its planets observed to be transiting would not generally be expected to attain a non-transiting configuration over secular timescales, although this stability may not hold over the age of the system. Another previous study (Volk & Gladman, 2015) found that currently observed multi-planet systems may be the remnants of tightly

packed compact systems, which may have lost planets over time through dynamical instabilities and collisions over the history of the system. On the other hand, Moriarty & Ballard (2016) found that these systems may be dynamically stable over spans of time much longer than secular timescales.

A comprehensive numerical analysis requires an average of 5000 – 8000 CPU hours on standard processors for each planetary system under investigation. For this reason, and others, the behaviour of the Kepler multi-planet systems in the presence of extra companions has not yet been evaluated numerically. For these compact planetary systems, this investigation thus provides a picture of the transiting behaviour of the inner planets in the presence of an extra companion.

As such, this work builds upon an earlier contribution (Becker & Adams, 2016), where we examined the possible self-excitation of inclination in a collection of the multi-planet systems discovered by the Kepler mission. These Kepler multi-planet systems are generally tightly packed, with four or more planets orbiting within ~ 0.5 AU. Self-excitation of inclination occurs when planets that are a part of such a tightly packed system trade angular momentum among their orbits. The end result is that one or more planets could have inflated inclinations at any given time. Over secular timescales, the particular planets that are excited to higher inclinations may change, and the width of the effective "plane" containing the planets may also vary. As a result of such interactions, a system where all planets start in a mutually transiting configuration from our line of sight could evolve such that one or more planets leave the transiting plane at later times (a related treatment of this problem can be found in Brakensiek & Ragozzine, 2016a).

For completeness, we note that the system could also evolve to a configuration where all of the planets are observed in transit from a different line of sight. The movement of planets in and out of the transiting plane could also excite large observed obliquities, as planets move out of the plane aligned with the stellar spin axis of the host star. Multiple authors (Li & Winn, 2016; Mazeh et al., 2015; Morton & Winn, 2014a) have found that the systems with multiple planets have lower obliquities.

Using a combination of secular and numerical analyses of the multi-planet systems observed by Kepler, previous work determined that self-excitation is not generally extreme enough to cause most of the observed systems to attain non-transiting configurations. For the sake of definiteness, we call the state of being in a continually mutually transiting configuration "CMT-stability". Note

that systems that are "CMT-unstable" are usually dynamically stable, in that they retain all of their planets (see also Brakensiek & Ragozzine 2016a for a more detailed discussion). However, for a more general set of systems — those motivated by the observed sample, but with a wider range of allowed properties — self-excitation can have a greater effect, leading to potentially CMT-unstable systems. In other words, planetary systems that are nearly the same as those observed, but with slightly different specific orbital elements, can oscillate in and out of transit. This effect — changes in the observability of a system over time due to dynamical interactions — has received much recent attention (see Ballard & Johnson, 2016a), including some studies of the effect of extra, unseen, perturbing bodies (prepared simultaneously with this work; see Lai, 2016; Mustill et al., 2016a; Hansen, 2017). This present chapter carries previous work forward by performing a more robust ensemble of numerical simulations for the systems with the highest multiplicity (with the caveat that numerical limitations prevent us from analysing the entire Kepler multi-planet sample in this way). This study also examines the effects of different priors on the end results by choosing three different versions of the priors. Finally, we provide predictions for specific systems (such as Kepler-20 and WASP-47).

In our previous chapter, we considered the systems to contain only the bodies observed thus far. It is unlikely that our observations are complete, and so it is useful to examine the effects of a perturbing body (giant planet or brown dwarf) on each compact, multi-planet system, using the same basic methodology that we did for the compact systems without perturbing bodies. Moreover, sufficiently distant companions are likely to be found outside the orbital plane of the inner system: the original molecular cloud cores that produce star/disk systems often have a range of angular momentum vectors and this complication, along with dynamical evolution, can often lead to companion orbits that are inclined (see Barclay et al. 2015b, Spalding et al. 2014a, and references therein).

This study derives statistical limits that constrain the presence of companions in the observed multi-planet Kepler systems, given that we see them in transit today. In this work, we place these limits by performing a large number of computationally-intensive simulations for 18 of the observed Kepler multi-planet systems. In Section 3.3, we discuss our numerical techniques and some typical results that characterise the effects of perturbing bodies for individual systems. Note that it is not

feasible to carry out a detailed numerical analysis for every compact system that will be discovered. Section 3.4 presents limits on potential unseen companions for the sub-sample of multi-planet systems considered in this work. These results provide a general picture of the CMT-stability for observed systems with planets in compact orbits and suggest methods for predicting the companion status of such systems. Section 3.5 presents specific results for the dynamically interesting systems Kepler-20 and WASP-47. The chapter concludes in Section 3.6 with a summary of our results and a discussion of some limitations of this analysis.

3.3 Evaluating the Effect of Unseen Companions on the Observed Kepler Multi-Planet Systems

The compact, multi-planet systems discovered by Kepler are remarkably stable in their currently observed transiting configurations, as long as there are no extra companions in the systems. If an additional body (giant planet or star) is introduced, however, the behaviour of the currently observed planets could be significantly altered over secular (and longer) timescales. Sufficiently large and/or close perturbing bodies could lead to the inner system becoming either dynamically unstable or CMT-unstable. Both of these scenarios would lead to a complete system with different properties than these observed by Kepler. Note that the perturbing bodies themselves could move in and out of transit with time, and would transit with low probability due to their large orbital separations. Notice also that the observed systems tend to have regularly-spaced orbits (Pu & Wu, 2015) with no large gaps where non-transiting planets could reside. We thus expect any additional planets to generally lie outside the observed compact systems.

Since the multi-planet systems were indeed discovered by Kepler, we can rule out the presence of companions in these systems that would disrupt their CMT-stability on short timescales. In addition, companions that disrupt CMT-stability on longer timescales are unlikely. For example, in all of the Kepler multi-planet systems considered in this work, a brown dwarf orbiting at 0.5 AU would disrupt the orbits of the inner planets, so that the inner system would fail to transit continually. The systems would thus be "CMT-unstable" and planetary systems of this type would not have been discovered by Kepler in their observed configurations. However, for a diametrically

different companion type — say, a super-Earth at $a = 700$ AU, analogous to the proposed Planet 9 in our own solar system (Batygin & Brown, 2016a) — none of the systems in our sample would be disrupted from their current transiting configurations. It is clear that for every compact multi-planet system, there is some regime of "acceptable" companions, which could very well exist in the observed systems as they do not alter the orbits of the compact system planets, and some other regime of "unacceptable" companions, which lead to the inner system being CMT-unstable. The goal of work is to determine these limits using numerical N-body integrations of the observed Kepler multi-planet systems.

3.3.1 The Necessity of N-body Integrations

In previous work, we used Laplace-Lagrange secular theory to evaluate the CMT-stability of the observed Kepler systems with four or more planets (Becker & Adams 2016; see also Lai 2016). In that context, secular theory is an appropriate approximation both because the planets attain fairly low eccentricities and inclinations through the natural orbital evolution, and because the systems are (as observed) dynamically stable. These systems do not experience orbit-crossing, scattering, or other dynamical complications that depend on the mean motions and could cause a system to change its orbital configuration.

When adding a perturbing companion to such a system, the opportunity arises for all of these mean-motion-dependent events to have significant effects on the evolution of the system. To illustrate this behaviour, Figure 3.1 shows a selection of such effects for one particular planet (Kepler-20c), and illustrates the (at times) significant discrepancy between numerical N-body evolution and secular evolution. The integrations shown in Figure 3.1 are drawn from the sample constructed for this work (which will be described in depth in Section 3.3.2). The secular analogues were generated using the same starting parameters that were used in the N-body integrations. The plots cover only 10^5 years for ease of viewing the relevant oscillations.

One major, well-known, unavoidable difference between secular theory and N-body integrations is the timescales of periodic evolution (this effect is explained, using Jupiter and Saturn as examples, in chapter 7 of Murray & Dermott 1999). This effect is illustrated in Case A of Figure 3.1, which shows the evolution of Kepler-20c in the presence of a 2 $M_{\rm jup}$ companion at 8 AU. In this case,

the evolution proceeds similarly in both secular and N-body cases, but the orbital elements evolve on somewhat different timescales. This kind of deviation will not compromise our results to a large degree, as it does not change the amplitude of the oscillations. Although there may be slight deviations when simultaneous transits occur (between multiple inner planets, each evolving on different timescales), this effect will likely be small. Moreover, these effects are unlikely to influence CMT-stability.

Case B in Figure 3.1 shows the ideal situation in which secular theory can be used to approximate the dynamics with high fidelity. In this case, a 1 $M_{\rm jup}$ companion in introduced at 20 AU. The orbits of the perturber and of the inner system are sufficiently spatially separated that no additional effects arise due to mean motions. In this case, all of the relevant dynamical variations are encapsulated by the secular approximation.

In contrast, Cases C and D in Figure 3.1 demonstrate the limitations of secular theory. Case C shows the effect of a 1 $M_{\rm jup}$ companion at 4 AU. Not only are the periods of the inclination oscillations different, as seen in Case A, but the amplitude of the oscillation shows a significant difference between the two calculations. This difference can be caused by a variety of factors which are not included in the secular approximation (including resonance-driven boosting of eccentricity or inclination, etc.). Since CMT-stability depends on the amplitude of inclination oscillations, a deviation of this magnitude will lead to different conclusions derived from using each method.

Case D shows the effect of a 1 $M_{\rm jup}$ companion at 1 AU. Note that the outer orbital radius of the planets in the observed Kepler-20 system is 0.35 AU, so this companion orbit is a factor of three larger than that of the observed system. This case illustrates another major imperfection in secular theory. Here, the inner system of planets becomes dynamically unstable due to the companion: In this particular integration, the eccentricities are increased to such an extent that orbit crossing occurs (but instability can occur in many other ways). This instability is plainly evident in the numerical integrations, but the secular theory is insensitive to such effects (which depend on where a planet is on its orbit when the orbits cross). The numerical integrations are thus necessary to evaluate whether the planets survive or not.

One additional limitation of secular theory that is not obvious from Figure 3.1 is its treatment of semi-major axis. In secular theory, the semi-major axes of the interacting planets are fixed and

only the evolution of other orbital properties (such as inclination, as plotted above, or eccentricity) is allowed to vary. On the other hand, numerical N-body simulations allow the semi-major axes to evolve. If the semi-major axes are expected to evolve (which would occur in scattering interactions with the perturber, for example), then it is necessary to use numerical techniques.

Although the secular approximation is a tremendously useful tool for making dynamically difficult problems tractable without significant investments of CPU time, it is insufficient for the particular problem considered in this chapter. Moreover, the secular theory fails for the regime of parameter space for which the planetary systems are dynamically active, i.e., the regime of interest in this study. As a result, we must turn to numerical methods.

3.3.2 Numerical methods

To evaluate the effects of unseen companions on the Kepler multi-planet systems, we use numerical N-body simulations to evaluate the dynamics and stability of the observed systems on secular timescales. These numerical integrations are carried out using the N-body code `Mercury6` (Chambers, 1999b).[1] Because the systems are chaotic, and because we need to consider a range of possible companions, many integrations of each system must be carried out. Toward this end, we use a Monte Carlo technique to generate multiple realisations of each compact multi-planet system discovered by Kepler, and introduce a perturbing companion with randomly chosen orbital elements. We then evaluate the CMT and dynamical stability of the system for each such realisation. The unseen companions are assumed to have orbits exterior to the observed compact Kepler systems. The distributions of the companion masses and other properties are described below.

3.3.2.1 Priors

Not every orbital parameter describing the planetary systems we consider can be measured. In order to complete the specification of the initial conditions for the N-body integrations, we have to determine the remaining parameters, both the the observed planets and for the unseen companion. These distributions of parameters – priors – are described below. Note that the priors for the observed planets are a means to specify unobserved properties of the system, e.g., setting

[1]Note that a numerical treatment is required for reasons explained in Section 3.3.1.

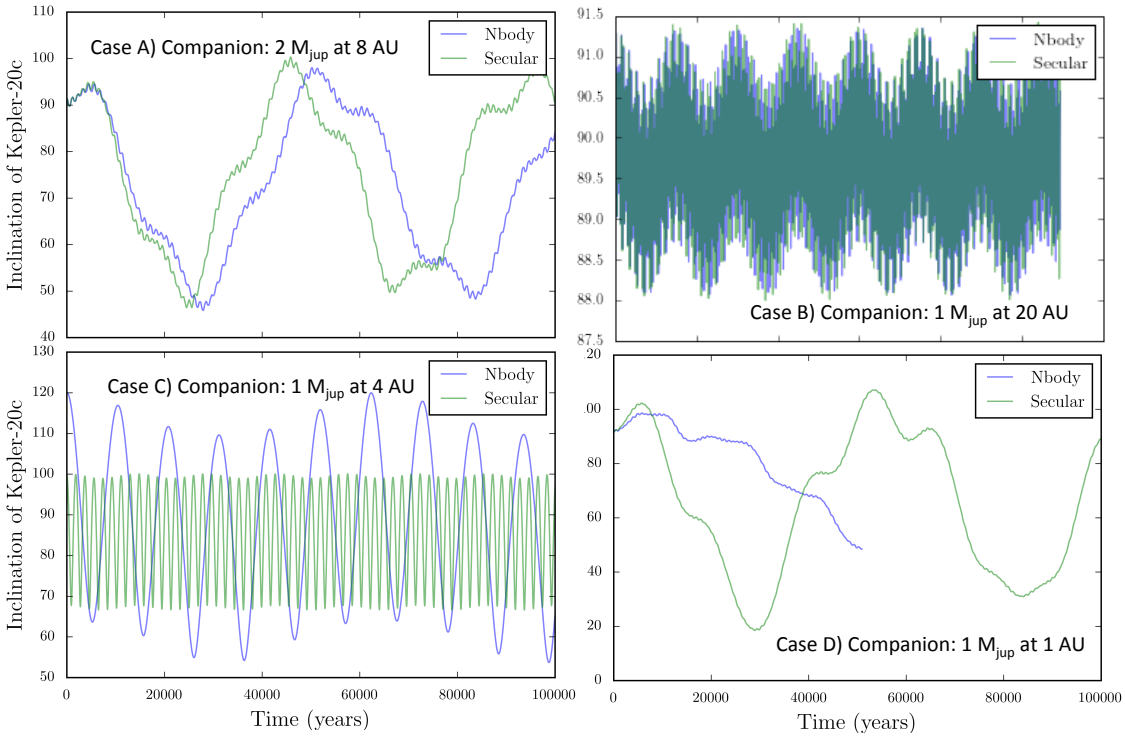

Figure 3.1 Differences Between Secular and N-Body Integrations. Four different companion types and their effects on the evolution of Kepler-20c, as computed using both secular and numerical methods. Case A shows the well-known effect of the potential inconsistency in the period of oscillations, which is important but unlikely to affect our results. Case B shows a case with good agreement between the two methods, and demonstrates that for large orbital separation companions, secular theory may be a good approximation. Case C shows differences in both the period and amplitude of the oscillations, an effect large enough to potentially skew results, which occurs when an additional planet in the system was ejected early in the simulation. Case D shows an example where the numerical integration identifies a dynamical instability that would be ignored in the secular approximation. For all cases, the realisations plotted were chosen from more than 4000 integrations, selected for illustrative purposes.

the planetary mass when the radius is measured. The priors for the putative companions are less constrained, as the additional bodies could have a wide range of orbits and other properties.

The orbital elements for the existing planets were drawn from observational priors (for the planets in our sample, these priors are found in Borucki et al., 2010; Lissauer et al., 2011a; Borucki et al., 2011; Fabrycky et al., 2012; Batalha et al., 2013; Borucki et al., 2013; Quintana et al., 2014; Rowe et al., 2014; Marcy et al., 2014, we use the values available as of January 2016). When observational priors do not exist (for example, for most planets, inclination has not yet been observationally determined), we draw from a prior chosen to be representative of the possible values of that parameter. We use the same methodology as in Becker & Adams (2016) to choose these values, and a more lengthy description of the choices made can be found in that chapter, but the most important choices will be described with brevity here.

Planetary Masses. Photometric light curves yield an excellent measure of planetary radii, but they do not provide direct measurement of the planetary masses. For this reason, it is necessary to use a mass-radius relation to choose starting masses for the simulations. The Wolfgang relationship from Wolfgang et al. (2015) provides a probabilistic mass-radius conversion function for planets in the range $R_P = 1.5 - 4R_\oplus$. For planets smaller than this lower limit, we use the relation from Weiss & Marcy (2014c). For planets larger than the upper limit, we use a characteristic gas giant density generated by a Gaussian draw from the observed gas giant densities (as done in Vanderburg et al., 2016b).

Orbital Inclinations. Mutual inclinations are generally parametrised by a Rayleigh distribution with some width (Fabrycky & Winn, 2009; Lissauer et al., 2012a; Fang & Margot, 2012; Ballard & Johnson, 2016a), which is typically taken to lie in the range 1 degree – 3 degree. For this application, we use a simple Rayleigh distribution with width 1.5degree (Fabrycky et al., 2014b) for planets without measured inclinations, with the constraint that all planets in the inner system must initially be transiting.

Additional Companion Properties. Because we do not fully understand the population of long-period planets, the priors for our injected companions can be chosen in a variety of ways. This regime of parameter space, with semi-major axes $a > 1$ AU, is not fully sampled observationally, and different techniques (RV, transit, direct imaging, micro-lensing) each have their own biases and

limitations.

In previous work concerning the stability of the Kepler systems, a variety of priors were used. For example, Mustill et al. (2016a) used priors representing stellar and planetary companions, and found that not only are the dynamical instability rates are different between the two cases, but so too is the amount of inclination excited. Hansen (2017) also performed numerical experiments that involved adding a perturbing body while using delta function priors and multiple trials, which provides a description of the average behaviour of the system for each companion type, but does not explain how susceptible results are to small changes in companion type.

In this chapter, we use three sets of priors for our population of perturbing bodies. The goal is to not only describe the behaviour of the inner systems in the presence of these extra bodies but also to determine the differences in computed stability thresholds using the different priors. As a result, for each observed system, we construct three samples of 2000 injected perturbing bodies by re-sampling our 4000 integrations with the following priors:

- **Transit-inspired prior.** The transit-inspired prior is intended to test the behaviour of perturbing bodies that may have formed in a plane with the inner system of planets, and remained roughly coplanar (see Section 3.5.2 for an example of a system that may have done this). For these companions, we choose a mass from a log-uniform distribution between 0.1 and 10 $M_{\rm jup}$. For inclination we use a Rayleigh distribution with a width of 3 degrees (which corresponds to the largest width given in recent papers that parametrise inclinations in this way; see Fang & Margot 2012, Ballard & Johnson 2016a, and Fabrycky et al. 2014b). The orbit of the perturbing planet is thus close to the plane(s) of the inner system. For this prior, we choose eccentricity from a beta distribution with shape parameters $\alpha = 0.867$ and $\beta = 3.03$ (an observationally motivated distribution derived in Kipping, 2013b), and choose the argument of periastron according to the asymmetric, sinusoidal distribution given in that same paper.

- **Uniform prior.** The uniform prior is intended to explore the entire parameter space that could potentially be populated by unseen companions. The semi-major axes are uniformly distributed in the range $a = 1 - 30$ AU. The planetary masses are uniformly distributed

in the range $M_p = 0 - 10\ M_{\rm jup}$. The inclination drawn from a uniform distribution with range $i = 0 - 90$ degrees. The eccentricity is drawn from a beta distribution, whereas the argument of pericentre has a corresponding asymmetric distribution with a sinusoidal prior (see Kipping 2014). Finally, the longitude of the ascending node Ω is taken to be uniform over the range $0 - 360$ degrees.

- **Non-transiting disk prior.** The non-transiting disk prior is intended to mimic the population of planets (and brown dwarfs) that could exist in these systems but be undetectable via transit methods. A large number of such planets have been discovered in existing systems (see, for example, Marcy et al. 2014; note that the non-transiting planets in these systems are generally exterior to the transiting system). As in the other two populations, we draw the eccentricity and argument of periastron from the distributions given in Kipping (2014). We draw the companion mass from a distribution uniform in log space, ranging between 0.1 and 10 $M_{\rm jup}$. We draw the inclination from a uniform distribution between 60 and 90 degrees, representing a 0 – 30 degree misalignment between the extra body and the plane of transiting planets. This 30 degree width is based on the maximum misalignment expected due to variations in the angular momentum direction between molecular cloud cores and their forming circumstellar disks (Goodman & Weare, 2010a; **?**). As discussed in Barclay et al. (2015b), there is no expectation of correlation within this range, and thus we use a uniform distribution in inclination (allowing up to 30 degrees of misalignment). Finally, we choose the semi-major axis from a uniform range between 1 and 30 AU.

In all three cases, the uniform sampling over semi-major axis does not bias our conclusions because we marginalise over semi-major axis (and later, periastron distance) in our results. We used the uniform prior to choose the orbital elements of all planets in the 4000+ trials (per system). To construct populations for the other two prior types, we resampled those initial 4000+ integrations and supplemented them with additional integrations for the Transit-inspired prior so as to have 2000 integrations for each prior. The results of a comparison between the three prior types can be seen in Figure 3.2 for a selection of example systems.

Figure 3.2 shows that the three choices of priors for the companion lead to similar results. The

three systems plotted in this figure represent two typical systems (Kepler-296, Kepler-169) and one system with particularly large CMT-instabilities (Kepler-20). For all three considered systems, the fraction of realisations that remain CMT-stable are a well-defined and increasing function of separation, measured here through the semi-major axis of the companion. The "transit prior", which has the lowest set of inclination angles for the companion, leads to a larger fraction of CMT-stable systems at $a \sim 5$ AU, but produces remarkably similar results at larger separations. In any case, for all three priors used here, the overall trend and extent of the populated region is roughly the same, even though the subtleties of the slopes may change between prior types. The differences between the systems are greater than the differences between the prior choices for a single system, so we are confident that the behaviour exhibited in our simulation results is attributable to the exoplanetary systems themselves, and not to our choice in prior.

Figure 3.3 shows the CMT stability curves for the same three systems considered in Figure 3.2. Instead of evaluating the difference of each prior type, the two curves here show the difference between the high- and low-mass (from the uniform prior, where high-mass is taken to be greater than 2 M_{jup} and low-mass is taken to be masses less than or equal to that value) values for the companion's mass. The low-mass companions are lead to a lower amount of CMT-instability in the inner system.

In Figure 3.2 and Figure 3.3, we plot the CMT-stability fraction against the semi-major axis of the perturber. This choice was motivated by our choices of priors: we naively sampled uniformly in semi-major axis with the intention to explore perturbers at all orbital radii, with the results marginalised over our three prior choices. Analogous plots to Figure 3.3 for eccentricity and inclination demonstrate significantly less variation between the high and low value populations for those quantities. As a result, we choose to plot the CMT-stability fraction against perturber periastron distance for the remainder of this work. Periastron is a more physically illustrative value than semi-major axis, since it describes the minimum distance attained between the perturber and the planets of the inner system.

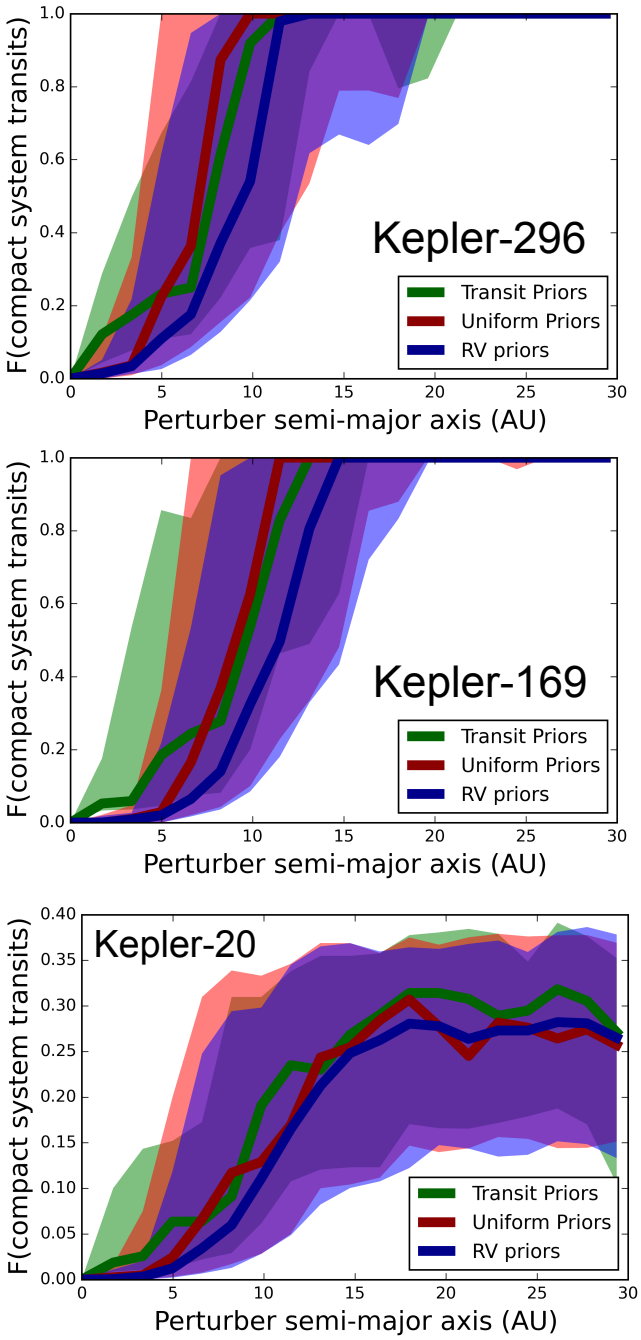

Figure 3.2 Effect of Prior on System Stability. The three different priors for the unseen companion lead to slightly different results for CMT-stability, as shown here for three representative systems. As expected, the transit prior (which has a much narrower range of allowed inclinations than the other two choices) tends to have a larger fraction of systems that are CMT-stable at close distances to the star. However, the difference is not as large as might be expected, due to the width of the Rayleigh distribution used as a prior for inclination.

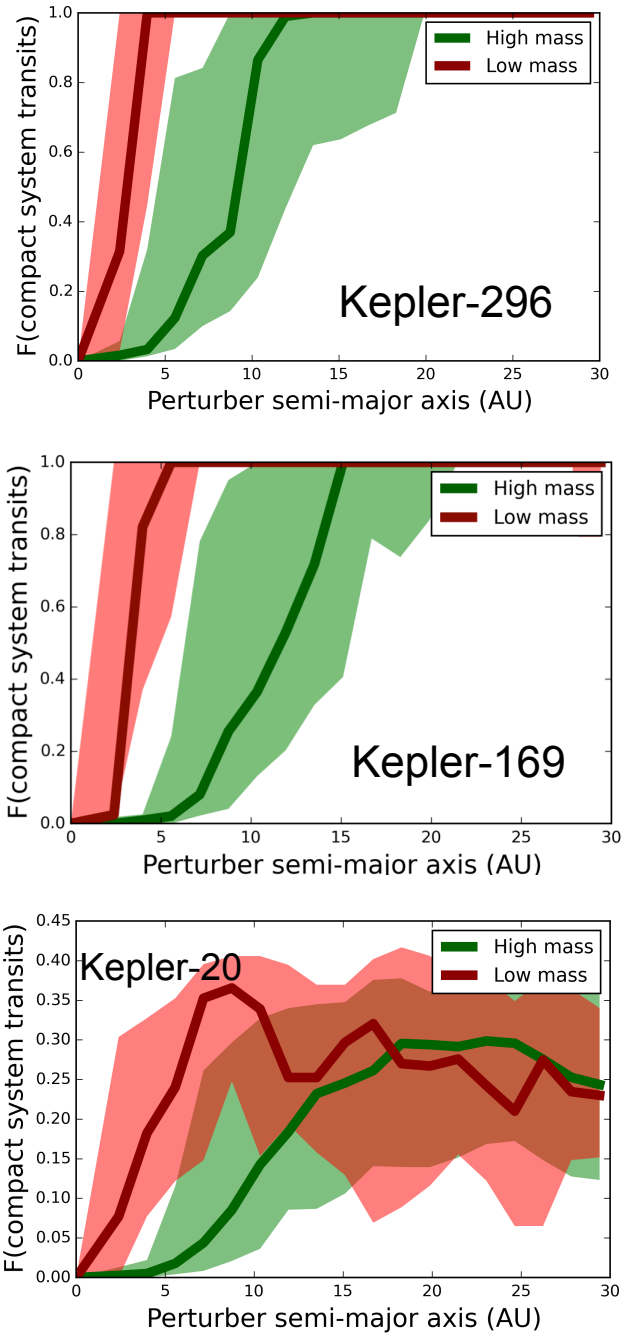

Figure 3.3 Activity Level by Perturber Type. For the same three systems considered in Figure 3.2, this figure shows the CMT-stability curves for systems with high-mass (green) and low-mass (red) perturbers. The high-mass companions cause systematically more CMT-instability of the inner system. Analogous plots for eccentricity and inclination (not shown here) do not show an obvious difference between the high- and low-quantity populations.

Priors for compact inner system of planets		
Orbital Element	Prior	Reference
semi-major axis, a	observational limits	(various[2])
planetary radius, R_p	observational limits	(various)
planetary mass, M_p	step function, converted from measured radius	Weiss & Marcy (2014c) Wolfgang et al. (2015)
inclination, i	mutual inc. from Rayleigh distribution with width 1.5^o	Fabrycky et al. (2014b)
argument of pericentre, ω	uniform on $(0^o, 360^o)$	
longitude of ascending node, Ω	uniform on $(0^o, 360^o)$	
eccentricity e	uniform on (0, 0.1)	

Table 3.1 Priors on Planetary Properties (for Kepler Multis). Priors for the Monte Carlo realisations of each planet in the observed Kepler multi-planet systems. Each system is comprised of the inner planets discovered by Kepler and a single outer, perturbing companion (whose orbital parameters are chosen using the three priors described in Section 3.3.2.1). Although mass measurements do not exist for most of these planets, the radii of the observed planets are derived from the transit light curves and stellar radii found in the literature. From these radii, we use the conversion procedures summarised in Becker & Adams (2016), which use relations from Wolfgang et al. (2015) and Weiss & Marcy (2014a) to estimate planetary mass for each realisation, which results in orbital parameters for each of the compact system planets in each studied system. (2) We downloaded best-fit orbital parameters from exoplanets.org as of January 2016, and updated when needed with parameters from Borucki et al. 2010; Lissauer et al. 2011a; Borucki et al. 2011; Fabrycky et al. 2012; Batalha et al. 2013; Borucki et al. 2013; Quintana et al. 2014; Rowe et al. 2014; Marcy et al. 2014.

3.3.2.2 Simulation Parameters

Every realisation of each system requires drawing the orbital elements for each planet, a process which has been described in Section 3.3.2.1. Once starting parameters for each planet have been chosen, we check for the Hill stability of the inner system of planets (ignoring the outer perturber) before beginning the computation for the realisation. If the initial conditions for the inner system of compact planets are not Hill stable, we discard that realisation (as it does not give us useful information about how an outer companion affects the behaviour of the inner system). We check for Hill stability, a criterion for stability that has the form

$$\frac{a_{out} - a_{in}}{R_H} > \Delta_{crit}\,, \tag{3.1}$$

where $\Delta_{crit} = 2\sqrt{3}$ is the critical separation for adjacent planets, and R_H is the mutual Hill radius, which is defined as

$$R_H \equiv \left(\frac{M_{in} + M_{out}}{3M_c}\right)^{1/3} \frac{a_{in} + a_{out}}{2}\,. \tag{3.2}$$

Since we are considering systems with more than three planets, we also require that $\Delta_{inner} + \Delta_{outer} > 18$ for each pairing of inner planets (as in Fabrycky et al., 2014b; Ballard & Johnson, 2016a). These initial conditions are intended to screen out systems where the inner system is dynamically unstable on its own, even without the perturber, due to unlucky draws from their observational priors. Since such unstable systems would not reflect the action of the perturber, these realisations are removed before the numerical integrations are run. Such cases are rare: Among the tens of thousands of realisations run, only a handful were discarded because of their failure to meet these constraints.

After the starting parameters for all bodies in the system are chosen and the inner system is confirmed to be Hill stable, we integrate the realisation forward for 10^7 years. If, during this time, any planets are ejected from the system, collide with the central body, or undergo a close encounter within 3 mutual Hill radii of another planet, we stop the integration and consider the system to be disrupted, and thus dynamically unstable for our purposes (this approach is consistent with the criteria used in other work such as Fabrycky et al., 2014b). We do not consider spin or tidal effects,

as additional evolution due to these effects would be inconsequential on the timescales we consider. We use the hybrid symplectic and Bulirsch-Stoer (B-S) integrator built into Mercury6 (Chambers, 1999b), and conserve energy to 1 part in 10^8.

To perform these computationally intensive simulations, we make use of both the Open Science Grid (Pordes et al., 2007; Sfiligoi, 2008) accessed through the Extreme Science and Engineering Discovery Environment (XSEDE; Towns et al., 2014), and personal computational resources for the simulations used in this work, with the bulk of numerical integrations being run by the former. In all cases, each integration was run on a single core. At least 4000 realisations were run for each system. The integrations were generally completed in less than 24 hours, with most integrations taking less than 6 hours to run to completion. The simulations resulted in more than 3 Terabytes of data files, and took roughly 100,000 CPU hours to generate. We integrated all of the 15 Kepler systems with 5 or more planets. After all integrations were complete, we also ran integrations of three representative four-planet systems, in order to verify that they exhibit similar behaviour.

Figure 3.5 and Figure 3.4 show each individual realisation of Kepler-102 and Kepler-20, respectively, as circular points, where we plot the fraction of time a compact inner system is CMT-stable in the presence of a companion with the periastron value given on the x-axis. These plots (and all analyses presented in this chapter) are marginalised over all of the other orbital elements chosen for the perturber. The population of points are significantly different for each system. Figures 3.5 and Figure 3.4 show two examples of systems: Kepler-20 is CMT-unstable a significant fraction of the time, for almost the full range of companion properties, although smaller orbital radii for the perturber do lead to an increase in CMT-instability (as expected). On the other hand, Kepler-102 has a clear threshold at roughly 10 AU where, external to this point, companions generally do not disrupt the behaviour of the inner system.

3.4 General Results: Limits on Unseen Companions in the Kepler Sample

In this section, we present the results of the simulations detailed in the previous section.

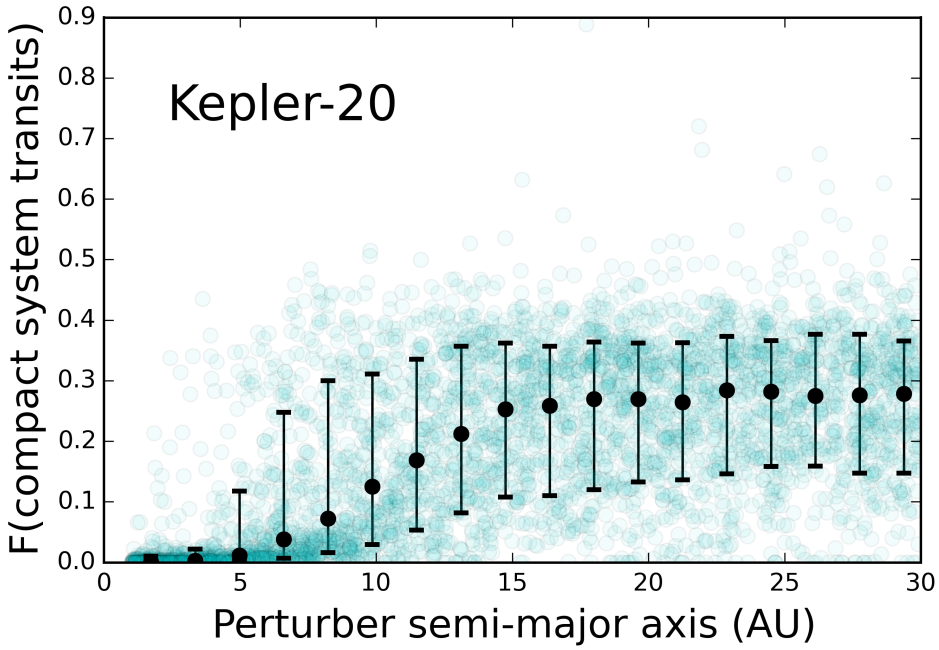

Figure 3.4 Kepler-20's Susceptibility to Destabilization. The Kepler-20 system appears to be an outlier in our sample of multi-planet systems, and is highly susceptible to being perturbed into a CMT-unstable configuration by a companion. For any companion with orbital separation in the range $a = 1 - 30$ AU, the inner system will be seen to be mutually transiting less than half (about one third) of the time. This result strongly suggests that if an additional close companion exists in this system, it is unlikely that we would see all of the planets in the inner system to be transiting.

3.4.1 General Trends

For all systems considered in this work, the general trend holds that pertubers closer to the compact system of planets causes a greater amount of movement out of the transiting plane by those inner planets. This mechanism can lead to the known planets in each system attaining non-transiting configurations (CMT-instability), meaning that they would not have been discoverable by the *Kepler* mission. There are two modes of motion due to an exterior companion that can lead to the aforementioned effects: (1) the excitation of relative inclination angles between the planets in the inner compact system, leading to an increase in the width of the inclination plane containing the compact system planets, and (2) Kozai-esqe oscillations of the entire plane of transiting planets, which may precess together. Both of these effects may occur, and both are encapsulated in our numerical integrations. Mode (1) will determine whether or not a system of planets can be seen in transit from any line of sight. In contrast, mode (2) could lead to a situation in which the system is not seen in transit from Earth's line of sight, but could be seen from another line of sight. For the sake of definiteness, we define the term CMT-stability to mean that the planets are continually mutually transiting from the original line of sight observed by Kepler (more specifically, all of planets can be seen in transit more than 95% of the time). This definition thus implies that both oscillation modes (1) and (2), as defined above, lead to CMT-unstable systems.

Figure 3.5 shows the Kepler-102 system, which serves as an example of the typical trend and demonstrates the different regimes of behaviour that can be excited by the injection of a perturbing companion into a known planetary system. In this figure (and everywhere in this chapter), the criterion F(compact system transits) = 1 means that the inner system of planets (which includes only those discovered to be transiting in the Kepler data) is continually mutually transiting. In other words, all planets can be seen to be transiting from Earth's line of sight for all time in the presence of the any considered perturbing companion. In contrast, the criterion F(compact system transits) = 0 means that the inner compact system that was found to be transiting by the Kepler mission will never attain a mutually transiting configuration in the presence of that companion. Figure 3.5 shows that for companions with orbits beyond 10 AU, the Kepler-102 system will continue to be mutually transiting. The fact that the Kepler spacecraft observed the Kepler-102 system to be transiting thus cannot exclude any companions beyond 10 AU. However,

for companions with periastron less than $\sim$ 5 AU, the Kepler-102 compact system will attain a non-transiting configuration a large fraction of the time, making it less likely that we would have discovered it.

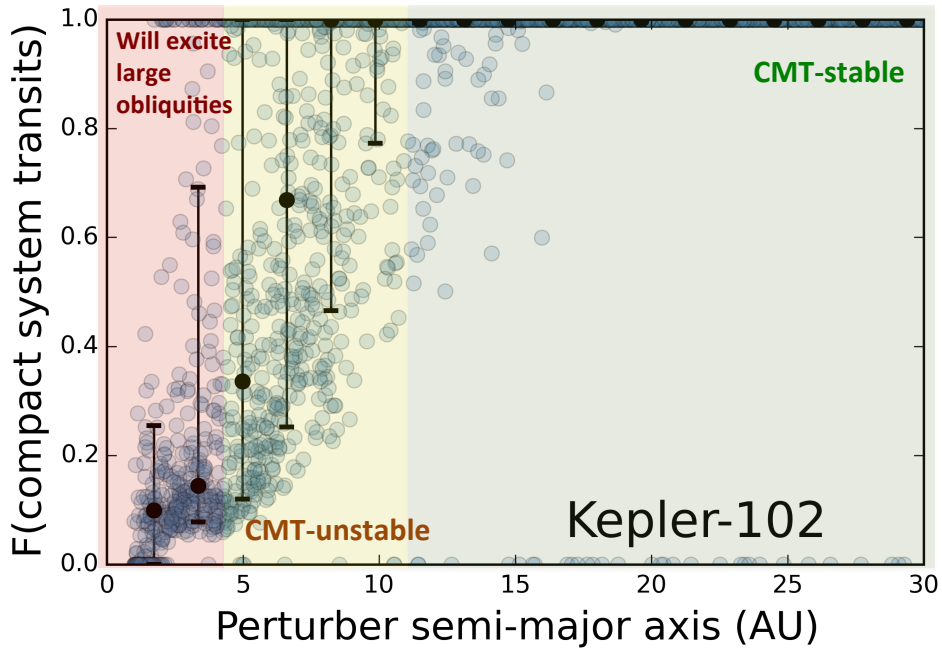

Figure 3.5 Fractional CMT-Stability by Perturber Properties: Kepler-102. The fraction of the time that the entire compact system transits depends on the orbital elements of the perturbing body. Here, this fraction is plotted against periastron of perturber for Kepler-102, where the non-transiting disk prior was used to choose companion orbital elements. If the body is far away from the inner planets, then that companion exerts only minimal perturbations on the compact system of planets, and the system will be CMT-stable, just as expected if no perturber is present. For an intermediate range of perturber parameters, the system will be CMT-unstable, but no large obliquities will be excited. For a selection of perturbing bodies, not only will the inner system be CMT-unstable, but the orbits of the planets in the compact system will become highly misaligned relative to their initial locations. These three regions for Kepler-102 are shown and labelled in the figure. Similar plots can be made for all stars in our sample, and for each of the sets of priors. The location of the different regimes depend on the properties of the planets and their orbits.

From the data used to construct Figure 3.5, and the analogous plots for the other planetary systems, we have computed the minimum periastron distance that allows the inner systems to remain in a CMT-stable configuration 95% of the time. This threshold at 95% ensures that the systems are likely to remain observable by Kepler over secular timescales, but the exact value is

arbitrary. These periastron values (computed for the 95% threshold) are useful for comparing the relative stability of systems, and for predicting/constraining the possible locations for any additional massive, external companions in these systems. This analysis was carried out for each system in our sample using each of the three prior choices described in Section 3.3.2.1. The results of this computation (for all systems and all priors) are presented in Table 3.2.

As outlined above, these limits correspond to the companion periastron required for the Kepler compact system to remain CMT-stable 95% of the time. The limits vary slightly between the three prior choices, demonstrating the effect of the priors of this dynamical analyses. The spread between the three prior choices $\delta p/p$ attains a median value of 11% and a mean value of 13% over the entire population of systems considered (the higher mean is due to the Kepler-32 system, which experienced particularly large variation between prior choices – if Kepler-32 is excluded from the sample, then the mean and median $\delta p/p$ values become equal). As a result, for the systems considered in this work, the choice of priors affects our results for the threshold values of the companion periastron at the level of 10-15%.

Each of these systems show the same general trend: For companions with sufficiently large orbital separations, the inner system becomes effectively decoupled from the perturber, so that the system is expected to stay in a CMT-stable configuration. In this context, the definition of being "sufficiently large" is given by the periastron values listed in Table 3.2. These results also depend on other properties of the compact systems. We provide limits in terms of periastron rather than semi-major axis, which folds in the distribution of eccentricity for each prior type. We also generated the limits in terms of semi-major axis, and the values were not significantly different. Periastron is a good variable to use here for two reasons: first, the periastron describes how close the outer planet gets to the inner system of planets, which controls the magnitude of mean motion-based perturbations; second, the high- and low-eccentricity cases (constructed and discussed in Section 3.3.2.1) do not exhibit significantly different behaviour, so our parametrisation in terms of periastron will not occlude any physical effects. For each planetary system, Table 3.2 also lists the surface density of the system, the corresponding angular momentum, and the inner system size (given by the semi-major axis of the outermost planet of the inner system). The outer radius of the compact system is included because planets with larger semi-major axis have lower

transit probabilities. Naively, it might seem that these systems would be easier to force into a non-transiting configuration. However, this expectation does not hold — the systems with the largest inner system radius are not necessarily those which are least CMT-stable in the presence of a companion. The dynamics of the inner system, not just the value of R_*/a, determines the CMT-stability of a system.

3.4.2 Surface Density as a predictor for susceptibility to perturbations

The results presented in Table 3.2 give the relative radii within with you expect significant misalignment to arise. Naively, it might seem that non-transiting planets will be observed more often in systems where the inner system has a larger outer radii (i.e., the semi-major axis of the furthest-out planet is larger). However, this value a_{out} does not predict the susceptibility of an inner system to perturbations. Instead, a better tracer of how susceptible a system is to perturbations is the surface density of the inner system of planets. In Figure 3.6, we plot the fraction of time that a system is CMT-stable as a function of the periastron of the distant perturbing planet. The lines are colour-coded by the surface density of the observed compact inner systems. The plotted surface densities were calculated by computing the surface density, Σ, of each realisation of the system according to the definition

$$\Sigma = \frac{1}{\pi(a_n^2 - a_1^2)} \sum_{i=1}^{n} m_i \,, \tag{3.3}$$

where n is the number of planets in the system, with planet n being the outermost planet, m_i are the planetary masses, and a_i are the orbital radii. Since we draw masses and periods from observationally-inspired priors, the exact value of the surface density varies between the different trials of our numerical integrations. For this plot, the chosen value of surface density was taken to be the median value of the surface density for all realisations of that system. The error on surface density, which is given for each system in Table 3.2, is given by the 1σ spread over all of the realisations.

If the surface density is higher, then the inner system acts more like a single ring, and perturbing bodies need to be closer to the inner system in order to excite individual inclinations away from a

System	N_p	Surface density	Angular momentum	a_n (AU)	$p_{\rm uniform}$ (AU)	$p_{\rm transit}$ (AU)	$p_{\rm disk}$ (AU)	$\rm F_{\mathit{jup}}$
Kepler-102	5	136 ± 26	20 ± 4	0.17	8.15	7.03	6.97	2%
Kepler-11	6	113 ± 10	206 ± 18	0.47	≥ 30[1]	≥ 30	≥ 30	0%
Kepler-122	5	406 ± 51	131 ± 16	0.23	8.57	8.3	7.2	0%
Kepler-169	5	55 ± 5	54 ± 5	0.36	14.7	13.15	11.7	4%
Kepler-186	5	19 ± 1	16 ± 1	0.43	19.5	16.4	15.2	1%
Kepler-20	5	77 ± 7	65 ± 8	0.35	≥ 30	≥ 30	≥ 30	2%
Kepler-292	5	534 ± 61	54 ± 7	0.14	6.9	6.9	5.4	18%
Kepler-296	5	98 ± 14	37 ± 6	0.26	11.6	10.1	10	1%
Kepler-32	5	539 ± 59	35 ± 4	0.13	8.7	11.8	7.03	0%
Kepler-33	5	473 ± 39	272 ± 23	0.25	≥ 30	≥ 30	≥ 30	0%
Kepler-444	5	48 ± 3	1 ± 1	0.08	6.3	5.5	5.1	8%
Kepler-55	5	240 ± 24	49 ± 4	0.20	8.5	10.6	7.5	0%
Kepler-62	5	11 ± 2	48 ± 9	0.72	≥ 30	≥ 30	≥ 30	0%
Kepler-84	5	184 ± 21	81 ± 9	0.25	7.4	9.8	7.2	2%
Kepler-90	7	48 ± 3	901 ± 53	1.01	≥ 30	≥ 30	≥ 30	0%
Kepler-150	4	352 ± 29	75 ± 6	0.19	8.3	6.9	5.6	4%
Kepler-197	4	82 ± 4	13 ± 1	0.16	6.9	6.9	6.7	11%
Kepler-402	4	571 ± 73	28 ± 3	0.10	5.2	5.3	5.3	16%

Table 3.2 Orbital and Physical Properties of High-Multiplicity Systems. Physical properties of each system considered in this chapter, along with the derived limits for the periastron of possible perturbing companions, when N_p is number of planets in each system. The periastron limit $p_{\mathbf{prior}}$ is the value of perturber periastron above which the inner system is CMT-stable 95% of the time, also marginalised over all other properties of the perturber (including periastron) for each selection of prior. The scale a_n is the outer orbital radius of the inner, compact system. For the three different types of priors, slightly different limits are computed, with the transit prior generally producing the more dynamically quiet systems. See Section 3.3.2.1 for a description of each of the three priors used. A selection of four-planet systems, which were not part of the original sample but included to check if the trends shown in Figure 3.6 appear to persist for additional systems, are presented in the lower part of the table. $\delta p/p$ between the three priors is a median of 11% and a mean of 13% for all systems, demonstrating that prior choice can affect dynamical stability in analysis of this nature to the 10-15% level. The final column, $\rm F_{\mathit{jup}}$, is the results of a separate experiment, where Jupiter-type planets (1 $\rm M_{\mathit{jup}}$ at 5 AU, with inclination and eccentricity similar to Jupiter's values) were injected into the system instead of the previously discussed perturbers. $\rm F_{\mathit{jup}}$ is the percentage of these realisations that were CMT-stable in the presence of this true Jupiter-like planet. (1) 30 AU is the maximum orbital separation tested for the perturber in our simulations, so this designation implies that the presence of any perturber within 30 AU causes the inner system to be CMT-unstable according to our simulations. The true limit for CMT-stability 95% of the time cannot be determined from our simulations.

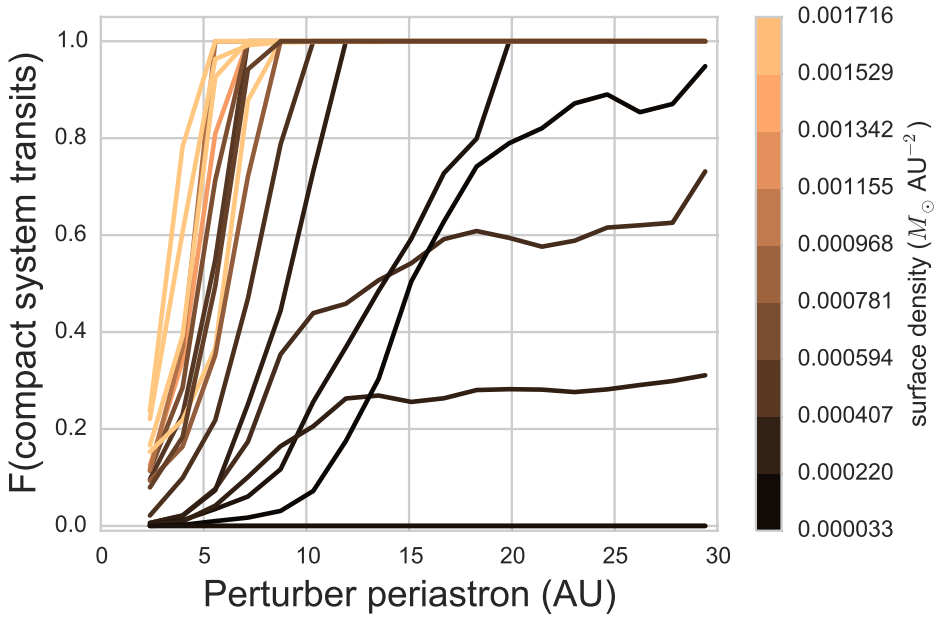

Figure 3.6 Fractional CMT-Stability by Perturber Properties: All Systems. The fraction of time a system is CMT-stable as a function of the periastron of the injected perturbing body, marginalised over all other properties of the perturber. Each line represents a different system, with the colour of the line showing the surface density of the compact inner system (computed using Equation 3.3). The colour bar on the right shows the scale. Systems with higher surface densities tend, with good uniformity, to allow a larger array of perturbing companions without becoming CMT-unstable.

mutually transiting configuration. It is clear from Figure 3.6 that surface density maps (almost) monotonically onto the periastron distance at which CMT-instability does occur. On the other hand, the periastron of the perturbing body is not the only quantity of interest. To construct Figure 3.6, we marginalised over the orbital parameters of the outer companion, using the non-transiting disk prior (see Section 3.3.2.1). An analogous plot can be constructed for the other priors types, but all three priors will produce results consistent on the 10-15% level (the value of periastron for the companion required to render the systems CMT-unstable varies by this amount over the different choices of priors).

Intuitively, the impact periastron distance has on the CMT-stability of the inner system makes sense because the periastron distance controls how closely the perturbing body passes to the inner system. In Becker & Adams (2016), we used secular theory to evaluate the long-term behaviours of these same systems. The expanded disturbing function in secular theory depends most strongly on semi-major axis, so the dynamics considered here must depend sensitively on a. In addition, eccentricity allows the companions to pass closer to the inner system. Previous studies have shown that the periastron of the perturbing companion is the most important variable for ejecting planets (David et al., 2003) and for stifling the formation of planets in binary systems (Quintana et al., 2007). As a result (and for brevity), we do not provide plots for CMT-stability as a function of mass, eccentricity, inclination, and other orbital properties.

In Figure 3.7, we plot the periastron of the most distant perturbing planet that allows the inner compact system to remain CMT-stable (mutually transiting 95% of the time) as a function of the surface density of the observed compact inner systems. The periastron values were taken from interpolated versions of the curves shown in Figure 3.6. For most of the transiting systems in our sample, a perturbing companion must be roughly $10 - 20$ AU away (or more) from the host star in order for the compact inner system to have a high probability of being observed in the configuration discovered by the Kepler mission. Note that systems with the largest orbital radius of their respective inner systems tend to have the lowest surface densities. This trend could suggest that they are either stalled at an earlier stage in their migratory histories (having not collapsed to the size of the smallest, densest multi-planet systems) or that our observations are incomplete. It remains possible that this trend reflects the diversity of possible planetary configurations.

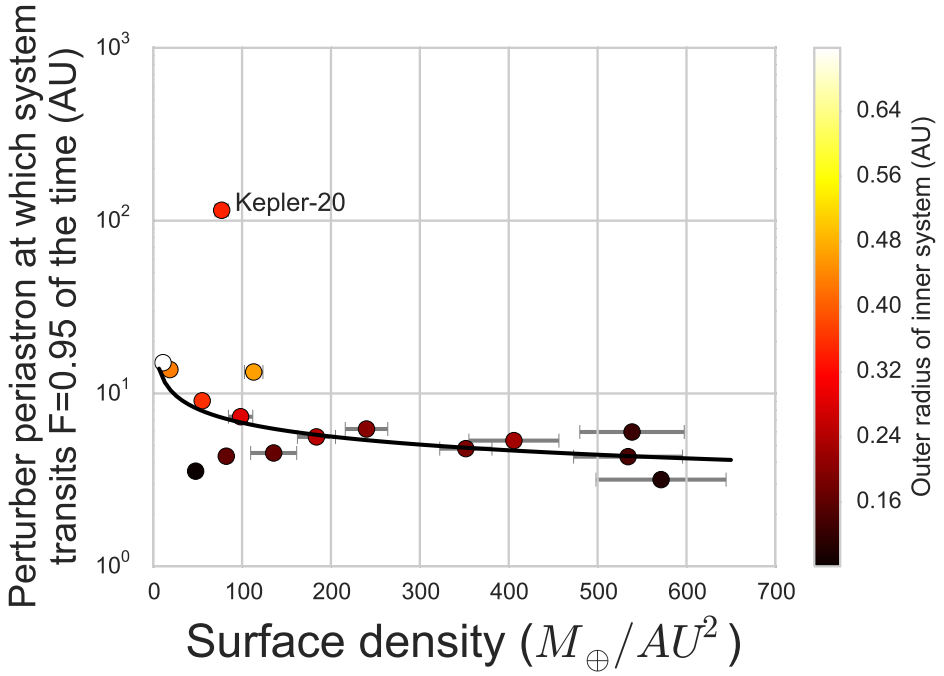

Figure 3.7 Allowed Perturbing Planet Locations by System Surface Density. The periastron of the most distant perturbing planet that allows the inner compact system to remain CMT-stable (mutually transiting 95% of the time), shown here as a function of the surface density of the observed compact inner systems. When the perturbing body has a sufficiently large orbit, it becomes effectively decoupled from the inner system. It is important to note that the lower surface density systems tend to have a larger radius within which companions would lead the inner system to be CMT-unstable. Kepler-20 appears to be a clear outlier compared to the other systems, with a large range of potential companions leading the inner system to be CMT-unstable. If the error bar is not visible, the error is smaller than size of the plotting symbol. The curve shows a model fit to all points except that of Kepler-20.

Using the limited number of systems analysed in this work, we can derive an approximate scaling relation that delineates how far a perturber must reside from the central body in order to excite CMT-instabilities in a transiting system with a given surface density. The model curve plotted in Figure 3.7 is a power-law, which was fit with a simple least-squares optimisation, with approximate best-fit functional form $p = 6.60 \text{ AU } (\Sigma/\Sigma_0)^{-0.27}$, where Σ is the surface density of the inner system of planets and p is the periastron beyond which companions do not disrupt the CMT-stability of the system 95% of the time. The constant $\Sigma_0 = 100\ M_\oplus \text{ AU}^{-2}$ is a reference surface density. This relation defines the region outside of which a companion could exist without affecting the inner system, i.e., so that it would not alter the transits of the observed planets. In contrast, any companions found within this boundary could cause significant misalignment of the orbital inclinations, perhaps knocking some inner planets out of an observable, transiting, configuration.

This relation is limited in two ways: First, the number of systems under consideration is small, by necessity, so that additional systems could display more complicated behaviour. Second, the relation is approximate, and depends on both the priors used and the relatively few low surface-density systems. As a result, this relation does not provide a definitive statement on the companion status of any particular system.

3.4.3 Examining the effect of Jupiter

Our own solar system has a gas giant planet with mass $m_P = 1 M_{\text{jup}}$ with semi-major axis $a \approx 5$ AU. The results of Table 3.2 indicate that 5 AU often falls within the radius at which additional companion cause the inner system to become misaligned. As a result, a true Jupiter analogue is unlikely to exist in any of these systems. However, the previous trials do not directly test for this possibility because the inclination variation of all three prior choices is larger than that of a true Jupiter analogue. For this reason, we performed an additional set of numerical simulations. In the work described thus far, we examined the effect that a perturber of varying orbital properties could have on compact systems of planets. However, it is also interesting to determine how the presence of a true Jupiter analogue would affect the CMT-stability of these systems. Toward this end, we ran another 100 realisations per system, including a Jupiter analogue as the perturber with

the following priors on its orbital elements: The mass is taken to be 1 $M_{\rm jup}$ and the semi-major axis $a = 5$ AU. The eccentricity is drawn from a uniform distribution in the range [0,0.05], and the inclination is drawn from a uniform distribution with a full width of 6 degrees, thus allowing the planet to attain a maximum inclination of three degrees out of the plane containing the inner system. All of the other orbital angles were randomised. We integrated these new realisations for 10 Myr and evaluated the fraction of the realisations that remained CMT-stable (mutually transiting 95% of the time). These percentages are reported in the final column of Table 3.2. In all but two of the systems containing more than four planets, more than 95% of trials were CMT-unstable. All of the systems were CMT-unstable a majority of the time. This finding indicates two things: First, it is unlikely that a Jupiter analog planet exists in any of these systems. Second, if such a system were to host a Jovian analog planet, it would (generally) lead to oscillations of the inclination angles of the orbits of the inner system. As a result, there could be additional unseen planets in the compact, inner part of that system.

The discussion thus far has not taken into account the stellar-spin axis, in particular its direction with respect to the orbital angular momentum vectors of the compact inner system. Morton & Winn (2014a) found that the obliquities of multi-planet systems tend to be lower than those in single-planet systems. [2] If the stellar-spin is observed to be aligned with the orbits, as seems to be common from observational results for multi-planet systems, then the most likely scenario is that the all of the angular momentum vectors point in their original directions. It is unlikely that both the stellar spin and all of the planetary orbits were disrupted in such a way that they maintain alignment. In contrast, systems with an observed misalignment between the stellar spin-axis and the orbital angular momentum vectors could have a variety of dynamical histories. One possibility is that the orbital inclination angles for the entire inner compact system are oscillating as a whole in response to a perturbing companion. Huang et al. (2017) and Gratia & Fabrycky (2017) both consider this mechanism in depth, and find that it is a feasible method of causing planet-star misalignment. Moreover, a number of other effects could lead to the stellar spin pointing in a different direction than the angular momentum of the planetary system. Possible processes include

[2]Some exceptions are expected. As one example, the Kepler-108 system, which hosts two planets, is thought to be misaligned (Mills & Fabrycky, 2017a). Another example is the well-studied, misaligned Kepler-56 system (Huber et al., 2013).

natal misalignment, interactions with unbound bodies, tidal precession, and many others. All of these effects should be explored in future work.

3.5 Results for Specific Systems

In addition to the general results presented in Section 3.4, this analysis also produces predictions and insights for individual systems. Here we consider the cases of Kepler-20 and WASP-47.

3.5.1 Kepler-20

Kepler-20 appears to be an outlier among the systems considered in this work, as shown by its unique placement in Figure 3.7. Kepler-20 requires an unusually large orbital separation between the added perturber and the inner system in order for the inner system to remain CMT-stable. Taken alone, this placement on the plot indicates that Kepler-20 is particularly susceptible to the effect of a companion; it is quite easy for a perturbing companion to knock the inner system into a non-transiting configuration.

This seems to be evidence of one of two things: either (1) there is no external companion in this system, because its existence would not allow the entire inner system to transit, or (2) the entire inner system is not transiting (the system is NOT continually, mutually transiting) and there is another planet that we do not know about.

The Kepler-20 considered in this work only included five planets, the original five reported in Gautier et al. (2012) and Fressin et al. (2012). After we had completed our simulations for this work, however, this system was found to host an additional planet with minimum mass 20 M_{earth} in an approximately 34-day orbit. This places the orbit of the new planet *between* the 20-day period Kepler-20f and the 78-day Kepler-20d (Buchhave et al., 2016). Because this newly detected planet lies between the orbits of the previously known planets, and because it was not observable by Kepler but is observable in the RV, it is likely to be slightly out of the transiting plane. The Kepler-20 system thus hosts five transiting planets and one non-transiting planet, with all six planets packed in a compact system. We now know that (2) is the correct conclusion for this particular system, which does not exclude the possibility that there is also an exterior, perturbing companion.

Additional work will help determine if such a companion is present, or if another explanation exists for the unusual configuration of Kepler-20. In general, compact planetary systems tend to have regularly spaced orbits, where all of the planets are seen in transit. If a system has a gap in its orbital spacing, there could be an additional massive planet of the type considered here.

3.5.2 WASP-47

The WASP-47 system was known to host a hot Jupiter (Becker et al., 2015b), was later found to contine two additional planetary companions with orbital periods less than 10 days (Hellier et al., 2012a). A super-Earth companion was discovered just inside the orbit of the hot Jupiter and a Neptune-sized planet was found just outside. Neveu-VanMalle et al. (2016a) reported simultaneously that the system also has a Jovian external perturber, a companion with $m \sin i = 1.24\ M_{\rm jup}$ and a period of 572 days. The hot Jupiter in this four-planet system was also found (Sanchis-Ojeda et al., 2015b) to have its orbital angular momentum vector aligned with the stellar spin axis of the star (implying that the two other transiting planets are also roughly aligned).

The fact that the inner three planets in the WASP-47 system appear to remain in their birth plane suggests that the external companion must allow for the persistent CMT-stability of the inner three-planet system. Because the RV measurements of the outer companion only determine the quantity $m \sin i$, and not the true mass, we do not know whether the companion is a highly inclined brown dwarf or a roughly co-planar Jovian planet. Using the techniques from this chapter, however, we can place probabilistic limits on the inclination and mass of the outer body in this system.

Toward that end, we ran 1000 integrations of the WASP-47 system for 10 Myr each. The orbital properties of the inner three planets were drawn from the posteriors found in Hellier et al. (2012a) from the transit and transit-timing-variation fits. For completeness we note that Dai et al. (2015) also provides mass estimates of the three inner planets from RV measurements, but the results are consistent with the TTV-estimated masses used here (within 1σ uncertainties). The inclination of the outer planet was allowed to vary over the full range from 0 to 90 degrees (we expect the 90 degree to 180 degree range to be symmetric; notice also that $i = 90$ degrees is defined as the midpoint of the transiting plane, i.e., where the inner three planets reside). The mass of the outer

planet was chosen for each trial to satisfy the observed $m \sin i$ measurement within the reported errors given the assigned inclination for that trial. The results are plotted in Figure 3.8.

In this systems, the spin-axis of the star is observed to be aligned with the orbital angular momentum of the inner three planets, so that the system is likely to have formed with such an alignment. The inclination of the orbit of the outer companion is unknown *a priori*. Our numerical results show that in order for the inner system to remain CMT-stable most of the time, the inclination of WASP-47c cannot be more than 2-3 degrees out of the transiting plane at 90 degrees (the plane that contains the inner three planets). Since the semi-major axis of WASP-47c is large, the inclination of its orbit can easily be large enough that the planet does not transit (as observed) but still lies within a couple degrees of the plane (as required by CMT-stability) — the inclination only needs to be a few tenths of a degree to keep WASP-47c from transiting. Notice also that further refinement of the masses of the inner system of planets will allow for a more robust exploration of this constraint.

The observed alignment between the spin-axis of the star and the angular momentum of WASP-47b's orbit, combined with the suggestion that WASP-47c is likely roughly coplanar with all three planets of the inner system, indicates a dynamically quiet history for the system. Indeed, it is easier to knock a system out of alignment than return it to alignment, so it is unlikely (although not impossible) that the WASP-47 system is dynamically active and we see it at an opportune moment. It is more likely that WASP-47 formed and migrated (in either order) in a dynamically quiet manner.

3.6 Conclusions

In this work, we have considered a collection of 18 Kepler multi-planet systems and evaluated their CMT-stability in the presence of a perturbing Jovian companion with a semi-major axis between 1 and 30 AU. A system that we define to be **C**ontinually **M**utually **T**ransiting is expected to remain transiting from our line of sight over many secular periods. In contrast, a system in a CMT-unstable configuration would be not be visible in transit all the time — sometimes one subset of planets might be visible, and another time a different subset might be visible. The sample we

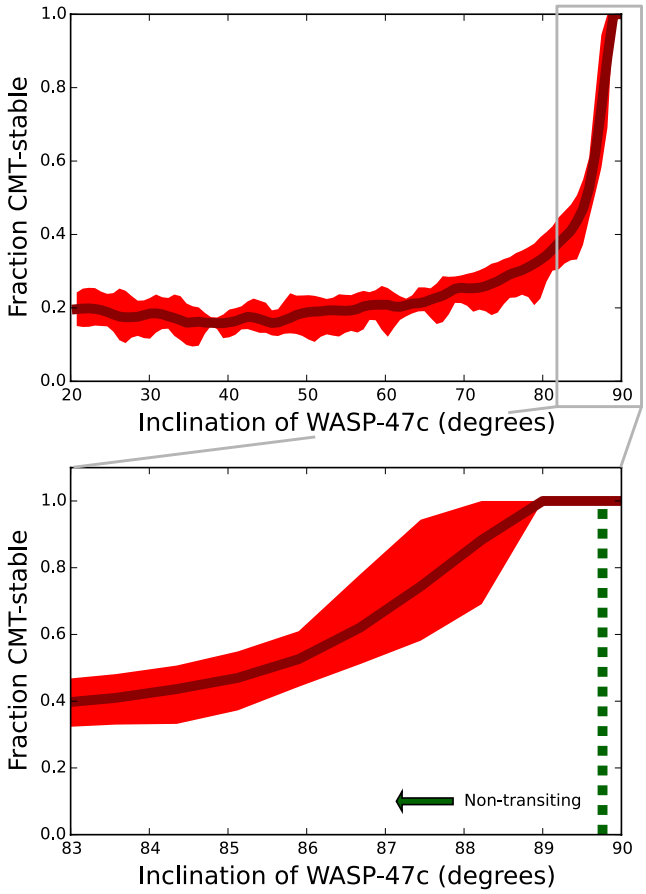

Figure 3.8 Stability of Inner Planets in WASP-47 System by Companion Properties. WASP-47, a good example of a planetary system with both a tightly packed inner system (WASP-47e, -47b, and -47d) and an outer perturber (WASP-47c) is a good test case for the methods used in this chapter. The line shows the median fraction of time the inner system is CMT-stable for a given inclination, and the color-block shows the entire parameter space populated by the 1000 trials. The CMT-stability of the inner system decreases to a paltry 20% if the outer companion is allowed to attain a significant inclination out of the plane containing the other planets (which, in parameterization, is the plane centered at 90 degrees). There is a large area in parameter space that allows the inner system to be CMT-stable and the outer planet to be non-transiting (see lower panel).

consider was chosen to include all observed systems with five or more planets, along with some additional four-planet systems for comparison. The total number of systems analyzed was limited by computational resources.

This work presents both general results and specific results for particular systems. We find that massive, close-in companions to the observed Kepler multi-planet systems will lead to CMT-instability. Table 3.2 gives the limits for each of the systems analyzed in this work. For most of the systems in the sample, the fraction of time that the system remains CMT-stable approaches unity at a well-defined value of the companion periastron (see Figure 5). Moreover, these periastron values fall in the range $p = 5 - 15$ AU for the majority of the systems. The specific values, for each of the sets of priors, are given in Table 3.2.

From the population of systems explored here, we can also deduce general limits on the presence of possible companions. These systems can remain CMT-stable provided that the companion periastron is greater than $p = 5 - 30$ AU, although some systems saturate this outer limit so that any companions must reside in even wider orbits. At one extreme, systems can be rendered CMT-unstable with a planet comparable in mass and orbital radius to Jupiter (e.g., Kepler-402). Most systems require companions to reside beyond $p \sim 10$ AU, whereas some systems are so sensitive to inclination angle oscillations that companions must lie beyond 30 AU. We can thus draw the following conclusion: If exterior companions (with periastron inside of 10 AU and masses of a few $M_{\rm jup}$) were common, we would often expect to see significant mis-alignments in at least some of the observed multi-planet systems. Since we do not see this effect in the sample, it is unlikely that this type of companion is common in the observed multi-planet systems.

We also find that the surface density of a compact system of planets can serve as a good prediction for whether systems are CMT-stable. Low surface density systems tend to be more susceptible to perturbations by additional companions (see Figure 6).

In addition to the general analysis summarized above, we considered the effects of adding Jupiter-analog planets (with mass of 1 $M_{\rm jup}$ and $a = 5$ AU) into the compact systems. The CMT-stability of the resulting systems is greatly compromised; these results are also presented in Table 3.2. This numerical experiment shows that none of the compact Kepler systems are allowed to have a Jupiter analog. If such a planet were present, the system would (almost always) be driven

to CMT-instability, so that the full set of planets would not be observed in transit.

This dynamical treatment also provides results for particular systems, specifically, WASP-47 and Kepler-20. The WASP-47 system is one where an analysis of this nature proves particularly useful: In order for the inner three planets of the system to remain CMT-stable, the inclination angle of the fourth (more distant) companion must be small, which in turn implies that it has a planetary mass (rather than a larger mass with the orbit observed at high inclination). In other words, CMT-stability of the WASP-47 system predicts that the fourth planet must be at low inclination with mass $m \approx m \sin i$. The finding that all four planets in this system exist in a roughly coplanar configuration has implications for the formation scenario of this system, and suggests that the system formed and migrated dynamically quietly. More work should be done to understand the dynamical history of this particular system, whose inclination spread is analogous to our own solar system.

Kepler-20 is another intriguing system. Our simulation results for the five-planet Kepler-20 showed that the system was particularly susceptible to excitations from a companion at a large range of orbital separations. Kepler-20 became CMT-unstable a large fraction of the time. A solution was recently found for this puzzling observation: Kepler-20 was recently discovered to have a sixth planet orbiting in a non-transiting configuration in between the orbits of the previously discovered planets. Since not all planets in the inner system of Kepler-20 actually transit, this case is actually a CMT-unstable system, as the inner compact system of planets does not continually, mutually transit.

In this work, we considered three choices for the priors used to specify the orbital properties of the companion: a uniform prior, a transit-inspired prior, and non-transiting disk prior. The results described above are largely insensitive to the choice of priors. We can quantify this effect as follows. The main result of this analysis is the threshold value of companion periastron, where companions must have larger values in order to not render the inner system CMT-unstable. These values are listed in Table 3.2. The spread between the three prior choices $\delta p/p$ are on the order of 10%-15%, so that this variation provides an estimate on the uncertainty of our quoted periastron thresholds.

For all three choices of priors, we have identified some Kepler systems as being probabilistically CMT-unstable in the presence of any additional perturbing companion (of the type considered

here). This result implies that if any additional, perturbing body were in the system, we would not expect all of the inner system planets to transit (at least not most of the time). These highly susceptible systems are Kepler-11, Kepler-20, Kepler-33, Kepler-62, and Kepler-90. If these systems actually have the planetary properties that are currently reported, then these systems are unlikely to host additional companions. In other words, either these planetary systems have no additional companions (of the class considered here) or their properties are not determined correctly.

It is interesting to note that the systems least capable of hosting an additional companion (see Table 3.2) fall into two categories. First, systems may have a large surface density (Kepler-33), which may be too tightly packed, such that any small perturbation from a companion excites the system into a non-CMT-stable state. Second, and more common, are systems like Kepler-90, Kepler-62, Kepler-20, Kepler-186, and Kepler-11, which have lower surface densities. The planets in these systems will attain higher inclinations more easily. The results of this work imply that the second case is more common. In other words, planetary systems with surface densities low enough to be easily perturbed are more common than the extremely dense ones. An extended analysis of additional Kepler, K2, and TESS systems will determine if this apparent trend holds. As more systems are discovered and characterized, the techniques of this chapter will be useful in constraining their possible architectures.

CHAPTER IV

Discovery of Two Additional Nearby Planetary Companions to Hot Jupiter WASP-47 b and Precise Density Determinations

Results in this chapter were published in: ***Becker, J. C.***, *Vanderburg, A., Adams, F. C., Rappaport, S. A., Schwengeler, H. M. 2015. WASP-47: A Hot Jupiter System with Two Additional Planets Discovered by K2. The Astrophysical Journal 812, L18.* and *Vanderburg, A.,* ***Becker, J. C.****, and 33 colleagues 2017. Precise Masses in the WASP-47 System. The Astronomical Journal 154, 237.* and are presented here with moderate revisions.

4.1 Abstract

Using new data from the K2 mission, we show that WASP-47, a previously known hot Jupiter host, also hosts two additional transiting planets: a Neptune-sized outer planet and a super-Earth inner companion. We measure planetary properties from the K2 light curve and detect transit timing variations, confirming the planetary nature of the outer planet. We performed a large number of numerical simulations to study the dynamical stability of the system and to find the theoretically expected transit timing variations (TTVs). The theoretically predicted TTVs are in good agreement with those observed, and we use the TTVs to determine the masses of two planets, and place a limit on the third. The WASP-47 planetary system is important because companion planets can both be inferred by TTVs and are also detected directly through transit observations. The depth of the hot Jupiter's transits make ground-based TTV measurements possible, and the

brightness of the host star makes it amenable for precise radial velocity measurements. The system serves as a Rosetta Stone for understanding TTVs as a planet detection technique.

Subsequently, we present precise radial velocity observations of WASP-47. We analyze our observations from the HARPS-N spectrograph along with previously published data to measure the most precise planet masses yet for this four-planet system. When combined with new stellar parameters and reanalyzed transit photometry, our mass measurements place strong constraints on the compositions of the two small planets. We find unlike most other ultra-short-period planets, the inner planet, WASP-47 e, has a mass and radius inconsistent with an Earth-like composition. Instead, WASP-47 e likely has a volatile-rich envelope surrounding an Earth-like core and mantle. We also perform a dynamical analysis to constrain the orbital inclination of WASP-47 c, the outer Jovian planet. This planet likely orbits close to the plane of the inner three planets, suggesting a quiet dynamical history for the system. Our dynamical constraints also imply that WASP-47 c is much more likely to transit than a geometric calculation would suggest. We calculate a transit probability for WASP-47 c of about 10%, more than an order of magnitude larger than the geometric transit probability of 0.6%.

4.2 Introduction

Due to their large sizes and short orbital periods, hot Jupiters (roughly Jupiter-mass planets with periods between 0.8 and 6.3 days; Steffen et al., 2012a) are among the easiest exoplanets to detect. Both the first exoplanet discovered around a main sequence star (Mayor & Queloz, 1995) and the first known transiting exoplanet (Charbonneau et al., 2000b; Henry et al., 2000) were hot Jupiters. Until the launch of the *Kepler* space telescope in 2009, the majority of known transiting exoplanets were hot Jupiters. Hot Jupiters allow for the determination of many planetary properties, including their core masses (Batygin et al., 2009) and atmospheres (Charbonneau et al., 2002). For these reasons, transiting hot Jupiters were and continue to be the subject of many follow-up studies (Kreidberg et al., 2014).

One such follow-up study is the search for additional planets in the system revealed by small departures from perfect periodicity in the hot Jupiter transit times (called transit timing variations

or TTVs). TTVs were predicted (Holman & Murray, 2005; Agol et al., 2005a) and searched for (Steffen & Agol, 2005; Gibson et al., 2009), but very little evidence for TTVs was found until the *Kepler* mission discovered smaller transiting planets on longer period orbits than the hot Jupiters detected from the ground (Holman et al., 2010; Lissauer et al., 2011a).

The lack of transit timing variations for hot Jupiters implies a dearth of nearby planets in these systems. While systems exist with a known hot Jupiter and a distant ($\gtrsim$ 200-day period) companion (Knutson et al., 2014c; **?**) or a warm Jupiter (orbital period 6.3 - 15.8 days) and a close-in planet (for example, KOI 191: Steffen et al., 2010; Sanchis-Ojeda et al., 2014a), searches for close-in, companions to hot Jupiters (as in Steffen et al., 2012a) have not yet been successful.

This apparent scarcity supports the idea that hot Jupiters form beyond the ice line and migrate inwards via high eccentricity migration (HEM), a process which would destabilize the orbits of short-period companions (Mustill et al., 2015a). Studies of the Rossiter-McLaughlin effect have also found the fingerprints of high eccentricity migration (Albrecht et al., 2012a). However, statistical work has shown that not all hot Jupiters can form in this way (Dawson et al., 2015), so some hot Jupiters may have close-in planets. Additionally, HEM may not exclude nearby, small planets (Fogg & Nelson, 2007).

In this chapter, we present an analysis of the WASP-47 system (originally announced by Hellier et al., 2012a) that was recently observed by the *Kepler* Space Telescope in its new K2 operating mode (Howell et al., 2014a). In addition to the previously known hot Jupiter in a 4.16-day orbit, the K2 data reveal two more transiting planets: a super-Earth in a 19-hour orbit, and a Neptune-sized planet in a 9-day orbit. We process the K2 data, determine the planetary properties, and measure the transit times of the three planets. We find that the measured TTVs are consistent with the theoretical TTVs expected from this system and measure or place limits on the planets' masses. Finally, we perform many dynamical simulations of the WASP-47 system to assess its stability. We also analyze radial velocity data taken with the HARPS-N spectrograph to better measure the masses and compositions of these planets, and perform a dynamical analysis of the entire four planet system.

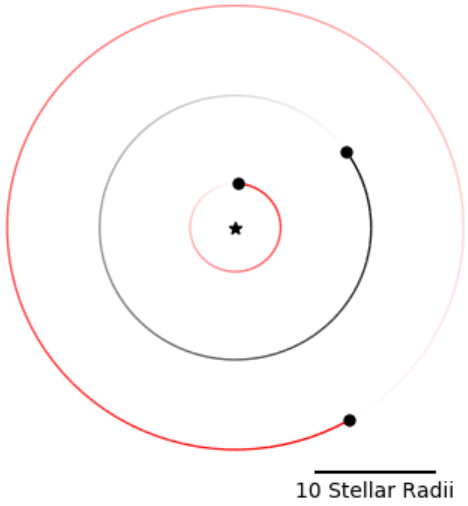

Figure 4.1 A schematic of the WASP-47 system, including planets b, and d. In the innermost part of the system, there are at least three planets. In grey, planets known previous to this work. In red, the two new planets discovered, the outer of which takes roughly nine days to orbit its host star.

4.3 Discovery of two nearby companions to WASP-47b

4.3.1 K2 Data

Kepler observed K2 Field 3 for 69 days between 14 November 2014 and 23 January 2015. After the data were publicly released, one of us (HMS) identified additional transits by visual inspection of the Pre-search Data Conditioned (PDC) light curve of WASP-47 (designated EPIC 206103150) produced by the *Kepler*/K2 pipeline. We confirmed the additional transits by analyzing the K2 pixel level data following Vanderburg & Johnson (2014). A Box-Least-Squares (BLS; Kovács et al., 2002a) periodogram search (as implemented in Muirhead et al., 2015) of the processed long cadence light curve identified the 4.16-day period hot Jupiter (WASP-47 b), a Neptune sized planet in a 9.03-day period (WASP-47 d), and a super-Earth in a 0.79-day period (WASP-47 e).

Because of the previously known hot Jupiter, WASP-47 was observed in K2's "short cadence"

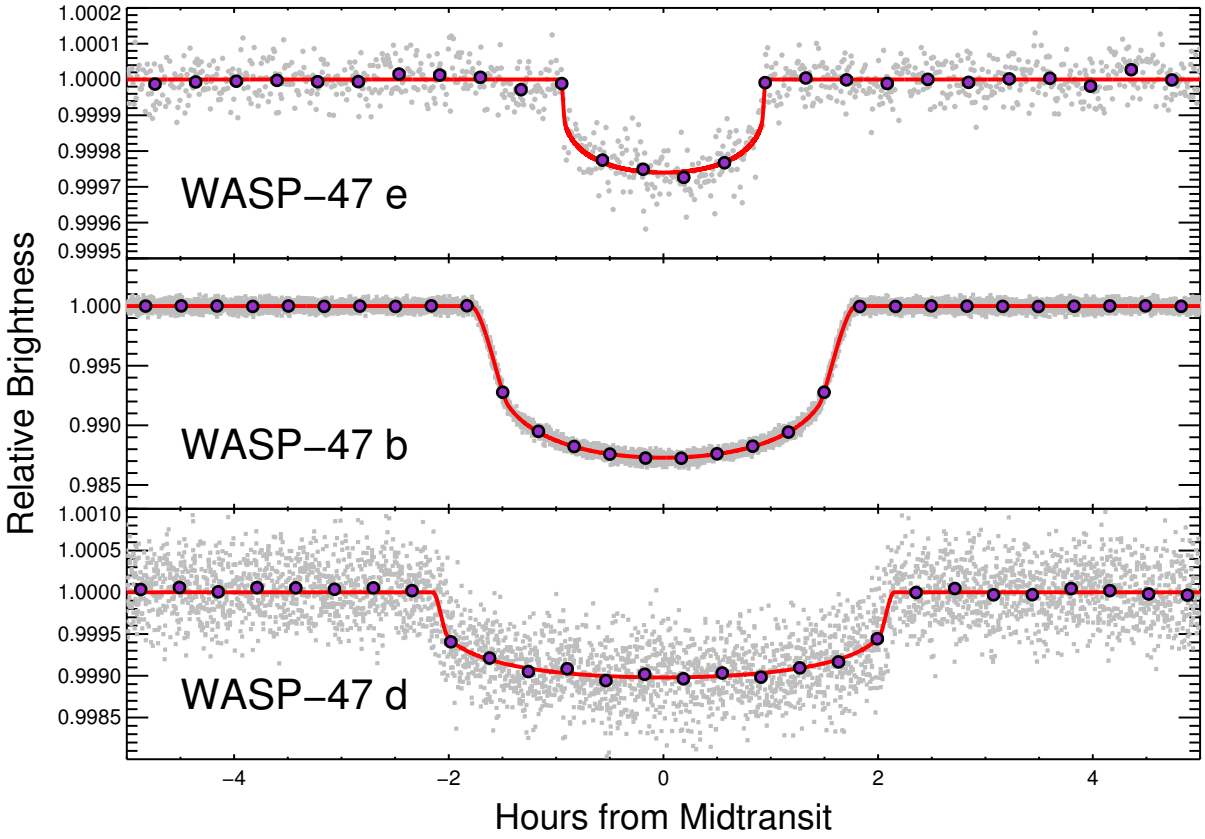

Figure 4.2 Phase-folded lightcurve of WASP-47 e, b, and d. Phase-folded short cadence K2 light curve overlaid with our best-fit transit model (red curves), and binned points (purple circles). In the top panel (WASP-47 e), the grey circles are bins of roughly 30 seconds. In the middle and bottom panels (WASP-47 b and WASP-47 d), the grey squares are the individual K2 short cadence datapoints.

mode, which consists of 58.3 second integrations in addition to the standard 29.41 minute "long cadence" integrations. K2 data are dominated by systematic effects caused by the spacecraft's unstable pointing which must be removed in order to produce high quality photometry. We began processing the short cadence data following Vanderburg & Johnson (2014) to estimate the correlation between K2's pointing and the measured flux (which we refer to as the K2 flat field). We used the resulting light curve and measured flat field as starting points in a simultaneous fit of the three transit signals, the flat field, and long term photometric variations (following Vanderburg et al., 2015b). The three planetary transits were fit with Mandel & Agol (2002a) transit models, the flat field was modeled with a spline in *Kepler*'s pointing position with knots placed roughly

every 0.25 arcseconds, and the long term variations were modeled with a spline in time with knots placed roughly every 0.75 days. We performed the fit using the Levenberg-Marquardt least squares minimization algorithm (Markwardt, 2009). The resulting light curve[1] shows no evidence for K2 pointing systematics, and yielded a photometric precision of 350 parts per million (ppm) per 1 minute exposure. For comparison, during its original mission, *Kepler* also achieved 350 ppm per 1 minute exposure on the equally bright (Kp = 11.7) KOI 279.

We measured planetary and orbital properties by fitting the short cadence transit light curves of all three planets with Mandel & Agol (2002b) transit models using Markov Chain Monte Carlo (MCMC) algorithm with affine invariant sampling (Goodman & Weare, 2010b). We used 50 walkers and 9000 links, and confirmed convergence with the test of Geweke (1992) and a comparison of the Gelman-Rubin statistics for each parameter. We fit for the q_1 and q_2 limb darkening parameters from Kipping (2013a), and for each planet, we fit for the orbital period, time of transit, orbital inclination, scaled semimajor axis $a/R_\star$, and $R_p/R_\star$. Our best-fit model is shown in Figure 4.2 and our best-fit parameters are given in Table 4.1. Our measured planetary parameters for WASP-47 b are consistent with those reported in Hellier et al. (2012a).

We also fitted for the transit times and transit shapes of each transit event in the short cadence light curve simultaneously (due to the relatively short orbital periods sometimes causing two transits to overlap) using MCMC. Our measured transit times[2] are shown in Figure 4.3. We find that the TTVs of WASP-47 b and WASP-47 d are detected at high significance. The two TTV curves are anti-correlated and show variations on a timescale of roughly 50 days. This is consistent with the TTV super-period we expect for planets orbiting in this configuration, which we calculate to be $P_{TTV} = 52.67$ days using Equation 7 of Lithwick et al. (2012).

4.3.2 Validation of WASP-47 e and WASP-47 d

Transiting planet signals like those we find for WASP-47 e and WASP-47 d can be mimicked by a variety of astrophysical false positive scenarios. In this section, we argue that this is unlikely in the case of the WASP-47 system. The hot Jupiter, WASP-47 b, was discovered by Hellier et al. (2012a)

[1]The short cadence light curve is available for download at www.cfa.harvard.edu/ avanderb/wasp47sc.csv
[2]Tables available at dept.astro.lsa.umich.edu/ jcbecker/

Parameter	Value		68.3% Confidence Interval Width	Comment
WASP-47 b				
Orbital Period, P [days]	4.1591287	±	0.0000049	B
Radius Ratio, $(R_P/R_\star)$	0.10186	±	0.00023	B
Scaled semimajor axis, $a/R_\star$	9.715	±	0.050	B
Orbital inclination, i [deg]	89.03	±	0.27	B
Transit impact parameter, b	0.164	±	0.045	B
Time of Transit t_t [BJD]	2457007.932131	±	0.000023	B
TTV amplitude [min]	0.63	±	0.10	B
M_P [$M_\oplus$]	341		$^{+73}_{-55}$	A,B,C
R_P [$R_\oplus$]	12.77	±	0.44	A,B
WASP-47 e				
Orbital Period, P [days]	0.789597	±	0.000013	B
Radius Ratio, $(R_P/R_\star)$	0.01456	±	0.00024	B
Scaled semimajor axis, $a/R_\star$	3.24	±	0.14	B
Orbital inclination, i [deg]	87.0	±	3.1	B
Transit impact parameter, b	0.17	±	0.15	B
Time of Transit t_t [BJD]	2457011.34849	±	0.00038	B
TTV amplitude [min]	<1.2 min for any TTV period < 80 days			B
M_P [$M_\oplus$]	<22		95% Confidence	C
R_P [$R_\oplus$]	1.829	±	0.070	A,B
WASP-47 d				
Orbital Period, P [days]	9.03081	±	0.00019	B
Radius Ratio, $(R_P/R_\star)$	0.02886	±	0.00047	B
Scaled semimajor axis, $a/R_\star$	16.33	±	0.87	B
Orbital inclination, i [deg]	89.36	±	0.67	B
Transit impact parameter, b	0.18	±	0.16	B
Time of Transit t_t [BJD]	2457006.36927	±	0.00044	B
TTV amplitude [min]	7.3	±	1.9	B
M_P [$M_\oplus$]	15.2		±7	C
R_P [$R_\oplus$]	3.63	±	0.14	A,B

Table 4.1 Planet Parameters for WASP-47 b, e, and d. A: Parameters come from Mortier et al. (2013). B: Parameters come from analysis of the K2 light curve. C. Parameters come from dynamical fits to the observed transit timing variations. D: We report the magnitude of the impact parameter, whereas the true value could be positive or negative.

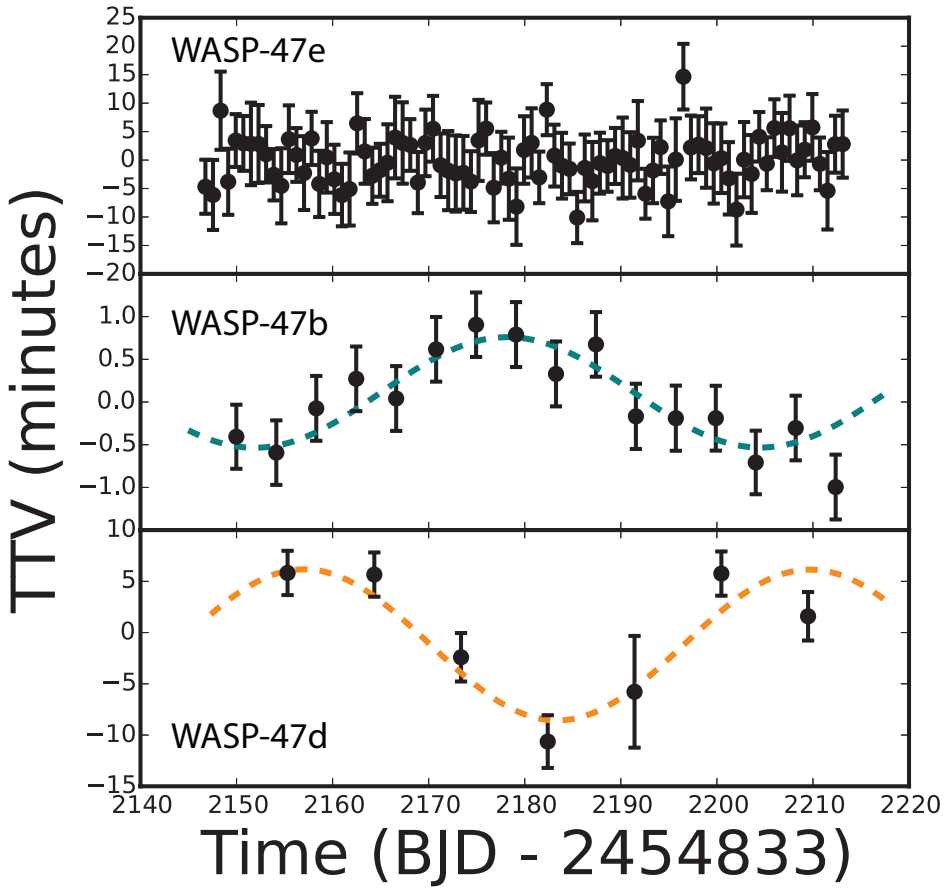

Figure 4.3 Derived TTVs for WASP-47 e, b, and d. Top: observed TTVs for WASP-47 e. Middle: observed TTVs for WASP-47 b, overlaid (for visual clarity) with a teal sine curve with period equal to the expected 52.67-day super-period. Bottom: Observed TTVs for WASP-47 d, overlaid (for visual clarity) with an orange sine curve with the expected super-period. When analyzing the transit times, we did not use the sine fits, they are simply to guide the eye.

and confirmed with radial velocity (RV) follow-up, which showed no evidence for stellar mass companions or spectral line shape variations, and detected the spectroscopic orbit of the planet. In the K2 data, we detect transit timing variations of WASP-47 b, which are anti-correlated with the transit timing variations of WASP-47 d, and which have a super-period consistent with what we expect if both of these objects are planets. The TTVs therefore confirm that WASP-47 d is a planet in the same system as WASP-47 b. We also fitted the transit durations with a power law and found that they followed the expected $P^{1/3}$ relation (when P is orbital period) for planets orbiting a single star.

The light curve is not of sufficiently high quality to detect TTVs for the smaller WASP-47 e, so we validate its planetary status statistically. We do this using `vespa` (Morton, 2015), an implementation of the procedure described in Morton (2012). Given constraints on background sources which could be the source of the transits, a constraint on the depth of any secondary eclipse, the host star's parameters and location in the sky, and the shape of the transit light curve, `vespa` calculates the probability of a given transit signal being an astrophysical false positive. Both visual inspection of archival imaging and a lucky imaging search (Wöllert et al., 2015) found no close companions near WASP-47, but the lucky imaging is not deep enough to rule out background objects that could cause the shallow transits of WASP-47 e. Following Montet et al. (2015), we define a conservative radius inside of which background sources could cause the transits. We adopt a radius of 12 arcseconds; we detect the transits with photometric apertures as small as 6 arcseconds in radius and allow for the possibility that stars outside of the aperture could contribute flux due to *Kepler*'s 6 arcsecond point spread function. We find that WASP-47 e has a false positive probability (FPP) of roughly 5×10^{-4}. We find using the expressions from Lissauer et al. (2012a) that since this is a three-planet system, its FPP decreases to less than 10^{-5}. As such, we consider WASP-47 e to be validated as a *bona fide* planet.

4.3.3 Dynamical Simulations

4.3.3.1 Stability Analysis

We test the dynamical stability of the WASP-47 planetary system with a large ensemble of numerical simulations. The K2 data determine the orbital periods of the three bodies to high precision and place constraints on the other orbital elements. We sample the allowed ranges of the orbital elements for all three planets, randomizing the orbital phases of the three bodies. We assigned masses by sampling the distribution of Wolfgang et al. (2015) for the measured planet radii. We chose eccentricities from a uniform distribution that extends up to e=0.3. We discard systems that do not satisfy the stability criteria enumerated in Fabrycky et al. (2014b).

Given a set of 1000 such initial conditions, we numerically integrate the systems using the `Mercury6` integration package (Chambers, 1999b). We use a Bulirsch-Stoer (B-S) integrator, re-

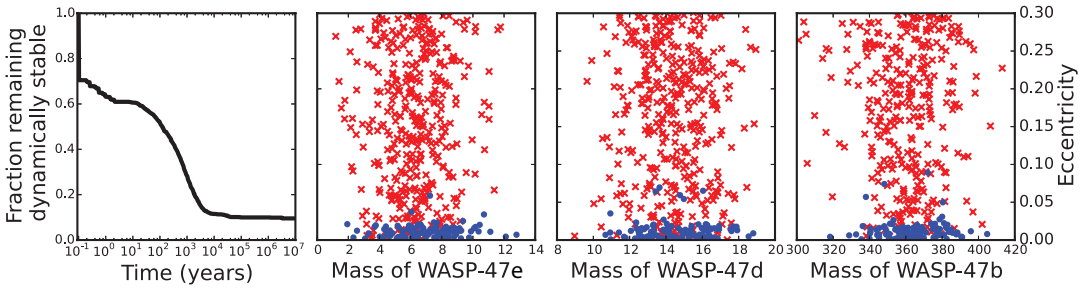

Figure 4.4 Stability Map for the WASP-47 System. Results from an ensemble of 1000 numerical integrations testing the stability of the system. The left panel shows the fraction of the systems that survive as a function of time. The other panels show the starting mass and eccentricity of the three planets sampled over 1000 trials; the blue points represent systems that are stable, whereas the red crosses depict systems that become dynamically unstable.

quiring that system energy be conserved to 1 part in 10^9. We integrate the system for a total simulation length of 10 Myr, unless the system goes unstable on a shorter time scale due to ejection of a planet, planetary collisions, or accretion of a planet by the central star. To perform these computationally intensive simulations, we use the Open Science Grid (OSG; Pordes et al., 2007) accessed through XSEDE (Towns et al., 2014).

The results from this numerical survey are shown in Figure 4.4. The left panel shows the fraction of systems remaining stable as a function of time. About 30% of the systems are unstable over short time scales, and almost 90% of the systems are unstable over long time scales. Once the systems reach ages of $\sim 10^4$ yr, they tend to survive over the next three orders of magnitude in integration time. The remaining three panels show the mass and initial eccentricity of the three planets, sampled from the distributions specified above. One clear trend is that low eccentricity systems tend to survive, whereas systems with $e_p > 0.05$ are generally unstable. A second trend that emerges from this study is that stability does not depend sensitively on the planet masses (provided that the orbits are nearly circular). Stable systems arise over a wide range of planet masses, essentially the entire range of masses allowed given the measured planetary radii.

WASP-47 b and WASP-47 d orbit within about 20% of the 2:1 mean motion resonance (MMR). For completeness, we carried out a series of numerical integrations where the system parameters varied over the allowed, stable range described above. In all trials considered, the resonance angles

were found to be circulating rather than librating, so there is no indication that the system resides in MMR.

Each of the numerical integrations considered here spans 10 Myr, which corresponds to nearly one billion orbits of the inner planet. Tidal interactions occur on longer timescales than this and should be considered in future work. In particular, the survival of the inner super-Earth planet over the estimated lifetime of the WASP-47 system could place limits on the values of the tidal quality parameters Q for the bodies in the system.

4.3.3.2 Theoretical TTVs

We performed a second ensemble of numerical simulations to estimate the magnitude of transit timing variations in the WASP-47 system. We used initial conditions similar to those adopted in the previous section, but with starting eccentricities $e < 0.1$.

We integrated each realization of the planetary system for 10 years using the `Mercury6` B-S integrator with time-steps < 0.5 seconds. We extracted transit times from each integration for each planet, resulting in theoretical TTV curves. The resulting distributions of predicted TTV amplitudes are shown in Figure 4.5. The three distributions have approximately the same shape and exhibit well defined peaks. The TTV amplitudes we measured in Section 4.3.1 are consistent with the distributions we produced theoretically.

4.3.3.3 Mass Measurements from the Transit Timing Variations

We measure the TTVs with high enough precision that dynamical fits can give estimates of the planetary masses. We use `TTVFAST` (Deck et al., 2014a) to generate model transit times for each observed epoch for each planet, and use `emcee` (Foreman-Mackey et al., 2013a), an MCMC algorithm with affine invariant sampling, to minimize residuals between the observed TTVs and these model TTVs. In these fits, we allow each planet's mass, eccentricity, argument of pericenter, and time of first transit to float. We imposed a uniform prior on eccentricity between 0 and 0.06 (as required for long-term stability). We initialized the chains with random arguments of pericenter and masses drawn from the Hellier et al. (2012a) mass posterior for WASP-47 b, and the distribution of Wolfgang et al. (2016) for WASP-47 e and WASP-47 d. We used 64 walkers and 20000 iterations

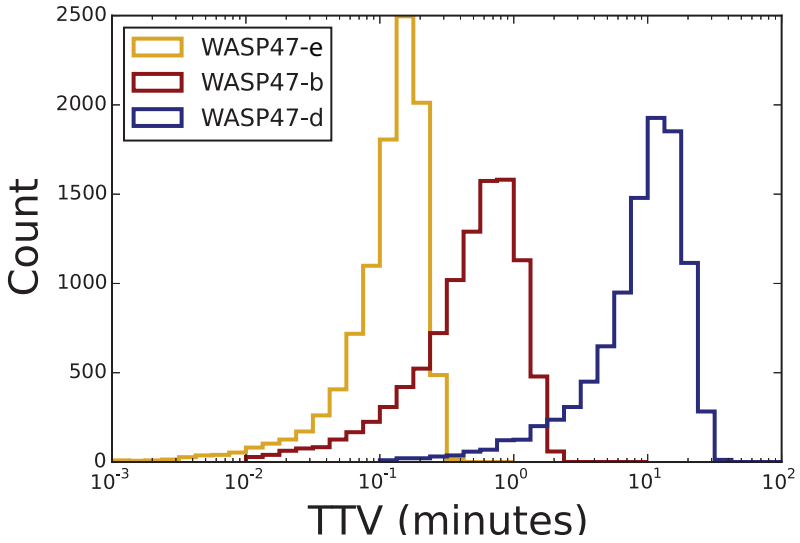

Figure 4.5 Expected TDVs for WASP-47 b, e, and d. Histograms of potential transit timing variations for each planet. For a large selection of (likely) dynamically stable initial conditions, we integrated the system forward over a ten-year timescale and extracted the expected TTV amplitude.

to explore the parameter space, and discarded the first 2500 iterations as 'burn-in'. We confirmed that the MCMC chains had converged using the test of Geweke (1992) and the Gelman-Rubin statistics (which were below 1.05 for every parameter). The best-fit model points are overlaid with the observed TTVs for the outer two planets in Figure 4.6.

We find that we are able to measure the masses of WASP-47 b and WASP-47 d, and place an upper limit on the mass of WASP-47 e. We additionally provide limits on the quantities $e_c \cos \omega_c - e_b \cos \omega_b$. These masses and limits are summarized in Table 4.1. We measure a mass of 3417.3 $M_\oplus$ for WASP-47 b, which is consistent with the mass measured by Hellier et al. (2012a) of 362 ± 16 $M_\oplus$ at the 1–σ level. The mass of WASP-47 d is 15.2±7 $M_\oplus$. Only an upper limit can be placed on WASP-47 e of $<22 M_\oplus$.

4.3.4 State of the field post Becker et al. 2015

WASP-47 is unusual: it is the first hot Jupiter discovered to have additional, close-in companion planets. Using the Exoplanet Orbit Database (Han et al., 2014), we found that among the 224 systems containing a planet with mass greater than 80 $M_\oplus$ and orbital period less than 10 days,

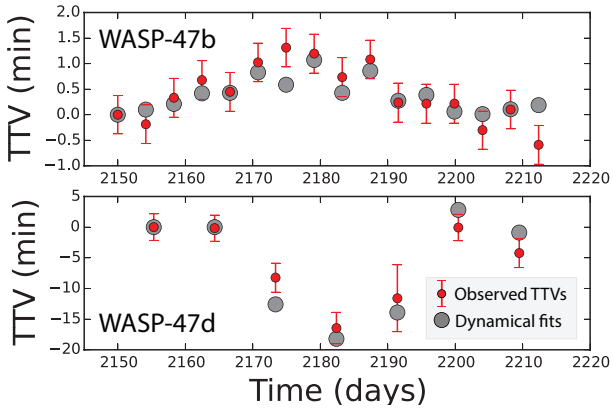

Figure 4.6 Agreement Between Observed TTVs and Theoretical TTVs. The best-fit theoretical points (red, with error bars) are overlaid with the observed TTVs (grey circles) for the best fit system parameters given in Table 4.1.

only six contain additional planets, and none of them have additional planets in orbital periods shorter than 100 days. That the additional planets in the WASP-47 system are coplanar with the hot Jupiter and that the planets are unstable with $e \gtrsim 0.05$ implies that the WASP-47 planets either migrated in a disk or some damping near the end of migration took place to bring them into their present compact architecture.

The continued existence of the companions in this system indicates that HEM cannot serve as the sole formation mechanism for hot Jupiters. HEM would likely have disrupted the orbits of the smaller planets. It is quite possible that there is more than one potential formation mechanism for hot Jupiters. Additionally, observations contemporaneous with the work in this section identified an additional Jupiter-mass planet in a estimated 571-day orbit (Neveu-VanMalle et al., 2016b, called WASP-47c;) in this system, making this the first hot Jupiter with both close-in companions and an external perturber.

WASP-47 is a rare system for which planet masses can be determined using TTVs measured from the K2 data set. This is because (a) the planets are far enough away from resonance that the super-period (52.7 days) is shorter than the K2 observing baseline (69 days), and (b) the planets are massive enough that the TTVs are large enough to be detectable. The detection of TTVs was also aided by the fact that WASP-47 was observed in short cadence mode, which is unusual for K2.

Finally, WASP-47 is a favorable target for future follow-up observations. The V-band magnitude

is 11.9, bright enough for precision RV follow-up studies. The K2 light curve shows no evidence for rotational modulation, indicating that WASP-47 is photometrically quiet and should have little RV jitter. Measuring the mass of the two planetary companions with RVs could both improve the precision of the inferred masses and test the consistency of TTV and RV masses, between which there is some tension (e.g. KOI 94: Weiss et al., 2013; Masuda et al., 2013). The 1.3% depth of the transits of WASP-47 b makes it easily detectable from the ground. Previous ground based searches for transit timing variations of hot Jupiters have attained timing uncertainties of $\sim$ 20 seconds, lower than the measured TTV amplitude for WASP-47 b (Gibson et al., 2009). Follow-up transit observations could place additional constraints on the masses of the WASP-47 planets.

In this work we have studied the WASP-47 planetary system by using data from the *Kepler*/K2 mission along with supporting theoretical calculations. Our main results can be summarized as follows:

1. In addition to the previously known hot Jupiter companion WASP-47 b, the system contains two additional planets that are observed in transit. The inner planet has a ultra-short period of only 0.789597 days, and radius of 1.829 $R_\oplus$. The outer planet has a period of 9.03081 days and a radius of 3.63 $R_\oplus$, comparable to Neptune.

2. The system is dynamically stable. We have run 1000 10 Myr numerical integrations of the system. The planetary system remains stable for the 10 percent of the simulations that start with the lowest orbital eccentricities.

3. The particular planetary system architecture of WASP-47 results in measurable TTVs, which are in good agreement with the TTVs we find from numerical integrations of the system. We use the TTVs to measure the masses of WASP-47 b (consistent with RV measurements) and WASP-47 d.

4. This compact set of planets in nearly circular, coplanar orbits demonstrates that at least a subset of Jupiter-size planets can migrate in close to their host star in a dynamically quiet manner, suggesting that there may be more than one migration mechanism for hot Jupiters.

The WASP-47 planetary system provides a rare opportunity where planets can be both inferred

from TTVs and seen in transit. Future observations comparing the system parameters inferred from TTVs with those inferred from RVs will qualitatively test TTVs as a general technique.

4.4 Improved Mass Measurements Using Radial Velocities

In Section 4.3, we described our discovery of two short-period planets in the hot-Jupiter-hosting system WASP-47. The WASP-47 planetary system was first discovered by the ground-based Wide Angle Search for Planets (WASP) survey (Hellier et al., 2012b). After detecting a candidate hot Jupiter in a 4.16 day orbital period with the WASP-South instrument, Hellier et al. (2012b) followed-up the system and confirmed the planetary nature of WASP-47 b with a transit observation with the EulerCam photometer and moderate precision radial velocity observations from the CORALIE spectrograph, both on the 1.2m Euler telescope at La Silla Observatory in Chile. Several years later, WASP-47 happened to lie in Field 3 of the K2 mission, and was observed by K2 between November 2014 and February 2015. In addition to the previously known hot Jupiter, the precise K2 photometry revealed two other transiting planets, an interior super-Earth in a 19 hour orbit, and an exterior Neptune-sized planet in a 9 day orbit, making WASP-47 the first and only hot Jupiter system with additional short-period transiting planets (Becker et al., 2015b). Meanwhile, long-term radial velocity monitoring of WASP-47 with CORALIE was also revealing interesting trends. Using 48 observations obtained over the course of almost 5 years, Neveu-VanMalle et al. (2016c) detected another giant planet orbiting WASP-47 in a nearly 600-day orbit, giving a total of four known planets around WASP-47.

Although in 2015, when WASP-47 c, d, and e were discovered, extra transiting planets in a hot Jupiter system seemed unusual and surprising, such planets were once believed likely to exist, and were in fact seen as a highly promising way to find small transiting planets before the launch of multi-million-dollar wide-field space telescopes like *Kepler* and CoRoT. Holman & Murray (2005) and Agol et al. (2005a) showed that a transiting planet would undergo small deviations from perfectly periodic transits (called transit timing variations or TTVs) in the presence of other nearby planets in the system, and Steffen & Agol (2005) showed that this method is highly sensitive to small planets orbiting near hot Jupiters. Frustratingly, however, after a decade of searching, the

TTV method's exquisite sensitivity to small planets near hot Jupiters had merely translated to exquisite upper limits on the presence of such planets (especially in mean motion resonances with the hot Jupiter, Steffen & Agol, 2005; Miller-Ricci et al., 2008; Collins et al., 2017).

Meanwhile, shortly after its launch, the *Kepler* telescope detected the first transit timing variations in systems of longer period and lower mass planets than the hot Jupiters on which previous searches had focused (Holman et al., 2010; Lissauer et al., 2011a). Over the course of its mission, *Kepler* found planets in nearly every configuration imaginable[3], including tightly packed systems of small planets with short orbital periods (Muirhead et al., 2012) and multi-planet systems with slightly longer period warm Jupiters (Bonomo et al., 2014; Sanchis-Ojeda et al., 2014b; Huang et al., 2016a), but *Kepler* found no evidence for any additional planets near a hot Jupiter. When detailed investigations and searches for companions to hot Jupiters in *Kepler* data came up empty (Steffen et al., 2012b), the scientific community largely considered the issue resolved — hot Jupiters evidently either cannot or almost never have nearby planetary companions.

Therefore, the planets around WASP-47 must represent a rare outcome of planet formation, and any observational or theoretical insights into their architecture and origins are important to help illuminate this new mode. Follow-up work came quickly. Sanchis-Ojeda et al. (2015a) detected the Rossiter McLaughlin effect for WASP-47 b, ruling out large misalignments between the inner transiting system's orbits and the star's sky-projected spin axis. Radial velocity monitoring with the Planet Finder Spectrograph (PFS) on the Magellan Clay telescope detected the reflex motion due to WASP-47 e and found that its composition was most likely rocky (Dai et al., 2015). More recently, a larger set of precise velocities from the HIgh Resolution Echelle Spectrometer (HIRES) on the Keck I telescope obtained by Sinukoff et al. (2017b) improved the precision on WASP-47 e's mass and detected WASP-47 d's RV signature. A photodynamical analysis by Almenara et al. (2016) and a simultaneous analysis of radial velocities and transit times by Weiss et al. (2016a) placed even stronger constraints on the planets' masses and eccentricities, showing that WASP-47 d had a mass close to that of Neptune, and that the eccentricities of the inner planets were small. Becker & Adams (2017) used the fact that the three inner planets all transit to place constraints

[3]Some exceptions to this statement include the lack of binary planets, Trojan planets, and circumtrinary planets among *Kepler*'s discoveries.

on the inclination of WASP-47 c. They showed that WASP-47 c's orbit is probably fairly well aligned with the transiting planets, though certain highly misaligned orbits could still allow the inner planets to transit.

Meanwhile, others have speculated about the origin of the WASP-47 planets. Batygin et al. (2016a) suggested that *in situ* formation could be an important channel for creating hot Jupiters, and that small planetary companions like those around WASP-47 (or in orbits misaligned with the hot Jupiter) would be a natural consequence of this mechanism. Huang et al. (2016a) also suggested *in situ* formation, noting that the planets around WASP-47 are much more reminiscent of planetary systems hosting warm Jupiters than other hot Jupiters, and speculating that WASP-47 might be an extreme short-period result of an *in situ* warm Jupiter formation mechanism. On the other hand, Weiss et al. (2016a) suggested that WASP-47's planets might have formed in a two-stage process, where the two Jovian planets formed far out in the disk, WASP-47 b migrated inwards, and then the two smaller planets formed nearby. More constraints on the planets' masses and compositions and the system architecture are needed to understand how these unusual planets formed and came to be in their present configuration.

In this section, we add to the already large body of follow-up work on the WASP-47 system, presenting 69 new precise radial velocity observations from the High Accuracy Radial velocity Planet Searcher for the Northern hemisphere (HARPS-N). We analyze these new observations along with previously collected data to determine the most precise values yet for the masses and radii of the WASP-47 planets.

4.4.1 HARPS-N Spectroscopy

We observed WASP-47 with the HARPS-N spectrograph on the 3.58m Telescopio Nazionale Galileo (TNG) on the island of La Palma, Spain (Cosentino et al., 2012). HARPS-N is a stabilized high resolution ($\lambda/\Delta\lambda = 115,000$) optical spectrograph designed specifically to make precise radial velocity measurements. We began observing WASP-47 on 23 July 2015, shortly after K2 data revealed the presence of two small transiting planets (WASP-47 e and WASP-47 d) in addition to the previously known hot Jupiter (WASP-47 b). We obtained 78 observations of WASP-47 with integration times of 30 minutes. We measured radial velocities for each exposure by cross-correlating

the HARPS-N spectra with a weighted binary mask (Baranne et al., 1996; Pepe et al., 2002). The 30 minute exposures of WASP-47 yielded radial velocity measurements with typical photon-limited uncertainties of 3 $\mathrm{m\,s^{-1}}$. HARPS-N is fed by two optical fibers going into the spectrograph - one fiber feeds the target starlight into the spectrograph, while the other fiber either feeds in a precise wavelength calibrator[4], or sky background light. HARPS-N is stable to better than 1 $\mathrm{m\,s^{-1}}$ over the course of a night, considerably more precise than our typical measurement uncertainties, so a simultaneous calibrator was not necessary for our observations. Instead, we fed sky background light into the instrument with the second fiber.

Because WASP-47 is somewhat faint for precise radial velocity measurements, and because it lies in the ecliptic plane near bright solar system objects like the moon, contamination from scattered sky background light can cause significant velocity errors in some conditions. We identified radial velocity observations contaminated by scattered light from a bright sky using the method described by Malavolta et al. (2017). In brief, we calculated radial velocities with and without sky contribution removed (using the sky spectrum obtained simultaneously with the instrument's second fiber), and flagged the exposures that showed a significant (2–σ) velocity difference with and without sky subtraction. We found that four of our 78 observations showed evidence for sky contamination and excluded them from our analysis (which we describe in Section 4.4.2).

4.4.1.1 Updated Spectroscopic Parameters

We used our HARPS-N spectra to measure spectroscopic parameters for WASP-47. We first used the Stellar Parameter Classification (SPC) method (Buchhave et al., 2012, 2014a). SPC works by cross-correlating a stellar spectrum with synthetic spectra from Kurucz (1992) model atmospheres and interpolating the resulting correlation peaks to determine stellar atmospheric parameters like effective temperature, surface gravity, metallicity, and line broadening. We ran SPC on 75 of the 78 HARPS-N spectra[5] and calculated the averages for all of the spectroscopic parameters. With SPC, we measure a temperature of $T_{\mathrm{eff,SPC}} = 5571 \pm 50$ K, a surface gravity

[4]The wavelength calibrator light source can be a Thorium Argon lamp, continuum light passed through a stabilized Fabry-Perot interferometer, or a stabilized laser frequency comb.

[5]We excluded several spectra due to their low signal-to-noise ratios. We did not exclude the sky-contaminated spectra from our SPC analysis because the small amount of sky contamination necessary to skew the radial velocity by ≈ 10 $\mathrm{m\,s^{-1}}$ does not significantly affect the SPC analysis.

of $\log g_{\rm cgs,SPC} = 4.39 \pm 0.1$, a metallicity $[{\rm M/H}]_{\rm SPC} = 0.42 \pm 0.08$, and place an upper limit on rotational velocity of $v_{\rm rot} < 2$ km s^{-1}. The error bars reported for SPC reflect systematic uncertainties in the stellar models used by SPC. The scatter in the parameters SPC reports for each of the 75 individual spectra is much smaller than the systematic uncertainty in these parameters.

We also measured spectroscopic parameters using the method described by Mortier et al. (2013) on our new HARPS-N spectra. We co-added all of the HARPS-N spectra, measured equivalent widths of iron lines using ARES2 (Sousa, 2014; Sousa et al., 2015), and determined atmospheric parameters using the 2014 version of MOOG[6] (Sneden, 1973). We then applied the surface gravity correction from Mortier et al. (2014) to adjust for systematic effects in the ARES/MOOG analysis method. This analysis yielded an effective temperature $T_{\rm eff,MOOG=}$ 5614 ± 67 K, surface gravity $\log g_{\rm cgs,MOOG} = 4.45 \pm 0.11$, and an iron abundance $[{\rm Fe/H}]_{\rm MOOG} = 0.39 \pm 0.05$.

The spectroscopic parameters that we determined through our SPC and ARES/MOOG analyses are consistent with one another, and are also consistent within errors with previous determinations. In this chapter, we adopt weighted averages of the spectroscopic parameters from our SPC analysis and our ARES/MOOG analysis, along with the spectroscopic analysis done by Sinukoff et al. (2017b) on a high signal-to-noise spectrum from Keck Observatory using another independent method, Spectroscopy Made Easy (SME, Brewer et al., 2015, 2016). Each of the three methods we use have their own systematics, so averaging the three methods could give more accurate spectroscopic parameters. The weighted averages were a temperature of $T_{\rm eff} = 5552$ K, a metallicity[7] of [M/H] = 0.38, and a stellar surface gravity of $\log g_{\rm cgs} = 4.32$. We assigned conservative error bars of 75 K in temperature, 0.05 dex in metallicity, and 0.1 dex in surface gravity to the weighted averages in order to account for systematic errors in the spectroscopic analyses.

4.4.1.2 Transit Re-analysis

Since the original analysis of the WASP-47 K2 light curve by Becker et al. (2015b), there have been new data collected (Sinukoff et al., 2017b) and additional dynamical analyses (Almenara et al., 2016; Weiss et al., 2016a) performed, which put tighter constraints on the planets' orbits

[6] `http://www.as.utexas.edu/~chris/moog.html`

[7] To calculate the weighted average metallicity, we use iron abundance as a proxy for the overall metallicity by assuming solar abundance ratios, where [M/H] = [Fe/H].

(in particular, their eccentricities). In this section, we re-analyze the K2 light curve using Kepler's third law to link together the planets' scaled semi-major axes while taking into account new, tighter constraints on the inner planets' orbital eccentricities. These constraints yield better measurements of the planets' scaled semi-major axes, and therefore better measurements of the planets' transit impact parameters and planet to star radius ratios.

We performed our new transit analysis using the same K2 light curve of WASP-47 produced and used by Becker et al. (2015b). *Kepler* observed WASP-47 for 69 days between 2014 November 14 and 2015 January 23 in short-cadence mode – an exposure of WASP-47 was recorded every 58.85 seconds instead of *Kepler*'s normal 29.4 minute "long cadence" integrations. After Becker et al. (2015b) processed the light curve to remove systematic effects due to *Kepler*'s unstable pointing (see also Vanderburg & Johnson, 2014; Vanderburg et al., 2016c), the photometric scatter in the light curve was about 350 ppm per minute.

We perform the transit analysis on the K2 light curve using a Markov Chain Monte Carlo (MCMC) algorithm with an affine invariant ensemble sampler (Goodman & Weare, 2010a). We fit the three transiting planet light curves with Mandel & Agol (2002b) model light curves (with a quadratic limb darkening law parameterized following Kipping 2013a). We fit for the planets' orbital periods, transit ephemerides[8], planet to star radius ratios ($R_p/R_\star$), orbital inclinations (i), and in some cases, the orbital eccentricity (e) and argument of periastron (ω_p). Instead of fitting for all three planets' scaled semi-major axis ratios ($a/R_\star$) independently, we fit for stellar density and calculated $a/R_\star$ for each planet using Kepler's third law. We also fit for a single flux offset parameter and the uncertainty of each K2 photometric datapoint.

We force the orbits of WASP-47 e and WASP-47 b to be circular; the tidal circularization timescales for these two planets (10^5 years and 10^7 years respectively, using the expression from Goldreich & Soter 1966 and reasonable values[9] of Q and k_2) are much shorter than the age of the system[10]. For WASP-47 d, while tidal dissipation is not strong enough to necessarily circularize the

[8]Even though small transit timing variations have been detected in the K2 light curve, for this analysis, we assumed the transits of the WASP-47 planets are perfectly periodic. We have also analyzed the K2 light curve while shifting the transit center times to account for the transit timing variations, and found the difference in fitted parameters was negligible.

[9]In particular, we used $Q/k_2 = 10^2$ for WASP-47 e and $Q/k_2 = 10^5$ for WASP-47 b and WASP-47 d.

[10]Planet-planet interactions will drive a small forced eccentricity but our dynamical calculations show that typical forced eccentricities for these planets are of order 10^{-3}, too small to affect our measured parameters.

orbit, strong dynamical constraints exist on any eccentricity. Both N-body simulations performed by Becker et al. (2015b) and simultaneous analysis of transit times and radial velocities by Almenara et al. (2016) and Weiss et al. (2016a) have showed that the eccentricity must be quite small. We imposed a half-Gaussian prior on eccentricity centered at 0 with a 1-σ width of 0.014, and solutions with eccentricity less than 0 forbidden. This prior matches the distribution of dynamically stable simulations from Becker et al. (2015b) and gives a 2-σ upper limit on eccentricity that matches the limit from Weiss et al. (2016a). In our MCMC fit, we explored eccentric models for WASP-47 d's orbit by stepping in $\sqrt{e}\sin\omega_p$ and $\sqrt{e}\cos\omega_p$.

We initialized an ensemble of 100 walkers, evolved them for 20,000 steps, and removed the first 10,000 steps, when the ensemble was "burning in" and not yet in a converged configuration. We assessed convergence of the resulting MCMC chains by calculating the Gelman Rubin statistic, which was less than 1.2 for all parameters, and less than 1.05 for most. The best-fit parameters and their uncertainties are reported in Table 4.1. The results are consistent with the previous transit analyses by Becker et al. (2015b) and Almenara et al. (2016), but in some cases are more precise because of the additional constraints we have imposed here. Thanks to the high signal-to-noise transits of WASP-47 b, we measure the stellar limb darkening coefficients[11] and importantly, we measure the stellar density with a precision of 1.4%, which we use in Section 4.4.1.3 to determine a precise stellar mass and radius. We also measure the radius ratios of WASP-47 e and WASP-47 d with 0.8% and 0.5% precision, respectively.

4.4.1.3 Stellar Parameters

In this section, we take advantage of the well measured stellar density we measure from the K2 transit photometry to derive precise stellar parameters (as has been done previously for other hot Jupiter hosts, e.g. Sozzetti et al., 2007). We base our analysis on the Yonsei-Yale (YY) isochrones (Yi et al., 2001), exploring parameter space stepping in stellar mass, age, and metallicity using MCMC with an affine invariant ensemble sampler. We interpolated the YY isochrones using

[11] We measure the linear coefficient $u_1 = 0.533 \pm 0.010$ and the quadratic coefficient $u_2 = 0.097 \pm 0.024$. These coefficients are in in reasonable agreement (within ≈ 0.1) with the theoretical predictions from Claret & Bloemen (2011) of $u_1 = 0.47$ and $u_2 = 0.22$.

code[12] written by Jason Eastman for EXOFASTv2 (Eastman et al. 2013a; Rodriguez et al. 2017a; Eastman et al. in prep). We impose Gaussian priors on WASP-47's density, metallicity, effective temperature, and surface gravity. The density prior's center and width come from our analysis of the K2 light curve. For the temperature, metallicity, and surface gravity priors, we use the values and uncertainties from the weighted average of the three different spectroscopic analyses we discussed in Section 4.4.1.1.

Thanks to our precise measurement of WASP-47's density from the transit light curves, our MCMC analysis yielded a stellar mass and radius with precisions of about 3% and 1% respectively. Stellar evolutionary models have not yet been tested at such high precisions on stellar parameters (Torres et al., 2010), so we performed tests to assess the scale of systematic errors in the isochrones we used. First, we compared the results of our analysis with the YY isochrones to the similar analysis performed by Almenara et al. (2016) using the Dartmouth isochrones (Dotter et al., 2008). Using the same priors and input stellar parameters, our YY analysis yielded a mass about 1.5% larger and a radius about 0.5% larger than the values Almenara et al. (2016) determined using the Dartmouth isochrones. The differences in mass and radius between the YY analysis and Dartmouth analysis are about half the size of the uncertainties from each analysis. We also performed an MCMC analysis to determine WASP-47's stellar parameters using the empirical mass and radius relations determined by Torres et al. (2010). We stepped in surface gravity, metallicity, and effective temperature, imposing Gaussian priors on the metallicity, temperature, and stellar density. The Torres relations have a known offset at one solar mass, over-predicting the mass of the Sun by about 5% and the radius of the Sun by about 2% (Torres et al., 2010), so we scaled the output masses and radii inside our model by those factors to correct for the offset – forcing the relations to correctly predict the Sun's density. Our analysis using the Torres relations yielded masses and radii that were about 0.7% and 0.1% larger than our analysis using the YY isochrones. These discrepancies again are considerably smaller than the uncertainties we determined in our stellar parameters. Finally, we repeated the analysis with the Torres relations while applying the empirical correction for solar-mass stars provided by Santos et al. (2013), and found that it also gave consistent values for the stellar mass and radius, with values about 0.5–σ larger than the YY value.

[12]Code available at `https://github.com/jdeast/EXOFASTv2/`.

Based on these tests showing different models and relations all predicting consistent stellar parameters for WASP-47, we conclude that systematic uncertainties in the stellar masses and radii we derive are small. This makes sense – stellar evolutionary models are calibrated off the Sun and incorporate physics known to be important for Sun-like stars, and therefore tend to be most accurate for stars with parameters close to those of the Sun. WASP-47 has a mass only 4% larger than the sun, and is only slightly more evolved, with a $\approx$ 14% larger radius and $\approx$ 200 K cooler stellar effective temperature. The biggest discrepancy between WASP-47 and the Sun is the composition – WASP-47 has a metallicity 2.5 times higher than that of the Sun, which is possibly the cause of the small discrepancies we do see between the different methods.

To take the 0.5–σ discrepancies we found into account, we re-determined the stellar mass and radius using our YY MCMC analysis after inflating the uncertainty on stellar density by adding an 0.5–σ systematic uncertainty in quadrature to the uncertainty we derived from our transit analysis. This analysis yielded a stellar mass of 1.040 $\pm$ 0.031 $M_\odot$ and a radius of 1.137 $\pm$ 0.013 $R_\odot$. Our constraint on stellar density is precise enough that we also measure an isochronal age of $6.7^{+1.5}_{-1.1}$ Gyr for WASP-47, although the precision of this age determination also pushes the level at which isochronal ages are accurate (isochronal ages can have systematic errors of up to 25%, Torres et al., 2010).

4.4.2 Radial Velocity Analysis

We analyzed our radial velocity observations and archival observations taken from the literature to measure masses and orbital parameters for the WASP-47 planets. In our analysis, we combined our HARPS-N observations with previously published radial velocities from CORALIE (Hellier et al., 2012b; Neveu-VanMalle et al., 2016c), PFS (Dai et al., 2015), and HIRES (Sinukoff et al., 2017b). From our HARPS-N dataset, we excluded the four points we found to be contaminated by sky background light and one point that was taken during poor conditions and which exhibited a photon-limited velocity uncertainty of 16 $m\,s^{-1}$, six times greater than the typical uncertainty in our dataset. From the HIRES dataset, we excluded the points taken on the night of their Rossiter-McLaughlin observation (Sanchis-Ojeda et al., 2015a; Sinukoff et al., 2017b). From all four RV datasets, we excluded points taken within two hours of the mid-transit time of WASP-47 b since

Parameter	Value	Comment
Stellar Parameters		
Right Ascension	22:04:48.7	
Declination	-12:01:08	
$M_\star$ $[M_\odot]$	1.040 ±0.031	A,B
$R_\star$ $[R_\odot]$	1.137 ± 0.013	A,B
Limb darkening q_1	0.396 ± 0.018	B
Limb darkening q_2	0.423 ± 0.017	B
Stellar Density$\rho_\star$ $[g\,cm^{-3}]$	0.999 ± 0.014	B
$\log g_\star$ [cgs]	4.3437 ± 0.0063	A,B,C
M/H	0.38 ± 0.05	C
$T_{\rm eff}$ [K]	5552 ± 75	C

Table 4.2 Updated Stellar Parameters for WASP-47. A: Parameters come from our stellar parameter analysis in Section 4.4.1.3. B: Parameters come from analysis of the K2 light curve in Section 6.4.2. C. Parameters come from weighted average of spectroscopic parameters from three different methods described in Section 4.4.1.1.

those points are affected by the planet's Rossiter-McLaughlin signal which we do not model[13]. The Rossiter-McLaughlin effects of the two other transiting planets are negligibly small so we retained points taken during their transits. We list our HARPS-N velocity observations in Table 4.3 and summarize the four datasets in Table 4.4.

We modeled the radial velocity of WASP-47 as a sum of four Keplerian functions, and do not attempt to model the gravitational interactions between the four planets. Even though mutual gravitational interactions do perturb the planets' orbits (Becker et al., 2015b; Almenara et al., 2016; Weiss et al., 2016a), the effect on the radial velocity curve is undetectably small (Dai et al., 2015; Sinukoff et al., 2017b). We confirmed this result holds over the longer time-span of our observations by numerically integrating the system. We used the same eccentricity priors for the RV analysis as we did for the transit analysis – specifically we forced the orbits of WASP-47 b and WASP-47 e to be circular, and we imposed a half-Gaussian prior on the eccentricity of WASP-47 d centered at 0 (without allowing negative eccentricity solutions) with a standard deviation of 0.014. For WASP-47 c, we allowed eccentricity and the argument of periastron to vary freely with only uniform priors imposed. For the three transiting planets, we imposed Gaussian priors on orbital period and time of transit at the values and uncertainties we derived in our transit analysis. We

[13]This led to the exclusion of four HARPS-N data points and two HIRES datapoints.

Radial Velocity Observations for WASP-47

BJD - 2454833	RV [m/s]	$\sigma_{\rm RV}$ [m/s]
2457226.561	-27014.60	6.43
2457226.699	-26987.90	4.84
2457226.721	-26982.21	6.71
2457227.561	-26937.25	2.63
2457227.713	-26954.63	2.55
2457228.566	-27113.16	4.71
2457228.700	-27142.69	4.98
2457229.562	-27219.22	5.11
2457229.703	-27190.29	3.24
2457230.572	-27039.26	2.59
2457230.711	-27010.20	2.34
2457254.520	-27210.88	3.77
2457256.548	-26932.08	2.20
2457256.641	-26933.99	3.06
2457257.644	-27101.64	3.34
2457267.487	-27151.78	2.43
2457267.602	-27127.38	2.23
2457268.521	-26968.72	7.43
2457268.624	-26945.85	2.77
2457269.542	-26995.84	2.31
2457270.526	-27188.86	1.85
2457271.530	-27172.97	1.88
2457272.568	-26967.95	2.45
2457273.544	-26970.22	2.09
2457301.412	-27017.29	1.95
2457301.521	-26992.78	2.21
2457302.411	-26931.79	2.08
2457302.524	-26936.49	2.99
2457324.337	-27134.85	3.00
2457325.323	-27192.62	3.33
2457325.417	-27190.58	2.67
2457330.315	-27046.38	2.67
2457330.443	-27031.60	2.93
2457331.316	-26930.42	2.97
2457331.421	-26929.30	2.55
2457333.328	-27202.65	2.60
2457336.316	-27018.83	2.47
2457336.398	-27036.13	2.99

Radial Velocity Observations for WASP-47

BJD - 2454833	RV [m/s]	σ_{RV} [m/s]
2457557.701	-27149.24	2.56
2457558.695	-27093.68	2.09
2457559.702	-26902.75	2.53
2457560.684	-26931.92	3.67
2457562.695	-27116.92	3.47
2457563.687	-26918.20	4.10
2457565.691	-27101.52	3.66
2457566.698	-27143.80	2.79
2457573.722	-27054.63	3.49
2457574.613	-27167.37	2.72
2457574.701	-27157.09	2.51
2457576.584	-26880.69	3.16
2457576.685	-26886.91	2.42
2457579.695	-27041.15	7.68
2457580.680	-26877.83	7.44
2457616.560	-27138.59	6.88
2457617.581	-26939.47	1.98
2457618.579	-26882.95	2.53
2457651.460	-26875.57	2.16
2457652.459	-26982.58	2.18
2457653.463	-27155.02	2.81
2457654.464	-27057.53	2.88
2457655.492	-26870.08	5.08
2457658.510	-27083.94	4.73
2457659.516	-26895.47	2.20
2457661.490	-27123.19	2.53
2457669.458	-27063.11	2.80
2457670.456	-27140.53	3.07
2457671.451	-26981.35	1.97
2457672.454	-26870.44	1.88
2457721.368	-27000.32	2.36

Table 4.3 HARPS-N Radial Velocities of WASP-47 (continuted). The measured radial velocity values for each spectra in our data set.

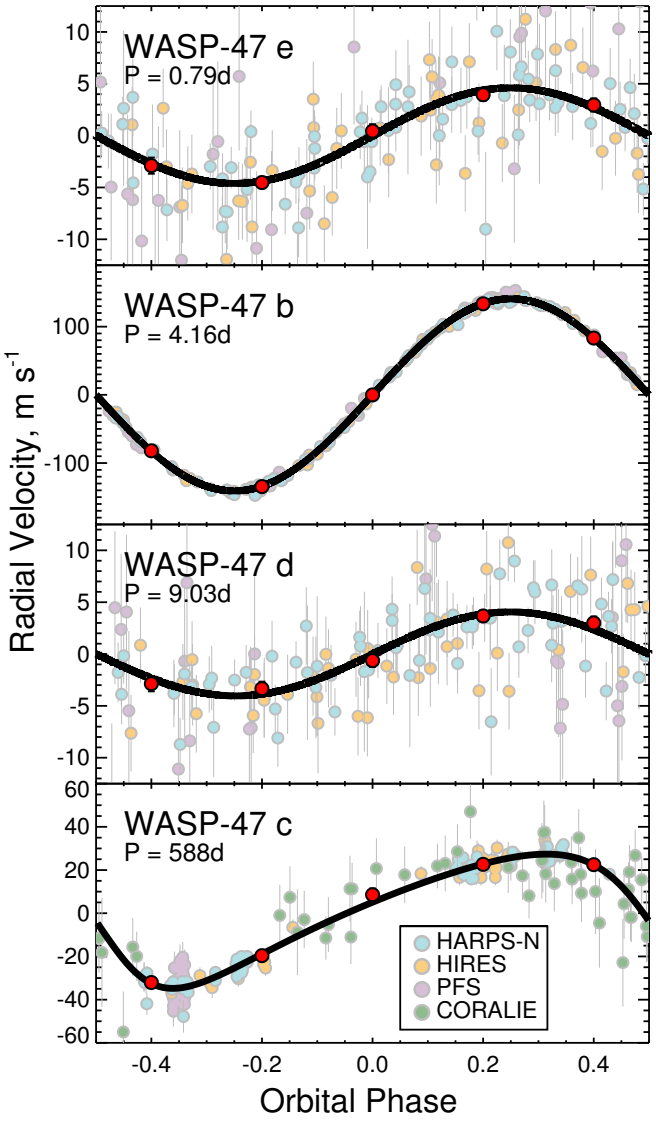

Figure 4.7 Radial Velocity Observations of WASP-47. Observations come from four spectrographs, and are folded on the periods of the four planets, with the best-fit model for each of the other three planets subtracted away. Data from HARPS-N are shown as pale blue dots, HIRES as pale orange dots, PFS as pale maroon dots, and CORALIE as pale green dots. The CORALIE data are only shown for WASP-47 c, as they are not of high enough precision to meaningfully constrain the orbits of WASP-47 e and WASP-47 d. The thick black lines are the best-fit models for each of the four planets, and the dark red dots are binned points. We note that we do not include the PFS velocities in our final analysis.

also imposed a prior that the RV semiamplitudes of all four planets be greater than zero, but the signals of all four planets were detected strongly enough that this prior had no effect.

WASP-47 is photometrically quiet, and we see no evidence in the radial velocities or activity

	HARPS-N	HIRES	PFS[a]	CORALIE
Number of usable observations	69	43	26	46
Standard deviation about best-fit	3.3 $\mathrm{m\,s^{-1}}$	3.7 $\mathrm{m\,s^{-1}}$	7.4 $\mathrm{m\,s^{-1}}$	13.5 $\mathrm{m\,s^{-1}}$
Mean photon-limited uncertainty	3.3 $\mathrm{m\,s^{-1}}$	2.0 $\mathrm{m\,s^{-1}}$	3.2 $\mathrm{m\,s^{-1}}$	12.1 $\mathrm{m\,s^{-1}}$
Time baseline	495 days	412 days	12 days	1622 days

Table 4.4 Summary of Radial Velocity Observations of WASP-47. *a*: In our final analysis, we exclude the PFS data. The standard deviation reported in the table is about the best-fit solution which did not include the PFS data. When the PFS data is included in the fit, its standard deviation about the best-fit model is 7.3 $\mathrm{m\,s^{-1}}$.

indicators of correlations due to stellar activity, so we used a white noise model for our RV analysis, with separate instrumental "jitter" terms for data from the four different telescopes. We also fit for velocity zero-point offsets for the four different instruments. We did not impose any informative priors on the jitter terms and zero-point offsets. We explored parameter space using an MCMC algorithm with affine invariant ensemble sampling, like for our transit analysis and our stellar parameter analysis. We used 100 walkers and evolved their positions for 150,000 steps each. To match the size of the chains from our transit analysis (Section 6.4.2) and our stellar parameter analysis (Section 4.4.1.3), we used the final 10,000 steps in our chains to estimate parameters. We confirmed the MCMC chains were converged by calculating the Gelman-Rubin statistics; the values were below 1.05 for all parameters.

We show the radial velocities from all four spectrographs and our best-fitting model in Figure 4.7. From our combined analysis with data from all four spectrographs, we measure masses that are more precise than, but consistent with previous determinations, except for the mass of WASP-47 e, which is somewhat at odds with the masses determined by Dai et al. (2015) and Sinukoff et al. (2017b). In particular, using data from all four spectrographs, we measure the mass of WASP-47 e to be 7.15 $\pm$ 0.67 $M_\oplus$, about 1.5–σ lower than both the measurements by Dai et al. (2015) of 12.2 $\pm$ 3.7 $M_\oplus$, and Sinukoff et al. (2017b) of 9.11 $\pm$ 1.17 $M_\oplus$.

We investigated the source of this discrepancy by repeating the RV fits with different datasets included and removed from the analysis. We found that the HIRES and HARPS-N datasets are quite consistent, both yielding masses for WASP-47 e between 6.5 and 7 $M_\oplus$, but that the PFS

dataset favors a planet mass almost a factor of two larger[14]. There are two possible explanations for the discrepancy betwen the PFS mass measurement and the HARPS-N/HIRES measurements.

1. The discrepancy is the result of random chance. The PFS measurement of WASP-47 e's semi-amplitude is only 1.5–σ away from the HARPS-N/HIRES solution, a discrepancy that should happen in about 6.5% of all similar datasets. If this explanation is correct, then including the PFS data in our solution is appropriate and will help the mass measurement converge to the true mass.

2. The discrepancy is the result of some time-correlated systematic errors in the PFS velocities. In this case including the data in our solution is not appropriate and will not help our measurements converge to the true mass.

There are reasons to believe the PFS velocities of WASP-47 could be systematically erroneous – the scatter of the PFS data about the solution is 7.3 $\mathrm{m\,s^{-1}}$, more than twice the photon-limited uncertainties listed by Dai et al. (2015), and considerably worse than both PFS's typical RV precision (better than 2 $\mathrm{m\,s^{-1}}$, Teske et al., 2016) and the radial velocity scatter from HARPS-N (3.3 $\mathrm{m\,s^{-1}}$) and HIRES (3.7 $\mathrm{m\,s^{-1}}$) in observations of WASP-47. Because the PFS observations were all taken over the course of only 12 days, if systematics are the cause of the large scatter in the velocities, any time correlations in the systematics would not necessarily average out.

Because of the risk of systematics contamination, and because the PFS data do not help much to constrain our velocity solution (the dataset is both smaller and less precise than the HARPS-N and HIRES observations, and the time baseline is not as long as the CORALIE observations), we choose to exclude the PFS observations from our final analysis. We re-ran the same MCMC analysis as before using only data from CORALIE, HARPS-N, and HIRES, and determined new planet masses. The masses and uncertainties of WASP-47 b, c, and d were essentially unchanged, but the mass of WASP-47 e decreased by about 0.5–σ while the uncertainty was unchanged. The results of this RV analysis are reported in Table 4.1.

We measure masses of 6.83 $\pm$ 0.66 $M_\oplus$ for WASP-47 e, 363.1 $\pm$ 7.3 $M_\oplus$ for WASP-47 b, 13.1

[14]The discrepancy between our combined mass measurement and that of Sinukoff et al. (2017b) is mostly due to the fact that Sinukoff et al. (2017b) included the PFS data in their analysis, which pulled their solution to higher masses.

$\pm$ 1.5 $M_\oplus$ for WASP-47 d, and a minimum mass of $M_p \sin i$ = 398.2 $\pm$ 9.3 $M_\oplus$ for WASP-47 c. WASP-47 c's orbit is significantly eccentric, with e_c =0.296 $\pm$ 0.017. The longer time-baseline of the HARPS-N observations compared to the previously published HIRES dataset and the higher precision compared to the CORALIE dataset gives a more precise measurement of the outer planet's orbital eccentricity and argument of periastron than before[15].

4.5 Dynamical Analysis for the Complete WASP-47 System

Unlike the three inner planets, which have precisely known (relative) orbital inclinations from their transit light curves, WASP-47 c has only been detected in radial velocity observations so far[16]. In this section, we use dynamical arguments to constrain the inclination of WASP-47 c. We perform a variation of the analysis done by Becker & Adams (2017), who constrained WASP-47 c's inclination by requiring that when perturbed by the outer planet, the three inner planets in the WASP-47 system all continually co-transit in the same orbital plane (where co-transit is defined as all of the planets crossing the star at any impact parameter, including grazing transits). Becker & Adams (2017) found that this requirement does not rule out orbits of WASP-47 c with high inclinations relative to the inner three planets, but that a realization of WASP-47 c with an inclination within a degree of the central projected plane of the star will always allow the inner three planets to transit.

Here we significantly strengthen the constraints placed by Becker & Adams (2017) by requiring that models of the WASP-47 system with WASP-47 c orbiting at various different inclinations reproduce other observed properties of the system. We relax the constraint that the planets all transit the star in the original orbital plane, and instead we require:

1. The inner planets around WASP-47 remain dynamically stable over integrations of 1 Myr.

[15]We note that another possible explanation for WASP-47 c's eccentricity is that it is caused by the un-modeled RV signal from an additional planet with half the orbital period of WASP-47 c (Anglada-Escudé et al., 2010), or the un-modeled signal from a longer-period planet (as postulated by Weiss et al., 2016a) contributing an RV acceleration. Our observations do not yet have the precision and time-baseline to distinguish these scenarios, so we interpret the signal as being caused by one eccentric planet.

[16]If WASP-47 c does happen to transit, it would not have been detected by K2 because it was at the wrong phase of its orbit during the 60 days of observations.

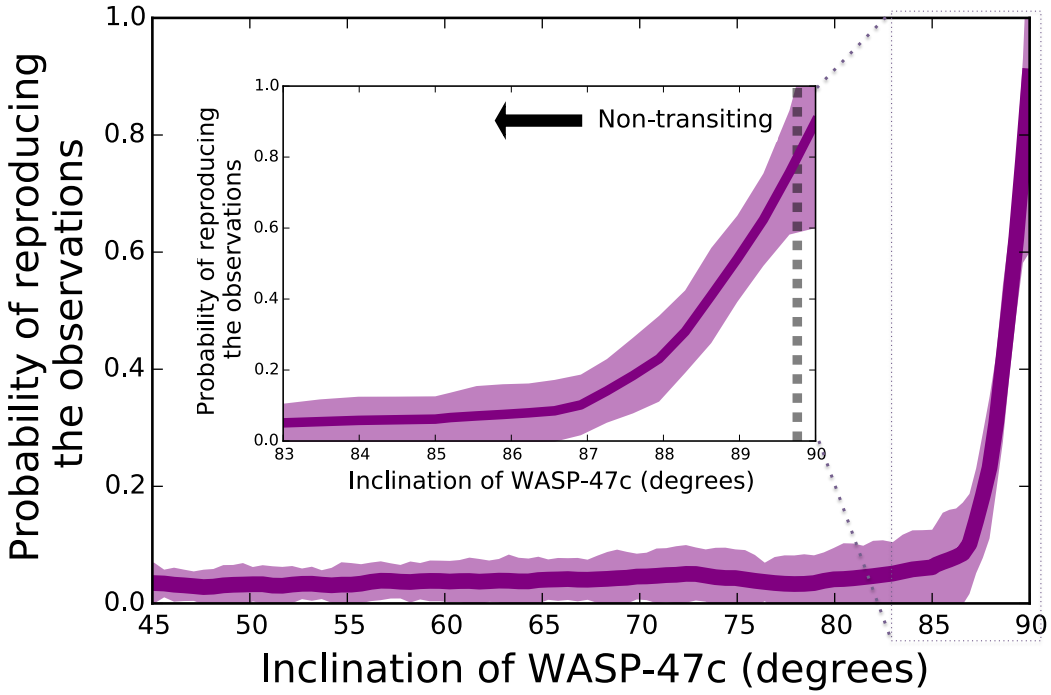

Figure 4.8 Constraints on the Orbital Inclination of WASP-47 c. This plot shows the fraction of time the WASP-47 system can reproduce our observations as a function of the inclination of WASP-47 c. The dark purple line is the average fraction of the time our simulations reproduce our observations of WASP-47, and the colored contours show the 1σ range calculated from the individual realizations. The inset diagram provides a zoomed-in version of the main figure to show the detail near $i_c = 90°$ (i.e., near the orbital plane of the inner planets).

2. The inner planets have mutual inclinations such that their transit impact parameters are as close to zero as we measure (at 3σ confidence)[17].

3. WASP-47 b has a sky-projected spin/orbit obliquity consistent with the result of Sanchis-Ojeda et al. (2015a).

We conduct numerical N-body simulations using the `Mercury6` (Chambers, 1999a) software package to evaluate the likelihood that WASP-47 c allows these three criteria to be satisfied — that is, the likelihood that the simulations reproduce the observations at varying values of WASP-47 c's orbital inclination. In our simulations, we use a hybrid symplectic and Bulirsch-Stoer (B-S)

[17]Here, although the fact that all three planets transit does not technically constrain their longitudes of ascending nodes, we assume the inner three planets are indeed coplanar. If the three planets did have high mutual inclinations, the probability that all three would transit is very small – a probability of about 1 in 1000 compared to a co-planar transit probability of roughly 1 in 15.

integrator, requiring energy conservation to a part in 10^{-8} or better, and allowing each integration to run for 1 Myr with a starting time-step of 14 minutes. We run 2000 total 1 Myr integrations, each with randomly drawn initial conditions.

The choice of 1 Myr as an integration time was chosen for two reasons: first, the short time-step required for these simulations is computationally demanding and integrations of 1 Myr remain feasible; second, 1 Myr encapsulates many ($> 10^8$) dynamical times of the inner planet, and several (3-4) secular time scales. These timescales are important because orbital instabilities will occur on dynamical time scales, while motions in a single secular cycle will be expected to repeat in subsequent secular cycles. A integration time of 1 Myr allows us to effectively evaluate any dynamical instabilities, as well as encapsulate any long-term secular variations that may occur.

The initial conditions for each planet in each integration are drawn from the observations presented in Table 4.1. For most orbital parameters of the inner three planets, we draw from a normal distribution with mean and error as reported in the table. For orbital inclination, all measured inclinations are reported to be below 90 degrees, as the degeneracy between planets orbiting slightly above and slightly below the plane cannot be broken with photometric measurements. As such, we choose an inclination from within the range of measured errors, then assign this inclination to be above or below 90 degrees with equal probability. This process is repeated independently for each of the inner three planets in each integration.

The orbital parameters of the outer planet, WASP-47 c, are also drawn from the observed values presented in Table 4.2. To disentangle M_p and i, we choose a value for the inclination of WASP-47 c for each integration, then choose a value of $M_p \sin i$ from the observed prior, and derive the planetary mass M_p.

Each integration results in one of two outcomes: (1) dynamical instabilities, in which planets collide with each other, collide with the central body, or are ejected from the system; or (2) dynamical stability. In this first case of dynamical instability, we assign a probability of those initial conditions reproducing the observations as being 0, as the system loses planets and/or changes orbits significantly. In the second, dynamically stable case, we can perform a second calculation using the results of the numerical simulations and determine the fraction of time that the set of initial conditions in a given integration reproduce the observations. The definition of

reproducing the initial conditions requires the satisfaction of three criteria: (1) all planets around WASP-47 remain dynamically stable for 1 Myr; (2) the inner planets have mutual inclinations such that their transit impact parameters are within the limits given in Table 4.1; (3) WASP-47 b has a sky-projected spin/orbit obliquity consistent with the result of Sanchis-Ojeda et al. (2014a) (since all three inner planets transit, this implies that all three inner planets share this alignment, but we require only WASP-47 b's alignment to match the measured value).

Each integration results in a pairing of WASP-47 c's orbital inclination with a measure of the probability that that particular inclination (and other initial conditions) reproduces the observations. We calculate the average fraction of time within the trials in which observations are reproduced as a function of inclination by smoothing the measurements from individual integrations with a Savitzky-Golay filter (a standard low-pass filter; Savitzky & Golay, 1964).

We show the results of our simulations in Figure 4.8. In particular, we show the smoothed function and the range of the fraction of time individual realizations of the system satisfy our observational criteria. Evidently, it is hard to reproduce the observed properties of the WASP-47 system if the outer planet is not aligned close to the inner planets' orbital plane. Unlike the result of Becker & Adams (2017), even a perfectly edge-on system with an inclination of 90° does not guarantee that the inner three planets reproduce the observations, mainly because of the increased precision on measured planetary impact parameters.

Our constraints on the orbital inclination of WASP-47 c also allow us to place approximate limits on the true mass of this planet by breaking the degeneracy in the measured $m \sin i$ between the planet's mass and orbital inclination. We find that the 68% limit on the mass of WASP-47 c is only 10% larger than the minimum mass, and that the true mass of WASP-47 c is smaller than double the minimum mass with 93% confidence.

4.6 Discussion

4.6.1 Constraints on the Composition of WASP-47 e

Our new measurements and analyses have yielded the most precise planetary masses and radii yet for the WASP-47 planets, which give us the ability to make strong inferences about the planets'

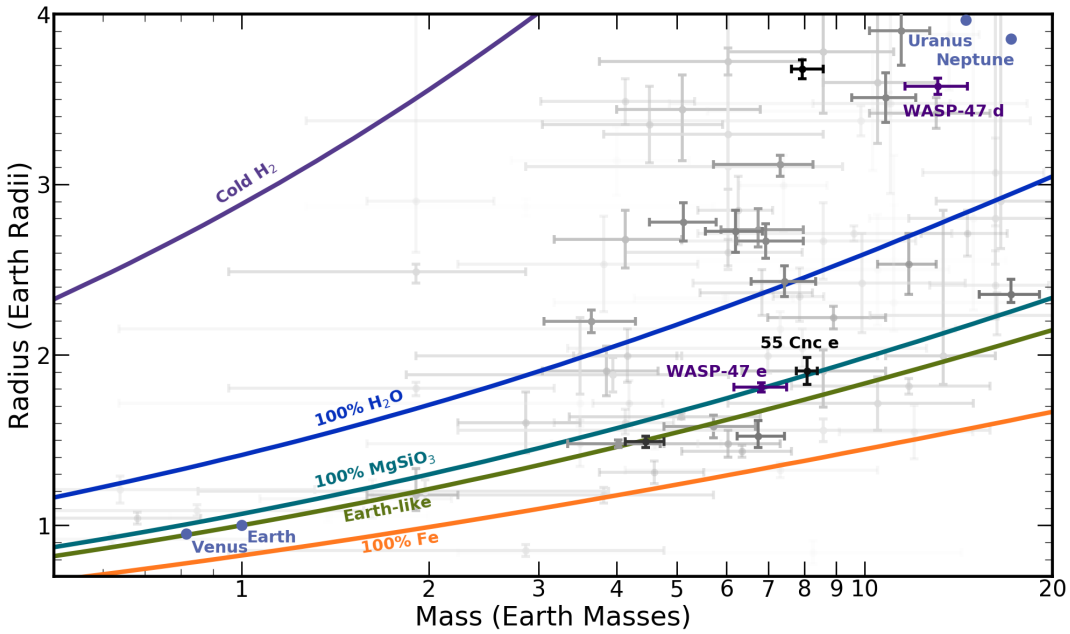

Figure 4.9 The Mass/Radius Diagram for Small Exoplanets. Planet masses and radii are taken from the NASA Exoplanet Archive (Akeson et al., 2013b), accessed 2017 Feb 22. The symbol darkness is proportional to the precision with which the masses and radii are determined. Overplotted are theoretical mass/radius relations for solid planets of different compositions from Zeng et al. (2016a) and for cold hydrogen planets from Seager et al. (2007). Solar system planets are shown in blue, and the WASP-47 planets are shown in purple. We also label 55 Cnc e to show the similarity in composition between it and WASP-47 e— both of these planets are less dense than an Earth-like composition, and likely have some volatiles around an Earth-like core.

compositions. We downloaded mass-radius relations for planets of various compositions[18] from Zeng et al. (2016a), and compared the measured mass (6.83 ± 0.66 $M_\oplus$) and radius (1.810 ± 0.027 $R_\oplus$) of WASP-47 e with these relations. We show a mass/radius diagram including the newly determined masses for WASP-47 e and WASP-47 d in Figure 4.9. Unlike most other small, highly irradiated planets (Dressing et al., 2015b), the mass and radius of WASP-47 e are not consistent with an Earth-like composition (32.5% iron core, 67.5% silicate mantle) at the $p = 5 \times 10^{-4}$, or roughly 3.3–σ level[19]. Instead, WASP-47 e is less dense than an Earth-like rocky planet, and falls

[18]The mass/radius relations are available at `https://www.cfa.harvard.edu/~lzeng/tables/mrtable3.txt`

[19]If we instead assume the slightly larger mass from our RV analysis including the PFS data, this conclusion still holds. Assuming a two-component iron core/rocky silicate mantle model, the median iron fraction for WASP-47 e would be 4.3% +/- 9.8%. An Earth-like 32.5% iron core fraction is excluded at the $p = 1.5 \times 10^{-3}$ or 3-σ level.

closer to the pure rock ($MgSiO_3$) mass/radius relation from Zeng et al. (2016a).

There are several possibilities for what the composition of WASP-47 e might be. One possibility is that WASP-47 e is a rocky planet with a very small iron core mass fraction compared to the Earth. Assuming a two-component iron core/rocky silicate mantle model, in this case, we would infer an iron fraction of 1.4% +/- 8.4%. We believe this scenario is unlikely. Theoretically, given the small scatter in chemical abundances of stars in the Solar neighborhood, rocky planet radii should not change much more than 2% due to differences in compositions (Grasset et al., 2009), while WASP-47 e's radius is 7% larger than an Earth-like planet with the same mass. Moreover, observations of small, likely rocky planets near their host stars have shown that rocky exoplanets tend to have compositions consistent with that of the Earth (Dressing et al., 2015b; Buchhave et al., 2016). It is unclear how a planet of this size, around a star of such high metallicity/iron content, could avoid accumulating any substantial amount of iron.

Instead, a more likely possibility is that WASP-47 e has an Earth-like core and mantle that is surrounded by a volatile-rich envelope. This type of interior structure is believed to be common among super-Earths and sub-Neptunes discovered by *Kepler* and K2 since RV observations have shown that most of these planets larger than about 1.6 $R_\oplus$ have densities too low to be explained by rocky compositions (Marcy et al., 2014; Weiss & Marcy, 2014a; Rogers, 2015b; Dressing et al., 2015b; Sinukoff et al., 2017a). Due to its short (19 hour) orbital period, WASP-47 e is so highly irradiated that any hydrogen/helium envelope would quickly be lost via photo-evaporation (Penz et al., 2008; Sanz-Forcada et al., 2011; Lopez et al., 2012), so any envelope around WASP-47 e must be made of water or some other high-metallicity volatile material (Lopez, 2016). Using the model described by Lopez (2016), we find that an Earth-like core and mantle surrounded by a water (or in this case, steam) layer making up 17% of the WASP-47 e's total mass is consistent with our observations.

WASP-47 e joins 55 Cnc e as the only ultra-short period (USP, $P < 1$ day) planets with densities too low to be consistent with an Earth-like composition[20] (Sanchis-Ojeda et al., 2014b). Mass measurements of other transiting USP planets from *Kepler* and CoRoT have all been consistent

[20]KOI 1843.03 must have a high density to avoid tidal disruption and therefore a larger iron core mass fraction than Earth (Rappaport et al., 2013).

with Earth-like compositions (*Kepler*-10 b, Batalha et al. 2011a; Dumusque et al. 2014; Weiss et al. 2016b; *Kepler*-78 b, Howard et al. 2013; Pepe et al. 2013; Grunblatt et al. 2015; CoRoT-7 b, Queloz et al. 2009; Haywood et al. 2014; K2-106 b, Sinukoff et al. 2017a; Guenther et al. 2017; and HD 3167 b, Christiansen et al. 2017b; Gandolfi et al. 2017).

Of all the USP planets with measured masses, WASP-47 e and 55 Cnc e are the two largest and most massive, so perhaps the largest USP planets preferentially retain some volatile materials. However, WASP-47 e and 55 Cnc e are also the two USP planets with the most precise mass determinations — it is possible that some of the other lower-mass USP planets also have densities too low to be explained by Earth-like compositions, and our data are not yet constraining enough to tell.

How might WASP-47 e and 55 Cnc e have come to possess such compositions? Previously it has been thought that USP planets might commonly be the remains of puffy planets (but probably not hot Jupiters, Winn et al., 2017a) after photo-evaporation stripped them of most or all of their volatile envelopes. Evidence for this includes the fact that almost all USP planets or candidates have radii smaller than about twice that of the Earth (Jackson et al., 2013; Sanchis-Ojeda et al., 2014b; Lopez, 2016), in contrast to the large population of less irradiated planets with radii between 2 and 4 $R_\oplus$ at longer orbital periods (Fressin et al., 2013a; Petigura et al., 2013c). WASP-47 e and 55 Cnc e might therefore be the remnants of larger planets that were massive enough to accrete a significant amount of both hydrogen and denser volatile materials before the hydrogen was subsequently lost to photoevaporation. On the other hand, WASP-47 e and 55 Cnc e may be unusual – in addition to being the only known USPs inconsistent with Earth-like interior structures, these planets are also the only well characterized USPs in systems with multiple Jovian planets. If this is not a coincidence and these planets are not typical of USPs, then a more exotic origin scenario may be required. One such possibility is that these planets are the remnant cores of hot Jupiters stripped by Roche lobe overflow (Valsecchi et al., 2014; Jackson et al., 2017). Although this mechanism cannot explain the general population of rocky USPs, this could explain WASP-47 e and 55 Cnc e's unusually low densities for such highly irradiated planets, their similar orbital periods (determined by the orbital radius at which Roche lobe overlow began), and the fact that these two objects were found in systems with multiple giant planets.

Finally, we note several additional similarities between the WASP-47 system and the 55 Cnc system. Both host stars have high metallicity (Valenti & Fischer, 2005), both systems have ultra-short-period planets which likely have a layer of dense volatile materials (WASP-47 e and 55 Cnc e), both systems have short-period giant planets (WASP-47 b and the 15d period warm Jupiter 55 Cnc b), and both systems have long-period giant planets (WASP-47 c and the 5000d period 55 Cnc d). While the 55 Cnc planets may not be as closely aligned with one another as the WASP-47 planets (only the innermost planet around 55 Cnc is known to transit, and astrometric measurements have shown a misalignment for the giant outer planet 55 Cnc d McArthur et al., 2004), the similarities between these two system architectures suggest similar origins.

4.6.2 Constraints on the Composition of WASP-47 d

We also determine a precise mass and radius for WASP-47 d of 13.1 $\pm$ 1.5 $M_\oplus$ and 3.576 $\pm$ 0.046 $R_\oplus$ respectively. On a mass/radius diagram (Figure 4.9), WASP-47 d is close to, but slightly smaller and less massive than the two Solar system ice giants, Uranus and Neptune. Like Uranus and Neptune, WASP-47 d must have a low density hydrogen/helium envelope to match our mass and radius measurements, but most of the mass of the planet's mass is in a dense core. Using the models from Lopez & Fortney (2014), we find that if the interior has an Earth-like composition with an iron core and rocky mantle, the hydrogen/helium envelope around WASP-47 d would have a mass fraction of about 5%. If instead, the solid core is rich in water or other high metallicity volatiles, the hydrogen/helium envelope mass fraction would be closer to 2%.

4.6.3 Orbital Inclination of WASP-47 c

Even though WASP-47 c has only been detected in radial velocities, in Section 4.5, we were able to put strong constraints on its orbital inclination by requiring dynamical perturbations from its orbit not disrupt the well aligned, co-transiting state of the inner three planets. We found that WASP-47 d likely has an inclination within a few degrees of an edge-on 90° orbit.

The fact that WASP-47 c likely orbits in the same plane as the three transiting planets suggests that the system formed in a dynamically quiet manner. If the hot Jupiter, WASP-47 b, formed beyond the snow-line and migrated after being scattered by WASP-47 c, we might expect the plane

of WASP-47 c's orbit to be different from the plane of the inner system. Instead, we see a picture more consistent with formation and migration that largely happened in the plane of the protoplanetary disk. In particular, the fact that WASP-47 e likely has a layer of dense volatile material like water suggests that it may have formed beyond the snow-line and migrated to its current location through the protoplanetary disk. WASP-47 c's relatively high eccentricity is somewhat difficult to explain in this context, because any eccentricity would have been damped by the disk. In this scenario, the eccentricity must have been excited after the disk dissipated, possibly by another, more distant planet, as suggested by Weiss et al. (2016a).

4.6.4 WASP-47 c's Transit Probability

Another, more practical, implication of the likely close alignment of WASP-47 c with the inner transiting system is that the probability of WASP-47 c transiting is greatly enhanced compared to the naive geometric transit probability. The expression for geometric transit probability is given by Sackett (1999):

$$P_{\text{transit,geom}} = \frac{\int_{i_t}^{90^\circ} \sin i \; di}{\int_{0^\circ}^{90^\circ} \sin i \; di} \tag{4.1}$$

where i is the planet's inclination, and i_t is the inclination above which the planet will transit, which depends on the orbital eccentricity e, argument of periastron ω_p, semi-major axis a, stellar radius $R_\star$, and planetary radius R_p as follows:

$$\cos i_t = \frac{R_p + R_\star}{a} \times \frac{1 + e \sin \omega_p}{1 - e^2} \tag{4.2}$$

We generalized the geometric expression by including a function $\mathcal{P}(i)$, the fraction of time our simulated systems reproduced observations of WASP-47 inside the integrals, giving:

$$P_{\text{transit,mod}} = \frac{\int_{i_t}^{90^\circ} \mathcal{P}(i) \sin i \; di}{\int_{0^\circ}^{90^\circ} \mathcal{P}(i) \sin i \; di} \tag{4.3}$$

Here, for $\mathcal{P}(i)$ we use the Savitzky-Golay filtered fraction of times that our numerical simulations reproduced observations of WASP-47, and for i_t we use 89.66°.

Without *a priori* knowledge of our inclination constraints for WASP-47 c, the transit probability is about 0.6%. When we take into account our dynamical inclination constraints, the probability increases by more than an order of magnitude to about 10% – the same *a priori* transit probability of a typical hot Jupiter.

If WASP-47 c is found to transit, it would open the door to future sophisticated investigations into the properties and formation history of the WASP-47 planets. It would be possible to study the atmosphere of both WASP-47 b and WASP-47 c in transit with the upcoming *James Webb Space Telescope*, determine and compare atmospheric abundances, and infer these planets' birthplaces (Öberg et al., 2011). A detection of a transit of WASP-47 c could make the WASP-47 system a key to unlocking the origin of hot Jupiters.

Detecting a transit of WASP-47 c should not be difficult - the transit depth would likely be about 1%, easily attainable by ground-based telescopes with moderate apertures. The transit duration will be long - an equatorial transit of WASP-47 c would last 14 hours, so a successful detection would likely require a coordinated ground-based campaign with several telescopes longitudally dispersed around the globe. At present, the largest obstacle to successfully recovering a transit of WASP-47 c is the uncertainty in the transit time. The last transit window happened around 9 January 2017, while WASP-47 was unobservable behind the Sun, with an uncertainty in transit time of 4.8 days. The next several transit windows will be around 21 August 2018 $\pm$ 6.5 days, 31 March 2020 $\pm$ 8.6 days, and 10 November 2021 $\pm$ 10.8 days. It would take a massive ground-based campaign to cover enough of these transit windows to ensure success. Although the uncertainties on the transit times are large now, they will sharpen considerably once precise RV spectographs have completed observing a full orbital period of WASP-47 c. We will continue to observe WASP-47 with HARPS-N in the coming years to refine the orbital period and ephemeris of WASP-47 c in preparation for the chance to detect the planet in transit.

4.7 Summary

We have investigated the WASP-47 planetary system, which is known to host a hot Jupiter, two smaller transiting planets flanking the hot Jupiter, and a long-period Jovian companion. Using

new data from the HARPS-N spectrograph and previously published data from the K2 mission and other ground-based spectrographs, we have measured the masses and radii of the transiting planets, and determined the orbit of the outer planet. Our main conclusions are summarized as follows:

1. We have measured the most precise masses and radii for the WASP-47 planets yet. The innermost planet, WASP-47 e, has a mass of 6.83 ± 0.66 $M_\oplus$ and a radius 1.810 ± 0.027 $R_\oplus$. The hot Jupiter, WASP-47 b has mass 363.1 ± 7.3 $M_\oplus$ and a radius 12.63 ± 0.15 $R_\oplus$. We find the Neptune-sized planet, WASP-47 d, has a mass 13.1 ± 1.5 $M_\oplus$ and radius 3.576 ± 0.046 $R_\oplus$. The outer Jovian planet, WASP-47 c is not known to transit, so from our radial velocity observations, we only measure the planet's minimum mass $m \sin i$ of 398.2 ± 9.3 $M_\oplus$.

2. WASP-47 e, unlike most other planets in ultra short period orbits, does not have an Earth-like composition. We find that WASP-47 e is not dense enough to have an iron core with the same mass fraction as terrestrial planets in the Solar system. Instead, WASP-47 e likely has a volatile rich (possibly water/steam) envelope comprising 17% its total mass on top of an Earth-like core.

3. We show using dynamical simulations that the inclination of WASP-47 c is likely well aligned with the inner transiting system. The orbital inclination of WASP-47 c is likely within a few degrees of edge on in order to not disrupt the inner transiting planets from their present-day well aligned configuration. This alignment, plus the alignment between the planets' orbits and the stellar spin axis (Sanchis-Ojeda et al., 2015a) suggests a dynamically quiet formation/migration scenario for the WASP-47 planets that kept all of the planets in the plane of the protoplanetary disk. The outer planet is much more likely to transit than the geometric transit probability, motivating campaigns to observe the transit in future opportunities. Additionally, this limit on the inclination suggests that the true mass of the WASP-47 c is likely close to the measured $M_P \sin i$.

Future radial velocity observations of WASP-47 will both continue to improve the precision on the masses of the two smaller planets, and will greatly improve the precision on the predicted

transit time of WASP-47 c. Sharpening the transit predictions will be hugely important to making a campaign to detect or rule out transits of WASP-47 c feasible.

Parameter	Value		68.3% Confidence Interval Width	Comment
WASP=47 e				
Orbital Period, P [days]	0.789592	±	0.000012	B
Radius Ratio, $(R_P/R_\star)$	0.01461	±	0.00013	B
Scaled semi-major axis, $a/R_\star$	3.205	±	0.014	B
Orbital inclination, i [deg]	85.98	±	0.75	B
Transit impact parameter, b	0.224	±	0.041	B
Time of Transit t_t [$\mathrm{BJD_{TDB}}$]	2457011.34861	±	0.00033	B
Transit Duration t_{14} [hours]	1.899	±	0.013	B
RV Semiamplitude K_e [$\mathrm{m\,s^{-1}}$]	4.61	±	0.44	D
M_P [$\mathrm{M_\oplus}$]	6.83	±	0.66	A,D
R_P [$\mathrm{R_\oplus}$]	1.810	±	0.027	A,B
Surface Gravity [cgs]	20.5	±	2.0	A,B,D
Mean Density [g $\mathrm{cm^3}$]	6.35	±	0.64	A,B,D
WASP-47 b				
Orbital Period, P [days]	4.1591289	±	0.0000042	B
Radius Ratio, $(R_P/R_\star)$	0.10193	±	0.00021	B
Scaled semi-major axis, $a/R_\star$	9.702	±	0.044	B
Orbital inclination, i [deg]	88.98	±	0.20	B
Transit impact parameter, b	0.173	±	0.032	B
Time of Transit t_t [$\mathrm{BJD_{TDB}}$]	2457007.932132	±	0.000021	B
Transit Duration t_{14} [hours]	3.5722	±	0.0030	B
RV Semiamplitude K_b [$\mathrm{m\,s^{-1}}$]	140.64	±	0.44	D
M_P [$\mathrm{M_\oplus}$]	363.1		7.3	A,D
R_P [$\mathrm{R_\oplus}$]	12.63	±	0.15	A,B
Surface Gravity [cgs]	22.33	±	0.27	A,B,D
Mean Density [g $\mathrm{cm^3}$]	0.993	±	0.021	A,B,D
WASP-47 d				
Orbital Period, P [days]	9.03077	±	0.00017	B
Radius Ratio, $(R_P/R_\star)$	0.02886	±	0.00016	B
Scaled semi-major axis, $a/R_\star$	16.268	±	0.074	B
Orbital inclination, i [deg]	89.32	±	0.23	B
Transit impact parameter, b	0.192	±	0.065	B
Time of Transit t_t [$\mathrm{BJD_{TDB}}$]	2457006.36931	±	0.00039	B
Transit Duration t_{14} [hours]	4.288	±	0.039	B
RV Semiamplitude K_d [$\mathrm{m\,s^{-1}}$]	3.93	±	0.43	D
M_P [$\mathrm{M_\oplus}$]	13.1		1.5	A,D
R_P [$\mathrm{R_\oplus}$]	3.576	±	0.046	A,B
Surface Gravity [cgs]	10.1	±	1.1	A,B,D
Mean Density [g $\mathrm{cm^3}$]	1.58	±	0.18	A,B,D
Eccentricity	< 0.014			E
WASP-47 c				
Orbital Period, P [days]	588.5	±	2.4	D
Time of Inferior Conjunction t_t [$\mathrm{BJD_{TDB}}$]	2457763.4	±	4.9	D
RV Semiamplitude K_d [$\mathrm{m\,s^{-1}}$]	31.01	±	0.43	D
$M_P \sin i$ [$\mathrm{M_\oplus}$]	398.2		9.3	A,D
Eccentricity	0.296	±	0.017	D
Argument of Periastron [degrees]	112.4	±	4.8	D
Semimajor Axis [AU]	1.393	±	0.014	A,D

Table 4.5 Updated Planetary Parameters for WASP-47 planets. A: Parameters come from our stellar parameter analysis in Section 4.4.1.3. B: Parameters come from analysis of the K2 light curve in Section 6.4.2. C. Parameters come from weighted average of spectroscopic parameters from three different methods described in Section 4.4.1.1. D: Parameters come from our radial velocity analysis in Section 4.4.2. E: The eccentricity of HIP 41378 d was fit with a strong Gaussian prior of 0 ± 0.014 from TTV and dynamical stability arguments. The argument of periastron was not constrained in our fits either by the data or prior.

CHAPTER V

Understanding Companions in Systems Around Cool Stars Hosting Hot Jupiters

Results in this chapter were published in: ***Becker, J. C.***, *Vanderburg, A., Adams, F., Khain, T., & Bryan, M. "Exterior Companions to Hot Jupiters Orbiting Cool Stars are Coplanar." 2017, The Astronomical Journal, 154, 230* and are presented here with minor revisions.

5.1 Abstract

The existence of hot Jupiters has challenged theories of planetary formation since the first extrasolar planets were detected. Giant planets are generally believed to form far from their host stars, where volatile materials like water exist in their solid phase, making it easier for giant planet cores to accumulate. Several mechanisms have been proposed to explain how giant planets can migrate inward from their birth sites to short-period orbits. One such mechanism, called Kozai-Lidov migration, requires the presence of distant companions in orbits inclined by more than ~ 40 degrees with respect to the plane of the hot Jupiter's orbit. The high occurrence rate of wide companions in hot Jupiter systems lends support to this theory for migration. However, the exact orbital inclinations of these detected planetary and stellar companions is not known, so it is not clear whether the mutual inclination of these companions is large enough for the Kozai-Lidov process to operate. This chapter shows that in systems orbiting cool stars with convective outer layers, the orbits of most wide planetary companions to hot Jupiters must be well aligned with the orbits of the hot Jupiters and the spins of the host stars. For a variety of possible distributions

for the inclination of the companion, the width of the distribution must be less than ~ 20 degrees to recreate the observations with good fidelity. As a result, the companion orbits are likely well-aligned with those of the hot Jupiters, and the Kozai-Lidov mechanism does not enforce migration in these systems.

5.2 Introduction

Hot Jupiters, or Jupiter-sized planets orbiting with periods of a few days and distances of about 2-5% of an astronomical unit, are an intriguing class of exoplanets with no analog in our own Solar system. Although hot Jupiters are thought to account for only about 0.9 – 1.5% of the total population of planets (Marcy et al., 2005; Cumming et al., 2008; Mayor et al., 2011; Wright et al., 2012; Wang et al., 2015a), they are over-represented in our current population of discovered exoplanets due to their large masses, large radii, and short orbital periods, which make them easy to detect in both transit and radial velocity observations. More than 300 hot Jupiters have been discovered to date[1].

Since the discovery of the first hot Jupiters, understanding their origins has been a challenge for planet formation theorists, who have proposed several different mechanisms for how these planets form and how the systems are assembled into the architectures we see today. One traditional model for giant planet formation, which has been highly successfully applied to the formation of giant planets in our own solar system, is called core accretion (Stevenson, 1982). In this model, a small core (likely composed of rocky and dense volatile materials) first forms in the proto-planetary disk, far enough away from its host star that dense volatile materials like water and/or methane are in solid, rather than gaseous, forms. Once a core has formed and become massive enough, it subsequently accretes a massive hydrogen/helium dominated envelope via runaway gas accretion, leaving planets roughly the size and mass of Jupiter in orbits similar to that of Jupiter – far away from their host stars.

In this traditional picture, in order for the newly formed giant planet to become a *hot* Jupiter, it must then migrate inwards towards its host star, halting its migration at an orbital distance of about

[1]As of 12 August 2017, the NASA Exoplanet Archive reports 315 known hot Jupiters. `https://exoplanetarchive.ipac.caltech.edu/cgi-bin/TblView/nph-tblView?app=ExoTbls&config=planets`

0.05 AU. Theorists have identified several mechanisms by which hot Jupiters might migrate from an orbit at tens of AU into their present-day short-period orbits. One migration mechanism involves torques arising from tidal-disk interactions ("disk torques"), which could cause the hot Jupiters to slowly spiral inwards towards their host stars in the plane of the protoplanetary disk (see Tanaka et al., 2002; Kley & Nelson, 2012). Another mechanism relies upon dynamical interactions between planets to excite high eccentricities in the proto-hot Jupiters after the gas disk has dissipated, bringing the planets into orbits whose perihelia distances are close to the surface of the host star. Tidal interactions when the planet comes close to the host star then might dissipate orbital energy, causing the orbit to shrink and result in the short-period orbits seen in hot Jupiter systems. There are a couple of ways to excite these high eccentricities. Eccentricity can be excited via the Kozai-Lidov effect, which we call Kozai-Lidov migration (and which requires an inclined exterior companion; Lidov, 1962; Kozai, 1962). In some, more rare, cases, eccentricity can also be excited via low-inclination secular interactions, which we call co-planar high eccentricity migration (Petrovich, 2015).

Another recently revived mechanism for hot Jupiter formation is *in situ* formation: instead of runaway accretion occurring far away from the host star, where dense volatile materials are abundant in their solid forms, the super-Earth-sized cores of the hot Jupiters form past the ice line, and migrate in to their modern orbital radii simultaneously with other material in the disk. At this new orbital radius, the gas surface density would then be high enough for the core to experience runaway gas accretion at that location, forming a hot Jupiter (Batygin et al., 2016b). This scenario builds on the idea that there exists a nearly ubiquitous population of super-Earth-sized planets orbiting close to their host stars (e.g. **?**), many of which have sufficient mass to undergo run-away accretion.

These four distinct mechanisms for hot Jupiter system assembly (disk torques, coplanar high-eccentricity migration, Kozai-Lidov high eccentricity migration, and *in situ* formation) have different observational outcomes. High eccentricity migration destabilizes the orbits of close-in companions and requires the presence of distant massive companions in hot Jupiter systems which originally helped excite those high eccentricities. If Kozai-Lidov migration is dominant, then these companions should have mutual inclinations with the hot Jupiters of $\gtrsim 40$ °. By contrast, disk migration

will likely result in dynamically quiet systems with low mutual inclinations. *In situ* formation initially produces a coplanar inner system, but subsequent secular interactions may eventually produce systems with either aligned (Batygin et al., 2016b) or misaligned (Batygin et al., 2016b; Spalding & Batygin, 2017) close-in exterior companions, such as those seen in the WASP-47 system (Becker et al., 2015b). Such interactions would not change the natal stellar obliquity.

A powerful way to understand the architectures and formation histories of hot Jupiter systems is through measurements of or constraints on the angles between the orbital angular momentum and the stellar spin axis. The difference between these angles is commonly called the stellar obliquity. There is a striking observed correlation between the photospheric temperature of the host star and the stellar obliquity. Observations of hot Jupiters (Winn et al., 2010a; Albrecht et al., 2012a), (and more tentatively, smaller planets as well, Mazeh et al., 2015) have shown that the orbits of planetary systems around cool stars ($T_* < 6200$ K) tend to be aligned with the spin of the host star, while the orbits of planets around hot stars ($T_* > 6200$ K) tend to be misaligned with the stellar spin axis. The boundary between the populations of hot and cool stars is commonly taken at stellar mass $M_* = 1.3$ $M_\odot$, or equivalently at surface temperature $T_* = 6200$ K. This threshold is often called the "Kraft break" (Kraft, 1967; van Saders & Pinsonneault, 2013). This mass limit corresponds to stellar configurations where the convective envelope becomes thin, which provides some clues to the physical processes involved.

Although the observed pattern of obliquities as a function of stellar surface temperature remains under study as additional stellar obliquity measurements are performed with methods such as Doppler tomography (recent measurements include Zhou et al., 2017; Johnson et al., 2017) or the Rossiter-McLaughlin technique (Ohta et al., 2005), the fact that hot Jupiters around cool stars tend to have orbits that are well-aligned with their host stars' spins axes appears to hold. However this alignment came about, it is difficult to produce it by random chance, and similarly difficult to reproduce it once it has been disturbed. This alignment could be primordial (for example, magnetic fields can realign a young star with its disk; see Spalding & Batygin, 2015), or it could come about by re-alignment of stellar spin axes due to the planets' tidal influence (Hut, 1980; Adams & Bloch, 2015; Albrecht et al., 2012a), a fairly slow process which takes hundreds of millions of years or more (Albrecht et al., 2012a; Lai, 2012). Therefore, in order for hot Jupiters to maintain their spin/orbit

alignment, their obliquities cannot be perturbed or changed on timescales significantly shorter than this benchmark value.

In this chapter, we ask the question: "What effect do distant perturbing bodies have on the alignment of hot Jupiter orbits and the spins of their host stars?" Many distant companions, both planetary and stellar, to hot Jupiters have been found, and in fact are more frequent around hot Jupiter hosts than around typical stars (Knutson et al., 2014d; Ngo et al., 2015; Bryan et al., 2016). These companions also seem to have little effect on the hot Jupiters' spin orbit alignments (Knutson et al., 2014d; Ngo et al., 2015; Bryan et al., 2016). But if these distant companions have a strong enough gravitational influence on the hot Jupiters and have large mutual inclinations, they could in principle disturb the spin orbit alignment of the hot Jupiters away from what we observe in cool stars. By calculating the effect of the observed distant companions to hot Jupiters, we can place constraints on the mutual inclination between these companions and the well aligned hot Jupiters.

Here, we *statistically* constrain the orbital inclinations of exterior long-period companions in hot Jupiter systems. We approach this problem by identifying a sample of hot Jupiters orbiting cool stars with known long-period companions and measured stellar obliquity and calculating the probability that each of these hot Jupiters will retain its low inclination as a function of the inclination of the distant perturbing companions using secular and N-body techniques. In Section 5.3, we describe our sample selection and analysis techniques. In Section 5.4, we present the statistical results of our analysis and show that most companions of hot Jupiters around cool stars orbit near the plane of the hot Jupiters' orbits. In Section 5.5, we discuss the implications of this result on hot Jupiter formation and suggest avenues for future work.

5.3 Methods

5.3.1 Sample selection

We focus in this chapter on transiting hot Jupiters with known companions detected via radial velocity observations. Since the hot Jupiters transit, it is often possible to measure components of the stellar obliquity via the Rossiter McLaughlin effect, a crucial ingredient in our calculations. Also, because the hot Jupiters transit, we know their orbital inclinations quite precisely to be nearly

90°. Therefore, any constraint on the orbital inclination of the distant companion constrains the mutual orientation of the two planets' orbits.

The systems we consider in this work are those with the following properties:

- The host star is cool (with an effective temperature below Kraft break; $T_* < 6200$ K)
- The star hosts a hot Jupiter (roughly Jupiter-mass planet with an orbital period between 0.8 and 6.3 days; as defined in Steffen et al., 2012b)
- There exists in the literature a measure of either the projected or true stellar obliquity (angle between the stellar spin axis and the planet's orbital angular momentum vector) for the host star. We do not require this obliquity to have any particular value or precision, but merely for a measurement to exist.
- There is evidence in the literature that the system has an additional companion in the system; this companion may be a Jupiter-like planet or a brown dwarf

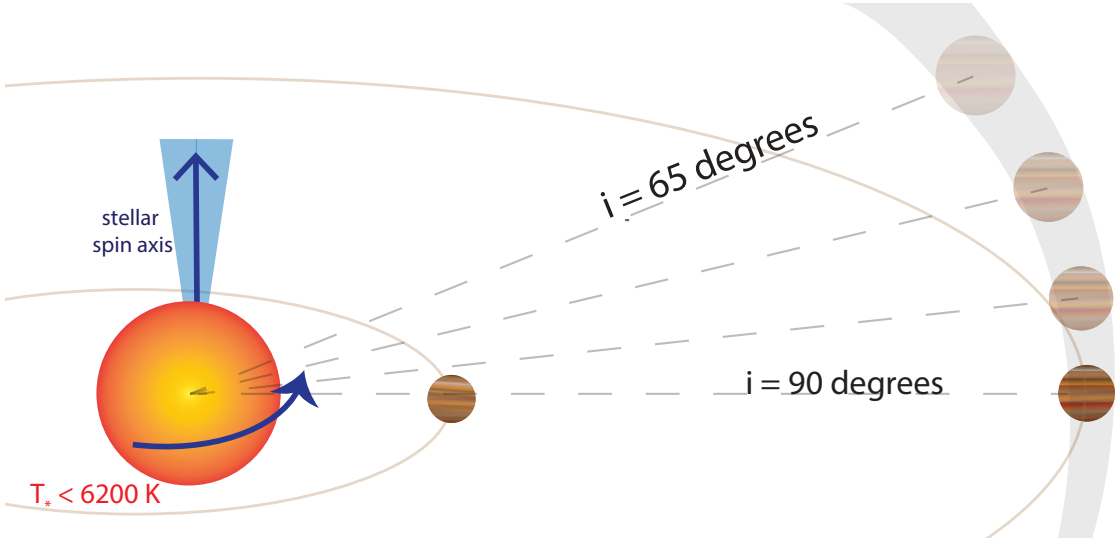

Figure 5.1 Schematic Diagram of Hot Jupiters Orbiting Cool Stars and their Companions. The systems we consider are those with stellar effective temperatures below the Kraft break ($T_* < 6200$K), a measured stellar obliquity, and evidence of an exterior companion whose residuals do not correlate with stellar activity level. The inclination of the outer companion is not known for any of the systems in our sample (this quantity is varied in the analysis).

Figure 5.1 illustrates the geometry of the type of systems we consider in this work. A list of all the stars that fit these criteria and their properties, as well as the measured orbital properties

of their planets, is given in Table 5.1. Additional companions in these systems come in two forms: First, there are systems for which the orbits of additional companions have been well-characterized, and the period of their orbits are known (such as WASP-41, WASP-47, and HAT-P-13). Second, there are systems in which a trend in the RV data has been identified, but the (putative) companion does not have a precisely measured period (such as HAT-P-4, WASP-22, and WASP-53). These latter systems only have constraints on the companion's orbits (see, for example, Figure 10 of Knutson et al., 2014b), which can be derived from the radial velocity curves. In this work, we use the posteriors from Bryan et al. (2016) for HAT-P-4 and WASP-22, and generate a new posterior for WASP-53 using the data in Triaud et al. (2017) and the method from Bryan et al. (2016), without any adaptive optics constraints on outer companions.

We exclude from our sample stars with companions and effective temperatures measured to be above the Kraft break. HAT-P-7, HAT-P-32, HAT-P-2 have temperatures right above Kraft break and have high projected obliquities, which is consistent with the convective realignment argument (the stars did not have a sufficient convective envelope to become realigned early in their lives). We exclude warm Jupiters (defined using the definition given in Steffen et al. 2012b to be Jupiter-mass planets with orbital periods between 6.3 days and 15.8 days) because these objects are not typically proposed to form through a high-eccentricity pathway and therefore, unlike hot Jupiters, are not expected to possess inclined companions (Huang et al., 2016b).

The system XO-2N contains a hot Jupiter (Burke et al., 2007), orbits a cool star, and has a projected stellar obliquity of 7 ± 11 degrees (Damasso et al., 2015). Knutson et al. (2014b) also presented RV evidence of a long-period signal in the system. However, Damasso et al. (2015) found a correlation between the RV residuals and the stellar activity index R_{HK}, indicating that the long period signal is likely stellar activity and not a companion. For this reason, we also exclude this system from our sample (although we note that this system and its companion would fit perfectly into the aligned paradigm we see in our sample, were the companion to be real).

Of the systems we include, some have additional components that do not significantly affect the evolution of the system. The WASP-47 system is unique among hot Jupiter-hosting systems because it contains two short-period planets in addition to the hot Jupiter WASP-47b. Both of these additional planets are roughly coplanar with the hot Jupiter orbit (as they were both discovered

via K2 transit photometry). In this work, we consider only the precession of the hot Jupiter, and do not impose additional constraints based on the transiting behavior or potential dynamical instability of the other planets (unlike the analyses done in Becker & Adams, 2017; Vanderburg et al., 2017). We choose to consider the hot Jupiter alone because it is the planet for which the Rossiter-McLaughlin measurement was made (Sanchis-Ojeda et al., 2015a). Excluding WASP-47 from the sample due to its unusual architecture would not change the results significantly since all hot Jupiters in our sample are aligned, so to maximize our sample size, we choose to include it.

HAT-P-13 actually has three planets, a hot Jupiter and its two companions. The first companion has a period of 428.5 ± 3.0 days, an eccentricity of 0.691 ± 0.018, and an $m \sin i$ of 15.2 ± 0.1 M_J (Bakos et al., 2009). The second companion does not have a measured period, but an RV trend indicates its existence (Winn et al., 2010b). The inner of those two (the middle body in the system) does not transit. Since the perturbations from the outermost body are expected to be adiabatic (Becker & Batygin, 2013), we ignore the effect of the outer planet in our analysis. We do note that the influence of the outer planet has the potential to adiabatically misalign both inner planets. However, given that we measure a low stellar obliquity, and will show later that the middle planet is probably also aligned, it is unlikely the outer companion is highly inclined. Future modelling efforts may readily test this prediction.

5.3.2 The Laplace-Lagrange Secular model

Additional exterior companions can alter the orbital inclination of the inner hot Jupiter through planet-companion interactions. As these interactions are mainly secular and non-resonant, we can approximate the system's orbital evolution over time using secular Laplace-Lagrange theory. This provides an approximation for the expected effect, which can be used to guide further analysis. Although we also use numerical N-body simulations (see below) to construct our final results in this work, this section outlines the analytic, guiding theory for describing the inclination evolution over time.

As we expect secular interactions to dominate, we can construct a disturbing function for the planetary system, excluding terms that depend on the relative positions of the planets in their orbits (Murray & Dermott, 1999). The result is an equation which treats the planets as smeared-out rings

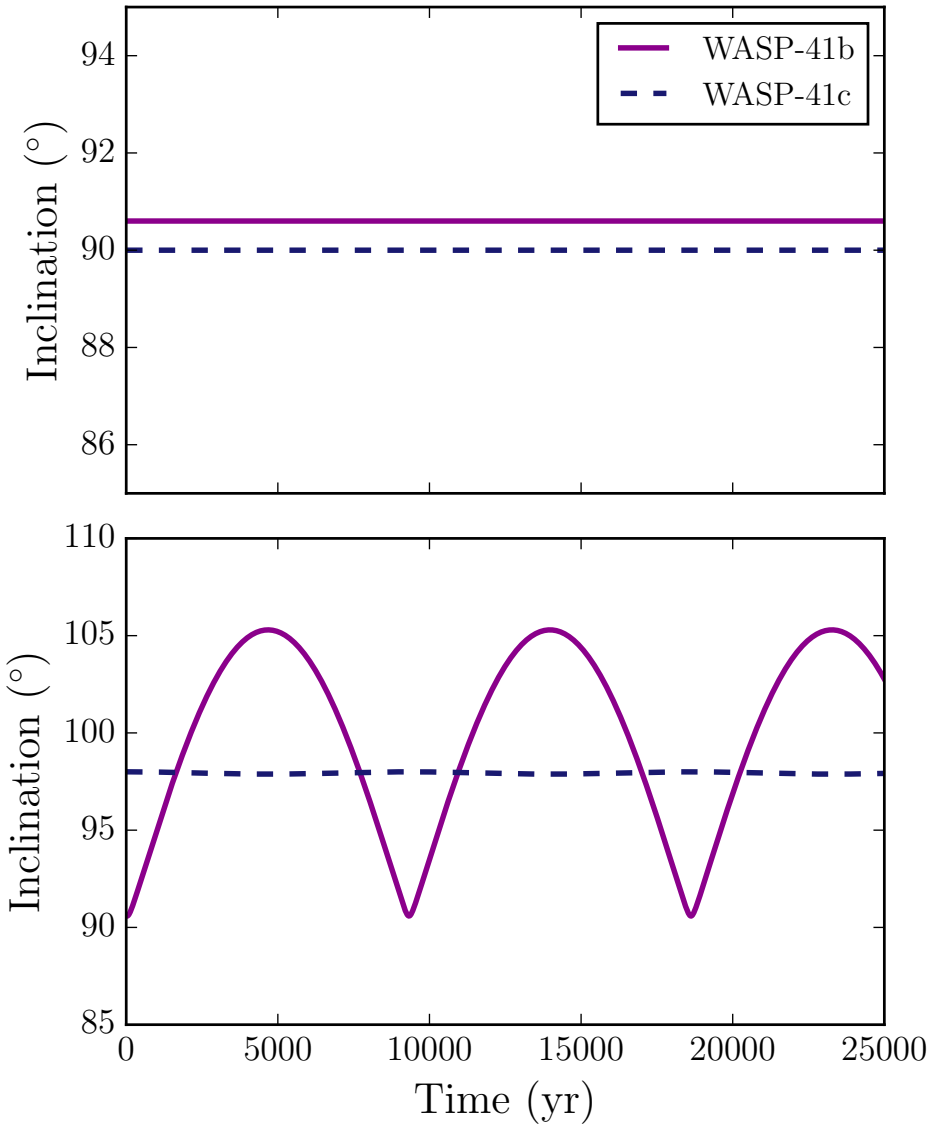

Figure 5.2 Secular Evolution of WASP-41b and -41c. The evolution of the inclination of WASP-41b and WASP-41c as given by Laplace-Lagrange secular theory: the secular theory was computed using inclinations centered around 0 degrees, and the inclination plotted is the secular result plus 90 degrees (to signify that WASP-41b is seen in an edge-on orbit). The companion's observed initial inclination differs in the two panels: $i_c = 90°$ (top panel) and $i_c = 98°$ (bottom panel). The presence of an inclined companion (-41c) results in an oscillating inclination angle for the hot Jupiter (-41b), affecting its angular momentum direction. In particular, a higher inclination of WASP-41c decreases the amount of time WASP-41b spends near its original orbital momentum direction, thereby increasing the likelihood of observing obliquity misalignments.

of mass. Including only the terms describing the inclination of each planet's orbit to second order, this result becomes

$$\mathcal{R}_j^{(\mathrm{sec})} = n_j a_j^2 \left[\frac{1}{2} B_{jj} I_j^2 + \sum_{k=1,\ j\neq k}^{N} \left(B_{jk} I_j I_k \cos\left(\Omega_j - \Omega_k\right)\right) \right], \tag{5.1}$$

where j is the planet number, n the mean motion, I the inclination, ω the argument of pericenter, and Ω is the longitude of the ascending node. In the case of a spherical central body, the quantities B_{ij} represent the interaction coefficients between pairs of planets and are given by

$$B_{jj} = -n_j \left[\frac{1}{4} \sum_{k=1,\ j\neq k}^{N} \frac{m_k}{M_c + m_j} \alpha_{jk} \bar{\alpha}_{jk} b_{3/2}^{(1)}(\alpha_{jk}) \right], \tag{5.2}$$

and

$$B_{jk} = n_j \left[\frac{1}{4} \frac{m_k}{M_c + m_j} \alpha_{jk} \bar{\alpha}_{jk} b_{3/2}^{(1)}(\alpha_{jk}) \right], \tag{5.3}$$

where m_k is the mass of the kth planet, M_c is the mass of the central star, the α_{jk} are the semi-major axis ratios a_j/a_k, and $\bar{\alpha}_{jk}$ are the semi-major axis ratios for $a_j/a_k < 1$. The function $b_{3/2}^{(1)}(\alpha)$ is the Laplace coefficient, which is defined by

$$b_{3/2}^{(1)}(\alpha) = \frac{1}{\pi} \int_0^{2\pi} \frac{\cos\psi \ d\psi}{(1 - 2\alpha\cos\psi + \alpha^2)^{3/2}}\,. \tag{5.4}$$

Further explanation of this theory and potential expansions of the model can be found in Murray & Dermott (1999). Using the standard transformation

$$p_j = I_j \sin\Omega_j \qquad \text{and} \qquad q_j = I_j \sin\Omega_j\,, \tag{5.5}$$

the solutions of the eigenvalue problem defined by matrix $\mathbf{B}$ take the form:

$$p_j(t) = \sum_{k=1}^{N} I_{jk} \sin(f_k t + \gamma_k) \tag{5.6}$$

and

$$q_j(t) = \sum_{k=1}^{N} I_{jk} \cos(f_k t + \gamma_k) \,. \tag{5.7}$$

To complete the initial condition problem, we define normalized eigenvectors $\mathcal{I}_{jk}$ and corresponding scaling factors T_k for the eigenvectors I_{jk},

$$I_{jk} = T_k \mathcal{I}_{jk} \,, \tag{5.8}$$

which allows us to use Equations (5.6) and (5.7) combined with the initial values of the inclination angles I_j and the angles Ω_j for each planet to solve for the scaling factors T_k, i.e.,

$$p_j(t=0) = \sum_{k=1}^{N} T_k \mathcal{I}_{jk} \sin \gamma_k \tag{5.9}$$

and

$$q_j(t=0) = \sum_{k=1}^{N} T_k \mathcal{I}_{jk} \cos \gamma_k \,. \tag{5.10}$$

The result is an expression defining the time evolution of the orbital inclination of each body in the system,

$$I_j(t) = \sqrt{[p_j(t)]^2 + [q_j(t)]^2} \,. \tag{5.11}$$

This equation can be used to generate the inclination evolution for planets in a system dominated by secular effects. By inspection, we see that the total angular momentum direction in the system will be conserved, but traded between planets in amounts mediated by the magnitude of the interaction coefficients. An example of the application of this theory is shown in Figure 5.2, which plots the orbital inclination angles (as computed with the Laplace-Lagrange secular theory detailed above) over time for two realizations of WASP-41b and WASP-41c. The first system is considered to be co-planar, whereas the second case assumes that the companion WASP-41c is slightly inclined. We note that when Equation 5.11 is used, the initial inclinations of transiting planets should be set to 0 degrees, rather than the 90 degrees traditionally reported observationally to denote edge-on orbits, due to the small angle approximation used in deriving the secular equations.

An inclined companion leads the orbit of hot Jupiter (-41b) to precess and allows the inclination

angles to oscillate over time. A precessing hot Jupiter will appear aligned with its host's spin axis some (small) fraction of the time. This exact value depends on the observational error on the obliquity measurement as well as the orbital elements of all bodies in the system. As a result, for a single system, the fact that a hot Jupiter is aligned with the stellar spin axis does not completely specify the inclination of the companion. It is possible that our observations happen to occur at a moment in the secular cycles where the system passes through alignment. However, if we observe the entire population of hot Jupiter hosts to have spin axes aligned with their hot Jupiter's orbital angular momentum, then it is unlikely that their companions are highly inclined. In other words, the assessment of alignment in hot Jupiter systems must be done statistically.

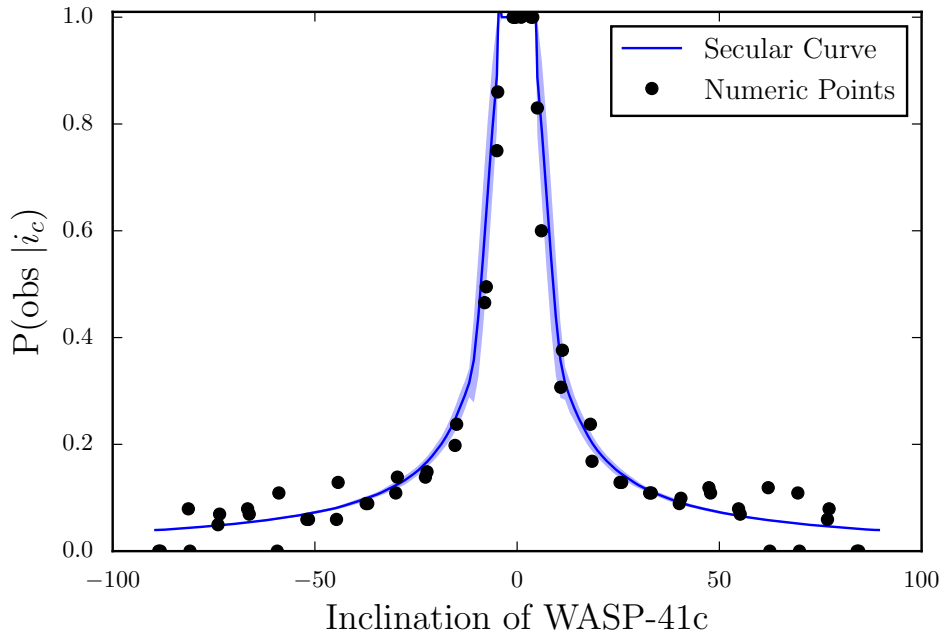

Figure 5.3 Probability of Reproducing Observations by Inclination for WASP-41c. Distribution for the probability of recreating the observations (obs), given some companion inclination for WASP-41c (i_c). This plots shows the comparison between the results computed from secular theory (solid blue curve) and the numerical N-body results (points). Here, an inclination of 0 degrees denotes an edge-on orbit (which observers report as having i=90 degrees). Except for the method used to generate the time series of orbital elements (secular theory versus the `Mercury6` N-body integrator), the probabilities in each case were generated the same way. The numerical simulations show good agreement with the secular calculation. The secular theory provides a robust motivation for this problem, and can be used to predict the interactions between planets at low mutual inclinations.

5.3.3 Numerical computation

In addition to the secular theory described above, we ran numerical N-body integrations of these systems, as such simulations are capable of recovering orbital behavior that is not apparent from the secular theory alone. In Figure 5.3, we show the comparison between the results computed using each method for one system in our sample (WASP-41, the same system visualized in Figure 5.2). The most important differences between the secular and numerical approaches are as follows: [1] The secular approach does not detect dynamical instabilities that result in ejections or collisions (see Figure 5.3 - the points which lie on the x-axis are points where such a dynamical instability occurred, the inner planet was lost, and thus the system would never recreate observations). [2] The numerical approach allows for time-dependence in semi-major axis, while the secular theory does not. [3] The numerical approach will correctly capture the behavior of mean motion resonances should they arise (although, we expect these to be rare for the particular geometry of this problem). The differences between the secular and numerical results in Figure 5.3 demonstrate that the secular theory is a good but not perfect approximation. To encompass all these behaviors, we treat the secular theory as motivation, and examine the behavior of each of the six systems in our sample using N-body integrations. In this numerical work, we use the system parameters and posteriors presented in Table 5.1.

Another reason to use N-body methods rather than the secular approximation is that, although the numerical computations are very expensive, we only have six systems in our sample, and thus the calculation is feasible. Notice that, on average, a single trial using a `Mercury6` N-body simulation takes $10^3 - 10^4$ longer than the corresponding `python`-generated secular evolution. For longer integration times, this discrepancy grows larger. Future analyses with a larger sample size might be able to use the secular approximation, which is generally accurate for sufficiently small mutual inclinations.

The purpose of these numerical experiments is to examine the effect that varying the inclination of the companion has on the alignment of the spin axis of the star and the orbital angular momentum vector direction of the hot Jupiter. Recall that for a single system, we cannot draw firm conclusions about its orbital geometry from the fact the hot Jupiter transits today because precessing orbits allow planets to transit from a given line of sight with some duty cycle. Similarly, we must make

an assumption about the underlying companion inclination distribution. Since we are testing the population as a whole, and not just individual systems, we consider three possible priors for the population of companion inclinations: a Fisher distribution, a uniform distribution, and a delta function. For each distribution, we assign the width of the distribution to be σ, when $\sigma^2 = \langle \sin^2 i \rangle$, and the functional forms of each probability distribution $dp = f di$ and width are given as follows:

- **Fisher distribution**. The Fisher distribution is often used (Fabrycky & Winn, 2009; Tremaine & Dong, 2012) to describe the inclinations of planetary orbits, especially relative to the spin axis of their host star (Morton & Winn, 2014b, see this paper for some illustrative plots describing the Fisher distribution). Its functional form can be written

$$f_f(i|\kappa) = \frac{\kappa}{2 \sinh \kappa} e^{\kappa \cos i} \sin i \,, \tag{5.12}$$

  when i is the orbital inclination angle. Then, we can find the width σ:

$$\sigma^2 = \langle \sin^2 i \rangle = \int f_\theta(\theta|\kappa) \sin^2 i di = 2\frac{\coth \kappa}{\kappa} - \frac{2}{\kappa^2} \tag{5.13}$$

  or

$$\sigma = \sqrt{2\frac{\coth \kappa}{\kappa} - \frac{2}{\kappa^2}} \tag{5.14}$$

  This form reduces to a Rayleigh distribution for large κ. For $\kappa \to 0$, the distribution becomes approximately isotropic.

- **Uniform distribution**. We assume that all companions come from a population with uniform scatter, but some maximum allowed inclination (defined as θ_m). For each iteration, we generate companions by drawing from a uniform inclination distribution between a 0 degree mutual inclination and some maximum inclination. The functional form for this distribution can be written as:

$$\frac{dp}{di} = f_u(i|\theta_m) = \frac{1}{2\theta_m} \tag{5.15}$$

  The width σ of this distribution is again defined by the expectation value of $sin^2 i$, where i

is the inclination drawn for each trial:

$$\sigma^2 = \langle \sin^2 i \rangle = \int f_u \sin^2 i di \tag{5.16}$$

For a distribution ranging between $-\theta_m$ and θ_m:

$$\sigma^2 = \int_{-\theta_m}^{\theta_m} \frac{1}{2\theta_m} \sin^2 i di = \frac{\theta_m - \cos\theta_m \sin\theta_m}{2\theta_m}, \tag{5.17}$$

or:

$$\sigma = \sqrt{\frac{1}{2} - \frac{\sin 2\theta_m}{4\theta_m}} \tag{5.18}$$

- **Delta function distribution**. We assume that all companions have the same inclination - so, the underlying companion distribution is a delta function at some inclination. This distribution has the probability function:

$$\frac{dp}{di} = f_\delta(i|\theta_x) = \delta(i - \theta_x) \tag{5.19}$$

and the width σ can also be found:

$$\sigma^2 = \langle \sin^2 i \rangle = \int f_\delta \sin^2 i di = \sin^2 \theta_x \tag{5.20}$$

So, the final width to the delta function companion distribution will be:

$$\sigma = \sin \theta_x \tag{5.21}$$

For each of those three priors, we initialized 1000 connected realizations of each of the six systems. (For example: a single realization includes all six planetary systems in independent integrations, all of which have inclinations drawn from the Fisher distribution of a given width. This process is then repeated 1000 times with different distributions widths. Then, the entire set of 1000 is repeated for each other prior type). In each realization, we sample from the known posteriors for each orbital element for all known planets. For the orbital elements of the hot Jupiter in each

system, we set its initial inclination to be 90 degrees, and draw its orbital period, mass, eccentricity, and argument of periastron from observational priors (see Table 5.1). For the orbital elements of the perturbing companions, we assign their orbital periods, masses, eccentricities, and arguments of periastron in the same way. We also draw an inclination for the perturbing companion from the prior being tested (either Equation [5.12], [5.15], or [5.19]). If a planet has an $m \sin i$ measurement instead of a true mass, we combine this measurement with our drawn inclination to find the true mass of the companion for that realization.

After the initial conditions for the systems are specified, we evolve the systems using `Mercury6` (Chambers, 1999b) with time-steps set initially to be 1% the orbital period of the innermost planet, and use the hybrid symplectic and Bulirsch-Stoer (B-S) integrator. We require energy conservation to a part in 10^{-8} or better, and allow each integration to run for 10 Myr (which encompasses many secular periods).

For each set of six systems, we then use the time-series of orbital elements computed by the N-body simulations to compute the projected stellar obliquity at each time-step. As each star in our sample has an observationally-measured projected obliquity, we then compute the probability that our simulated stellar obliquity would be measured to be consistent with this value (assuming the observational errors on our simulated measurement are equal to the error on the true measurement; see the third row of Table 5.1 for the projected obliquities and errors). The result of this computation is the probability that an observer would observe the stellar obliquity to be consistent with the true value we measure observationally at the current epoch.

Since each realization we have simulated includes six integrations (one for each planetary system), we then compute for each time-step the product of these six individual probabilities. This product is the probability that a simulated telescope making an observation at that time-step would measure a set of six projected stellar obliquities consistent with the true, current-day values. Then, using the entire time-series of probabilities, we compute a single marginalized probability $P(\mathrm{obs}|\sigma)$, when σ is computed directly from the functional form of each prior (the final forms of which are given in Equation [5.14], Equation [5.13], and Equation [5.21]). This single probability describes the chance that we would observe all the same stellar obliquities presented in the third row of Table 5.1 given the prior we chose for the underlying distribution of companion inclinations. We also plot

in Figure 5.4 a smoothed curve representing the mean probability for each distribution width, with contoured error bars representing the 1σ scatter at each distribution width.

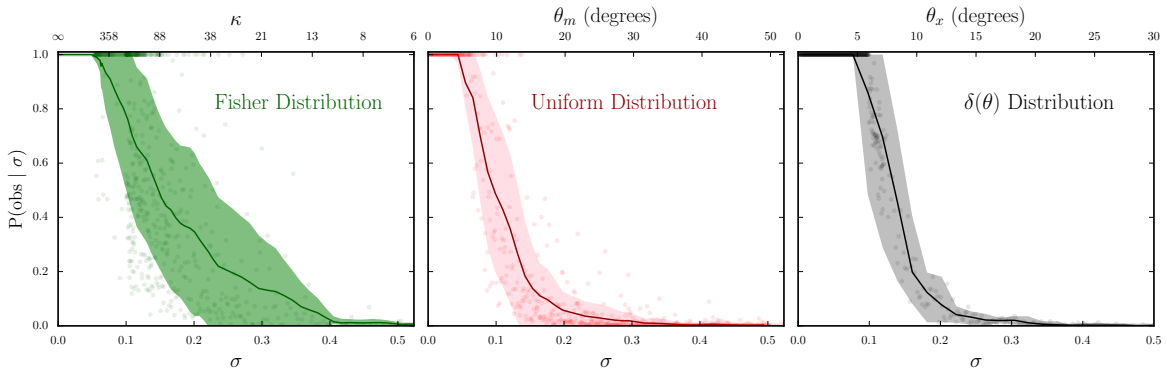

Figure 5.4 The Final Probability Distributions for Companion Inclinations. For three different choices for the underlying companion inclination distributions with expectation value for orbital inclination of $\sigma^2 = \langle \sin^2 i \rangle$, these curves show the probability that we would measure the observed obliquities between the stellar spin axis and hot Jupiter orbital angular momentum for the entire population of systems in our sample (obs), given some companion inclination distribution i_c. Each panel uses a different prior on the type of distribution from which we draw the inclination of the companion orbit: the left panel is a Fisher distribution, the middle panel a uniform distribution with varying maximum inclinations, and the right panel is a delta function at each inclination. For all choices of the priors, the allowable range in inclination for the underlying distribution of the companion's orbit is less than ~ 20 degrees out of the plane containing the hot Jupiter.

5.4 Results

5.4.1 The companion population tends to have nearly co-planar orbits

Figure 5.4 illustrates the main result of this work. We have considered systems containing hot Jupiters orbiting cool stars for which an obliquity measurement exists and which exhibit evidence for a companion. For three different types of distributions for the (unknown) inclination angle of the companion orbit, the numerical N-body simulations show that a large fraction of the cases with large mutual inclination angles result in a low probability of recreating the observations. As a result, it is unlikely that the companions to these cool hot Jupiter hosts generally have a high mutual inclination. Indeed, for all three prior choices (which range from the restrictive delta function distribution to the physically motivated and commonly used Fisher distribution), the

allowable range of orbital planes for the companions is within 20–30 degrees of the orbital plane of the hot Jupiter: the probability curves in Figure 5.4 are plotted against $\sigma = \sqrt{\langle \sin^2 i \rangle}$, and the top axis of each panel presents for physically intuitive units for each prior (the definitions of which can be found in Section 5.3.3). From these curves, we can compute the 95% confidence interval for each prior, which will define an upper limit on the value we can expect $\sqrt{\langle \sin^2 i \rangle}$ to assume, and then convert this to an angle, i_c, describing the likely maximum misalignment of exterior, coupled companions in these systems. For the Fisher distribution, this value is $i_c \sim$24 degrees. For the uniform distribution, this value is $i_c \sim$13 degrees. For the delta function distribution, this value is $i_c \sim$13 degrees.

Although the sample of known hot Jupiters with both stellar obliquity measurements and known exterior companions is small (only six such systems have been discovered at the time that this chapter was written), we can nonetheless make significant inferences on the underlying distribution of possible orbital inclinations for the population of companions. The dynamical calculations carried out here show that, through primarily secular evolution, the inclination angles of the orbits are expected to evolve in the presence of an inclined companion. The fact that the stellar obliquity with respect to the hot Jupiter tends to be low constrains the secular evolution histories in these systems. If the underlying population of companions to systems containing hot Jupiters around cool stars has a random distribution of uniformly distributed inclination angles, the chance that our observations happened to catch the six known systems at times where the orbits of the hot Jupiters are aligned with the stellar spin axis is only $\sim 10^{-7}$. As shown in Figure 5.4, the orbits of the underlying companion population in these hot Jupiter systems are likely to be confined near the plane of the hot Jupiter orbit.

5.4.2 Implications for Hot Jupiter Formation and Migration

Our conclusion that orbits of distant exterior companions to hot Jupiters are likely co-planar with hot Jupiter orbits has important implications for migration scenarios. The narrow distribution of inclination angles inferred here favors disk-driven migration mechanisms for hot Jupiters around cool stars. In this case, the disk and planets remain in nearly the same plane, and disk is generally aligned (within about 30 degrees) with the stellar spin axis (for additional discussion, see Lee et al.

2014; Becker et al. 2015b; Huang et al. 2016b; Weiss et al. 2017 for discussions of alignment, and Lai et al. 2011; Spalding et al. 2014b; Lai 2014; Fielding et al. 2015 for mechanisms to excite misalignments, particularly with systems around hot stars). In situ formation of hot Jupiters would also lead to well-aligned planetary orbits (Batygin et al., 2016b). In contrast, high-eccentricity migration does not generally lead to low mutual inclinations. In this latter scenario, the migrating hot Jupiter attains high eccentricity, and hence a small periastron, so that tidal dissipation can circularize the orbit with a small semimajor axis. The mechanisms invoked to excite the high eccentricity — including the Kozai-Lidov effect from stellar companions, planet-planet scattering, and secular interactions between planets — generally result in high inclination configurations (Fabrycky & Tremaine, 2007a; Nagasawa et al., 2008a; Naoz et al., 2011a). As these high-inclination configurations are found in hot Jupiter systems around hot stars ($T_* > 6200$ K), it is possible either that (a) hot stars, lacking a convective envelope, fail to realign the stellar spin-axis with orbital angular momentum early in their lives, or (b) the systems orbiting hot stars assemble via a different pathway. In either case, for cool stars, we favor a disk-driven migration scenario for dynamically coupled companions.

On the other hand, some exceptions are possible (Petrovich, 2015), and the number of hot Jupiter systems for which we can carry out the analysis of this chapter remains small. Fortunately, future observations should find an increasing number of hot Jupiter systems with additional companions orbiting cool stars. If these upcoming observations find a large number of misaligned systems, then high eccentricity migration will remain a viable alternative. On the other hand, if future observations find more systems with aligned obliquities, then it will support the paradigm advanced in this work of a coplanar companion population for cool hot Jupiter hosts.

5.4.3 Inclination of Companions to Hot Jupiters around Hot Stars

In this chapter, we only consider the inclinations of distant companions to hot Jupiters around cool stars because their obliquity angles are conveniently well aligned, making this type of analysis possible. This raises the question: "Are companions to hot Jupiters around hot stars also coplanar?"

One possibility is that distant companions to hot Jupiters around hot stars are not well aligned with the hot Jupiters' orbits, and that their gravitational perturbations either cause or contribute

to the the increased scatter in spin/orbit angles that are observed for these stars. This scenario hints at the explanation for correlation between stellar obliquity and stellar effective temperature by Batygin (2012a), who suggests that the increased prevalence of stellar companions for more massive stars can explain the misalignment of hot Jupiter orbits with the spin axes of hot stars. Batygin (2012a) suggests that torques from distant, misaligned companions on the proto-planetary disks can cause the misalignments that are observed; our results demonstrate the well-known (ex: Lai & Pu, 2017) result that closer misaligned companions can cause misalignments via secular interactions with the planet itself.

Another possibility is that most distant companions to hot Jupiters around stars of all temperatures and masses are roughly co-planar with the hot Jupiters, and the large scatter in stellar obliquity observed in hot stars comes from some other mechanism. In this case, although the companions do not disturb the hot Jupiters' spin/orbit angles, we cannot tell because there is no apparent pattern for distant companions to disrupt.

5.4.4 Caveats

The major caveats on the results quoted above can be summarized as follows. First, even in this paradigm, individual systems containing hot Jupiters around cool stars could (rarely) be found to have high-inclination companions due to unusual dynamical histories. For this reason, the methods and results of this work provide a statistical statement on the population of companions to hot Jupiters around cool stars, and cannot be used to determine true inclinations for individual systems.

Second, the temperature cut-off that we use in this work is chosen based on effective temperature. As these measurements are improved, some systems may move into or out of our sample. The ideal way to define the sample would be to include stars with thick convective envelopes, but currently, effective temperature is the best proxy for envelope size. As such, systems with host stars close to the temperature cut-off may be incorrectly categorized.

Third, only dynamically coupled companions can be included in analyses of this nature. Companions with sufficiently large orbital radii may become decoupled from the dynamics of the inner system, and no longer affect the orbital precession of the hot Jupiter. Our statistical result does

not apply to these very distant decoupled companions. Field surveys indicate that the occurrence rate of brown dwarfs (with masses ranging from 13 - 80 M_J) around Sun-like stars is low (Ma & Ge, 2014), with exact fractions ranging from 0.6% to 0.8% (Vogt et al., 2002; Patel et al., 2007; Wittenmyer et al., 2009; Sahlmann et al., 2011), suggesting that the companions for which we do not have fitted orbits (HAT-P-4, WASP-22, WASP-52) are more likely to be planetary companions rather than distant (potentially decoupled) brown dwarfs.

5.5 Conclusion

In this work, we have shown statistically that distant exterior companions to hot Jupiters around cool stars must typically orbit in roughly the same plane as the hot Jupiter itself. Specifically, companion orbits must generally fall within 20 – 30 degrees of the plane containing the hot Jupiter (see Figure 5.4)[2]. We constructed a sample of six hot Jupiter systems around cool stars (specifically, HAT-P-4, HAT-P-13, WASP-22, WASP-41, WASP-47, and WASP-53) and calculated the dynamical effects of distant perturbing companions as a function of the companion's orbital inclination. We performed a large ensemble of numerical simulations to show that if the inclination distribution companions to these systems extended much more than 20° away from coplanar, then we would have been unlikely to observe the measured obliquities in our sample. We have also used secular theory for comparison; this approach is in good agreement with the full N-body simulations and can provide a time-saving alternative (see Figure 5.3).

The fact that companions to hot Jupiters tend to orbit in nearly the same plane as the hot Jupiters themselves disfavors formation and migration models involving planet/planet scattering for hot Jupiters around cool stars. In particular, Kozai-Lidov migration typically requires a perturbing planetary (or stellar) companion with a mutual inclination of about 40° or more. Mutual inclinations this large are strongly disfavored by our statistical analysis. This finding — along with the fact that too few highly eccentric proto-hot Jupiters have been detected in *Kepler* data to explain the hot Jupiter population (Dawson et al., 2015) — suggests that Kozai-Lidov migration is not the dominant mode for forming hot Jupiter systems. Instead, this result favors formation sce-

[2]Note that we expect any additional planets to also be roughly in the same plane (see, for example, WASP-47).

narios that take place mostly within the plane of the proto-planetary disk, such as disk migration, *in situ* formation, or in some cases, coplanar high-eccentricity migration.

Stellar Properties

	M_* ($M_\odot$)	R_* ($R_\odot$)	λ (deg)	T_*(K)
HAT-P-4	1.26 ± 0.10 (1)	$1.617^{+0.057}_{-0.05}$ (1)	-4.9 ± 11.9 (2)	5860 ± 80 (1)
HAT-P-13	$1.22^{+0.05}_{-0.10}$ (5)	1.281 ±0.079 (5)	1.9 ± 8.5 (6)	5653 ± 90 (5)
WASP-22	$1.249^{+0.088}_{-0.17}$ (7)	$1.255^{+0.035}_{-0.034}$ (7)	22 ± 16 (8)	6153 ± 50 (7)
WASP-41	0.987 ± 0.047 (7)	0.886 ± 0.017 (7)	6 ± 11 (7)	5546 ± 33 (7)
WASP-47	1.00 ± 0.05 (13)	1.15 ± 0.04 (14)	0 ± 24 (15)	5400 ± 100 (16)
WASP-53	0.87 ± 0.08 (17)	0.96 ± 0.24 (17)	-4 ± 12 (17)	4950 ± 60 (17)

Hot Jupiter Properties

	Mass (M_J)	Period (days)	e_b
HAT-P-4	0.68 ± (1)	3.056536 $\pm 5.7 \times 10^{-5}$ (1)	0 (1,2)
HAT-P-13	$0.853^{+0.029}_{-0.046}$ (5)	2.916260 $\pm 1.0 \times 10^{-5}$ (5)	0.0133 ± 0.0041 (5)
WASP-22	$0.617^{+0.033}_{-0.022}$ (7)	3.5327313 $\pm 5.8 \times 10^{-5}$ (8)	0.023 ± 0.012 (9)
WASP-41	0.977 ± 0.037 (7)	3.0524 ± 10^{-5} (10)	< 0.026 (11)
WASP-47	1.12 ± 0.04 (13)	4.15912 ± 10^{-5} (13)	0.0028 ± 0.0028 (13)
WASP-53	$2.132^{+0.09}_{-0.09}$ (17)	3.3098443 $\pm 2 \times 10^{-6}$ (17)	< 0.03 (17)

	i_b (deg.)	ω_b (deg.)
HAT-P-4	$88.76^{+0.89}_{-1.38}$ (1)	-
HAT-P-13	83.4 ± 0.6 (5)	181 ± 45 (5)
WASP-22	89.2 ± 0.5 (8)	27^{51}_{-78}
WASP-41	$89.4^{+0.3}_{-0.3}$ (11)	-
WASP-47	$89.2^{0.5}_{0.7}$	51 ± 82
WASP-53	$87.08^{+0.16}_{-0.15}$ (17)	-

Companion Properties

	$m \sin(i)$ (M_J)	Period (days)	e_c	ω_c (deg.)
HAT-P-4	(3,4) [1]	(3,4) (3,4)	(3,4)	
HAT-P-13	14.28±0.28 (6)	446.27±0.22 (6)	0.662±0.005 (6)	176.7±0.5 (5)
WASP-22	(3,4) [1]	(3,4)	(3,4)	(3,4)
WASP-41	3.2±0.20 (11)	421 ± 2 (11)	0.294±0.024 (11)	353±6 (11)
WASP-47	1.24±0.22 (11)	572 ± 7 (11)	0.13±0.10 (11)	144±53 (11)
WASP-53	(17)[1]	(17)	(17)	(17)

Table 5.1 Orbital parameters used for the analysis in this work, with the literature sources for each measured value. [1]: this companion does not have a fitted orbit, but a trend indicating the presence of a companion with an orbital period longer than our observational baseline. In this work, we sample the orbital elements of these companions from the posteriors provided in Bryan et al. (2016). [2]: Using the method of Knutson et al. (2014b) and Bryan et al. (2016), we create a posterior for WASP-53, using radial velocity measurements from Triaud et al. (2017). References: (1) Kovács et al. 2007 (2) Winn et al. 2011 (3) Knutson et al. 2014b (4) Piskorz et al. 2015 (5) Bakos et al. 2009 (6) Winn et al. 2010b (7) Southworth et al. 2016 (8) Anderson et al. 2011 (9) Maxted et al. 2010 (10) Maxted et al. 2011 (11) Neveu-VanMalle et al. 2016a (12) Vanderburg et al. 2017 (13) Weiss et al. 2017 (14) Hellier et al. 2012a (15) Sanchis-Ojeda et al. 2015b (16) Hellier et al. 2012b (17) Triaud et al. 2017

CHAPTER VI

Dynamically Constraining Ambiguous Orbital Periods from Transit Data

Results in this chapter were published in: ***Becker, J. C.**, Vanderburg, A., and 24 colleagues 2019. A Discrete Set of Possible Transit Ephemerides for Two Long-period Gas Giants Orbiting HIP 41378. The Astronomical Journal 157, 19.* and *Vanderburg, A., **Becker, J. C.**, and 16 colleagues 2016. Five Planets Transiting a Ninth Magnitude Star. The Astrophysical Journal 827, L10.* and are presented here with moderate revisions.

6.1 Abstract

The *Kepler* mission has revealed a great diversity of planetary systems and architectures, but most of the planets discovered by *Kepler* orbit faint stars. Using new data from the K2 mission, we present the discovery of a five planet system transiting a bright (V = 8.9, K = 7.7) star called HIP 41378. HIP 41378 is a slightly metal-poor late F-type star with moderate rotation ($v \sin i \simeq 7$ km s^{-1}) and lies at a distance of 116 $\pm$ 18 pc from Earth. We find that HIP 41378 hosts two sub-Neptune sized planets orbiting 3.5% outside a 2:1 period commensurability in 15.6 and 31.7 day orbits. In addition, we detect three planets which each transit once during the 75 days spanned by K2 observations. One planet is Neptune sized in a likely ∼160 day orbit, one is sub-Saturn sized likely in a $\sim$ 130 day orbit, and one is a Jupiter sized planet in a likely $\sim$ 1 year orbit. We show that these estimates for the orbital periods can be made more precise by taking into account dynamical stability considerations. We also calculate the distribution of stellar reflex velocities expected for this system, and show that it provides a good target for future radial velocity observations. If a

precise orbital period can be determined for the outer Jovian planet through future observations, it will be an excellent candidate for follow-up transit observations to study its atmosphere and measure its oblateness.

We then consider the system in the updated context of new data: the 2015 K2 observations only spanned 74.8 days, and the outer three long-period planets in the system were only detected with a single transit, so their orbital periods and transit ephemerides could not be determined at that time. We report on 50.8 days of new K2 observations of HIP 41378 from summer 2018. These data reveal additional transits of the long-period planets HIP 41378 d and HIP 41378 f, yielding a set of discrete possible orbital periods for these two planets. We identify the most probable orbital periods for these two planets using our knowledge of the planets' transit durations, the host star's properties, the system's dynamics, and data from the ground-based HATNet, KELT, and WASP transit surveys. Targeted photometric follow-up during the most probable future transit times will be able to determine the planets' orbital periods, and will enable future observations with facilities like the *James Webb Space Telescope*. The methods developed herein to determine the most probable orbital periods will be important for long-period planets detected by the *Transiting Exoplanet Survey Satellite*, where similar period ambiguities will frequently arise due to the mission's survey strategy.

6.2 Introduction

The *Kepler* spacecraft (launched in 2009) has been a tremendously successful planet discovering mission (Borucki et al., 2010, 2011; Koch et al., 2010). Over the course of its four year original mission, *Kepler* discovered thousands of planetary candidates around distant stars (Coughlin et al., 2015), demonstrating the diversity and prevalence of planetary systems (e.g. Muirhead et al., 2012; Fabrycky et al., 2014b; Orosz et al., 2012b; Morton & Swift, 2014). *Kepler*'s contributions include measuring the size distribution of exoplanets (Howard et al., 2012a; Fressin et al., 2013a; Petigura et al., 2013c), understanding the composition of planets intermediate in size between the Earth and Neptune (Weiss & Marcy, 2014a; Wolfgang et al., 2016), measuring the prevalence of rocky planets in their host star's habitable zones (Dressing & Charbonneau, 2013b, 2015; Petigura et al.,

2013b; Foreman-Mackey et al., 2014; Burke et al., 2015), and uncovering the wide range of orbital architectures like tightly packed planetary systems (Campante et al., 2016), and planets in and (more commonly) near low order mean motion resonances (Carter et al., 2012a; Steffen & Hwang, 2015).

After the original *Kepler* mission came to an end in 2013, the K2 extended mission (Howell et al., 2014a) has conducted a series of ∼70–80 day observations in different locations along the ecliptic plane. Since the conception of the K2 Mission, one of its major goals has been to detect small transiting planets orbiting nearby bright stars (Howell et al., 2014a). Due to the original *Kepler* mission's narrow and deep survey strategy, most of its discoveries orbit stars that are too distant and faint for detailed follow-up study, so that only limited information can be gleaned about the physical properties of the newly discovered planet population beyond those discernible from the light curves.

Because it only observes stars for about 80 days before moving onto new fields, K2 is not as sensitive to planetary systems with complex architectures as the original *Kepler* mission. While *Kepler* detected systems with up to seven transiting planets (Schmitt et al., 2014; Cabrera et al., 2014), K2 had not (as of early 2016) yet discovered any systems with more than three transiting planet candidates[1] (Sinukoff et al., 2015; Vanderburg et al., 2016c). This limitation is one of the signatures of the survey design: the short orbital baselines change the nature of the biases in the transit data. While transit campaigns always have a preference for discovering short period planets, a shorter observational baseline makes this bias even more evident.

In this chapter, we first describe the discovery (first reported in Vanderburg et al. 2016b) of a system of five transiting planets using K2 data. The host star (HIP 41378) is one of the brightest planet host stars from either *Kepler* or K2, with a V magnitude of 8.9 and a K magnitude of 7.7. The planetary system displays a rich architecture, with two sub-Neptunes slightly outside of mean motion resonance and three larger planets in longer period orbits. The subsequent focus of this chapter is on our efforts (published in Becker et al., 2019) to recover accurate orbital period estimates of the outer three planets, each of which transited only once during K2 Campaign 5

[1]The WASP-47 system hosts four planets, only three of which are known to transit (Hellier et al., 2012a; Becker et al., 2015b; Neveu-VanMalle et al., 2016b).

(abbreviated henceforth as C5, which was the campaign in which they were originally discovered). These 2015 K2 observations only spanned 74.8 days, and the outer three long-period planets in the system were only detected with a single transit, so their orbital periods and transit ephemerides could not be determined from the C5 data alone.

Following a proposal by Vanderburg, Becker, et al. to re-observe this target, in Campaign 18 (C18), HIP 41378 was observed for another 50.8 days. The new K2 observations of HIP 41378 from summer 2018 revealed additional transits of the long-period planets HIP 41378 d and HIP 41378 f, yielding a set of discrete possible orbital periods for these two planets. In the latter half of this chapter, I describe the dynamical and statistical methods we used in Becker et al. (2019) to identify the most probable orbital periods for these two planets. The methods used combine our knowledge of the planets' transit durations, the host star's properties, the system's dynamics, and data from the ground-based HATNet, KELT, and WASP transit surveys in order to provide the best possible system characterization moving forwards. Targeted photometric follow-up during the most probable future transit times will be able to determine the planets' orbital periods, and will enable future observations with facilities like the *James Webb Space Telescope*. The methods developed herein to determine the most probable orbital periods will be important for long-period planets detected by the *Transiting Exoplanet Survey Satellite*, where similar period ambiguities will frequently arise due to the mission's survey strategy.

6.3 Observations

HIP 41378 was observed by *Kepler* for a total of about 126 days in both Campaigns 5 (C5) and 18 (C18) of the K2 mission. The data from K2 C5 showed evidence of the transits of five planets, three of which transited once each during the original 74-day campaign (Vanderburg et al. (2016b)). HIP 41378 has also been observed by several ground-based planet-hunting surveys, including the Hungarian-made Automated Telescope (HAT), Kilodegree Extremely Little Telescope (KELT) surveys, and the Wide Angle Search for Planets (WASP).

6.3.1 K2 data

During C5, HIP 41378 was only observed in long-cadence mode (29.4 minute co-added exposures), but it was observed in short-cadence mode (58.34 second co-added exposures) during Campaign 18 due to the discovery of its planetary system. Analysis of the short-cadence data will likely yield improved parameters for the planets in the system and a detection of asteroseismic oscillations, but we defer this work until the final, pipeline-calibrated data is released by K2 team later in 2018. In this work, we focus on analysis of the long-cadence data to determine precise possible orbital periods for HIP 41378 d and f, with a goal of determining the orbital periods as soon after the last transit of each planet as possible, so that the periods we identify as most likely can be monitored and eventually the true orbital periods will be identified by follow-up work.

6.3.1.1 Campaign 5

HIP 41378 was observed along with 25,850 other targets by the *Kepler* space telescope during C5 (2015 April 27 - 2015 July 10) of the K2 mission. Upon downlink of the data, the K2 team processed the data with their photometric pipeline, to produce calibrated pixel files. Vanderburg et al. (2016b) downloaded the pixel-level data, produced a light curve using the methodology of Vanderburg & Johnson (2014), and then rederived the K2 systematics correction by simultaneously fitting the long-term stellar variability, pointing-related systematics, and transits of the five detected planets following the method of Vanderburg et al. (2016c). We use the highly-precise (38 ppm scatter per 30 minute exposure) light curve produced from the simultaneous fit by Vanderburg et al. (2016b) for our analysis. The C5 light curve is plotted in the second panel of Figure 6.1.

6.3.1.2 Campaign 18

HIP 41378 was observed along with 20,419 other targets by the *Kepler* space telescope during C18 (2018 May 12 – 2018 July 02) of the K2 mission. After the data was downlinked from the spacecraft, the raw cadence files were immediately uploaded to the Mikulski Archive for Space Telescopes (MAST), before pixel-level calibration had been performed by the K2 team. In the interest of time, we used the raw, un-calibrated cadence files to produce a quick-look light curve of HIP 41378. We downloaded the cadence files from the MAST and used the *kadenza* software

tool (Barentsen & Cardoso, 2018) to produce a pseudo-target pixel file containing the long-cadence *Kepler* images from the postage stamp region around HIP 41378. We then used the procedure of Vanderburg & Johnson (2014) to process the K2 pixel data into a systematics-corrected light curve. We manually identified and excluded cadences from our systematics correction when *Kepler* was undergoing a reaction wheel desaturation event. We also manually excluded a continuous stretch of seven hours of data around time BJD - 2454833 = 3431.85 when *Kepler* experienced a pointing anomaly. The systematics corrected light curve showed transits of four of the five known HIP 41378 planets: HIP 41378 b, c, d, and f. After performing a first-pass systematics correction with the Vanderburg & Johnson (2014) method, we re-derived the systematics correction and re-processed the light curve following the method of Vanderburg et al. (2016c) to simultaneously fit for the long-term variability, pointing-related systematics, and the transits of the four planets seen in C18. The photometric precision of the light curve is about 40% worse (51 ppm scatter per 30 minute exposure) than the light curve from C5 as a result of using the un-calibrated pixel data.

Once the K2 team released their pipeline-processed target pixel files from Campaign 18, we downloaded these newly processed data and analyzed them in an identical manner to the Campaign 5 data, following Vanderburg & Johnson (2014) and Vanderburg et al. (2016c) to extract light curves, produce a first-pass systematics correction, and then fit simultaneously for the systematics correction, transit model, and low-frequency variability. The resulting light curve has photometric precision nearly identical to that of the Campaign 5 light curve (38 ppm per 30 minute exposure). Although the *kadenza* light curves were used to conduct our preliminary analysis, the re-processed light curve is plotted in the second panel of Figure 6.1, and we use this updated light curve in the final version of our analysis included in the remainder of this chapter.

6.3.2 KELT data

The Kilodegree Extremely Little Telescope (KELT) survey (Pepper et al., 2007, 2012) is a ground-based transit survey consisting of two 4.2cm-aperture, wide-field (26 by 26 degrees) automated telescopes (KELT-North is located in Arizona, and KELT-South is located in South Africa). KELT's primary goal is the detection of transiting Jupiter-sized planets, and it has had much success finding these planets (Zhou et al., 2016; Stevens et al., 2017; Lund et al., 2017; Gaudi et al.,

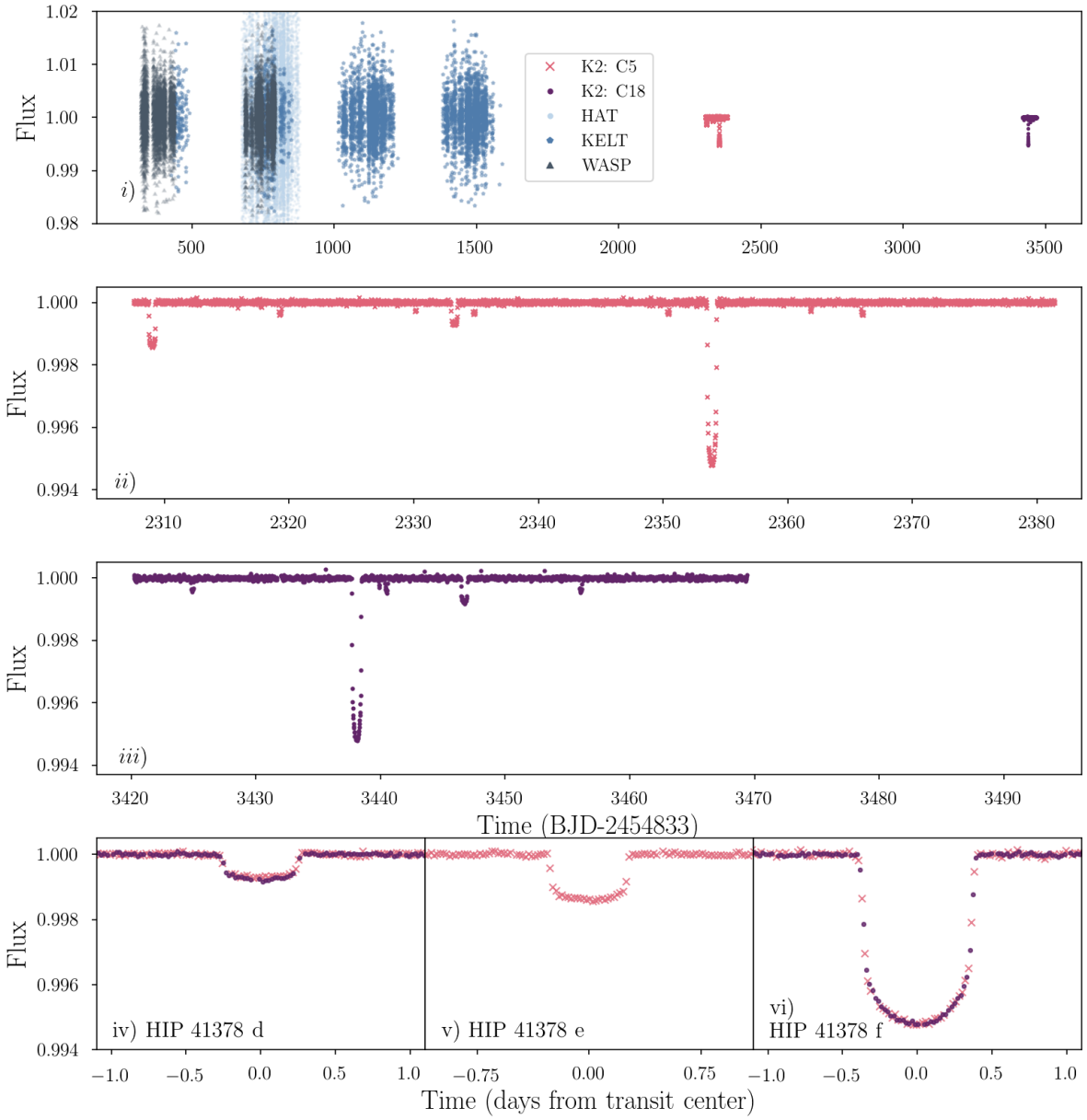

Figure 6.1 Full Light Curve Data of HIP 41378. HIP 41378 was observed in C5 and C18 of the K2 mission, which were separated by a little over 1000 days. (top panel) The K2 data, plotted by time of acquisition, plotted alongside the KELT, HAT, and WASP observations of the same star. All values have been converted to relative flux. (middle two panels) The K2 campaigns, expanded. In both campaigns, many transits of HIP 41378 b and c are observed, while single transits of HIP 41378 d and f are observed in each campaign. HIP 41378 e transits only once in the first campaign (C5). (bottom panels) The phase-folded light curves for planets HIP 41378 d, e and f, each of which transited only once during the K2 C5. Although we do not know the true orbital period of any of these three planets, we plot the results of a Levenberg-Marquardt fit of the transit model to the transit center for each event and center the plot on each fitted center. Planets d and f have data from both C5 and C18, while e has no data from C18 since it did not transit during this newer campaign.

2017; Pepper et al., 2017; Siverd et al., 2018). The candidate selection process is described in (Siverd et al., 2012) and (Kuhn et al., 2016); KELT is primarily searching for planets with V-band magnitudes between 8 and 10, and HIP 41378 was observed by both KELT telescopes for several years before Kepler's K2 mission began. Roughly 4700 observations of HIP 41378 were taken by KELT-North and KELT-South between March 2, 2010, and May 10, 2013. The reduction pipeline and candidate selection process is described in Siverd et al. (2012) and Kuhn et al. (2016). The full KELT data set for HIP 41378 is plotted in Figure 6.1.

6.3.3 HATNet data

HIP 41378 was a target observed by HATNet (Bakos et al., 2004) between November 2, 2010 and June 3, 2011. HATNet is a telescope network which consists of six 11-cm, wide-field (10.6 degrees by 10.6 degrees field of view) aperture lenses on six different fully-automated telescope mounts, four of which are in Arizona and two of which are in Hawaii (Bakos et al., 2004). The HATNet observations for HIP 41378 were reduced as in Bakos et al. (2010), using aperture photometry routines from image processing software FITSH (Pál, 2012). The resultant light curves were outlier-clipped, smoothed, and detrended using the TFA (Kovács et al., 2005). Due to the brightness of HIP 41378 the innermost pixels containing the center of the point spread function (PSF) are saturated in the HATNet observations of this star. Because the Apogee U16m 4K×4K CCDs used by HATNet incorporate anti-blooming gates, electrons exceeding the full pixel well are suppressed rather spilling over into neighboring pixels. To account for this, aperture photometry is performed only on the unsaturated pixels and then corrected for the flux not counted in the saturated pixels using the estimated PSF. This leads to bright/saturated stars having lower photometric precision than somewhat fainter/unsaturated stars. For HIP 41378 the HATNet observations have a RMS scatter of 14 mmag, compared to ~ 4 mmag for the brightest unsaturated stars in the same images.

The full HAT data set for HIP 41378 is also plotted in Figure 6.1, and consists of 12903 observations.

6.3.4 WASP data

HIP 41378 was also target observed by the WASP survey (Pollacco et al., 2006) between Nov 20, 2009 and March 3, 2011. WASP consists of two robotic telescope arrays with eight Canon lenses (each with a field of view of 7.8 degrees by 7.8 degrees). The arrays are located in South Africa and the Canary Islands. Data taken post January 2009 benefit from improved red noise reduction (Barros et al., 2011; Faedi et al., 2011). WASP data are detrended using SysRem (Tamuz et al., 2005) and TFA.

The WASP light curve for HIP 41378 was further processed: all points with error bars greater than 2% were excluded, as were points with flux values smaller than 10% the median flux value. The remaining points include are expected to be good quality, and are plotted in Figure 6.1.

6.3.5 Adaptive Optics Imaging

We observed HIP 41378 with the Robo-AO adaptive optics (AO) system on the 2.1 meter telescope at the Kitt Peak National Observatory (Baranec et al., 2014; Law et al., 2014; Riddle et al., 2016). Robo-AO is a robotic laser guide star adaptive optics system, which has recently moved to the 2.1 meter telescope at Kitt Peak from the 1.5 m telescope at Palomar Observatory. We obtained an image on 2 April 2016 with an i'-band filter. The observation consisted of a series of exposures taken at a frequency of 8.6 Hz, which were then shifted and added using HIP 41378 as the tip–tilt guide star. The total integration time was 120 seconds.

The resulting image showed no evidence for any companions to HIP 41378 within the 36 arcsec×36 arcsec Robo-AO field of view. The AO observations allow us to exclude the presence of companion stars two magnitudes fainter than HIP 41378 at a distance of 0.25 arcsec, and stars four magnitudes fainter at a distance of 0.7 arcsec with 5-σ confidence.

6.3.6 High Resolution Spectroscopy

We observed HIP 41378 with the Tillinghast Reflector Echelle Spectrograph (TRES) on the 1.5 meter telescope at Fred L. Whipple Observatory on Mt. Hopkins, Arizona. We obtained spectra on four different nights in January and February 2016. The spectra were obtained at a spectral

resolving power of $\lambda/\Delta\lambda = 44{,}000$, and exposures of 360 - 450 seconds yielded spectra with signal-to-noise ratios of 90 to 110 per resolution element. We see no evidence for chromospheric calcium II emission from the H-line at 396.85 nm. We cross correlated the four spectra with a model spectrum and inspected the resulting cross correlation functions (CCFs). There is no evidence in the CCFs for additional second sets of stellar lines. We measure an absolute radial velocity for HIP 41378 of 50.7 $\mathrm{km\,s^{-1}}$, and the four individual spectra show no evidence for high-amplitude radial velocity variations. We measured relative radial velocities by cross correlating each observation with the strongest observation and found no evidence for RV variations greater than TRES's intrinsic RV precision of 15 $\mathrm{m\,s^{-1}}$.

6.4 Analysis

6.4.1 Updated Stellar Parameters

Our analysis to determine the most likely orbital periods of the long-period HIP 41378 planets depends directly on the adopted stellar parameters, especially the stellar density. We used the observations described in Section 6.3.6 to derive spectroscopic properties (including stellar metallicity, temperature, and V band magnitude) using the Stellar Parameter Classification (SPC, Buchhave et al., 2012, 2014a) method. These values are shown in Table 6.1. To derive fundamental stellar parameters (like the stellar mass and radius), we use a parallax from the *Gaia* (Gaia Collaboration et al., 2016c, 2018a) Data Release 2 (reported in Table 6.1). Using an online interface[2], we interpolate onto Padova stellar evolution tracks (da Silva et al., 2006). The resulting values of stellar mass, stellar radius, and surface gravity are presented in Table 6.1. We also obtained an independent, empirical measure of the stellar radius via the method described by Stassun et al. (2018). Briefly, we performed a fit to the full broadband spectral energy distribution (SED) using a Kurucz model atmosphere with the same stellar $T_{\rm eff}$, $\log g$, and [Fe/H], and their uncertainties, reported in Table 6.1. The free parameters of the SED fit are then only the extinction (A_V) and an overall flux normalization. The bolometric flux at Earth ($F_{\rm bol}$) is then obtained simply by direct summation of the (non-reddened) SED model. Finally, the stellar radius then follows from the $F_{\rm bol}$

[2] `http://stev.oapd.inaf.it/cgi-bin/param_1.3`

Parameter	Value
Stellar Parameters	
Right Ascension	8:26:27.85
Declination	+10:04:49.35
Age [Gyr]	4.279 ± 0.931
Parallax [mas]	9.379940 ± 0.059038
V magnitude	8.93
$M_\star$ [$M_\odot$]	1.140 ± 0.033
$R_\star$ [$R_\odot$]	1.35 ± 0.03
(B-V)	0.599 ± 0.012 mag
Limb darkening q_1	0.311±0.048
Limb darkening q_2	0.31±0.13
$\log g_\star$ [cgs]	4.20 ± 0.03
Metallicity [M/H]	-0.11±0.08
$T_{\rm eff}$ [K]	6199±50

Table 6.1 Parameters for host star HIP 41378. Stellar properties ($M_\star$, $R_\star$, stellar age, B-V magnitude, and $\log g_\star$) have been derived using the Gaia parallax (9.37993950 mas ± 0.059037831).

and $T_{\rm eff}$ via the Stefan-Boltzmann relation.

We constructed the observed stellar SED using broadband fluxes spanning 0.2–20 μm from *GALEX* NUV, *Tycho-2* $B_T V_T$, APASS $BVgri$, 2MASS JHK_S, and *WISE* 1–4. We limited the maximum permitted A_V to be that of the full line-of-sight extinction from the Galactic dust maps of Schlegel et al. (1998a). The resulting best fit SED model, with a reduced χ^2 of 2.9, gives $A_V = 0.01 \pm 0.01$ and $F_{\rm bol} = 6.91 \pm 0.16 \times 10^{-9}$ erg s^{-1} cm^{-2}. Adopting the *Gaia* DR2 parallax, but adjusted by +0.08 mas to account for the systematic offset found by Stassun & Torres (2018a), we obtain $R_\star = 1.35 \pm 0.02$ R$_\odot$, consistent with the radius from our analysis using the Padova isochrones. For the rest of our analysis, we adopt the parameters from the isochrone analysis (reported in Table 6.1).

Importantly, we note that when we first published our discovery of this system Vanderburg et al. (2016b), the *Gaia* parallax was not available, and we used the *Hippacos* parallax instead. This resulted a much less precise measurement of the stellar density (see Figure 6.2). The *Gaia* parallax for this system was first used in Becker et al. (2019).

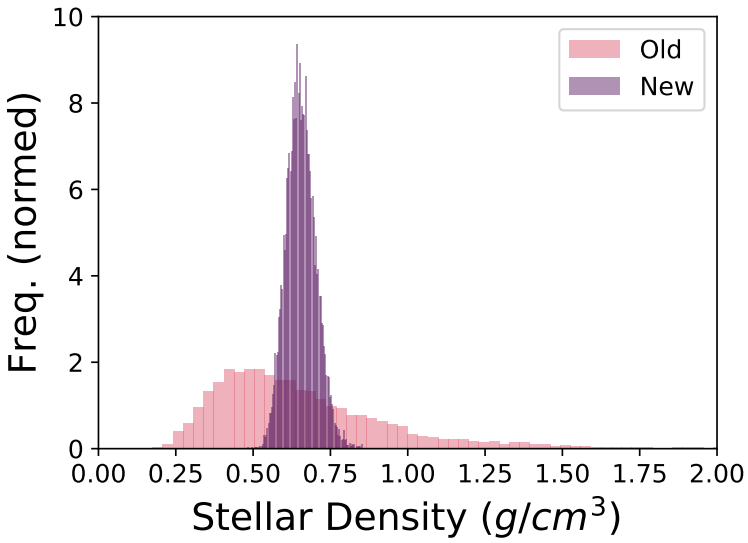

Figure 6.2 Stellar Density Estimates for HIP 41378. Comparisons of the posteriors for stellar density for the old set of stellar parameters given in Vanderburg et al. 2016b, computed using the *Hippacos* parallax, and the new set used in Becker et al. 2019 and this thesis chapter, computed using the Gaia parallax (this is the set given in Table 6.1). The increased precision of the stellar density has a significant impact on the fidelity of the dynamical analyses.

6.4.2 Transit Analysis

We analyzed the K2 light curve by simultaneously fitting the five transiting planet candidates and a model for low frequency variability using a Markov Chain Monte Carlo algorithm with an affine invariant ensemble sampler (Goodman & Weare, 2010a). We fit the five transiting planet candidates with Mandel & Agol (2002b) transit models, and we modeled the low frequency variations with a basis spline. For the two inner candidates, we fit for the orbital period, time of transit, scaled semi-major axis ($a/R_\star$), orbital inclination, and planet to star radius ratio ($R_P/R_\star$). For the three outer candidates with only one transit, we fit for the transit time, duration (from the first to fourth contact), transit impact parameter, and planet to star radius ratio. We fit for quadratic limb darkening coefficients for all five transits simultaneously, using the the q_1 and q_2 parametrization from Kipping (2013a). We imposed no priors on these parameters other than requiring impact parameters be positive. We accounted for the effects of the *Kepler* long cadence exposure time by oversampling each model data point by a factor of 30 and performing a trapezoidal numerical integration. We did not account for any asymmetry in the transit light curve due to eccentricity –

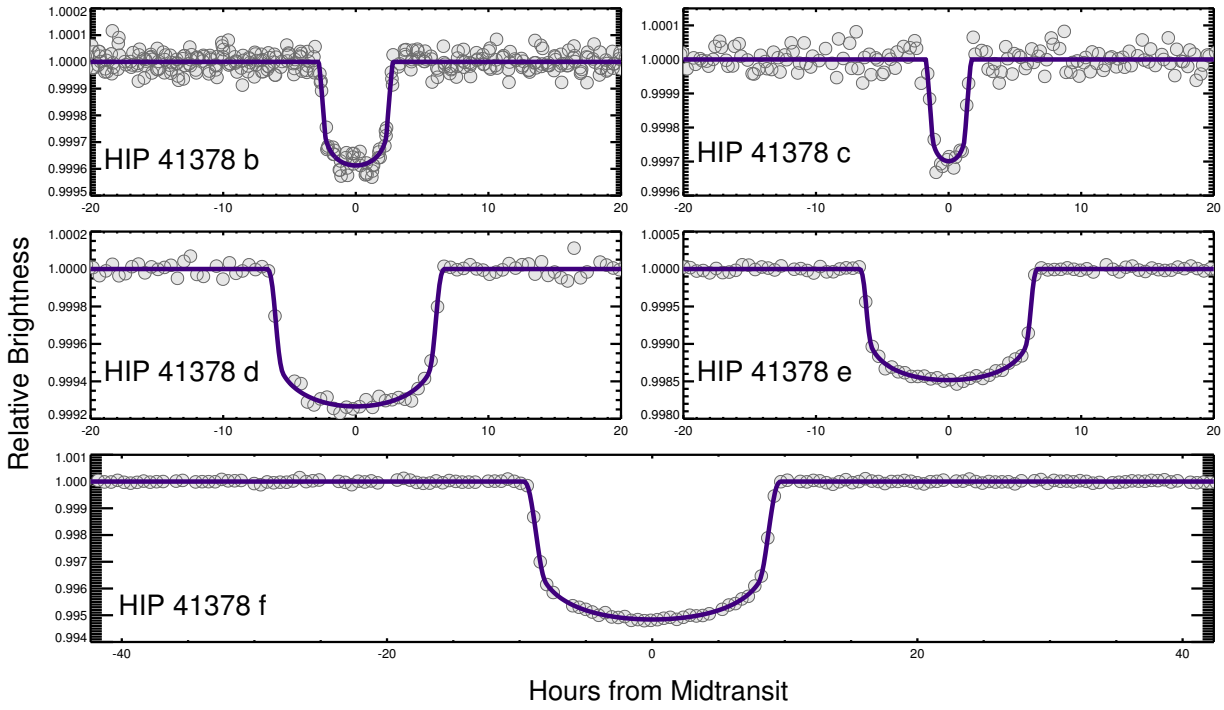

Figure 6.3 Phase-folded Light Curve for HIP 41378. Phase-folded light curve for each of the five transiting planets in the HIP 41378 system. The individual K2 long cadence data points are shown as grey circles, and the best-fit transit model is shown as a thick purple line. The scaling on the x-axis is the same for each sub-panel. In each panel, we have subtracted the best-fit transit model for the other four planets for clarity.

this effect scales with $(a/R_\star)^{-3}$ and is too small to detect for long period planets like these (Winn, 2010). We note that our choice to parameterize the orbits by their inclinations is an approximation – although orbits are uniformly distributed in $\cos i$, not i, the difference is negligible for nearly edge on orbits like those of the planets transiting HIP 41378. We performed a Monte Carlo calculation and found that the different parameterizations only change our final measured inclinations by roughly 10^{-4} degrees, much less than our measured uncertainties in inclination.

We sampled the parameter space using 150 walkers evolved through 40,000 links, and removed the first 20,000 links during which time the chains were "burning-in" to a converged state. This yielded a total of 3,000,000 individual samples. We tested the convergence of the MCMC chains by calculating the Gelman-Rubin statistic (Gelman & Rubin, 1992). For each parameter, the Gelman-Rubin statistic was below 1.04, indicating our MCMC fits were well converged.

We plot the transit light curves for each planet and the best-fitting transit model in Figure 6.3.

6.4.3 Measured center of transit times in C18 for new transits of HIP 41378 d and HIP 41378 f

We measured the mid-time of the two newly detected transits of HIP 41378 d and HIP 41378 f in the C18 data in order to precisely determine the time between the transit observed in C5 and the newly detected transit from C18. We determined mid-transit times for the new transits of HIP 41378 d and f by fitting the C18 light curve using a Mandel & Agol (2002b) transit model using a Levenberg-Marquardt least-squares minimization algorithm. We performed the Levenberg-Marquardt minimization over one free parameter, the mid-transit time, while fixing the transit shape parameters (R_p^2/R_*^2, transit duration, impact parameter, and quadratic limb darkening parameters) to the values reported by Vanderburg et al. (2016b).

The resulting mid-transit times from our one-parameter optimizations of the C18 light curve and the mid-transit times determined by Vanderburg et al. (2016b) from C5 are given in Table 6.2. Further refinement of the system parameters, including an asteroseismic analysis, will be completed in Chontos et al. (2019, in prep).

6.4.4 Statistical Validation

The transit signals in the K2 light curve of HIP 41378 that we attribute to transiting planets could in principle have a non-planetary astrophysical origin. In this subsection, we argue that astrophysical false positive scenarios are unlikely in the case of the HIP 41378 system, and a planetary interpretation of the transit signals is well justified.

We began by calculating the false positive probability (FPP) of the inner two planet candidates, which both have precisely measured orbital periods from multiple transits in the K2 light curve, using the `vespa` software package (Morton, 2012, 2015). `Vespa` takes information about the transit shape, orbital period, host star parameters, location in the sky, and observational constraints and calculates the likelihood that a given transit signal has an astrophysical origin other than a transiting planet. We used `vespa` to calculate the FPP of HIP 41378 b and HIP 41378 c given constraints on the depth of any secondary eclipse from the K2 light curve and limits on any nearby companion stars in the K2 aperture from Robo-AO. We also used the fact that our radial velocity measurements

of HIP 41378 show no variations greater than about 15 $\mathrm{m\,s^{-1}}$ to exclude all foreground eclipsing binary false positive scenarios. Given these constraints, we calculate that the FPP for HIP 41378 b is very small, of order 2×10^{-6}, and the FPP of HIP 41378 c is 3×10^{-3}, somewhat larger but still quite low. These FPPs do not take into account the fact that we detect five different candidate transit signals towards HIP 41378 and that the vast majority of *Kepler* multi-transiting candidate systems are real planetary systems (Latham et al., 2011; Lissauer et al., 2012a). Lissauer et al. (2012a) estimate that being in a system of three or more candidates increases the likelihood of a given transit signal being real by a factor of $\sim$ 50-100. Taking this multiplicity argument into account, the FPP for HIP 41378 b decreases to roughly 10^{-7} and the FPP for HIP 41378 c decreases to roughly 10^{-4}. We therefore consider HIP 41378 b and HIP 41378 c to be validated as genuine planets.

It is more difficult to calculate the false positive probability for the outer planet candidates. Because the orbital period is unconstrained, a `vespa`-like false positive analysis loses an important piece of information (namely, the duration of the transit compared to the orbital period). Even though we can estimate the orbital period of the outer three planets (assuming they indeed transit HIP 41378), we have no constraint on orbital periods for the scenario where the single transit signals are astrophysical false positives. We do, however, know that the three single-transits are detected in a multi-transiting planet candidate system and can use this fact to estimate the false positive probabilities without any knowledge of the transit shapes and orbital periods. Lissauer et al. (2012a) give expressions for estimating the likelihood of false positive signals in multiple planet systems. Using these expressions with numbers from the recent Data Release 24 *Kepler* planet candidate catalog (Coughlin et al., 2015), we find that the probability of a given target having two planets and three false positives is roughly 10^{-12}, the probability of the target having three planets and two false positives is roughly 10^{-9}, and the probability of the target having four planets and one false positive is roughly 5×10^{-7}. From the observed number of systems with five or more transiting planets discovered by *Kepler*, the probability of a star hosting such a system is roughly 18/198646 or 10^{-4}. When we compare these probabilities, we find that, *a priori*, it is 10^8 times more likely HIP 41378 hosts five transiting planets than two planets and three false positives, 10^5 times more likely HIP 41378 hosts five transiting planets than three planets and

two false positives, and about 200 times more likely that HIP 41378 hosts five transiting planets than four planets and one false positive. When this information is combined with the fact that the transits are u-shaped (consistent with small planets) rather than v-shaped (consistent with a background false positive), the second transits in the C18 data for two of the three outer planets, and our adaptive optics imaging which rules out many possible background contaminants, we have high confidence that all five candidates in the HIP 41378 system are genuine planets.

6.4.5 Dynamics

The richness of the HIP 41378 planetary system gives rise to questions about its dynamics and architecture. In this section, we aim to address and place constraints on the dynamical stability of the system and the resonance state of the inner two planets. The dynamical stability arguments we make in this section are useful for constraining the orbital periods of the outer two planets (which we do in Section 6.5.1).

6.4.5.1 Inner Planets

In the original sample of planets discovered by Kepler, it appears that the observed population of planets are preferentially close to, but not in, mean motion resonances (Veras & Ford, 2012). As such, we first considered the two inner planets, which both show multiple transit events in the K2 light curve and therefore have precisely measured orbital periods. The ratio of the orbital periods of the two inner planets is just 3.57% larger than 2:1, so we tested whether the two planets orbit in a 2:1 mean motion resonance (MMR).

We assessed the resonant state of the inner two planets by conducting 10,000 numerical simulations of the orbits of the inner two planets over 100,000 years using the `Mercury6` N-body integrator (Chambers, 1999a). For each trial, we drew the orbital elements of each planet from the posterior probability distribution from the MCMC transit fit (Section 6.4.2). We assigned masses to the planets using the the methodology of Becker & Adams (2016) – to summarize, given the planet radii, we draw masses from several published mass-radius relations: the Weiss & Marcy (2014a) relation for planets with $R_p < 1.5R_\oplus$, the Wolfgang et al. (2016) relation for planets with $4R_\oplus > R_p > 1.5R_\oplus$, and for planets larger than $4\mathrm{R}_\oplus$ we solve for mass by drawing the mean planetary density from a

normal distribution centered at $\rho = 1.3 \pm 0.5$ g / cm^3, taking the hot Jupiter radius anomaly into account using the relation from Laughlin et al. (2011).

We tested each of the 10,000 realizations of the system for resonant behavior. The condition for resonance is more stringent than that of a period commensurability: for a pair of planets to be resonant, they must have oscillating (rather than circulating) resonance angles, which means that the longitude of conjunction (the location where the the planets pass closest together) has an approximately stable location. Resonances are sometimes referred to as a "bound states" because planets can be trapped in the energetically favorable configuration where the resonance angles oscillate back and forth in a potential well, like a pendulum with an energy low enough to swing back and forth rather than swing 360 degrees over the top (Ketchum et al., 2013a). At the same time, a pair of planets can have a period ratio slightly out of an integer ratio and still be in resonance. We examined the resonance argument of the inner two planets, φ, which is defined as:

$$\varphi = (p+q)\lambda_{inner} - p\lambda_{outer} - q\varpi_{outer}, \tag{6.1}$$

where $p/(p+q)$ is the order of the resonance (which is 2:1, so $p = 1$ and $q = 1$ for these planets), ϖ is longitude of pericenter, and λ is angular location in orbit.

Out of the 10,000 system realizations that we tested, none of them were in resonance (all had circulating rather than oscillating resonant arguments). Therefore, we conclude that the inner two planets orbiting HIP 41378 do not orbit in a mean motion resonance. This conclusion is not surprising – the sample of multi-planet systems from *Kepler* shows that planets more often orbit near, but not in, mean motion resonances (Veras & Ford, 2012). The fact that these planets orbit slightly outside of mean motion resonance is also reminiscent of trends seen in *Kepler* multi-planet systems. Fabrycky et al. (2014b) found that period ratios slightly larger than 2:1 (as is the case for these two planets) are overrepresented in the population of observed systems, and slightly smaller ratios are underrepresented. Thus, there is no evidence to suggest that these planets are in resonance, but they are a part of the overabundance of planets that pile up slightly outside the 2:1 MMR.

We note that in this analysis, we have examined only the behavior of the two inner planets.

The three outer planets in the system contribute additional terms in Equation 6.1, which we have ignored because of their poorly constrained orbits, but which could presumably alter the resonant behavior of the inner two planets. However, we believe it is unlikely that the outer planets would significantly affect the inner planets' resonant state. The periods of the outer three planets are likely significantly longer (by an order of magnitude or so, see Section 6.5.1) than the periods of the inner two planets, so the outer planets will act like distant static perturbers.

6.4.5.2 Outer Planets

We performed a separate dynamical analysis to study possible orbits and configurations of the outer three planets in the HIP 41378 system. The outer three planets only transited HIP 41378 once during the 75 days of K2 observations, so their orbital periods are not uniquely determined from the light curve. We do, however, measure the transit duration, radius ratio, and impact parameter of the three single-transit events, and our follow-up spectroscopy and analysis measures the mean stellar density, which allows us to estimate the semi-major axes and orbital periods of the three outer planets (see Table 6.2 for the best-fit values for each parameter).

We assessed the dynamical stability of the system by performing 4000 N-body simulations using the `Mercury6` hybrid integrator. We initialized the N-body simulations with orbital elements drawn from either the posterior probability distributions of transit parameters or from reasonable priors.

We estimated the outer three planets' orbital periods (and therefore semimajor axes) from the transit and stellar parameters using an analytical expression (e.g., Seager & Mallén-Ornelas, 2003) with a correction for nonzero eccentricity from Ford et al. (2008).

We solved Equation this expression numerically 4000 times for each outer planets' orbital period (which we then converted to semimajor axis). For each of the 4000 realizations, we drew the quantities $t_{d,i}$, P_i, $R_{P,i}$, and b_i from the light curve posterior probability distributions from the MCMC transit fits. We generated the planet masses $m_{p,i}$ from the measured planet radii using the same piece-wise mass-radius relation as was used in 6.4.5.1. Values for M_* and R_* were drawn from the posterior probability distributions generated in Section 4.4.1.3, and values for e were drawn from a beta distribution with shape parameters $\alpha = 0.867$ and $\beta = 3.03$ (derived from the population of observed planets given in Kipping, 2013b, 2014; Kipping & Sandford, 2016). We used

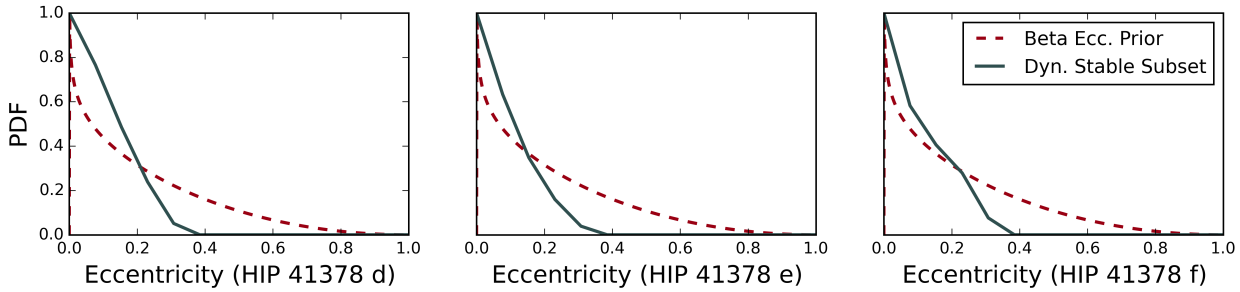

Figure 6.4 Dynamically Derived Limits on Eccentricity. Comparison of input planet eccentricity to dynamical simulations (red dashed lines) and the eccentricity of planets in dynamically stable systems (black solid lines). The input to the dynamical simulations is the distribution of eccentricities in all exoplanets detected with radial velocities (Kipping, 2013b). The difference in shape between the two curves demonstrates which eccentricities are preferred in dynamically stable systems. Evidently planets with eccentricities larger than $e \sim 0.37$ or so will cause the system to go dynamically unstable. The maximum of each curve is normalized to one to show the difference in shape between the two distributions.

an asymmetric prior for the argument of periastron ϖ to account for the fact that the planet is observed to be transiting (the value of which is dependent on the drawn eccentricity; see Equation 19 in Kipping & Sandford, 2016).

After determining initial parameters, we integrated each of the 4000 systems forward in time for 1 Myr, long enough to examine interactions over many secular periods, while requiring energy be conserved to one part in 10^8. Of the total 4000 realizations, only a subset (roughly 10%) were dynamically stable over 1 Myr timescales, meaning that dynamical arguments can help constrain the system architecture, including the orbits of the three outer planets. We found that the most important variables for determining the stability of the system are the orbital eccentricities of the individual planets. For a given transit duration, the orbital period and eccentricity are degenerate. As a result, the eccentricities' constraints translate into limits on the orbital periods of the outer planets.

Figure 6.4 shows the difference in initial eccentricity distribution (namely, the beta distribution prior) and the eccentricity distribution of the planets in systems that remained dynamically stable. These distributions are visibly different, and the eccentricities of stable systems are preferentially lower. Among our 4000 realizations, all systems containing planets with eccentricities above $e \sim 0.37$ became dynamically unstable, suggested that the true eccentricities are less than this value.

6.5 Towards Constraining Ambiguous Orbital Periods

6.5.1 Period constraints from the transit baseline and transit likelihood: when only one transit is seen

In this section, we estimate the orbital period of the three outer planets transiting HIP 41378 under various assumptions and taking different information into account. We calculate orbital periods with a similar analysis to that described in the previous section, in particular by solving Equation 6.7 numerically after drawing parameters from the MCMC transit fit posterior probability distributions or from priors.

We first calculated orbital periods under the assumption of strictly circular orbits. We also required that the orbital periods be longer than the baseline of K2 observations before and after each event – otherwise, we would have seen multiple transits. We find that when we assume a circular orbit, we obtain relatively tight limits on the periods of the outer three planets, in particular the two deepest transits with precisely measured durations and impact parameters. For long period planets like these, however, the assumption of a circular orbit is in general not justified, so we believe these orbital period estimates are artificially tight. The distributions of orbital periods for the outer three planets assuming circular orbits are shown in Figure 6.5.

We also calculated orbital periods with the assumption of circular orbits relaxed to allow orbital eccentricities and arguments of periastron drawn from the same beta distribution and asymmetric prior described in the previous section (and which we used as an input to the dynamical simulations). As noted previously, this distribution matches the observed distribution of orbital eccentricity for exoplanets detected by radial velocities. When we do not assume circular orbits, the limits on are much looser. Although the median orbital periods we derived under the assumption of circular orbits and eccentric orbits are relatively similar, the width of the distribution changes drastically. In the case of HIP 41378 f, the uncertainty on the orbital period increases by an order of magnitude when taking into account nonzero eccentricity. The orbital period distributions given this prior on orbital eccentricity are also shown in Figure 6.5, where they can be compared to the case of circular orbits.

The fact that the eccentricity of exoplanets tends to follow a beta distribution is not the only

information we have about the system architecture or orbital eccentricities of the outer three planets. We can place additional constraints on the orbital eccentricities (and therefore orbital periods) by requiring that the system be dynamically stable. In Section 6.4.5.2, we found that the HIP 41378 system is dynamically unstable on 1 Myr timescales when any of the planets have eccentricities greater than 0.37, so we remove all orbital periods with eccentricities greater than 0.37. We also remove all systems that are not Hill stable (using the criterion from Fabrycky et al., 2014b). Enforcing these dynamical stability criteria narrow the distributions of plausible orbital periods by about 30%. The orbital period distributions with dynamical stability enforced are also shown in Figure 6.5, along with distributions without dynamical stability enforced for comparison.

Finally, we took into account the fact that we observed these three planets to be transiting during the 75 days of K2 observations. Planets with shorter orbital periods are more likely to transit during a limited baseline than planets with longer orbital periods. We take this information into account by imposing a prior of the form:

$$\mathcal{P}(P_i, t_{d,i}, B) = \begin{cases} 1 & \text{if } P_i - t_{d,i} < B \\ (B + t_{d,i})/P_i & \text{else,} \end{cases} \tag{6.2}$$

where $\mathcal{P}$ is the probability of observing a transit of planet i, B is the time baseline of the observations, $t_{d,i}$ is the ith planet's transit duration, and P_i is the orbital period of the planet i. Here, we define the planet being 'observed to transit' as any part of its ingress or egress occurring during K2 observations. We imposed this prior on the orbital period distribution taking into account nonzero orbital eccentricity and dynamical stability, and we show the result in Figure 6.6. The effect of this prior is to narrow the period distributions by another $\sim$30% and to shift the period distributions to slightly lower values. The effect is most pronounced on the period distribution of HIP 41378 d which had a weakly constrained orbital period because of its shallow transit.

We summarize our orbital period estimates under these various assumptions in Table 6.3. We report the median values and 1σ widths of each distribution. In this chapter, we choose to adopt the period distributions which were calculated taking into account nonzero eccentricity, dynamical stability, and the fact that the planets transiting during the K2 observations as our best estimate

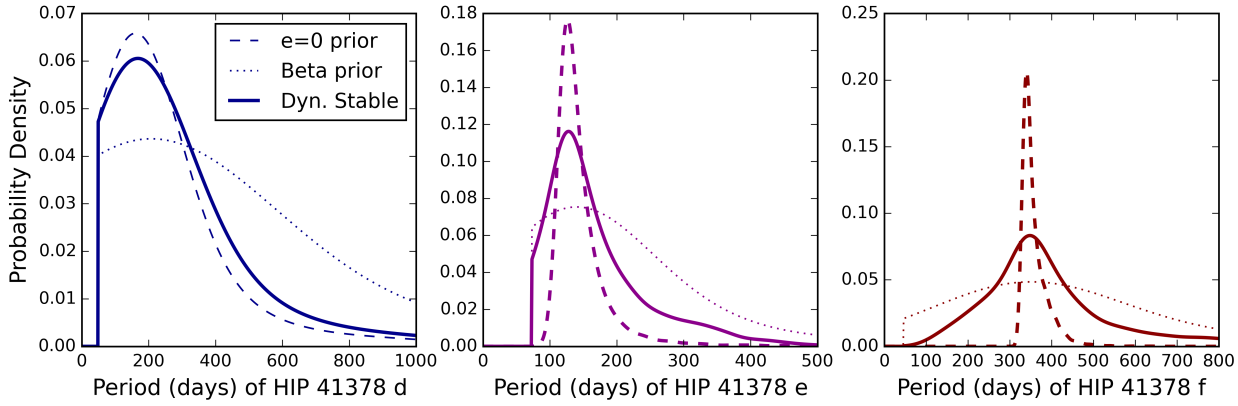

Figure 6.5 Probability Distributions for the Periods of HIP 41378 d, e, and f. Probability distributions for the orbital period of each of the outer planets in the system (detected by only a single transit in K2 data). The dashed lines used a prior of null eccentricity for all three planets. The dotted lines used the Kipping beta distribution as the prior for eccentricity, with the prior for ϖ being that from Kipping & Sandford (2016), which accounts for both geometrical and observational biases. The solid lines use the Kipping eccentricity and ϖ priors, but impose two additional priors of dynamical stability and transit probability. The area under each curve is normalized to one for ease of comparison.

for the outer planets' orbital periods. These distributions incorporate the most information we have about the system to give the best possible period estimates.

6.5.2 Period constraints from the transit baseline and transit likelihood: when two transits are seen

In our work in the previous section, when we only had detected a single transit each of HIP 41378 d, e, and f, we were able to place broad constraints on their orbital periods. In the C18 data, HIP 41378 d and f each transit one more time each, yielding a discrete spectrum of possible orbital periods. Here, we combine broad constraints on the orbital periods and the discrete possible periods based on the times of the two detected transits to determine the most likely orbital periods for HIP 41378 d and f. The techniques used in this section will be more generally applicable to any system where variable baselines (as seen in K2, TESS) result in ambiguous periods but two observed transits.

Our analysis to place broad constraints on the orbital periods of these planets closely follows that of Vanderburg et al. (2016b), with a handful of differences. In particular, Vanderburg et al.

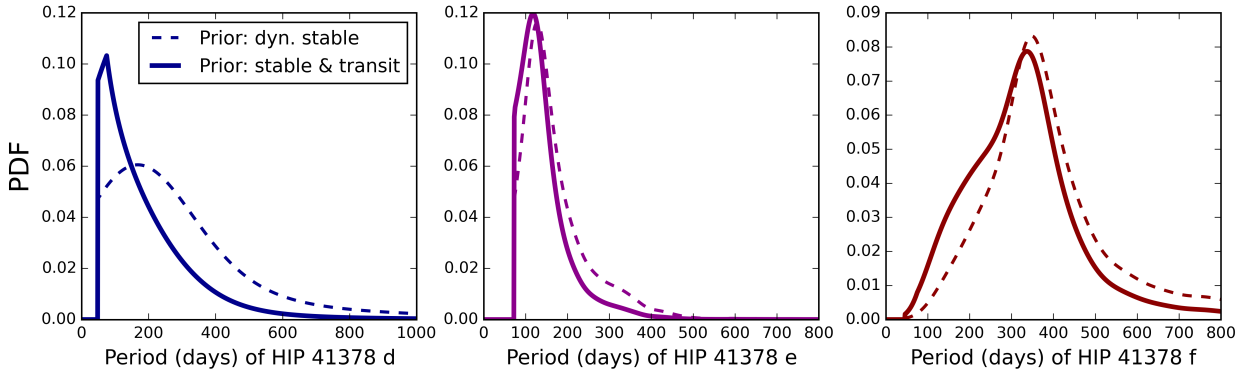

Figure 6.6 Probability of Period for Single-Transit Events. Probability distributions for the orbital period of each of the single-transit planets in the system, incorporating dynamical stability alone (dashed lines) and incorporating dynamical stability and the probability of detecting a single transit with K2 (solid lines). The distribution only taking into account dynamical stability is the same as the solid lines shown in Figure 6.5. Incorporating the prior information that these three planets transited during K2 observations sharpens our predictions of the orbital periods of the three outer planets.

(2016b) imposed a transit prior on the calculated orbital periods to account for the fact that planets HIP 41378 d, e, and f transited once during the 74-day baseline of C5 (see Equation 6.2). Now that we have re-detected planets d and f in C18, we can update our prior on the orbital periods based on these new observations. As such, we impose a prior on both planets orbital periods which account for the fact that both HIP 41378 d and f were detected during both C5 and C18:

$$\mathcal{P}_i(P_i, D_i, B_5, B_{18}) = \begin{cases} 1 & \text{if } P_i - D_i < B_5 \\ (B_5 + D_i)/P_i & \text{if } B_{18} < P_i - D_i < B_5 \\ (B_5 + D_i)(B_{18} + D_i)/P_i^2 & \text{else,} \end{cases} \tag{6.3}$$

where $\mathcal{P}_i$ is the chance of seeing planet i, B_k the time baseline of the observations for campaign k, D_i the planet's transit duration, and P_i the orbital period of the planet in question. In Figure 6.7, we show the comparison between this analytic prior and a Monte Carlo simulation of transit probabilities for 20000 randomly chosen periods on the interval $(0, 1000]$ days, with random centers of transit times on the same interval, and with randomly selected baseline separations (defined as

the time between the last data point of the first campaign with baseline B_1 and the first data point of the second campaign with baseline B_2) on the range $[0, 3000)$ days. The true separation between the end of C5 and the start of C18 was 1037.13 days, but Equation 6.3 describes the general transit probability for a planet with a given period which transits only twice in the K2 data: once in one campaign, and once in another. This prior (Eq. 6.3) describes generally the relative chances of planets with various orbital periods transiting over two observing campaigns. This general result can be applied to targets with unknown periods seen over multiple K2 campaigns, and will also be applicable to similar planets observed in two separated baselines by TESS. In this work, we will apply this probability as a prior in our calculation of the likelihood of each possible period for HIP 41378 d and f, as shorter period planets are more likely to transit over the observed baselines.

As done in Vanderburg et al. (2016b), we can find lower limits on the periods of HIP 41378 d and HIP 41378 f from then length of out-of-transit observations taken on either side of each event (see the middle two panels of Figure 6.1 to see visually the out-of-transit baseline on each side of each transit event). In C5, the data was acquired at times (BJD-2454833) between 2307.55 and 2381.41, for an official baseline of 73.86 days[3]. For C18, the data was acquired at times (BJD-2454833) between 3418.56 and 3469.40 days, for a total baseline of 50.86 days. We assumed that for a 'detection' to occur, any part of the planet's ingress or egress must have occurred during the K2 observations. Using these times, as well as the center of transit times and duration for each transit event, we can compute the minimum periods which are allowed given the single detection in each campaign as follows:

$$P_{min} = \max(\mathrm{t_c} + \mathrm{D}/2 - \mathrm{B_i},\ \mathrm{B_f} - \mathrm{t_c} + \mathrm{D}/2) \tag{6.4}$$

where B_i denotes the beginning time of the campaign, B_f denotes the end time of the campaign, t_c denotes the measured center time of transit for the observed transit event, and D denotes the planetary transit duration. The C5 center for HIP 41378 d (with transit duration 12.71 hours) was 2457166.2629 BJD, and the C18 center was 2458279.709 BJD. Similarly, the C5 center for HIP 41378 f (with transit duration 18.998 hours) was 2457186.91451 BJD, and the C18 center was

[3]The total time baseline of C5 was 74.8 days, but Vanderburg et al. (2016b) clipped out the first day of data while *Kepler* was thermally settling into the campaign.

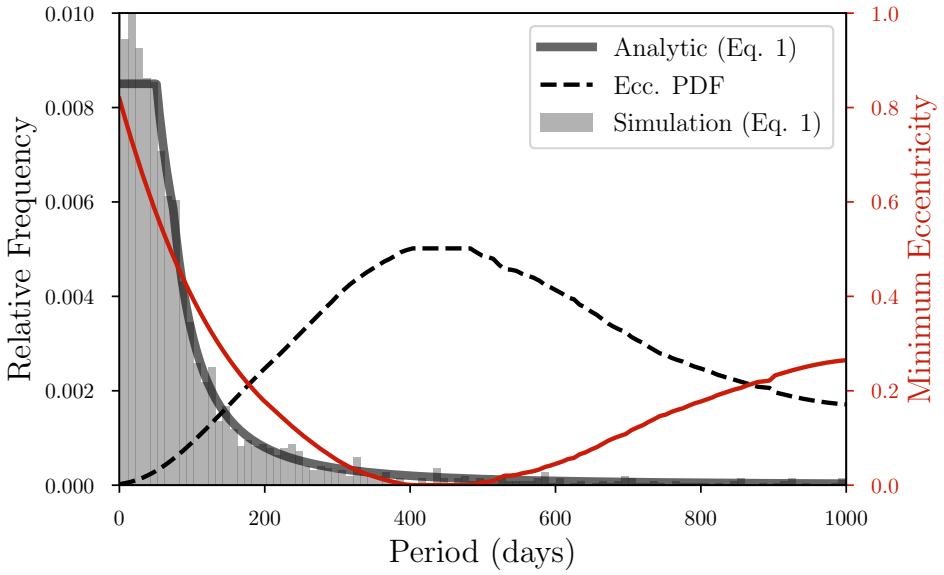

Figure 6.7 Probability Density Function for Observing Two Transit Events. We show the normalized probability density function for the chance of observing *at least* two transits, with at least one in each of two K2 campaigns, for some planet. Plotted here is a comparison of the analytically derived Equation 6.3 (solid line) with a numerically computed Monte Carlo simulation of observability probability by orbital period (histogram). The distributions plotted here were computed for planet HIP 41378 f, for two K2 campaigns with baselines $B_1 = 74$ days and $B_2 = 51$ days, separated by some unspecified length of time. This generalized form describes the chance that only two transits of a planet would be seen over two K2 campaigns, and the good agreement between the simulation and analytic form suggests that Eq. 6.3 can be adopted as the baseline prior in cases where a planet with an unknown period is observed over multiple K2 campaigns. Also plotted in comparison is the minimum value of eccentricity (in red) at each orbital period that allows recreation of the observed duration, and (black dotted line) the probability distribution for each eccentricity, as derived from the cumulative density function of the Kipping beta distribution eccentricity prior (where all values larger than the minimum eccentricity at each period are considered able to reproduce the true transit duration).

2458271.0740 BJD.

From this, we compute a minimum period of 48.1 days for HIP 41378 d and a minimum period of 46.4 for HIP 41378 f. Both of these limits come from the C5 data, which had a longer observational baseline. From these limits, we can exclude any periods for these planets less than these values: if the true periods were smaller than these values, we should have seen evidence of a second transit in the C5 data.

Finally, the fact that HIP 41378 d and HIP 41378 f transit twice allows us to define their orbital periods as

$$P_j = \frac{t_{j,18} - t_{j,5}}{i}, \tag{6.5}$$

when j denotes the planet and i is some positive integer. This equation, combined with the lower limits previously derived, provides a discrete set of possible orbital periods for each planet. For example, there are 23 possible orbital periods for HIP 41378 f, ranging between ∼47.1 days (the lowest possible value that exceeds our lower limit on the period) and ∼1084 days (if no intermediate transits occurred in between the two we observed). The possible periods for each planet are given in the first column of Table 6.4 and Table 6.5 respectively.

6.5.3 Excluding orbital periods using all HAT/KELT/WASP data

In Equation 6.5, we gave an expression for the possible orbital periods for each planet, based on the time at which the two observed events occur for each planet. The HAT/KELT/WASP data subtend a significant observational baseline, and the transit event of HIP 41378 f is relatively deep (0.5%). As such, these ground-based surveys should be able to detect the transit, if the transit happened to occur while the surveys were observing the star. There are a large number of possible orbital periods for HIP 41378 f, so we evaluate the KELT/HAT/WASP evidence for each possible orbital period by computing the likelihood ratio for two models: a flat line and the transit model. We chose our outlier rejection threshold so that on average, we reject only one 'good' data point from each photometric dataset. We found the significance level that corresponds to the single most extreme data point in each data set (where the KELT data had 4709 unique points, HAT had 12903 points, and WASP had 6732 points), and then utilized sigma-clipping to remove outliers.

The threshold we use is $3.7/3.9/3.8\sigma$ (for KELT/HAT/WASP) away from the median flux level of each survey, which was computed from the number of data points for each survey. Then, we phase-folded the light curve at each possible orbital period, and computed the following likelihood ratio:

$$\mathcal{L} = \frac{\exp\left[-\sum_{i=0}^{i=N}(0.5(f(t_i) - m(t_i))^2\sigma_i^{-2})\right]}{\exp\left[-\sum_{i=0}^{i=N}(0.5(f(t_i) - \bar{f})^2\sigma_i^{-2})\right]} \tag{6.6}$$

where $f(t_i)$ denotes the KELT, HAT, or WASP flux at each exposure time t_i, $m(t_i)$ denotes the transit model (using the best-fit parameters from Table 6.2 and the transit model from Mandel & Agol 2002b) at some exposure time, $\bar{f}$ denotes the weighted mean KELT/HAT/WASP flux (a flat line model set to be the weighted mean of the out-of-transit baseline, which is expected to be the best model if no transit occurs; Kovács et al., 2002b), and σ_i denotes the error on the flux measurements, which is set to be $\sigma_i = k\sigma_{\rm obs,i}$, where the measured errors $\sigma_{\rm obs}$ for all data points of the each data set have independently been scaled by a factor of k, so that the reduced χ^2 for the flat line model for each full data-set is roughly 1. The errors on the KELT, HAT, and WASP data-sets are derived and scaled independently.

The likelihood ratio defined in Eq. 6.6 is the ratio of the likelihood of the flat line model to the likelihood of the transit model. In Figure 6.8, we show the phase folded HAT/KELT/WASP light curve at each orbital period. For each orbital period, we compute the likelihood ratio using the entire HAT/KELT/WASP combined, phase-folded data-set. The result is one likelihood ratio $\mathcal{L}$ for each orbital period, describing the relative likelihood of the two models. For likelihood ratios $\mathcal{L}$ greater than 10^4, where the flat line model is highly preferred to the transit model, we consider the corresponding orbital period ruled out.

In each panel of Figure 6.8, we label the orbital period depicted and color the text corresponding to the computed value of the likelihood ratio $\mathcal{L}$: red text indicates that an orbital period can be considered ruled out, and blue text indicates that a particular period cannot be ruled out. For likelihood ratios less than 10^4, we consider the evidence too weak to discriminate between the models. We note that for a single orbital period - $\sim$ 180 days - the likelihood ratio was roughly 3000, a marginal case which our strict criterion of rejection ($\mathcal{L} > 10000$) does not reject. Our choice of 10^4 as the significant likelihood ratio was purposefully conservative, decreasing the probability

of incorrectly rejecting a particular orbital period. For the orbital periods we could rule out based on this test, we set the probabilities to be unlikely (defined as $< 0.1\%$) in Table 6.5. The analysis of the combined KELT, HAT, and WASP data allowed us to eliminate 16 of the 23 possible orbital periods for HIP 41378 f to this significance level. We note that analysis of any of the individual data sets alone could not rule out all 16 orbital periods: the full result of this method was achieved by combining the three ground-based data sets.

We also performed the same algorithm described above on the predicted orbital periods for HIP 41378 d, but no periods could be excluded (as expected for a transit event of the much smaller measured depth of HIP 41378 d). The depth of HIP 41378 d is $\sim$1 mmag, and its duration $\sim$ 12.7 hours. For the three ground-based surveys considered, typical scaled photometric uncertainties were reported to be 0.5%, 0.3%, and 1% for KELT, WASP, and HAT, respectively, which we roughly corresponds to a median precision of 5 mmag. For a best-case 100 points in transit at this precision, this corresponds to a SNR of $\sqrt{100}(1 \text{ mmag}/5 \text{ mmag}) = 2$. Once the orbital period for HIP 41378d is uniquely determined, or more ground-based data points become available, this signal may be detectable in the HAT/KELT/WASP data.

Additionally, we conducted a pre-recovery search in the KELT data using the fixed-duration and fixed T_C BLS method, as implemented in the VARTOOLS package (Hartman & Bakos, 2016), with an approach described in Yao et al. (2018). Using the transit time and transit duration for HIP 41378 f as determined from Vanderburg et al. (2016b), we searched 300,000 trials evenly spaced in frequency from 150 to 450 days. The strongest peak in the BLS output corresponds to 328.59 days, with a signal-to-pink noise statistic of 2.4, which is below the 10% confidence level for a transit with the corresponding depth and duration, as determined in Yao et al. (2018). As such, this is not considered a plausible detection.This period is not predicted by Eq. 6.5; as such, the only way that the signal detected by this algorithm is real is if HIP 41378 f has significant ($\sim$ month amplitude) transit timing variations (TTVs). As this scenario is *a posteriori* unlikely and the SPN of this peak is low, we do not consider this a plausible detection.

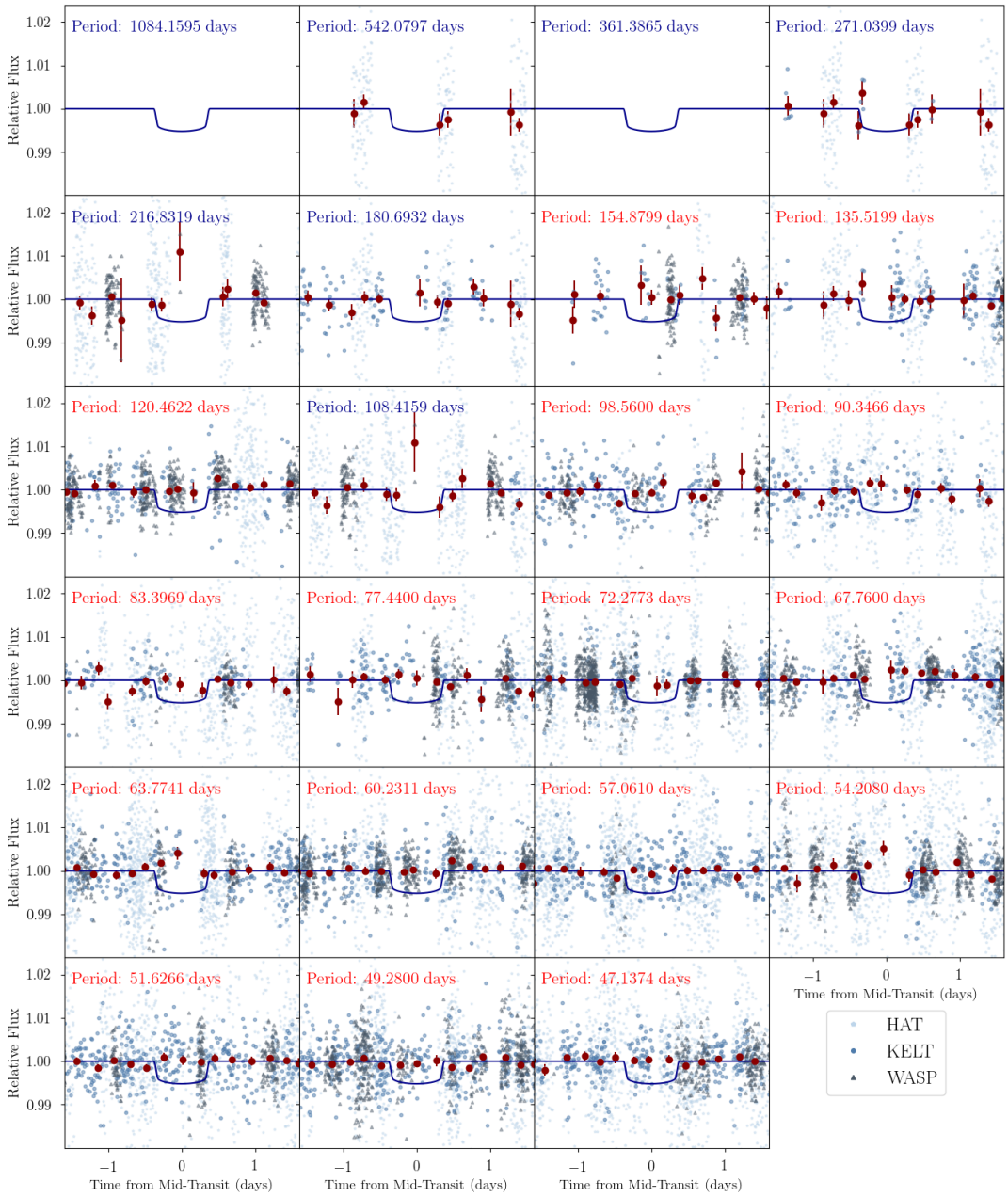

Figure 6.8 The HAT/KELT/WASP Data Folded Over Each Possible Period for HIP 41378 f. For each possible orbital period of HIP 41378 f derived from Equation 6.5, we phase-fold the KELT, HAT, and WASP data and fit two models around where the transit would be expected to be: the transit model, plotted in blue, which we would expect to see if the tested orbital period were the true orbital period of the planet; and the best-fit flat model with no transit (not shown), which we expect to see if that orbital period is incorrect. In red are orbital periods where the flat line model is heavily preferred. In blue are orbital periods for which a determination between the two models cannot be made. Blue points are true data points from the KELT, HAT, and WASP surveys, and red points are the weighted mean for each bin, with errors equal to the weighted error on the mean.

6.5.4 Dynamically Feasible Periods

From the K2 data, we have well-measured values of the transit duration, transit impact parameter, center time of transit, and $(R_P/R_\star)$ for HIP 41378 d and HIP 41378 f. These known values are presented in Table 6.2. Using these values and priors on the unmeasured quantities (orbital eccentricity and longitude of perihelion), we can estimate the orbital period that corresponds to a transit duration of a given value using (e.g., Seager & Mallén-Ornelas, 2003; Ford et al., 2008):

$$D_i = \frac{P_i}{\pi} \arcsin \left[\left(\frac{G(M_* + m_{p,i})P_i^2}{4\pi^2} \right)^{-1/3} \times \sqrt{(R_{P,i} + R_*)^2 - (b_i^2 \times R_*^2)} \right] \frac{\sqrt{1 - e_i^2}}{1 + e_i \cos \varpi_i} \qquad (6.7)$$

where we define D_i is the transit duration of the ith planet (from first to fourth contact) and $R_{P,i}$ is the planetary radius, P_i its orbital period (the quantity for which we would like to solve), $m_{p,i}$ the mass of the ith planet, e_i the orbital eccentricity, ϖ_i the longitude of periastron, b_i the impact parameter, M_* the stellar mass, R_* the stellar radius, and finally G the gravitational constant.

In a method reminiscent of the analysis in Vanderburg et al. (2016b), we generated 10000 feasible orbital periods by solving the above equation with draws from the following probability distributions: $t_{d,i}$, $R_{P,i}$, and b_i were drawn from the posteriors given in Table 6.2; M_* and R_* were drawn from the Gaia posterior probability distributions (see also Table 6.1); eccentricity e was drawn from a beta distribution with shape parameters $\alpha = 0.867$ and $\beta = 3.03$ (Kipping, 2013b, 2014; Kipping & Sandford, 2016); ϖ_i was chosen using Equation 19 of Kipping & Sandford (2016); $m_{p,i}$ was drawn from the Weiss & Marcy (2014a) mass-radius relation for planets with $R_p < 1.5R_\oplus$, drawn from the Wolfgang et al. (2016) relation for planets with $4R_\oplus > R_p > 1.5R_\oplus$, and the mean planetary density is drawn from a normal distribution centered at $\rho = 1.3 \pm 0.5$ g / cm^3 for planets larger than 4R$_\oplus$. With only P_i left as a free parameter in the equation, we solve Eq. 6.7 numerically for each set of draws. The resultant series of 10000 orbital periods all geometrically produce the observed transit durations, and can as such be considered plausible.

The orbital periods drawn from this distribution are not necessarily equally physically likely, however. To ensure their feasibility, we use two additional criteria based on the dynamical stability of the planetary system as a whole. In Section 6.4.5.2, we used an extensive set of numerical simulations to determine that eccentricities above $e \sim 0.37$ lead to dynamical instability (defined as

collisions or ejections within 1 Myr) in the five-planet HIP 41378 system. Additionally, systems are generally expected to be dynamically unstable when their drawn initial conditions are Hill-unstable (Fabrycky et al., 2014b). As such, we exclude from our distribution of dynamically feasible periods any draw which either is Hill-unstable or has planetary eccentricities above 0.37. The result is roughly 5100 orbital periods for each planet that are both consistent with the measured transit duration and adhere to our dynamical stability criterion. A normalized histogram of these orbital periods is shown for each planet in Figure 6.9. This histogram represents the probability distribution for the orbital period of each planet, based on only its measured duration and the orbital elements physically likely to cause such a duration.

We note that for future analysis for other systems, the eccentricity cut we use to exclude dynamically unstable systems will need to be re-derived, as it was derived from numerical simulations for this specific system. The probabilistic exclusion used here will not apply to all systems.

6.5.5 Final period constraints for HIP 41378 d and HIP 41378 f

In this chapter, we have constructed various constraints from direct analysis of the light curve, statistical analysis, and dynamical modeling. We list here the constraints that we have placed on the planetary periods:

- A list of possible periods based on the measured times of transit center for each planet (Eq. 6.5)
- The statistical baseline prior (Sec. 6.5.2; also see Figure 6.7)
- Lower limits on the orbital periods from the out-of-transit C5 baseline (Section 6.5.2)
- A distribution of dynamically feasible periods, based on the measured durations and orbital stability
- Exclusions of particular orbital periods from the combined KELT, HAT, and WASP data (this constraint is available only for HIP 41378 f, which had the deeper transit event)

In Figure 6.9, we illustrate the final continuous probability distribution with a solid line. This distribution is the normalized product of the baseline transit probability (Eq. 6.3) and the PDF

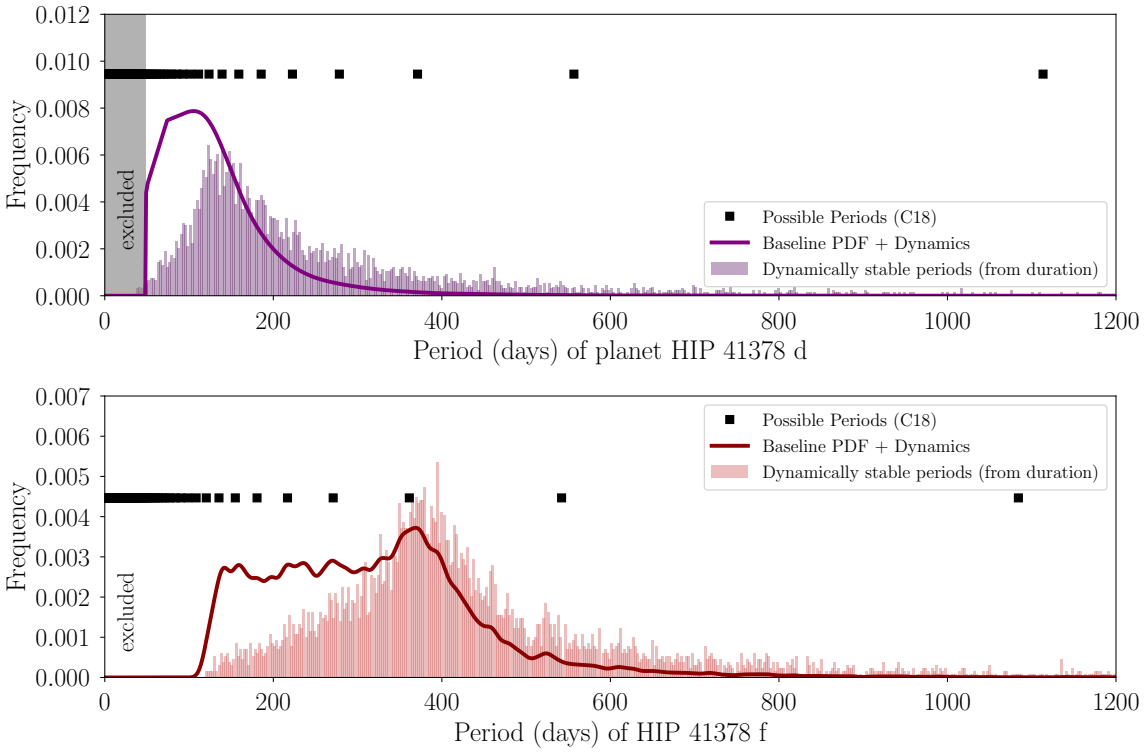

Figure 6.9 Derived Probability Distributions for Orbital Period of HIP 41378 d and f. The derived probability distributions for orbital period for HIP 41378 d (top panel) and HIP 41378 f (bottom panel). The histogram denotes the periods consistent with the measured transit duration, and the height of each bin describes the relative likelihood of each period from dynamical constraints alone. The solid line is the product of the histogram convolved with a Gaussian kernel and the baseline prior (Eq. [6.3]), which assigns a higher probability to orbital periods with a higher likelihood of transiting during the observed K2 campaigns. At each square point (which correspond to the possible discrete orbital periods), we read off the value of the solid line to get the relative probabilities, which must subsequently be normalized once all possible periods are identified. The results of this analysis at each discrete period are presented in Tables 6.4 and 6.5.

constructed by convolving a Gaussian kernel with the histogram of dynamically feasible periods (generated from Eq. 6.7 and described in the previous section). Squares denote the possible orbital periods based on Eq. 6.5, and some of these periods can be excluded using the KELT, HAT, and WASP data. Notably, all of the periods below $\sim$ 100 days can be excluded for HIP 41378f.

Using these constraints, we construct individual probability estimates for the possible orbital periods in the following way. First, we exclude all orbital periods generated by Eq. 6.5 that fall below the lower limit derived by Eq. 6.4. Then, for each remaining orbital period, we extract

the probability from the interpolated product of the baseline prior and the PDF of dynamically feasible periods (this function is plotted as the solid line in Fig. 6.9) at exactly that orbital period. We repeat this for each possible period, and then normalize the total probability for all discrete periods to be equal to one. The resultant periods and their corresponding normalized probabilities are presented in Table 6.4 and Table 6.5.

6.5.6 Final period constraints for HIP 41378 e

HIP 41378 e transited once during K2 C5, but did not transit during C18 (see Fig. 6.1). As such, we do not have discrete guesses for its true orbital period; however, we can exclude any orbital period that would have led to a transit being observable during C18. To construct an additional PDF that represents this scenario, we test each possible orbital period for HIP 41378 e between 72 days (the minimum orbital period permitted by Eq. [6.4]) and 1200 days. Then, we allow $t_{e,18}$ to vary between the times of the first and last data points of C18. If Eq. 6.5 is satisfied for some integer i for any value of $t_{e,18}$ on this range, then we consider this particular period "observable" in C18, and set the probability that it is the true orbital period of HIP 41378 e to zero. The result of this pruning (normalized so the maximum probability is equal to the maximum probability of the PDF constructed from the results of the baseline PDF and dynamical analysis) is shown in grey in Figure 6.10.

The final orbital period for HIP 41378 e cannot be directly constrained due to the lack of a transit in the C18 data; the best that can be done without follow-up observations is the probabilistic period estimation presented in the bottom panel of Figure 6.10.

6.6 Discussion

6.6.1 Strategies for observational follow-up in the HIP 41378 system

In this work, we have identified a discrete set of precise possible orbital periods for the long-period transiting planets HIP 41378 d and HIP 41378 f, and have assessed the likelihood that each of these possible orbital periods is indeed the true orbital period. While we have significantly constrained the possible orbital periods of these two planets (we have ruled out about 25% of the

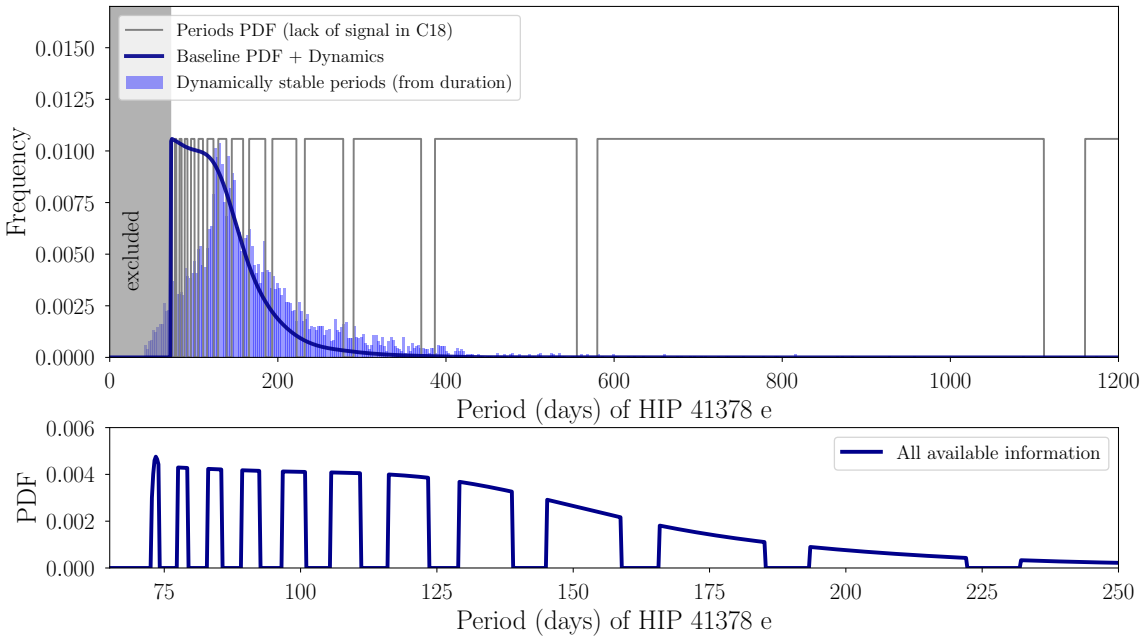

Figure 6.10 Derived Probability Distribution for Orbital Period of HIP 41378 e. The derived probability distributions for the orbital period of HIP 41378 e. The histogram (top panel) denotes the periods consistent with the measured transit duration. The solid line is the product of the histogram convolved with a Gaussian kernel and the baseline prior (Eq. [6.3]), constructed the same way as for HIP 41378 d and f in Figure 6.9. The grey line describes the relative probability of each orbital period, given that HIP 41378 e did not transit during C18. This line has been normalized so that the maximum value of the Baseline + Dynamics PDF matches its maximum value for illustrative purposes. In the bottom panel, we show the normalized product of the Baseline + Dynamics PDF and the grey curve.

possible periods at confidence <1.5% for planet d and 80% of possible periods for planet f), our analysis is so far unable to uniquely determine the true orbital periods of these planets. Additional follow-up observations will be necessary to ultimately identify the true orbital periods and enable future studies with facilities like JWST.

To determine the true orbital periods for HIP 41378 d and f, the strategy is fairly straightforward. The additional transits during C18 and our identification of precise possible orbital periods makes it possible to schedule targeted transit follow-up observations at these most likely periods. The 0.5% transit depth of HIP 41378 f makes it possible to detect the transit with ground-based telescopes, although the long (19 hour) transit duration will make it impossible to observe the transit from a single observatory. The multi-site Las Cumbres Observatory telescopes, which have demonstrated the ability to produce continuous precise light curves across multiple observing sites around the globe (Boyajian et al., 2018), may be well suited to detect the long duration transit of HIP 41378 f. The shallower (800 ppm) transits of HIP 41378 d, however, will likely require space-based resources such as the *Spitzer* Space Telescope, or potentially the CHEOPS space telescope once it launches in 2019, for confirmation.

Because of HIP 41378 d's shorter orbital period, and the fact that our ground-based data from HAT and KELT were unable to detect or rule out its shallow transits, there are a large number of possible orbital periods, many of which have roughly equal probabilities of being the true orbital period. Observing transits at all of these possible transit times would be an expensive observing program for a precious resource like *Spitzer*. However, it should be possible to significantly increase the efficiency of *Spitzer* follow-up observations for these possible orbital periods because of how many of these periods are related to one another by harmonics. For example, a single *Spitzer* non-detection of a transit of HIP 41378 d on the observation opportunity on 2019 June 16 (371.149 days after the C18 transit) would rule out four possible orbital periods (371.149, 185.574, 123.716, and 61.858 days). Taking advantage of these harmonic relationships between the possible orbital periods may significantly decrease the amount of observing time needed to identify the true period of HIP 41378 d.

Determining the orbital period of HIP 41378 e is significantly more difficult than HIP 41378 d and f. Since K2 reobserved HIP 41378 for 51 days and did not detect a second transit of HIP 41378

e, it is likely the orbital period is longer than that of HIP 41378 d, despite their very similar transit durations. The shallow transit depth of only about 0.15% will likely require long stares with highly precise space-based photometers to redetect. The first opportunity for a re-detection will come fairly soon with the newly commissioned TESS spacecraft. TESS will observe HIP 41378 f in early 2019 (2019 January 7 to 2019 February 2) during Sector 7 of its prime mission[4] and should have sufficient photometric precision to detect the transit of HIP 41378 e. If no transits are detected during the Sector 7 TESS monitoring of HIP 41378, TESS may monitor HIP 41378 for a longer period of time in an extended mission, which could provide additional opportunities to detect the transit of this planet. If TESS is unable to re-detect HIP 41378 e, CHEOPS may be able to, if HIP 41378 is added to its monitoring program. The long duration of the transit could make it an efficient CHEOPS target, where only sparse observations are necessary to sample the transit shape.

6.6.2 The uniqueness of HIP 41378 f

The detection of a second transit of HIP 41378 d and f provides a path towards determining their precise orbital periods and enabling follow-up opportunities for these two long-period gas giant planets. While both planets present intriguing prospects for observations like transmission spectroscopy, HIP 41378 f is a particularly unique target. Depending on its true orbital period, the equilibrium temperature of HIP 41378 f likely ranges between 300 K and 400 K (assuming an albedo similar to Jupiter's), significantly cooler than all other transiting gas giant planets well suited for transmission spectroscopy. We queried the NASA Exoplanet Archive[5] Confirmed Planet Table on 2 September 2018, and identified all transiting planets larger than 0.8 R_J and orbital periods longer than 150 days. Among the nine stars which host planets satisfying these criteria, HIP 41378 is the brightest by a factor of about 15 in H-band. Once a unique transit ephemeris has been determined, the brightness of HIP 41378 should make transmission spectroscopy observations of this long-period temperate gas giant feasible.

HIP 41378 f will likely remain a uniquely interesting target for transmission spectroscopy into the TESS era as well. We downloaded the predicted TESS planet detection yields from Sullivan

[4] `https://heasarc.gsfc.nasa.gov/cgi-bin/tess/webtess/wtv.py`

[5] `http://exoplanetarchive.ipac.caltech.edu/cgi-bin/TblView/nph-tblView?app=ExoTbls&config=planets`

et al. (2015) and searched again for planets larger than 0.8 R_J with orbital periods longer than 150 days. Over the course of its two year prime mission, TESS is expected to detect only about three such planets. In the TESS realization from Sullivan et al. (2015), none of the host stars of these planets are brighter than HIP 41378. It is also likely that any similar long-period planets detected by TESS will have similar orbital period ambiguities to those posed by HIP 41378 (more than 1200 single-transit planets are expected to be found in the full frame images, some of which will have periods longer than 250 days; Villanueva et al., 2018), so it may be a long time before any long-period TESS discoveries will have precisely determined transit ephemerides to enable follow-up. Now that HIP 41378 f has a straightforward path towards a well determined orbital period, it is likely this planet will be one of the best to study the atmosphere of Jovian planets in temperate, nearly Earth-like irradiation environments.

6.6.3 Deriving planetary masses

HIP 41378 is a compelling candidate for follow-up observations due to its brightness, the accessible size of the planets, and the system's rich architecture. HIP 41378 is the second brightest multi-transiting system, behind *Kepler*-444 (Campante et al., 2016), a system of five sub-Earth sized planets with expected RV semi-amplitudes below the noise-floor of current instrumentation. Unlike the *Kepler*-444 system, the planets orbiting HIP 41378 should each have measurable RV semi-amplitudes. We have estimated the likely range of RV semi-amplitudes for each planet assuming planetary masses drawn from the Wolfgang et al. (2016) distribution and periods and eccentricities drawn from our analysis in Sections 6.4.5.2 and 6.5.1. The RV semi-amplitude distributions, shown in Figure 6.11, are all centered above 1 $\mathrm{m\,s^{-1}}$, and could therefore be detectable with spectrographs like HARPS-N (Cosentino et al., 2012) and HIRES (Vogt et al., 1994) in the north, and HARPS (Mayor et al., 2003) and PFS (Crane et al., 2010) in the south. It will be most challenging to detect HIP 41378 d which has an unknown period (unlike the inner two planets) and most likely induces an RV semiamplitude of only 2 $\mathrm{m\,s^{-1}}$, but such signals have been detected previously in intensive observing campaigns (e.g. Lovis et al., 2011).

Radial velocity measurements will be particularly valuable for two reasons. First, precise mass measurements of the inner two planets can probe the mass radius diagram in the regime of low

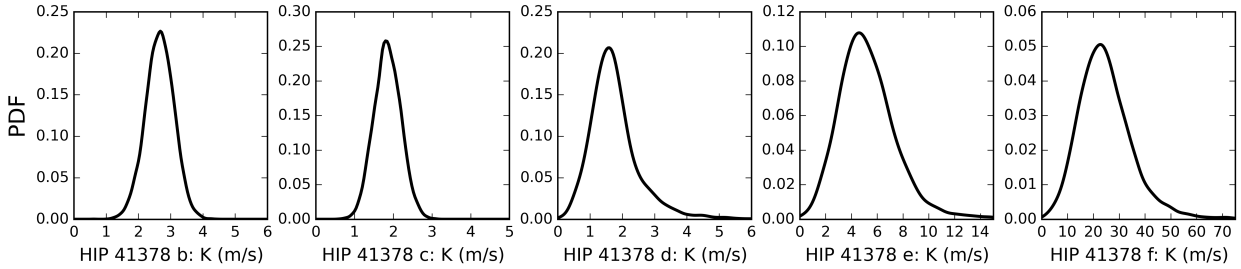

Figure 6.11 Expected Stellar Reflex Velocity of HIP 41378. Probability density function for the expected stellar reflex velocities caused by the motion of each planet in this system. Planets b and c have well measured orbital periods and ephemerides which will make it easier to measure their masses despite the low amplitudes of their RV signals.

incident flux. Most transiting planets with precise masses orbit very close to their host stars, where any gaseous envelopes originally present might have been stripped by the intense stellar radiation. Planet masses measured from transit timing variations have shown that some planets on longer periods are likely less dense than most short period planets. Measuring precise masses of planets in longer period orbits (like the inner two planets in this system) can help show whether or not a planet's radiation environment affects its density.

6.7 Summary

In this chapter, we have described the discovery of five planets in the HIP 41378 system. We provide our results from an MCMC analysis of the K2 light curve to derive planetary parameters, and use data from several additional sources to better model the stellar properties. The final result is a detailed characterization of the system, barring a radial velocity analysis to determine system masses.

Subsequently, once additional data was taken of HIP 41378 in C18 of the K2 mission, we refined the estimates for the orbital periods of HIP 41378 d and HIP 41378 f to provide updated predictions of the transit ephemerides. Although unique orbital periods cannot yet be determined, we have constrained the possibilities and have identified the most likely candidate orbital periods. Additional observations that probe each of the most likely orbital periods will allow a determination of the true orbital period for each planet. The orbital periods that should be tested are presented

in Tables 6.4 and 6.5. One of the primary motivations for this analysis is to recover the transit of HIP 41378 f, a Jupiter-size planet which may be a particularly interesting target for additional in-transit study (such as transit spectroscopy).

The methods developed in this work can be applied to multi-planet systems discovered in the future (e.g., where only single transits are observed). The TESS mission is expected to discover many such systems. In addition, some of the TESS targets are expected to have variable baselines between continuous viewing periods, resulting in a cadence similar to the gaps between campaigns in K2. As a result, true period and ephemeris determinations will be imperative for the subsequent study of many planetary systems discovered by TESS.

6.8 Emergent Properties: Learning more from Transit Data

A additional motivation of the work in this chapter is to provide a blueprint for future period-recovery efforts. In the era of TESS, many more planets for which the exact orbital period cannot be determined will be discovered. Due to the TESS survey strategy, in some cases, stars will be observed with significant gaps in between periods of observations. For example, according to the Web TESS Viewing Tool[6], the southern circumpolar star δ Mensae will be observed by TESS during Sectors 1,5,8,12, and 13 for 28 days each, with gaps of 84 days, 56 days, and 84 days between subsequent periods of observation. Any planet detected by TESS in this region of sky with a period longer than about 28 days could have ambiguous orbital periods due to the observational strategy. The different constraints we used to narrow down the possible orbital periods for the HIP 41378 planets provided in Section 6.5.5 can serve as a starting point for future analysis on TESS planets with similar orbital period ambiguities.

Some results, such as the generalized transit probability by transit baseline (Eq. [6.3]), can be derived merely by substituting in the values for campaign baseline and other easily obtained parameters. Similarly, the expected period distribution can be derived from transit duration (Eq. [6.7]), as long as sensible priors are applied. For example, in Vanderburg et al. (2016b), we pointed out the importance of allowing planets to have non-zero eccentricities when computing period

[6] `https://heasarc.gsfc.nasa.gov/cgi-bin/tess/webtess/wtv.py`

estimates from transit durations: a null eccentricity prior artificially narrows the distribution of possible orbital periods. It is reasonable to say that the observed multi-planetary systems such as HIP 41378 have the emergent property of dynamical stability: in order for the system to be seen now when the star's age is estimated in this chapter to be around 4.2 Gyr old, the system must reside in a dynamically stable and favorable configuration. In this chapter, we used that fact to place limits on where in the system the planets could reside and what orbits were allowable. In this way, emergent properties can be used to very easily yield constraints on the system.

On the other hand, some additional constraints may take significantly more work to derive for some systems. In particular, for multi-planet systems with ambiguous orbital periods, dynamical constraints should be derived uniquely (either using numerical simulations or other dynamical techniques) for each system, and may place tighter limits in some systems than others.

Finally, period estimations can be improved by using additional data. The analysis in this paper also shows the importance of legacy ground-based surveys in the TESS era. Through a combination of existing photometric data from such as HAT and KELT and dynamical analysis, the most likely orbital periods for individual planets can be determined, which allows for an efficient use of limited follow-up telescope resources.

6.8.1 Implications on Future Work

The K2 mission has discovered transiting planets and candidates around bright stars (Vanderburg et al., 2016e; Rodriguez et al., 2017b; Christiansen et al., 2017c; Niraula et al., 2017a; Rodriguez et al., 2018a; Mayo et al., 2018a; Yu et al., 2018; Brahm et al., 2018), which are particularly amenable to follow-up studies, such as precise radial velocities and transit transmission spectroscopy. In particular, the yield from K2 includes six of the ten small planets (with $R_p < 3R_\oplus$) with the best prospects for transmission spectroscopy discovered to date (Rodriguez et al., 2018d). These kinds of follow-up observations could significantly improve our understanding of these planets, yielding information about their interior structure and bulk composition (Dressing et al., 2015b), how they have been sculpted by processes like photoevaporation (Ehrenreich et al., 2015), how, why and to what extent some planets form aerosols and hazes high in their atmospheres (Crossfield & Kreidberg, 2017a; May et al., 2018), and what kind of molecules constitute their atmospheres

(Morley et al., 2017). The HIP 41378 system (and in particular Jupiter-radius planet HIP 41378 f) is an excellent and (so far) unique target for these efforts, which could yield important constraints on where in the disk these planets formed. The HIP 41378 system appears to be particularly amendable to efforts to derive its formation and migration history.

Parameter	Value
HIP 41378 b	
Orbital Period, P [days]	15.5712±0.0012
Radius Ratio, $(R_P/R_\star)$	0.0188±0.0011
Scaled semimajor axis, $a/R_\star$	19.5±4.5
Orbital inclination, i [deg]	88.4±1.6
Transit impact parameter, b	0.55±0.28
Time of Transit t_t [BJD]	2457152.2844± 0.0021
R_P [$R_\oplus$]	2.90±0.44
HIP 41378 c	
Orbital Period, P [days]	31.6978± 0.0040
Radius Ratio, $(R_P/R_\star)$	0.0166± 0.0012
Scaled semimajor axis, $a/R_\star$	73± 18
Orbital Inclination, i [deg]	89.58± 0.52
Transit Impact parameter, b	0.53± 0.29
Time of Transit t_t [BJD]	2457163.1659± 0.0027
R_P [$R_\oplus$]	2.56± 0.40
HIP 41378 d	
Radius Ratio, $(R_P/R_\star)$	0.0259±0.0015
Transit Impact Parameter, b	0.50±0.27
Time of Transit (C5) $t_{t,5}$ [BJD]	2457166.2629± 0.0016
Time of Transit (C18) $t_{t,18}$ [BJD]	2458279.709± 0.003
Transit Duration D [hours]	12.71± 0.26
HIP 41378 e	
Radius Ratio, $(R_P/R_\star)$	0.03613± 0.00096
Transit Impact Parameter, b	0.31± 0.17
Time of Transit t_t [BJD]	2457142.01656± 0.00076
Transit Duration D [hours]	13.007± 0.088
R_P [$R_\oplus$]	5.51±0.77
HIP 41378 f	
Radius Ratio, $(R_P/R_\star)$	0.0672±0.0013
Transit Impact Parameter, b	0.227±0.089
Time of Transit (C5) $t_{t,5}$ [BJD]	2457186.91451± 0.00032
Time of Transit (C18) $t_{t,18}$ [BJD]	2458271.0740± 0.0008
Transit Duration D [hours]	18.998± 0.051

Table 6.2 Parameters for the known planets in the HIP 41378 system. Planetary data in this table comes from analysis in Vanderburg et al. (2016b) and Becker et al. (2019). The time of transits for single-transit planets are reported for both campaign 5 (C5) and campaign 18 (C18).

Eccentricity Prior	**HIP 41378 d period**	**HIP 41378 e period**	**HIP 41378 f period**
$e = 0$	157^{+195}_{-41}	132^{+37}_{-14}	348^{+37}_{-13}
e beta distribution	188^{+397}_{-87}	143^{+129}_{-52}	367^{+311}_{-130}
e beta distribution, stable only	174^{+260}_{-68}	140^{+92}_{-43}	361^{+182}_{-103}
Adopted: e beta, stable + baseline	156^{+163}_{-78}	131^{+61}_{-36}	324^{+121}_{-127}

Table 6.3 Estimated Periods for the Three Outer Planets Using Four Choices of Priors. The $e = 0$ prior produces the smallest errors on period, but it is likely these are underestimated. We adopt the results from the fourth line, which uses a the beta distribution for eccentricity and incorporates priors accounting for dynamical stability and transit likelihood (Equation 6.3) as our best estimates of the orbital periods in this system.

Orbital Period (days)	**Normalized Probability**
1113.4465 ± 0.0034	< 0.1 %
556.7233 ± 0.0017	< 0.1 %
371.1488 ± 0.0011	0.1 %
278.3616 ± 0.0009	0.5 %
222.6893 ± 0.0007	1.1 %
185.5744 ± 0.0006	2.4 %
159.0638 ± 0.0005	4.1 %
139.1808 ± 0.0004	5.7 %
123.7163 ± 0.0004	6.7 %
111.3447 ± 0.0003	7.1 %
101.2224 ± 0.0003	7.1 %
92.7872 ± 0.0003	7.0 %
85.6497 ± 0.0003	6.9 %
79.5319 ± 0.0002	6.8 %
74.2298 ± 0.0002	6.8 %
69.5904 ± 0.0002	6.3 %
65.4969 ± 0.0002	5.9 %
61.8581 ± 0.0002	5.5 %
58.6024 ± 0.0002	5.1 %
55.6723 ± 0.0002	4.8 %
53.0213 ± 0.0002	4.5 %
50.6112 ± 0.0002	4.2 %
48.4107 ± 0.0001	1.4 %

Table 6.4 Possible orbitals periods and their relative likelihoods, based on the analysis described in Section6.5.1. Values may not add up to 100% due to rounding. Errors on orbital periods were computed with $\sigma = (t_{c,5}^2 + t_{c,18}^2)^{1/2}/n$, when n denotes the number of full cycles between C5 and C18, and t_c denotes the uncertainty on center time of transit in each campaign. Errors on the orbital period are lower when a larger number of periods have elapse since the C5 observation.

Orbital Period (days)	**Normalized Probability (w/o KELT/HAT/WASP)**	**Normalized Probability (w/ KELT/HAT/WASP)**
1084.15946 ± 0.00086	< 0.1 %	< 0.1 %
542.07973 ± 0.00043	2.2 %	3.2 %
361.38649 ± 0.00029	19.9 %	29.7 %
271.03986 ± 0.00022	15.7 %	23.6 %
216.83189 ± 0.00017	15.2 %	22.8 %
180.69324 ± 0.00014	13.4 %	20.1 %
154.87992 ± 0.00012	14.8 %	< 0.1 %
135.51993 ± 0.00011	13.4 %	< 0.1 %
120.46216 ± 0.00010	5.0 %	< 0.1 %
108.41595 ± 0.00009	0.4 %	0.6 %
98.55995 ± 0.00008	< 0.1 %	< 0.1 %
90.34662 ± 0.00007	< 0.1 %	< 0.1 %
83.39688 ± 0.00007	< 0.1 %	< 0.1 %
77.43996 ± 0.00006	< 0.1 %	< 0.1 %
72.27730 ± 0.00006	< 0.1 %	< 0.1 %
67.75997 ± 0.00005	< 0.1 %	< 0.1 %
63.77409 ± 0.00005	< 0.1 %	< 0.1 %
60.23108 ± 0.00005	< 0.1 %	< 0.1 %
57.06102 ± 0.00005	< 0.1 %	< 0.1 %
54.20797 ± 0.00004	< 0.1 %	< 0.1 %
51.62664 ± 0.00004	< 0.1 %	< 0.1 %
49.27998 ± 0.00004	< 0.1 %	< 0.1 %
47.13737 ± 0.00004	< 0.1 %	< 0.1 %

Table 6.5 Possible orbitals periods and their likelihoods. The second column comes from only dynamical analysis, and the third column excludes periods that our analysis of the KELT/HAT/WASP data found to be unlikely. Values may not add up to 100% due to rounding. Errors on orbital periods were computed with $\sigma = (t_{c,5}^2 + t_{c,18}^2)^{1/2}/n$, when n denotes the number of full cycles between C5 and C18, and t_c denotes the uncertainty on center time of transit in each campaign.

CHAPTER VII

A Compact Multi-Planet System With A Significantly Misaligned Ultra Short Period Planet

Results through Section 7.7 in this chapter were published in: *Rodriguez, J. E.,* ***Becker, J. C.****, Eastman, J. D., et al. "A Compact Multi-Planet System With A Significantly Misaligned Ultra Short Period Planet." 2018, The Astronomical Journal, 156, 245.*

Results in Section 7.8 onwards are as of yet unpublished work.

7.1 Abstract

We report the discovery of a compact multi-planet system orbiting the relatively nearby (78pc) and bright (K = 8.9) K-star, K2-266 (EPIC248435473). We identify up to six possible planets orbiting K2-266 with estimated periods of P_b = 0.66, $P_{.02}$ = 6.1, P_c = 7.8, P_d = 14.7, P_e = 19.5, and $P_{.06}$ = 56.7 days and radii of R_P = 3.3 $R_\oplus$, 0.646 $R_\oplus$, 0.705 $R_\oplus$, 2.93 $R_\oplus$, 2.73 $R_\oplus$, and 0.90 $R_\oplus$, respectively. We are able to confirm the planetary nature of two of these planets (d & e) from analyzing their transit timing variations ($m_d = 8.9^{+5.7}_{-3.8} M_\oplus$ and $m_e = 14.3^{+6.4}_{-5.0} M_\oplus$), confidently validate the planetary nature of two other planets (b & c), and classify the last two as planetary candidates (K2-266.02 & .06). From a simultaneous fit of all 6 possible planets, we find that K2-266 b's orbit has an inclination of 75.32° while the other five planets have inclinations of 87–90°. This observed mutual misalignment may indicate that K2-266 b formed differently from the other planets in the system. The brightness of the host star and the relatively large size of the sub-Neptune sized planets d and e make them well-suited for atmospheric characterization efforts

with facilities like the Hubble Space Telescope and upcoming James Webb Space Telescope. We additionally provide a dynamical mechanism that can explain the observed rare system geometry in the K2-266 system.

7.2 Introduction

Our understanding of exoplanet demographics has rapidly expanded as a direct result of the success of the *Kepler* and K2 missions. With the successful launch of the Transiting Exoplanet Survey Satellite (*TESS*) mission, which is expected to discover thousands of new exoplanetary systems (Ricker et al., 2015), the community is now focused on understanding the mechanisms responsible for the diversity of exoplanet architectures. We now know of over 700 multi-planet systems and a total of more than 3700 confirmed or validated planets to date[1]. From these discoveries, we know that the most commonly known planets with periods P<100 days are smaller than Neptune, a large fraction of which are super-Earths and mini-Neptunes (R_P = 1.5 – 4 $r_\oplus$; Fressin et al., 2013b). With no analogues in our own Solar System, our understanding of these planets is limited.

The large number of multi-planet systems discovered may provide key information to facilitate our understanding of the formation of our own Solar System. From studying multi-planet systems using Kepler data, it has been determined that ∼30% of Sun-like stars have compact and closely aligned architectures, with planetary radii R$_P$¿$r_\oplus$ and orbital periods less than 400 days (Zhu et al., 2018). Planets in systems with *large* mutual inclinations, however, might not all transit. The mutual inclination could be dependent on the number of planets in the system. Specifically, systems with fewer planets have larger mutual inclinations, possibly explaining the observed excess of Kepler single planet systems (Zhu et al., 2018). If unaccounted for, this bias can affect our understanding of planet formation. Fortunately, typical mutual inclinations within transiting systems can be constrained by measuring the ratio of transit durations of adjacent transiting planets. Studies that constrain the underlying multiplicity and distribution of inclinations suggest that transiting multi-planet systems are close to aligned, with mutual inclinations typically less than a few degrees (Fang & Margot, 2012; Figueira et al., 2012; Swift et al., 2013; Fabrycky et al., 2014b; Ballard & Johnson,

[1] `https://exoplanetarchive.ipac.caltech.edu/`

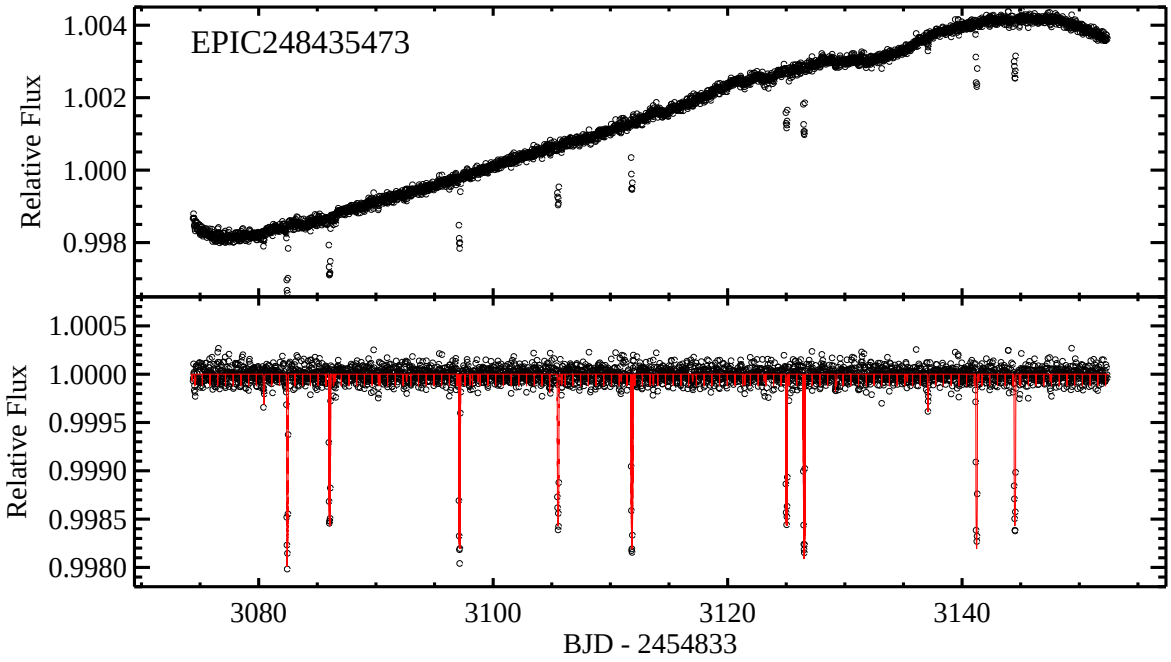

Figure 7.1 K2 Light Curve for K2-266. (Top) The full K2 light curve of K2-266 from Campaign 14, corrected for systematics using the technique described in Vanderburg & Johnson (2014) and Vanderburg et al. (2016c). The observations are plotted in open black circles, and the best fit models are plotted in red. (Bottom) The flattened final *K2* light curve used in the EXOFASTv2 fit.

2016b). However, many studies have shown that the observed population is not well represented by a single-component model (Lissauer et al., 2011b; Ballard & Johnson, 2016b), and this claim is supported by simulations of late-stage planet formation (Hansen & Murray, 2013); the underlying population may consist of some well-aligned systems and some with large mutual inclinations.

Ultra Short-period Planets (USPs), planets that orbit with periods less than a day, may provide insight into the origin of mutually misaligned planetary systems. These are relatively rare objects (0.5% of all stars, Sanchis-Ojeda et al., 2014c), but their close proximity to their host star allows them to transit at a larger range of inclinations relative to our line of sight. This relatively high transit probability makes the USP in a multi-planet system more likely to transit than the longer-period planets in the system (e.g., 55 Cancri, Fischer et al., 2008; Batalha et al., 2011b). It also makes it more likely that *misaligned* systems containing USPs will be observed to host multiple transiting planets, which affords greater opportunities for detailed investigations of the physical

and dynamical properties of the planets. USPs therefore have the potential to help us understand the origin of planetary systems with high mutual inclinations.

Since young stars are larger in radius than their sizes on the main sequence, by factors of 3 – 4, it is unlikely that USPs could form in situ: the host star would have engulfed some of the known USPs based on stellar properties derived from pre-main-sequence evolutionary tracks (Palla & Stahler, 1991; D'Antona & Mazzitelli, 1994). As a result, one possible origin scenario is that USP migration is influenced by gravitational interactions with other planets or stars, increasing the planet's orbital eccentricity. This "High Eccentrictiy Migration" mechanism (HEM), has also been proposed to explain the origin of hot Jupiters (Petrovich et al., 2018, see, e.g.,). These systems initially retain their primordial eccentricities from these interactions (Rasio & Ford, 1996; Wu & Murray, 2003; Fabrycky & Tremaine, 2007b; Nagasawa & Ida, 2011; Wu & Lithwick, 2011), but subsequent tidal interactions should circularize the orbit (e.g., Adams et al. 2006). However, the inclination excited by HEM may remain, resulting in highly misaligned planetary orbits.

Another possible explanation for misaligned planetary systems is that they originate from misaligned disks around young stars. It is known that young stars are surrounded by circumstellar disks of gas and dust that eventually form the planetary systems that are observed today. From high resolution observations of these circumstellar disks, for example using the Atacama Large Millimeter/submillimeter Array (ALMA), we know that these disks are not smooth and uniform. Instead they contain gaps or rings (ALMA Partnership et al., 2015), and display misalignment with their disks and even multiple disks (e.g., see Beta Pic, Heap et al., 2000). Additionally, wide binary systems where each star has its own circumstellar disk have been shown to be mutually misaligned (e.g., Jensen & Akeson, 2014, and references therein).

Using high precision photometric observations from *Spitzer* and K2 there has been a sub-class of young stellar objects identified called "dippers" that display large amplitude (>10%) dimming events that occur on timescales of days (Alencar et al., 2010; Morales-Calderón et al., 2011; Cody et al., 2014; Ansdell et al., 2016b). The observed variability has been attributed to extinction by dust in the inner disk, implying that disks would need to be relatively edge-on, as suggested for the archetypal dipper AA Tau (Bouvier et al., 1999). However, recent high spatial resolution millimeter mapping of AA Tau by ALMA shows a modestly inclined disk at 59.1° (Loomis et al., 2017). Even

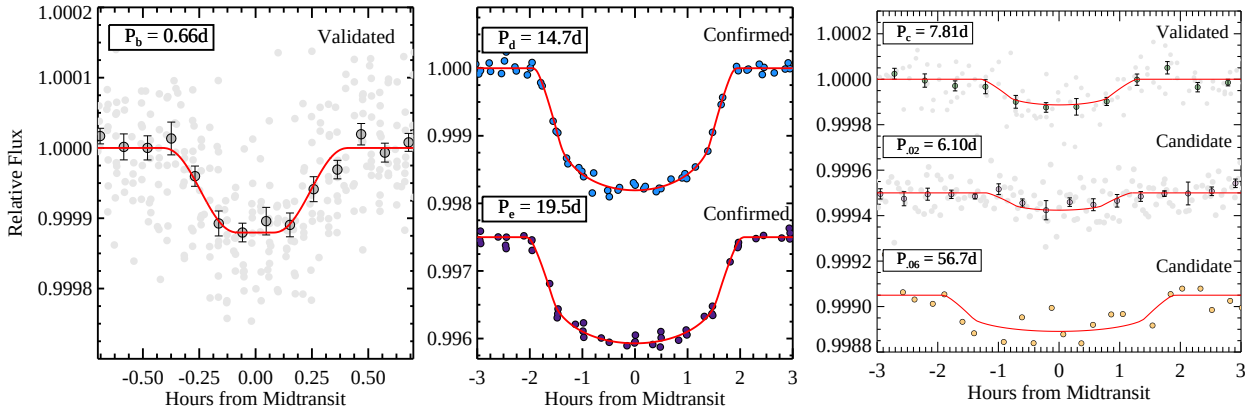

Figure 7.2 Phase-Folded K2 Light Curve for Planets Orbiting K2-266. The phase-folded corrected *K2* light curve for the four validated planets in the system K2-266 b (Left), d (middle), e (middle), and c (right), and the two additional planet candidates .02 (right) and .06 (right). For planets b, d, and candidate c, the full phasefolded LC is shown in light gray and the binned points are shown in color with error bars. The red line corresponds to the final EXOFASTv2 transit model.

more extreme examples exist, such as the dipper J1604-2130, for which ALMA observations reveal the disk to be nearly face-on (Ansdell et al., 2016a). These observations, combined with the photometric dimming events observed suggest that the inner disk is more aligned to our line of sight, and therefore, misaligned relative to the outer disk. Finally, we note that molecular cloud cores that form stars do not have perfectly well-ordered distributions of angular momentum, so that the formation of disks, and later planets, naturally produces some mis-alignment (e.g., see Spalding & Batygin 2014 and references therein).

Multi-planet systems also allow us to determine key physical planet parameters, such as mass and orbital eccentricity, through the detection and analysis of transit timing and duration variations (TTV & TDV, respectively, see Agol et al., 2005b; Holman & Murray, 2005). The slight variations in the timing between consecutive transits are caused by another planet in the system, and result from exchanging energy and angular momentum due to their mutual gravitational interaction. Systems that have planets in or near mean motion resonance (MMR) can produce large amplitude timing variations, allowing the measurement of mass and eccentricity for small planets with longer periods. Efforts to analyze the TTVs for a large sample of planetary systems have provided mass and eccentricity measurements for planets that would not be accessible from other techniques, such

as radial velocities (Steffen et al., 2013b; Holczer et al., 2016; Jontof-Hutter et al., 2016; Hadden & Lithwick, 2017).

In this paper, we present the discovery and characterization of a compact multi-planet system orbiting the late K-star K2-266. Using observations from the K2 mission, we have identified up to six planets orbiting K2-266, with periods of 0.66, 6.1, 7.8, 14.7, 19.5, and 56.7 days. We are able to confidently confirm the planetary nature of two of these planets (P_d = 14.7 days & P_e = 19.5 days), validate two more as planets (P_b = 0.66 days & P_c = 7.8 days), and we classify the other two (weaker) signals as planetary candidates. From a simultaneous global model of all six planets and candidates, we find that the orbit of K2-266 b has an inclination of 75.32 degrees, while the other five planets and candidates have inclinations of 87 degrees to 90 degrees. This significant misalignment of the inner planet has interesting implications for the dynamical history of the system, and may suggest that it had a different evolutionary path than the rest of the planets.

The chapter is organized in the following way: We first discuss our photometric and spectroscopic observations in Section 7.3. Our EXOFASTv2 global model methodology and results are then presented in §7.4.

7.3 Observations, Archival Data, and Validation

7.3.1 K2 Photometry

Since the failure of the second reaction wheel, the *Kepler* spacecraft has been re-purposed to observe a set of fields along the ecliptic. Each K2 campaign lasts ∼80 days (Howell et al., 2014b), achieving similar precision to the original *Kepler* mission (Vanderburg et al., 2016c). K2-266 was observed during K2 Campaign 14 from UT 2017 Jun 02 until UT 2017 Aug 19, obtaining 3504 observations on a 30 minute cadence (see Figure 7.1). Following the strategy described in Vanderburg & Johnson (2014) and Vanderburg et al. (2016c), the light curves were extracted from the *Kepler*-pipeline calibrated target pixel files from the Mikulski Archive for Space Telescopes[2], corrected for the K2 spacecraft-motion-induced systematics, and searched for transiting planet candidates. From our search of K2-266, we identified three super-Earth/sub-Neptune sized transiting

[2]MAST; `https://archive.stsci.edu/`

Other identifiers		EPIC 248435473 2MASS J10314450+0056152 K2-266	
Parameter	Description	Value	Source
α_{J2000}	Right Ascension (RA)	10:31:44.506	1
δ_{J2000}	Declination (Dec)	+00:56:15.27	1
Bdotfill	APASS Johnson B mag.	13.001 ± 0.02	2
V	APASS Johnson V mag.	11.808 ± 0.02	2
G	Gaia G mag.	11.3527±0.0009	7,8
g'	APASS Sloan g' mag.	12.407 ± 0.02	2
r'	APASS Sloan r' mag.	11.311 ± 0.02	2
i'	APASS Sloan i' mag.	10.927 ± 0.04	2
J	2MASS J mag.	9.611 ± 0.05	3, 4
H	2MASS H mag.	9.041 ± 0.03	3, 4
K_S	2MASS K_S mag.	8.897 ± 0.02	3, 4
WISE1	*WISE1* mag.	8.805 ± 0.022	5
WISE2	*WISE2* mag.	8.897 ± 0.02	5
WISE3	*WISE3* mag.	8.787 ± 0.02	5
WISE4	*WISE4* mag.	8.789 ±0.437	5
μ_α	Gaia DR2 proper motion in RA (mas yr^{-1})	56.871 ± 0.151	7, 8
μ_δ	Gaia DR2 proper motion in DEC (mas yr^{-1})	-68.828 ± 0.242	7,8
π	Gaia Parallax (mas)	12.87 ± 0.06	7,8
RV	Systemic radial velocity (km s^{-1})	10.848 ± 0.066	§7.3.2

Table 7.1 K2-266 Magnitudes and Kinematics. The uncertainties of the photometry have a systematic error floor applied. Even still, the global fit requires a significant scaling of the uncertainties quoted here to be consistent with our model, suggesting they are still significantly underestimated for one or more of the broad band magnitudes. References are: [1]Cutri et al. (2003),[2]Henden et al. (2016),[3]Cutri et al. (2003), [4]Skrutskie et al. (2006), [5]Cutri & et al. (2014), [6]Zacharias et al. (2017),[7]Gaia Collaboration et al. (2016a), [8]Gaia Collaboration et al. (2018b)

exoplanet candidates with periods of 0.66, 14.7, and 19.5 days with signal-to-noise (S/N) values of 13.0, 114.6, and 111.5. In addition, some of us (MHK, MO, HMS, IT) performed a visual inspection of the light curve using the LCTOOLS[3] software (Kipping et al., 2015). From this visual inspection, we identified two additional Earth sized exoplanet candidates with periods of 6.1 and 7.8 days with S/N values of 8.3 and 10.6. An additional visual inspection of the K2 light curve led to the identification of a sixth planet candidate at 56.7 days with a S/N value 6.6. The phase-folded light curves for each planet candidate is shown in Figure 7.2. We note that the two transits of this candidate overlap with other candidates in the system. The K2 light curve was reprocessed where all six planets were simultaneously fit along with the stellar variability and known K2 systematics. The corresponding light curve was flattened by dividing out the best-fit stellar variability using a spline fit with breakpoints every 0.75 days. The final light curve for K2-266, shown in Figure 7.1, has a 30 minute cadence noise level of 70 ppm, and a 6 hour photometric precision of 19 ppm.

7.3.2 TRES Spectroscopy

Using the Tillinghast Reflector Echelle Spectrograph (TRES; Fűrész, 2008)[4] on the 1.5 m Tillinghast Reflector at the Fred L. Whipple Observatory (FLWO) on Mt. Hopkins, AZ we obtained 8 observations of K2-266 between UT 2017 Nov 23 and UT 2018 Apr 10. TRES has a resolving power of $\lambda/\Delta\lambda = 44000$, and an instrumental radial velocity (RV) stability of 10–15 $\mathrm{m\,s^{-1}}$. The spectra were optimally extracted, wavelength calibrated, and cross-correlated to derived relative RVs following the techniques described in (Buchhave et al., 2010). We cross-correlate each spectrum, order by order, against the strongest observed spectrum, and fit the peak of the cross-correlation function summed across all orders to derive the relative RVs. Uncertainties are determined from the scatter between orders for each spectrum. We use RV standard stars to track the instrumental zero point over time, and apply these zero point shifts (typically < 15 $\mathrm{m\,s^{-1}}$) to the relative RVs and propagate uncertainties in the zero point shifts to the RVs. This is why the strongest spectrum, correlated against itself, does not have an RV of 0 $\mathrm{m\,s^{-1}}$. The final relative RVs are given in Table 7.2. Using the RV standards to set the absolute zero point of the TRES system, we also determine

[3] `https://sites.google.com/a/lctools.net/lctools/home`

[4] `http://www.sao.arizona.edu/html/FLWO/60/TRES/GABORthesis.pdf`

BJD_{TDB}	**RV (m s^{-1})**	σ_{RV} **(m s^{-1})**	**Target**
2458081.028322	-30.1	17.7	K2-266
2458090.980928	-2.5	32.0	K2-266
2458106.965261	-3.2	43.6	K2-266
2458107.923621	-55.5	28.2	K2-266
2458211.644609	-26.3	21.2	K2-266
2458212.644636	-36.5	25.6	K2-266
2458213.663584	-23.9	33.3	K2-266
2458218.808648	-30.0	32.5	K2-266

Table 7.2 Relative Radial Velocities for K2-266.

the RV of K2-266 on the IAU standard system to be 10.848 ± 0.066 km s^{-1}, where the uncertainty is dominated by the uncertainty in the shift from relative to absolute RV.

7.3.3 Palomar TripleSpec Observations

We refined the characterization of K2-266 by acquiring near-infrared spectra using TripleSpec on the 200" Palomar Hale telescope on 1 December 2017. TripleSpec has a fixed slit of 1" x 30" slit, enabling simultaneous observations across J, H, and K bands (1.0 - 2.4 microns) at a spectral resolution of 2500-2700 (Herter et al., 2008). Following Muirhead et al. (2014), we obtained our observations using a 4-position ABCD not pattern to reduce the influence of bad pixels on our resulting spectra. As in Dressing et al. (2017), we reduced our data using a version of the publicly available `Spextool` pipeline (Cushing et al. 2004) that was modified for use with TripleSpec data (available upon request from M. Cushing). We removed telluric contamination by observing an A0V star at a similar airmass and processing both our observations for both the A0V star and K2-266 with the `xtellcor` telluric correction package (Vacca et al., 2003).

After reducing the spectra, we estimated stellar properties by applying empirical relations developed by Newton et al. (2014, 2015) and Mann et al. (2013b,a). Specifically, we estimated the stellar effective temperature and radius by measuring the widths of Al and Mg features using the publicly available, IDL-based `tellrv` and `nirew` packages (Newton et al., 2014, 2015). We then employed the stellar effective temperature-mass relation developed by Mann et al. (2013a) to infer the stellar mass from the resulting stellar effective temperature estimate. We also estimated the

stellar metallicity ([M/H] and [Fe/H]) using the relations developed by Mann et al. (2013b). For more details about our TripleSpec analysis methods, see Dressing et al. (2017), Dressing et al., (in prep).

The resulting stellar properties were $T_{\rm eff} = 4192 \pm 77$ K, $M_\star = 0.67^{+0.08}_{-0.07} M_\odot$, and $R_\star = 0.63 \pm 0.03$. This values for the stellar mass is consistent with those estimated from our EXOFASTv2 analysis (see Table 3). However, the radius is $\sim 3\sigma$ different from the EXOFASTv2 fit using the broadband photometry and Gaia DR2 parallax.

7.3.4 Archival "Patient" Imaging

To check for nearby stars (either physically associated companions or coincidental alignments) that may influence our results, we examined archival observations from National Geographic Society Palomar Observatory Sky Survey (NGS POSS) from 1952. The proper motion of K2-266 is $\mu_\alpha =$ 56.9 mas and $\mu_\delta =$ -68.8 mas, and has moved $\sim$6 in the 66 years since the original POSS observations were taken. The present-day position of K2-266 is located right at the edge of the saturated point-spread-function of K2-266 in the original POSS plates. While the present-day position of K2-266 is not completely resolved in the POSS image, if there was a bright-enough background star at the present-day position of K2-266, we would expect to see some elongation of the POSS point spread function at that position. We see no evidence for such an elongation in POSS plates with either a red-sensitive or blue-sensitive emulsion. We estimate that we can rule out background stars at the present-day position of K2-266 down to a magnitude of about 19 in blue, and a magnitude of about 18 in the red. Figure 7.3 shows our archival imaging overlaid with the K2 photometric aperture used to extract the light curves.

We used modern imaging from the Pan-STARRS data release to search for faint companions at distances greater than a few arcseconds from K2-266 (Flewelling et al., 2016). In the Pan-STARRS images, we identified one star located inside our best photometric aperture about 9 magnitudes fainter than K2-266. In principle, if this star were a fully eclipsing binary (with 100% deep eclipses[5]), it could contribute a transit-like signal to the light curve of K2-266 with a depth of

[5]While the greatest eclipse depth possible from two main-sequence eclipsing binaries is about 50% (caused by an equal-brightness binary), we also consider the worst-case scenario of 100% deep eclipses caused by, for example, a bright, hot white dwarf being eclipsed by a cool M-dwarf or brown dwarf (e.g. Rappaport et al.,

at most about 250 ppm. This is shallower than the transits of the two sub-Neptunes, but could in principle contribute the transits of the other four candidates. We therefore extracted the K2 light curve from a smaller aperture (shown in Figure 7.3 as a navy blue outline overlaid on the Pan-STARRS image of K2-266), which excludes the companion star detected in Pan-STARRS imaging (see Rodriguez et al. 2018c for more discussion of this companion). We find in the noisier light curve extracted from the smaller aperture, the transits of the ultra-short-period and 7.8d planets are convincingly detected, but the transits of the two weaker candidates (at 6.1 and 56.7 days) do not convincingly appear (due to the increased noise in the light curve). We therefore cannot rule out a blended background eclipsing binary origin for at least one of those candidates.

7.3.5 Keck/NIRC2 AO Imaging

We obtained high resolution images of K2-266 using the Near Infrared Camera 2 (NIRC2) on the W. M. Keck Observatory. Two observations of each target were taken on UT 2017 December 28, one in the Br-γ filter and the other in the J-band (see Figure 7.3). NIRC2 has 9.942 mas pix^{-1} pixel scale and 1024×1024 pixel array. The lower left quadrant of the array suffers from higher noise levels. To exclude this part of the detector, a 3-point dither pattern was used. The final image shown in Figure 7.3 is created by shifting and co-adding the observations, after flat-fielding and sky subtraction. We see no other star in the 10 field-of-view for K2-266. Our sensitivity to nearby companions is determined by injecting a simulated source with a S/N of 5. The final 5σ sensitivity curves as a function of spatial separation and the corresponding images for K2-266 in both Br-γ and J filters are shown in Figure 7.3.

7.3.6 Statistical Validation

We attempted to statistically validate each of the six candidates in K2-266, a process in which the probability of planethood is estimated. If the probability is above some threshold value the candidate is upgraded to validated planet. Our method of validation followed the approach taken by Mayo et al. (2018b). In detail, we made use of `vespa` (Morton, 2015), a Python package based on the work of Morton (2012). `vespa` calculates the false positive probability (FPP) of an exoplanet

2017).

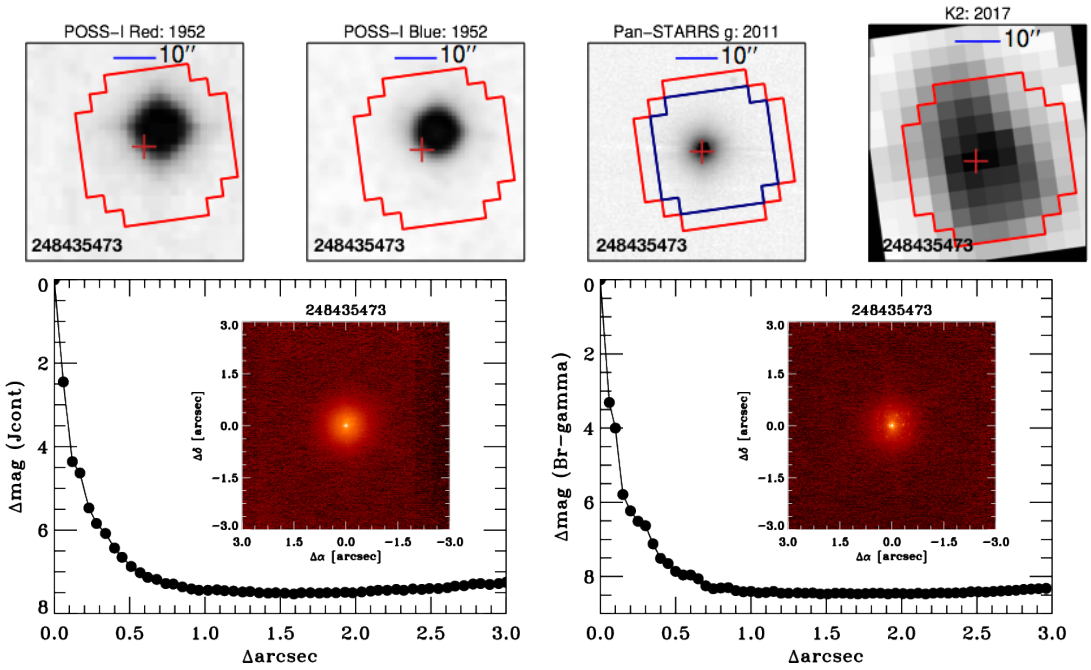

Figure 7.3 Archival Imaging for K2-266. Archival imaging from the National Geographic Society Palomar Observatory Sky Survey (NGS POSS) of K2-266 taken with a (1st panel) red and (2nd panel) blue emulsion in 1952. (3rd panel) Archival imaging from the Pan-STARRS survey of K2-266 taken in 2011. (Right panel) Summed image of K2-266 from K2 observations. The aperture selection is described in Vanderburg et al. (2016c).

candidate by first simulating a population of synthetic stellar systems, each of which creates a transit signal due to a planet or eclipsing binary scenario. Then, `vespa` calculates the FPP by determining which synthetic systems are consistent with the input observations and calculating the fraction of those systems that correspond to an eclipsing binary scenario.

This determination is made based on inputs such as the sky position of the target, the transit signal, various stellar parameters, and contrast curves from any available high-resolution imaging. (A contrast curve relates the angular separation between the target star and an undetected companion to the maximum brightness for the putative companion.) In the case of K2-266, we provided as input to `vespa` the RA and Dec, the phase-folded light curve of the candidate in question (with transits from other candidates removed), J, H, and K_S bandpass stellar magnitudes from 2MASS (Cutri et al., 2003; Skrutskie et al., 2006) and the Kepler magnitude, stellar parameters (6199, 4.18, and) calculated in Section 7.4, and contrast curves from two AO images.

After we subjected each of our six candidates to validation, we made two additional adjustments

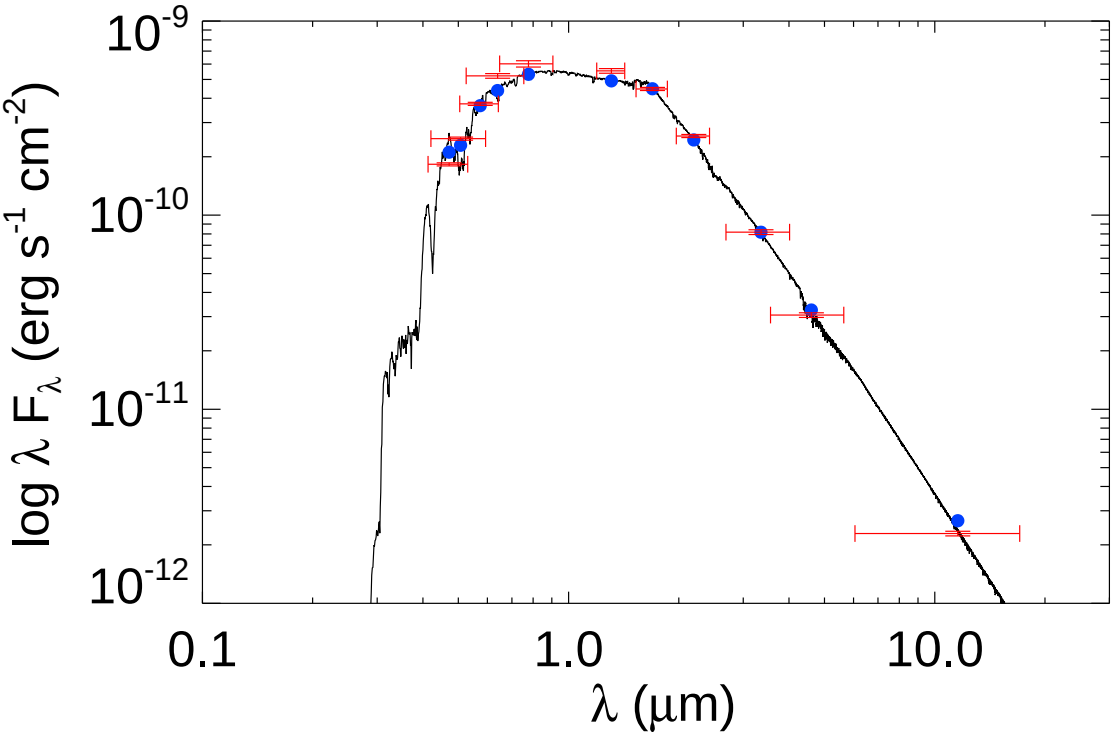

Figure 7.4 The SED Fit for K2-266 from EXOFASTv2. The blue points are the predicted integrated fluxes and the red points are the observed values at the corresponding passbands. The width of the bandpasses are the horizontal red error bars and the vertical errors represent the 1σ uncertainties. The final model fit is shown by the solid line.

to their FPP estimates. First, there are eight spectra and corresponding RV measurements collected with TRES from 2017 Nov 23 to 2018 Apr 10. The RV measurements derived from the TRES spectra did not indicate any large variations indicative of a simple eclipsing binary, so we were able to eliminate that scenario. (Note that this is different from a background eclipsing binary or hierarchical eclipsing binary scenario, which we also consider.) By eliminating the possibility of a simple eclipsing binary, the probability of the planet scenario (and each false positive scenario) was increased so that the total probability remained at unity.

Second, according to Lissauer et al. (2012b), the likelihood of one or more false positives decreases significantly when there is more than one candidate in a system. In the case of a system with more than 2 candidates, they estimate that a multiplicity boost factor of 50 is appropriate. As a result, we decreased the FPP for each candidate by a factor of 50.

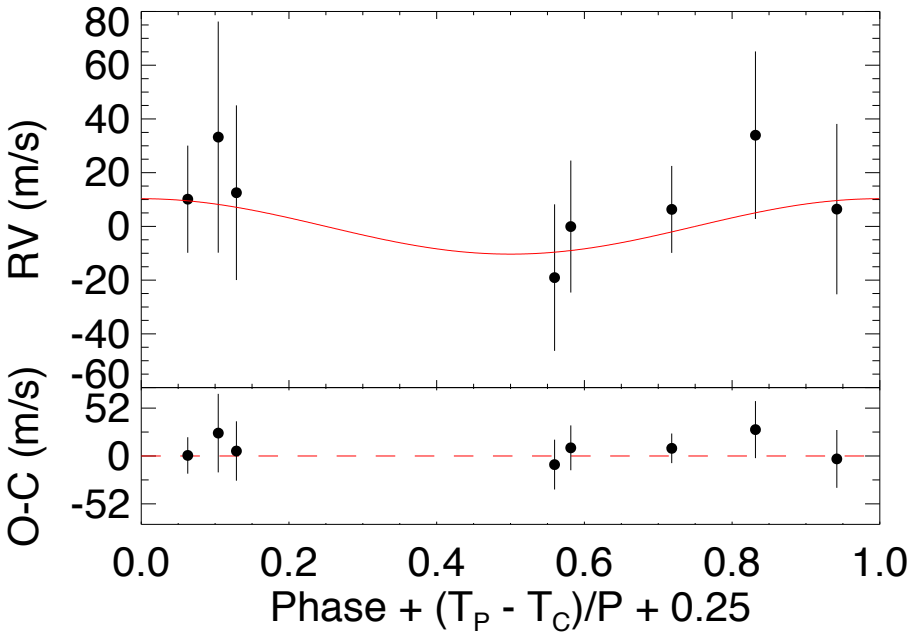

Figure 7.5 TRES Radial Velocities for K2-266. The TRES radial velocity measurements phase-folded to the best-fit ephemeris of K2-266 b. The primary transit occurs at a phase of 0.25, where T_P is the time of periastron, T_C is the time of transit, and P period of planet b.

After calculating FPP values for our six candidates, reducing the eclipsing binary scenario to 0 probability, and including a multiplicity boost of 50, we found final FPP values of $3.02e-05$, $7.34e-06$, $9.40e-06$, $6.80e-11$, $1.16e-12$, and $4.90e-06$ for candidates K2-266.01, .02, .03, .04, .05, and .06. These values would each be low enough to easily validate all six candidates (e.g. Mayo et al. (2018b) used a FPP threshold value of 1e-4). However, given the inability to rule out the possibility that the faint background star we identified in Section 7.3.4 is an eclipsing binary, we were only able to conclusively validate candidates K2-266.01, .03, .04, and .05, naming them K2-266 b, c, d, and e, respectively. We also refrain from validating candidates .02 and .06 because they have the lowest signal-to-noise ratios that do not pass our threshold (8.3 and 6.6, respectively). Validating such low S/N candidates is challenging because it is difficult to prove that the weakest signals detected in *Kepler* or K2 data are astrophysical, and not the result of residual instrumental systematics or artifacts (Mullally et al., 2018).

7.4 EXOFASTv2 Global Fit for K2-266

Using the global exoplanet fitting suite, EXOFASTv2 (Eastman, 2017), we perform a simultaneous fit of the existing observations to determine the final system parameters for K2-266. Based largely on the original EXOFAST (Eastman et al., 2013b), EXOFASTv2 provides the unique flexibility to simultaneously fit the spectral energy distribution (SED) and RV observations from multiple instruments, in combination with fitting the time series photometry for every planet in the system. Using EXOFASTv2, we simultaneously fit the flattened K2 light curve (accounting for the 30 minute cadence smearing, see Figure 7.1 and 7.2), the SED (see Table 7.1), and the radial velocity observations from TRES (see Figure 7.5). To characterize the host star radius within the fit, we include the the broad band photometry and Gaia DR2 parallax (See Table 7.1) (Gaia Collaboration et al., 2016a, 2018b). We add 0.082 mas to the DR2 parallax, as determined by Stassun & Torres (2018b) and impose a systematic error floor on the uncertainty of 0.1 mas since all systematics and uncertainties should be below this (Gaia Collaboration et al., 2018b). To constrain the mass of the star, we used a Gaussian prior of $0.677 \pm 0.034 M_{\odot}$ from Mann et al. (2015), but with the uncertainties inflated to 5%. In a separate global fit (not reported), we used the MIST stellar isochrones (Dotter, 2016; Choi et al., 2016; Paxton et al., 2011, 2013, 2015) instead of the Gaussian prior from Mann et al. (2015) as the primary constraint of the stellar mass and arrived at $0.748^{+0.047}_{-0.045} M_{\odot}$, a 1.3σ difference. We favor the Mann et al. (2015) relations due to their empirical approach and the known problems with all model isochrones at low stellar masses.

Additionally, we enforce an upper limit in the V-band extinction (A_V) from the Schlegel et al. (1998b) dust maps of 0.0548 at the position of K2-266. The final SED fit is shown in Figure 7.4, the phase-folded RVs from TRES to planet b's period is shown in Figure 7.5, and the best fit transit models are shown in Figures 7.1 and 7.2. Given the near resonance orbit of K2-266 d and e, which would have the largest transit timing variations (TTVs), we fit for the TTVs of these two planets while fitting a linear ephemeris for planets/candidates b, .02, c, and .06. The final determined stellar and planetary parameters from our global fit are shown in Tables 7.3 and 7.4.

The grazing geometry of planet b means the upper limit of the planet radius is unconstrained by the light curve. However, during the global fit, we simultaneously model the radial velocities,

Stellar Parameters		**K2-266**
M_*	Mass ($M_\odot$)	0.686 ± 0.033
R_*	Radius ($R_\odot$)	$0.703^{+0.024}_{-0.022}$
L_*	Luminosity ($L_\odot$)	0.1502 ± 0.0057
ρ_*	Density (cgs)	$2.79^{+0.29}_{-0.30}$
$\log g$	Surface gravity (cgs)	$4.581^{+0.032}_{-0.037}$
$T_{\rm eff}$	Effective Temperature (K)	4285^{+49}_{-57}
[Fe/H]	Metallicity	$-0.12^{+0.40}_{-0.42}$
A_v	V-band extinction	$0.029^{+0.018}_{-0.019}$
σ_{SED}	SED photometry error scaling	$5.0^{+1.6}_{-1.1}$
$\pi^\dagger$	Parallax (mas)	12.960 ± 0.100
d	Distance (pc)	$77.16^{+0.60}_{-0.59}$

Table 7.3 Median values and 68% confidence intervals for the stellar parameters of the K2-266 from EXOFASTv2. † The MIST Isochrones were not used in the EXOFASTv2 fit for K2-266.

which provide a robust upper limit on its mass. This upper limit is translated to a radius upper limit during the global fit using EXOFASTv2's integrated Chen & Kipping (2017) exoplanet mass-radius relation, which excludes Jupiter-radius solutions (and even higher inclinations). Because the radial velocities are not precise enough for a measurement, the prior, which is uniform in $log(K)$, can have a significant impact on the posteriors for the RV-semi amplitude, mass, radius, and inclination of planet b and tends to favor smaller planets and smaller inclinations (in line with our prior expectation that such planets are intrinsically more numerous).

Because the Chen & Kipping (2017) relations only use a sample of planets with robustly detected masses and radii, and we can typically measure robust radii for smaller planets than we can measure the corresponding masses, there is likely a selection effect in the Chen & Kipping (2017) relations that bias it toward larger masses at low signal to noise. As a consequence, for a given mass, we expect to over-estimate the radius. Our radius upper limit would likely be somewhat smaller if we used a relation that accounted for non-detections within our fit.

The Weiss & Marcy (2014c) exoplanet mass-radius relations are an often used alternative which attempts to account for the bias from non-detections. However, they only apply to rocky planets ($R_p < 4r_\oplus$), and so could not be used to exclude large planets, whereas the Chen & Kipping (2017) relations are defined and continuous from rocky planets to stars.

Planetary Parameters:		b	K2-266.02	c	d	e	K2-266.06
P	Period (days)	0.658524 ± 0.000017	$6.1002^{+0.0015}_{-0.0017}$	$7.8140^{+0.0019}_{-0.0016}$	$14.69700^{+0.00034}_{-0.00035}$	19.4820 ± 0.0012	$56.682^{+0.019}_{-0.018}$
R_P	Radius ($R_\oplus$)	$3.3^{+1.8}_{-1.3}$	$0.646^{+0.099}_{-0.091}$	$0.705^{+0.096}_{-0.085}$	$2.93^{+0.14}_{-0.12}$	$2.73^{+0.14}_{-0.11}$	$0.90^{+0.14}_{-0.12}$
T_C	Time of conjunction (BJD_{TDB})	$2457945.7235^{+0.0032}_{-0.0030}$	$2457913.413^{+0.013}_{-0.011}$	$2457907.5812^{+0.0099}_{-0.012}$	2457944.8393 ± 0.0012	2457938.5410 ± 0.0013	$2457913.436^{+0.014}_{-0.013}$
T_0	Optimal conjunction Time (BJD_{TDB})	$2457949.6747^{+0.0032}_{-0.0030}$	$2457943.9143^{+0.0066}_{-0.0064}$	2457946.6510 ± 0.0064	2457944.8393 ± 0.0012	2457938.5410 ± 0.0013	$2457913.436^{+0.014}_{-0.013}$
a	Semi-major axis (AU)	$0.01306^{+0.00020}_{-0.00021}$	$0.05761^{+0.00090}_{-0.00093}$	0.0679 ± 0.0011	$0.1035^{+0.0016}_{-0.0017}$	$0.1249^{+0.0019}_{-0.0020}$	$0.2546^{+0.0040}_{-0.0041}$
i	Inclination (Degrees)	$75.32^{+0.62}_{-0.70}$	$87.84^{+0.84}_{-0.46}$	$88.28^{+0.81}_{-0.41}$	$89.46^{+0.32}_{-0.25}$	$89.45^{+0.25}_{-0.18}$	$89.40^{+0.26}_{-0.14}$
e	Eccentricity	–	$0.051^{+0.051}_{-0.036}$	$0.042^{+0.043}_{-0.030}$	$0.047^{+0.043}_{-0.032}$	$0.043^{+0.036}_{-0.030}$	$0.31^{+0.11}_{-0.17}$
ω_*	Argument of Periastron (Degrees)	–	88^{+60}_{-62}	87 ± 61	87 ± 62	89^{+57}_{-58}	83^{+57}_{-59}
M_P	Mass ($M_\oplus$)	$11.3^{+11}_{-6.5}$	$0.209^{+0.15}_{-0.089}$	$0.29^{+0.17}_{-0.11}$	$9.4^{+2.9}_{-2.0}$	$8.3^{+2.7}_{-1.8}$	$0.70^{+0.87}_{-0.30}$
K	RV semi-amplitude (m/s)	$10.3^{+10.}_{-5.9}$	$0.094^{+0.067}_{-0.040}$	$0.119^{+0.073}_{-0.046}$	$3.17^{+0.99}_{-0.69}$	$2.53^{+0.84}_{-0.56}$	$0.158^{+0.20}_{-0.068}$
δ	Transit depth (fraction)	$0.0018^{+0.0025}_{-0.0012}$	$0.000071^{+0.000022}_{-0.000018}$	$0.000085^{+0.000023}_{-0.000019}$	$0.001465^{+0.000055}_{-0.000043}$	$0.001270^{+0.000048}_{-0.000043}$	$0.000136^{+0.000046}_{-0.000033}$
T_{14}	Total transit duration (days)	$0.01389^{+0.0012}_{-0.00085}$	$0.083^{+0.014}_{-0.012}$	$0.094^{+0.016}_{-0.014}$	$0.1420^{+0.0014}_{-0.0015}$	$0.1527^{+0.0014}_{-0.0015}$	$0.143^{+0.024}_{-0.023}$
b	Transit Impact parameter	$1.011^{+0.027}_{-0.024}$	$0.64^{+0.13}_{-0.25}$	$0.60^{+0.14}_{-0.28}$	$0.29^{+0.12}_{-0.17}$	$0.36^{+0.10}_{-0.16}$	$0.64^{+0.17}_{-0.33}$
ρ_P	Density (cgs)	$1.77^{+1.9}_{-0.88}$	$4.27^{+0.79}_{-0.66}$	$4.51^{+0.81}_{-0.67}$	$2.03^{+0.64}_{-0.43}$	$2.21^{+0.70}_{-0.47}$	$5.27^{+1.5}_{-0.87}$
$loggg_P$	Surface gravity	$3.00^{+0.14}_{-0.13}$	2.69 ± 0.12	2.75 ± 0.11	$3.026^{+0.12}_{-0.100}$	$3.03^{+0.12}_{-0.10}$	$2.93^{+0.18}_{-0.12}$
$ecos\omega_*$		–	$-0.000^{+0.044}_{-0.045}$	0.000 ± 0.037	-0.000 ± 0.043	$-0.000^{+0.036}_{-0.035}$	0.00 ± 0.24
$esin\omega_*$		–	$0.026^{+0.046}_{-0.022}$	$0.022^{+0.038}_{-0.018}$	$0.025^{+0.035}_{-0.020}$	$0.025^{+0.034}_{-0.020}$	$0.19^{+0.16}_{-0.15}$
$M_P \sin i$	Minimum mass (Earth masses)	$10.9^{+11}_{-6.3}$	$0.208^{+0.15}_{-0.089}$	$0.29^{+0.17}_{-0.11}$	$9.4^{+2.9}_{-2.0}$	$8.3^{+2.7}_{-1.8}$	$0.70^{+0.87}_{-0.30}$

Table 7.4 Median values and 68% confidence intervals for planetary parameters of K2-266 from EXOFASTv2. Selected outputs from the EXOFASTv2 presented here; for complete table with all parameters, see Rodriguez et al. (2018c).

Planet	Period (days)	$R_P(R_\oplus)$	S/N[a]	Reference	Discovery
GJ 1214 b	1.58	2.85	1.00	Charbonneau et al. (2009)	MEarth
55 Cnc e	0.74	1.91	0.41	Dawson & Fabrycky (2010)	RVs
HD 97658 b	9.49	2.35	0.27	Dragomir et al. (2013)	RVs
TRAPPIST-1 f	9.21	1.04	0.24	Gillon et al. (2017)	*Spitzer*
K2-136 c	17.31	2.91	0.19	Ciardi et al. (2018); Livingston et al. (2018); Mann et al. (2018)	K2
GJ 9827 b	1.21	1.75	0.18	Niraula et al. (2017b); Rodriguez et al. (2018b)	K2
K2-167 b	9.98	2.82	0.16	Mayo et al. (2018b)	K2
K2-266 e	**14.70**	**2.93**	**0.15**	**This Work**	**K2**
GJ 9827 d	6.20	2.10	0.15	Niraula et al. (2017b); Rodriguez et al. (2018b)	K2
HIP 41378 b	15.57	2.90	0.14	Vanderburg et al. (2016d)	K2
HD 3167 b	0.96	1.70	0.14	Vanderburg et al. (2016f); Christiansen et al. (2017a)	K2
K2-233 d	24.37	2.65	0.13	David et al. (2018)	K2
K2-266 f	**19.48**	**2.73**	**0.12**	**This Work**	**K2**
K2-28 b	2.26	2.32	0.12	Hirano et al. (2016)	K2
K2-199 c	7.37	2.84	0.12	Mayo et al. (2018b)	K2
K2-155 c	13.85	2.60	0.11	Diez Alonso et al. (2018); Hirano et al. (2018)	K2
Kepler-410 A b	17.83	2.84	0.10	Van Eylen et al. (2014)	*Kepler*
HD 106315 b	9.55	2.40	0.10	Rodriguez et al. (2017c); Crossfield et al. (2017)	K2

Table 7.5 The Best Confirmed or Validated Planets for Transmission Spectroscopy with $R_P < 3\ R_\oplus$. [a]The predicted signal-to-noise ratios relative to GJ 1214 b. All values used in determining the signal-to-noise were obtained from the NASA Exoplanet Archive (Akeson et al., 2013c). If a system did not have a reported mass on NASA Exoplanet Archive or it was not a 2σ result, we used the Weiss & Marcy (2014c) Mass-Radius relationship to estimate the planet's mass. [b]Our calculation for the S/N of 55 Cnc e assumes a H/He envelope since it falls just above the pure rock line determined by Zeng et al. (2016b). However, 55 Cnc e is in a ultra short period orbit, making it unlikely that it would hold onto a thick H/He envelope. We do not include HIP 41378 b due to its grazing configuration.

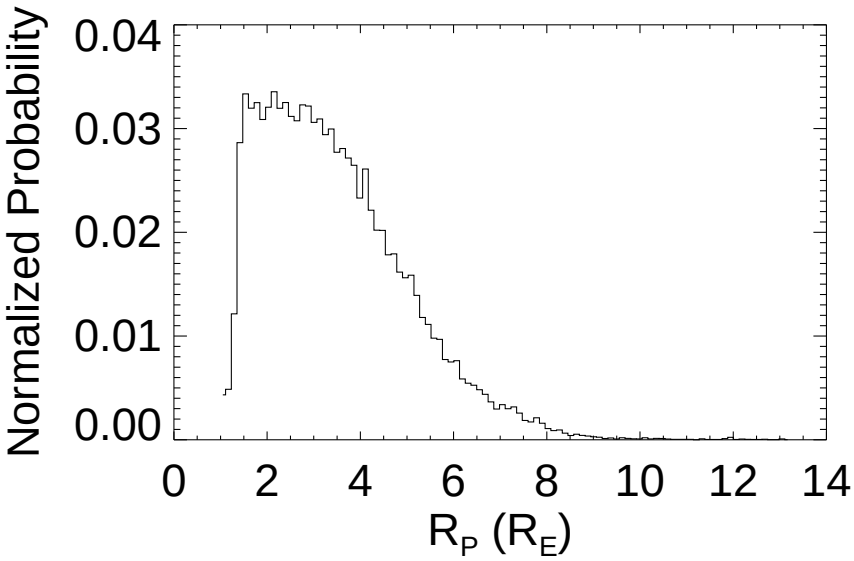

Figure 7.6 The Probability Distribution Function for the Radius of K2-266 b. It shows the depth of the transit sets a hard lower limit of $\sim 1 r_{\oplus}$. Due to the grazing geometry, the upper envelope is not constrained by the light curve, and instead set by the upper limit on the mass through an RV non-detection and the Chen & Kipping (2017) exoplanet mass-radius relation.

7.5 Dynamics of K2-266

Given its multiplicity and mutually-transiting nature, the six-planet system orbiting K2-266 can be classified as one of the Systems of Tightly Packed Inner Planets (STIPs) common in the *Kepler* data (Lissauer et al., 2011b; Van Laerhoven & Greenberg, 2012; Swift et al., 2013). However, this system is unique due to the innermost planetary orbit displaying a remarkable 75 degree inclination and a grazing transit. Members of the *Kepler* multi-planet systems have smaller mutual inclinations, typically within a few degrees of each other (Fang & Margot, 2012; Figueira et al., 2012; Fabrycky et al., 2014b). Moreover, these systems do not tend to excite high mutual inclinations without some external factor (Becker & Adams, 2016; Mustill et al., 2017; Hansen, 2017; Becker & Adams, 2017; Jontof-Hutter et al., 2017a; Denham et al., 2018). In this section, we discuss the information gained through combining the observed light curve with dynamical analysis, and attempt to constrain the current dynamical state of the system.

Wavelength Parameters:		Kepler		
u_1	linear limb-darkening coeff	$0.630^{+0.064}_{-0.10}$		
u_2	quadratic limb-darkening coeff	$0.107^{+0.082}_{-0.054}$		
Telescope Parameters:		TRES		
$\gamma_{\rm rel}$	Relative RV Offset (m/s)	$-29.9^{+7.4}_{-8.6}$		
σ_J	RV Jitter (m/s)	$0.00^{+19}_{-0.00}$		
σ_J^2	RV Jitter Variance	-130^{+480}_{-140}		
Transit Parameters:				
Planet	Transit Date	Added Variance $\sigma^2 \times 10^{-10}$	Transit Mid Time $\rm BJD_{TDB}$	Baseline flux F_0
b,c,d,g	Full K2 LC	$7.6^{+2.9}_{-2.7}$	N/A	1.0000035 ± 0.0000030
e	K2 UT 2017-06-10	19^{+26}_{-18}	$2457915.44761 \pm 0.00106$	0.999981 ± 0.000016
f	K2 UT 2017-06-14	10^{+21}_{-15}	$2457919.05628 \pm 0.00088$	1.000012 ± 0.000014
e	K2 UT 2017-06-25	-3^{+15}_{-11}	$2457930.13813 \pm 0.00101$	$1.000002^{+0.000013}_{-0.000012}$
f	K2 UT 2017-07-04	25^{+26}_{-18}	$2457938.54211 \pm 0.00108$	$0.999986^{+0.000016}_{-0.000017}$
e	K2 UT 2017-07-10	16^{+25}_{-17}	$2457944.83597 \pm 0.00137$	$0.999971^{+0.000016}_{-0.000015}$
f	K2 UT 2017-07-23	54^{+41}_{-27}	$2457958.03343 \pm 0.00112$	$0.999986^{+0.000020}_{-0.000021}$
e	K2 UT 2017-07-25	13^{+21}_{-14}	$2457959.52590 \pm 0.00090$	$1.000000^{+0.000014}_{-0.000015}$
e	K2 UT 2017-08-08	30^{+26}_{-19}	$2457974.23919 \pm 0.00114$	1.000009 ± 0.000017
f	K2 UT 2017-08-12	5^{+23}_{-15}	$2457977.50614 \pm 0.00120$	1.000007 ± 0.000015

Table 7.6 Median values and 68% confidence intervals for the additional parameters of HIP 41378 from EXOFASTv2.

7.5.1 Transit Timing Variations

The transit timing measurements for planets d and e listed in Table 7.5 can be used to derive dynamical constraints on their masses and orbits. In this section, we invert the planet pairs' TTVs to infer their masses and, in combination with the planet radii derive from out light-curve fitting, their densities. We model the planets' TTVs using the TTVFast code developed by Deck et al. (2014b) and use the emcee package's (Foreman-Mackey et al., 2013b) ensemble sampler, based on the algorithm of Goodman & Weare (2010), to sample the posterior distribution of the planetary masses and orbital elements. We model only the dynamical interactions of planets d and e, and ignore any perturbations from the other (potential) members of the system.[6] We assume planets d and e orbit in the same plane since small mutual inclinations have negligible influence on TTVs. We approximate the mid-transit uncertainties to be Gaussian-distributed about the median transit time determined by EXOFASTv2, with variances set to the larger of the two asymmetric error bars in Table 7.6. Our likelihood function is then computed based on the standard chi-squared

[6]The variations induced by the additional planets in the system are expected to be negligible. For example, assuming a 1 $M_\oplus$ planet c and circular orbits, it induces variations of less than 10 seconds in planet d's transit times. Allowing for modest eccentricities does not significantly enhance the induced TTVs. The influence of the other additional planets is expected to be even weaker given as they are more widely separated and do not fall near any significant resonances with d or e.

statistic as $\ln \mathcal{L} = -\frac{1}{2}\chi^2$. We impose a Gaussian prior with 0 mean and a variance of $\sigma = 0.05$ on the eccentricity vector components, $e_i \cos \omega_i$ and $e_i \sin \omega_i$, typical for eccentricities of multi-planet, sub-Neptune systems (Hadden & Lithwick, 2014, 2017; Van Eylen & Albrecht, 2015; Xie et al., 2016) We found that the inferred planet masses are insensitive to the assumed eccentricity priors after running additional MCMC fits with $\sigma = 0.025$ and $\sigma = 0.1$. We initialize our MCMC with 200 walkers and run for 120,000 iterations, saving all walker positions every 1000 iterations.

Figure 7.7 shows the observed timing variations of planets d and e, along with N-body solutions drawn from our MCMC posterior. From our TTV dynamical fit, we determine planet-star mass ratios of $m_d/M_* = 3.9^{+2.5}_{-1.7} \times 10^{-5}$ for planet d and $m_e/M_* = 6.3^{+2.8}_{-2.2} \times 10^{-5}$ for planet e. The TTVs yield no strong constraint on planet eccentricities and the posterior distributions largely mirror our assumed priors. We convert the dynamical constraints on planet-star mass ratios to constraints on the planetary masses and densities by combining the posterior samples from our TTV fit with posterior samples of our fit to stellar mass and planet radii computed with EXOFASTv2. The resulting posterior distributions of the planets' masses and densities are plotted in Figure 7.8. The inferred median and 1σ planet mass values are $m_d = 8.4^{+5.4}_{-3.6} M_\oplus$ and $m_e = 13.6^{+6.1}_{-4.7} M_\oplus$ and densities are $\rho_d = 2.7^{+1.8}_{-1.2}$ g/cm^3 and $\rho_e = 5.6^{+2.6}_{-2.0}$ g/cm^3.

Our N-body dynamical model contains 10 free parameters which are fit to only nine data points. This means that, at face value, our model is under-constrained and we are at risk of over-fitting. To understand the origin of our dynamical mass constraints and ensure that they are not merely the result of over-fitting, we analyze the TTVs using the analytic model of Hadden & Lithwick (2016). This analytic treatment reduces the dimensionality of the TTV model so that it is no longer under-constrained. Note that we adopt the masses derived from the more complete N-body model as our best fit values; we present the analytic model simply as a consistency check to ensure the N-body results are not over-fitting the data because of poor MCMC convergence.

We use the formulas of Hadden & Lithwick (2016) to construct an analytic model for the TTVs of planets d and e as a function of planet periods P_i, initial transit times T_i, planet-star mass ratios μ_i, and the complex 'combined eccentricity'

$$\mathcal{Z} \approx \frac{1}{\sqrt{2}}(e_e e^{i\omega_e} - e_d e^{i\omega_d}) \ . \tag{7.1}$$

The analytic model reduces the total number of model parameters to 8 by combining the planets' eccentricities and longitudes of perihelia into the single complex quantity, $\mathcal{Z}$. The nth transit of planet d and e are modeled as

$$t_i(n) = T_i + nP_i + \delta t_{\mathcal{C},i}(n) + \delta t_{\mathcal{F},i}(n) \tag{7.2}$$

where $\delta t_{\mathcal{C}} \propto \mu'$, $\delta t_{\mathcal{F}} \propto \mu' \mathcal{Z}$ with μ' the perturbing planet's planet-star mass ratio. Expressions for $\delta t_{\mathcal{C}}$ and $\delta t_{\mathcal{F}}$ are given in Hadden & Lithwick (2016). We use the Levenberg-Marquardt minimization algorithm to fit our analytic model to the observed transit times and estimate uncertainties from the local curvature of the χ^2 surface (e.g., Press et al., 1992). The analytic fit, plotted in Figure 7.7, yields masses $m_d/M_* = 3.0 \pm 0.8 \times 10^{-5}$ for planet d and $m_e/M_* = 4.6 \pm 1.0 \times 10^{-5}$ for planet e, which are consistent with the N-body MCMC constraints.

The origins of the mass constraint can be qualitatively understood from the analytic model as follows: at conjunction, planets impart impulsive kicks to one another that change their instantaneous orbital periods. This effect is captured by the so-called 'chopping' terms, $\delta t_{\mathcal{C}}$, in Equation (7.2) (see also Nesvorný & Vokrouhlický, 2014; Deck & Agol, 2015). Indeed, we obtain nearly identical mass constraints from an analytic fit that drops the $\delta t_{\mathcal{F}}$ terms from Equation (7.2) (and thereby further reduces the number of free parameters to 6 as the model no longer depends on the complex number $\mathcal{Z}$). Because these $\delta t_{\mathcal{F}}$ terms vary over a timescale much longer than the baseline of our observations, they are well-approximated by a linear trend and essentially degenerate with small changes to the $T_i + nP_i$ terms in Equation (7.2). Thus, we have identified the the origin of our mass constraints with the measurement of the chopping signals, $\delta t_{\mathcal{C},i}$, in d and e's TTVs. Over the course of our observing baseline, planet d and e experience a single conjunction, at the time marked by a dashed line in Figure 7.7. The power of the TTV signal for constraining the planets' masses comes mainly from the impulsive changes in the planets' osculating orbital periods experienced at this conjunction causing the planets to arrive early (in the case of e) or late (in the case of d) at their next transits.

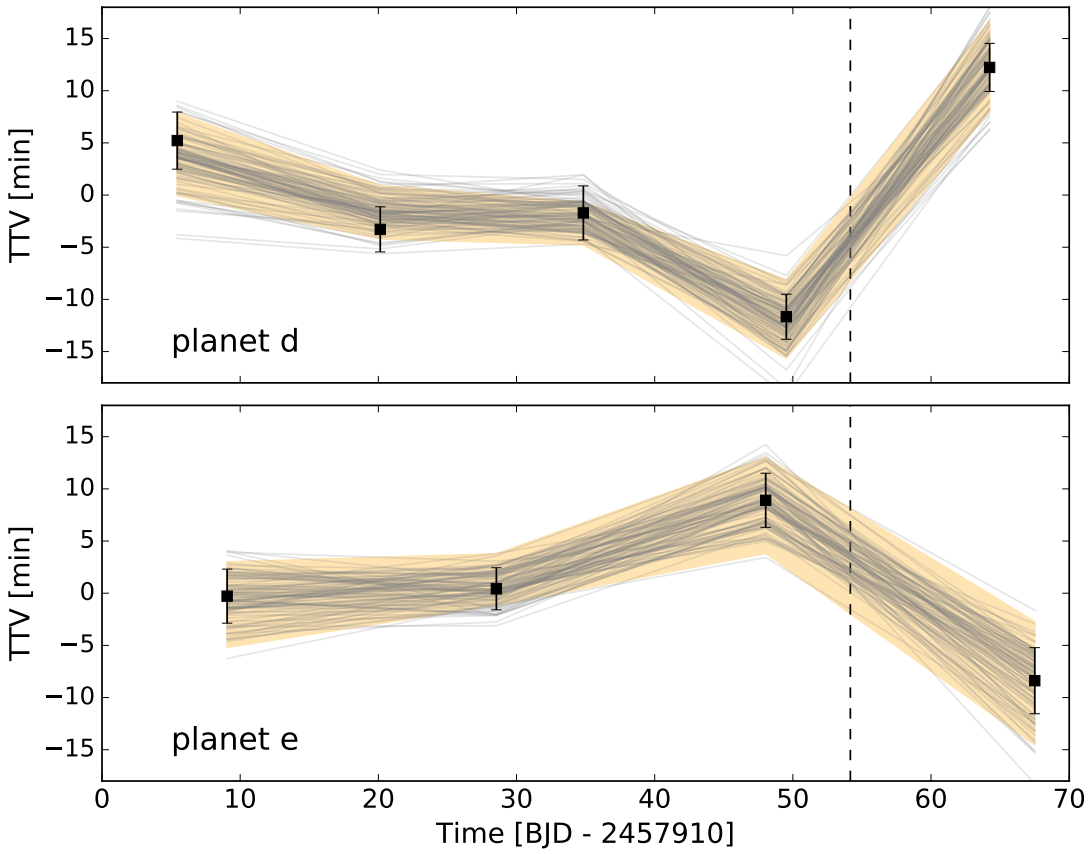

Figure 7.7 Observed TTVs for Planets d and e. The observed transit timing variations of planet's d and e are shown by black squares with error bars showing the 1σ uncertainties. A sample of 100 N-body solutions drawn from our MCMC fit posteriors are shown in gray. The shaded orange region shows the 1σ uncertainty in the analytic TTV model fit via least-squares. The time at which d and e experience a conjunction is indicated by the dashed vertical.

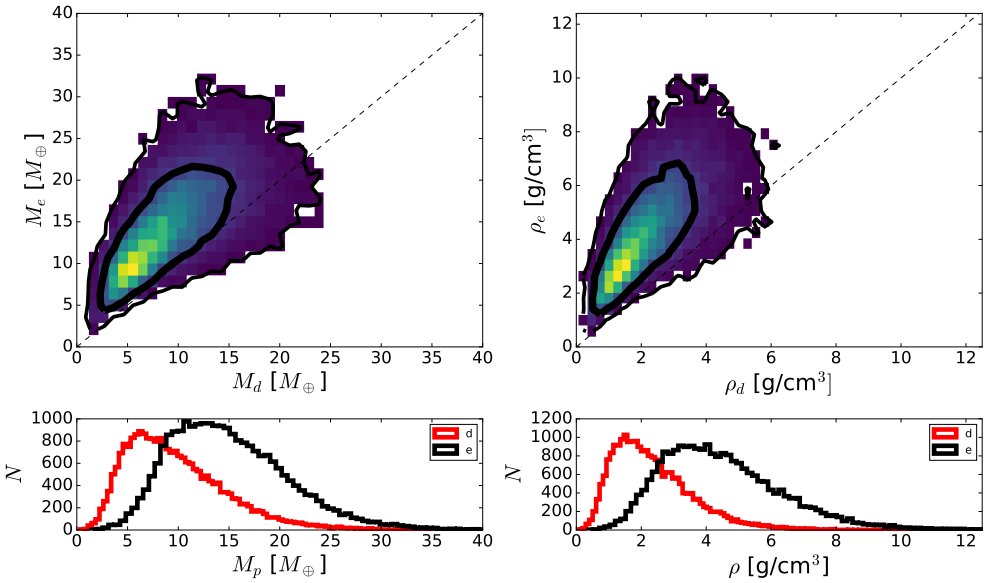

Figure 7.8 Mass Estimates from TTV Modeling. Posterior distributions of planet d and e's masses and densities derived from TTV dynamical modeling. Joint posterior distributions are plotted as intensity maps in the top two panels with 68% and 95% credible region contours plotted in black. Equal mass and density are indicated with dashed lines. Bottom panels show one dimensional histograms of the marginalized posterior distribution of planet d (red) and e's (back) mass and density.

7.5.2 Dynamical Stability and Transit Likelihood

Next we consider the dynamical stability of the system, along with the probability that all of the putative planets can be seen in transit. Although most Kepler multi-planet systems tend to have low mutual inclinations, this system is unique to date because there is a significant mutual inclination between the innermost planet and the other five. In the context of the known set of multi-planet systems, this appears significant. Ballard & Johnson (2016b) found that the Kepler planet-hosting systems around cool stars appears to be drawn from two populations: a set of multi-transit systems and a second set of single-transit planets, which may also have statistically higher obliquities Morton & Winn (2014c) (this concept of these two populations is commonly called the 'Kepler dichotomy'). One solution to the Kepler dichotomy is that the two populations are actually all multi-planet systems, and that the ones that appear to be singly-transiting are systems with larger mutual inclinations, which can see seen as single-transit systems from a particular line of sight. Although most Kepler multi-planet (4 planets or more) are fairly tightly confined to a roughly coplanar region, there is some precedent for multi-planet systems: Mills & Fabrycky (2017b) found a two-planet system with a 24 degree mutual inclination. In cases like this, the question of how many planets in a multi-transiting system might be seen in transit at any one time becomes relevant (Brakensiek & Ragozzine, 2016b), as large mutual inclinations can lead to only a subset of the planets being seen from a given line of sight. K2-266 b is currently observed to have a grazing transit and a high mutual inclination with the remainder of the planets, the five of which reside in a roughly coplanar configuration. With an aim towards assessing where this system fits into the Kepler dichotomy, we in this section conduct an analysis of the transit likelihood for various numbers of planets in this system.

To test the dynamical and transit stability of these planets, we ran 250 N-body simulations of the system, drawing the initial orbital elements from the posteriors generated from the EXOFAST transit fit (more specifically, we draw a single link from the MCMC posterior at random for each of the 250 simulations, and then use all orbital elements from that link). We assigned the longitude of ascending node to be 2π, as it cannot be measured from the transit fits. The planetary masses are drawn from the posteriors provided by the EXOFAST fit, as are stellar mass and radius. For all calculated values of inclination, we broke the above/below solar mid-plane degeneracy by

randomly assigning the value to be either greater or smaller than 90 degrees. We also assume that the stellar obliquity is aligned with the plane containing the outer five planets (but there are no system-specific observations to support this assumption; instead, we make this assumption as a computational necessity, although we expect the stellar obliquity to be more aligned in multi-planet systems; Morton & Winn 2014c). These 250 simulations were carried out using the hybrid Wisdom-Holman and Bulirsch-Stoer (B-S) integrator `Mercury6` (Chambers, 1999c) for integration times of 10^5 years, and with an initial time-step of 8.5 minutes. Energy was conserved to better than one part in 10^8 over the course of the simulations. When physical collisions occur, particles are removed from the simulation. The integration time was chosen to include many secular timescales of the system (Figure 7.9 shows that many periods of secular oscillations are included in 10^5 years time span).

In roughly 66% of our suite of 250 simulations, at least two planets in the system attain orbits which cross. In 23% of the simulations, the system experiences a true dynamical instability, in which a planet is ejected from the system or physically collides with another body. In the cases in which orbits cross, planets 0.02 and c are the culprits of the instability roughly 80% of the time. On the 10^5 year integrations considered in this work, a size-able fraction (roughly a third) remain dynamically stable. As such, we cannot use dynamical arguments to argue against the existence of planet candidate 0.02, whose close orbit with planet c might otherwise be suspect.

As neither of the planet candidates can clearly be ruled out based on dynamical arguments, we next consider the dynamical evolution that leads to only a subset of the six known planets being seen in transit. We currently observe the system to be a six-planet system, but the innermost planet K2-266 b has a high measured impact parameter, meaning that is barely transiting. The simulations show significant inclination evolution over time for both K2-266 b and the other planets in the system. In Figure 7.9, we plot a representative case from our set of 250 simulations, where the semi-major axes and eccentricities of all planets remain confined relatively close to their currently-measured values, but the orbital inclination of all six planets evolves.

One notable feature of the numerical simulations is the inclination evolution of all six planets. Secular evolution of the system causes the planetary orbits to evolve with time, resulting in configurations in which not all planets can be seen in transit simultaneously. Inspired by the present-day

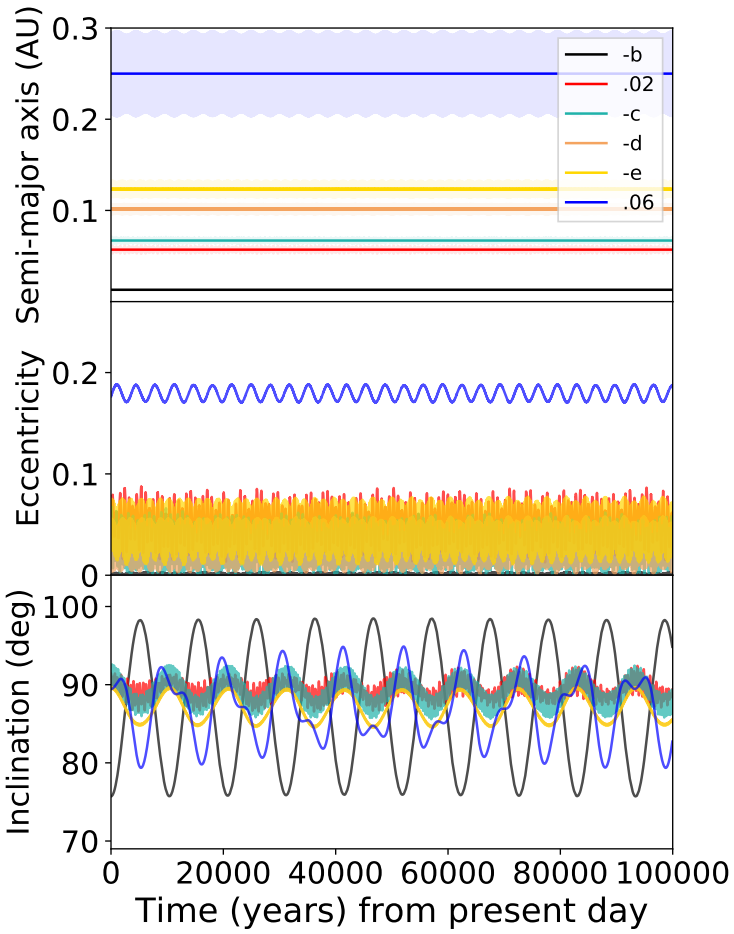

Figure 7.9 Sample N-body Integration for K2-266. A sample integration from the suite of 250 run for this work, plotted for illustrative purposes. A typical dynamically stable integration, where planetary orbits do not wander far from their initial values of semi-major axis or eccentricity. (top panel) The semi-major axis of each planet, with shaded regions to denote the extent of the perihelion and aphelion distances. (middle panel) The eccentricity evolution of each planet, which oscillate but remain confined near their initial values. (bottom panel) Inclination values for each planet. The inclination values for all planets oscillate with varying amplitudes, as is typical for all integrations.

(apparently serendipitous) geometry, we extracted from the simulations the transit probability over time for varying numbers of planets in this system. The result of this analysis is presented in Figure 7.10 for two lines of sight. The first case considers the fixed line of sight corresponding to our current location (that of the Solar System). The second case uses an optimized variable line of sight, which is re-computed at each time-step of each integration to determine the largest multiplicity that can be observed from *any* location in the galaxy.

This analysis shows that observing six transiting planets in the system is rare given the known components of the system. No matter which line of sight is considered, the system will appear to contain the six 'known' planets a minority of the time. More commonly, the system will be seen as a five-planet system from the most favorable line of sight, and as a one- or two-planet system from our current line of sight. Most of the time, the inclinations of the outer five planets evolve and cause them to reside in non-transiting configurations. On the other hand, the probabilities are not vanishingly small. We expect to be able to re-observe a six-planet transiting system about 2.2 percent of the time in the future from our current line of sight, given the currently measured orbits of these planets. It is also important to note that we cannot be sure that the observed six planets are the only planets in this system: additional, non-transiting planets would alter the dynamics described here.

7.5.3 Resonant state of the two sub-Neptunes

The sub-Neptunes K2-266 d and e, with periods of 19.482 days and 14.697 days, have a period ratio of 1.326, which is 0.59% away from the $4:3$ mean motion commensurability. These planets reside in nearly the same orbital plane (with 89.73 and 89.74 degree inclinations). As such, the orbital periods of these planets suggest that they may reside in orbital resonance. However, true resonance is characterized by a librating resonance angle, and it is not clear from the orbital elements alone whether the resonance angle will librate or circulate. To determine the true resonance behavior of these two planets, we used the subset of the 250 simulations which did not experience orbit-crossing during the 10^5 year integation time, and post-process the results to search for resonances.

We have performed a resonance-finding algorithm to identify the time intervals in the simulations where the planets were in true resonance. We found regimes with nearly constant period ratio

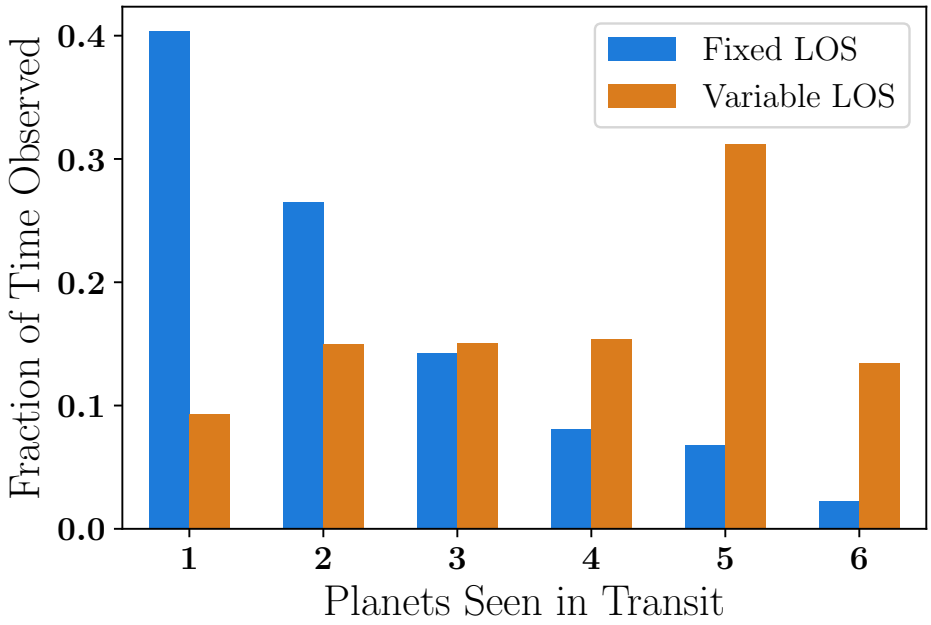

Figure 7.10 [Transit Probability by Planet Count. The future simultaneous transit fraction by the number of planets seen in transit. These fractions were computed using the numerical simulations for two lines of sight: a fixed line of sight (Fixed LOS), set to be the current line of sight from the earth, and a variable line of sight (Variable LOS), computed at each time-step to be the line of sight from which the greatest number of planets can be seen in transit at any time. The simulations used to construct this plot are the subset of the 250 simulations run in this section. Given the measured orbital elements of the planets around K2-266, the system is expected to be observed as a six-planet system a minority of the time (assuming there are no extra unseen planets in the system).

(constant P_e/P_d), generated arrays of resonance angles for all $p : q$ resonances up to 29th order (while $p \leq 30$), and automatically generated plots using the simulated orbital elements of planets K2-266 d and e for each resonance angle for each resonance order for all of the 250 simulations. Using the resulting resonance angles, we searched for librating behavior by breaking the time series into 5000 year intervals and searching for gaps in resonance angle space: Note that a circulating resonance angle will populate the entire 360 degree range of possible angles, whereas a librating angle will have gaps.

We find that in our simulations, planets K2-266 d and e exhibit orbital resonances approximately 8.1% of the time over the simulations under consideration. The resonance angles populated in these

cases have the forms

$$\psi_1 = 4\lambda_o - 3\lambda_i - \varpi_o \,, \tag{7.3}$$

and

$$\psi_2 = 4\lambda_o - 3\lambda_i - \varpi_i \,, \tag{7.4}$$

where λ is mean longitude and ϖ is longitude of pericenter. The subscripts denote the inner (i) and outer (o) planets. The four types of resonance behavior exhibited by this system, in order of occurrence rate, include: non-resonance, continuous resonance for the entire simulation lifetime, an initial condition close to resonance that loses the resonance as the system evolves, and very rarely, the attainment of a resonance after an initial period of non-resonance (see Ketchum et al. 2013b for a more detailed discussion of this process). We find that for trials that start out in a resonant configuration, the typical libration width of the resonance is generally consistently around 190 degrees. Although this width may evolve slightly as the simulation progresses, the resonances are not typically much deeper than this initial value.

Two examples of resonant behavior exhibited in our simulations are shown in Figure 7.11. The top panel shows results from a simulation where both planets reside in resonance for the entire 10^5 year integration; the bottom panel shows a simulation where K2-266 e and f start in resonance, but leave the resonance after roughly 45,000 years.

7.5.4 Chaotic Behavior

Dynamical systems are often chaotic and we would like to quantify the chaotic behavior of K2-266. The system, as observed, has six planets in a compact configuration with a relatively large mutual inclination between the innermost planet and the others. Our numerical simulations, described above, indicate that while the outer planets (K2-266 d, e, and .06) are generally dynamically stable, the middle planets (K2-266.02 and d) can experience scattering or other non-periodic time evolution, potentially leading to orbit crossing. Non-periodic behavior of this nature can be indicative of chaos.

The evolution of a chaotic planetary system is extremely sensitive to its initial conditions. Chaos is often parameterized by the Lyapunov exponents of the system, which determine the rate

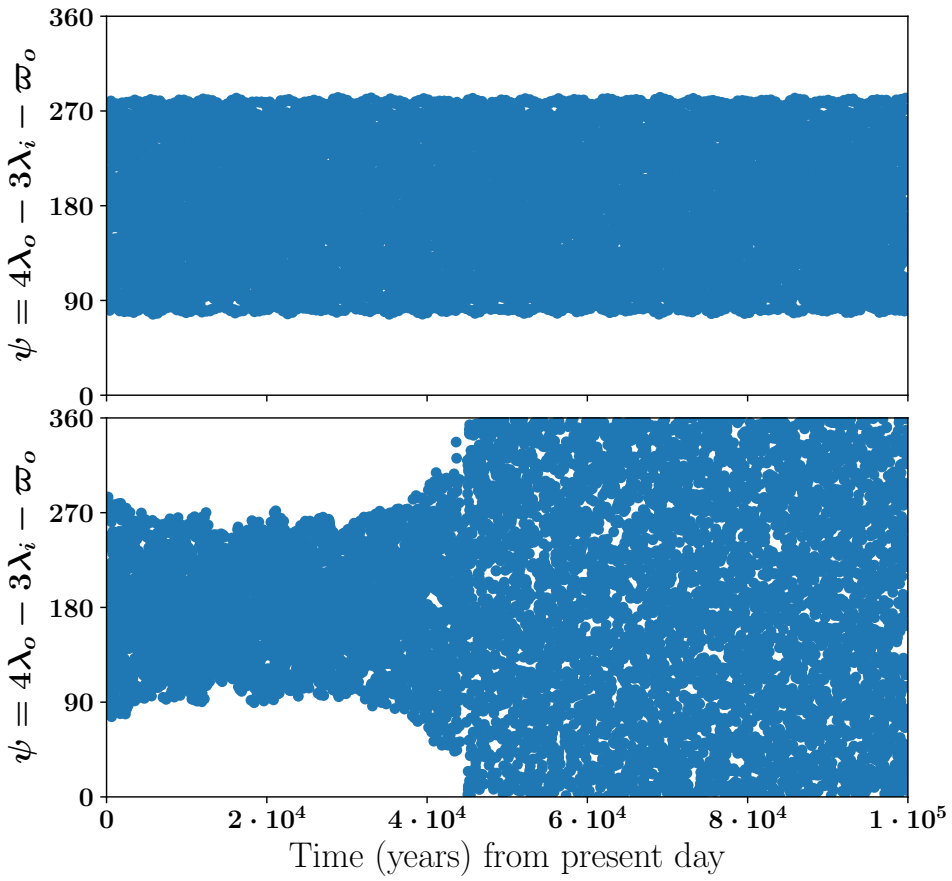

Figure 7.11 Resonance Angle over Time while in Resonance. The evolving resonance angles for two sample integrations for the two super-Earths, drawn from the suite of 250 integrations run with `Mercury6`. Initial orbital parameters drawn from the posteriors generated from the transit fit, and all six planets were included in the integration. These two frames are characteristic of two of the four types of resonant behavior exhibited by this system: in the top panel, we plot a stable resonance for the entire 10^5 years of the integration, as exhibited by its librating resonance angle; in the bottom panel, we plot a trial that begins in resonance, and then nods out of resonance during the evolution of the system. The third case, total non-resonance for the entire time of the integration, is not plotted (but is characterized by circulating resonance angles). The fourth case, initial non-resonance followed by temporary attainments of resonances, is extremely rare and also not plotted here.

of exponential divergence of orbits with similar initial conditions. In contrast, general observational uncertainties in the orbital elements can also lead to non-chaotic divergence if initial orbital elements are drawn from different locations of the posteriors (in cases where ensembles of simulations are used to sample the uncertainties). Either sufficiently large observational errors or the sufficiently rapid onset of chaos will thus make both numerical integrations and analytic explorations less

certain.

To test the chaotic behavior of the K2-266 system, we ran 400 integrations of this system, with the orbital parameters and masses drawn from the posteriors generated by the transit fit. Each simulation was carried out using the Rebound N-Body integration package (Rein & Liu, 2012), where we used a total integration time of 1000 years, the `IAS15` integrator (Rein & Tamayo, 2015b), and an initial time-step of 8 minutes. For each of these integrations, we evaluate the chaotic nature of the initial conditions by employing the Mean Exponential Growth factor of Nearby Orbits (MEGNO) indicator (Cincotta et al., 2003), implemented in the `Rebound` N-body code. For chaotic trajectories, the MEGNO indicator, Y, grows linearly in time at a rate of $1/t_{Ly}$ where t_{Ly} is the Lyapunov time, while for regular trajectories it asymptotically approaches $Y = 2$. We compute MEGNO values for the 400 draws from the posteriors of this system at times between 1 and 1000 years. These realizations provide a good sample of the parameter space spanned by the observational posteriors. Of the 400 realizations, only 4.5% can be categorized as unambiguously regular at the end of the integration (where the criterion for regularity is taken to be MEGNO< 4). Moreover, we find no strong correlations between planetary parameters and MEGNO values using our current simulation set. We attempted to trace chaotic behavior using the period ratio of the resonant planets d and e (as done in Figure 3 of Deck et al. 2012), the ratio perihelion/aphelion of .02 and c, and by using the orbital elements of planet b, but no trends emerged. This finding is likely due to the high multiplicity and tightly packed nature of the system: there are multiple equally-important sources of dynamical chaos. In Figure 7.12, we plot the median MEGNO indicator value for these 400 simulations considered in this section at periodic intervals in the 1000 year integrations. A MEGNO indicator less than 4 denotes regular orbits, while a MEGNO of 4 or greater denotes measured chaos. The median MEGNO indicator reaches 4 (denoting the measurable onset of chaos) at roughly 100 years.

From this MEGNO analysis, we know that the majority of orbits allowed by the transit posteriors are chaotic. It is important to note that, while some of these chaotic posterior points are likely destined to experience instabilities based on our 10^5 year numerical simulations, a chaotic system does not necessarily mean a dynamically unstable system, or even a particularly active system (the planetary orbits in our solar system are known to be chaotic, as is the Kepler-36 planetary system,

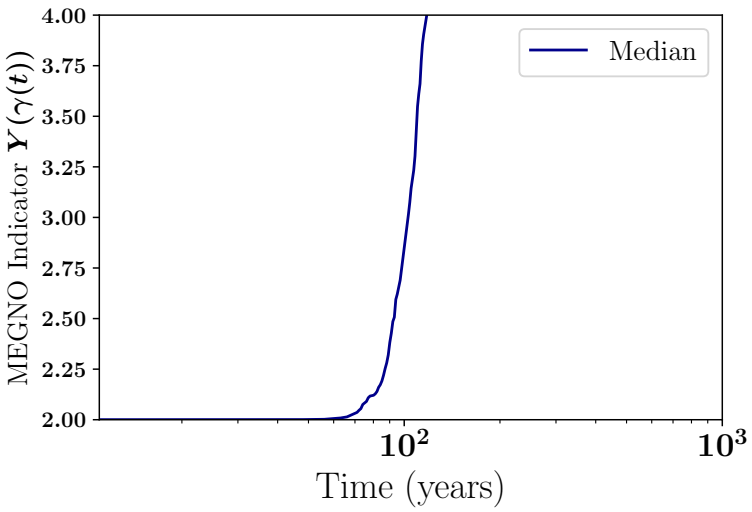

Figure 7.12 Median MEGNO Indicator. The median MEGNO indicator value as a function of time during the thousand-year `Rebound` integrations (among 400 realizations). The median value reaches $Y = 4$, indicating chaotic behavior, after only 100 years. The light blue shaded region delineates the quartile values of the MEGNO indicator. For the majority of posterior draws, this system is thus highly chaotic.

Deck et al. 2012). Chaos implies that similar initial conditions will diverge over some time scale, so that precise future predictions of planetary orbits can no longer be made. Specifically, for two given sets of similar initial conditions, integrations of both cases could result in systems that are dynamically stable and continuously transit, but the values of the phase space variables (including planet locations) can diverge over time if the system is chaotic. One implication of this analysis is that a large amount of uncertainty in forward integrations comes from chaos, rather than only from the uncertainty of the transit posteriors.

7.6 Discussion

The complex architecture of the planetary system surrounding K2-266 makes it an intriguing target for further characterization. Additionally, the host star is relatively bright (V=11.8, K=8.9) and up to 6 planets orbit the host star in a compact configuration. At the present time, we are only able to validate planets b, c, d, and e, so that more data is needed to confirm the remaining two candidates.

7.6.1 Atmospheric Characterization

The origin of Neptune sized planets is not clear, yet they appear to be one of the most common types of planets. The planets range in size from 2-6$R_\oplus$ and have been discovered orbiting >25% of all stars (Howard et al., 2012b; Fressin et al., 2013b; Buchhave et al., 2014b; Fulton et al., 2017). Recent statistical studies of the observed amplitude of transmission spectral features of warm Neptunes show a correlation with equilibrium temperature or its bulk H/He mass fraction (Crossfield & Kreidberg, 2017b). However, there are only a small number of Neptune sized planets that are amenable to transmission spectroscopy with current facilities like the *Hubble Space Telescope (HST)*.

To understand if the planets orbiting K2-266 would be viable targets for transmission spectroscopic measurements, we follow the technique described in Vanderburg et al. (2016c) to calculate their expected atmospheric scale height and signal-to-noise (S/N) per transit. Using data from NASA's Exoplanet archive (Akeson et al., 2013c), we also calculate the atmospheric scale height and S/N for all planets with $R_p < 3R_\oplus$(see Table 7.5), updating this table from Rodriguez et al. (2018b). The calculations are done in the H-band to understand their accessibility using the Wide Field Camera 3 instrument on HST, as well as the future feasibility to observe them with the suite of instruments on the upcoming James Webb Space Telescope (JWST). Purely based on the inferred sizes of the planets, it is expected that K2-266 b, d, and e might all have thick gaseous atmospheres (Weiss & Marcy, 2014c), but the uncertainty in the size of planet b (due to the grazing transit configuration) and its proximity to its host star makes this unclear (see Figure 7.6 for the probability distribution of planet b's radius from our global fit). While our transit fit indicates that the most probable size of planet b is about three times the size of the Earth, virtually all known ultra-short-period planets known are smaller than 2 $R_\oplus$ (Sanchis-Ojeda et al., 2014c; Winn et al., 2017b)

K2-266 b is a particularly interesting target for atmospheric followup because of its status as an ultra-short period (USP) exoplanet. Lopez (2017) suggests that in order for USP planets to have radii larger than $\sim 2R_\oplus$, they should have formed with high-metallicity, water-rich envelopes, and are likely to remain water-rich today. In addition, the theoretical models of Owen & Wu (2013) and Owen & Wu (2017) suggest that planets with the radial size and orbital period of K2-266 b reside near the boundary in parameter space where photoevaporation becomes an important source of

mass loss. In addition, if K2-266 b has a typical magnetic field strength, its close proximity allows for interactions between the magnetospheres of the star and the planet (Adams, 2011). Combinations of mass measurements of K2-266 b, refined radius measurements, and atmospheric constraints on water abundance could be used together to paint a complete picture of where in the disk this planet originated and when it reached its current-day location.

K2-266 d and e are two of the best sub-Neptune sized planets for atmospheric characterization and their longer periods (as compared to the others in Table 7.5) provide a valuable opportunity for a comparative atmospheric study between hot and warm sub-Neptune sized planets. Interestingly, the Near-IR and IR brightness of K2-266 should allow for high S/N observations using short exposure time for all four instruments on JWST: Near Infared Camera (NIRCam), Near Infrared Imager and Slitless Spectrograph (NIRISS), Near-Infrared Spectrograph (NIRSpec), and the Mid-Infrared Instrument (MIRI) (Beichman et al., 2014; Kalirai, 2018).

7.6.2 Dynamical Classification

The dynamics of the K2-266 system is characterized by several remarkable features: The innermost planet (K2-266 b) is highly inclined relative to the rest of the planets, the orbits of planet candidate K2-266.02 and validated planet K2-266 c are in close proximity, the two sub-Neptunes (K2-266 d, e) are either in or extremely close to a mean-motion resonance, and the outer candidate K2-266.06 has a moderately eccentric orbit. Taken together, these factors place the planetary system orbiting K2-266 in a particularly unique realm.

Among the exoplanetary systems discovered thus far, only a small number have been determined to be in true resonance (Rivera et al., 2010; Lissauer et al., 2011b; Carter et al., 2012b; Barclay et al., 2013; Mills et al., 2016; Luger et al., 2017; Shallue & Vanderburg, 2018; Millholland et al., 2018). From our numerical simulations initialized with orbital elements from the transit fit, we find in the stable simulations in which no planetary orbits cross, planets K2-266 d and K2-266 e are in true resonance for 8.1% of the time, as characterized by a librating resonance angle. This significant fraction makes K2-266 another member of the short list of stars hosting systems containing potentially resonant exoplanets. Additional transits, which will improve orbital period precision, would enable future refinement of this resonance fraction.

From the time-evolution of the MEGNO indicator, we find that the average draw from the posterior becomes noticeably chaotic after roughly 100 years. The high mutual inclination between validated planet K2-266 b and the rest of the planets is also intriguing. As shown in Figure 7.10, because of the high present day inclination of K2-266 b, this system is rarely (perhaps 5 percent of the time) in a configuration where all six planets can be seen simultaneously from our current line of sight. A smaller number of planets are expected to be seen in transit most of the time. Similarly, it is possible that the system hosts more than six planets, but we are seeing only six of them in transit at the current epoch. Tighter limits on the planetary posteriors will allow for a more precise determination of the future transit probability for each (known) planet, and will place constraints on any additional bodies in the system. In future work, a numerical survey of the parameter space subtended by the measured posteriors might allow for additional constraints on planetary parameters based on dynamical stability limits.

The formation of misaligned orbits, such as that of K2-266 b, remains an open problem. Petrovich et al. (2018) proposes that most ultra-short period planets form through non-linear secular interactions ("secular chaos"). In this scenario, the proto-USP starts with an orbital period of $5-10$ days, is excited to high eccentricity, and is subsequently tidally captured onto a short-period orbit. Note that the process that leads to high eccentricity (e.g., planet-planet scattering) could also produce inclined orbits. As a result, one potential signature of this process could be a high mutual inclination for the USP relative to the other planets, as seen in this system. However, most companions to a USP generated in this manner would generally have orbital periods of 10 days or larger, whereas the K2-266 system has two planets with shorter periods of only 6 and 7 days. For this secular chaos mechanism to form this system, the 6- and 7-day planets would need to migrate inward after the eccentricity excitement and subsequent circularization of the USP; yet, as K2-266 b may have an un-evaporated atmosphere based on current radius estimates, a dynamical history allowing it to form further from the star (subject to less photoevaporation) seems favorable.

7.7 Summary of Planet Discoveries

We present the discovery of up to six planets transiting the bright (K=8.9) nearby (∼78 pc) star K2-266 (EPIC248435473). From a global model where we simultaneously fit all six planetary signals, we find that the six planets have periods between 0.66 to 56.7 days, and radii of 0.65 to 3.3 $R_\oplus$. From analyzing transit timing variations, we are able to confirm the two warm Neptunes (d & e), constraining their masses to be $m_d = 8.9^{+5.7}_{-3.8} M_\oplus$ and $m_e = 14.3^{+6.4}_{-5.0} M_\oplus$. Additionally, we are able to validate the planetary nature of planets b and c. Future followup observations should aim to confirm the transits of K2-266.02 and .06 through high photometric precision observations with facilities like NASA's *Spitzer Space Telescope*. Our analysis shows that the inner ultra-short period planet, K2-266 b, has an inclination of 75.3 degrees while the other five planets are consistent with an inclination between 87–90 degrees. This corresponds to a mutual misalignment of >12.5 degrees which may indicate that planet b did not form in the same way as the others. The brightness of K2-266 combined with the relatively large size of the sub-Neptune planets d and e make them great targets for atmospheric characterization observation with current facilities like *HST* and future facilities like *JWST*.

7.8 Explaining the Misalignment in the K2-266 Planetary System

In Chapters III and IV of this thesis, we modeled how the inclination evolution of an inner system of multiple planets changes in the presence of an outer pertruber. In the case of WASP-47 (Chapter IV), the perturbing extra planet was real (WASP-47c), while in the case of the Kepler compact systems (Chapter III), the perturbing planets were hypothetical. For all those systems, the effect of the perturbers was destabilizing: the extra angular momentum provided by the companion resulted in a greater spread in inclinations.

In particular, in Figure 2.10 of Chapter II, we showed that systems with a higher surface density of planetary mass (defined as the mass of the planets spread out over an annulus the distance of the inner to outer planets) are more susceptible to perturbations.

The K2-266 system of validated planets (b, c, d, and e; from this point forwards, we do not include .02 and .06 in our analysis since they are not yet validated planets) has a surface density

(computed using Equation 2.19) of 2782.059 $M_\oplus$ / AU^2 for its median posteriors. This is by far the highest value of any Kepler STIP, with a large amount of the mass being contributed by the inner ultra-short-period planet. The Kepler STIPs, in comparison, have surface densities ranging from $\sim$ a few to $\sim$ 850 $M_\oplus$ / AU^2 (again, see Figure 2.10).

This high surface density, combined with the result from Chapter II that it tends to be easier to perturb systems with high surface densities out of mutually transiting configurations, indicates that were the K2-266 system to be perturbed in such a way, it might lose its mutually transiting configuration. Clearly, due to the misalignment between the K2-266 b and the other known planets, something has excited different rates of inclination evolution for the inner planet compared to the outer ones.

One explanation for this misalignment consistent with the spirit of Chapter III is that an additional unseen companion resides in the K2-266 system. In that case, the strength of its dynamical coupling could vary between each of the inner planets, potentially resulting in different inclination evolution amplitudes for the inner planets and even causing the observed misalignment.

The companion needed in the K2-266 system would need to both create a misalignment between the inner ultra-short-period planet K2-266 b and the other planets, but also keep the other planets (c, d, and e) confined to a plane small enough that they all transit and appear as coplanar as they do in the transit data described in the previous section. We next turn our attention to whether such a companion can exist.

7.8.1 Deriving Perturbing Planet Parameters: General Techniques

There are two ways to tackle this problem: secular theory and numerical N-body simulations. In this section, we describe the ways that we will utilize both to derive the companion parameters that would recreate the observed geometry of K2-266.

7.8.1.1 Secular Theory

The secular model we use here is similar to that of Chapter II, with one major change: where before we neglected the oblateness of the central body, we now add quadrupole moment J_2 into the disturbing function, as follows. The general form of the disturbing function remains:

What was once Equation 2.2 now becomes:

$$\mathcal{R}_j^{(\mathrm{sec})} = n_j a_j^2 \left[\frac{1}{2} B_{jj} I_j^2 + \sum_{k=1}^{N} \left(B_{jk} I_j I_k \cos\left(\Omega_j - \Omega_k\right) \right) \right], \tag{7.5}$$

where as before, j is the planet number, n is the mean anomaly, I the inclination, ω the argument of pericenter, and Ω is the longitude of the ascending node.

The form of coefficients B_{ij} changes, as we introduce a dependence on solar oblateness:

$$B_{jj} = -n_j \left[\frac{3}{2} J_2 \left(\frac{R_c}{a_j} \right)^2 - \frac{27}{8} J_2^2 \left(\frac{R_c}{a_j} \right)^4 - \frac{15}{4} J_4^2 \left(\frac{R_c}{a_j} \right)^4 + \frac{1}{4} \sum \frac{m_k}{M_c + m_j} \alpha_{jk} \bar{\alpha}_{jk} b_{3/2}^{(1)}(\alpha_{jk}) \right], \tag{7.6}$$

and

$$B_{jk} = n_j \left[\frac{1}{4} \frac{m_k}{M_c + m_j} \alpha_{jk} \bar{\alpha}_{jk} b_{3/2}^{(1)}(\alpha_{jk}) \right], \tag{7.7}$$

where J_2 and J_4 describe the oblateness of the central star (the quadrupole and octopole moments respectively), R_c is the stellar radius, m_k indicates the mass of the kth planet, M_c denotes the mass of the central star, α_{jk} denotes the semi-major axis ratio a_j/a_k, and $\bar{\alpha}_{jk}$ denotes the semi-major axis ratio $a_j/a_k < 1$. The quantities $b_{3/2}^{(1)}$ is the Laplace coefficient.

Otherwise, the procedure of solving these equations proceeds identically as in Chapter II. The reason that we introduce these terms into the disturbing function is that for ultra-short-period planets, the contribution of the stellar quadrupole field becomes significant. K2-266 b's extremely short orbital period (0.66 days) places it squarely in the regime where this effect is more important. To construct the inclination time-series, we chose starting parameters for each planet equal to the median value from the EXOFASTv2 posterior, including planets K2-266 b, c, d, and e in the evolution. We ignore the candidate planets due to their unvalidated nature. Our choice of starting parameters is an important distinction from previous work: for much of this thesis, we have sampled starting parameters for simulations from the full range of the transit fit posteriors, with the goal of better understanding the parameter space.

In an effort to reduce the number of degrees of freedom in the system and better understand the effect of a companion, we choose to use the median posterior value for all measured planetary and stellar parameters, meaning that the starting parameters are identical in all integrations except for

the semi-major axis, inclination, and mass of the injected companion. Additionally, since the secular theory presented here is to second order, inclination and eccentricity are decoupled, meaning that the starting values of eccentricity do not affect the final result. We also draw the staring planetary inclinations from a Rayleigh distribution with a width of 0.5 degrees (including K2-266 b), to simulate the planets starting in a 'normal' STIP configuration typical to what we expect from the Kepler data. We then allow the system to evolve forwards in the presence of the outer companion, and measure the inclination over time.

7.8.1.2 N-body Integrations

Our second avenue of generating evolution time-series is by using numerical N-body simulations. We use the `Mercury6` N-body integration package (Chambers, 1999b), using the Bulirsch-Stoer (B-S) integrator, requiring that system energy be conserved to 1 part in 10^9. For the simulations suites presented in this work, we integrate the system for a total simulation length of 10,000 years, with a time-step of 0.005 days (the short time step is needed since the orbital period of the inner planet is so short). Importantly, the numerical timescale, being only 10,000 years, is not long enough to resolve secular resonances.

In the N-body integrations, we include the validated planets (K2-266 b, c, d, e). For all star and planet parameters, we taken the median value of the EXOFASTv2 posterior. To further simplify the system and stay consistent with the secular integrations (in which eccentricity and inclination are decoupled), we also set all planetary eccentricities to zero. We also draw the staring planetary inclinations from a Rayleigh distribution with a width of 0.5 degrees as in the previous section.

To perform these computationally intensive simulations, we use the Open Science Grid (OSG; Pordes et al., 2007) accessed through XSEDE (Towns et al., 2014).

7.8.2 Deriving Emergent Properties from Initial Parameters

The K2-266 has two apparent emergent properties:

- The plane of outer 5 candidate planets (3 of which are validated planets) is at present day confined to a fairly narrow plane in impact parameters. The inclinations of these planets range between 88.28 and 89.46 degrees.

- The innermost planet, K2-266 b, has an inclination of 75.32 degrees, which is a significant misalignment compared to the outer plane of planets.

Note that since the data on this system came from for all inclinations, the standard (above/below) plane degeneracy applies: K2-266 b may have a true inclination of either ~ 75 or ~ 105 degrees. In either case, the misalignment between the planes remains ~ 15 degrees.

Running simulations (secular or N-body) as described above, starting the planetary inclinations to all be drawn from a Rayleigh distribution measured the effect of the companion on the inclination evolution of the other planets. Since we start the known planets in roughly the same plane, the first of our two emergent properties is immediately satisfied (as it is in all the Kepler systems of tightly packed inner planets). Over time, the presence of the companion may cause the evolution of inclination of the inner planets. Simultaneously, the inner most planet's oscillation mode is also strongly affected by the stellar quadrupole moment. The potential result is that for a particular type of companion, a strong dynamical coupling between the outer transiting planets and the companions results in the evolution of their inclination relative to the inclination evolution of the inner planet. When this occurs and simultaneously the outer plane of transiting planets remains fairly tightly confined, the observed geometry of the system can be reproduced.

In the remainder of this section, we study the companion parameters that reproduce the above geometry.

7.8.2.1 No Companion

We first check whether the two observed emergent properties can be recreated when the system is started in a confined plane of inclinations (drawn from a Rayleigh distribution with a width of 1.4 degrees) and allowed to evolve forwards in the presence of only the known planets. We include the stellar quadrupole moment and the effect of general relativistic precession, but do not include a companion. The purpose of this analysis is to check whether the observed geometry is actually as strange as it first appears, or if it is a natural consequence of the planetary parameters.

We run 100 N-body simulations using the parameters given in Section **??**, and compare the result with 1000 secular evolutions. In Figure 7.13, we plot a sample N-body integration, showing the inclination evolution for the four validated planets as they evolve under the influence of GR

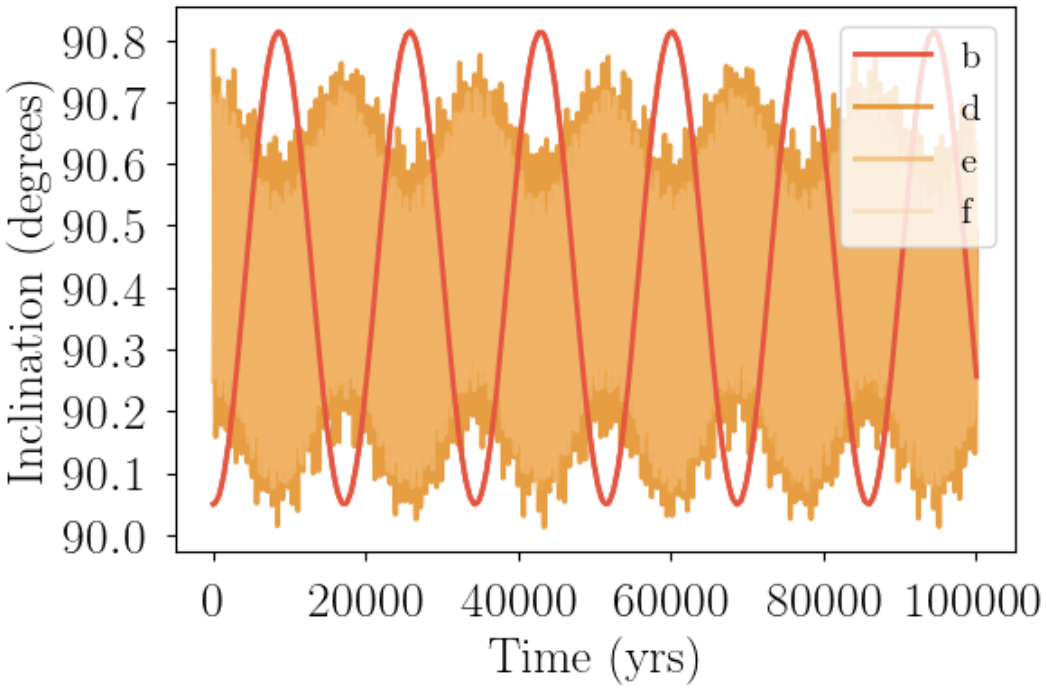

Figure 7.13 N-body Evolution Without a Companion. The four validated planets in the K2-266 system were evolved forwards in the known system, starting their orbits in a plane with inclinations drawn from a Rayleigh distribution with a width of 1.4 degrees (Fabrycky et al., 2014b).

and the stellar quadrupole moment (when $J_2 = 10^{-7}$). Although the secular period of the inner planet K2-266 b is significantly different from the other planets, a misalignment as large as that measured in the system today is not naturally produced in this trial.

The full results from the integrations are presented in Figure 7.14, and show that the maximum plane size attained for all of these integrations is less than the 14 degree of observed misalignment between the ultra-short-period planet and the other three planets. As such, the observed misalignment cannot be reproduced in the system as observed when only the other known planets and the effects of GR and stellar J_2 are considered, and we must turn to another explanation.

7.8.2.2 Saturn-mass Companions

To begin, we assume that a Saturn-mass companion exists somewhere in this system. We emphasize that the choice of a Saturn-mass companion does not come from any observational motivation: there is no observational evidence that a companion of that size exists in the system; instead,

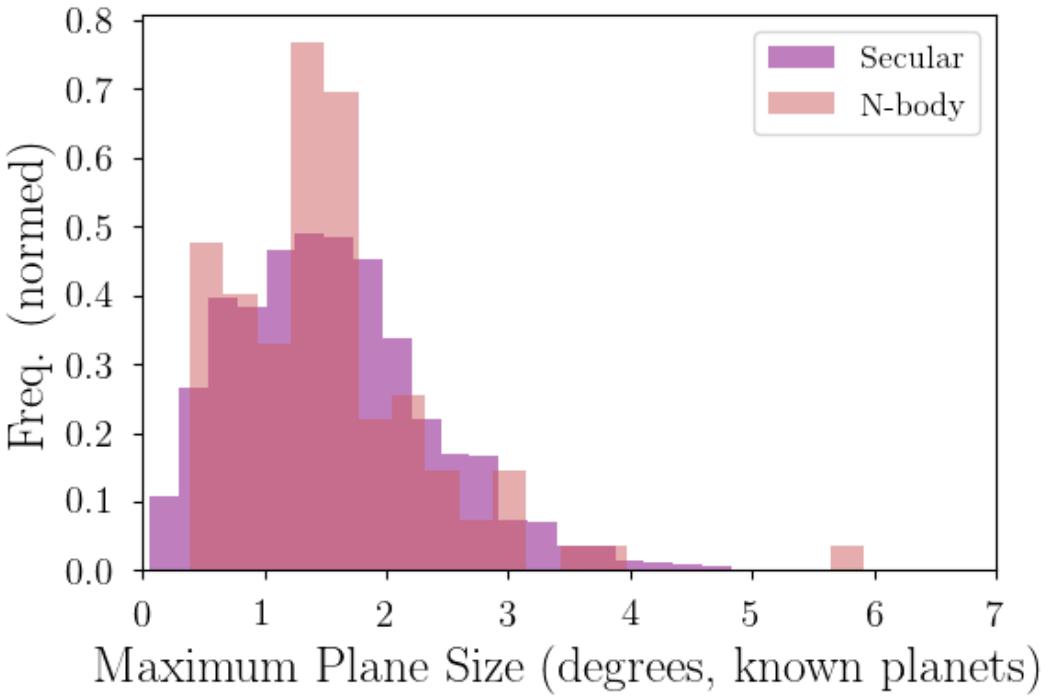

Figure 7.14 Control Distributions of Orbital Inclinations. Here, we plot two normalized histograms, both showing the *maximum* plane size for all planets (including the inner planet) attained in each integration for test sets of 100 N-body integrations and 1000 secular solutions. Even the maximum plane attained does not reproduce the observed misalignment.

we merely test whether the presence of such a companion could create the observed misalignment for the innermost planet.

The host star in the K2-266 system is 0.686 $M_{\odot}$. Several stars in this mass range host planets more massive than our tested companion (which is the mass of Saturn, or 0.3 $M_{\odot}$): Kepler-45, a 0.59 $M_{\odot}$ star, hosts a 0.5 M_{jup} hot Jupiter (Johnson et al., 2012); WASP-80, a 0.58 $M_{\odot}$ star, hosts a 0.55 M_{jup} hot Jupiter (Triaud et al., 2013); HIP 57274, a 0.73 $M_{\odot}$ star, hosts a 0.4 M_{jup} planet with an orbital period of 32 days, as well as two additional planets (Triaud et al., 2013). Nature has shown that a $\sim$0.7 $M_{\odot}$ star can host a planet in the mass range 0.3 to 0.4 M_{jup}, even in multi-planet systems.

To test the regime in which our injected Saturn-mass companion can reproduce both (1) the coplanarity of the outer transiting planets, and (2) the misalignment of the ultra-short-period planet, we perform a Monte Carlo study of the companion parameters space between (0, 90) degrees mutual inclination with the starting plane of inner planets and a semi-major axis of (0.1, 2) AU, by drawing a and i uniformly between those bounds and then evolving the system forward in time for 10,000 years under the effect of a $J_2 = 10^{-7}$. In Figure 7.15 we plot two example outcomes. We note that the 10,000 year integrations are not long enough to resolve the full secular cycle of the system; see Section 7.8.4 for a discussion of how this might be a good extension to request in revisions.

In Figure 7.16, we plot the possible parameter space that meets the following specific criteria:

- The plane of outer 3 validated planets (b, c, d) reside in a plane with a width of inclination of less than two degrees for the entire integration time.
- The median of the misalignment between the innermost planet, K2-266 b, and the plane of outer transiting planets is greater than 14 degrees.

as computed by both secular and N-body methods. The result is plotted in Figure 7.16. We note that the secular solution spans a slightly larger parameter space, but the general area is the same for both methods: companions with semi-major axis between 0.5 and 0.7 AU and inclinations spanning the majority of the range of inclinations succeed in reproducing the observed geometry. This region is defined by two boundary conditions: first, the companion must be sufficiently distant that it does

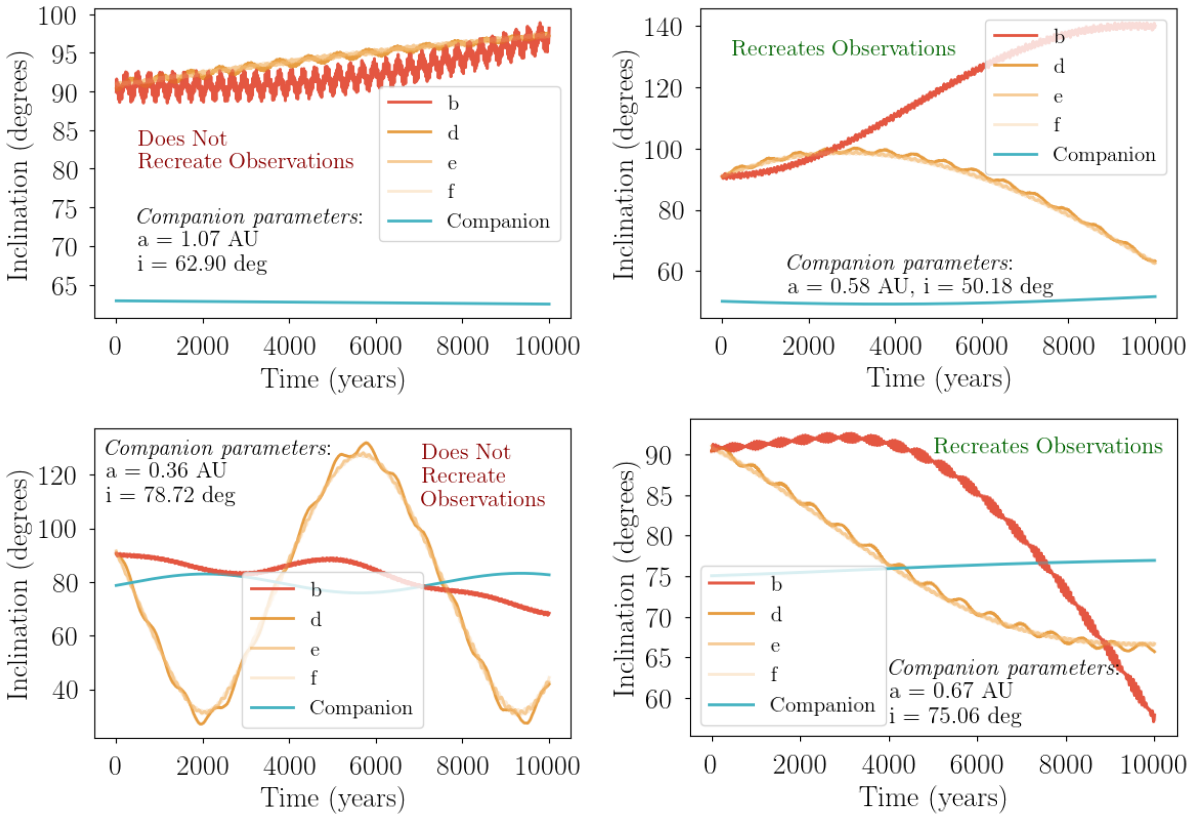

Figure 7.15 Sample N-body Integrations with a Saturn-mass Companion. (left panels) Some companion parameters do not recreate the observed observations due to (top left) a failure to misalign the ultra-short period planet or (bottom left) an inability to keep the outer transiting planets as coplanar as they are observed to be, while others (right panels) do reproduce both the compactness of the outer transiting planets and their misalignment with the ultra-short-period planet. The parameters of each tested companion are marked on the plot. As evident from the plots, longer integrations are required to fully resolve the parameters space in which companions could reside to recreate the observed system.

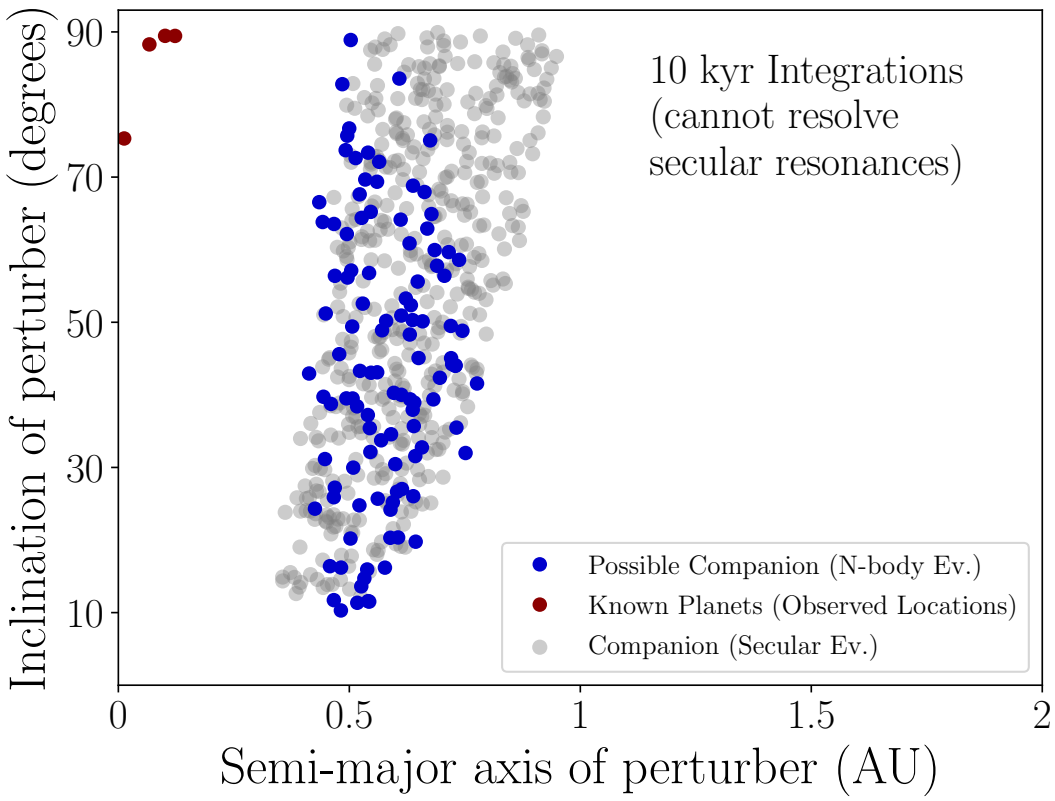

Figure 7.16 Possible Parameter Space for a Saturn-Mass Companion. The measured planet parameters of K2-266 are plotted as red points, while the companion parameters computed as allowed by Monte Carlo N-body (blue) and secular (grey) models are plotted as points. These solutions were generated with 10kyr integrations for both methods.

not perturb the outer transiting planets out of a narrow plane of inclination space; second, it must be close enough that it causes those same planes to experience (coherent) inclination oscillations. For all companions plotted here, the coupling with K2-266 b (the USP) is weak compared to K2-266 b's coupling with the stellar quadrupole moment, leading to its inclination evolution being incoherent with the outer plane of transiting planets.

7.8.3 Implications

The results of Dai et al. (2018) show that planets with ultra-short orbital period populate a larger fraction of the 'transiting' range of inclinations than do planets with slightly longer periods. In inclination space, the outer system is planar, while inner systems in comparison tend to be more puffy and fills the full allowable transiting parameter space. K2-266 fits this paradigm: K2-266

with its grazing transit resides at the absolute maximum mutual inclination that is still observable, while the outer system is very compact in vertical space.

Some authors have proposed dynamically hot mechanisms for generating these ultra-short-period misaligned planets, such as secular chaos (Petrovich et al., 2018), which requires significant eccentricities on the other nearby planets. The mechanism presented in this chapter provides the observed misalignment, reproduces the observed compact nature of the outer transiting planets, and does not require the excitation of eccentricity for any planets. Instead, our proposed mechanism functions via decoupling the timescales of the inclination evolution for the outer transiting planets (which are coupled strongly to the companion) and the ultra-short-period planet (which is coupled strongly to the stellar quadrupole field).

This mechanism could also be at play in other systems hosting ultra-short-period misaligned planets with multiple other transiting planets, a class of system only recently being discovered. Rodriguez et al. (2018c) provided the first such discovery, and Quinn et al. (2019) detected a potential second such system, with hosts five total planets / candidates with an ultra-short period super-Earth at 0.52 days and 72.80 degrees inclination. The existence of companions could explain the mutual inclinations in both of these systems.

7.8.4 Caveats

The majority of the integrations run in this section were only 10,000 years, which is not long enough to resolve secular resonances or even full secular cycles for most companions. To fully recover the long-term secular cycles, we probably need to run 100,000 year integrations at the least, with longer integrations being preferable but computationally difficult.

In this thesis, we have only tested a $0.3 M_{jup}$ companion. It would be useful to try other values for the mass of the companion and observe how the resultant parameter space changes as a result. We could also derive an analytic expression for the allowed companion parameter space.

We used the median values of the posteriors and fixed the eccentricities to 0 in order to save on computation time. If the true planet parameters are slightly different from those used, the location of the allowed parameter space for companions will vary. Similarly, if the companion mass is different that the masses used here, the location of its (a,i) will change as well. This work

demonstrates that a companion may cause the observed effects, but makes no guarantees about the particular parameters of the companion.

CHAPTER VIII

The Dynamical Evolution of the Most Extreme TNOs in the Presence of Planet Nine

Results in this chapter were published in: ***Becker, J. C.**, Adams, F., Khain, T., Hamilton, S., & Gerdes, D. "Evaluating the Dynamical Stability of Outer Solar System Objects in the Presence of Planet Nine." 2017, The Astronomical Journal, 154, 61* and are presented here with minor revisions.

8.1 Introduction

In our solar system, a large population of small, rocky objects resides beyond the orbit of Neptune, and the collective structure of this population is anomalous, exhibiting trends unexplained by random chance. Many of these objects appear to occupy a region close to the plane containing the eight known planets, leading to this region being called the Kuiper Belt. The existence of these objects has implications for the formation mechanism of our solar system; however, we have yet discovered only a small fraction of the objects orbiting beyond Neptune. Since the turn of the century, many new objects have been discovered in the Kuiper Belt. The subset of objects orbiting outside of Neptune's orbit are called Trans-Neptunian objects (TNOs), and they often have dynamically interesting orbits. In particular, some of these objects have large semi-major axes and large perihelion distances, including, for example, Sedna (Brown et al., 2004), 2004 VN_{112} (Becker et al., 2008), 2010 GB_{174} (Chen et al., 2013), and 2012 VP_{113} (Trujillo & Sheppard, 2014).

When Trujillo & Sheppard (2014) reported the discovery of 2012 VP_{113}, they also noted a curious clustering in argument of perihelion for the population of TNOs with high-a, high-q orbits.

The authors proposed that the high-q orbits could be generated in three ways: first, by the ejection of a solar system body that left behind the observed clustering as a signature of its ejection; second, through a stellar fly-by encounter that perturbed the orbits of some TNOs into their current configurations (Morbidelli & Levison, 2004), where such interactions are relatively common in the birth cluster (Li & Adams, 2015c); third, through the presence of an additional planet in the solar system. Notably, this third mechanism could also explain the clustering of this population of TNOs, as the proposed ninth planet's repeated secular interactions with the shorter-period TNOs could force the TNOs to keep their ω confined to be near either 0 degrees or 180 degrees (for example, this could occur via the Kozai mechanism).

Batygin & Brown (2016a) also suggested the existence of an additional planet (Planet Nine), which is differentiated from the potential planet discussed in Trujillo & Sheppard (2014) in the way it interacts with the TNOs. The Batygin & Brown (2016a) version of Planet Nine functions by explaining both the apsidal and ascending node alignment of a selection of objects in the Kuiper Belt. The objects under consideration in Batygin & Brown (2016a) were two overlapping sets of objects: first, those that have perihelion distance $q > 30$ AU and semi-major axis $a > 150$ AU, while being dynamically stable in the presence of Neptune; second, any objects which have $q > 30$ AU and semi-major axis $a > 250$ AU, all of which exhibit clustering in ϖ (when ϖ is defined as the longitude of perihelion, $\varpi = \omega + \Omega$). The orbit for Planet Nine presented in Batygin & Brown (2016a) was a rough estimate, with semi-major axis $a = 700$ AU, eccentricity $e = 0.6$, inclination $i = 30$ degrees, longitude of ascending node $\Omega = 113$ degrees, and argument of perihelion $\omega = 150$ degrees. The authors estimated the planet to have a mass of roughly 10 Earth masses, but all of these orbit predictions were noted as approximate. This mass estimate was supported in a follow-up effort by the predicting authors (Brown & Batygin, 2016), which placed constraints on the orbital elements of the potential Planet Nine by using N-body simulations to determine which Planet Nine realizations lead to clustered TNOs in simulations. In this work, the authors determined that a 10 Earth mass Planet Nine was more likely to recreate the observed clustering than a 20 Earth mass Planet Nine.

The possibility of a new planet has led to a great deal of recent work, e.g., to evaluate the likelihood of Planet Nine's existence given the known properties of the Solar System. For example,

Fienga et al. (2016) and Holman & Payne (2016b) examined the measured Earth-Saturn distance, and determined that Planet Nine is likely to have a true anomaly near 117 degrees (based on the upper limit to the amplitude of the residuals for that distance measurement). In complementary work, Malhotra et al. (2016a) evaluated the potential resonant behavior that Planet Nine could invoke in the population of long-period TNOs, and predicted that Planet Nine should have a semi-major axis of $a = 665$ AU in order to support stability-boosting resonances. Other authors (Lawler et al., 2016; de la Fuente Marcos et al., 2016) have examined the dynamical effects that Planet Nine would have on the populations of objects that exist in the Solar System. Finally, additional work was carried out to explain how Planet Nine would fit into our existing picture of the Solar System. For example, multiple groups found that the existence of such a ninth planet can be invoked to explain the six-degree obliquity of the sun (Bailey et al., 2016a; Lai, 2016; Gomes et al., 2016). Several previous works have also suggested that the mechanism by which Planet Nine shapes the orbits of the TNOs may be orbital resonances (Batygin & Brown, 2016a; Beust, 2016; Malhotra et al., 2016a; Millholland & Laughlin, 2017).

The conclusion in Batygin & Brown (2016a) was based only on six of the (at the time) thirteen discovered extreme TNOs. These six TNOs (2004 VN_{112}, 2007 TG_{422}, 2010 GB_{174}, 2012 VP_{113}, 2013 RF_{98}, and Sedna) were chosen because they exhibit clustering in ϖ and have $a > 250$ AU, meaning they are expected to be influenced by Planet Nine. Sheppard & Trujillo (2016) also announced the discovery of two new objects (2014 SR_{349} and 2013 FT_{28}) that also fit into the class of objects used by Batygin & Brown (2016a) to predict the existence of Planet Nine. In order for Planet Nine to be capable of forcing the orbits of the TNOs into aligned configurations, the TNOs must remain dynamically stable on secular timescales, to allow apsidal alignment to occur. Objects whose orbital elements are affected by short-period scattering events can be used to understand the scattering event itself, but not the long-period, secular effects in the system. Numerical simulations in Batygin & Brown (2016a) and Sheppard & Trujillo (2016) determined that some of the high semi-major axis ($a > 250$) objects' orbits change significantly over 1 Gyr timescales. They used numerical simulations to evaluate the stability of these bodies in the presence of the four giant planets, and found that some objects were not dynamically stable. If two of the six objects used to infer the existence of Planet Nine are dynamically unstable (for example, being susceptible to

scattering events) in the presence of Neptune, it is less likely that those objects could reside in their current orbits long enough to be influenced by Planet Nine and become apsidally aligned via that mechanism. de la Fuente Marcos et al. (2016) also found that the six aforementioned extreme TNOs can become dynamically unstable on relatively short timescales in the presence of both Neptune and the nominal Planet Nine, which could potentially prevent the observed apsidal alignment from occurring on secular timescales.

Of course, dynamical stability is a function of timescale. The objects with perihelion distances in the range 30-40 AU can be termed a part of the scattered disk (Lykawka & Mukai, 2007). The objects in this population are characterized by repeated (potentially scattering) interactions with Neptune (Nesvorný & Roig, 2001). An integration of the solar system run for an indefinite amount of time (without the presence of Planet Nine) will eventually lead to all objects in the scattered disk leaving the solar system. However, our solar system is only 4.5 Gyr old, and it does not take this long for Planet Nine to align the TNOs into the pattern reported in Batygin & Brown (2016a). For this reason, 'dynamical stability' in this work refers to objects which remain in orbits comparable to their current orbits for 4.5 Gyr.

Sheppard & Trujillo (2016) reported two new TNOs in the regime of interest for consideration of Planet Nine, and the population of discovered TNOs and Kuiper Belt Objects is rapidly growing. The Canada-France Ecliptic Plane Survey (Petit et al., 2011), which ran from 2003–2007, detected 169 TNOs with a preference for larger TNOs (size $R > 100$ km). A 32-square-degree survey running from 2011–2012 by Alexandersen et al. (2014) detected 77 TNOs. The Outer Solar System Origins Survey (Bannister et al., 2016a), which is currently in progress, has thus far detected 85 TNOs. The Panoramic Survey Telescope and Rapid Response System (Pan-STARRS) is intended to discover comets and asteroids (particularly near-Earth objects), but has also found Kuiper Belt Objects (Chen et al., 2016a) and giant planet Trojans (Horner et al., 2012; Guan et al., 2012; Lin et al., 2016a). In addition to these dedicated Solar System searches, cosmological searches also allow for the serendipitous discovery of foreground TNOs. For example, the Dark Energy Survey has experienced great success in discovering TNOs and other solar system objects (Gerdes et al., 2016a; Dark Energy Survey Collaboration et al., 2016a), including a new dwarf planet (Gerdes et al., 2017a).

This ever-growing population of TNOs will allow for increasingly stronger constraints on the possible orbital elements of Planet Nine and its current location in the Solar System. These objects will also provide a clearer picture of the dynamical regimes of bodies in the outer Solar System, where these orbits are sculpted by Neptune on the inside and could be influenced by Planet Nine from the outside.

In this chapter, we use as our sample the TNOs with $a > 250$ AU from Batygin & Brown 2016a and two newly discovered objects (announced in Sheppard & Trujillo, 2016) expected to be dynamically stable in the presence of the solar system objects. We use N-body techniques to simulate the behavior of these objects in the presence of Planet Nine to place limits on the possible orbital elements (a, e) of Planet Nine. In Section 8.2, we describe the sets of simulations carried out in this work and present some results. Our treatment uses a Monte Carlo sample of 1500 Planet Nine realizations, and thus extends most previous work, which generally considered only a single nominal orbit or small number (generally $N \leq 3$) of potential orbits. The simulations enable us to estimate the mean lifetime of each TNO in the presence of each of the Planet Nine realizations under consideration. In Section 8.3, we develop and provide a posterior probability distribution for the most likely values (a, e) for the Planet Nine orbit, given that we observe the eight TNOs in their current orbits. In Section 8.4, we discuss the different dynamical instability mechanisms contributing to the potentially shortened lifetimes for the TNOs, and identify some interesting differences between objects in our sample. In Section 8.5, we explore the relationship between the period of our injected Planet Nine and the period of each TNO, and show that TNOs living in dynamically stable configurations tend to attain integer period ratios with Planet Nine. Remarkably, some TNOs do not remain in the same commensurability for their entire lifetimes; instead, they transition between multiple near-resonant locations. The chapter concludes, in Section 8.6, with a summary of our main results and a discussion of avenues for future study.

8.2 Numerical Simulations of TNO orbital evolution in the presence of Planet Nine

Brown & Batygin (2016) provided a relative posterior probability distribution for the (a, e) of

Planet Nine. This posterior was constructed using clustering arguments of the same type that were used in Batygin & Brown (2016a) to predict the existence of Planet Nine. The logic used in both these works can be summarized as follows: the observed TNOs' orbits are aligned in physical space (the longitudes of perihelion ϖ and longitudes of ascending node Ω are confined to a narrow range in angles instead of uniformly populating all allowed angles), and the probability of this occurring by chance is low, even accounting for potential bias in the observations. Numerical N-body simulations of a selection of test-particles at varying orbital radii do not recreate the observed clustering unless Planet Nine is included in the simulations; even then, some orbits of Planet Nine are more likely to recreate the observed clustering than others. From a suite of numerical integrations, Brown & Batygin (2016) predicted the combinations of (a, e) that were most likely to allow a population of test particles that exhibited the observed clustering in longitude of perihelion.

The physical orientation of orbits is not the only observed physical property that can be measured from the known TNOs. The most basic property that the observed TNOs share is orbital stability: although merely seeing the TNO orbits today does not ensure that they are dynamically stable in those current orbits, the observed (Trujillo & Sheppard, 2014; Batygin & Brown, 2016a) physical clustering of the orbit directions suggests that the orbits have been dynamically stable for a long enough time for this alignment to develop. Whether or not the aligning agent is the theorized Planet Nine, this alignment would have to have taken place over secular timescales, suggesting that these TNOs must have been dynamically stable over such timescales.

The dynamical stability of these objects is thus a fundamental and necessary property. As such, any allowable Planet Nine would have to allow the continued dynamical stability of the TNOs over secular and solar system lifetimes. To evaluate the likelihood of any particular realization of Planet Nine, we must evaluate the lifetimes of the TNOs in the presence of said Planet Nine.

8.2.1 Numerical Methods

To determine how the lifetimes of the TNOs vary in the presence of different combinations of the semi-major axis and eccentricity of Planet Nine, we run a large number of numerical N-body integrations, each including one potential realization of Planet Nine and the population of TNOs we are testing. This population includes the six TNOs considered in Batygin & Brown (2016a) (2004

VN_{112}, 2007 TG_{422}, 2010 GB_{174}, 2012 VP_{113}, 2013 RF_{98}, and Sedna) and two additional objects discovered by Sheppard & Trujillo (2016) (2014 SR_{349} and 2013 FT_{28}) that appear to fit in the same dynamical class as the previous six. The orbital elements of all eight objects in our sample are reported in Table 8.1. The objects we consider in this work are those with semi-major axis $a > 250$ AU and perihelion distance $q > 30$ AU. This is a different sample, with a stricter semi-major axis cut, than was originally used in Trujillo & Sheppard (2014) to identify the clustering effect (Trujillo & Sheppard, 2014, used $a > 150$ AU). We limited the objects considered in this chapter to those with $a > 250$ AU for three reasons: first, these are the objects which are found in Batygin & Brown (2016a) to exhibit both confinement in the longitude of perihelion and in the longitude of ascending node; second, these large-a objects exhibit a variability in semi-major axis (Batygin & Brown, 2016a) that can potentially lead to dynamical instability; third, we expect the dynamics of these long period orbits to be dominated by Planet Nine rather than by Neptune (Sheppard & Trujillo, 2016).

We choose to explore the effect of Planet Nine's a and e because the orbital angles of Planet Nine are directly oppositional to those of (all but one of) the discovered ETNOs, and the current location of Planet Nine can be estimated using other methods (for example, Fienga et al., 2016; Holman & Payne, 2016b). For this work, the inclination and orbital angles of Planet Nine were taken to be the nominal values presented in Batygin & Brown (2016a). The robust consideration of a wider range of angles is beyond the scope of this work, but we report a basic reproduction of the experiments of this work while allowing the orbital angles to vary in Appendix 9.9. We choose to fix these angles for the remainder of the main manuscript for two reasons: first, to examine the effect of (a, e), we take a cross section in the other angles in order to remove the degeneracies that would be imposed by allowing these angles to vary; second, considering all orbital angles would be too computationally intensive, so we choose the best values we can and proceed under the assumption that altering these angles will not change the broad trends of the results.

To evaluate the dynamical stability (and thus, expected mean orbital lifetimes) of these eight TNOs in the presence of Planet Nine, we ran 1500 numerical N-body integrations using the hybrid symplectic and Bulirsch-Stoer (B-S) integrator built into `Mercury6` (Chambers, 1999b), and conserved energy to 1 part in 10^{10}. We replaced the three inner giant planets (Jupiter, Saturn

and Uranus) with a solar J2 (as done in Batygin & Brown, 2016a). We included Neptune as an active particle because the orbital motion of Neptune may induce scattering or resonant effects on the TNOs, potentially leading to dynamical instabilities (rapid, drastic orbital evolution for the TNOs). For each realization, we included each TNO with orbital elements drawn from observational constraints, sampling each orbital element from reported 1σ errors. Then, we integrated each of the 1500 realizations forward for 4.5 Gyr using computational resources provided by Towns et al. (2014). For data management, we used the `pandas` python package (McKinney, 2010).

Some of the TNOs (2013 RF_{98}, for example) have very rough observational priors. Since we are sampling from observational priors in the orbital elements we assign to these small bodies, the lifetimes of these objects (compared to Sedna, whose orbital properties are much better constrained) include the degeneracy of both Planet Nine and also of the TNO itself. This leads to smoothed distributions, which are effectively convolutions of the true lifetimes with an uncertainty kernel including the errors of the measured orbital properties of the object.

The final result of these simulations is 1500 measures of dynamical lifetime for each object, which can be plotted on a (a, e) grid as shown in the top panel of Figure 8.1 (which shows the points for 2012 VP_{113}). We do not expect the lifetimes to form a smooth function for several reasons: first, for each object, we draw orbital parameters from observational priors, resulting in some expected scatter in results for even a single Planet Nine realization; second, chaotic effects will cause scatter in outcomes between realizations. For that reason, we must run enough simulations that we can treat the averaged value from all results near a Planet Nine (a, e) point as a good average of the behavior that a given Planet Nine would engender.

We construct the contour plots in Figure 8.2 and Figure 8.4 by using a polyharmonic spline (from Jones et al., 2001) to smooth and interpolate between the points generated by our Monte Carlo simulations. We investigated the effects of different interpolation methods, and found that for our sample size ($N \sim 1500$ realizations), the interpolation scheme does not drastically affect the final result. However, it is important to note that when we attempted to use $N \sim 100$ realizations, the results varied drastically between different interpolation schemes. Since our sample size does not show such variations between methods, we consider the (a, e) parameter space well-sampled. Figure 8.1 demonstrates the smoothed two-dimensional lifetime function and provides a comparison

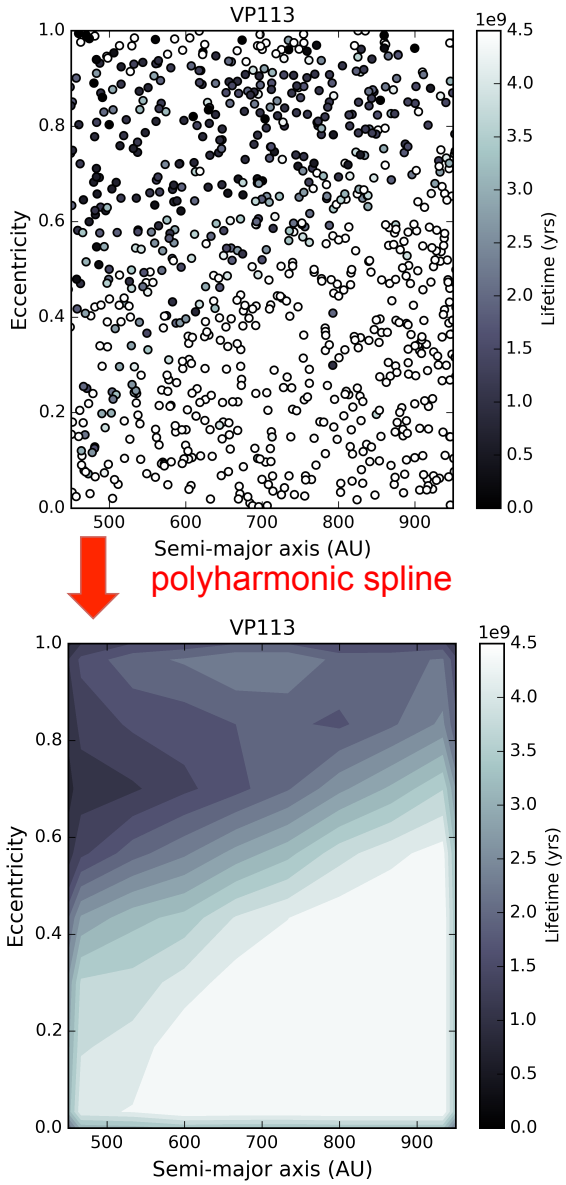

Figure 8.1 Converting Simulation Results to a Stability Heat Map. (Top panel) The points for one object in our sample, 2012 VP_{113}, which are color coded by the amount of time the system remained dynamically stable. (Bottom panel) The same points, turned into a contour plot by use of a polyharmonic spline. The contour plot allows for easier comparison of the posterior for each object, and visualizes the interpolation up for the Monte Carlo sampling.

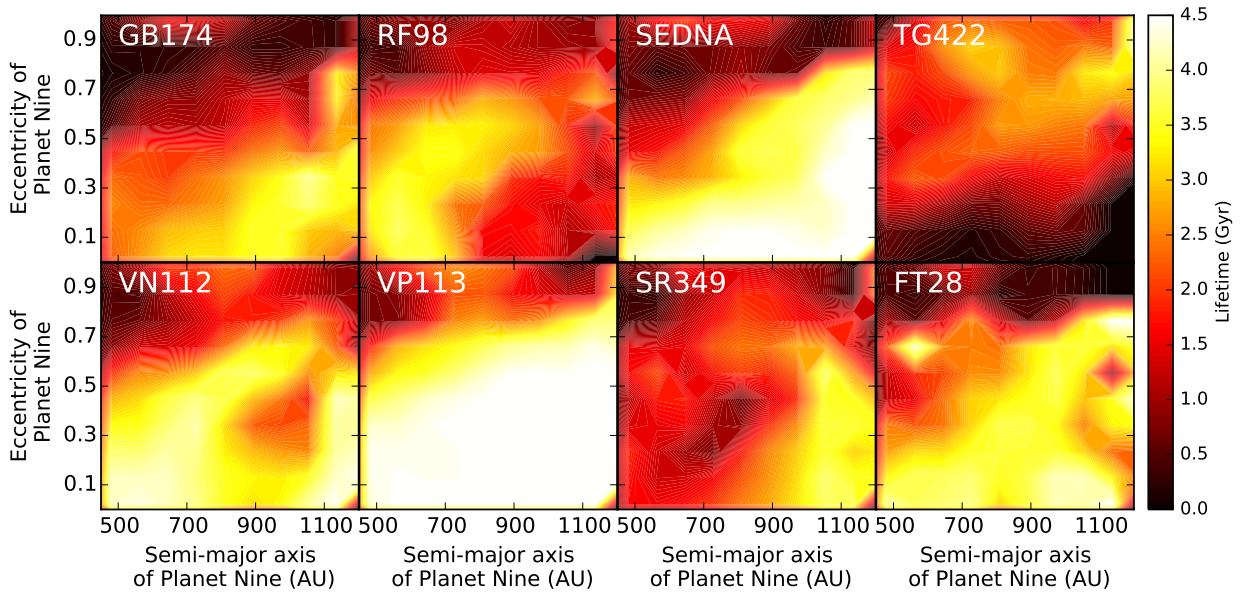

Figure 8.2 Lifetimes of TNO by Planet Nine Properties. Individual contour plots of the lifetimes of each of the eight TNOs considered. The lifetime plots do not exhibit the same general trends, indicating that the different objects may be members of different dynamical classes of objects. Table 8.1 presents the complete list of their orbital properties; the title of each subplot here is the short name of the object it portrays.

to the raw points for one object (2012 VP_{113}) in our sample. Analogous plots (not presented) can be constructed for each of the eight objects in our sample.

8.2.2 Numerical Results

The results of the simulations are plotted in Figure 8.2, which presents contour plots for the expected orbital lifetimes of the eight TNOs in the presence of various realizations of Planet Nine. The main results that we get from this experiment fit into three categories: we affirm the potential stability of all eight TNOs in the presence of Neptune and Planet Nine, we find that different TNOs prefer different parameter spaces of Planet Nine, and we examine the fate of the TNOs that do go dynamically unstable.

Stability of TNOs. For all objects in our sample, there are realizations of Planet Nine that allow them to remain dynamically stable for the lifetime of the solar system. Here, dynamical stability requires that a TNO remain within 100 AU of its starting orbit, and not experience collisions with the planets or central body. This value of 100 AU was chosen from examination of

Object	a **(AU)**	e	i **(deg)**	ω **(deg)**	Ω **(deg)**	**% Stable**	$\bar{\delta t}$[1]
2003 VB_{12}	499	0.85	11.92	311.5	144.5	45.3%	300 Myr
2004 VN_{112}	318	0.85	25.56	327.1	66.0	28.4%	625 Myr
2007 TG_{422}	482	0.93	18.59	285.8	113	14.6%	1.24 Gyr
2010 GB_{174}	371	0.87	21.54	347.8	130.6	17.9%	1.03 Gyr
2012 VP_{113}	261	0.69	24.06	292.8	90.8	56.5%	9 Myr
2013 RF_{98}	325	0.88	29.61	316.5	67.6	18.7%	1.01 Gyr
2013 FT_{28}	310	0.86	17.3	40.2	217.8	19.9%	709 Myr
2014 SR_{349}	288	0.84	18.0	341.3	34.8	18.1%	917 Myr

Table 8.1 Stability of ETNOs in Presence of Neptune and Planet Nine. A list of the TNOs used for the dynamical survey. The dynamical stability of each object was evaluated using a suite of numerical N-body simulations. The orbital elements of each object provided in this table are the best fit observational values. In the simulations, the orbital elements were drawn from the 1σ distribution for each realization of each object. Also provided in this table is the percentage of realizations of each object that are dynamically stable. It is important to note that this percentage reported (which is the percentage of realizations of each object that are dynamically stable) is marginalized over all realizations of Planet Nine included in the simulations, and thus the exact percentage is not meaningful. What is meaningful is that the percentages are all non-zero, indicating that for a selection of orbital parameters and Planet Nine realizations, each object in our sample can be dynamically stable. [1]: $\bar{\delta t}$ is the difference in median lifetime (over all Planet Nine realizations) between two cases: case one being when the definition of dynamical instability does not include migration, and case two being when migration of more than 100 AU constitutes dynamical instability. Larger values indicate that TNOs are susceptible to significant ($\delta a > 100$) migrations in semi-major axis.

the time-evolution of the bulk set of TNOs. We find that when orbits vary by less than 100 AU, the objects are generally confined to a network of mean motion resonances (MMRs), an outcome that we describe in Section 8.5.

When orbits change by more than 100 AU, they potentially change dynamical class. The criteria in Batygin & Brown (2016a) included the cut that $a_{TNO} > 250$ AU, and 100 AU of migration inwards would change this dynamical classification of 5 of the 8 TNOs considered in this work. Since this choice of cutoff is somewhat arbitrary, we present in Table 8.2 the frequency of final dynamical outcome for each TNO in our sample. Migration is in outcome in between 7%-30%, depending on the TNO under consideration, so future work that uses a different criterion for migratory instability can expect variation from our results of this magnitude.

Table 8.1 provides a 'Percent Stable' column, which gives for each object the percentage of our

1500 realizations (which all have different a, e for Planet Nine) which allowed that object to remain dynamically stable for the entire 4.5 Gyr simulation. Since our simulations also include Neptune as an active particle, all of these objects *can* be dynamically stable in the presence of both Neptune and Planet Nine. Notably, 18 of our 1500 realizations of Planet Nine allowed all eight TNOs to remain dynamically stable for 4.5 Gyr. The 18 trials that allowed all tested TNOs to survive had semi-major axes varying between 600 AU and 800 AU and eccentricities between 0.35 and 0.55. The small sample ($N \sim 18$) that allowed all TNOs to survive limits any further conclusions based on their orbital parameters. Sheppard & Trujillo (2016) found that 2007 TG_{422} and 2013 RF_{98} were both dynamically unstable in the presence of Neptune, but they did not include a potential Planet Nine in their integrations. We find that 2007 TG_{422} and 2013 RF_{98} have stability percentages of less than 20%, making them less stable on average than, for example, 2012 VP_{113}. However, with a dynamically favorable realization of Planet Nine, both of these objects can remain dynamically stable for a solar system lifetime. This result, combined with the result from Sheppard & Trujillo (2016) that these two objects are not dynamically stable in the presence of Neptune alone, suggests that Planet Nine can boost the orbital stability of these objects.

Variations between behavior of different TNOs. For each object in our sample, different realizations of Planet Nine lead to differing object lifetimes. This is shown in Figure 8.2, which plots the lifetime of each TNO as a function of the semi-major axis and eccentricity of Planet Nine. These stability maps look very different for different objects. For example, large-a, low-e orbits lead to a longer lifetime for 2012 VP_{113}. For this object, shorter object lifetimes occur if Planet Nine has a shorter perihelion distance (lower a or higher e). This is intuitive. In contrast, 2007 TG_{422} is dynamically unstable in the presence of these same long perihelion-distance objects that 2012 VP_{113} preferred. Since different objects prefer different regions of Planet Nine's possible parameter space, a better understanding of the constraints they provide can be obtained by considering all objects simultaneously. We will discuss how this can be done, as well as find constraints using our results thus far, in Section 8.3.

Fate of the TNOs. To construct the lifetime contours in Figure 8.2, we defined the lifetime of an object as the length of time it lived in our simulation without significant alterations in its orbit. We defined significant alterations in orbit to be any of the following: (1) migration in semi-major

Object	Migration > 100 AU	Close Encounter	Collision w/ Central Body	Ejection	Survive 4.5 Gyr
2003 VB_{12}	16.0%	19.3%	0.1%	19.3%	45.3%
2004 VN_{112}	14.9%	30.6%	0.7%	25.4%	28.4%
2007 TG_{422}	29.3%	32.9%	0.0%	23.1%	14.6%
2010 GB_{174}	17.8%	31.2%	0.4%	32.7%	17.9%
2012 VP_{113}	7.1%	21.1%	0.5%	14.8%	56.5%
2013 RF_{98}	14.0%	40.6%	0.0%	26.7%	18.7%
2013 FT_{28}	17.2%	30.7%	0.0%	32.2%	19.9%
2014 SR_{349}	22.0%	39.5%	0.7%	19.8%	18.1%

Table 8.2 Outcomes of ETNOs in Presence of Neptune and Planet Nine. For each TNO used in the dynamical simulations, the percentage of integrations that ended in each major instability outcome.

axis by more than 100 AU from the starting orbit of the object, (2) collisions or a close encounter (defined as passing within 3 Hill radii of the larger body) with Planet Nine or Neptune, (3) collision with the central body, and (4) ejection from the solar system. It is clear that each of these criteria have different thresholds for importance, as well as different outcomes for the object. In particular, while ending methods (2-4) result in a violent end for the TNO, method (1) does not necessarily remove the TNO from the solar system: instead, the TNO's orbit is significantly altered, but the TNO may continue to be a part of the solar system, merely in a different location. Numerical simulations allow these effects to be disentangled. In particular, we find that the two objects (2007 TG_{422} and 2013 RF_{98}) that do not prefer the high-a, low-e realizations of Planet Nine tend to exhibit the migratory end in those realizations, rather than experiencing a violent instability. We will further discuss this effect in Section 8.4.

8.3 Deriving constraints on the orbital elements of Planet Nine

Given the predicted lifetime distributions constructed in the previous section, we can constrain the orbital properties of Planet Nine by determining which (a, e) combinations allow the continued dynamical stability of the observed clustered TNOs. We make an assumption here that in order for the TNOs to attain their observed ϖ clustering, they must have remained in their currently observed orbits for at least secular timescales. This would require those orbits being dynamically

stable in the presence of Planet Nine. The process of constructing these constraints will be detailed in this section.

8.3.1 Bayesian inference towards a posterior probability distribution for the orbital elements of Planet Nine

The ultimate goal of our dynamical stability analysis is to determine the posterior probability distribution for the orbital elements (a, e) of Planet Nine. This will serve as a check and supplement to previous orbital posteriors in the literature, which were estimated using different techniques. We define A to be the orbital elements of Planet Nine, T_i to be the expected dynamical lifetime of the i^{th} TNO, and I to be all prior information that we can incorporate into our models (for example: the fact that Planet Nine exists is a prior we impose, as are the observational errors of the discovered TNOs, which lead to uncertainties on their orbits). With these definitions, the property we wish to measure is $P(A|T_i, I)$, the probability of A (Planet Nine's orbital elements), given the lifetimes of the observed TNOs and our other knowledge. This posterior probability function can be represented using Bayes' Theorem as follows:

$$P(A|T_i, I) = \frac{P(T_i, I|A)P(A)}{P(T_i, I)} \tag{8.1}$$

However, upon inspection of this expression, there is one clear problem: $P(T_i, I|A)$ requires knowledge of T_i, the actual lifetimes of the observed TNOs in our solar system. This is not a property that can be measured. As an added difficulty, the prior information encapsulated in I includes large uncertainties on the orbital elements of the observed TNOs.

To overcome this difficulty, we define a new parameter, D_i. D_i is defined to be the computed lifetimes of the *observed* TNOs, where these lifetimes are marginalized over the observational priors of the TNOs' orbital elements and our other uncertainties that were before folded into I. Although we cannot measure the true lifetimes T_i, we have constructed TNO lifetime estimates D_i as they depend on our priors by using numerical N-body simulations. These simulations are described in the previous section, and a visualization of the derived lifetimes is presented in Figure 8.2.

Now, we can rewrite the Bayesian statement of our posterior in terms of this new variable:

$$P(A|D_i) = \frac{P(D_i|A)P(A)}{P(D_i)} \tag{8.2}$$

when $P(D_i|A)$ is the probability of getting the numerically measured lifetimes conditional on the orbital elements of Planet Nine, $P(A)$ is our priors on Planet Nine's orbital elements, and $P(D_i)$ is the occurrence probability of our computed lifetimes. Of course, we have N TNOs to consider in this analysis, so what we really need to compute is the posterior probability distribution as it depends on the numerically estimated lifetimes of all N objects:

$$P(A|D_1, D_2...D_N) = \frac{P(D_1, D_2...D_N|A)P(A)}{P(D_1, D_2...D_N)},$$

which, using the definition of Bayes' theorem, reduces into the form:

$$\begin{aligned} P(A|D_1, D_2...D_N) = \frac{P(D_1) \times P(D_2) \times ...P(D_N)}{P(D_1, D_2...D_N)} \times \\ \frac{P(D_1|A) \times P(D_2|A) \times ...P(D_N|A)}{P(A)^{N-1}} \end{aligned} \tag{8.3}$$

We can say that $D_1, D_2...D_N$ are conditionally independent, since we treated all TNOs as test particles in the simulations used to generate $\{D_i\}$. Since each TNO has zero mass in the simulations, removing one will not alter the lifetime maps for the other objects. As a result, the first term of the right-hand side of Equation 8.3 can be treated as a normalization coefficient, which is needed only when comparing different versions of $P(A|D_1, D_2...D_N)$ constructed with different numbers N of TNOs. We need only a relative posterior probability distribution, which will identify the most likely realization of Planet Nine and identify the parameter space in which it is likely to reside.

The final result we need to compute, then, is:

$$P(A|D_1, D_2...D_N) = a\frac{\prod_{n=1}^{n=N} P(D_i|A)}{P(A)^{N-1}} \tag{8.4}$$

when D denotes the lifetime of a TNO in the presence of Planet Nine as measured from simulations, i denotes the TNO considered, A denotes the orbital elements (a, e) of Planet Nine. $P(A)$ is

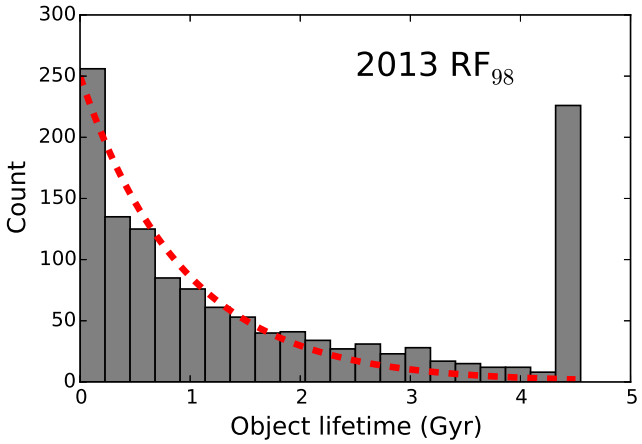

Figure 8.3 Measured Lifetimes for 2013 RF98. A histogram of lifetimes (measured from time $t = 0$ at the start of the N-body simulation) for 2013 RF_{98}. Barring a pile-up at lifetimes of $t = 4.5$ Gyr (corresponding to realizations that were stable for the duration of the simulation; these were not included in the fit), the decay appears to have an approximately exponential trend.

a known quantity, and $P(D_i|A)$ can be measured from the stability maps constructed using the N-body integrations.

8.3.2 Converting TNO lifetime maps to probability distributions

Equation 8.4, which can be used to construct our goal posterior probability distribution, requires $P(D_i|A)$ for each TNO in the sample. $P(D_i|A)$ is the probability of the TNOs' lifetimes as they depend on the orbital elements of Planet Nine. To compute this term, we must convert the lifetime maps presented in Figure 8.2 into probability distributions.

Each realization of Planet Nine will lead to a different time of dynamical instability (defined as the time at which an object experiences one of the four instability mechanisms described in Section 8.2.2), with some objects never experiencing dynamical instability. In Figure 8.3, we plot a histogram of the object lifetimes for 2013 RF_{98}, as derived from the 1500 numerical integrations run with varying realizations of Planet Nine.

Although the longer object lifetimes can intuitively be interpreted as corresponding to more likely realizations of Planet Nine, we would like to convert these lifetimes into a relative probability function. Since an exponential decay trend appears to be a good, empirical fit for the lifetimes of

an object marginalized over all integrations (regardless of the fact that the realization of Planet Nine varies between the different trials), we can fit a decay constant λ from the lifetime histogram for all decaying realizations of a single TNO:

$$f_{\text{decay}}(t) = C_0 e^{-\lambda t} \tag{8.5}$$

when $f_{\text{decay}}(t)$ is the fraction of realizations decaying at each time t, C_0 a normalization constant, and λ the decay constant to be fit. For each object in our sample, the histogram of instability times was fit with exponential curve using a simple Levenburg-Marquardt optimization scheme, with all objects that do not experience dynamical instability (which have lifetimes $t = 4.5$ Gyr) excluded from the fit. The results of this fit for 2013 RF_{98} are plotted in Figure 8.3. For this particular object, if we extend the exponential curve to infinite time, we expect only 0.4% of these dynamically stable objects to become dynamically unstable, indicating that the majority of objects that have not decayed after 4.5 Gyr are truly dynamically stable.

To construct a final probability distribution, we need to account for the fact that for each object, some fraction of trials were dynamically stable for the entire 4.5 Gyr integration length. For this reason, we construct a piecewise probability function for $P(D_i|A)$, the probability we get these lifetimes from our simulation given a particular set of A, Planet Nine's orbital elements:

$$P(D_i|A) = \begin{cases} N_s/N & \text{if } \mathrm{D}_i\text{=4.5 Gyr} \\ C_1 \times e^{-\lambda D_i} & \text{else} \end{cases} \tag{8.6}$$

when $P(D_i|A)$ is the probability of computing the object lifetime D_i for the ith TNO in the presence of a Planet Nine with orbital elements A, N_s the number of integrations for which the object did not experience dynamical instability, N the total number of integrations, λ the decay constant determined from the previous fit, and C_1 is a normalization constant of the form:

$$C_1 = \frac{N - N_s}{N} \times \left[\int_0^{4.5 \text{ Gyr}} e^{-\lambda t} dt \right]^{-1} \tag{8.7}$$

The substitution of Equation 8.6 into Equation 8.4 results in a final expression of the posterior

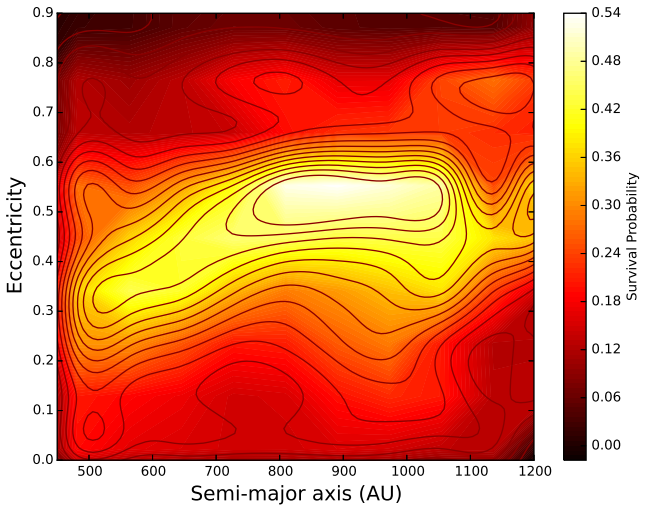

Figure 8.4 Overall Stability Posterior for the Semi-Major Axis and Eccentricity of Planet Nine. This posterior was constructed by taking a summation of the posteriors for each individual object, including the six objects used in Batygin & Brown (2016a) and the two new high-a, low-e objects from Sheppard & Trujillo (2016).

probability distribution $P(A|D_1, D_2...D_N)$. For the eight objects considered in this work, this final distribution is plotted in Figure 8.4. It is important to note that this process required multiple steps of normalization, which depend on $P(A)$, the priors, and the populations of TNOs used to derive constraints. Since we (by necessity) treated the objects used in this analysis as conditionally independent, the posterior presented in Figure 8.4 provides relative, rather than absolute, measures of the likelihood of each (a, e) realization of Planet Nine. The derived decay constant must be re-derived if different populations of TNOs or different orbits of Planet Nine are tested in the future; the values used in this work are particular to our sample of eight TNOs in the presence of our particular population of Planet Nines. For this reason, we do not provide the decay constants in this work, as they cannot be used for these objects in general but only for our particular choices of Planet Nine's priors.

8.3.3 The posterior probability distribution for Planet Nine's orbital elements

Figure 8.4 presents the final posterior probability distribution for Planet Nine's orbital elements (a, e), based on the observed dynamical stability of the eight TNOs considered in this work. This distribution provides a relative measure of the likelihood of differing combinations of Planet Nine's

semi-major axis and eccentricity. The nominal orbit of Planet Nine (700 AU, 0.6 eccentricity) appears to lie in a less preferred region, with slightly smaller eccentricities (0.3-0.4) being preferred. Remarkably, the large-a, low-e orbits appear to be excluded based on our dynamical stability arguments. This is roughly consistent with the posterior generated using clustering arguments, provided in Brown & Batygin (2016), which also preferred a middling eccentricity and excluded large-a, low-e iterations of Planet Nine.

8.3.4 Comparing our prediction of Planet Nine's Orbit with constraints derived via different methods

The posterior probability distribution we present in Figure 8.4 was generated using dynamical stability arguments. Specifically, Planet Nine realizations that allow the observed TNOs to remain dynamically stable are considered to be more likely than those that cause dynamical instabilities. Brown & Batygin (2016) also provided a probability map showing the most likely regions for Planet Nine based on the observed orbital alignment of the TNOs. In Figure 8.5, we compare the two probability distributions presented in Brown & Batygin (2016) to the distribution derived in this work (along with additional contours described below). For these distributions, we plot a single contour in Figure 8.5 using the value 1σ below the maximum probability of the distribution. The level of this contour is chosen so that the single contours visually reflect the highest probability regions for each posterior type. The choice of the (maximum - 1σ) level is representative, but by no means the only way to visualize the comparisons between the posterior types.

The regions showing the most overlap between the 10 $M_{\oplus}$ alignment result from Brown & Batygin (2016) and our dynamical stability result are those with a semi-major axis between 525–675 AU and an eccentricity of 0.40–0.55, and the region with a semi-major axis between 700–800 AU and an eccentricity of 0.25–0.35. A recent paper by Millholland & Laughlin (2017) also used dynamical stability arguments and resonance considerations to choose a best-fit (a, e) of (654 AU, 0.45). This point is also plotted in Figure 8.5 and appears to be consistent with the region showing overlap between both the dynamical stability results of this work and those of (Brown & Batygin, 2016).

The posteriors plotted in Figure 8.5 include four curves based on N-body simulations and

one analytical curve. The analytical curve encompasses the regime where the equation of motion $d\omega/dt \approx 0$. It is important to note that this analytic approximation is not a true analysis of the dynamics of the system, as the derivation (the complete form of which is presented in Appendix 8.7) assumes all bodies are coplanar, and solves for alignment rather than anti-alignment. Thus, this analytic model is more an order-of-magnitude estimate of the effect we expect to see, rather than a true prediction.

The functional form for $d\omega/dt$ is derived from the secular Hamiltonian, and assumes the form:

$$\begin{aligned}\frac{d\omega}{dt} \propto & \frac{3}{4M_c}\sum_{i=1}^{4} m_i a_i^2 (e^2-1)^{-2} a^{-2} \\ & -\frac{15}{16}\frac{m_9}{M_c}\frac{e_9}{e}\left(\frac{a}{a_9}\right)^4 \frac{\sqrt{1-e^2}}{(1-e_9^2)^{5/2}}(1-9e^2/4)\cos(\omega-\omega_9) \\ & -\frac{3}{4}\frac{m_9}{M_c}\left(\frac{a}{a_9}\right)^3 \frac{\sqrt{1-e^2}}{(1-e_9^2)^{3/2}},\end{aligned} \tag{8.8}$$

where the subscript 9 denotes the orbital elements of Planet Nine, the subscript i within the summation in the first term denotes the four giant planets, c denotes the central body, and a lack of subscript denotes the TNO for which the equation of motion is written. This equation of motion can be split into two parts: $d\omega_{SS}/dt$, which denotes precession due to the effect of the gas giants, and $d\omega_9/dt$, which denotes the precession due to the effect of Planet Nine. The magnitudes of these terms can be written in the form

$$\begin{aligned}\frac{d\omega_{SS}}{dt} \propto & \frac{3}{4M_c}\sum_{i=1}^{4} m_i a_i^2 (e^2-1)^{-2} a^{-2} \\ \frac{d\omega_9}{dt} \propto & \frac{15e_9}{16e}\frac{m_9}{M_c}\left(\frac{a}{a_9}\right)^4 \frac{\sqrt{1-e^2}}{(1-e_9^2)^{5/2}}(1-\frac{9e^2}{4})\cos(\omega-\omega_9) \\ & + \frac{3}{4}\frac{m_9}{M_c}\left(\frac{a}{a_9}\right)^3 \frac{\sqrt{1-e^2}}{(1-e_9^2)^{3/2}}\end{aligned} \tag{8.9}$$

where $d\omega_{TNO}/dt = d\omega_{SS}/dt - d\omega_9/dt$. At the point where $d\omega_{SS}/dt \approx d\omega_9/dt$, the precession rates due to Planet Nine and the inner solar system cancel each other out, and the TNO orbit is not expected to precess. For each TNO, we can construct a curve in the (a, e) plane for which these precession rates cancel. The region presented in Figure 8.5 is the superposition of these curves for all eight TNOs, and it encompasses the range of Planet Nine realizations which will allow alignment

by preventing precession.

Figure 8.5 also presents (in green) a posterior based on alignment of the TNOs, as derived from our set of numerical simulations. Our simulations were intended to test dynamical stability, but one output of the N-body simulation is the orbital elements ω and Ω of the TNOs over time. Using a similar technique to that used to construct the dynamical stability posterior in Figure 8.4, we tested how well aligned the TNOs were for each realization of Planet Nine. Alignment was measured by looking at the fraction of time for which all eight TNOs were aligned with each other (and thus anti-aligned with Planet Nine: we counted dispersions of less than 94 degrees in $\varpi = \omega + \Omega$ between all eight TNOs as aligned). We constructed a contour plot of the percentage of the integrations during which alignment was visible for all eight TNOs, which exhibited between near 0% alignment to a maximum of $\sim$10% alignment in the green regions. The alignment rate expected for pure chance would be about 2×10^{-5} (for alignment among all eight TNOs). As a result, the numerical simulations show an overabundance of alignment in certain, preferred regions (denoted by the green contour of Figure 8.5).

The constraints provided by the three methods in this work and the two literature results show rough agreement: the region of Planet Nine parameter space looking most attractive extends over the range 500–700 AU in semi-major axis, and 0.3-0.6 in eccentricity. Notably, low eccentricities are disfavored. Notice also that the contours preferred for TNO stability are somewhat parallel to those for orbital alignment. In order for Planet Nine to be close enough to the TNOs to enforce alignment, it must be close enough that the TNO orbit is close to instability. As a result, the preferred region is given by the boundary between the stablity contours and the alignment contours in Figure 8.5.

8.4 End States for Trans-Neptunian objects under the influence of Planet Nine

The numerical simulations that we use to create distributions of TNO lifetime in the presence of Planet Nine evaluate the long-term evolution of these TNOs. As discussed in Section 8.2, there are five main outcomes for these TNOs: (1) migration in semi-major axis, which is defined in the simulations as the orbit's semi-major axis attaining a value more than 100 AU from the

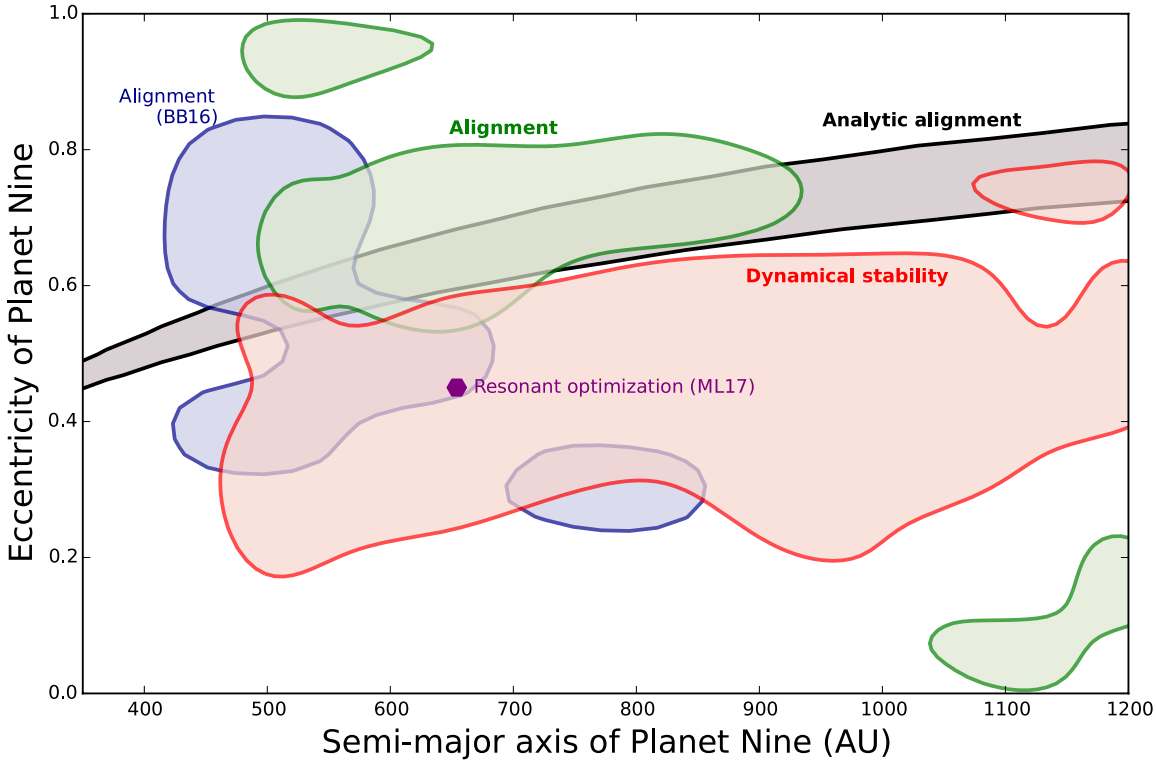

Figure 8.5 Phase Space Representation of the Most Favorable Orbits for Planet Nine. A comparison between the preferred regions for Planet Nine's orbit, as computed using a variety of different methods. Bold labels indicate that the posterior was derived in this work. In red, we plot the region that maximizes the survival probability for the TNOs in our N-body simulations (based on their dynamical stability; see Figure 8.4). In green, we plot the realizations of Planet Nine orbital parameters in our N-body simulations that allowed the TNOs to be aligned as observed in nature. In black, we plot the analytic approximation for the region where we expect the observed alignment to occur (see Equation 8.8 and its derivation in the Appendix 9.9). In blue, we plot the region reported in Brown & Batygin (2016) that allows the alignment of TNOs in a suite of numerical N-body simulations (unlike the green curve, these simulations used randomized test particles). The purple point denotes the best-fit orbit as reported by Millholland & Laughlin (2017), which was found by optimizing the resonant behavior of the TNOs in the presence of Planet Nine. Each method prefers somewhat different regimes of parameter space, with the dynamical stability argument allowing the largest region. There is significant overlap between the results derived from the different methods. The optimal orbital elements for Planet Nine exist in the overlap region, which corresponds to eccentricity in the range $e_9 = 0.4 - 0.6$ and semimajor axis in the range $a_9 = 500 - 700$ AU.

starting orbit; (2) a close encounter (defined as passing within 3 Hill radii of the larger body) with Planet Nine or Neptune, which would result in the TNO being captured by or colliding with the large planet; (3) collision with the central body; (4) ejection from the solar system, where the ejection radius is taken to be 10,000 AU[1]; and finally, (5) dynamical stability, where none of the aforementioned effects occur over the 4.5 Gyr timescale of the simulation. This final result (5) corresponds to scenarios that are consistent with observations, where the TNO can remain in its orbit over solar system lifetimes. This scenario allows the secular alignment of the TNOs' longitude of perihelion by Planet Nine. However, if this last result does not occur, then the TNO will experience one of the first four (1-4) outcomes.

Within these four dynamical instability outcomes, there is further stratification in the effects of each mechanism. The violent ends (collision with a planet, the star, or ejection from the system) generally remove the TNO from the solar system entirely, while the migratory outcome is more nuanced. TNOs that are in the process of migrating cannot necessarily be used as evidence of the Planet Nine hypothesis, since their orbital elements are in flux and may not have had sufficient time in their current orbits to attain the alignment that serves as a hallmark of Planet Nine's influence.

2007 TG_{422} was one of the more interesting objects in the sample of TNOs considered in this work. Although found in Sheppard & Trujillo (2016) to be dynamically unstable in the presence of Neptune, we reevaluated the stability of 2007 TG_{422} in the presence of Planet Nine in Section 8.2, and found that adding Planet Nine to the solar system can actually stabilize the orbit of this object. 2007 TG_{422} has a particularly high semi-major axis and eccentricity, suggesting that its dynamical instability might be due to orbit crossing with other planets. However, this is not the case. The most common dynamical instability mechanism for 2007 TG_{422} is actually migration, leading this object to remain present in the solar system but wander from its starting orbit. This migratory outcome is likely what Sheppard & Trujillo (2016) found in their work, and we reproduce this instability in the case of large-a, low-e realizations of Planet Nine (which is dynamically very similar to the case of no Planet Nine, as considered in Sheppard & Trujillo (2016)).

[1]This choice in ejection radius will remove objects which become unbound; it is important to note that there may be second order effects due to stellar encounters (see, for example, Li & Adams, 2016a). The effect on TNO motion due to these external perturbations is expected to be small, and is neglected in this work.

The top panels of Figure 8.6 show the instability lifetime map for 2007 TG_{422} when only violent instability methods are considered (top panel) and when migratory instabilities are also considered (middle panel). The significantly shortened lifetimes present in this middle panel show that migration is the main explanation for 2007 TG_{422}'s dynamical instability in the presence of Planet Nine. The bottom panel of Figure 8.6 shows the difference in expected dynamical stability lifetime for this object between the cases depicted in the top two panels: when this difference is low, migration does not have a large effect in ending the integrations, and when it is high, migration is a very common outcome for 2007 TG_{422} in the presence of that particular Planet Nine realization. This difference plot highlights the regions where migration acts as the main cause of dynamical instability. The large-a, low-e realizations of Planet Nine tend to cause migration of 2007 TG_{422}, but not violent dynamical instabilities.

The susceptibility of an object to migration in the presence of Planet Nine can also be summarized as $\bar{\delta t}$, the difference in median lifetime (over all Planet Nine realizations) for an object between the case when migration is considered to be a dynamically unstable outcome and when it is ignored. Larger values of $\bar{\delta t}$ indicate that the TNO is more susceptible to significant migration in semi-major axis ($\delta a > 100$ AU), and that such migrations significantly change the dynamical stability map of that object. The choice of $\delta a > 100$ AU as the threshold criterion for migration is somewhat arbitrary. It is chosen to represent the condition for which an object has drifted significantly from its observed orbit. Migration in semi-major axis with deviations greater than 100 AU generally results in an orbit with significantly different orbital elements, rather than oscillation of the orbital elements around well-defined central values. As a result, objects that migrate by more than 100 AU are unlikely to remain part of the same dynamical class of object.

For 2007 TG_{422} , $\bar{\delta t} = 1.07$ Gyr, meaning that Planet Nine incites migration in this object often enough to decrease its dynamically stable lifetime by more than one billion years. In contrast, 2012 VP_{112} has a $\bar{\delta t} = 32$ Myr, indicating that migration does not play a large role in its outcomes. The values of $\bar{\delta t}$ for each object in our sample are reported in Table 8.1, which presents in its last two columns both $\bar{\delta t}$ and the percentage of trials out of all our simulations that are dynamically stable. As the percentage increases (or, as an object is more stable in the presence of any considered Planet Nine realization), the value of $\bar{\delta t}$ tends to decrease (or, the TNO experiences migration as

an instability outcome with a lower frequency). This suggests that susceptibility to migration is a major factor leading to differences in orbit lifetimes between different TNOs in the presence of Planet Nine.

In this work, we have made the assumption that since the eight TNOs in our sample exhibit alignment in longitude of perihelion attributable to Planet Nine, these objects by necessity have lived in their current orbits for a significant length of time. In constructing the stability posterior presented in Figure 8.4, we assumed that since significant, unbounded migration alters orbits and potentially disrupts this alignment, a migratory instability provides equal information against Planet Nine's orbital elements as does a violent dynamical instability. In this way, we used migratory instabilities (such as those caused by large-a, low-e realizations of Planet Nine for 2007 TG_{422}) as evidence against the iterations of Planet Nine that excited the migration.

The TNOs affected by Planet Nine appear to fall into two categories: some of them (Sedna, 2012 VP_{113}) are generally stable against this migratory process, while others (2007 TG_{422}, 2013 RF_{98}) can be easily caused to migrate in semi-major axis with an improperly chosen realization of Planet Nine. The best orbit of Planet Nine can be determined not only from the orbit-crossing constraint that rules out small-a, large-e orbits for all TNOs, but also by the constraint from this second population of objects, which are unstable in the presence of large-a, low-e Planet Nine orbits (and are additionally unstable in the presence of no Planet Nine at all). These two populations explain the unintuitive structure of the posterior probability distribution given in Figure 8.4.

Even though we require a Planet Nine iteration that does not cause the aligned TNOs to migrate significantly (more than 100 AU) over secular timescales, we expect there is a further population of objects that do migrate in the presence of Planet Nine. Indeed, some populations of objects in our solar system can be explained by this process. Batygin & Brown (2016b) uses the nominal Planet Nine orbit from Batygin & Brown (2016a) to explain the existence of a population of highly inclined KBOs with $a \leq 100$: these objects can be explained as a migratory end-state of objects that started as members of the extreme TNO populations. The fact that some TNOs appear to experience migratory instabilities under the influence of Planet Nine is not inconsistent with our assumptions, but it does engender further questions. Clearly, some degree of migration is acceptable and will not alter the orbital alignment of the TNOs - the 100 AU threshold we use allows significant movement

in semi-major axis without declaring objects dynamically unstable. However, the fact that objects can migrate in semi-major axis but remain confined to a comparably narrow range (disallowing above 100 AU of migration does not allow objects to move into entirely different object populations as seen in Batygin & Brown 2016b) begs the question: how are objects moving when they migrate in what we have defined as a dynamically *stable* way? The answer to this question will be addressed in the following section.

8.5 Proximity of the Trans-Neptunian Objects' Orbits to Resonances with Planet Nine

In the previous section, we identified that for some TNOs, migration in semi-major axis is an outcome for a significant fraction of integrations. In this section, we delve deeper into the nature of that migration and consider the question of resonance between the TNOs and Planet Nine. Specifically, if the TNOs migrate in semi-major axis, they are likely to pass through the locations of mean-motion commensurabilities with Planet Nine, and one might expect the TNOs to fall into the stable configurations afforded by resonances, and stop migrating.

The fact that proximity to resonance boosts dynamical stability can be directly applied to the Planet Nine - TNO system. In particular, Malhotra et al. (2016a) considered the possibility that Planet Nine should be at an orbital radius that would allow it to be closest to low-order resonances for several TNOs, based on the currently measured orbits of those TNOs. The benefit to this configuration is that Planet Nine could stabilize the orbits of TNOs such as 2007 TG_{422}, which might otherwise migrate in semi-major axis. Similarly, Millholland & Laughlin (2017) used numerical N-body simulations to determine the best orbit of Planet Nine by testing which locations close to resonances allow the observed alignment of the TNOs. Millholland & Laughlin (2017) found the best semi-major axis of Planet Nine to be $a_9 \sim 654$ AU (with a $e_9 \sim 0.45$), and Malhotra et al. (2016a) found the best-fit orbit to have a semi-major axis of $a_9 \sim 665$ AU.

Clearly, resonance is an important aspect of the Planet Nine problem, as suggested by Batygin & Brown (2016a), Beust (2016), Malhotra et al. (2016a), and Millholland & Laughlin (2017). In Figure 8.7, we plot two histograms of the orbital period ratio (P_9/P_{TNO}) for each of the eight

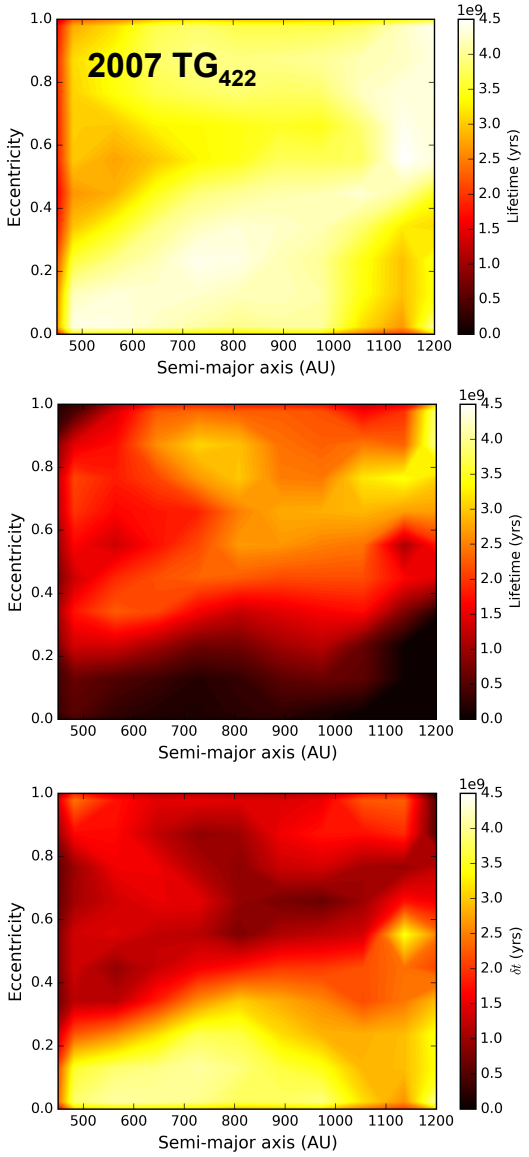

Figure 8.6 2007 TG_{422}'s Orbital Evolution in the Presence of Planet Nine. The lifetime of 2007 TG_{422} in the presence of realizations of Planet Nine with semi major axis between 450 and 1200 AU, and eccentricities between 0 and 1. *(top panel)* Stability lifetimes when dynamical instability is only caused by violent ends for 2007 TG_{422}, including collision with a solar system planet, collision with the sun, or ejection from the solar system (the outer boundary of which is defined to be 10000 AU). *(middle panel)* Stability lifetimes, when dynamical instability is caused by the violent end depicted in the top panel and also migration in semi-major axis by more than 100 AU. *(bottom panel)* The difference δt in stability lifetimes between the two cases, demonstrating which realizations of Planet Nine are most likely to cause 2007 TG_{422} to change its orbit significantly. Planet Nine realizations with low eccentricity and large semi-major axis cause 2007 TG_{422}'s orbit to migrate, but not meet with a violent end.

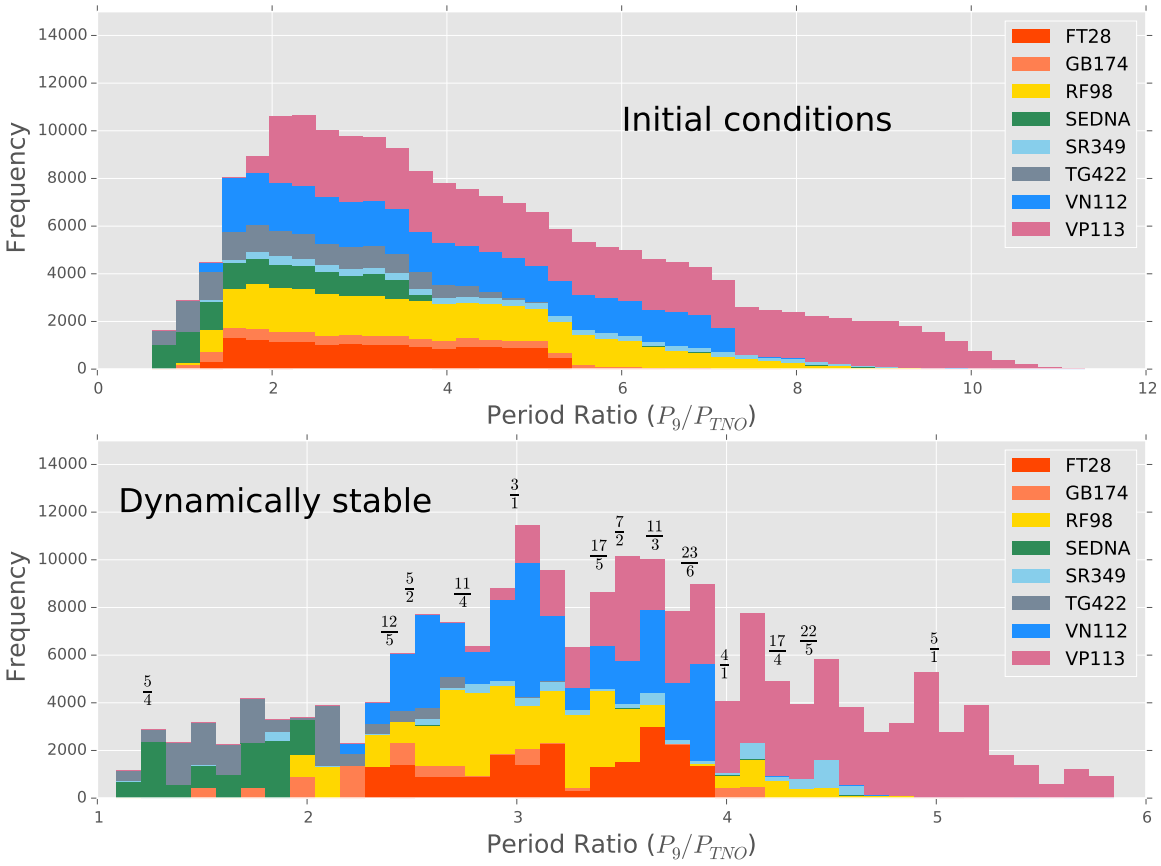

Figure 8.7 Comparison of TNO Period Ratios at Simulation Initialization Versus at Completion. (top panel) A sample of period ratios P_9/P_{TNO}, drawn from the initial conditions of the N-body simulations. This histogram shows the period ratio distribution that we would expect to see from the simulations if no period ratio were more dynamically stable than any other period ratio. This set serves as the control, and does not have the condition of dynamical stability imposed. (bottom panel) Period ratios P_9/P_{TNO} for the dynamically stable integrations at time-steps of one million years, demonstrating a peaked distribution, as some period ratios are preferred to others. In both panels, colors correspond to the values for each TNO, and the area of histograms was normalized.

TNOs in our sample. In the top panel, we plot random draws from our initial conditions that were used to initialize the N-body simulations described in Section 8.2. The total number of draws in the top histogram was chosen to match the number of dynamically stable time-steps for each individual TNO, but the draws are from a raw distribution of the ratio P_9/P_{TNO} for all numerical trials, including those that are not dynamically stable. This top panel does not include the effect of certain ratios becoming more common due to gravitational interactions. In the bottom panel, we plot the dynamically stable trials for each TNO, with the period ratio sampled every million years. The sharp peaks in this second histogram demonstrate clear overabundances of particular period ratios P_9/P_{TNO}. These values occur near resonances — in the trials where dynamical stability is found — and is markedly different from the continuum of period ratios shown in the upper panel. Keep in mind that the initial conditions of our simulations were chosen independently of resonance locations, unlike the set of simulations in Millholland & Laughlin (2017). As a result, the behavior shown in the figure indicates that systems found to be dynamically stable in the simulations also show a clear preference for near-resonant locations.

The results of this work show an important departure from the assumptions used previously (Malhotra et al., 2016a; Millholland & Laughlin, 2017). This earlier work assumes that the TNOs remain in a single resonant configuration over the lifetime of the Solar System. For example, Sedna might live in either the 9:8 or 6:5 mean motion commensurability, depending on the semi-major axis of Planet Nine, but it is considered to remain in a single resonance. In this approximation, the orbits of the extreme TNOs that we observe today are consistent with their past orbits. This assumption allows for the estimate found in Malhotra et al. (2016a) to be carried out: if the TNOs reside in the same orbits over their entire lifetimes, and if they must be near resonance, then their current orbital properties can be used to compute the expected orbital elements of Planet Nine. However, our simulations show that TNOs do not always remain in the same orbits: Although they often remain near some resonance with Planet Nine, the TNOs change orbits and hence change resonances.

In Figure 8.8, we plot time series for 2004 VN_{112} (top), 2007 TG_{422} (middle), and Sedna (bottom) to demonstrate the potential resonant outcomes. The behavior of 2004 VN_{112} is consistent with the assumption made by Malhotra et al. (2016a) and Millholland & Laughlin (2017): that

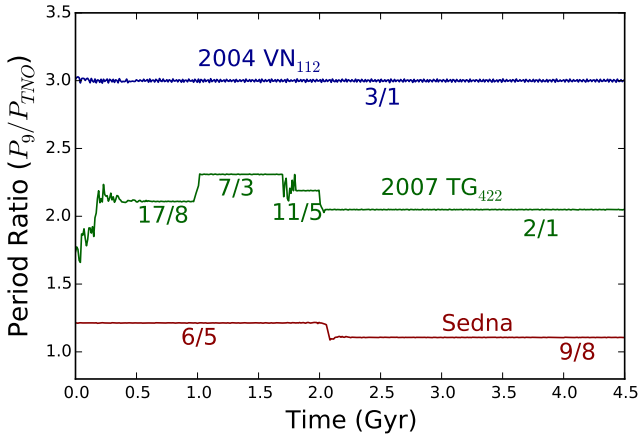

Figure 8.8 Period Ratio Over Time for Three TNOs. For three integrations (top curve: 2004 VN_{112}; middle curve: 2007 TG_{422}; bottom curve: Sedna), we plot the period ratio P_9/P_{TNO} as function of simulation time. The numbers denote resonances within $\Delta a_{\rm res}$ of the semi-major axis of each TNO, at each time-step. The top time series, showing the evolution of 2004 VN_{112} during a typical integration, demonstrates how an object might remain in a single mean-motion commensurability for the entire lifetime of the solar system. The middle series, for 2007 TG_{422}, shows the behavior we call 'resonance hopping,' where a TNO attains multiple mean-motion commensurabilities over the course of the simulation. The bottom series shows a less extreme version of this 'resonance hopping,' where Sedna switches between two commensurabilities during the solar system lifetime. In all cases, the period of Planet Nine does not change over the course of the simulation: it is the motion of the TNO that leads to changing values of P_9/P_{TNO}.

TNOs would live in a single resonance for the age of the solar system. The other two TNOs plotted in Figure 8.8 show behavior we call 'resonance hopping,' where a TNO attains multiple mean-motion commensurabilities over the course of the simulation. When liberated from one mean-motion commensurability, both TNOs are captured into another resonance instead of being ejected from the system entirely. Planet Nine's semi-major axis did not change over the course of a single simulation, so all the change in P_9/P_{TNO} within a single integration is due to migration by the TNO.

As illustrated in Figure 8.2, each TNO has a different dynamically stability map, preferring different regions of Planet Nine's potential parameter space. Similarly, when we take the subset of dynamically stable integrations for each TNO, each TNO has a different behavior relating to resonance. In this work, we take the definition of being 'in' resonance to be living close to a resonant period ratio; as with the exoplanetary systems near resonance, the boost in dynamically stability provided by proximity to resonance applies even when systems are not in a perfect resonance. Malhotra et al. (2016a) and Millholland & Laughlin (2017) use a criterion for the proximity to resonance that is close enough to afford such benefits:

$$\Delta a_{\rm res} \approx 0.007 a_{\rm TNO} \mid \frac{m_9 a_{\rm TNO} \mathcal{A}}{3 M_\odot a_9} \mid^{1/2} \tag{8.10}$$

when $\Delta a_{\rm res}$ is the width, in AU, of the band of space close enough to a resonance to count as being 'near' said resonance, subscript TNO denotes the TNO's semi-major axis a and the subscript 9 denotes Planet Nine's semi-major axis a_9 and mass m_9. $\mathcal{A}$ is a unitless coefficient. We choose to use $\mathcal{A} = 3$ as done in Malhotra et al. (2016a) and Millholland & Laughlin (2017). The numerical value of $\Delta a_{\rm res}$ tends to be close to 5-10 AU for the TNOs in our sample, meaning that the simulation results allow us to determine the nearest resonance and identify TNOs that 'hop' between resonances. Figure 8.8 shows three examples from our set of simulations: 2004 $\rm VN_{112}$ does not change resonances during the integration, 2007 $\rm TG_{422}$ changes resonances three times, and Sedna changes resonance once. For two objects in our sample (2004 $\rm VN_{112}$ and 2012 $\rm VP_{113}$), we see no hopping behavior.

However, it is important to note that the simulations used to construct Figure 8.7 and the curves in Figure 8.8 are the set run for this chapter, which uses the quadrupole moment of the central

part of the system (J_2) to replace the active motions of Jupiter, Saturn and Uranus (JSU). This approximation allows the simulations in this work to be completed in a total of roughly 100,000 total CPU hours, rather than the nearly 2 million CPU hours that would be required to run the full integrations with all active giant planets. This approximation is appropriate for the tests of dynamical stability and alignment considered thus far in this work, but when considering the question of resonance, some discrepancies arise. In Figure 8.9, we present a comparison between a few test simulations run with the J_2 approximation and the JSU case of active particles for Jupiter, Saturn, and Uranus. The test simulations were run for 1 Gyr each, with a single realization of Planet Nine (a = 700 AU, e = 0.5) and otherwise identical to the cases run in the previous set of simulations. For the JSU set of simulations, we lowered the time-step to 20 days.

When active JSU particles are included in the integrations, two major differences occur as compared to the J_2 approximation: (1) the period ratios are not as tightly confined, experiencing a larger degree of scatter even while living in a single apparent resonance; (2) the number of times objects hop between resonances can be both increased (due to repeated accelerations from Uranus) and decreased (as shown in the top panel of Figure 8.9, hops we resolve in the J_2 case are un-physical in the JSU case).

Regarding point (1), the second panel of Figure 8.9 illustrates a case where in both the J_2 and JSU cases, a TNO lives close to the 8/5 mean motion resonance. In the J_2 case, the TNO stays within 0.3% of its average period ratio. In the JSU case, the TNO stays within 5% of its averege period ratio (this value is larger than in the J_2 case due to the inclusion of accelerations from the inner three giant planets). Due to this complication, we have chosen the bin size in Figure 8.7 to be commensurate with the period ratio confinement experienced by TNOs in the JSU case, which is typically around 8%.

Regarding point (2), it is unclear without running a large suite of JSU integrations how the hopping frequency changes with the inclusion of the giant planets. For this reason, we do not present in this work detailed results of the resonance hopping in our simulations. In order to accurately assess this behavior, a complete set of simulations with active giants planets (JSU) should be carried out.

Our simulations show that dynamically stable integrations of the TNOs tend to attain mean-

motion commensurabilities. Depending on the TNO, it may attain a single resonant location and stay there, or it may hop between resonant locations. This 'resonance hopping' is an important effect, and for TNOs that exhibit this behavior, their past semi-major axis may be different than the current values. The numerical computation of the specifics of this behavior should be a fruitful avenue for future work.

8.6 Conclusions

In this work, we have evaluated the dynamical stability and orbital alignment of eight TNOs (Sedna, 2004 VN_{112}, 2007 TG_{422}, 2010 GB_{174}, 2012 VP_{113}, 2013 RF_{98}, 2013 FT_{28}, and 2014 SR_{349}) in the presence of a Monte Carlo assortment of Planet Nine realizations with varying semi-major axis and eccentricity. We used the results to predict the most probable (a, e) of Planet Nine by deriving the posterior probability distributions for Planet Nine's orbital elements (a, e). The distribution based on dynamical stability considerations for the TNOs is presented in Figure 8.4. We have also constructed an analogous probability distribution based on the requirement that the orbits of the TNOs remain aligned. Both of these posterior distributions demonstrate that the preferred orbits for Planet Nine have intermediate values of eccentricity ($0.3 < e < 0.5$) and semi-major axis ($650 < a < 900$ AU), as shown in Figure 8.5. Moreover, these values are roughly consistent with the regime suggested in Brown & Batygin (2016), which constructed its probability map using clustering arguments only. Our stability posterior and that from Brown & Batygin (2016) were constructed based on different fundamental orbital properties (dynamical stability and secular evolution patterns, respectively). Despite this significant difference in construction, the two results are consistent, in that they both prefer non-zero eccentricities and a similar range in semi-major axis for Planet Nine. The comparison between our results and those of Brown & Batygin (2016) is shown in Figure 8.5. Notably, similar dynamical stability arguments in Millholland & Laughlin (2017) produce a best-fit Planet Nine of 654 AU and 0.45 eccentricity, which is consistent with the overlap region between the results of this work and of Brown & Batygin (2016).

Using numerical N-body simulations, we also demonstrated that 2007 TG_{422} and 2013 RF_{98}, while found in the past to be dynamically unstable in the presence of Neptune alone, can attain

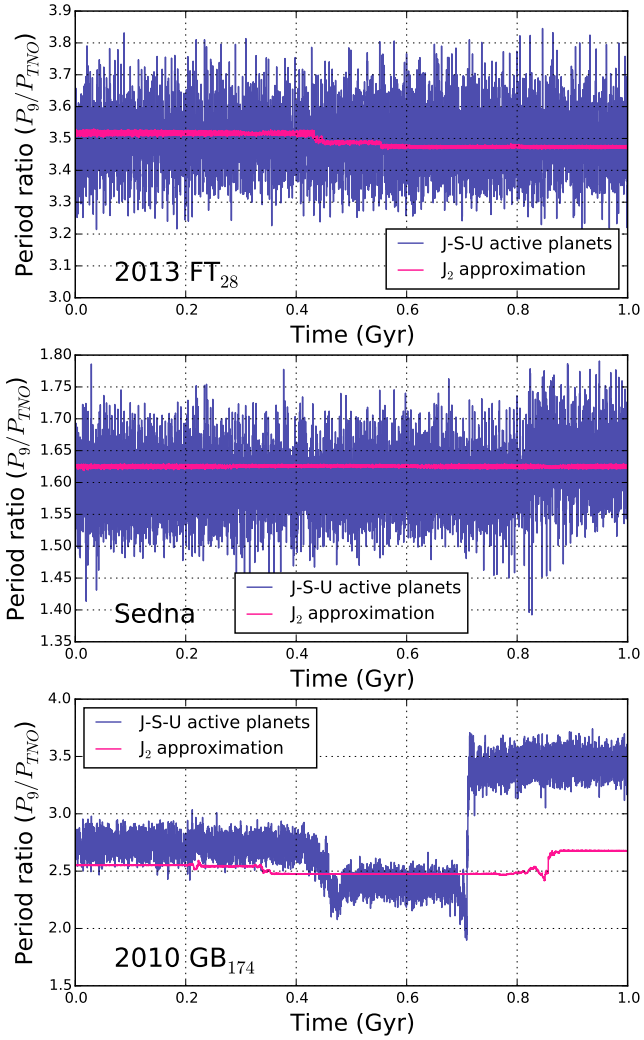

Figure 8.9 Numerical Comparison of Full Model to J2 Approximation. A check of our integrations (which used solar J_2 in place of the inner three giant planets) and integrations run with active Jupiter, Saturn, and Uranus (JSU) show that although both sets exhibit the same hopping behavior, the J_2 approximation underestimates the noise in period ratio and overestimates the degree to which the resonances can be differentiated.

dynamically stable states in the presence of Planet Nine. Our simulation results support the prediction of Sheppard & Trujillo (2016) that since 2007 TG_{422} and 2013 RF_{98} exhibit the same orbital clustering as the dynamically stable TNOs, Planet Nine likely dominates over Neptune interactions. In addition, we find that different TNOs exhibit very different stability maps, with some objects (such as Sedna and 2012 VP_{113}) contributing relatively little unique information to the stability posterior and others (such as 2007 TG_{422} and 2013 RF_{98}) exhibiting unintuitive preference against large-a, low-e orbits of Planet Nine. These two categories suggest that there may be two dynamical classes of objects in this TNO sample, which interact differently with Planet Nine. However, we have considered in this work only a small ($N = 8$) number of objects that fit into the desired high-a, trans-Neptunian-q, apsidally aligned category identified in Batygin & Brown (2016a). The discovery of additional objects in this population (expected in the near future) will allow for a more robust test of this two-population hypothesis.

We have also evaluated the different dynamical outcomes for these extreme TNOs in the presence of Planet Nine. The objects that are dynamically unstable in the presence of large-a, low-e orbits of Planet Nine (2007 TG_{422} and 2013 RF_{98}) tend to experience migration rather than violent collisions or ejections as their main outcome in dynamically unstable cases. These objects are also dynamically unstable in the presence of only Neptune and the other giant planets, i.e., in the absence of Planet Nine. In Table 8.1, we present the difference $\bar{\delta t}$ in average dynamical lifetime between the case where migration is considered to be a dynamical instability mechanism and when it is not. Table 8.2 presents the relative occurrence rates for each type of outcome. For cases where the TNOs are not stable over the lifetime of the Solar System, the fraction of trials that lose objects to migration (with $a > 100$ AU), close encounters with giant planets, and ejection from the system are roughly comparable. A small minority of the simulations end with accretion onto the Sun (less than 1%).

Next, we suggest a generalized description for the interactions between the TNOs and Planet Nine. We propose that the paradigm is neither that (1) mean motion resonance is unimportant, nor (2) TNOs reside in a single resonance with Planet Nine for the age of the solar system. Instead, while some TNOs (such as 2004 VN_{112} and 2012 VP_{113}) can sometimes live in a single resonance for solar system lifetimes, others exhibit a behavior that we call 'resonance hopping.' This term

means that the TNO is near-continually in close proximity to a mean motion resonance (Figure 8.7), but it is not necessarily near the *same* resonance for the age of the Solar System (Figure 8.8). Instead, the TNOs can transition between closely-spaced resonances, often those described by relatively large integer ratios. The long-term effect of this process is that the orbital anti-alignment caused by Planet Nine is able to persist, but the TNO is protected against small kicks in energy provided by interactions with Neptune. In this paradigm, an interaction with Neptune might lead to the movement of a TNO into a new resonance, but not to its ejection from the solar system (see also Malhotra et al. 2016a; Millholland & Laughlin 2017). A useful avenue for future work would be the full numerical computation of this effect, as the J_2 approximation used in this work precludes an accurate calculation of the true frequency of resonance hopping.

Another important avenue for future work exists in our prediction that the eight TNOs considered in this work populate two distinct dynamical classes: first, a class of objects such as 2012 VP_{113} or Sedna, which are more dynamically stable in the presence of large a, low e realizations of Planet Nine (which reduce closely to the case of having no ninth planet); second, a class of objects that are dynamically unstable in the presence of only Neptune and no Planet Nine (and also in the case of a high-a, low-e Planet Nine). This second class of objects may have higher e and a than the first, and require a stabilizing influence in the form of an eccentric Planet Nine to prevent destabilizing interactions with Neptune. To truly understand if this is a valid division, it is hoped that a large number of high-a, trans-Neptunian-q, apsidally aligned TNOs will be discovered in the next few years. The classification of these objects, and exploration of the mechanism by which Planet Nine may stabilize their orbits, should be explored in the future.

8.7 Appendix: Precession Equations of Motion for TNOs

To consider the secular motion of the TNOs in the presence of Planet Nine, we can treat the problem with a coplanar approximation, as done in Batygin & Brown (2016a). It is important to note that this is a very rough approximation, as the TNOs and Planet Nine are expected to be inclined relative to the inner solar system and each other.

The Hamiltonian for this system, as used in Batygin & Brown (2016a), is:

$$\begin{aligned}\mathcal{H} = &-\frac{1}{4}\frac{GM}{a}(1-e^2)^{-3/2}\sum_{i=1}^{4}\left(\frac{m_i a_i^2}{Ma^2}\right) - \frac{Gm_9}{a_9}\left[\frac{1}{4}\left(\frac{a}{a_9}\right)^2\frac{1+3e^2/2}{(1-e_9^2)^{3/2}}\right.\\ &\left.-\frac{15}{16}\left(\frac{a}{a_9}\right)^3 e\ e_9\frac{1+3e^2/4}{(1-e_9^2)^{5/2}}\cos\left(\omega_9-\omega\right)\right]\end{aligned} \tag{8.11}$$

when M is the mass of the central body, the subscript 9 denotes the properties of Planet Nine, the subscript i within the summation in the first term denotes the four giant planets, and a lack of subscript denotes the TNO for which the Hamiltonian is being written.

Using canonical variable $\epsilon = \sqrt{1-e^2}$, we can find the equation of motion for the argument of perihelion ω by taking the derivative of Equation 8.11, such that $d\omega/dt \propto d\mathcal{H}/d\epsilon$. The result of this yields

$$\begin{aligned}\frac{d\omega}{dt} \propto &\left[\frac{3}{4}\sum_{i=1}^{4} m_i a_i^2 (e^2-1)^{-2}a^{-2} - \frac{15}{16}m_9\frac{e_9}{e}\left(\frac{a}{a_9}\right)^4\frac{\sqrt{1-e^2}}{(1-e_9^2)^{5/2}}(1-9e^2/4)\cos(\omega-\omega_9)\right.\\ &\left.-\frac{3}{4}m_9\left(\frac{a}{a_9}\right)^3\frac{\sqrt{1-e^2}}{(1-e_9^2)^{3/2}}\right],\end{aligned} \tag{8.12}$$

when leading constants have been dropped, since in this work we care only about the relative contributions of the terms of the equation of motion. The first term of Equation 8.12 represents the apsidal precession of a TNO with orbital elements (a, e, ω) that is caused by the inner solar system (where the outer four giant planets are treated as a solar oblateness and the terrestrial planets ignored). The latter two terms of Equation 8.12 include dependences on the mass of Planet Nine (m_9), eccentricity of Planet Nine (e_9), semi-major axis of Planet Nine (a_9), and argument of perihelion of Planet Nine (e_9). These two terms represent the apsidal precession of the TNO due to Planet Nine's influence.

Alone, the influence of Planet Nine *or* of the inner solar system would lead to precession of each TNO's ω. Taken together, the two precession terms can either boost precession rates or slow them. With the proper choice of orbital elements for Planet Nine, $d\omega/dt$ can be set to be zero, leading to no net precession relative to the Katti-Range vector of Planet Nine's orbit. Such a situation could result in a selection of TNOs exhibiting orbits that remain in roughly the same regime of parameter space over time, potentially leading to alignment like that observed in the TNOs in our

solar system.

For completeness, we note that Equation 8.12 can also be derived from the disturbing function using Lagrange's planetary equations. We use the disturbing function as formulated in Mardling (2013), which is written to work in the dimensions of energy. The disturbing function can be written as

$$\begin{aligned}\mathcal{R} = -\frac{1}{4}\frac{GMm}{a}(1-e^2)^{-3/2}\sum_{i=1}^{4}\left(\frac{m_i a_i^2}{Ma^2}\right) \\ + \frac{Gm_9 m}{a_9}\left[\frac{1}{4}\left(\frac{a}{a_9}\right)^2\frac{1+3/2e^2}{(1-e_9^2)^{3/2}} - \frac{15\ e\ e_9}{16}\left(\frac{a}{a_9}\right)^3\frac{1+3e^2/4}{(1-e_9^2)^{5/2}}\cos(\omega-\omega_9)\right]\right],\end{aligned} \tag{8.13}$$

This equation has been simplified under the assumption $m << m_p << M$. We can use Lagrange's planetary equations to find the equation of motion analogous to that in Equation 8.12. Specifically:

$$\frac{d\omega}{dt} = \frac{\epsilon}{m\nu a^2 e}\frac{d\mathcal{R}}{de} \tag{8.14}$$

when ν is the orbital frequency of the TNO. Substituting Equation 8.13 into the relevant Lagrange equation (Equation 8.14) yields the full equation of motion:

$$\begin{aligned}\frac{d\omega}{dt} = \frac{m_9\nu}{M}\left[\frac{3}{4}\sum_{i=1}^{4} m_i a_i^2 (e^2-1)^{-2}a^{-2} - \frac{15}{16}m_9\frac{e_9}{e}\left(\frac{a}{a_9}\right)^4\frac{\sqrt{1-e^2}}{(1-e_9^2)^{5/2}}(1-9e^2/4)\cos(\omega-\omega_9)\right. \\ \left. -\frac{3}{4}m_9\left(\frac{a}{a_9}\right)^3\frac{\sqrt{1-e^2}}{(1-e_9^2)^{3/2}}\right],\end{aligned} \tag{8.15}$$

which is equivalent to the result presented in Equation 8.12.

It is very important to note that the preceding derivation makes several major approximations:

- We assume a coplanar system and neglect orbital inclination of all bodies,
- In the construction of the Hamiltonian and the disturbing function, we ignore all short-order, resonant terms[2]

For all of these reasons, this analytic result should be treated as approximate. To do the problem properly, it is important to use numerical N-body simulations.

[2]and as shown in Section 8.5, this is probably dangerous to do

8.8 Appendix: Effects of allowing orbital elements to vary in N-body simulations

In the set of N-body simulations that we describe in Section 8.2 and use to construct the posterior probability distribution given in Section 8.3, we use a population of Planet Nine realizations with fixed inclination $i = 30$ degrees, argument of perihelion $\omega = 150$ degrees, and longitude of the ascending node $\Omega = 113$ degrees. This was done because the amount of uncertainty in each of these measurements would require a computationally unfeasible number of integrations to well-sample the parameter space. Instead, we chose the approximate best values for each angle, as reported and used in prior literature.

However, we can recreate the probability posterior presented in Figure 8.4 for an additional set of 1500 N-body integrations, while allowing these orbital angles to vary, and examine the amount of difference between this new posterior and the old one as a first test. To do this, we ran 1500 more numerical N-body integrations with the same numerical properties as our other set (hybrid symplectic and Bulirsch-Stoer (B-S) integrator in `Mercury6` (Chambers, 1999b), conserving energy to 1 part in 10^{10}, replacing the three inner giant planets with a solar J2, including each TNO with orbital elements drawn from observational constraints). In this set of integrations, we sampled a_9 from a uniform range between (400, 1200) AU, and e_9 between (0,1). However, instead of fixing the orbital angles, we sampled from normal distributions centered on the Batygin & Brown (2016a) estimates ($i_9 = 30$ degrees, $\omega_9 = 150$ degrees, $\Omega_9 = 113$ degrees) with widths of 30 degrees in each case. Then, we integrated each of the 1500 realizations forward for 4.5 Gyr.

The results of this new, second suite of integrations is presented in Figure 8.10, which can be directly compared to Figure 8.4 (which was constructed with our original set of simulations). Comparing the two figures presents three major conclusions: [1] The main parameter space preferred in each set is similar, with high eccentricities being less preferred and the range from 0.3-0.5 eccentricity, 600-1000 AU being good in both sets. [2] The overall survival probabilities are lower for the case where Planet Nine's orbital angles are allowed to vary, which indicates that altering these values too much decreases dynamical stability of the TNOs overall. [3] The posterior presented in Figure 8.10, with varying orbital angles, has less variation between peaks and valleys, which is

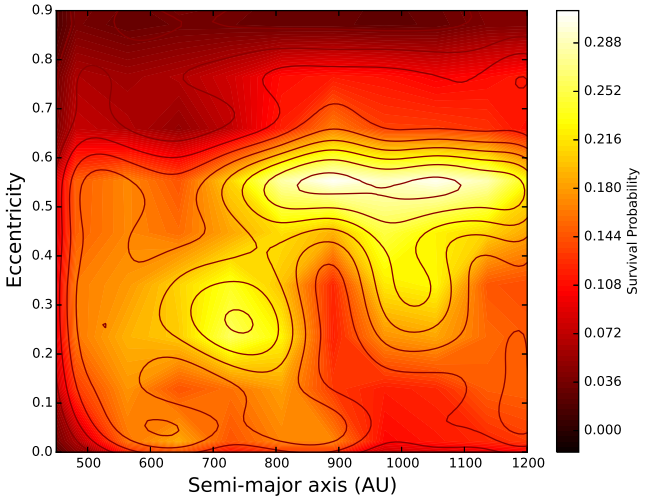

Figure 8.10 Full Stability Contour for Planet Nine Parameters. The overall stability posterior for the semi-major axis and eccentricity of Planet Nine, when Planet Nine's orbital angles were allowed to vary over a normal distribution centered on the best-guess values. This posterior was constructed by taking a summation of the posteriors for each individual object, including the six objects used in Batygin & Brown (2016a) and the two new high-a, low-e objects from Sheppard & Trujillo (2016). As compared to Figure 8.4, which did not allow the orbital angles to vary, the survival probability is lower when orbital angles are allowed to vary, suggesting that the best-guess values leading to more probable alignment also lead to more dynamically stable configurations.

the danger of adding additional layers of variation (which we did by allowing three orbital angles to vary).

The reason that we do not use this set of simulations that allow initial orbital angles of Planet Nine to vary as the main set in this chapter is that the parameter space is not well-sampled. Additionally, the three additional free parameters bring with them three additional sources of variations. The robust exploration of this parameter space is outside the scope of this work.

CHAPTER IX

Discovery and Dynamical Analysis of an Extreme Trans-Neptunian Object with a High Orbital Inclination

Results in this chapter were published in: ***Becker, J. C.**, Khain, T., Hamilton, S. J., Adams, F., et al. "Discovery and Dynamical Analysis of an Extreme Trans-Neptunian Object with a High Orbital Inclination." 2018, The Astronomical Journal, 156, 81* and are presented here with minor additions.

9.1 Abstract

We report the discovery and dynamical analysis of 2015 BP_{519}, an extreme Trans-Neptunian Object detected by the Dark Energy Survey at a heliocentric distance of 55 AU, perihelion of ∼36 AU, and absolute magnitude $H_r = 4.3$. The current orbit, determined from an 1110-day observational arc, has semi-major axis $a \approx 450$ AU, eccentricity $e \approx 0.92$, and inclination $i \approx 54$ degrees. With these orbital elements, 2015 BP_{519} is the most extreme TNO discovered to date, as quantified by the reduced Kozai action, $\eta_0 = (1 - e^2)^{1/2} \cos i$, which is a conserved quantity at fixed semi-major axis a for axisymmetric perturbations. We discuss the orbital stability and evolution of this object, and find that under the influence of the four known giant planets 2015 BP_{519} displays rich dynamical behavior, including rapid diffusion in semi-major axis and more constrained variations in eccentricity and inclination. We also consider the long term orbital stability and evolutionary behavior within the context of the Planet Nine hypothesis, and find that 2015 BP_{519}

adds to the circumstantial evidence for the existence of this proposed new member of the solar system, as it would represent the first member of the population of high-i, ϖ-shepherded TNOs.

9.2 Introduction

The most extreme members of any dynamical class of solar system objects serve as particularly acute test cases for theories of our solar system's formation and evolution. In particular, Trans-Neptunian Objects (TNOs) with very large semi-major axes probe the most distant observable regions of the solar system, aiding to reveal the migration histories of the giant planets. Very high inclination TNOs and centaurs mostly remain puzzling. Both classes of objects may also be dynamically influenced by distant, yet-unseen perturbers. Indeed, the apparent clustering in orbital and physical space of the so-called "extreme TNOs" with $a > 250$ AU and perihelion distances $q > 30$ AU was used by Batygin & Brown (2016a) to argue for the existence of a distant super-Earth known as Planet Nine.

The 13 currently known extreme TNOs have an average orbital inclination of 17.3°. The most highly-inclined of these objects, 2013 RF_{98}, was discovered in our earlier work (Dark Energy Survey Collaboration et al., 2016b) and has an inclination of 29.6°, consistent with other members of the scattered disk population. In this work, we report the discovery by the Dark Energy Survey of 2015 BP_{519}, a TNO with a semi-major axis of 450 AU (the sixth-largest among known TNOs), an eccentricity of 0.92, and a remarkable inclination of 54 degrees. The orbital elements of this object make it the "most extreme" of the extreme TNOs, in a sense that we make precise in Section 9.4.2. With a perihelion distance of $q = 35.249 \pm 0.078$ AU, it may also be the first purely trans-Neptunian member of the Planet-Nine-induced high-inclination population first predicted in Batygin & Morbidelli (2017).

Objects in the outer solar system populate several distinct dynamical categories (Gladman et al., 2008). Cold classical Kuiper Belt Objects (CKBOs) are dynamically cool, with perihelion distances greater than 40 AU, low orbital eccentricities, and low orbital inclinations (Tegler & Romanishin, 2000; Elliot et al., 2005). The orbits of these objects are not controlled by dynamical interactions with Neptune, and they may originate from material left over from the formation of

the solar system. On the contrary, hot classical KBOs as well as resonant KBOs are believed to have been placed in the trans-Neptunian region from smaller original heliocentric distances. Another class of objects have orbits that are perturbed significantly through scattering interactions with Neptune (Duncan & Levison, 1997; Gladman et al., 2002). Yet another set of objects have high eccentricities, but also have sufficiently large perihelia that they are not influenced by either scattering or resonant interactions with Neptune. A summary of the types of objects present in the Kuiper Belt is given in Figure 9.1.

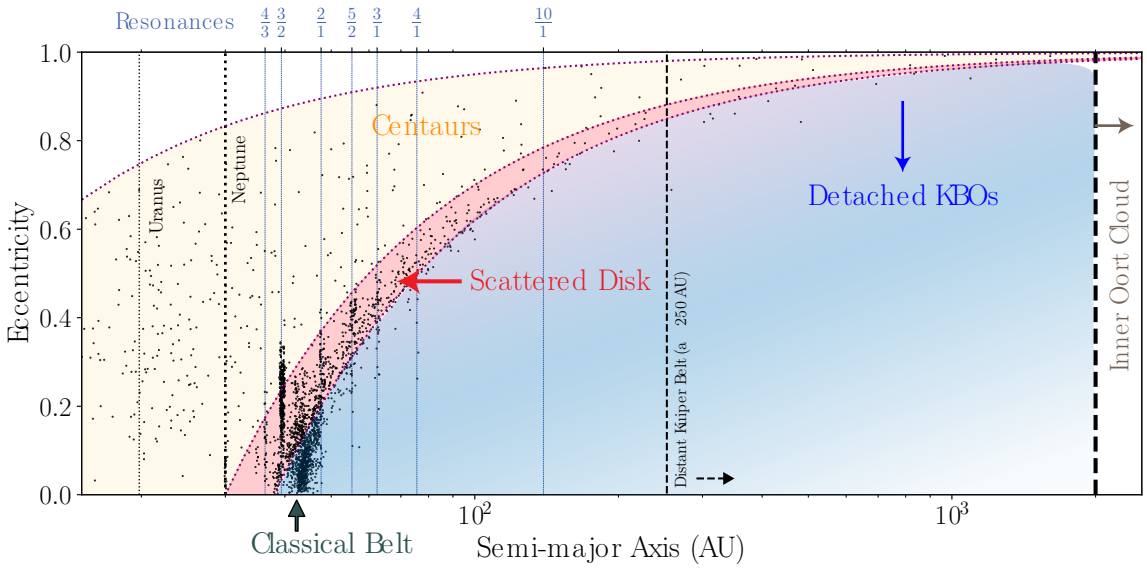

Figure 9.1 Dynamical Classes of Kuiper Belt Objects. The different classes of objects present in the outer solar system. Objects can be approximately delineated into dynamical classes according to their orbital elements, but exact classification require numerical simulations. The discovered objects (as of December 2018) are plotted as grey points. 2015 BP_{519} resides in the scattered disk. This figure was also published in Batygin et al. (2019).

Recently, a new subset of objects has attracted considerable attention. The TNOs with semi-major axes $a > 150$ AU and perihelia distances beyond 30 AU were found in Trujillo & Sheppard (2014) to exhibit a clustering in their argument of perihelion, ω. Batygin & Brown (2016a) subsequently noted that this clustering persists in physical space (as measured by the longitude of perihelion ϖ, where $\varpi = \omega + \Omega$, where Ω is the longitude of ascending node). Trujillo & Sheppard (2014) noted that one explanation for the clustering might be a ninth planet, and Batygin & Brown (2016a) suggested that the existence of a ninth planet of about 10 Earth masses in the outer solar system could explain the apparent alignment of large-semi-major axis objects (Batygin & Brown,

2016a). The motions of objects with $a > 250$ AU would in this case be dominated by Planet Nine, while TNOs falling in the intermediate regime, with $a = 150 - 250$ AU, may experience differing degrees of influence from Planet Nine. The TNOs with $a > 250$ AU constitute the "extreme" TNOs, or ETNOs. The evidence and consequences of the Planet Nine hypothesis have been explored in previous literature from both dynamical and observational perspectives (Batygin & Brown, 2016b; Li & Adams, 2016b; Malhotra et al., 2016b; Mustill et al., 2016b; Kenyon & Bromley, 2016; Bromley & Kenyon, 2016; Chen et al., 2016b; Holman & Payne, 2016a,c; de la Fuente Marcos & de la Fuente Marcos, 2016; Sheppard & Trujillo, 2016; Shankman et al., 2017a; Millholland & Laughlin, 2017; Saillenfest et al., 2017a; Becker et al., 2017; Batygin & Morbidelli, 2017; Hadden et al., 2017; Parker et al., 2017; Eriksson et al., 2018; Khain et al., 2018a). The Planet Nine hypothesis has been invoked to explain the detachment of perihelia distance for the most distant class of TNOs (Khain et al., 2018a), the 6 degree solar obliquity (Bailey et al., 2016b; Gomes et al., 2017), and the existence of highly inclined objects in the outer solar system (Batygin & Brown, 2016b). The subset of objects discovered so far to have semi-major axis greater than 250 AU and perihelion distances greater than 30 AU (the extreme TNOs) includes 2003 VB_{12} (known as Sedna, Brown et al., 2004), 2004 VN_{112} (MPC), 2007 TG_{422} (MPC), 2010 GB_{174} (Chen et al., 2013), 2012 VP_{113} (Trujillo & Sheppard, 2014), 2013 FT_{28} (Sheppard & Trujillo, 2016), 2013 RF_{98} (MPC), 2013 SY_{99} (Bannister et al., 2017), 2014 FE_{72} (Sheppard & Trujillo, 2016), 2014 SR_{349} (Sheppard & Trujillo, 2016), 2015 GT_{50} (Shankman et al., 2017b), 2015 KG_{163} (Shankman et al., 2017b), and 2015 RX_{245} (Shankman et al., 2017b). The orbital elements of these objects are listed in the Appendix for reference. These objects have inclinations ranging from nearly zero up to a maximum of about 30 degrees.

The orbital inclinations of these high-a objects are of particular interest dynamically. Gladman et al. (2009) discovered 2008 KV_{42} (Drac), the first retrograde Centaur (where a Centaur is an object with a semi-major axis between 5 AU and 30 AU, placing its orbit in the region of the solar system containing the gas giants). This object does not appear to be primordial and could imply the existence of a reservoir of high inclination TNOs. The discovery of the retrograde centaur 2011 KT_{19} (Niku) (Chen et al., 2016) added to the small collection of such objects, and suggested that they may cluster in a common orbital plane.

Batygin & Brown (2016a) predicted that Planet Nine could create such a supply of objects by

sourcing them from a more distant population of high-inclination orbits, which are in turn generated by Planet Nine. Batygin & Morbidelli (2017) presented a dynamical model for the orbital evolution of high-inclination, long period ($a > 250$ AU) objects and compared the model to the existing high-a, high-i objects. However, the objects then known to reside in that population have perihelia $q < 30$ AU, and thus experience orbit crossing with the giant planets, complicating their ability to test the Planet Nine hypothesis. To better test this particular prediction of the Planet Nine model, high-a, high-i objects with perihelion $q > 30$ AU are needed.

Apart from the Planet Nine debate, the continued discovery of new objects in the outer solar system enables a better understanding of how the solar system arrived at its present state. For this reason, many groups have conducted surveys to increase the census of objects known in the outer solar system and better understand their properties (including Millis et al., 2002; Elliot et al., 2005; Müller et al., 2010; Lellouch et al., 2010; Lim et al., 2010; Fornasier et al., 2013; Bannister et al., 2016b; Lin et al., 2016b). Data from other surveys or archival data sets have also been utilized to enable solar system science (Fuentes & Holman, 2008; Solontoi et al., 2012; Ahn et al., 2014). The Dark Energy Survey (DES, Dark Energy Survey Collaboration et al. 2016a) follows in these footsteps, enabling study of new populations including high-inclination objects like 2015 BP_{519}.

This chapter is organized as follows. We start with a description of the discovery of 2015 BP_{519} by DES in Section 9.3. Given the extreme status of this object, Section 9.4 considers its dynamical status using a secular approach, starting with an analytic treatment of the problem. The dynamics of this object are rich and complicated, so that a complete characterization requires full N-body numerical simulations to include interactions with Neptune and the other giant planets, as well as other complexities. These numerical simulations are presented in Section 9.5 for the dynamics of 2015 BP_{519} in the context of the currently known solar system. Section 9.6 then considers the dynamics of this new object in the presence of the proposed Planet Nine. The chapter concludes with a discussion of the implications (Section 9.7) and a summary of the results (Section 9.8).

9.3 Discovery of 2015 BP_{519}

DES Dark Energy Survey Collaboration et al. 2016a is an optical survey targeting nearly 5000 square degrees of sky. It uses the Dark Energy Camera (DECam, Flaugher et al., 2015) on the 4-meter Blanco telescope at the Cerro Tololo Inter-American Observatory in Chile. DECam is a prime-focus imager on Blanco with a 3 square degree field of view and a focal plane consisting of 62 $2K \times 4K$ red-sensitive science CCDs. DES saw first light in 2012, and the nominal survey period of 520 nights over five years ran from August 2013 through February 2018. During this time, DES has operated in two survey modes. The Wide Survey observes the full of the survey area roughly twice per year in each of the *grizY* bands. The Supernova Survey (Bernstein et al., 2012) consists of ten 3 square degree regions that are observed roughly every 6 days in the *griz* bands. Due to the large survey area, high repetition, and deep limiting magnitude for single-epoch exposures (r ∼23.8 magnitude), DES has many applications in addition to its main cosmological objectives (Dark Energy Survey Collaboration et al., 2016b). It is well-suited for solar-system science, and in particular to the study of high-inclination populations.

In this chapter, we report the discovery of 2015 BP_{519}, which has the largest semi-major axis of any object yet found by DES, and the highest inclination of any known extreme TNO. 2015 BP_{519} was first detected at a heliocentric distance of 55 AU in the same set of observations from 2013-16 that were used to discover the dwarf planet candidate 2014 UZ_{224} (Gerdes et al., 2017b). The original detection of 2015 BP_{519} came from a difference-imaging analysis of the wide field images (using software from Kessler et al., 2015). Transient objects are found by image subtraction. Artifacts and low-quality detections are rejected using the techniques described in Goldstein et al. (2015). The surviving sources are compiled into a catalog of measurements, each of which corresponds to a transient at one epoch. From those, TNOs are extracted by identifying pairs of detections within 60 nights of each other whose angular separation is consistent with what would be expected for an object with perihelion $q > 30$ AU given Earth's motion. These pairs are linked into chains of observations that correspond to the same object by testing the goodness of fit of the best-fit orbit for each chain. A reduced chi-squared $\chi^2/N < 2$ (Bernstein & Khushalani, 2000) is considered a detection of a TNO.

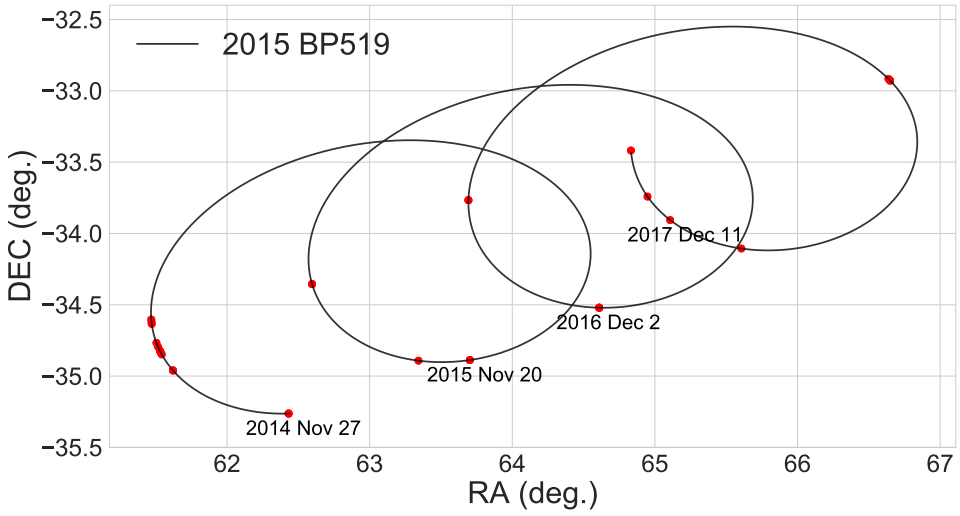

Figure 9.2 Trajectory of 2015 BP519. Trajectory of 2015 BP519 over its measured four-opposition arc. Larger, red dots along the trajectory indicate points at which it was observed by DES.

Although 2015 BP_{519} was originally identified using data from observing campaigns 2-4, we have obtained additional observations in two ways: first, some of the subsequent planned DES exposures provided additional serendipitous observations of this object. Second, we performed three targeted observations on 2 Feb. 2017 and 6-7 August 2017. The result is a series of 30 observations over four oppositions between 27 Nov. 2014 and 15 Feb. 2018, shown in Figure 9.2. We computed astrometric positions using the WCSFIT software described in Bernstein et al. (2017), which provides astrometric solutions referenced to the Gaia DR1 catalog (Gaia Collaboration et al., 2016b). This includes corrections for the effects of tree-ring and edge distortions on the DECam CCDs, as well as for chromatic terms from lateral color and differential atmospheric refraction. We obtain barycentric osculating orbital elements using the method of Bernstein & Khushalani (2000). For consistency with the orbital elements and uncertainties used in the simulation results presented below, our fit uses the 27 observations available through 11 Dec. 2017. The resulting fit has a χ^2 of 48.2 for 48 degrees of freedom, and a mean residual of 29 mas. These orbital elements are shown in Table 9.1. 2015 BP_{519}'s inclination and orbital orientation relative to the other extreme TNOs is also visualized in Fig. 9.3 (where the orbital elements used for the other plotted extreme TNOs are given in the Appendix, Table 9.3).

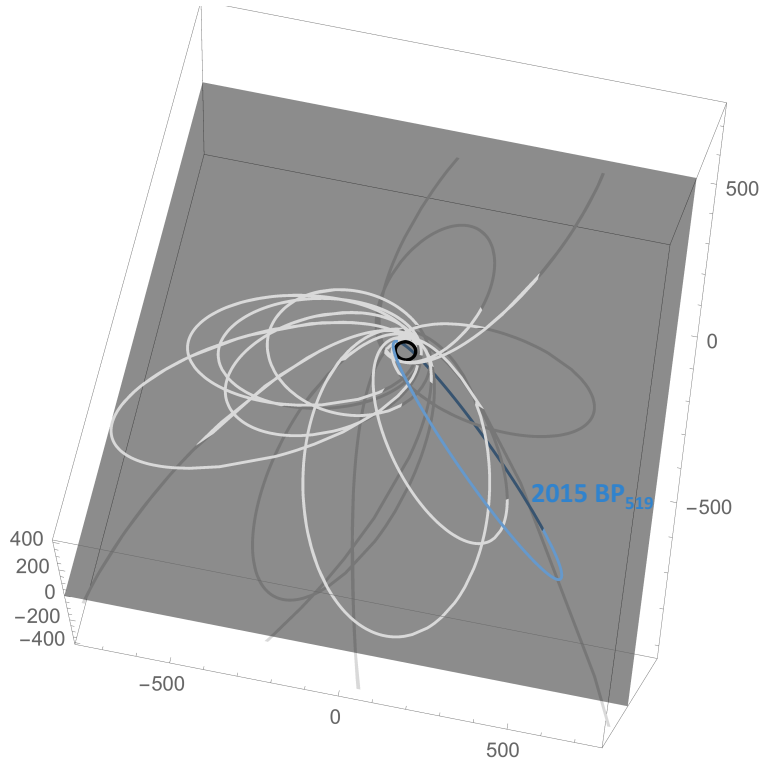

Figure 9.3 Three Dimensional Orbit Diagram. A visual representation of the orbit of 2015 BP_{519}, plotted with the other ETNOs as comparisons. For each orbit, the darker regions on the curve denote where an object falls below the plane of the solar system. 2015 BP_{519} has the highest inclination of any extreme TNO discovered to date. The full, interactive 3D orbit visualization can be found at `https://smillholland.github.io/BP519/`.

These 27 observations of 2015 BP519 include 8 measurements in the g-band, 9 in r-band, 6 in i-band, and 4 in z-band. Few of these observations were taken in close temporal proximity. To compute the colors of this object, we therefore compute the corresponding absolute magnitude H of each measurement to correct for the varying object-sun and object-earth distances as well as differences in observational phase. The g-r color, for example, is then computed as $< H_g > - < H_r >$, and its uncertainty is $(< H_g^2 > + < H_r^2 >)^{1/2}$. The moderately red g-r and r-z colors are consistent with the values measured in (Pike et al., 2017) for objects identified as dynamically excited.

For TNOs with magnitudes in the range $H \sim 2-4$, measured visual albedos have been found to range between 0.07 and 0.21 (Brucker et al., 2009; Lellouch et al., 2013; Fraser et al., 2014; Gerdes et al., 2016b; Holman et al., 2018). With $H_r = 4.3$, the diameter of 2015 BP_{519} could range from

400-700 km, depending on whether the albedo falls near the high or low end of this range.

Because the DES survey area lies predominantly out of the ecliptic, the status of 2015 BP_{519} as the highest inclination TNO of those with semi-major axis $a > 250$ AU and perihelion $q > 30$ AU must be considered in the context of possible bias of the DES selection function. To explore this issue, we simulate an ensemble of clones of 2015 BP_{519} and test their recoverability in the DES TNO search pipeline. The orbital elements of these clones are drawn from the observed posteriors provided in Table 9.1, but with the inclination angle i drawn from a uniform distribution between 0 and 180 degrees. We then compute the orbits of these objects and where the clones would fall on the nights DES observed.

Using these synthetic orbital elements, we first remove any object that is not detectable by DES because it is either too faint or outside the survey area. We then compute the position of each remaining clone at the time of every DES exposure belonging to the data set in which 2015 BP_{519} was discovered, and determine which clones could be linked together into an orbit. The clones that could be identified as candidates are those with at least three observations on three different nights separated by less than 60 nights, and with observations on at least five different nights in total.

The distribution of clones that survives this process, and hence is potentially detectable, is presented in Fig. 9.4. This plot thus shows the sensitivity function for objects with the orbital parameters (a, e, ω, Ω) of 2015 BP_{519}, but with varying orbital inclinations and mean anomalies. The resulting sensitivity function shows some structure, but is not heavily biased toward the observed inclination angle of 2015 BP_{519}.

2015 BP_{519} has the highest inclination of any known TNO (defined as objects with $q > 30$ AU). 2015 BP_{519} also has an extreme eccentricity (0.92). Figure 9.5 compares the inclination and eccentricity occurrences by semi-major axis of the regular and extreme ($a > 250$ AU) TNO populations. Compared to the other known TNOs, 2015 BP_{519} has the largest orbital inclination. Since the number of known ETNOs is small, however, is it unclear where 2015 BP_{519}'s inclination places it in the true distribution of ETNO inclinations. For regular TNOs (objects with perihelion distance $q > 30$ AU but any semi-major axis), for which nearly 1500 have been discovered, 2015 BP_{519} is the most extreme and seems to lie at the upper tail of the inclination distribution of known objects; among TNOs, 2015 BP_{519} has the highest currently measured value, but this population

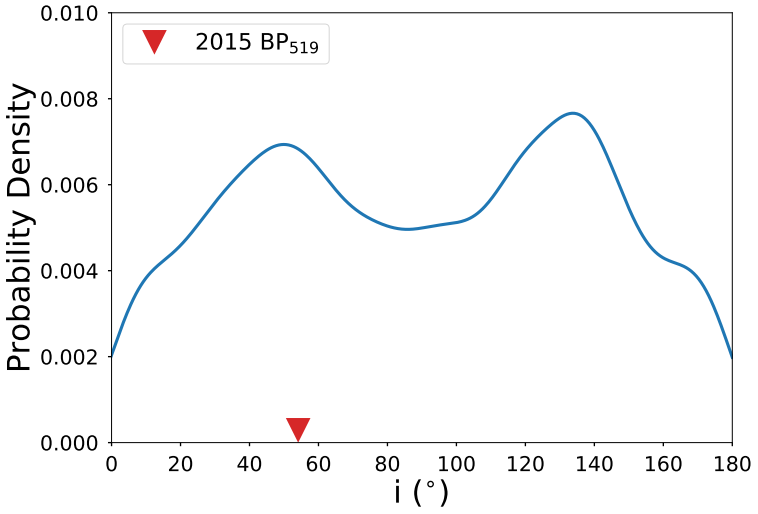

Figure 9.4 DES Selection Function. The DES selection function for the discovery of objects with the orbital elements of 2015 BP_{519}, but with varying inclination angles. The value for 2015 BP_{519} is shown as the red triangle. The probability distribution is normalized so that the area under the curve is unity.

is by no means complete.

In Fig. 9.6, we plot a sensitivity histogram computed in the method described above, but for objects with the orbital parameters (a, e, i) of 2015 BP_{519}, and varying ω and Ω. As was true for the previous sensitivity function, the final sensitivity histogram shows some structure in each orbital angle of interest, but is not heavily biased towards the measured angles of 2015 BP_{519} (which happen to be consistent with the region of clustering that was used to predict Planet Nine, as will be discussed further in later sections of this chapter. See also Figure 9.7; Trujillo & Sheppard 2014; Batygin & Brown 2016a).

9.4 Characterization of 2015 BP_{519}

As a starting point, we consider the dynamical behavior of 2015 BP_{519} using a secular treatment. The basic approach is outlined and compared with numerical N-body experiments in subsection 9.4.1, and this formalism is used to elucidate the extreme nature of this object in subsection 9.4.2.

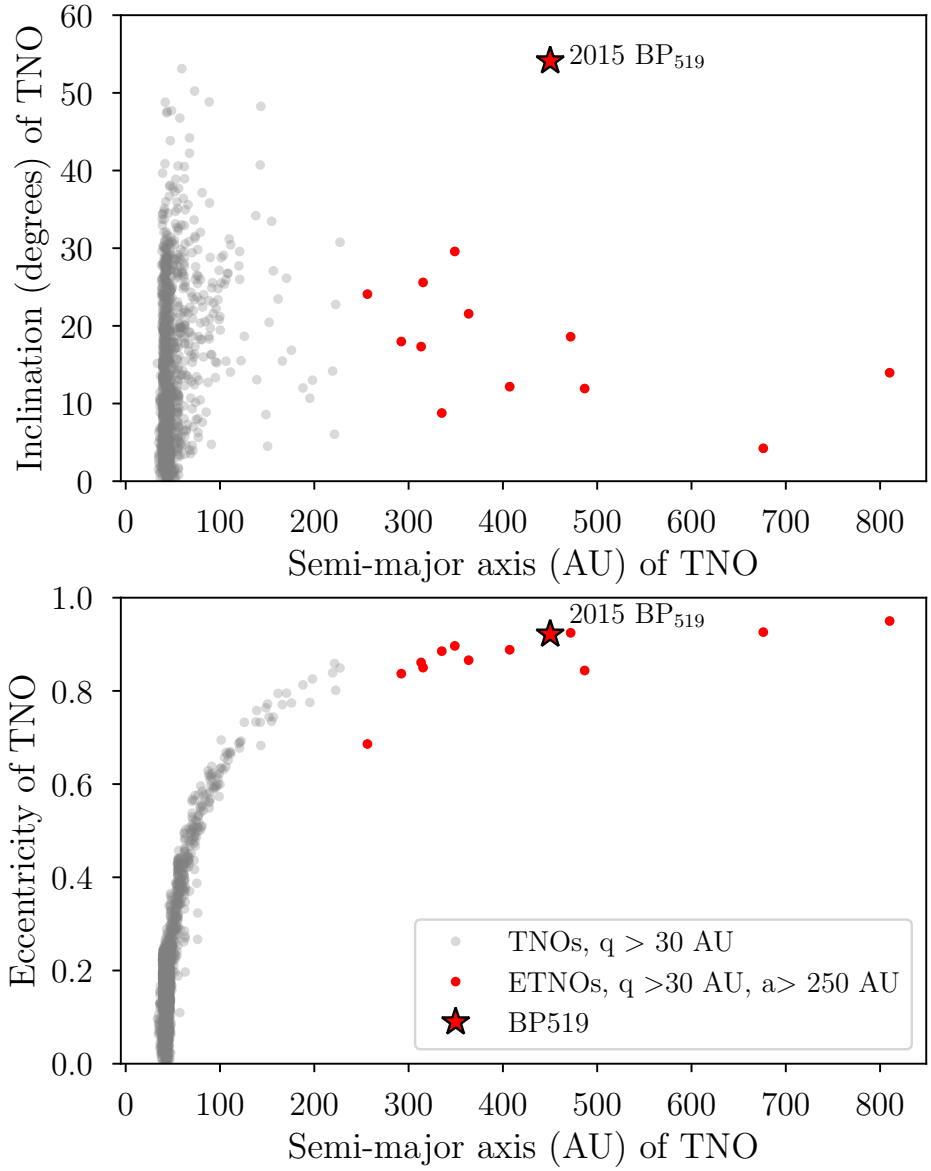

Figure 9.5 Distribution of Orbital Elements for all TNOs. The distributions of inclinations (top panel) and eccentricities (bottom panel) for the two populations of TNOs considered in this work: all objects with perihelia distances greater than 30 AU, and then the subset of those with semi-major axes greater than 250 AU. Orbits of known objects are fit from observations posted to the Minor Planet Center database. 2015 BP_{519} represents the tail of the inclination distribution of the known TNOs, as well as the upper limit of eccentricities populated by TNOs.

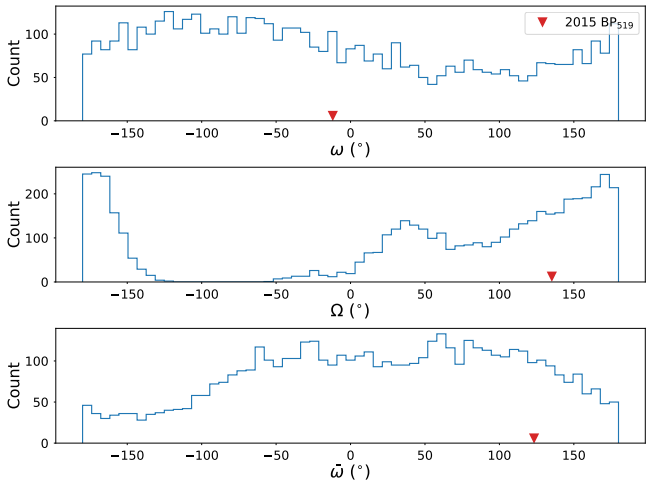

Figure 9.6 DES Angular Selection Function. The DES selection function for the discovery of objects with the orbital elements (a, e, i) of 2015 BP_{519}, but with varying angles ω, Ω. The observed values for 2015 BP_{519} are shown as red triangles on each panel. For objects with the orbital elements (a, e, i) of 2015 BP_{519}, the DES observation bias allows discovery of ω and Ω subtending most of the allowable ranges.

9.4.1 Secular Dynamics

A secular approach averages over the mean motion of solar system objects and thus allows for a simplified treatment of the long-term dynamics. Kozai (1962) provided secular equations for the orbital evolution of small bodies with high inclinations and eccentricities in the presence of an inner perturber. Here we want to describe the behavior of 2015 BP_{519}, which orbits outside a system of four interior perturbers (namely, the known giant planets). The contribution from the terrestrial planets is negligible in this context. We can write the mean perturbing function R_m for a test particle evolving in the presence of a set of inner planets in the form

$$R_m = \frac{G}{16a^3\left(1-e^2\right)^{3/2}}\left[\sum_j^N (m_j a_j^2)(1+3\cos 2i) + \frac{9\sum_j^N (m_j a_j^4)\left(2+3e^2\right)\left(9+20\cos 2i+35\cos 4i\right)}{512a^2\left(1-e^2\right)^2} + \frac{9\sum_j^N (m_j a_j^4)\ 40e^2(5+7\cos 2i)\cos 2\omega \sin^2 i}{512a^2\left(1-e^2\right)^2}\right], \tag{9.1}$$

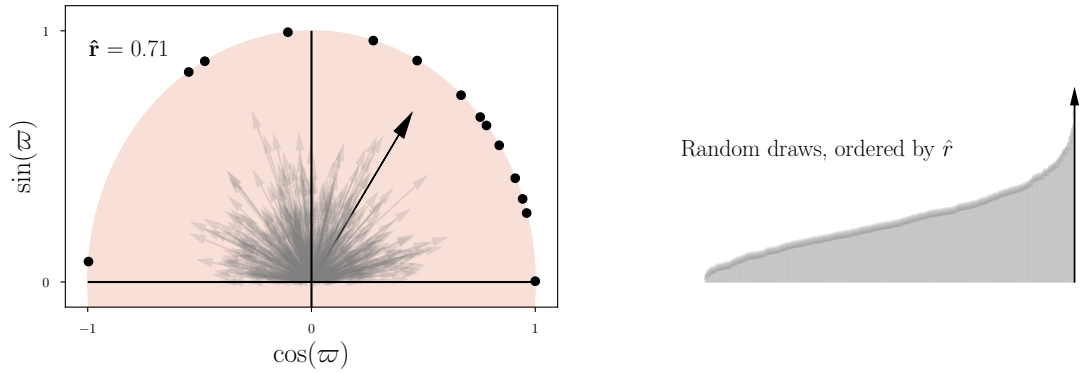

Figure 9.7 Circular Signal Analysis. An adapted circular signal analysis (CSA) (similar to that done in **?**; for original technique see Lutz 1985). To account for the alignment and anti-alignment predictions, we fold the unit circle on the predicted ϖ of Planet Nine. The points on the circumference of the circle are the known extreme TNOs ($a > 250$ AU, $q > 30$ AU), including 2003 VB_{12} (Sedna), 2004 VN_{112}, 2007 TG_{422}, 2010 GB_{174}, 2012 VP_{113}, 2013 FT_{28}, 2013 RF_{98}, 2013 SY_{99}, 2014 FE_{72}, 2014 SR_{349}, 2015 GT_{50}, 2015 KG_{163}, and 2015 RX_{245} as well as our new object, 2015 BP_{519}. The length of vector $\hat{r} = \sqrt{\langle x \rangle^2 + \langle y \rangle^2}$ increases with increasing strength of clustering to a maximum at $\hat{r} = 1$, with $\hat{r} = 0$ being totally uncorrelated. This clustering visualization does not account for the bias of the surveys that discovered the TNOs in this population. Grey arrows are simulated observations from a uniform angular distribution, and the right panel orders by $\hat{r}$ the simulated draws (grey) and true observed clustering (black). *Note:* this analysis does not account for the observational biases inherent in the surveys that discovered each known TNO. Future work (Hamilton et al., *in prep*) will attempt to quantify the biases inherent in the DES detection.

Parameter	Value
a	448.99 ± 0.49 AU
e	0.92149 ± 0.00009
i	54.1107 ± 0.00001 deg
ω	348.058 ± 0.00136 deg
Ω	135.2131 ± 0.00010 deg
Time of Perihelion (JD)	2473015.55 ± 0.56
Perihelion	35.249 ± 0.078 AU
Aphelion	862.733 ± 0.972 AU
Orbital Period	9513.84 ± 15.42 years
Absolute magnitude	$H_r = 4.3$
g-*r* (mag)	0.79 ± 0.17
r-*i* (mag)	0.19 ± 0.12
r-*z* (mag)	0.42 ± 0.15
i-*z* (mag)	0.23 ± 0.15

Table 9.1 Orbital Elements of 2015 BP_{519}. 2015 BP_{519} barycentric osculating elements at epoch 2456988.83, based on 27 observations over a 1110-day arc from 27 Nov. 2014 to 12 Dec. 2017. 2015 BP_{519} has a mean anomaly 358.34 degrees and will reach perihelion on 14 Oct. 2058.

where the effects of the inner planets are included here as a mean moment of inertia (Gallardo et al., 2012). In this expression, G is the gravitational constant ($G = 4\pi^2$; we work in units of solar mass, AU, and year), (a, e, i) are the orbital elements of the test particle, $\sum_j^N (m_j a_j^2)$ is the moment of inertia in the direction out of the plane containing the giant planets, and the label j denotes each giant planet under consideration.

From this secular Hamiltonian, we can derive an expression for the time evolution of the inclination angle using Lagrange's planetary equations, which takes the form

$$\frac{di}{dt} = -\tan(i/2)(na^2\sqrt{1-e^2}\,)^{-1}\left(\frac{dR_m}{d\epsilon} + \frac{dR_m}{d\varpi}\right) - (na^2\sqrt{1-e^2}\sin i)^{-1}\frac{dR_m}{d\Omega}\,. \tag{9.2}$$

where $n = (GM/a^3)^{1/2}$ is the mean motion, M is the mass of the central body, and ϵ is the mean longitude at epoch. Combining the previous two expressions yields the equation of motion for i:

$$\frac{di}{dt} = \frac{45e^2G^{1/2}\sum_j^N (m_j a_j^4)}{1024\ M^{1/2}\ a^{11/2}(1-e^2)^4}(5 + 7\cos 2i)\sin 2i \sin 2\omega\,. \tag{9.3}$$

Analogous equations can also be constructed using the other Lagrange planetary equations, resulting in equations of motion for de/dt, $d\omega/dt$, $d\Omega/dt$ (see Equations 7-11 of Gallardo et al. 2012), and $da/dt = 0$. Using the known (estimated) orbital elements for 2015 BP_{519} (see Table 9.1) as initial conditions, we simultaneously solved these five equations of motion, resulting in predicted secular evolution for 2015 BP_{519}'s orbital evolution. This result is shown in Fig. 9.8 as the solid curve. The figure shows additional curves in thinner grey lines corresponding to the orbital evolution computed for the same initial conditions, but using full N-body integrations instead of secular theory. These simulations are described in full in the following section, and their parameters are also summarized as Set 1 in Table 9.2. As a quick summary, these integrations are computed using the `Mercury6` integration package (Chambers, 1999b), using the hybrid symplectic and Bulirsch-Stoer (B-S) integrator and a time-step of 20 days. In these simulations, all four of the known giant planets are treated as active bodies (rather than being modeled using the J_2 approximation that is often used).

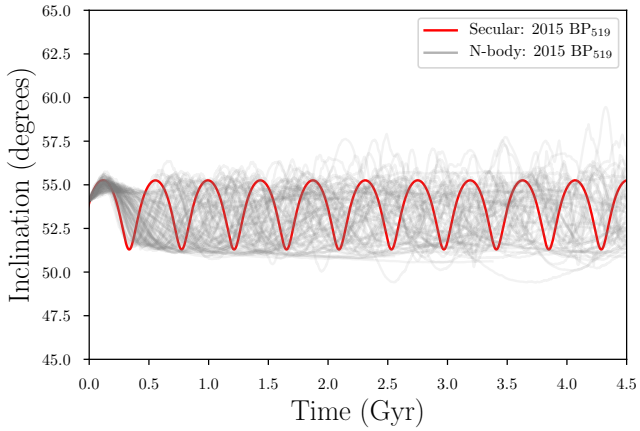

Figure 9.8 Evolution of 2015BP519 in Known Solar System: Secular vs. Numerical. The future evolution of 2015 BP_{519} (using its current day best-fit orbital parameters as initial conditions) in the presence of the known solar system. The secular curve plotted as a solid dark line was solved from the disturbing function (Equation 9.1) and the best-fit orbital elements of 2015 BP_{519}. The numerical results, plotted as grey lines, are drawn from simulation Set 1, where the orbit of 2015 BP_{519} is evolved in the presence of the known solar system for 4.5 Gyr. See Table 9.2 for more details on the simulation parameters.

Figure 9.8 shows that the secular approximation provides a good order of magnitude description of the time evolution of the inclination angle, even through the secular approximation does not include the scattering interactions that lead to slight divergence in the N-body simulations. Both

the secular and N-body treatments predict that, in the known solar system, the inclination of 2015 BP_{519} will remain fairly well constrained around its presently observed value.

9.4.2 The Extreme Nature of 2015 BP_{519}

Although the orbit of 2015 BP_{519} is highly unusual among known TNOs, we need a quantitative assessment of its properties relative to other TNOs of its dynamical class. Toward that end, we consider the Kozai Hamiltonian written in Delaunay coordinates (Thomas & Morbidelli, 1996), for which the action H is defined as:

$$H = \sqrt{a(1-e^2)}\cos i\,. \tag{9.4}$$

Note that this action is equivalent to the standard '$\mathcal{H}$' variable in Delaunay coordinates (**?**) and is a constant of the motion in the quadrupolar approximation. The action $L = \sqrt{a}$ will also be constant, as the Kozai Hamiltonian averaged over the mean anomaly and thus rotationally invariant and thus depends only on action $G = \sqrt{a(1-e^2)}$ and coordinate $g = \omega$, with actions L and H being conserved. Next, we define a reduced Kozai action η_0, which has the form

$$\eta_0 = \sqrt{(1-e^2)}\cos i\,. \tag{9.5}$$

As action L is conserved for the Kozai Hamiltonian, this reduced form of action H should also be conserved. Note that η_0 is the specific angular momentum vector in the direction out of the plane of the solar system (Kinoshita & Nakai 1999; we follow the notation in Saillenfest et al. 2016). For sufficiently distant TNOs, the potential of the solar system is effectively axially symmetric (but not spherically symmetric), so that the z-component of angular momentum (but not total angular momentum) is conserved. In the known solar system, TNOs with constant semi-major axis are thus expected to evolve in (i, e) space along contours of constant η_0. In Fig. 9.9, we overlay curves of constant η_0 on a plot comparing the i, e of all TNOs and ETNOs discovered so far. Compared to previously discovered objects, 2015 BP_{519} has the lowest η_0 value which signifies its relative extremeness.

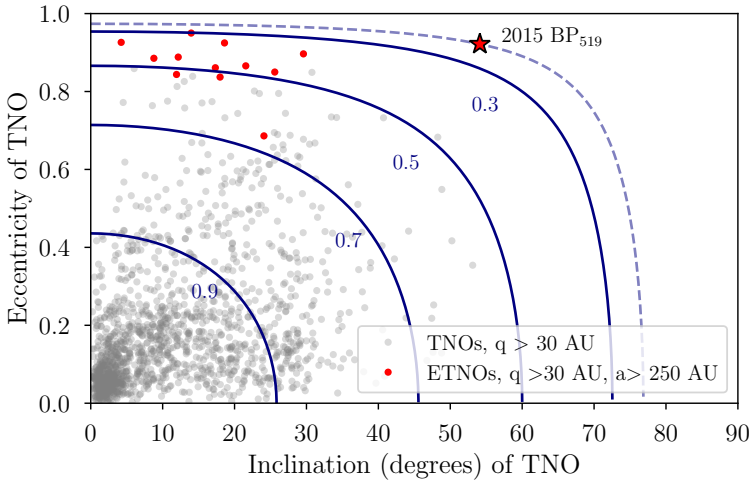

Figure 9.9 Comparison of the Kozai Action for all Discovered TNOs. We plot curves of constant η_0 in (i, e) space (see Equation 9.5). Also plotted are (in grey) the orbital elements of all objects with perihelion distances outside of Neptune and data quality flags of 6 or better, as reported to the Minor Planet Center database (files downloaded 10/25/2017) and (in red) the subset of those objects that also have a semi-major axis measured to be $a > 250$ AU. With $\eta_0 = 0.2274$, 2015 BP_{519} has the lowest value of η_0 out of any TNO with $q > 30$ AU that has been discovered thus far. This metric, which measures the extremeness of the (i, e) of each object, characterizes 2015 BP_{519} as the most extreme of the extreme TNOs.

9.5 Full Dynamics of 2015 BP_{519} in the Known Solar System

The analytic formulation presented in Section 9.4 classifies 2015 BP_{519} as the most extreme TNO discovered in the outer solar system to date, due to its high inclination, high eccentricity, and large semi-major axis. However, the secular approximation used in the previous section neglects the importance of interactions with Neptune, which will occur when 2015 BP_{519} reaches its perihelion. 2015 BP_{519}'s relatively small perihelion distance ($\approx$ 35 AU) suggests that it will be subject to repeated strong interactions with Neptune, which will change the energy of 2015 BP_{519}'s orbit by a factor of roughly 6×10^{-6} per perihelion crossing (when this process can be modeled as a random walk; see Fig. 1 of Duncan et al., 1987). The change in orbital energy will also lead to change in the semi-major axis of the orbit, and as a result, the level curves presented in Fig. 9.9 may not truly represent the evolution of 2015 BP_{519} over extended spans of time. Instead, quantities which appear as constants of motion in the previous section (η_0) will no longer be conserved as 2015 BP_{519} changes its orbital elements, in particular its semi major axis, due to interactions with

Neptune. The true orbital evolution, being the result of a chaotic process, will also vary widely between trials in numerical integrations. As shown in Fig. 9.8, the numerically computed orbital evolution does not perfectly match the secular expectation, and multiple integrations of the same object will give slightly different periods and amplitudes of evolution.

To fully test the effect of additional dynamics not encapsulated by the secular analysis of the previous section, we perform a suite of numerical N-body simulations using computing resources provided by Open Science Grid (Pordes et al., 2007; Sfiligoi, 2008; Sfiligoi et al., 2009) through the Extreme Science and Engineering Discovery Environment (XSEDE) portal (Towns et al., 2014). These simulations include the new body 2015 BP_{519} and all of the relevant known solar system objects (the case of Planet Nine is considered in the following section, but is excluded from this initial set of simulations).

9.5.1 Numerical Evolution of 2015 BP_{519} in the Known Solar System

The precession time scales and orbital evolution of 2015 BP_{519} can be tested more directly with numerical N-body simulations. To examine the complete evolution of 2015 BP_{519} in the known solar system, we perform a suite of numerical integrations using the `Mercury6` integration package (Chambers, 1999b). We exclude the terrestrial planets from the simulations, but include the gas giants (Jupiter, Saturn, Uranus, and Neptune) as active, massive particles with their currently measured masses and orbital elements. We start with a time-step of 20 days, which is roughly 0.5% of Jupiter's orbital period. We use the hybrid symplectic and Bulirsch-Stoer (B-S) integrator built into `Mercury6` and conserve energy to better than 1 part in 10^9 over the course of the 4.5 Gyr integrations. The orbital elements for 2015 BP_{519} are drawn from the covariance matrix derived from the fit to the DES data. Fifty-two simulations are run of the solar system, each with five clones of 2015 BP_{519}. Half of these simulations are integrated forward in time from the current day, and the other half evolve back in time for 4.5 Gyr. Other parameters used for this set of simulations (which we call Set 1 in this work) are given in Table 9.2.

The results of these integrations are presented in Fig. 9.10, and demonstrate that the semi-major axis of 2015 BP_{519} diffuses widely in the presence of the known giant planets. The perihelion distance tends to remain fairly well-confined near the initial value of even as the orbital energy

Set	**Initial Timestep**	**Active Planets**	J_2	**Abs. Radius**	**Backwards Clones**	**Forward Clones**	**Details**
Set 1	20 days	4 (JSUN)	2×10^{-7}	4.65×10^{-3} AU	130	130	No P9
Set 2	3000 days	1 (P9)	0.00015244	20 AU	0	1000	low i[1], P9[2]
Set 3	3000 days	1 (P9)	0.00015244	20 AU	0	1000	P9[2]
Set 4	200 days	2 (N,P9)	0.00036247	9.8 AU	0	600	P9[2]
Set 5	20 days	5 (JSUN, P9)	2×10^{-7}	4.65×10^{-3} AU	0	130	P9[2]

Table 9.2 Simulation Sets Used in This Work. A list of the sets of simulations used in this work, with their relevant parameters listed. When included as active particles in a simulation, gas giant planets are denoted by their first initials (J for Jupiter, S for Saturn, U for Uranus, N for Neptune) and when Planet Nine is included, it is denoted by P9. The absorbing radius is the radius of the central body in the simulations. The ejection radius is set to 10000 AU for all simulation sets, and all integrations are run for 4.5 Gyr. Except when denoted otherwise, the orbital elements of 2015 BP_{519} are drawn from the covariance matrix describing the best-fit values and errors in Table 9.1. Simulations were run in batches; for simulation Sets 1 and 5, 5 clones of 2015 BP_{519} were included as test particles in each individual integration. For simulation Sets 2, 3, and 4, 10 clones were included in each integration. [1] Inclination of 2015 BP_{519} was drawn from a half-normal distribution around 0 degrees with a width of 5 degrees. [2] The best-fit version of Planet Nine from Batygin & Morbidelli (2017) was used (700 AU, 0.6 eccentricity, 20 degrees inclination). The solar quadrupole moment J_2 is defined by Eq. 9.6 when any giant planets are absorbed, and set to the solar value otherwise (Pireaux & Rozelot, 2003).

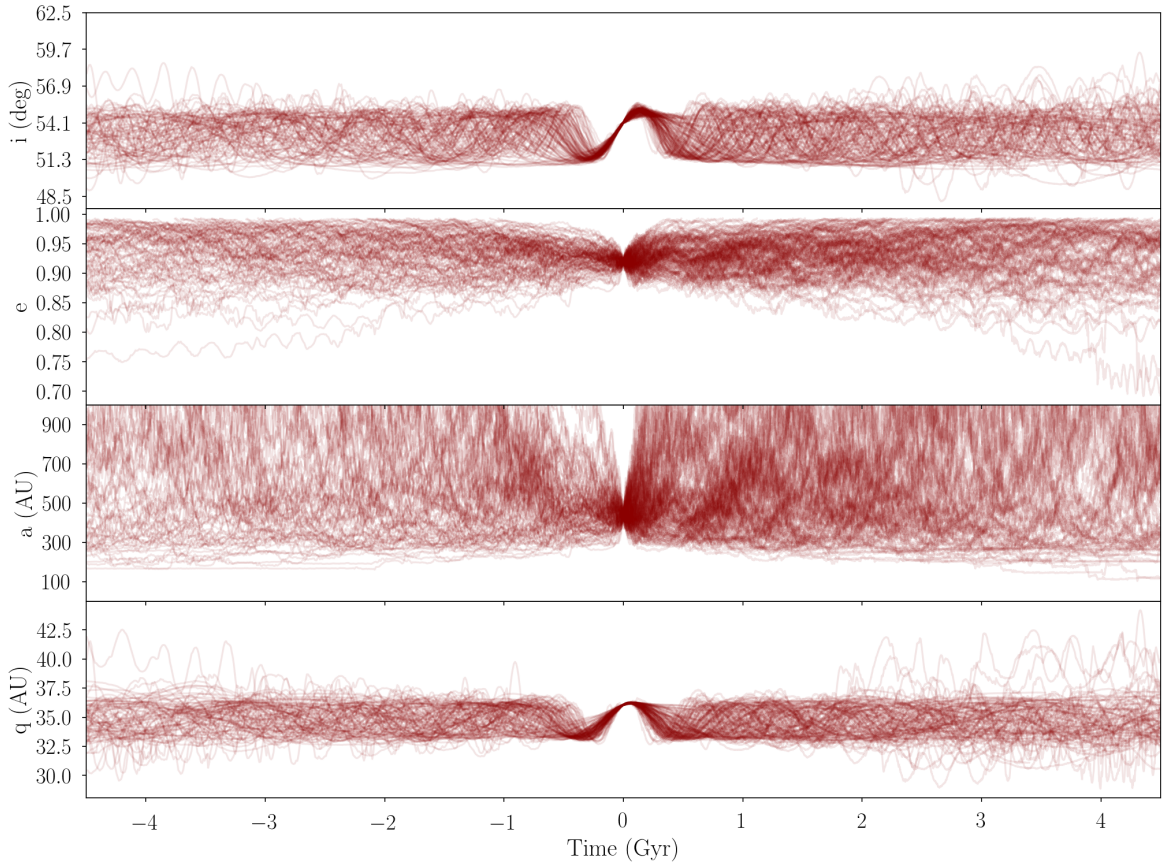

Figure 9.10 Evolution of 2015BP519 in Known Solar System. The results of numerical simulations where 2015 BP_{519} is evolved forward and backward in time in the presence of the four giant planets (Set 1; see Table 9.2). All trials are plotted here; curves that end prematurely before 4.5 Gyr correspond to the integrations where a clone becomes dynamically unstable (collision into the central body, ejection from the system, physical collision with a planet, or a scattering event resulting in an unbound orbit). For trials that remain dynamically stable, the inclination and eccentricity are relatively well constrained to values near their initial conditions. The semi-major axis of 2015 BP_{519} diffuses rapidly.

changes due to repeated kicks from Neptune.

The Hamiltonian used in Section 9.4.2 requires that the semi-major axis of the particle remain roughly constant. From these simulations, it is clear that the semi-major axis of 2015 BP_{519} tends to change significantly over relatively rapid ($\sim 10^6 - 10^7$ year) timescales. As such, Equation 9.5 is a good model for 2015 BP_{519}'s short-term dynamical behavior, but not its long-term orbital evolution.

9.5.2 Generating Highly Inclined Objects in the Known Solar System

In the previous section, we used numerical simulations to determine the expected evolution of 2015 BP_{519} in the presence of the four known gas giants. The results show that the inclination of 2015 BP_{519} tends to be confined to within a range of roughly 5 degrees. Although the semi-major axis diffuses over a wide range of values, the corresponding evolution in eccentricity is constrained by the behavior of the perihelion: to leading order, the perihelion distance of 2015 BP_{519} remains well confined. Specifically, q is constant to within $\sim$5 AU over the entire envelope of all dynamically stable clones. The eccentricity evolution of 2015 BP_{519} is thus explained by the requirement that the perihelion remains nearly constant as the semi-major axis varies. Moreover, this behavior is mediated by Neptune. The orbital evolution is consistent with that expected for a member of the scattered disk.

The high present-day inclination of 2015 BP_{519} is more difficult to explain. In the numerical simulations shown in Figure 9.10 in the context of the currently-observed solar system, the orbital inclination of 2015 BP_{519} is found to remain roughly constant. This trend holds for simulations running both backwards and forwards in time. Since the solar system formed from a disk, we expect the orbital inclination of 2015 BP_{519} to be low at birth. The transition from an initially low inclination orbit to the present-day (high) value must be explained by some mechanism that is not included in our simulations. Some possible explanations include the following: a passing star could excite objects to highly inclined and eccentric orbits; a particularly favorable impact parameter during a close encounter with Neptune could excite an object out of the plane of the solar system; the high inclination could be a fossil from violent migration processes in the early solar system; the self-gravity of a large disk of planetesimals in the scattered disk; and finally, the

existence of proposed solar system member Planet Nine, which could lead to secular evolution in eccentricity and inclination for long-period TNOs, thereby producing the current-day orbit of 2015 BP_{519}. In this section, we briefly consider the first three possibilities, and then examine the Planet Nine hypothesis in detail in Section 9.6.

Scattering interactions with other stars As most planetary systems form in clusters (Lada & Lada, 2003; Porras et al., 2003), the solar system is likely to have formed in such an environment (Adams, 2010). Dynamical interactions between cluster members can shape the dynamics of the constituent planetary systems (Brasser et al., 2012a). The interactions tend to have a moderate effect (Adams et al., 2006), but can nonetheless sculpt the outer portions of the planetary system or the original disk, which are of interest here. Interactions in the birth cluster are expected to dominate over those that occur later on in the field, but the latter can still be significant. If the trajectory of a binary or single star brings it sufficiently close to a star hosting a planetary system, the geometry of the planetary system can be altered (Jiménez-Torres et al., 2011). For example, Kenyon & Bromley (2004) discuss the possibility that Sedna's orbit is the result of a passing star perturbing the orbit of objects in the Kuiper Belt. They find that if such a star had its own disk of planets and planetesimals, then some objects could be captured into our solar system onto high-inclination orbits. It is thus possible that 2015 BP_{519} is the result of interactions between our solar system and another external, perturbing body. The interaction cross sections for such events are much larger at the low fly-by speed realized in young embedded clusters (Li & Adams, 2015d), so that the required event is more likely to occur in the birth cluster (compared to the field).

Scattering interactions with Neptune As discussed in Duncan et al. (1987), TNOs will experience a perturbation in orbital energy at each periapsis, when the TNO passes closest to the orbit of Neptune. Although Fig. 9.10 demonstrates that in our set of backwards integrations 2015 BP_{519} has retained *roughly* the same inclination for the past 4.5 Gyr, there is some variation among the individual trials. More specifically, one particular integration in the backwards time direction attained (at one point) an orbital inclination of 60 degrees, although such a large value was not attained in any of the other integrations in either direction. With a large enough set of simulations, one could find the probability that 2015 BP_{519} could originate in an orbit closer to the plane of the solar system, and subsequently evolve into its present orbit. In this scenario, 2015 BP_{519} could

have reached its high inclination from a series of extreme scattering events with Neptune. Our current set of numerical simulations shows that this scenario is possible, but unlikely.

Remnant of planetary migration

The Nice model (Tsiganis et al., 2005; Morbidelli et al., 2005; Gomes et al., 2005) suggests that even if the solar system starts as a roughly co-planar disk, the planets attain their small eccentricities and inclinations through scattering events with the large reservoir of planetesimals in the outer solar system. Some of these bodies will be forced to high eccentricities and inclinations, while others will be able to maintain their lower (e, i) distributions (Levison et al., 2008). This scenario is characterized by a short period of extreme instability, which corresponds to the Late Heavy Bombardment inferred in the history of our solar system (at an age of ∼600 Myr). As a result of this violent period, high-inclination objects can be created from objects originating at the outer edge of the planetesimal disk. Although it is unclear how an object with a semi-major axis as high as that of 2015 BP_{519} would be generated in this process, we cannot exclude the idea that 2015 BP_{519}'s currently observed orbital inclination may come from a period of violent instability in the early history of the solar system.

Another explanation for high semi-major axis, high eccentricity orbits could be the diffusion hypothesis proposed in Bannister et al. (2017) for the generation of 2013 SY_{99}'s orbit. Objects with the longest orbital periods may sequentially scatter outwards, detach their perihelia through galactic tides, and then diffuse inwards into orbits with long periods and detached perihelia. Galactic tides start to dominate once an object attains a semi-major axis of roughly 3000 AU or more (Duncan et al., 1987), meaning that the currently-observed TNOs are not generally susceptible to these effects. This mechanism does appear to describe 2013 SY_{99}, an object with a semi-major axis $a \approx 730$ AU and an eccentricity of 0.93, which fits into the dynamical class of objects that would be produced by this mechanism. However, 2015 BP_{519}'s perihelion is not sufficiently detached (35 AU vs. 50 AU for 2013 SY_{99}) for this mechanism to operate.

Another explanation for this object's extreme orbit could be galactic tides acting on remnants of the inner Oort cloud. It has been suggested (Brasser et al., 2012b) that centaurs may come from the inner Oort cloud rather than the scattered disk. Brasser et al. (2012a) shows that the median inclination of the inner Oort cloud should be around 50 degrees. As mentioned in Brasser et al.

(2012a), the number and orbital parameters of objects with large semi-major axis can be used to constrain birth cluster properties. An object at 450 AU would be near the inner 2-5% of the cloud, depending on the density profile used. However, objects formed via this mechanism (such as SY99, Bannister et al. 2017) would be expected to have detached perihelia distances, which 2015 BP_{519} does not.

Silsbee & Tremaine (2018) discuss the possibility that a potentially planetary-mass object (sub-earth mass) could have formed among the giant planets, and its influence during Neptune's migration could have excited TNOs to present-day high inclinations. This object is distinct from the Planet Nine discussed in the next section.

Self-gravity of the scattered disk A sufficiently large (1-10 Earth masses in total mass), eccentric disk would experience an instability due to the self-gravity of the disk (Madigan & McCourt, 2016). This proposed instability could cause clustering in ω (as observed) for the objects experiencing the instability, and a subsequent pumping of inclination for objects that find their apocenter above the orbital plane (Madigan et al., 2018). This would result in the population of high inclinations for eccentric objects. 2015 BP_{519} could undergo this mechanism if the scattered disk contains enough mass to cause the instability: for this explanation to be feasible, a large number of additional objects in the scattered disk will need to be found, as the early mass of the scattered disk must have been high for this instability to occur.

9.6 Dynamics in the Presence of Planet Nine

Many recent papers have considered the existence of a possible ninth planet. In this section, we consider how the existence of Planet Nine would alter the orbital behavior and evolution of 2015 BP_{519}. In considering possible dynamical interactions between 2015 BP_{519} and Planet Nine, there are two main classes of effects that may be relevant:

- Constant-a evolution (while in or near resonance with another body). Due to 2015 BP_{519}'s large semi-major axis, we do not expect Neptune resonances to be relevant. The longest period objects known to be in resonance with Neptune have semi-major axis of $\sim$130 AU (Volk et al., 2018). 2015 BP_{519}'s semi-major axis of $\sim$450 AU is likely too large for these

processes to be relevant. However, resonances with Planet Nine may be important.

- Diffusion and scattering in a due to close encounters with Neptune or Planet Nine. These encounters may be very close (<3 AU) and lead to significant changes in the orbit of 2015 BP_{519}, or may be more distant (5-15 AU) and act more as a series of perturbations than an abrupt change.

Both of these modes of evolution can occur over the entire history of the solar system. For example, Fig. 9.11 shows one sample numerical realization of the orbital evolution of 2015 BP_{519}, which demonstrates these two evolutionary modes within a single 4.5 Gyr integration.

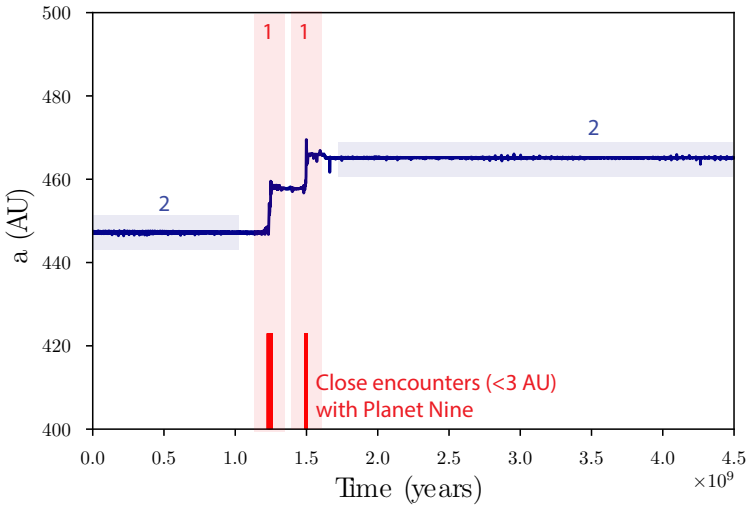

Figure 9.11 Illustrative Resonance Hopping Diagram. A single clone of 2015 BP_{519} in the presence of Planet Nine drawn from Set 3 of our simulations. There are two modes of evolution, both shown and labeled in this panel. The first (1) occurs when 2015 BP_{519} passes physically close to Planet Nine (a close encounter), and the orbit of the TNO may be slightly jostled. Times when 2015 BP_{519} passes within 3 AU of Planet Nine are denoted with red vertical lines. When close encounters occur, the orbit of 2015 BP_{519} is altered and appears to migrate for some time before settling into a new equilibrium semi-major axis. These jumps are the same 'resonance hopping' discussed in previous work (Becker et al., 2017). The second mode of evolution shown here (2) occurs when the semi-major axis remains constant, but the inclination and eccentricity of 2015 BP_{519} may still evolve. The work in Batygin & Morbidelli (2017) describes what happens during these (2) regions of constant semi-major axis.

9.6.1 Evolution with Constant Semi-major Axis

The existence of Planet Nine can lead to a behavior in which TNOs "hop" between resonances (Becker et al., 2017). This is differentiated from 'resonance sticking' (Duncan & Levison, 1997; Robutel & Laskar, 2001; Lykawka & Mukai, 2006), where scattered disk objects are temporarily captured into resonances with Neptune. In the Planet Nine paradigm, TNOs generally spend more time living in resonances than not, with relatively short periods between the attainment of resonances.

An example of what resonance hopping looks like is given in Fig. 9.11, where the semi-major axis makes sudden transitions between relatively long periods at nearly constant values (note that further examples can be found in Figures 8 and 9 of Becker et al. 2017). The transitions in the resonance hopping paradigm are generally caused by close encounters with either Neptune or Planet Nine.

Batygin & Morbidelli (2017) conducted a thorough analytic and numerical exploration of the evolution of TNOs in the case where the TNOs remain at a nearly constant semi-major axis. Fig. 9.11 demonstrates the typical behavior of 2015 BP_{519} in the presence of Planet Nine – for extended periods of time, it orbits with a roughly constant semi-major axis, until a close encounter (denoted by red vertical bars in the figure) perturbs the semi-major axis into a different value. A new equilibrium is quickly attained, and the object returns to evolution with nearly constant semi-major axis a. During the long periods of constant-a orbital motion, the dynamics described in Batygin & Morbidelli (2017) will apply, as described below.

To study the evolution of 2015 BP_{519} under the same conditions starting in the early solar system and integrating to the current day, we conduct another set of simulations (Set 2; see Table 9.2). In contrast to the earlier Set 1 integrations, where the giant planets were considered as active bodies, these simulations absorb all four gas giants into the quadrupole moment of the central body. The corresponding contribution of the planets to the value of J_2 is given by

$$J_2 = \frac{1}{2} \sum_{j=1}^{4} \frac{m_j a_j^2}{M R_{abs}^2}\,, \tag{9.6}$$

where is R_{abs} is the absorbing radius, within which objects are removed from the simulation, the

index j counts through the four gas giants, m_j and a_j denote planetary masses and semi-major axes, and M denotes the mass of the central body. This approximation minimizes perturbations in a-space, allowing for an easier study of the orbital evolution at constant-a. As was done in Batygin & Morbidelli (2017), we initialize the inclination of 2015 BP_{519} to be drawn from a half-normal distribution with mean 0 degrees and width 5 degrees, which simulates the expected initial conditions in the early solar system. We also include Planet Nine, using the best-fit values of its orbital elements (a = 700 AU, e = 0.6, i = 20, ω = 150, Ω = 90), which come from Millholland & Laughlin (2017) and Batygin & Morbidelli (2017). We also run an additional set of simulations (Set 3) with identical parameters, but using the observed inclination of 2015 BP_{519} as drawn from the observationally-derived covariance matrix. Simulation Set 2 is intended to study the behavior of an object like 2015 BP_{519}, but starting from early in solar system history, before the inclination of 2015 BP_{519} is perturbed to its current-day value. Simulation Set 2 is intended to answer the following question: assuming that 2015 BP_{519} started in the same plane as the outer solar system objects that were present in the early solar system, can secular interactions with Planet Nine excite 2015 BP_{519}'s inclination to its current day value? For comparison, simulation Set 3 studies the behavior of 2015 BP_{519} from the current day forwards (but using the same approximations that are used in Set 2; namely, neglecting perturbations caused by scattering interactions with the giant planets and treating evolution as occurring at constant-a).

In Fig. 9.12, we plot the action-angle evolution of the results of Set 2, using angle

$$\theta = \Delta\varpi = 2\Omega - \varpi - \varpi_9 \tag{9.7}$$

and coordinate action

$$\Theta = \frac{\sqrt{1-e^2}}{2}(1-\cos i) \tag{9.8}$$

as done in Batygin & Morbidelli (2017).

The resulting evolution of 2015 BP_{519} in this action-angle phase space is plotted in Fig. 9.12. The lines trace the 4.5 Gyr evolution of the realizations of 2015 BP_{519} from simulation Set 2. The star symbol marks the present-day location of 2015 BP_{519} in this parameter space, using its observed inclination, eccentricity, and (expected) $\Delta\varpi$. It is important to note that the remarkably high

observed inclination of 2015 BP_{519} is not a guaranteed outcome of these simulations. Nonetheless, the star symbol lies along the teal contours, which describe regions of the phase space to which an initially-coplanar 2015 BP_{519} could evolve. These simulations demonstrate that in the case where 2015 BP_{519} starts its life close to the plane containing the solar system planets, 2015 BP_{519} is able to attain its current day inclination, eccentricity, and orbital orientation through secular interactions with Planet Nine alone.

As a result, Set 2 of our simulations shows that orbital evolution with constant semi-major axis (a) evolution can explain how 2015 BP_{519} achieves its observed inclination in the presence of Planet Nine. In other words, the existence of Planet Nine is sufficient to explain the currently observed orbit of 2015 BP_{519}.

9.6.2 Orbital Evolution with Planet Nine and Neptune

The constant-a evolution is relevant for the majority of the lifetimes of the TNOs in the presence of Planet Nine, and the behavior of the TNOs will generally behave as described in the previous section during those times. Close encounters with Planet Nine do occur even in the idealized simulation Set 2, but they are rare and tend to lead to only small hops between nearby resonances with Planet Nine. However, as the current perihelion distance of 2015 BP_{519} brings it fairly close to the orbit of Neptune during each perihelion passage, the true evolution of 2015 BP_{519} will be affected heavily by those Neptune-2015 BP_{519} interactions. In Fig. 9.11, we show a sample orbital evolution of 2015 BP_{519} without Neptune. During a close encounter with Planet Nine, 2015 BP_{519}'s orbit is rapidly altered, where the average distance of its orbit diffuses until it is trapped into or near a new resonance. The inclusion of Neptune as an active body increases the number of close encounters experienced by 2015 BP_{519}, as it will interact with both Planet Nine and Neptune. This increase in interactions, in turn, allows for the orbit of 2015 BP_{519} to become more heavily perturbed over time.

To test the effect of these kicks from Neptune, we set up another set of simulations (Set 4; see Table 9.2). In this case, we replace Jupiter, Saturn, and Uranus with an effective J_2 term to represent the potential of those three planets. However, this time we include Neptune as an active body, which allows Neptune scattering events to be resolved. As before, the energy is conserved to

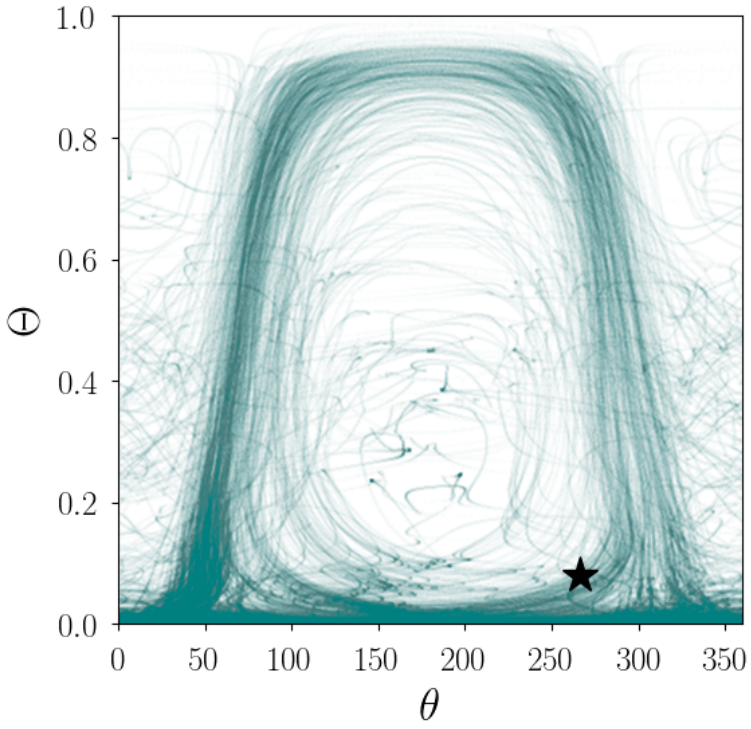

Figure 9.12 Action-Angle Evolution of 2015BP519 in Presence of Planet Nine. Orbital evolution of 2015 BP_{519} in action-angle space. This figure shows results from simulations where the initial inclination of 2015 BP_{519} was drawn from a half-normal distribution centered at 0 degrees, with a width of 5 degrees (Set 2; see Table 9.2). This plot should be compared to the bottom panel of Fig. 11 in Batygin & Morbidelli (2017). The currently observed action-angle coordinates θ and Θ (computed using the simulated version of Planet Nine) is marked by the star symbol. The current-day orbital elements of 2015 BP_{519} are easily reproduced in the scenario with Planet Nine and with 2015 BP_{519} starting in the plane with the other solar system objects.

one part in 10^9 and the hybrid symplectic-Bulirsch-Stoer integrator is used. The other parameters of this set of simulations are summarized in in Table 9.2, and the results are plotted in Fig. 9.13. As expected, in this new set of simulations, 2015 BP_{519} appears to be significantly less

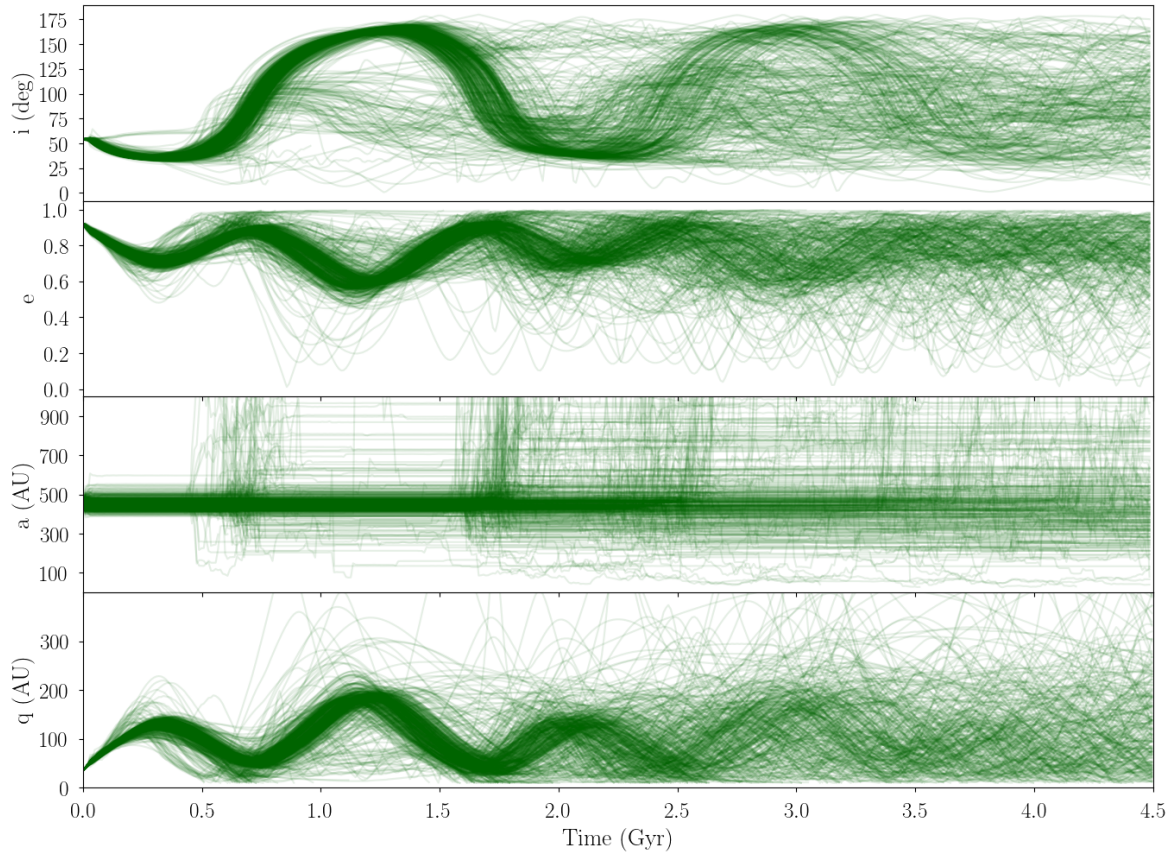

Figure 9.13 Orbital Evolution of 2015BP519 in Presence of Planet Nine with J2. The orbital evolution of 2015 BP_{519} as computed using N-body simulations for Simulation Set 4, which includes Neptune as an active particle, replaces the other three gas giants with an effective J_2, and includes Planet Nine. These integrations do describe well the secular dynamics of *surviving* particles. The evolution of semi-major axis also shows the horizontal banding structure in semi-major axis, which is characteristic of resonance hopping.

dynamically stable than in the previous sets (which do not include an active Neptune). However, part of this apparent dynamical instability is due to the nonphysical absorbing radius used in the simulations: specifically, we remove particles from the simulation when they reach orbital radii within the absorbing radius. This inner boundary is set to be 9.8 AU in this case, since we are replacing the Sun and inner three giant planets with an oblate central body with a larger radius, to represent the effective quadrupole term of the entire system.

As a result of the complication outlined above, ensembles of simulations that use effective J_2 terms (like Set 4) to represent time-averaged planetary orbits cannot be used to study the final outcomes of these objects. For example, if the orbit of a realization of 2015 BP_{519} was to evolve to the point where the clone becomes a Jupiter-family comet, simulation Set 4 would not resolve this end state, and would instead classify the clone as dynamically unstable. On the other hand, this approximation can be used to describe the expected secular evolution for objects that remain a part of the same dynamical population.

9.6.3 Orbital Evolution with Planet Nine and the Four Giant Planets

Both of the previous sections discussing the orbital evolution of 2015 BP_{519} in the presence of Planet Nine replaced some (or all) of the gas giants with an effective J_2 term. This time-saving integration strategy has been used extensively in the Planet Nine literature (Batygin & Brown, 2016a; Brown & Batygin, 2016; Millholland & Laughlin, 2017; Hadden et al., 2017). In Section 9.6.2, we showed that the physical presence of Neptune leads to a greater number of transitions ('hops') between Planet Nine (true or near) resonances. Next, our final set of simulations (Set 5) investigates the effect of including all four gas giants as active bodies. The details of Set 5 are given in Table 9.2. One important detail about this set of simulations is that since all the gas giants are included as active particles (and terrestrial planets ignored), no planets need be modeled as perturbations on the solar J_2. As such, the absorbing radius of the central body is set equal to the Solar radius. This aspect of the simulations allows for the resolution of outcomes where 2015 BP_{519} settles into a stable orbit with a perihelion distance that passes into the inner solar system; the results of this set of simulations is shown in Fig. 9.14. This figure appears very similar to 9.13, but describes the full motion of 2015 BP_{519}. The striking similarity between the two figures can be used as justification for using the J_2 approximation when secular evolution is being studied.

9.7 Discussion

In this work, we present the discovery and dynamical analysis of a new extreme TNO, a population defined as those objects with $a > 250$ AU and $q > 30$ AU. Because 2015 BP_{519} has the largest

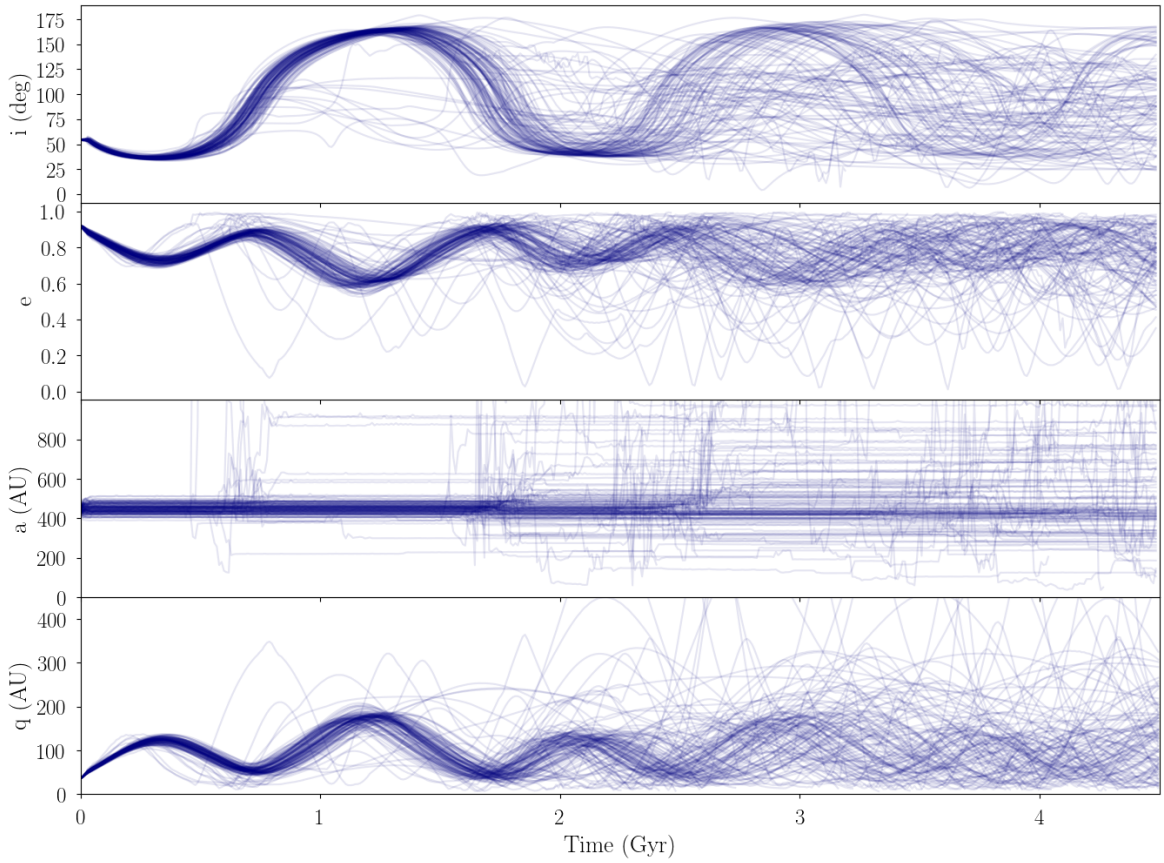

Figure 9.14 Orbital Evolution of 2015BP519 in Presence of Planet Nine. The orbital evolution of 2015 BP_{519} as computed using N-body simulations for Simulation Set 5, which includes all four gas giants as active particles and also includes Planet Nine. The integrations show the same horizontal banding structure in semi-major axis characteristic of resonance hopping. The evolution computed here is very similar in secular trajectory to that of Set 4 (Fig. 9.13).

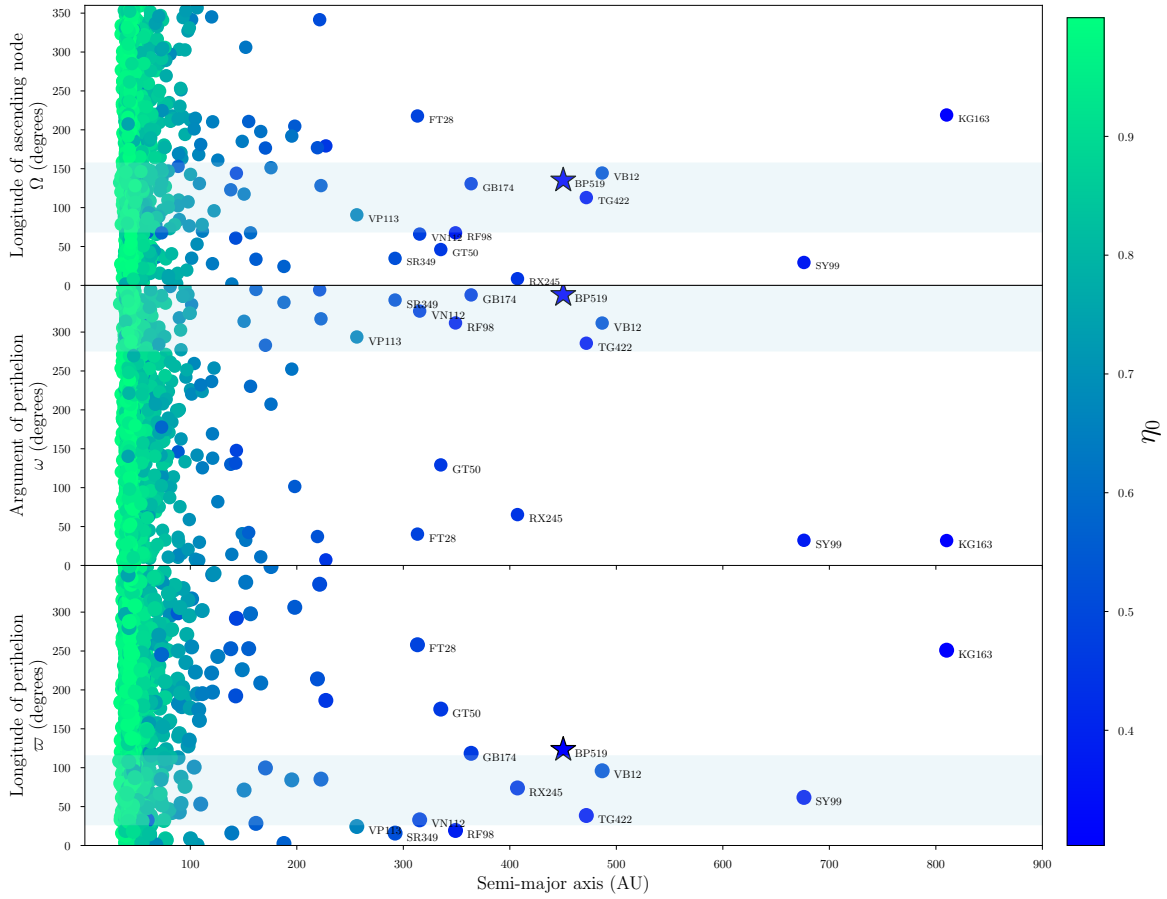

Figure 9.15 Orbital Angles and Clustering. A visualization of the two orbital angles Ω (longitude of ascending node, top panel) and ω (argument of perihelion, middle panel), along with their sum longitude of perihelion $\varpi = \omega + \Omega$ (top panel). The points are color coded by the specific angular momentum of the orbit $\eta_0 = \sqrt{1-e^2}\cos i$. The plot includes all objects with $q > 30$ AU and data quality $U < 6$ from the MPC database (Marsden et al., 1978), with 2015 BP_{519} denoted as a star. Horizontal bars denote the approximate regions of clustering in each angle, as identified in Batygin & Brown (2016a).

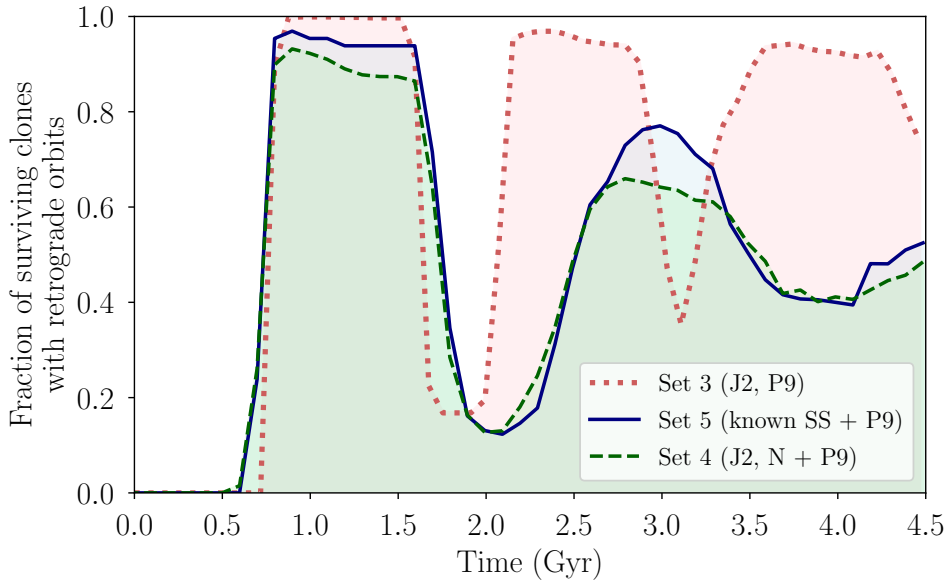

Figure 9.16 Retrograde TNOs. A measure of the fraction of 2015 BP_{519} clones that attain retrograde orbits as a function of time in the numerical simulations that include Planet Nine. The coherence between all sets of simulations is due to a single realization of Planet Nine's orbital elements being used for all simulations. The good agreement between the simulations that used a J_2 approximation (Set 4) and those that included all gas giants as active particles (Set 5) suggests that the J_2 approximation (while keeping Neptune an active particle) is appropriate for studying the orbital evolution of surviving particles, even if it does not work well on its own for studying the dynamical stability. The integrations in Set 1 (which included the known solar system and no Planet Nine) never attain retrograde geometries.

eccentricity and inclination of any of the extreme TNOs, it allows us to probe the behavior of a new regime in the solar system. Ideally, DES and other surveys will find more of these high-inclination, large semi-major axis objects. Once such a population is found and grows to a sufficient size, it will inform a variety of hypotheses about the structure of the outer solar system and the migration of the giant planets. For now, while the number of such known objects is small, we have performed an in-depth study of the dynamical evolution of 2015 BP_{519} in various scenarios with two goals: first, we would like to make whatever insights are possible with a single object to improve our understanding of the outer solar system; second, we would like to determine which hypotheses and analyses will be most fruitful for future study once more of these objects are found.

Our analysis of the orbital evolution of 2015 BP_{519} using forward and backwards integrations has revealed that it is difficult to reproduce 2015 BP_{519}'s high current-day inclination in the known solar system without considering some other mechanism. In Simulation Set 1, which studied the evolution of this object in the known solar system, 0 out of the 260 simulated clones of 2015 BP_{519} attained inclinations less than 48 degrees or greater than 60 degrees, when integrations were initialized with 2015 BP_{519}'s measured inclination of $\sim$54 degrees. This strong confinement in inclination space that is evident in the numerical simulations requires us to consider other mechanisms to excite the inclination of this object. Some potential explanations (discussed in Section 9.5.2) include a stellar fly-by, a remnant excitation from the early migration of the giant planets, a particularly serendipitous outcome not captured by our 260 N-body simulations, or an inclination instability caused by the self-gravity of a massive scattered disk.

One additional explanation to those listed above is the existence of a ninth planet in our solar system, as proposed by Trujillo & Sheppard (2014) and Batygin & Brown (2016a). As shown in Fig. 9.12, in the presence of Planet Nine 2015 BP_{519} can start out with a relatively low inclination and easily attain its current-day inclination. Additionally, as shown in Fig. 9.15, 2015 BP_{519}'s orbital angles ω, Ω, and ϖ appear to be consistent with the clustering first noted in Trujillo & Sheppard (2014). This clustering in physical space has been proposed to be caused by the $\sim$10 Earth-mass Planet Nine at 700 AU (Batygin & Brown, 2016a) and is the line of evidence most commonly used to support the existence of Planet Nine. Although 2015 BP_{519} does appear to fit into this paradigm, the physicality of the clustering remains a contentious piece of evidence for

Planet Nine (Shankman et al., 2017b; Brown, 2017). In Fig. 9.6, we showed the bias in DES detections of objects with varying orbital angles ω, Ω, but the same (a, e, i) as 2015 BP_{519} has. For 2015 BP_{519}, at least, the biases are sufficiently mild that it seems that 2015 BP_{519} can be used as evidence towards the existence of the clustering. However, the observational biases we determine for 2015 BP_{519} do not tell us anything about other objects that may be found by DES or other surveys: without fully accounting for the observational biases for each individual survey that has discovered these ETNOs, it cannot fully be determined how much of the clustering is physical and how much is due to observational bias. Past surveys have been able to quantify this: the Deep Ecliptic Survey had well-documented pointings, and as a result was able to construct a model of its detection biases (Adams et al., 2014). Similarly, the Outer Solar Systems Origin Survey has quantified its own biases (Lawler et al., 2018). Future work (Hamilton et al., in prep) will do the same for the Dark Energy Survey, and enable a better understanding of whether the clustering suggesting Planet Nine's existence is real or a sampling bias.

However, 2015 BP_{519} does provide additional diagnostics unrelated to angular clustering which inform the Planet Nine debate. Batygin & Brown (2016a) predicted that high inclination KBOs would serve as an important constraint on Planet Nine's properties. Subsequently, dynamical analysis presented in Batygin & Morbidelli (2017) suggests that the population of highly inclined centaurs can be explained by the presence of Planet Nine. Shankman et al. (2017a) predicted that if there is a ninth planet in the solar system, there should also be a reservoir of high-i TNOs that exhibit clustering of their orbits with the existing population. Finally, Batygin & Morbidelli (2017) provided a model of the secular evolution expected for high-i, high-a objects, but was only able to test it on objects with $q < 30$ AU. 2015 BP_{519} is the first known high-a ($a > 250$ AU), high-i ($i > 40$ degrees), high-q ($q > 30$ AU) object, a class of objects whose existence is predicted by Batygin & Morbidelli (2017). 2015 BP_{519} is the first discovered high-i object, and it fits into the Planet Nine paradigm as predicted by this previous work.

In Fig. 9.16, we show the fraction of surviving objects that have retrograde orbits for three of the different simulations sets used in this work. A sizable fraction of 2015 BP_{519}'s potential future orbits attain retrograde orientations, an outcome predicted in Batygin & Brown (2016b) and Batygin & Morbidelli (2017). A subset of these also evolve to lower semi-major axes, potentially

resulting in 2015 BP_{519} eventually becoming a retrograde centaur; however, our simulations show that it is more likely that 2015 BP_{519} retains a large semi-major axis and retrograde configuration than that it migrates inwards and becomes a centaur. In the presence of Planet Nine, TNOs with orbits as extreme as 2015 BP_{519} would appear to cycle though populations, changing their orbital inclinations and perihelion distances rather than living at roughly constant perihelion distances (as they would in the known solar system without Planet Nine; see Fig. 9.10). Finally, the presence of Planet Nine in the solar system naturally produces objects with orbits like that of 2015 BP_{519}, a feature which cannot be reproduced in the solar system without Planet Nine without invoking some other mechanism (such as interaction with a passing star, or a 1-10 Earth mass scattered disk that can cause an inclination instability, Madigan & McCourt 2016; Madigan et al. 2018).

Although 2015 BP_{519} appears to fit well into the Planet Nine paradigm and aid in a better differentiation between these two potential scenarios – a solar system with or without Planet Nine – more objects of this type need to be found. Future work using the Dark Energy Survey will both identify additional high-semi-major axis, high-inclination objects which will help us better understand the high-inclination structure of the outermost regions of the solar system, and make a more definitive statement on the existence of Planet Nine.

9.8 Conclusion

This chapter reports the detection and initial dynamical analysis of the extreme Trans-Neptunian Object 2015 BP_{519}. This object was discovered as part of the Dark Energy Survey and adds to the growing inventory of unusual bodies in the outer solar system. Our main results can be summarized as follows:

[1] The estimated orbital elements for this new (minor) member of the solar system include semi-major axis $a \approx 450$ AU, eccentricity $e \approx 0.92$, and inclination $i \approx 54$ degrees. With these orbital properties, j resides well outside the classical Kuiper Belt. On the other hand, the perihelion distance is only $q \sim 36$ AU, close enough to be influenced by Neptune.

[2] The newly discovered body 2015 BP_{519} is the most extreme TNO found to date. This claim can be quantified using the reduced Kozai action η_0 (see Equation 9.5), which is equivalent to the

Object	a (AU)	e	i (deg)	ω (deg)	Ω (deg)	H
2003 VB_{12}	507 ± 10	0.8496 ± 0.003	11.9 ± 0.1	311.3 ± 0.1	144.4 ± 0.1	1.5
2007 TG_{422}	503 ± 0.35	0.93 ± 0.001	18.6 ± 0.1	285.7 ± 0.1	112.9 ± 0.1	6.2
2010 GB_{174}	351 ± 9	0.862 ± 0.004	21.6 ± 0.1	347.2 ± 0.1	130.7 ± 0.1	6.6
2012 VP_{113}	$266\ ^{+26}_{-17}$	0.69 ± 0.03	24.1 ± 0.1	292.7 ± 0.1	90.8 ± 0.1	4
2013 FT_{28}	295 ± 7	0.853 ± 0.004	17.4 ± 0.1	40.7 ± 0.1	217.7 ± 0.1	6.7
2013 RF_{98}	363 ± 5	0.9 ± 0.001	29.6 ± 0.1	311.8 ± 0.1	67.6 ± 0.1	8.7
2013 SY_{99}	735 ± 15	0.932 ± 0.007	4.2 ± 0.1	32.2 ± 0.1	29.5 ± 0.1	6.8
2014 SR_{349}	299 ± 12	0.841 ± 0.007	18 ± 0.1	341.2 ± 0.1	34.9 ± 0.1	6.6
2015 GT_{50}	312 ± 2	0.877 ± 0.001	8.8 ± 0.1	129 ± 0.1	46.1 ± 0.1	8.3
2015 KG_{163}	680 ± 2	0.94 ± 0.001	14 ± 0.1	32.1 ± 0.1	219.1 ± 0.1	8.1
2015 RX_{245}	430 ± 20	0.894 ± 0.001	12.1 ± 0.1	65.2 ± 0.1	8.6 ± 0.1	6.1
2004 VN_{112}	316 ± 1	0.8505 ± 0.0005	25.6 ± 0.1	327.1 ± 0.1	66 ± 0.1	6.5
2014 FE_{72}	1655 ± 336	0.98 ± 0.02	20.64 ± 0.1	133.89 ± 0.04	336.84 ± 0.1	6.1

Table 9.3 Orbital Elements of Extreme TNOs. Barycentric osculating elements for the currently known set of TNOs with $a > 250$ AU and $q > 30$ AU. H is absolute magnitude. Excluding our new object 2015 BP519, solutions were drawn from Shankman et al. (2017b) and Bannister et al. (2017) for all objects except 2013 RF98, 2007 TG422, and 2014 FE72. The barycentric orbital solutions for these three objects were fit using the OSSOS (Bannister et al., 2016b) implementation[a] of the Bernstein & Khushalani (2000) orbit fitter, using the observations of each object available[b] at the Minor Planet Center.

[a] Available at `https://github.com/OSSOS/liborbfit`, and from the Python Package Index via `pip install mp_ephem`

[b] `https://www.minorplanetcenter.net/db_search/asof2/1/2018`

z-component of the specific orbital angular momentum. Among all known solar system objects, 2015 BP_{519} has the most extreme value of this parameter, as shown in Fig. 9.9.

[3] 2015 BP_{519} provides support for the Planet Nine hypothesis. If the object is formed in the plane of the solar system, as expected, then there is a low probability that its orbit can attain the observed high inclination through dynamical processes involving only the known planets. In contrast, the observed orbital elements of 2015 BP_{519} are readily produced through dynamical interactions if the solar system also contains Planet Nine (see Fig. 9.12).

9.9 Appendix: The relevance of Neptune resonances

2015 BP_{519}'s large semi-major axis (450 AU) places it in an regime where mean motion resonances with Neptune are very unlikely. Were 2015 BP_{519} to be trapped in a resonance with Neptune,

the period ratio of that resonance would be around 58:1. However, even if 2015 BP_{519} were to be subject to such a resonance, it would not be affected strongly by Neptune-induced equilibrium points. For this long-period object, despite its short perihelion distance, Neptune resonances will not be relevant.

Figure 9.17 plots the regions in which the TNO's orbits are susceptible to influence by Neptune. These regions were derived in Saillenfest et al. (2017b) through a numerical exploration of which values of η_0 create libration islands in (q, ω) space. TNOs with a value of η_0 that lies within a colored contour will interact strongly with Neptune *if* in that resonance; the range in η_0 colored on the plot is the range of η_0 that allows libration centers for each resonance. Objects in the outside this range will have more peaceful evolution when in resonance with Neptune; instead of living in libration islands, these objects will live in a constant q but circulate through values of ω.

2015 BP_{519}, with its unusually low value of η_0, will not become trapped in a libration center even were it in resonance with Neptune (an already unlikely event due to its large orbital period).

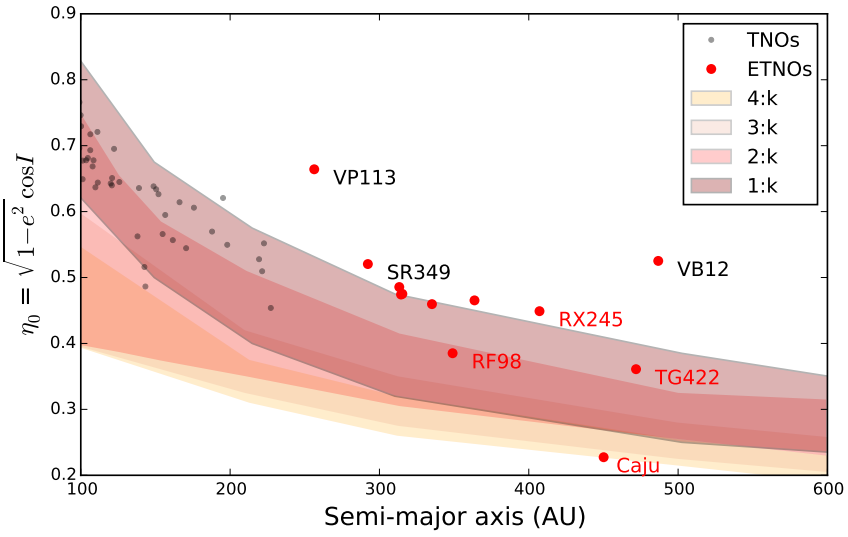

Figure 9.17 Proximity to Neptune Resonance. A reproduction of Fig. 10 from Saillenfest et al. (2017b), with the newly discovered object from this work and the most extreme (a>250 AU) TNOs included as red points. The contours signify which values of η_0 allow the long-term dynamics of each TNO to be influenced by mean-motion resonance with Neptune. Having a value of H that lies within a contour means that a TNO in that particular resonance with Neptune will be influenced by nearby equilibrium points.

CHAPTER X

Current State of the Field and Future Directions

10.1 General Contributions of This Work

As Kepler (Borucki et al., 2010), K2 (Howell et al., 2014a), and now TESS (Ricker et al., 2015) have discovered planets and collected data on an increasing number of systems, we have begun to understand better the diversity of planetary systems in the galaxy. As the number of known planets has increased, some logical assumptions of planet formation have been confirmed. For example, the data has supported the idea that ultra-short-period planets, being so close to their host stars, have evaporated atmospheres (Lopez, 2016). White dwarfs, previously known to at times have photospheric metal enrichments (Zuckerman et al., 2003), are now confirmed to sometimes have transiting, disintegrating planets (Vanderburg et al., 2015a). However, many of the assumptions about the underlying distributions of planets in the galaxy have been turned on their heads as unexpected observational correlations have been found: for example, instead of a uniform or monotonic distribution of planetary radii, there appears to be a valley in planet occurrence around 1.5 to 2 $R_\oplus$ (Fulton et al., 2017), which may in fact depend on the mass of the planet-hosting star (Fulton & Petigura, 2018). The discovery of more planets has both increased our understanding of the underlying distribution of exoplanets in the galaxy and engendered new questions about how and why exoplanets form and migrate.

This thesis has endeavored to move towards a more coherent understanding of planet formation by studying the emergent properties of exoplanetary systems; that is, the properties which can only be understood when a system is considered in its entirety. Conclusions cannot be drawn

about planet formation from the existence of an exoplanet system unless all factors affecting its long-term evolution and dynamics are understood. Although observational biases conspire to make such complete analysis difficult, we show in this thesis that using theoretical techniques combined with observational data can help fill in the gaps.

We do not yet know all of the factors which may affect the dynamics of exoplanet systems, although we can use numerical simulations and analytic methods to model factors of which we are aware. To use a system's geometry to make meaningful insights about planet formation, we must be confident that we understand the dominant factors affecting the evolution of the system, which most simply include the masses and locations of planets, and any planet-planet interactions that significantly affect their orbits. Although it would be nice to have all data possible about every system, the exact dynamics of (for example) the exo-Kuiper belt in an exoplanet system to draw the most important conclusions. It is often not immediately clear how important some factors - say, for example, the possible presence of distant companions to tightly packed systems - might be in modeling the long-term evolution of these systems, but by studying and modeling emergent properties, the relative importance of various factors can be determined.

In this thesis, I have presented a series of analyses that demonstrate multiple ways in which emergent properties can be used to better understand the components and dynamics of exoplanetary systems. If the complete system is known, its emergent properties can be derived, and subsequently used to predict the origin of other properties of the system. This was done in Chapter II and VI. There is one caveat to deriving and using emergent properties in this way: if not all components are known, the conclusions can be wrong, which requires a complete understanding of the relevant parameter space. Commonly, this is the case and the complete system is not known. In this case, some emergent properties can be observed and used to reverse engineer the components that must or cannot be present in the system. We attempted to do this in Chapter III (using the emergent property of system stability), Chapter IV (using the emergent property of TTVs), Chapter VI (using again the emergent property of system stability), Chapter VII (using the dual emergent properties of dynamical stability and secular evolution of inclination), and in Chapters VIII and IX, in both of which we considered how the dynamics of the outer solar system could be explained by an additional solar system planet or other theories. Furthermore, the interplay between emergent

and independent properties can be exploited to construct a feedback loop, where independent and emergent properties can be used to inform each other and provide a more accurate final picture of the system, as was done in Chapter VI (the measured transit durations were used to predict the possible orbits for the planets, then system stability was checked on that subset to further constrain the orbital periods, and then those predictions were compared again with observational data to determine which theoretically derived values best fit the data).

The methods laid out in this thesis will enable a deeper understanding of the dynamics in the possibly under-studied systems that will be discovered with TESS. Such understandings of the dynamics will in turn immediately enable more efficient utilization of follow-up resources, in a manner as was done with Chapter VI.

10.2 Specific Contributions of This Work

In addition to the general development of techniques that allow the coherent unification of dynamics and observations, this thesis has also presented several significant scientific results.

Figure 10.1 is a re-imagining of Figure 1.1, except that in this iteration the planets studied or discovered as part of this thesis are highlighted. Although my thesis is primarily theoretical in nature, through the work described in this thesis I have led and contributed to the discovery of 11 validated planets (marked on Figure 10.1), 2 (unplotted) planet candidates, and 4 (unplotted) Kuiper Belt Objects (see Chapter IX, as well as Gerdes et al. 2017a, Khain et al. 2018b) in our own solar system.

Beyond the discovery of new objects, the theoretical analyses presented in this thesis have made progress towards answering many significant science questions, as well as answering one open question and opening several new lines of inquiry.

10.2.1 Understanding the dynamics of multi-planet systems

The Kepler mission's initial goal was to target sun-like stars, with the goal of finding Earth-analogues orbiting Sun-analogues in habitable orbits. One surprising result of the Kepler mission was that M-dwarfs, the most common and coolest type of star, seem to host large numbers of

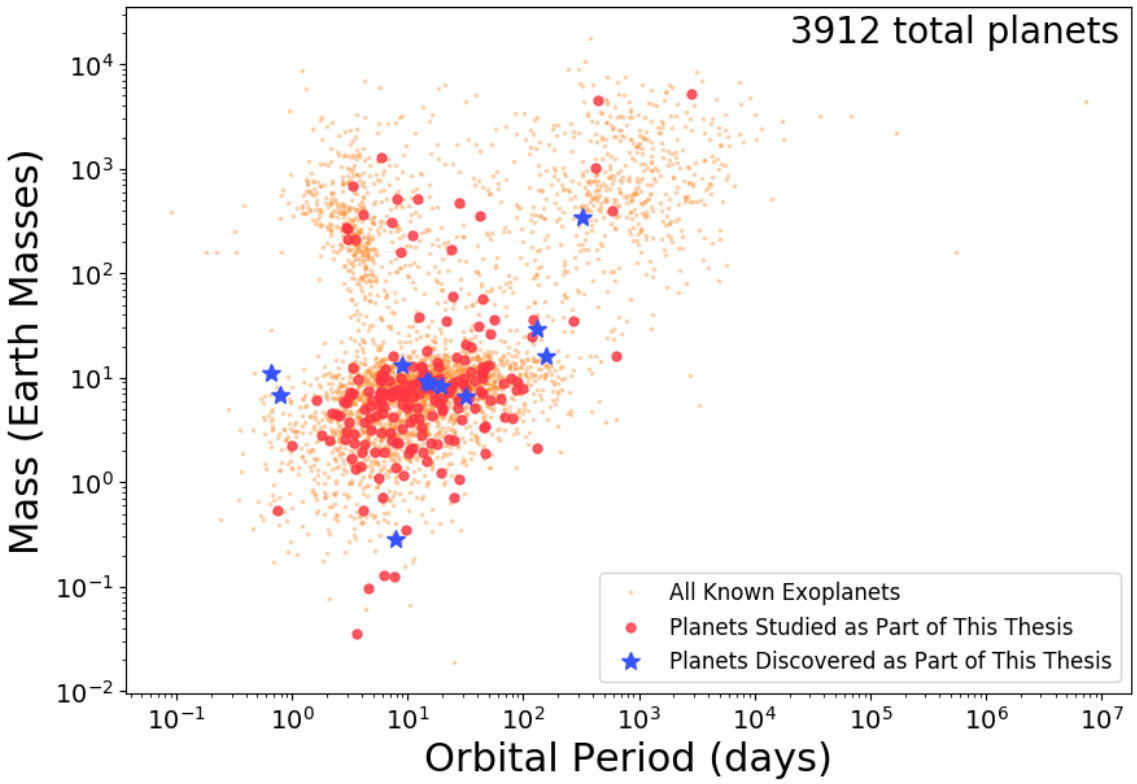

Figure 10.1 Exoplanets Considered and/or Discovered in This Work. A recreation of the diagram given in Figure 1.1 of the orbital periods and masses all planets discovered so far. This time, we mark the exoplanets explicitly studied in this work as red circles and exoplanets discovered as part of this work as blue stars.

tightly packed multi-planet systems. These systems are much more tightly packed than our own solar system, and teeter near the edge of dynamical stability. Indeed, at first glance, it was surprising that such tightly packed systems would remain dynamically stable over the long life spans of these cool stars. Chapter II evaluates the dynamical stability of the observed orbital configurations for Kepler systems with high multiplicities, and finds that they are actually very dynamically stable (see also Becker & Adams, 2016).

The follow-up work to Chapter II, given in Chapter III (and published in Becker & Adams 2017), asked the question 'What if these systems have companions?'. This timely question was also addressed in several other works in the literature (Hansen, 2017; Mustill et al., 2017; Lai & Pu, 2017; Jontof-Hutter et al., 2017b, 2018; Granados Contreras & Boley, 2018; Denham et al., 2019). The conclusion from Chapter III and these other works was that although vastly exterior

companions can exist in the Kepler systems of tightly packed inner planets, nearby or particularly massive companions destabilize the system. Given the abundance of such tightly packed systems, there are a few possible explanations.

First, it is possible that planet formation is even more relentlessly efficient than is thought, that these companions do (or did) exist, and a large number of systems that started out with high-multiplicity have since been destabilized. In this case, dynamical violence could lead systems to end up being seen as single-transiting systems, even if they did not start that way. This first explanation could also serve as an answer to the Kepler Dichotomy, the idea that the single- and multi-planet systems appear to be drawn from different distributions (Ballard & Johnson, 2016a; Morton & Winn, 2014b): the destabilized systems are just the fraction where a large perturber did form.

Second, it is possible that these massive exteriors companions do not tend to form around the same stars that the multi-planet systems do. Since many of the highest multiplicity systems orbit the smallest type of star (M-dwarfs), which should have started with smaller disks masses, it is possible that large planets do not form efficiently in these disks (Johnson et al., 2010). In this case, the correlation coefficient between tightly packed systems of planets and large, longer period companions would be lower. This explanation is a good example of why the emergent properties of systems must be considered; if the correlation coefficient between multi-planet systems and giant planet-hosting systems is damped, then extrapolating system contents from uniformly derived exoplanet abundance rates will miss this important behavior.

10.2.2 Hot Jupiter formation and migration

In 2012, analysis of the Kepler data indicated that hot Jupiters were generally lonely, meaning that they did not tend to have nearby companions. The only examples of companions to hot Jupiters were similarly sized or much larger vastly external companions, with periods upwards of hundreds of days (Knutson et al., 2014a). Nearby (with orbital periods within an order of magnitude of the hot Jupiter's orbital period) companions to hot Jupiters should have been detectable in TTVs in the Kepler sample (Steffen & Hwang, 2015), but none had been found. That no such companions were found in the Kepler data set was taken as evidence that these companions did not exist,

necessitating an explanation for the universal loneliness of hot Jupiters. One explanation for their loneliness was that their system geometries were enforced by their migratory pathways (Mustill et al., 2015b): if hot Jupiters never have nearby planetary companions, that means that whatever process by which they form and migrate destabilized potential companions, since we have begun to understand that planet formation is generally efficient. This was commonly taken as evidence that tidal migration (i.e., Fabrycky & Tremaine, 2007b) was the correct mechanism by which hot Jupiters formed.

However, in 2015, we announced the discovery of two nearby planetary companions to the hot Jupiter WASP-47 (Becker et al. 2015b, see also Chapter IV). This discovery reinvigorated the debate regarding how hot Jupiters form: clearly the existence of nearby companions to hot Jupiters is possible, though perhaps not common, meaning that the mechanisms by which hot Jupiter systems are assembled include as one possible outcome tightly packed systems of planets (including the Jupiter).

The three main possible mechanisms by which hot Jupiter-hosting systems can form are shown in Figure 10.2: (1) disk migration, whereby a super-Earth seed (which will become the core of the Jupiter) forms in the outer disk, undergoes runaway accretion in the outer disk where the surface density is favorable, then migrates inwards to its final orbital position via disk torques; (2) *in situ* formation, whereby a super-Earth-sized seed forms in the outer disk, quickly migrates inwards via disk torques, then accretes its envelope in its final orbital position, requiring a steady inflow of gas to create the environment needed for runaway accretion; or (3) tidal migration, a violent class of mechanisms in which the Jupiter forms in the outskirts of the disk and resides there until after the disk dissipates, before having its eccentricity excited by some force (be it secular interactions, a violent scattering event, or some other mechanism) and subsequently experiencing tidal decay of its orbit until it reaches its final orbital position (Fabrycky & Tremaine, 2007b; Nagasawa et al., 2008b; Wu & Lithwick, 2011; Beaugé & Nesvorný, 2012).

Tidal migration explains a lot of the observational correlations of hot Jupiters, including the observed high obliquities of many hot Jupiters (Albrecht et al., 2012b; Teyssandier et al., 2013), the apparent lack of nearby planets (Steffen et al., 2012a), the existence of retrograde hot Jupiters (Naoz et al., 2011b), the existence of eccentric hot Jupiters (Bakos et al., 2007), and the existence

of the so-called 'sub-Jovian desert' (Owen & Lai, 2018).

Subsequent to the discovery of WASP-47's companions, however, *in situ* formation has been considered in depth and has seemed to become a more plausible explanation for the origin of at least some hot Jupiters (Batygin et al., 2016a; Boley et al., 2016). *In situ* formation can also explain the particular parameter-space shape of the sub-Jovian desert (Bailey & Batygin, 2018). A disk driven mechanism would also explain the fact that hot Jupiters appear no more likely than warm ones to have exterior companions (Schlaufman & Winn, 2016), a fact which seems inconsistent with many tidal mechanisms, which require exterior companions.

Disk migration, in which planets form and migrate while the protoplanetary disk is still present, generally produces dynamically quiet systems with low mutual inclinations. However, particular starting conditions could explain the misalignments in some hot-Jupiter systems even with a disk-driven migratory pathway (Batygin, 2012b).

These three mechanisms, also summarized in Figure 10.2, will each produce different distributions of hot Jupiter envelope abundances (Ali-Dib, 2017) and orbital architectures (Batygin et al., 2016a; Bailey & Batygin, 2018). Future work will need to both (a) determine the general branching ratios of the formation pathways, and (b) determine how those ratios depend on other factors such as spectral type of the host star and its metallicity. WASP-47's two inner companions to the hot Jupiter remain a solid boundary condition on our understanding of these pathways.

After we announced the discovery of WASP-47's companions, many other groups have searched other hot Jupiters for similar companions, with the goal of better constraining the particular properties such systems contain as a population. The first candidate has come only recently in the Kepler-730 system (Thompson et al., 2018; Zhu et al., 2018; Cañas et al., 2019). In the Kepler-730 system, the hot Jupiter has an orbital period of 6.49 days, and the companion is an inner Earth-sized planet with an orbital period of 2.85 days. This architecture is consistent with WASP-47, which also has an inner companion, but not the prediction of the types of companions generated by *in situ* formation by Batygin et al. (2016a), which predicted companions exterior to the hot Jupiter.

Our understanding of hot Jupiter migration and formation was fundamentally changed by WASP-47, and will be improved further by the discovery of additional systems with such compan-

ions.

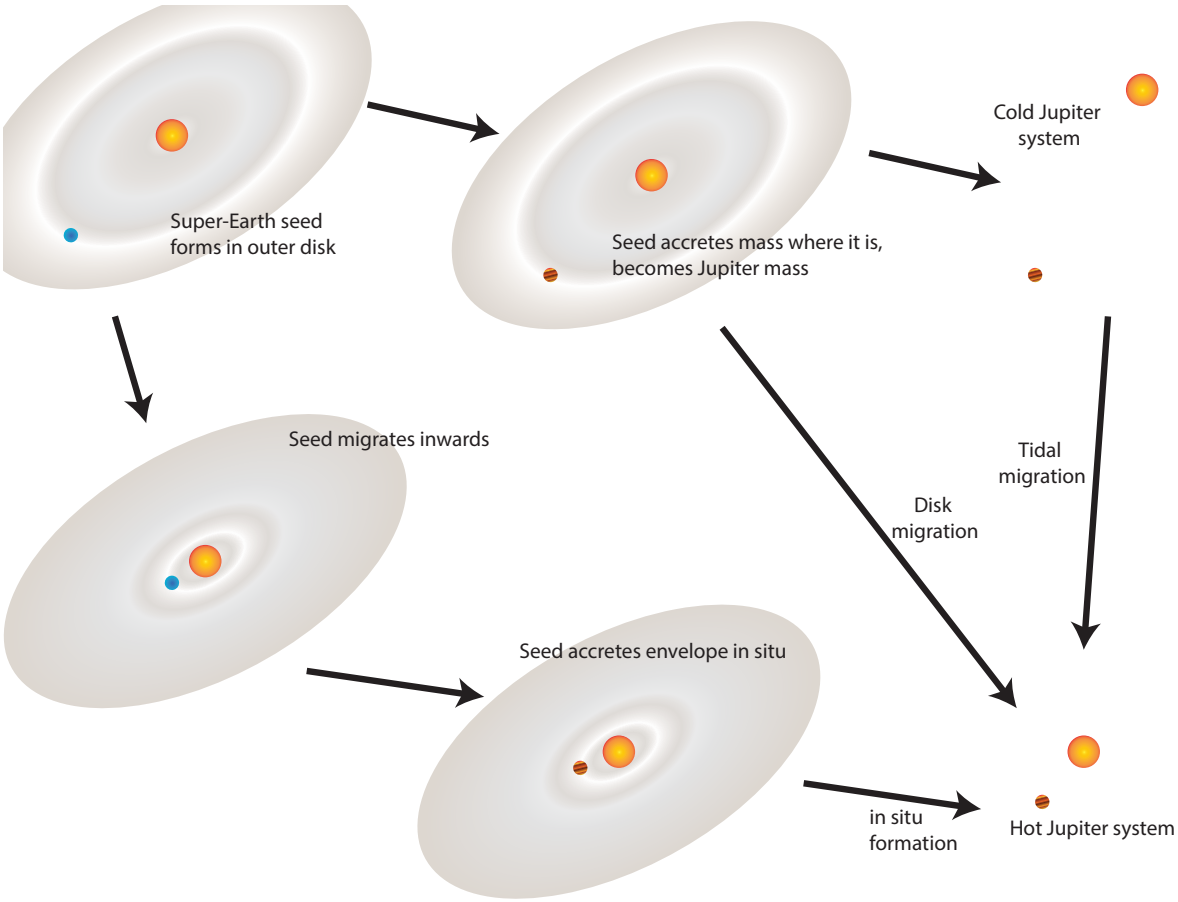

Figure 10.2 Formation Pathways for Hot Jupiters. A schematic of the three main mechanisms by which hot Jupiters could form. In (1) *in situ* formation, a super-Earth-sized seed (which becomes the core of the Jupiter) forms in the outer disk, migrates inwards via disk torques, then accretes its envelope in its final orbital position. In (2) disk migration, the super-Earth seed forms in the outer disk, but undergoes runaway accretion to assemble its envelope before it migrates inwards to its final orbital position. In (3) tidal migration, a category which encompasses many specific mechanisms, the Jupiter forms its core and undergoes runaway accretion in the outer disk, the disk dissipates, and the Jupiter-size planet has its eccentricity pumped by some external force, resulting in a slow decay of its orbital radius as it dissipates energy each perihelion crossing.

10.2.3 Informing Observations of High-Interest Systems

In Chapters III, IV, VI, and VII, we provided predictions and guidance for future observations in an attempt to allow more efficient utilization of follow-up telescope resources.

Observations can be avoided of systems where such observations would be unlikely to glean any new useful information about the system. In Chapter III, we tested whether the Kepler compact systems could host additional planets without destabilizing the continually mutually transiting state of the inner system. We found rough limits for where such companions could reside, including that system Kepler-20 could not host companions without causing its inner systems to excite at least one planets into a non-transiting state. Contemporaneous radial velocity observations of Kepler-20 found that in fact, the system did have a non-transiting planet in that inner system. Some systems, in contrast, were completely unsuscecptible to excitation from any reasonably placed companions: in these systems, where the inner system is decoupled from the outer perturbing system, such coupled analyses present less useful information.

In the era of TESS, many more planets for which the exact orbital period cannot be determined will be discovered. Due to the TESS survey strategy, in some cases, stars will be observed with significant gaps in between periods of observations. For example, according to the Web TESS Viewing Tool[1], the southern circumpolar star δ Mensae will be observed by TESS during Sectors 1,5,8,12, and 13 for 28 days each, with gaps of 84 days, 56 days, and 84 days between subsequent periods of observation. Any planet detected by TESS in this region of sky with a period longer than about 28 days could have ambiguous orbital periods due to the observational strategy. In Chapter VI, we showed how to combine multiple types of constraints in order to narrow down the possible orbital periods for the HIP 41378 planets. This analysis will serve as a starting point for future analysis on TESS planets with similar orbital period ambiguities. The HIP 41378 system is currently being studied via follow-up Spitzer observations, the timing of which was optimized to observe the highest probability events based on the predictions of Chapter VI, cutting down on the total follow-up time needed to inform the dynamics of the system

Similarly, in Chapter IV, we estimate the transit probability for the outermost planet WASP-47c, which was discovered via radial velocities, using a suite of numerical simulations combined with all known observations of the system (including stellar obliquity, the stability of the system and the transiting nature of the planets, and their physical and orbital parameters). Although only 10%, its transit probability is much higher than would normally be expected for a planet of its orbital

[1] `https://heasarc.gsfc.nasa.gov/cgi-bin/tess/webtess/wtv.py`

period ($\sim$ 590 days). If a transit could be observed of this planet, it would provide significant constraints on the dynamical history and evolution of the system (see Chapter V). Observations are underway to determine whether this planet transits or not.

In the latter half of Chapter VII, we show that the existence of an additional unseen companion in the system could explain the observed emergent property of the observed evolution of planetary inclinations. We also provide guidance for where in the system such a companion might reside. Such a companion might be detectable with radial velocity data. The methods developed in these works can be used in the analysis of future systems in order to increase the information gained from observations.

10.2.4 Providing a Mechanism for the Misalignment of Ultra-Short Period Exoplanets

The discovery detailed in the first half of Chapter VII revealed an intriguing system geometry: a outer plane of coplanar planets with an inner ultra-short period *misaligned* companion. A similar geometry has also been revealed in the TOI-125 system (Quinn et al., 2019). Due to these new detections, which seem to go against the previously accepted dogma of "tighly packed, very coplanar multiplanet systems" considered in, for example, Chapter II, the question of how a geometry of this nature can be generated has just begun to be pondered in the literature. (Petrovich et al., 2018) suggests a secular chaos model whereby planet-planet interactions excite the eccentricity of the inner ultra-short-period planet and its nearest companions, which are subsequently damped as the orbit circularizes. This mechanism requires nearby companions, but not too nearby - the closest companions to the ultra-short-period planet are predicted to have orbital periods outside of 10 days, which is not true in the K2-266 system.

In the second half of Chapter VII, we show that an additional undiscovered planet in the system could explain the observed system geometry. Such companions must reside in very particular regimes of parameter space in order to maintain both the ultra-short-period planet's misalignment and the observed coplanarity of the outer transiting planets. Further studies will determine whether the occurrence rates of such companions are consistent with the occurrence rates of systems like K2-266 and TOI-125. The mechanism proposed in this work may solve or partially solve the mystery

of K2-266 and TOI-125.

10.3 Future Directions

The mapping of the universe beyond our solar system began long ago with naked-eye observations of the brightest stars. However, a statistical understanding of their orbiting planets did not emerge until the Kepler spacecrafts discovery of thousands of transiting planets. Initial studies from Kepler's data (Borucki et al., 2010; Batalha et al., 2013; Petigura et al., 2013c; Dressing et al., 2015a), which focus on statistics and planet cataloging, have not only shown that planet formation is relentlessly efficient within the Galaxy, but that the dominant mode of planet formation appears to be one that produces planets with typical masses a few times that of Earth (termed super-Earths), and orbital periods less than $\sim$100 days, rather than solar system analogues. However, Kepler targets are usually too faint for detailed follow-up observations, limiting the degree to which the discovered systems can be fully characterized.

TESS, a planet-hunting mission launched earlier this year, was carefully designed to answer scientific questions that Kepler did not by focusing on brighter stars, for which detailed follow-up observations will be more feasible. While Kepler was a statistical survey, TESS will enable detailed planet profiles. However, while TESS will discover transiting planets and enable detailed studies of those individual planets, by design a large parameter space in each system will remain unstudied. Many transiting systems are accompanied by giant companions which are unseen in transit (Bryan et al., 2019). An intriguing aspect of such paired orbital configurations is that theoretical studies (e.g. Batygin et al. 2016a, Izidoro et al. 2015) suggest that the mere existence of low-mass, close-in exoplanets is incompatible with long-range migration of giant planets, evoking an intriguing observational constraint on the physics of orbital transport. And yet, TESS is already discovering short-period planets with long- period companions (Huang et al., 2018; Gandolfi et al., 2018). Without knowing the full census of planets present in each system, it is impossible to determine their formation histories.

The field of exoplanets has reached a crossroads between being a counting game, where we accumulate individual discoveries of systems, to a statistical game, in which we start to make

larger insights about the underlying planet populations in the galaxy. Through the assembly of this larger statistical sample, some of our early misconceptions about the properties of these distributions have been corrected. However, despite our progress thus far, many misconceptions assuredly persist. Each of the exoplanet discovery methods used thus far have their own individual biases, as discussed in Chapter I. The results of this is that our exoplanet discoveries are biased, and although many efforts have been made to correct for the biases and derive the true underlying abundances of exoplanets, there are still a large degree of uncertainty on these estimates. Further, the most important factor for making insights towards planet formation is understanding not just the bulk abundances of various types of planets, but the correlations inherent in planet occurrence.

The correlations in planet occurrence can also be described as what types of planets are likely to occur together, and what system geometries are common versus which geometries do not occur in nature. For example: do hot Jupiters have companions in only the rarest of cases? Do misaligned ultra-short period planets occurring in multi-planet systems usually have exterior massive companions? These correlations which have only recently begun to be studied in the literature, with Bryan et al. (2019) being an excellent examaple. To continue to construct these occurrences, it is necessary to combine data on the same systems that come from different sources. The most successful detection methods thus far have been transits and radial velocities, but both of these methods are biased to find larger planets at shorter orbital radii. Future missions will allow an increased number of discoveries using other methods such as direct imaging. Although direct imaging has its own set of biases, the biases are different than those of transits and radial velocities, and allow the study of a new regime in parameter space: the outermost parts of systems which may host large planets or brown dwarfs. Moving forward, the increased precision of newly developed instrumentation will allow the detection of transit and radio velocity discoveries to smaller signal amplitudes. The combination of all these techniques, together with the supplemental dynamical analyses like those done in this thesis, will allow more complete mappings of the components of exoplanetary systems.

The difficulty with completing the aforementioned cohesive analysis on Kepler targets is that the Kepler targets skew faint, meaning that follow-up efforts are often not possible. The value of Kepler is not in the follow-up, but in its uniform statistical survey, which is the most robust

exoplanet survey that exists to date. Indeed, it is unlikely that Kepler's statistical completeness and the uniformity of its sample will be surpassed for many decades to come. The specific planet characterization mission TESS, which launched last year in 2018, is built to survey the brightest stars in the sky, the purpose of its mission being to find exoplanet-hosting stars that are ripe for observational follow-up with other missions in the style described above. TESS will enable detailed characterization of a large number of systems orbiting very bright stars.

The importance of emergent properties in the TESS systems is immediately quite evident: TESS systems, being bright, are very conducive to follow-up, meaning that there will soon be a large quantity of data for various sources available on a large number of TESS systems. If this data is combined effectively, we will be able to glean more information out of the coherent analysis of all data than any one individual group would with a single channel of data. Additionally, supplementing these data-focused analysis with dynamical efforts (such as the secular theory and numerical simulations used in this work) will improve our understandings of the systems even further. Chapter VI is a good example of what exactly this will look like: as described in that chapter, an analysis of the K2 data alone provided only a limited amount of information on the five exoplanets in the HIP 41378 system. In particular, the orbital periods of the outer three planets could not even be measured precisely due to the limited and non-continuous observational baseline. Separately, ground-based missions WASP, KELT, and HAtNet all had observed HIP 41378 in the past (unrelated to the K2 observations) since it was a bright star. None of those missions had done anything with their data on this star because they all had non-detections at the ground-based photometric precision. However, when we combined all of these data sources (K2, HAT, KELT, WASP) together with additional numerical simulations to constrain the dynamically allowable orbits for the entire system, we were able to get tighter constraints on the unknown orbital parameters than was possible with any set of data or simulations alone. This is a good example of the way forward in exoplanet studies: many analyses from the Kepler mission used only Kepler data to get strong constraints on systems, since the Kepler sample was uniform and well characterized. Going forward, using data from only the space space transit mission TESS will (by design) not be enough. The observational baseline limitation suffered by the HIP 41378 data will be extremely common with TESS systems, since TESS' pointings tile the entire sky, 27 days per pointing, in

sequence. Only the poles will be viewed continuously, with all other regions exhibiting varying (but all non-continuous) baseline. As such, the TESS data must be combined with additional data from other sources as well as dynamical analyses. The important question, then, is how to best choose what data to acquire and combine it effectively.

We advocate in this thesis for the importance of supplemental applications of dynamical theory in this process. Secular theory and numerical simulations can enable better results from a set of observational data.

The focus on emergent properties has two aspects: first, to understand the true evolution of a planetary system one needs to know enough parameters about the planets and the dominant mode of oscillation in order to model the system; second, if one has a measure of some emergent property of the system (for example, a measure of the transit timing variations), one can use it to determine what additional components of the system are missing from the current model. An example of this would be an apparently single-planet system having evidence of sinusoidal TTVs. These TTVs could be evidence of an additional planet in the system, and even if the signal is not due to a planet, there must be something else causing the TTV signal (be it stellar activity or instrumental systematics or something else; Barros et al. 2013). Combining the amplitude of the signal with mathematical models of the possible causes of the effect can result in a measure of the parameter space in which the companion causing the effect must reside.

The Kepler data set has not yet be exhausted - Dotson et al. (2019) estimates that on 30% of the planets in the K2 data have been found so far, leaving a large number of new planets hiding in the K2 data. Even as the K2 data set is underutilized, TESS is already starting to discover planets (Huang et al., 2018; Gandolfi et al., 2018; Vanderspek et al., 2019; Wang et al., 2019). The TESS discoveries will allow the beginning of in-depth characterization of individual systems. One of the major difficulties of the Kepler/K2 sample was that many of the stars were too faint to construct radial velocity time series. This resulted in observational determinations of their masses often being impossible. Surveys such as Marcy et al. (2014); Weiss & Marcy (2014a) did measure masses for the planets orbiting the brightest stars, but a large number of Kepler planets have masses that remain unmeasured. Although efforts such as Wolfgang et al. (2016); Ning et al. (2018) constructed (non-parametric) models to convert between radius and mass, TESS will provide a new population

of exoplanets for which such extrapolations will not be necessary. The stars will be bright enough that in most cases the masses will be directly determined or hard limits will be found. One major uncertainty in much of the work in this thesis (Chapters II, III, VI, V) was the masses that should be used as inputs into the dynamical models. Since the masses of planets matter a lot for their subsequent evolution, this was a major source of potential error. The TESS systems will eventually have more accurate mass determinations, enabling better dynamical constraints in turn. By nature of their favorability to follow-up observations, the TESS targets will be heavily studied by many groups using many facilities. This also means that these are the systems we will be able to study the best of any systems that will be found in the future. We want to get the most that we can out of this data, and we also want to know how to efficiently utilize telescope resources going forward. There remains a limited amount of telescope observing time available, particularly on high-profile instruments such as those on JWST, and the number of TESS systems of interest will be much higher than the capacity of these observatories to make the needed observations.

To plan efficient follow-up observations, numerical simulations and other dynamical techniques should be used to predict which systems have easily detectable companions, do not have such companions, or are the most ripe for the breaking of existing degeneracies. As shown in Chapter VI, efficient utilization of existing data can often cut down the amount telescope time needed in the future. Without the most likely orbital periods that we derived in that chapter, it would have been unclear which of the epochs were most important for follow-up observing. Eliminating some of the orbital periods that were unlikely cut down on the amount of follow-up observation time that must be devoted to the system in order to recover the true orbital period of planet f.

One major current goal in the field of exoplanets is to understand how planets and systems of planets form. We remain now at a relatively early stage in this process. Even the formation mechanism of our own solar system, for which we have the additional information encoded in the orbits of asteroids, comets, and Kuiper Belt objects, is not yet understood. Although our solar system is likely the most detailed study we will ever be able to do of the components of a planetary system, there are some additional benefits afforded by using a population-wide analysis of all discovered exoplanets.

Studies towards understanding properties of exoplanets will focus on their physical properties

(interior structures and bulk compositions; Batygin et al. 2009; Dressing et al. 2015b; Fortney & Nettelmann 2010), chemical properties (how they have been sculpted by processes like photoevaporation and form aerosols and hazes high in their atmospheres, Ehrenreich et al. 2015; Crossfield & Kreidberg 2017a; May et al. 2018, what molecules constitute their atmospheres Morley et al. 2017), and what orbital and system properties correlate with these factors. With additional information afforded by these studies of physical parameters combined with dynamical insights gleaned via the methods described in this thesis, we will take a step closer to making broader statements about the ways by which planets form.

10.4 Emergence Moving Forwards

The reductionist days of studying exoplanets are coming to a close, as we move from merely hunting for individual exoplanets to trying to understand exactly how planets form and what factors mediate the development of particular system geometries.

The reductionist trap mentioned in the introduction to this thesis acts directly in opposition to our desire to understand the deeper principles underlying planet formation. When we construct theories assuming that the discovered exoplanets in each system are the only ones that affect the evolution of the system, we inadvertently condense a complex interacting system to a much more simple but incomplete subset of its true dynamics.

The clear way forward is to directly and explicitly consider additional (perhaps unseen) components in the systems we study. This thesis has argued that moving forward, the study of planet formation requires explicit consideration of the emergent properties in exoplanetary systems, and the additional constraints which can be derived through their use. To understand planet formation, we must derive population-level constraints and correlations by using the known relationship between the independent properties of the system and its resultant emergent properties. By using this knowledge in a cohesive model, it can be leveraged to provide a better understanding of the system as a whole, which is necessary for our eventual development of a coherent understanding of planet formation.

APPENDIX

APPENDIX A

Additional Acknowledgements

A.1 Additional Acknowledgements

In addition to the acknowledgements listed at the start of this thesis, I would like to thank the following groups, organizations, and facilities for help with specific projects.

For the work described in Chapter II, we would like to thank Konstantin Batygin, Kathryn Volk, Ben Montet, Andrew Vanderburg, and Doug Lin for useful conversations. We would like to additionally thank Konstantin Batygin for his careful review of the manuscript and helpful suggestions. We would like to thank the referee for the journal publication, Darin Ragozzine, for his thoughtful and helpful suggestions. J.B. was supported by the National Science Foundation Graduate Research Fellowship, Grant No. DGE 1256260.

The work described in Chapter III used the Extreme Science and Engineering Discovery Environment (XSEDE), which is supported by National Science Foundation grant number ACI-1053575. This research was done using resources provided by the Open Science Grid, which is supported by the National Science Foundation and the U.S. Department of Energy's Office of Science. JCB is supported by an NSF graduate fellowship. We would also like to thank Daniel Tamayo, Christopher Spalding, and Andrew Vanderburg for useful conversations. Finally, we thank the referee for many useful comments that improved the manuscript.

Regarding the work described in Chapter IV, we are grateful to Kat Deck and Tim Morton for significant assistance. We thank Marion Neveu-VanMalle, Eric Bell, Moiya McTier, Mark Omohundro, and Alexander Venner for useful conversations. We thank John Johnson for his guidance and the anonymous referee for their very useful comments. We acknowledge the Planet Hunters team for its community. This work used the Extreme Science and Engineering Discovery Environment (NSF ACI-1053575) and the OSG (NSF, DoE). This research has used the Exoplanet Data Explorer at `http://www.exoplanets.org`. The data in this chapter were obtained from the Mikulski Archive for Space Telescopes. This chapter includes data collected by the Kepler/K2 mission (funding provided by the NASA Science Mission directorate), and we gratefully acknowledge the efforts of the entire Kepler/K2 team. We also thank Jason Eastman, Jonathan Irwin, Laura Kreidberg, Willie Torres, Lauren Weiss, and George Zhou for helpful conversations. We thank Josh Winn for helpful comments on the manuscript and the anonymous referee for a thoughtful report. A.V. and J.C.B are supported by the NSF Graduate Research Fellowship, grant nos. DGE 1144152 and DGE 1256260, respectively. This work was performed in part under contract with the California Institute of Technology/Jet Propulsion Laboratory funded by NASA through the Sagan Fellowship Program executed by the NASA Exoplanet Science Institute. D.W.L. acknowledges partial support from the from the TESS mission through a sub-award from the Massachusetts Institute of Technology to the Smithsonian Astrophysical Observatory. The research leading to these results has received funding from the European Union Seventh Framework Programme (FP7/2007-2013) under Grant Agreement n. 313014 (ETAEARTH). Parts of this work have been supported by NASA under grants No. NNX15AC90G and NNX17AB59G issued through the Exoplanets Research Program. This publication was made possible through the support of a grant from the John Templeton Foundation. The opinions expressed in this publication are those of the authors and do not necessarily reflect the views of the John Templeton Foundation. This work is based on observations made with the Italian Telescopio Nazionale Galileo (TNG) operated on the island of La Palma by the Fundacin Galileo Galilei of the INAF (Istituto Nazionale di Astrofisica) at the Spanish Observatorio del Roque de los Muchachos of the Instituto de Astrofisica de Canarias. The HARPS-N project was funded by the Prodex Program of the Swiss Space Office (SSO), the Harvard University Origin of Life Initiative (HUOLI), the Scottish Universities Physics Alliance

(SUPA), the University of Geneva, the Smithsonian Astrophysical Observatory (SAO), and the Italian National Astrophysical Institute (INAF), University of St. Andrews, Queens University Belfast and University of Edinburgh. This work was supported in part by the NASA Exoplanets Research Program.

Regarding the work described in Chapter V, we thank Gongjie Li, Heather Knutson, Josh Winn, Ben Montet, Danielle Piskorz, Sarah Millholland, Clara Eng, and Iryna Butsky for useful conversations. We also thank Michael Dieterle for visualization suggestions, and thank the referee, Chris Spalding, for prompt and useful feedback. J.C.B and A.V. are supported by the NSF Graduate Research Fellowship grant nos. DGE 1256260 and 1144152, respectively. This work was performed in part under contract with the California Institute of Technology (Caltech)/Jet Propulsion Laboratory (JPL) funded by NASA through the Sagan Fellowship Program executed by the NASA Exoplanet Science Institute. This work used both the Extreme Science and Engineering Discovery Environment (XSEDE; NSF grant number ACI-1053575) and resources provided by the Open Science Grid, which is supported by the National Science Foundation and the U.S. Department of Energy's Office of Science.

For the work described in Chapter VI, we would like to thank the anonymous referee for helpful comments on the manuscript. A.V. and J.C.B are supported by the NSF Graduate Research Fellowship, Grants No. DGE 1144152 and DGE 1256260, respectively. D.W.L. acknowledges partial support from the Kepler mission under NASA Cooperative Agreement NNX13AB58A with the Smithsonian Astrophysical Observatory. C.B. acknowledges support from the Alfred P. Sloan Foundation. This research has made use of NASA's Astrophysics Data System and the NASA Exoplanet Archive, which is operated by the California Institute of Technology, under contract with the National Aeronautics and Space Administration under the Exoplanet Exploration Program. This work used the Extreme Science and Engineering Discovery Environment (XSEDE), which is supported by National Science Foundation grant number ACI-1053575. This research was done using resources provided by the Open Science Grid, which is supported by the National Science Foundation and the U.S. Department of Energy's Office of Science. The National Geographic Society–Palomar Observatory Sky Atlas (POSS-I) was made by the California Institute of Technology with grants from the National Geographic Society. The Oschin Schmidt Telescope is

operated by the California Institute of Technology and Palomar Observatory. This chapter includes data collected by the *Kepler* mission. Funding for the *Kepler* mission is provided by the NASA Science Mission directorate. Some of the data presented in this chapter were obtained from the Mikulski Archive for Space Telescopes (MAST). STScI is operated by the Association of Universities for Research in Astronomy, Inc., under NASA contract NAS5–26555. Support for MAST for non–HST data is provided by the NASA Office of Space Science via grant NNX13AC07G and by other grants and contracts. Robo-AO KP is a partnership between the California Institute of Technology, University of Hawaii, University of North Carolona, Chapel Hill, the Inter-University Centre for Astronomy and Astrophysics, and the National Central University, Taiwan. Robo-AO KP was supported by a grant from Sudha Murty, Narayan Murthy, and Rohan Murty. The Robo-AO instrument was developed with support from the National Science Foundation under grants AST-0906060, AST-0960343, and AST-1207891, the Mt. Cuba Astronomical Foundation, and by a gift from Samuel Oschin.

During the preparation of the manuscript in which the work of Chapter VI was first published (Becker et al., 2019), we became aware of a parallel chapter on the new K2 observations of HIP 41378: Berardo et al. (20189; under review). These manuscripts were prepared independently, and we did not discuss the results with the other team before submission. We thank David Berardo and collaborators for coordinating submission of these papers. We thank Tali Khain for her careful reading of the manuscript and useful suggestions. A.C. and D.H. acknowledge support by the National Aeronautics and Space Administration under Grants NNX17AF76G and 80NSSC18K0362 issued through the K2 Guest Observer Program. This work has made use of data from the European Space Agency (ESA) mission *Gaia* (`https://www.cosmos.esa.int/gaia`), processed by the *Gaia* Data Processing and Analysis Consortium (DPAC, `https://www.cosmos.esa.int/web/gaia/dpac/consortium`). Funding for the DPAC has been provided by national institutions, in particular the institutions participating in the *Gaia* Multilateral Agreement.

For the work described in Chapter VII, we thank Chelsea Huang, Laura Kreidberg, George Zhou, and Li Zeng for their valuable conversations. Work performed by J.E.R. was supported by the Harvard Future Faculty Leaders Postdoctoral fellowship. AV's contribution to this work was performed under contract with the California Institute of Technology (Caltech)/Jet Propulsion

Laboratory (JPL) funded by NASA through the Sagan Fellowship Program executed by the NASA Exoplanet Science Institute.

This work has made use of data from the European Space Agency (ESA) mission *Gaia* (`https://www.cosmos.esa.int/gaia`), processed by the *Gaia* Data Processing and Analysis Consortium (DPAC, `https://www.cosmos.esa.int/web/gaia/dpac/consortium`). Funding for the DPAC has been provided by national institutions, in particular the institutions participating in the *Gaia* Multilateral Agreement.

This chapter includes data collected by the K2 mission. Funding for the K2 mission is provided by the NASA Science Mission directorate.

A portion of this work was supported by a NASA Keck PI Data Award, administered by the NASA Exoplanet Science Institute. Data presented herein were obtained at the W. M. Keck Observatory from telescope time allocated to the National Aeronautics and Space Administration through the agency's scientific partnership with the California Institute of Technology and the University of California. The Observatory was made possible by the generous financial support of the W. M. Keck Foundation.

The authors wish to recognize and acknowledge the very significant cultural role and reverence that the summit of Maunakea has always had within the indigenous Hawaiian community. We are most fortunate to have the opportunity to conduct observations from this mountain.

For the work described in Chapter VIII, we thank Konstantin Batygin for a thorough review of the manuscript and many useful suggestions. We thank Andrew Vanderburg, Sarah Millholland, Jaehan Bae, Marina Kounkel, and Ellen Price for useful conversations. We thank Michael Dieterle and Clara Eng for helpful suggestions on how to effectively visualize the simulation results. We also thank Gary Bernstein for reviewing the manuscript and suggesting several improvements. Finally, we thank the referee for many useful comments that improved the chapter. This work was supported by NSF Grant AST-1515015. J.C.B and S.J.H. are also supported by the NSF Graduate Research Fellowship Grant No. DGE 1256260. The computations for this work used the Extreme Science and Engineering Discovery Environment (XSEDE), which is supported by National Science Foundation grant number ACI-1053575. This research was done using resources provided by the Open Science Grid, which is supported by the National Science Foundation and

the U.S. Department of Energy's Office of Science.

The work described in Chapter IX is based upon work supported by the National Aeronautics and Space Administration under Grant No. NNX17AF21G issued through the SSO Planetary Astronomy Program, and by NSF grant AST-1515015. We would like to thank Andrew Vanderburg, Ellen Price, Linn Eriksson, Melaine Saillenfest and Mike Brown for many useful conversations. We would like to thank Michele Bannister for useful discussions and methods advice. We would like to thank Konstantin Batygin for his careful review of the manuscript and suggestions that greatly improved this work. We thank Marty Kandes and Mats Rynge for help running simulations on Open Science Grid's high-throughput computing resources (operated through XSEDE). J.C.B, S.J.H, and L.M. are supported by the NSF Graduate Research Fellowship Grant No. DGE 1256260. This work used the Extreme Science and Engineering Discovery Environment (XSEDE), which is supported by National Science Foundation grant number ACI-1053575. This research was done using resources provided by the Open Science Grid, which is supported by the National Science Foundation and the U.S. Department of Energy's Office of Science, through allocations number TG-AST150033 and TG-AST170008. This research has made use of data and services provided by the International Astronomical Union's Minor Planet Center.

Funding for the DES Projects has been provided by the U.S. Department of Energy, the U.S. National Science Foundation, the Ministry of Science and Education of Spain, the Science and Technology Facilities Council of the United Kingdom, the Higher Education Funding Council for England, the National Center for Supercomputing Applications at the University of Illinois at Urbana-Champaign, the Kavli Institute of Cosmological Physics at the University of Chicago, the Center for Cosmology and Astro-Particle Physics at the Ohio State University, the Mitchell Institute for Fundamental Physics and Astronomy at Texas A&M University, Financiadora de Estudos e Projetos, Fundação Carlos Chagas Filho de Amparo à Pesquisa do Estado do Rio de Janeiro, Conselho Nacional de Desenvolvimento Científico e Tecnológico and the Ministério da Ciência, Tecnologia e Inovação, the Deutsche Forschungsgemeinschaft and the Collaborating Institutions in the Dark Energy Survey.

The Collaborating Institutions are Argonne National Laboratory, the University of California at Santa Cruz, the University of Cambridge, Centro de Investigaciones Energéticas, Medioambientales

y Tecnológicas-Madrid, the University of Chicago, University College London, the DES-Brazil Consortium, the University of Edinburgh, the Eidgenössische Technische Hochschule (ETH) Zürich, Fermi National Accelerator Laboratory, the University of Illinois at Urbana-Champaign, the Institut de Ciències de l'Espai (IEEC/CSIC), the Institut de Física d'Altes Energies, Lawrence Berkeley National Laboratory, the Ludwig-Maximilians Universität München and the associated Excellence Cluster Universe, the University of Michigan, the National Optical Astronomy Observatory, the University of Nottingham, The Ohio State University, the University of Pennsylvania, the University of Portsmouth, SLAC National Accelerator Laboratory, Stanford University, the University of Sussex, Texas A&M University, and the OzDES Membership Consortium.

Based in part on observations at Cerro Tololo Inter-American Observatory, National Optical Astronomy Observatory, which is operated by the Association of Universities for Research in Astronomy (AURA) under a cooperative agreement with the National Science Foundation.

The DES data management system is supported by the National Science Foundation under Grant Numbers AST-1138766 and AST-1536171. The DES participants from Spanish institutions are partially supported by MINECO under grants AYA2015-71825, ESP2015-66861, FPA2015-68048, SEV-2016-0588, SEV-2016-0597, and MDM-2015-0509, some of which include ERDF funds from the European Union. IFAE is partially funded by the CERCA program of the Generalitat de Catalunya. Research leading to these results has received funding from the European Research Council under the European Union's Seventh Framework Program (FP7/2007-2013) including ERC grant agreements 240672, 291329, and 306478. We acknowledge support from the Australian Research Council Centre of Excellence for All-sky Astrophysics (CAASTRO), through project number CE110001020, and the Brazilian Instituto Nacional de Ciência e Tecnologia (INCT) e-Universe (CNPq grant 465376/2014-2).

This manuscript has been authored by Fermi Research Alliance, LLC under Contract No. DE-AC02-07CH11359 with the U.S. Department of Energy, Office of Science, Office of High Energy Physics. The United States Government retains and the publisher, by accepting the article for publication, acknowledges that the United States Government retains a non-exclusive, paid-up, irrevocable, world-wide license to publish or reproduce the published form of this manuscript, or allow others to do so, for United States Government purposes.

BIBLIOGRAPHY

BIBLIOGRAPHY

Adams, E. R., Dupree, A. K., Kulesa, C., & McCarthy, D. 2013, *AJ*, 146, 9

Adams, E. R., Gulbis, A. A. S., Elliot, J. L., et al. 2014, *AJ*, 148, 55

Adams, F. C. 2010, *ARA&A*, 48, 47

—. 2011, *ApJ*, 730, 27

Adams, F. C., & Bloch, A. M. 2015, *MNRAS*, 446, 3676

Adams, F. C., & Laughlin, G. 2001, Icarus, 150, 151

Adams, F. C., Proszkow, E. M., Fatuzzo, M., & Myers, P. C. 2006, *ApJ*, 641, 504

Agol, E., Steffen, J., Sari, R., & Clarkson, W. 2005a, *MNRAS*, 359, 567

—. 2005b, *MNRAS*, 359, 567

Ahn, C. P., Alexandroff, R., Allende Prieto, C., et al. 2014, *ApJS*, 211, 17

Akeson, R. L., Chen, X., Ciardi, D., et al. 2013a, *PASP*, 125, 989

—. 2013b, *PASP*, 125, 989

—. 2013c, *PASP*, 125, 989

Albrecht, S., Winn, J. N., Johnson, J. A., et al. 2012a, *ApJ*, 757, 18

—. 2012b, *ApJ*, 757, 18

Alencar, S. H. P., Teixeira, P. S., Guimarães, M. M., et al. 2010, *A&A*, 519, A88

Alexandersen, M., Gladman, B., Kavelaars, J. J., et al. 2014, ArXiv e-prints, arXiv:1411.7953

Ali-Dib, M. 2017, *MNRAS*, 467, 2845

ALMA Partnership, Brogan, C. L., Pérez, L. M., et al. 2015, *ApJ*, 808, L3

Almenara, J. M., Díaz, R. F., Bonfils, X., & Udry, S. 2016, *A&A*, 595, L5

Almond, D. P., Budd, C. J., Freitag, M. A., et al. 2013, Physica A Statistical Mechanics and its Applications, 392, 1004

Anderson, D. R., Collier Cameron, A., Gillon, M., et al. 2011, *A&A*, 534, A16

Anderson, R., C. Jackson, H., May, R., & D. M. Smith, A. 1981, Nature, 289, 765

Angerbjorn, A., Tannerfeldt, M., & Erlinge, S. 1999, Journal of Animal Ecology, 68, 34

Anglada-Escudé, G., López-Morales, M., & Chambers, J. E. 2010, *ApJ*, 709, 168

Ansdell, M., Gaidos, E., Williams, J. P., et al. 2016a, *MNRAS*, 462, L101

Ansdell, M., Gaidos, E., Rappaport, S. A., et al. 2016b, *ApJ*, 816, 69

Antoninus, M. 161 - 180 A.D., The Meditations Of The Emperor, ed. G. Chrystal

Applegate, J. H. 1992, *ApJ*, 385, 621

Armitage, P. J. 2018, A Brief Overview of Planet Formation, 135

Bailey, E., & Batygin, K. 2018, *ApJ*, 866, L2

Bailey, E., Batygin, K., & Brown, M. E. 2016a, ArXiv e-prints, arXiv:1607.03963

—. 2016b, *AJ*, 152, 126

Bakos, G., Noyes, R. W., Kovács, G., et al. 2004, *PASP*, 116, 266

Bakos, G. Á., Kovács, G., Torres, G., et al. 2007, *ApJ*, 670, 826

Bakos, G. Á., Howard, A. W., Noyes, R. W., et al. 2009, *ApJ*, 707, 446

Bakos, G. Á., Torres, G., Pál, A., et al. 2010, *ApJ*, 710, 1724

Ballard, S., & Johnson, J. A. 2016a, *ApJ*, 816, 66

—. 2016b, *ApJ*, 816, 66

Ballard, S., Fabrycky, D., Fressin, F., et al. 2011, *ApJ*, 743, 200

Bannister, M. T., Kavelaars, J. J., Petit, J.-M., et al. 2016a, *AJ*, 152, 70

—. 2016b, *AJ*, 152, 70

Bannister, M. T., Shankman, C., Volk, K., et al. 2017, *AJ*, 153, 262

Baraffe, I., Homeier, D., Allard, F., & Chabrier, G. 2015, *A&A*, 577, A42

Baran, A. S., Zola, S., Blokesz, A., Østensen, R. H., & Silvotti, R. 2015, *A&A*, 577, A146

Baranec, C., Ziegler, C., Law, N. M., et al. 2016, *AJ*, 152, 18

Baranec, C., Riddle, R., Law, N. M., et al. 2014, *ApJ*, 790, L8

Baranne, A., Queloz, D., Mayor, M., et al. 1996, *A&AS*, 119, 373

Barclay, T., Quintana, E. V., Adams, F. C., et al. 2015a, *ApJ*, 809, 7

—. 2015b, *ApJ*, 809, 7

Barclay, T., Rowe, J. F., Lissauer, J. J., et al. 2013, *Nature*, 494, 452

Barentsen, G., & Cardoso, J. V. d. M. 2018, Kadenza: Kepler/K2 Raw Cadence Data Reader, Astrophysics Source Code Library, ascl:1803.005

Barros, S. C. C., Boué, G., Gibson, N. P., et al. 2013, *MNRAS*, 430, 3032

Barros, S. C. C., Faedi, F., Collier Cameron, A., et al. 2011, *A&A*, 525, A54

Barr-Sinoussi, F., & Montagutelli, X. 2015, Future science OA, 1, FSO63

Basri, G., Walkowicz, L. M., Batalha, N., et al. 2011, *AJ*, 141, 20

Batalha, N. M., Rowe, J. F., Gilliland, R. L., et al. 2010, *ApJ*, 713, L103

Batalha, N. M., Borucki, W. J., Bryson, S. T., et al. 2011a, *ApJ*, 729, 27

—. 2011b, *ApJ*, 729, 27

Batalha, N. M., Rowe, J. F., Bryson, S. T., et al. 2013, *ApJS*, 204, 24

Batygin, K. 2012a, *Nature*, 491, 418

—. 2012b, *Nature*, 491, 418

Batygin, K., Adams, F. C., Brown, M. E., & Becker, J. C. 2019, arXiv e-prints, arXiv:1902.10103

Batygin, K., Bodenheimer, P., & Laughlin, G. 2009, *ApJ*, 704, L49

Batygin, K., Bodenheimer, P. H., & Laughlin, G. P. 2016a, *ApJ*, 829, 114

—. 2016b, *ApJ*, 829, 114

Batygin, K., & Brown, M. E. 2016a, *AJ*, 151, 22

—. 2016b, ArXiv e-prints, arXiv:1610.04992

Batygin, K., & Morbidelli, A. 2017, *AJ*, 154, 229

Batygin, K., Morbidelli, A., & Tsiganis, K. 2011, *A&A*, 533, A7

Beaugé, C., & Nesvorný, D. 2012, *ApJ*, 751, 119

Beaulieu, J.-P., Bennett, D. P., Fouqué, P., et al. 2006, *Nature*, 439, 437

Becker, A. C., Arraki, K., Kaib, N. A., et al. 2008, *ApJ*, 682, L53

Becker, J. C., & Adams, F. C. 2016, *MNRAS*, 455, 2980

—. 2017, *MNRAS*, 468, 549

Becker, J. C., Adams, F. C., Khain, T., Hamilton, S. J., & Gerdes, D. 2017, *AJ*, 154, 61

Becker, J. C., & Batygin, K. 2013, *ApJ*, 778, 100

Becker, J. C., Johnson, J. A., Vand erburg, A., & Morton, T. D. 2015a, The Astrophysical Journal Supplement Series, 217, 29

Becker, J. C., Vanderburg, A., Adams, F. C., Rappaport, S. A., & Schwengeler, H. M. 2015b, *ApJ*, 812, L18

Becker, J. C., Vanderburg, A., Rodriguez, J. E., et al. 2019, *AJ*, 157, 19

Beichman, C., Benneke, B., Knutson, H., et al. 2014, *PASP*, 126, 1134

Bennett, D. P., Bhattacharya, A., Anderson, J., et al. 2015, *ApJ*, 808, 169

Bernhardt, J., Borschmann, K., Boyd, L., et al. 2016, International Journal of Stroke, 11, 454, pMID: 27073187

Bernstein, G., & Khushalani, B. 2000, *AJ*, 120, 3323

Bernstein, G. M., Armstrong, R., Plazas, A. A., et al. 2017, *PASP*, 129, 074503

Bernstein, J. P., Kessler, R., Kuhlmann, S., et al. 2012, *ApJ*, 753, 152

Beust, H. 2016, *A&A*, 590, L2

Bodman, E. H. L., Quillen, A. C., Ansdell, M., et al. 2017, *MNRAS*, 470, 202

Boley, A. C., & Ford, E. B. 2013, arXiv e-prints, arXiv:1306.0566

Boley, A. C., Granados Contreras, A. P., & Gladman, B. 2016, *ApJ*, 817, L17

Boley, A. C., Payne, M. J., & Ford, E. B. 2012, *ApJ*, 754, 57

Bonomo, A. S., Sozzetti, A., Lovis, C., et al. 2014, *A&A*, 572, A2

Borucki, W. J., Koch, D., Basri, G., et al. 2010, Science, 327, 977

Borucki, W. J., Koch, D. G., Basri, G., et al. 2011, *ApJ*, 736, 19

Borucki, W. J., Agol, E., Fressin, F., et al. 2013, Science, 340, 587

Bouvier, J., Chelli, A., Allain, S., et al. 1999, *A&A*, 349, 619

Boyajian, T. S., Alonso, R., Ammerman, A., et al. 2018, *ApJ*, 853, L8

Brahm, R., Espinoza, N., Jordán, A., et al. 2018, *MNRAS*, 477, 2572

Brakensiek, J., & Ragozzine, D. 2016a, *ApJ*, 821, 47

—. 2016b, *ApJ*, 821, 47

Brasser, R., Duncan, M. J., Levison, H. F., Schwamb, M. E., & Brown, M. E. 2012a, Icarus, 217, 1

Brasser, R., Schwamb, M. E., Lykawka, P. S., & Gomes, R. S. 2012b, *MNRAS*, 420, 3396

Brewer, J. M., Fischer, D. A., Basu, S., Valenti, J. A., & Piskunov, N. 2015, *ApJ*, 805, 126

Brewer, J. M., Fischer, D. A., Valenti, J. A., & Piskunov, N. 2016, *ApJS*, 225, 32

Bromley, B. C., & Kenyon, S. J. 2016, *ApJ*, 826, 64

Brown, M. E. 2017, *AJ*, 154, 65

Brown, M. E., & Batygin, K. 2016, *ApJ*, 824, L23

Brown, M. E., Trujillo, C., & Rabinowitz, D. 2004, *ApJ*, 617, 645

Brucker, M. J., Grundy, W. M., Stansberry, J. A., et al. 2009, Icarus, 201, 284

Bryan, M. L., Knutson, H. A., Lee, E. J., et al. 2019, *AJ*, 157, 52

Bryan, M. L., Knutson, H. A., Howard, A. W., et al. 2016, *ApJ*, 821, 89

Buchhave, L. A., Bakos, G. Á., Hartman, J. D., et al. 2010, *ApJ*, 720, 1118

Buchhave, L. A., Latham, D. W., Johansen, A., et al. 2012, *Nature*, 486, 375

Buchhave, L. A., Bizzarro, M., Latham, D. W., et al. 2014a, *Nature*, 509, 593

—. 2014b, *Nature*, 509, 593

Buchhave, L. A., Dressing, C. D., Dumusque, X., et al. 2016, *AJ*, 152, 160

Burke, C. J., McCullough, P. R., Valenti, J. A., et al. 2007, *ApJ*, 671, 2115

Burke, C. J., Christiansen, J. L., Mullally, F., et al. 2015, *ApJ*, 809, 8

Cañas, C. I., Wang, S., Mahadevan, S., et al. 2019, *ApJ*, 870, L17

Cabrera, J., Csizmadia, S., Lehmann, H., et al. 2014, *ApJ*, 781, 18

Campante, T. L., Schofield, M., Kuszlewicz, J. S., et al. 2016, *ApJ*, 830, 138

Carter, J. A., Agol, E., Chaplin, W. J., et al. 2012a, Science, 337, 556

—. 2012b, Science, 337, 556

Caselli, P., Benson, P. J., Myers, P. C., & Tafalla, M. 2002, *ApJ*, 572, 238

Chambers, J. E. 1999a, *MNRAS*, 304, 793

—. 1999b, *MNRAS*, 304, 793

—. 1999c, *MNRAS*, 304, 793

Charbonneau, D., Brown, T. M., Latham, D. W., & Mayor, M. 2000a, *ApJ*, 529, L45

—. 2000b, *ApJ*, 529, L45

Charbonneau, D., Brown, T. M., Noyes, R. W., & Gilliland, R. L. 2002, *ApJ*, 568, 377

Charbonneau, D., Berta, Z. K., Irwin, J., et al. 2009, *Nature*, 462, 891

Charpinet, S., Fontaine, G., Brassard, P., et al. 2011, *Nature*, 480, 496

Chen, J., & Kipping, D. 2017, *ApJ*, 834, 17

Chen, Y.-T., Kavelaars, J. J., Gwyn, S., et al. 2013, *ApJ*, 775, L8

Chen, Y.-T., Lin, H. W., Holman, M. J., et al. 2016a, *ApJ*, 827, L24

—. 2016b, *ApJ*, 827, L24

Chen, Y.-T., Lin, H. W., Holman, M. J., et al. 2016, The Astrophysical Journal Letters, 827, L24

Cheng, K. S., Ho, C., & Ruderman, M. 1986, *ApJ*, 300, 500

Chilcote, J., Pueyo, L., De Rosa, R. J., et al. 2017, *AJ*, 153, 182

Choi, J., Dotter, A., Conroy, C., et al. 2016, *ApJ*, 823, 102

Christiansen, J. L., Clarke, B. D., Burke, C. J., et al. 2013, *ApJS*, 207, 35

—. 2015, *ApJ*, 810, 95

Christiansen, J. L., Vanderburg, A., Burt, J., et al. 2017a, *AJ*, 154, 122

—. 2017b, ArXiv e-prints, arXiv:1706.01892

—. 2017c, *AJ*, 154, 122

Ciardi, D. R., Crossfield, I. J. M., Feinstein, A. D., et al. 2018, *AJ*, 155, 10

Cincotta, P. M., Giordano, C. M., & Simó, C. 2003, Physica D Nonlinear Phenomena, 182, 151

Claret, A., & Bloemen, S. 2011, *A&A*, 529, A75

Cochran, W. D., Fabrycky, D. C., Torres, G., et al. 2011, The Astrophysical Journal Supplement Series, 197, 7

Cody, A. M., Stauffer, J., Baglin, A., et al. 2014, *AJ*, 147, 82

Collins, K. A., Kielkopf, J. F., & Stassun, K. G. 2017, *AJ*, 153, 78

Cosentino, R., Lovis, C., Pepe, F., et al. 2012, in Society of Photo-Optical Instrumentation Engineers (SPIE) Conference Series, Vol. 8446, Society of Photo-Optical Instrumentation Engineers (SPIE) Conference Series

Coughlin, J. L., Mullally, F., Thompson, S. E., et al. 2015, ArXiv e-prints, arXiv:1512.06149

Crane, J. D., Shectman, S. A., Butler, R. P., et al. 2010, in Society of Photo-Optical Instrumentation Engineers (SPIE) Conference Series, Vol. 7735, Society of Photo-Optical Instrumentation Engineers (SPIE) Conference Series

Crossfield, I. J. M., & Kreidberg, L. 2017a, *AJ*, 154, 261

—. 2017b, *AJ*, 154, 261

Crossfield, I. J. M., Ciardi, D. R., Isaacson, H., et al. 2017, *AJ*, 153, 255

Cucker, F., & Smale, S. 2007, Japanese Journal of Mathematics, 2, doi:https://doi.org/10.1007/s11537-007-0647-x

Cumming, A., Butler, R. P., Marcy, G. W., et al. 2008, *PASP*, 120, 531

Currie, T., Debes, J., Rodigas, T. J., et al. 2012, The Astrophysical Journal, 760, L32

Cutri, R. M., & et al. 2014, VizieR Online Data Catalog, 2328, 0

Cutri, R. M., Skrutskie, M. F., van Dyk, S., et al. 2003, VizieR Online Data Catalog, 2246, 0

da Silva, L., Girardi, L., Pasquini, L., et al. 2006, *A&A*, 458, 609

Dai, F., Masuda, K., & Winn, J. N. 2018, *ApJ*, 864, L38

Dai, F., Winn, J. N., Arriagada, P., et al. 2015, *ApJ*, 813, L9

Damasso, M., Biazzo, K., Bonomo, A. S., et al. 2015, *A&A*, 575, A111

D'Antona, F., & Mazzitelli, I. 1994, *ApJS*, 90, 467

Dark Energy Survey Collaboration, Abbott, T., Abdalla, F. B., et al. 2016a, *MNRAS*, 460, 1270

—. 2016b, *MNRAS*, 460, 1270

David, E.-M., Quintana, E. V., Fatuzzo, M., & Adams, F. C. 2003, *PASP*, 115, 825

David, T. J., Crossfield, I. J. M., Benneke, B., et al. 2018, *AJ*, 155, 222

Dawson, R. I., & Fabrycky, D. C. 2010, *ApJ*, 722, 937

Dawson, R. I., Murray-Clay, R. A., & Johnson, J. A. 2015, *ApJ*, 798, 66

de la Fuente Marcos, C., & de la Fuente Marcos, R. 2016, *MNRAS*, 462, 1972

de la Fuente Marcos, C., de la Fuente Marcos, R., & Aarseth, S. J. 2016, *MNRAS*, 460, L123

Deck, K. M., & Agol, E. 2015, *ApJ*, 802, 116

Deck, K. M., Agol, E., Holman, M. J., & Nesvorný, D. 2014a, *ApJ*, 787, 132

—. 2014b, *ApJ*, 787, 132

Deck, K. M., Holman, M. J., Agol, E., et al. 2012, *ApJ*, 755, L21

Denham, P., Naoz, S., Hoang, B.-M., Stephan, A. P., & Farr, W. M. 2018, ArXiv e-prints, arXiv:1802.00447

—. 2019, *MNRAS*, 482, 4146

Diez Alonso, E., Suarez Gomez, S. L., Gonzalez Hernandez, J. I., et al. 2018, ArXiv e-prints, arXiv:1801.06249

Dotson, J. L., Barentsen, G., Hedges, C., & Coughlin, J. L. 2019, Research Notes of the American Astronomical Society, 3, 23

Dotter, A. 2016, *ApJS*, 222, 8

Dotter, A., Chaboyer, B., Jevremović, D., et al. 2008, *ApJS*, 178, 89

Doyle, L. R., Carter, J. A., Fabrycky, D. C., et al. 2011, Science, 333, 1602

Dragomir, D., Matthews, J. M., Eastman, J. D., et al. 2013, *ApJ*, 772, L2

Dressing, C. D., & Charbonneau, D. 2013a, *ApJ*, 767, 95

—. 2013b, *ApJ*, 767, 95

—. 2015, *ApJ*, 807, 45

Dressing, C. D., Newton, E. R., Schlieder, J. E., et al. 2017, *ApJ*, 836, 167

Dressing, C. D., Charbonneau, D., Dumusque, X., et al. 2015a, *ApJ*, 800, 135

—. 2015b, *ApJ*, 800, 135

Dumusque, X., Bonomo, A. S., Haywood, R. D., et al. 2014, *ApJ*, 789, 154

Duncan, M., Quinn, T., & Tremaine, S. 1987, *AJ*, 94, 1330

Duncan, M. J., & Levison, H. F. 1997, Science, 276, 1670

Dwyer, G., Levin, S. A., & Buttel, L. 1990, Ecological Monographs, 60, 423

Eastman, J. 2017, EXOFASTv2: Generalized publication-quality exoplanet modeling code, Astrophysics Source Code Library, ascl:1710.003

Eastman, J., Gaudi, B. S., & Agol, E. 2013a, *PASP*, 125, 83

—. 2013b, *PASP*, 125, 83

Ehrenreich, D., Bourrier, V., Wheatley, P. J., et al. 2015, *Nature*, 522, 459

Elliot, J. L., Kern, S. D., Clancy, K. B., et al. 2005, *AJ*, 129, 1117

Eriksson, L. E. J., Mustill, A. J., & Johansen, A. 2018, *MNRAS*, 475, 4609

Fabrycky, D., & Tremaine, S. 2007a, *ApJ*, 669, 1298

—. 2007b, *ApJ*, 669, 1298

Fabrycky, D. C., & Winn, J. N. 2009, *ApJ*, 696, 1230

Fabrycky, D. C., Ford, E. B., Steffen, J. H., et al. 2012, *ApJ*, 750, 114

Fabrycky, D. C., Lissauer, J. J., Ragozzine, D., et al. 2014a, *ApJ*, 790, 146

—. 2014b, *ApJ*, 790, 146

Faedi, F., Barros, S. C. C., Anderson, D. R., et al. 2011, *A&A*, 531, A40

Faigler, S., Tal-Or, L., Mazeh, T., Latham, D. W., & Buchhave, L. A. 2013, *ApJ*, 771, 26

Fang, J., & Margot, J.-L. 2012, *ApJ*, 761, 92

Fekel, F. C. 1997, Publications of the Astronomical Society of the Pacific, 109, 514

Fűrész, G. 2008, PhD thesis, University of Szeged, Hungary

Fielding, D. B., McKee, C. F., Socrates, A., Cunningham, A. J., & Klein, R. I. 2015, *MNRAS*, 450, 3306

Fienga, A., Laskar, J., Manche, H., & Gastineau, M. 2016, *A&A*, 587, L8

Figueira, P., Marmier, M., Boué, G., et al. 2012, *A&A*, 541, A139

Finzer, P. 2017, EMBO Reports, 18, 515518

Fischer, D. A., Marcy, G. W., Butler, R. P., et al. 2008, *ApJ*, 675, 790

Flaugher, B., Diehl, H. T., Honscheid, K., et al. 2015, *AJ*, 150, 150

Flewelling, H. A., Magnier, E. A., Chambers, K. C., et al. 2016, ArXiv e-prints, arXiv:1612.05243

Fogg, M. J., & Nelson, R. P. 2007, *A&A*, 461, 1195

Ford, E. B., Quinn, S. N., & Veras, D. 2008, *ApJ*, 678, 1407

Foreman-Mackey, D., Hogg, D. W., Lang, D., & Goodman, J. 2013a, *PASP*, 125, 306

—. 2013b, *PASP*, 125, 306

Foreman-Mackey, D., Hogg, D. W., & Morton, T. D. 2014, *ApJ*, 795, 64

Foreman-Mackey, D., Morton, T. D., Hogg, D. W., Agol, E., & Schölkopf, B. 2016, *AJ*, 152, 206

Fornasier, S., Lellouch, E., Müller, T., et al. 2013, *A&A*, 555, A15

Fortney, J. J., & Nettelmann, N. 2010, *Space Sci. Rev.*, 152, 423

Fox, O. D., Silverman, J. M., Filippenko, A. V., et al. 2015, *MNRAS*, 447, 772

Fraser, W. C., Brown, M. E., Morbidelli, A., Parker, A., & Batygin, K. 2014, *ApJ*, 782, 100

Fressin, F., Torres, G., Rowe, J. F., et al. 2012, *Nature*, 482, 195

Fressin, F., Torres, G., Charbonneau, D., et al. 2013a, *ApJ*, 766, 81

—. 2013b, *ApJ*, 766, 81

Fuentes, C. I., & Holman, M. J. 2008, *AJ*, 136, 83

Fulton, B. J., & Petigura, E. A. 2018, *AJ*, 156, 264

Fulton, B. J., Petigura, E. A., Howard, A. W., et al. 2017, *AJ*, 154, 109

Gaia Collaboration, Brown, A. G. A., Vallenari, A., et al. 2018a, ArXiv e-prints, arXiv:1804.09365

—. 2018b, ArXiv e-prints, arXiv:1804.09365

—. 2016a, *A&A*, 595, A2

—. 2016b, *A&A*, 595, A2

Gaia Collaboration, Prusti, T., de Bruijne, J. H. J., et al. 2016c, *A&A*, 595, A1

Gallardo, T., Hugo, G., & Pais, P. 2012, Icarus, 220, 392

Gandolfi, D., Barragán, O., Hatzes, A. P., et al. 2017, ArXiv e-prints, arXiv:1706.02532

Gandolfi, D., Barragán, O., Livingston, J. H., et al. 2018, *A&A*, 619, L10

Gaudi, B. S., Naber, R. M., & Sackett, P. D. 1998, *ApJ*, 502, L33

Gaudi, B. S., Bennett, D. P., Udalski, A., et al. 2008, Science, 319, 927

Gaudi, B. S., Stassun, K. G., Collins, K. A., et al. 2017, *Nature*, 546, 514

Gautier, Thomas N., I., Charbonneau, D., Rowe, J. F., et al. 2012, *ApJ*, 749, 15

Gautschy, A., & Saio, H. 1996, Annual Review of Astronomy and Astrophysics, 34, 551

Gelman, A., & Rubin, D. B. 1992, Statistical science, 457

Gerdes, D. W., Jennings, R. J., Bernstein, G. M., et al. 2016a, *AJ*, 151, 39

—. 2016b, *AJ*, 151, 39

Gerdes, D. W., Sako, M., Hamilton, S., et al. 2017a, *ApJ*, 839, L15

—. 2017b, *ApJ*, 839, L15

Geweke, J. 1992, in IN BAYESIAN STATISTICS (University Press), 169–193

Gibson, N. P., Pollacco, D., Simpson, E. K., et al. 2009, *ApJ*, 700, 1078

Gilliland, R. L., Marcy, G. W., Rowe, J. F., et al. 2013, *ApJ*, 766, 40

Gillon, M., Jehin, E., Lederer, S. M., et al. 2016, *Nature*, 533, 221

Gillon, M., Triaud, A. H. M. J., Demory, B.-O., et al. 2017, *Nature*, 542, 456

Gladman, B., Holman, M., Grav, T., et al. 2002, Icarus, 157, 269

Gladman, B., Marsden, B. G., & Vanlaerhoven, C. 2008, Nomenclature in the Outer Solar System

Gladman, B., Kavelaars, J., Petit, J.-M., et al. 2009, *ApJ*, 697, L91

Goldreich, P., & Julian, W. H. 1969, *ApJ*, 157, 869

Goldreich, P., & Soter, S. 1966, Icarus, 5, 375

Goldstein, D. A., D'Andrea, C. B., Fischer, J. A., et al. 2015, *AJ*, 150, 82

Gomes, R., Deienno, R., & Morbidelli, A. 2016, ArXiv e-prints, arXiv:1607.05111

—. 2017, *AJ*, 153, 27

Gomes, R., Levison, H. F., Tsiganis, K., & Morbidelli, A. 2005, *Nature*, 435, 466

Gong, Y.-X., & Ji, J. 2017, *AJ*, 154, 179

Goodman, J., & Weare, J. 2010a, Communications in Applied Mathematics and Computational Science, 5, 65

—. 2010b, Communications in Applied Mathematics and Computational Science, 5, 65

Goodman, J., & Weare, J. 2010, Communications in Applied Mathematics and Computational Science, Vol. 5, No. 1, p. 65-80, 2010, 5, 65

Granados Contreras, A. P., & Boley, A. C. 2018, *AJ*, 155, 139

Grasset, O., Schneider, J., & Sotin, C. 2009, *ApJ*, 693, 722

Gratia, P., & Fabrycky, D. 2017, *MNRAS*, 464, 1709

Grunblatt, S. K., Howard, A. W., & Haywood, R. D. 2015, *ApJ*, 808, 127

Guan, P., Zhou, L.-Y., & Li, J. 2012, Research in Astronomy and Astrophysics, 12, 1549

Guenther, E. W., Barragan, O., Dai, F., et al. 2017, ArXiv e-prints, arXiv:1705.04163

Hadden, S., Li, G., Payne, M. J., & Holman, M. J. 2017, ArXiv e-prints, arXiv:1712.06547

Hadden, S., & Lithwick, Y. 2014, *ApJ*, 787, 80

—. 2016, *ApJ*, 828, 44

—. 2017, *AJ*, 154, 5

Han, C., Udalski, A., Choi, J.-Y., et al. 2013, *ApJ*, 762, L28

Han, E., Wang, S. X., Wright, J. T., et al. 2014, *PASP*, 126, 827

Handler, G., Balona, L. A., Shobbrook, R. R., et al. 2002, *MNRAS*, 333, 262

Hansen, B. M. S. 2017, *MNRAS*, 467, 1531

Hansen, B. M. S., & Murray, N. 2012, *ApJ*, 751, 158

Hansen, B. M. S., & Murray, N. 2013, *ApJ*, 775, 53

Hartman, J. D., & Bakos, G. Á. 2016, Astronomy and Computing, 17, 1

Haywood, R. D., Collier Cameron, A., Queloz, D., et al. 2014, *MNRAS*, 443, 2517

Heap, S. R., Lindler, D. J., Lanz, T. M., et al. 2000, *ApJ*, 539, 435

Hellier, C., Anderson, D. R., Collier Cameron, A., et al. 2012a, *MNRAS*, 426, 739

—. 2012b, *MNRAS*, 426, 739

Henden, A. A., Templeton, M., Terrell, D., et al. 2016, VizieR Online Data Catalog, 2336

Henderson, C. B., & Shvartzvald, Y. 2016, *AJ*, 152, 96

Henry, G. W., Marcy, G. W., Butler, R. P., & Vogt, S. S. 2000, *ApJ*, 529, L41

Hermes, J. J. 2018, Timing by Stellar Pulsations as an Exoplanet Discovery Method, 6

Hernández, J., Hartmann, L., Megeath, T., et al. 2007, *ApJ*, 662, 1067

Herter, T. L., Henderson, C. P., Wilson, J. C., et al. 2008, in *Proc. SPIE*, Vol. 7014, Ground-based and Airborne Instrumentation for Astronomy II, 70140X

Hirano, T., Fukui, A., Mann, A. W., et al. 2016, *ApJ*, 820, 41

Hirano, T., Dai, F., Livingston, J. H., et al. 2018, *AJ*, 155, 124

Holczer, T., Mazeh, T., Nachmani, G., et al. 2016, *ApJS*, 225, 9

Holman, M. J., & Murray, N. W. 2005, Science, 307, 1288

Holman, M. J., & Payne, M. J. 2016a, *AJ*, 152, 80

—. 2016b, ArXiv e-prints, arXiv:1604.03180

—. 2016c, *AJ*, 152, 94

Holman, M. J., Fabrycky, D. C., Ragozzine, D., et al. 2010, Science, 330, 51

Holman, M. J., Payne, M. J., Fraser, W., et al. 2018, *ApJ*, 855, L6

Horner, J., Lykawka, P. S., Bannister, M. T., & Francis, P. 2012, *MNRAS*, 422, 2145

Howard, A. W., Marcy, G. W., Bryson, S. T., et al. 2012a, *ApJS*, 201, 15

—. 2012b, *ApJS*, 201, 15

Howard, A. W., Sanchis-Ojeda, R., Marcy, G. W., et al. 2013, *Nature*, 503, 381

Howell, S. B., Sobeck, C., Haas, M., et al. 2014a, *PASP*, 126, 398

—. 2014b, *PASP*, 126, 398

Huang, C., Wu, Y., & Triaud, A. H. M. J. 2016a, *ApJ*, 825, 98

—. 2016b, *ApJ*, 825, 98

Huang, C. X., Petrovich, C., & Deibert, E. 2017, *AJ*, 153, 210

Huang, C. X., Burt, J., Vanderburg, A., et al. 2018, *ApJ*, 868, L39

Huber, D., Carter, J. A., Barbieri, M., et al. 2013, Science, 342, 331

Hut, P. 1980, *A&A*, 92, 167

Izidoro, A., Raymond, S. N., Morbidelli, A. r., Hersant, F., & Pierens, A. 2015, *ApJ*, 800, L22

Jackson, B., Arras, P., Penev, K., Peacock, S., & Marchant, P. 2017, *ApJ*, 835, 145

Jackson, B., Stark, C. C., Adams, E. R., Chambers, J., & Deming, D. 2013, *ApJ*, 779, 165

Jain, C., Paul, B., Sharma, R., Jaleel, A., & Dutta, A. 2017, *MNRAS*, 468, L118

James, A. I., Eldridge, D. J., Koen, T. B., & Moseby, K. E. 2011, Biological Invasions, 13, 3027

Janson, M., Carson, J. C., Lafrenière, D., et al. 2012, The Astrophysical Journal, 747, 116

Jensen, E. L. N., & Akeson, R. 2014, *Nature*, 511, 567

Jiménez-Torres, J. J., Pichardo, B., Lake, G., & Throop, H. 2011, *MNRAS*, 418, 1272

Johnson, J. A., Aller, K. M., Howard, A. W., & Crepp, J. R. 2010, Publications of the Astronomical Society of the Pacific, 122, 905

Johnson, J. A., Gazak, J. Z., Apps, K., et al. 2012, *AJ*, 143, 111

Johnson, M. C., Cochran, W. D., Addison, B. C., Tinney, C. G., & Wright, D. J. 2017, ArXiv e-prints, arXiv:1708.01291

Jones, E., Oliphant, T., Peterson, P., et al. 2001, SciPy: Open source scientific tools for Python, [Online; accessed 2018]

Jontof-Hutter, D., Truong, V. H., Ford, E. B., Robertson, P., & Terrien, R. C. 2018, *AJ*, 155, 239

Jontof-Hutter, D., Weaver, B. P., Ford, E. B., Lissauer, J. J., & Fabrycky, D. C. 2017a, *AJ*, 153, 227

—. 2017b, *AJ*, 153, 227

Jontof-Hutter, D., Ford, E. B., Rowe, J. F., et al. 2016, *ApJ*, 820, 39

Kalas, P., Graham, J. R., Chiang, E., et al. 2008, Science, 322, 1345

Kalas, P., Graham, J. R., Chiang, E., et al. 2008, Science, 322, 1345

Kalirai, J. 2018, Contemporary Physics, 59, 251

Kenyon, S. J., & Bromley, B. C. 2004, *Nature*, 432, 598

—. 2016, *ApJ*, 825, 33

Kerr, P. J. 2012, Antiviral research, 93, 387

Kessler, R., Marriner, J., Childress, M., et al. 2015, *AJ*, 150, 172

Ketchum, J. A., Adams, F. C., & Bloch, A. M. 2013a, *ApJ*, 762, 71

—. 2013b, *ApJ*, 762, 71

Khain, T., Batygin, K., & Brown, M. E. 2018a, ArXiv e-prints, arXiv:1804.11281

Khain, T., Becker, J. C., Adams, F. C., et al. 2018b, *AJ*, 156, 273

Kinoshita, H., & Nakai, H. 1999, Celestial Mechanics and Dynamical Astronomy, 75, 125

Kipping, D. M. 2009, *MNRAS*, 392, 181

—. 2011, The Transits of Extrasolar Planets with Moons

—. 2013a, *MNRAS*, 435, 2152

—. 2013b, *MNRAS*, 434, L51

—. 2014, *MNRAS*, 444, 2263

Kipping, D. M., Huang, X., Nesvorný, D., et al. 2015, *ApJ*, 799, L14

Kipping, D. M., & Sandford, E. 2016, ArXiv e-prints, arXiv:1603.05662

Kley, W., & Nelson, R. P. 2012, *ARA&A*, 50, 211

Knutson, H. A., Benneke, B., Deming, D., & Homeier, D. 2014a, *Nature*, 505, 66

Knutson, H. A., Fulton, B. J., Montet, B. T., et al. 2014b, *ApJ*, 785, 126

—. 2014c, *ApJ*, 785, 126

—. 2014d, *ApJ*, 785, 126

Koch, D. G., Borucki, W. J., Basri, G., et al. 2010, *ApJ*, 713, L79

Kopparapu, R. K., Hébrard, E., Belikov, R., et al. 2018, *ApJ*, 856, 122

Kostov, V. B., McCullough, P. R., Carter, J. A., et al. 2014, *ApJ*, 784, 14

Kovács, G., Bakos, G., & Noyes, R. W. 2005, *MNRAS*, 356, 557

Kovács, G., Zucker, S., & Mazeh, T. 2002a, *A&A*, 391, 369

—. 2002b, *A&A*, 391, 369

Kovács, G., Bakos, G. Á., Torres, G., et al. 2007, *ApJ*, 670, L41

Kozai, Y. 1962, *AJ*, 67, 591

Kraft, R. P. 1967, *ApJ*, 150, 551

Kramer, M., Stairs, I. H., Manchester, R. N., et al. 2006, Science, 314, 97

Kratina, P., LeCraw, R. M., Ingram, T., & Anholt, B. R. 2012, Ecosphere, 3, art50

Kreidberg, L., Bean, J. L., Désert, J.-M., et al. 2014, *ApJ*, 793, L27

Krzesinski, J. 2015, *A&A*, 581, A7

Kuhn, R. B., Rodriguez, J. E., Collins, K. A., et al. 2016, *MNRAS*, 459, 4281

Kurucz, R. L. 1992, in IAU Symposium, Vol. 149, The Stellar Populations of Galaxies, ed. B. Barbuy & A. Renzini, 225

Lada, C. J., & Lada, E. A. 2003, *ARA&A*, 41, 57

Lai, D. 2012, *MNRAS*, 423, 486

—. 2014, *MNRAS*, 440, 3532

—. 2016, ArXiv e-prints, arXiv:1608.01421

Lai, D., Foucart, F., & Lin, D. N. C. 2011, *MNRAS*, 412, 2790

Lai, D., & Pu, B. 2017, *AJ*, 153, 42

Latham, D. W., Rowe, J. F., Quinn, S. N., et al. 2011, *ApJ*, 732, L24

Laughlin, G., & Adams, F. C. 2000, Icarus, 145, 614

Laughlin, G., Crismani, M., & Adams, F. C. 2011, *ApJ*, 729, L7

Law, N. M., Morton, T., Baranec, C., et al. 2014, *ApJ*, 791, 35

Lawler, S. M., Kavelaars, J., Alexandersen, M., et al. 2018, ArXiv e-prints, arXiv:1802.00460

Lawler, S. M., Shankman, C., Kaib, N., et al. 2016, ArXiv e-prints, arXiv:1605.06575

Lee, E. J., Chiang, E., & Ormel, C. W. 2014, *ApJ*, 797, 95

Lees, A. C., & Bell, D. J. 2008, Mammal Review, 38, 304

Lellouch, E., Kiss, C., Santos-Sanz, P., et al. 2010, *A&A*, 518, L147

Lellouch, E., Santos-Sanz, P., Lacerda, P., et al. 2013, *A&A*, 557, A60

Levison, H. F., Morbidelli, A., Van Laerhoven, C., Gomes, R., & Tsiganis, K. 2008, Icarus, 196, 258

Li, G., & Adams, F. C. 2015a, *MNRAS*, 448, 344

—. 2015b, *MNRAS*, 448, 344

—. 2015c, *MNRAS*, 448, 344

—. 2015d, *MNRAS*, 448, 344

—. 2016a, *ApJ*, 823, L3

—. 2016b, *ApJ*, 823, L3

Li, G., Hadden, S., Payne, M., & Holman, M. J. 2018, *AJ*, 156, 263

Li, G., & Winn, J. N. 2016, *ApJ*, 818, 5

Li, X.-G., Gao, Z.-Y., Li, K.-P., & Zhao, X.-M. 2007, Physical review. E, Statistical, nonlinear, and soft matter physics, 76, 016110

Lidov, M. L. 1962, *Planet. Space Sci.*, 9, 719

Lim, T. L., Stansberry, J., Müller, T. G., et al. 2010, *A&A*, 518, L148

Lin, H. W., Chen, Y.-T., Holman, M. J., et al. 2016a, *AJ*, 152, 147

—. 2016b, *AJ*, 152, 147

Lissauer, J. J., Fabrycky, D. C., Ford, E. B., et al. 2011a, *Nature*, 470, 53

Lissauer, J. J., Ragozzine, D., Fabrycky, D. C., et al. 2011b, *ApJS*, 197, 8

Lissauer, J. J., Marcy, G. W., Rowe, J. F., et al. 2012a, *ApJ*, 750, 112

—. 2012b, *ApJ*, 750, 112

Lithwick, Y., Xie, J., & Wu, Y. 2012, *ApJ*, 761, 122

Livingston, J. H., Dai, F., Hirano, T., et al. 2018, *AJ*, 155, 115

Loeb, A., & Gaudi, B. S. 2003, *ApJ*, 588, L117

Londono, C., Loureiro, M. J., Slater, B., et al. 2014, Proceedings of the National Academy of Sciences, 111, 1807

Loomis, R. A., Öberg, K. I., Andrews, S. M., & MacGregor, M. A. 2017, *ApJ*, 840, 23

Lopez, E. D. 2016, ArXiv e-prints, arXiv:1610.01170

—. 2017, *MNRAS*, 472, 245

Lopez, E. D., & Fortney, J. J. 2014, *ApJ*, 792, 1

Lopez, E. D., Fortney, J. J., & Miller, N. 2012, *ApJ*, 761, 59

Lovis, C., Ségransan, D., Mayor, M., et al. 2011, *A&A*, 528, A112

Luger, R., Sestovic, M., Kruse, E., et al. 2017, Nature Astronomy, 1, 0129

Lund, M. B., Rodriguez, J. E., Zhou, G., et al. 2017, *AJ*, 154, 194

Lutz, T. M. 1985, *Nature*, 317, 404

Lykawka, P. S., & Mukai, T. 2006, *Planet. Space Sci.*, 54, 87

—. 2007, Icarus, 189, 213

Ma, B., & Ge, J. 2014, *MNRAS*, 439, 2781

Ma, S., Mao, S., Ida, S., Zhu, W., & Lin, D. N. C. 2016, *MNRAS*, 461, L107

Maciejewski, G., Niedzielski, A., Wolszczan, A., et al. 2013, *AJ*, 146, 147

Madigan, A.-M., & McCourt, M. 2016, *MNRAS*, 457, L89

Madigan, A.-M., Zderic, A., McCourt, M., & Fleisig, J. 2018, ArXiv e-prints, arXiv:1805.03651

Maeder, A., & Meynet, G. 2000, Annual Review of Astronomy and Astrophysics, 38, 143

Malavolta, L., Borsato, L., Granata, V., et al. 2017, ArXiv e-prints, arXiv:1703.06885

Malhotra, R., Volk, K., & Wang, X. 2016a, *ApJ*, 824, L22

—. 2016b, *ApJ*, 824, L22

Mandel, K., & Agol, E. 2002a, *ApJ*, 580, L171

—. 2002b, *ApJ*, 580, L171

Mann, A. W., Feiden, G. A., Gaidos, E., Boyajian, T., & von Braun, K. 2015, *ApJ*, 804, 64

Mann, A. W., Gaidos, E., & Ansdell, M. 2013a, *ApJ*, 779, 188

Mann, A. W., Gaidos, E., Kraus, A., & Hilton, E. J. 2013b, *ApJ*, 770, 43

Mann, A. W., Vanderburg, A., Rizzuto, A. C., et al. 2018, *AJ*, 155, 4

Marcy, G., Butler, R. P., Fischer, D., et al. 2005, Progress of Theoretical Physics Supplement, 158, 24

Marcy, G. W., Isaacson, H., Howard, A. W., et al. 2014, *ApJS*, 210, 20

Mardling, R. A. 2013, *MNRAS*, 435, 2187

Markwardt, C. B. 2009, in Astronomical Society of the Pacific Conference Series, Vol. 411, Astronomical Data Analysis Software and Systems XVIII, ed. D. A. Bohlender, D. Durand, & P. Dowler, 251

Marois, C., Macintosh, B., Barman, T., et al. 2008, Science, 322, 1348

Marois, C., Zuckerman, B., Konopacky, Q. M., Macintosh, B., & Barman, T. 2010, *Nature*, 468, 1080

Marsden, B. G., Sekanina, Z., & Everhart, E. 1978, *AJ*, 83, 64

Masuda, K., Hirano, T., Taruya, A., Nagasawa, M., & Suto, Y. 2013, *ApJ*, 778, 185

Maxted, P. F. L., Anderson, D. R., Gillon, M., et al. 2010, *AJ*, 140, 2007

Maxted, P. F. L., Anderson, D. R., Collier Cameron, A., et al. 2011, *PASP*, 123, 547

May, E. M., Zhao, M., Haidar, M., Rauscher, E., & Monnier, J. D. 2018, *AJ*, 156, 122

Mayo, A. W., Vanderburg, A., Latham, D. W., et al. 2018a, *AJ*, 155, 136

—. 2018b, *AJ*, 155, 136

Mayor, M., & Queloz, D. 1995, *Nature*, 378, 355

Mayor, M., Pepe, F., Queloz, D., et al. 2003, The Messenger, 114, 20

Mayor, M., Marmier, M., Lovis, C., et al. 2011, ArXiv e-prints, arXiv:1109.2497

Mazeh, T., Perets, H. B., McQuillan, A., & Goldstein, E. S. 2015, *ApJ*, 801, 3

McArthur, B. E., Endl, M., Cochran, W. D., et al. 2004, *ApJ*, 614, L81

Mccann, K., & Hastings, A. 1997, Proceedings of the Royal Society of London. Series B: Biological Sciences, 264, doi:10.1098/rspb.1997.0172

McKinney, W. 2010, in Proceedings of the 9th Python in Science Conference, ed. S. van der Walt & J. Millman, 51 – 56

Mena-Lorcat, J., & Hethcote, H. W. 1992, Journal of Mathematical Biology, 30, 693

Michtchenko, T. A., & Malhotra, R. 2004, Icarus, 168, 237

Mill, J. S. 1843, 3, doi:10.1098/rsfs.2011.0046

Miller-Ricci, E., Rowe, J. F., Sasselov, D., et al. 2008, *ApJ*, 682, 586

Millholland, S., & Laughlin, G. 2017, *AJ*, 153, 91

Millholland, S., Laughlin, G., Teske, J., et al. 2018, *AJ*, 155, 106

Millis, R. L., Buie, M. W., Wasserman, L. H., et al. 2002, *AJ*, 123, 2083

Mills, S. M., & Fabrycky, D. C. 2017a, *AJ*, 153, 45

—. 2017b, *AJ*, 153, 45

Mills, S. M., Fabrycky, D. C., Migaszewski, C., et al. 2016, *Nature*, 533, 509

Montet, B. T., Morton, T. D., Foreman-Mackey, D., et al. 2015, ArXiv e-prints, arXiv:1503.07866

Morales-Calderón, M., Stauffer, J. R., Hillenbrand, L. A., et al. 2011, *ApJ*, 733, 50

Morbidelli, A., & Levison, H. F. 2004, *AJ*, 128, 2564

Morbidelli, A., Levison, H. F., Tsiganis, K., & Gomes, R. 2005, *Nature*, 435, 462

Morbidelli, A., & Raymond, S. N. 2016, Journal of Geophysical Research (Planets), 121, 1962

Moriarty, J., & Ballard, S. 2016, *ApJ*, 832, 34

Morley, C. V., Knutson, H., Line, M., et al. 2017, *AJ*, 153, 86

Mortier, A., Santos, N. C., Sousa, S. G., et al. 2013, *A&A*, 558, A106

Mortier, A., Sousa, S. G., Adibekyan, V. Z., Brandão, I. M., & Santos, N. C. 2014, *A&A*, 572, A95

Morton, T. D. 2012, *ApJ*, 761, 6

—. 2015, VESPA: False positive probabilities calculator, Astrophysics Source Code Library, ascl:1503.011

Morton, T. D., & Swift, J. 2014, *ApJ*, 791, 10

Morton, T. D., & Winn, J. N. 2014a, *ApJ*, 796, 47

—. 2014b, *ApJ*, 796, 47

—. 2014c, *ApJ*, 796, 47

Muirhead, P. S., Johnson, J. A., Apps, K., et al. 2012, *ApJ*, 747, 144

Muirhead, P. S., Becker, J., Feiden, G. A., et al. 2014, *ApJS*, 213, 5

Muirhead, P. S., Mann, A. W., Vanderburg, A., et al. 2015, *ApJ*, 801, 18

Mulders, G. D., Pascucci, I., & Apai, D. 2015, *ApJ*, 798, 112

Mullally, F., Thompson, S. E., Coughlin, J. L., Burke, C. J., & Rowe, J. F. 2018, *AJ*, 155, 210

Müller, T. G., Lellouch, E., Stansberry, J., et al. 2010, *A&A*, 518, L146

Murphy, S. J., Bedding, T. R., & Shibahashi, H. 2016, *ApJ*, 827, L17

Murray, C. D., & Dermott, S. F. 1999, Solar system dynamics

Mustill, A. J., Davies, M. B., & Johansen, A. 2015a, *ApJ*, 808, 14

—. 2015b, *ApJ*, 808, 14

—. 2016a, ArXiv e-prints, arXiv:1603.09506

—. 2017, *MNRAS*, 468, 3000

Mustill, A. J., Raymond, S. N., & Davies, M. B. 2016b, *MNRAS*, 460, L109

Nagasawa, M., & Ida, S. 2011, *ApJ*, 742, 72

Nagasawa, M., Ida, S., & Bessho, T. 2008a, *ApJ*, 678, 498

—. 2008b, *ApJ*, 678, 498

Naoz, S., Farr, W. M., Lithwick, Y., Rasio, F. A., & Teyssandier, J. 2011a, *Nature*, 473, 187

—. 2011b, *Nature*, 473, 187

Nesvorný, D., Kipping, D., Terrell, D., et al. 2013, *ApJ*, 777, 3

Nesvorný, D., & Roig, F. 2001, Icarus, 150, 104

Nesvorný, D., & Vokrouhlický, D. 2014, *ApJ*, 790, 58

Neveu-VanMalle, M., Queloz, D., Anderson, D. R., et al. 2016a, *A&A*, 586, A93

—. 2016b, *A&A*, 586, A93

—. 2016c, *A&A*, 586, A93

Newton, E. R., Charbonneau, D., Irwin, J., et al. 2014, *AJ*, 147, 20

Newton, E. R., Charbonneau, D., Irwin, J., & Mann, A. W. 2015, *ApJ*, 800, 85

Ngo, H., Knutson, H. A., Hinkley, S., et al. 2015, *ApJ*, 800, 138

Ning, B., Wolfgang, A., & Ghosh, S. 2018, The Astrophysical Journal, 869, 5

Niraula, P., Redfield, S., Dai, F., et al. 2017a, *AJ*, 154, 266

—. 2017b, *AJ*, 154, 266

Öberg, K. I., Murray-Clay, R., & Bergin, E. A. 2011, *ApJ*, 743, L16

Ohta, Y., Taruya, A., & Suto, Y. 2005, *ApJ*, 622, 1118

Orosz, J. A., Welsh, W. F., Carter, J. A., et al. 2012a, Science, 337, 1511

—. 2012b, Science, 337, 1511

Owen, J. E., & Lai, D. 2018, *MNRAS*, 479, 5012

Owen, J. E., & Wu, Y. 2013, *ApJ*, 775, 105

—. 2017, *ApJ*, 847, 29

Paddock, G. F. 1913, *PASP*, 25, 208

Pál, A. 2012, *MNRAS*, 421, 1825

Palla, F., & Stahler, S. W. 1991, *ApJ*, 375, 288

Parker, R. J., Lichtenberg, T., & Quanz, S. P. 2017, *MNRAS*, 472, L75

Parrish, J. K., Viscido, S. V., & Grnbaum, D. 2002, The Biological Bulletin, 202, 296, pMID: 12087003

Patel, S. G., Vogt, S. S., Marcy, G. W., et al. 2007, *ApJ*, 665, 744

Paxton, B., Bildsten, L., Dotter, A., et al. 2011, *ApJS*, 192, 3

Paxton, B., Cantiello, M., Arras, P., et al. 2013, *ApJS*, 208, 4

Paxton, B., Marchant, P., Schwab, J., et al. 2015, *ApJS*, 220, 15

Peña Ramírez, K., Béjar, V. J. S., & Zapatero Osorio, M. R. 2016, *A&A*, 586, A157

Pedler, R. D., Brandle, R., Read, J. L., et al. 2016, Conservation Biology, 30, 774

Penny, M. T., Gaudi, B. S., Kerins, E., et al. 2018, arXiv e-prints, arXiv:1808.02490

Penz, T., Micela, G., & Lammer, H. 2008, *A&A*, 477, 309

Pepe, F., Mayor, M., Galland, F., et al. 2002, *A&A*, 388, 632

Pepe, F., Cameron, A. C., Latham, D. W., et al. 2013, *Nature*, 503, 377

Pepper, J., Kuhn, R. B., Siverd, R., James, D., & Stassun, K. 2012, *PASP*, 124, 230

Pepper, J., Pogge, R. W., DePoy, D. L., et al. 2007, *PASP*, 119, 923

Pepper, J., Rodriguez, J. E., Collins, K. A., et al. 2017, *AJ*, 153, 215

Petigura, E. A., Howard, A. W., & Marcy, G. W. 2013a, Proceedings of the National Academy of Science, 110, 19273

—. 2013b, Proceedings of the National Academy of Science, 110, 19273

Petigura, E. A., Marcy, G. W., & Howard, A. W. 2013c, *ApJ*, 770, 69

Petigura, E. A., Schlieder, J. E., Crossfield, I. J. M., et al. 2015, *ApJ*, 811, 102

Petit, J.-M., Kavelaars, J. J., Gladman, B. J., et al. 2011, *AJ*, 142, 131

Petrovich, C. 2015, *ApJ*, 805, 75

Petrovich, C., Deibert, E., & Wu, Y. 2018, ArXiv e-prints, arXiv:1804.05065

Petrovich, C., Tremaine, S., & Rafikov, R. 2014, *ApJ*, 786, 101

Pfalzner, S., Steinhausen, M., & Menten, K. 2014, *ApJ*, 793, L34

Pfalzner, S., Davies, M. B., Gounelle, M., et al. 2015, Physica Scripta, 90, 068001

Pike, R. E., Fraser, W. C., Schwamb, M. E., et al. 2017, *AJ*, 154, 101

Pireaux, S., & Rozelot, J.-P. 2003, *Ap&SS*, 284, 1159

Piskorz, D., Knutson, H. A., Ngo, H., et al. 2015, *ApJ*, 814, 148

Polis, G. A. 1991, The American Naturalist, 138, 123

Pollacco, D. L., Skillen, I., Collier Cameron, A., et al. 2006, *PASP*, 118, 1407

Pordes, R., OSG Consortium, Petravick, D., et al. 2007, Journal of Physics Conference Series, 78, 012057

Porras, A., Christopher, M., Allen, L., et al. 2003, *AJ*, 126, 1916

Post, R. M., & Weiss, S. R. B. 1997, Development and Psychopathology, 9, 907929

Press, W. H., Teukolsky, S. A., Vetterling, W. T., & Flannery, B. P. 1992, Numerical recipes in C. The art of scientific computing

Pu, B., & Wu, Y. 2015, *ApJ*, 807, 44

Puranam, A., & Batygin, K. 2018, *AJ*, 155, 157

Pl, A., & Kocsis, B. 2008, Monthly Notices of the Royal Astronomical Society, 389, 191

Queloz, D., Bouchy, F., Moutou, C., et al. 2009, *A&A*, 506, 303

Quinn, S. N., Becker, J. C., Rodriguez, J. E., et al. 2019, arXiv e-prints, arXiv:1901.09092

Quintana, E. V., Adams, F. C., Lissauer, J. J., & Chambers, J. E. 2007, The Astrophysical Journal, 660, 807

Quintana, E. V., Barclay, T., Raymond, S. N., et al. 2014, Science, 344, 277

Ragozzine, D., & Holman, M. J. 2010, arXiv e-prints, arXiv:1006.3727

Rappaport, S., Sanchis-Ojeda, R., Rogers, L. A., Levine, A., & Winn, J. N. 2013, *ApJ*, 773, L15

Rappaport, S., Vanderburg, A., Nelson, L., et al. 2017, *MNRAS*, 471, 948

Rasio, F. A., & Ford, E. B. 1996, Science, 274, 954

Reid, C. R., Lutz, M. J., Powell, S., et al. 2015, Proceedings of the National Academy of Sciences, 112, 15113

Rein, H., & Liu, S.-F. 2012, *A&A*, 537, A128

Rein, H., & Tamayo, D. 2015a, *MNRAS*, 452, 376

—. 2015b, *MNRAS*, 452, 376

Ricker, G. R., Winn, J. N., Vanderspek, R., et al. 2015, Journal of Astronomical Telescopes, Instruments, and Systems, 1, 014003

Riddle, R. L., Baranec, C., Law, N. M., et al. 2016, in American Astronomical Society Meeting Abstracts, Vol. 227, American Astronomical Society Meeting Abstracts, 427.03

Rivera, E. J., Laughlin, G., Butler, R. P., et al. 2010, *ApJ*, 719, 890

Robutel, P., & Laskar, J. 2001, Icarus, 152, 4

Rodriguez, J. E., Vanderburg, A., Eastman, J. D., et al. 2018a, *AJ*, 155, 72

—. 2018b, *AJ*, 155, 72

Rodriguez, J. E., Zhou, G., Vanderburg, A., et al. 2017a, ArXiv e-prints, arXiv:1701.03807

—. 2017b, *AJ*, 153, 256

—. 2017c, *AJ*, 153, 256

Rodriguez, J. E., Ansdell, M., Oelkers, R. J., et al. 2017d, *ApJ*, 848, 97

Rodriguez, J. E., Becker, J. C., Eastman, J. D., et al. 2018c, *AJ*, 156, 245

—. 2018d, ArXiv e-prints, arXiv:1806.08368

Roettenbacher, R. M., & Kane, S. R. 2017, *ApJ*, 851, 77

Roettenbacher, R. M., Monnier, J. D., Harmon, R. O., Barclay, T., & Still, M. 2013, *ApJ*, 767, 60

Rogers, L. A. 2015a, *ApJ*, 801, 41

—. 2015b, *ApJ*, 801, 41

Rowe, J. F., Bryson, S. T., Marcy, G. W., et al. 2014, *ApJ*, 784, 45

Sackett, P. D. 1999, in NATO Advanced Science Institutes (ASI) Series C, Vol. 532, NATO Advanced Science Institutes (ASI) Series C, ed. J.-M. Mariotti & D. Alloin, 189

Sahlmann, J., Lazorenko, P. F., Ségransan, D., et al. 2013, *A&A*, 556, A133

Sahlmann, J., Ségransan, D., Queloz, D., et al. 2011, *A&A*, 525, A95

Saillenfest, M., Fouchard, M., Tommei, G., & Valsecchi, G. B. 2016, Celestial Mechanics and Dynamical Astronomy, arXiv:1611.04457

—. 2017a, Celestial Mechanics and Dynamical Astronomy, 129, 329

—. 2017b, Celestial Mechanics and Dynamical Astronomy, 127, 477

Sallum, S., Follette, K. B., Eisner, J. A., et al. 2015, *Nature*, 527, 342

Sanchis-Ojeda, R., Rappaport, S., Winn, J. N., et al. 2014a, *ApJ*, 787, 47

—. 2014b, *ApJ*, 787, 47

—. 2014c, *ApJ*, 787, 47

Sanchis-Ojeda, R., Winn, J. N., Dai, F., et al. 2015a, *ApJ*, 812, L11

Sanchis-Ojeda, R., Rappaport, S., Pallé, E., et al. 2015b, ArXiv e-prints, arXiv:1504.04379

Santos, N. C., Sousa, S. G., Mortier, A., et al. 2013, *A&A*, 556, A150

Sanz-Forcada, J., Micela, G., Ribas, I., et al. 2011, *A&A*, 532, A6

Savitzky, A., & Golay, M. J. E. 1964, Analytical Chemistry, 36, 1627

Schlaufman, K. C., & Winn, J. N. 2016, *ApJ*, 825, 62

Schlegel, D. J., Finkbeiner, D. P., & Davis, M. 1998a, *ApJ*, 500, 525

—. 1998b, *ApJ*, 500, 525

Schmitt, J. R., Wang, J., Fischer, D. A., et al. 2014, *AJ*, 148, 28

Seager, S., Kuchner, M., Hier-Majumder, C. A., & Militzer, B. 2007, *ApJ*, 669, 1279

Seager, S., & Mallén-Ornelas, G. 2003, *ApJ*, 585, 1038

Sfiligoi, I. 2008, in Journal of Physics Conference Series, Vol. 119, Journal of Physics Conference Series, 062044

Sfiligoi, I., Bradley, D. C., Holzman, B., et al. 2009, in WRI World Congress on Computer Science and Information Engineering, Vol. 2, WRI World Congress on Computer Science and Information Engineering, 428–432

Shallue, C. J., & Vanderburg, A. 2018, *AJ*, 155, 94

Shankman, C., Kavelaars, J. J., Lawler, S. M., Gladman, B. J., & Bannister, M. T. 2017a, *AJ*, 153, 63

Shankman, C., Kavelaars, J. J., Bannister, M. T., et al. 2017b, *AJ*, 154, 50

Shapiro, S. L., & Teukolsky, S. A. 1983, Black holes, white dwarfs, and neutron stars : the physics of compact objects

Sheppard, S. S., & Trujillo, C. 2016, *AJ*, 152, 221

Shin, I. G., Yee, J. C., Gould, A., et al. 2019, arXiv e-prints, arXiv:1902.10945

Silsbee, K., & Tremaine, S. 2018, *AJ*, 155, 75

Silvotti, R., Charpinet, S., Green, E., et al. 2014, *A&A*, 570, A130

Sinukoff, E., Howard, A. W., Petigura, E. A., et al. 2015, ArXiv e-prints, arXiv:1511.09213

—. 2017a, *AJ*, 153, 271

—. 2017b, *AJ*, 153, 70

Siverd, R. J., Beatty, T. G., Pepper, J., et al. 2012, *ApJ*, 761, 123

Siverd, R. J., Collins, K. A., Zhou, G., et al. 2018, *AJ*, 155, 35

Skrutskie, M. F., Cutri, R. M., Stiening, R., et al. 2006, *AJ*, 131, 1163

Slawson, R. W., Prša, A., Welsh, W. F., et al. 2011, *AJ*, 142, 160

Slettebak, A., Collins, G. W., I., Boyce, P. B., White, N. M., & Parkinson, T. D. 1975, The Astrophysical Journal Supplement Series, 29, 137

Sneden, C. 1973, *ApJ*, 184, 839

Snellen, I. A. G., & Brown, A. G. A. 2018, Nature Astronomy, 2, 883

Solontoi, M., Ivezić, Ž., Jurić, M., et al. 2012, Icarus, 218, 571

Sousa, S. G. 2014, ARES + MOOG: A Practical Overview of an Equivalent Width (EW) Method to Derive Stellar Parameters, ed. E. Niemczura, B. Smalley, & W. Pych, 297–310

Sousa, S. G., Santos, N. C., Adibekyan, V., Delgado-Mena, E., & Israelian, G. 2015, *A&A*, 577, A67

Southworth, J., Tregloan-Reed, J., Andersen, M. I., et al. 2016, *MNRAS*, 457, 4205

Sowicka, P., Handler, G., Dębski, B., et al. 2017, *MNRAS*, 467, 4663

Sozzetti, A., Torres, G., Charbonneau, D., et al. 2007, *ApJ*, 664, 1190

Spalding, C., & Batygin, K. 2014, *ApJ*, 790, 42

—. 2015, *ApJ*, 811, 82

—. 2017, *AJ*, 154, 93

Spalding, C., Batygin, K., & Adams, F. C. 2014a, *ApJ*, 797, L29

—. 2014b, *ApJ*, 797, L29

Stassun, K. G., Corsaro, E., Pepper, J. A., & Gaudi, B. S. 2018, *AJ*, 155, 22

Stassun, K. G., & Torres, G. 2018a, *ApJ*, 862, 61

—. 2018b, *ApJ*, 862, 61

Steffen, J. H., & Agol, E. 2005, *MNRAS*, 364, L96

Steffen, J. H., & Farr, W. M. 2013, *ApJ*, 774, L12

Steffen, J. H., & Hwang, J. A. 2015, *MNRAS*, 448, 1956

Steffen, J. H., Batalha, N. M., Borucki, W. J., et al. 2010, *ApJ*, 725, 1226

Steffen, J. H., Ragozzine, D., Fabrycky, D. C., et al. 2012a, Proceedings of the National Academy of Science, 109, 7982

—. 2012b, Proceedings of the National Academy of Science, 109, 7982

Steffen, J. H., Fabrycky, D. C., Agol, E., et al. 2013a, *MNRAS*, 428, 1077

—. 2013b, *MNRAS*, 428, 1077

Stevens, D. J., Collins, K. A., Gaudi, B. S., et al. 2017, *AJ*, 153, 178

Stevenson, D. J. 1982, *Planet. Space Sci.*, 30, 755

Struve, O. 1931, *ApJ*, 74, 225

—. 1952, The Observatory, 72, 199

Sturrock, P. A. 1971, *ApJ*, 164, 529

Sullivan, P. W., Winn, J. N., Berta-Thompson, Z. K., et al. 2015, *ApJ*, 809, 77

Swift, J. J., Johnson, J. A., Morton, T. D., et al. 2013, *ApJ*, 764, 105

Szabó, G. M., Pál, A., Derekas, A., et al. 2012, *MNRAS*, 421, L122

Tamuz, O., Mazeh, T., & Zucker, S. 2005, *MNRAS*, 356, 1466

Tanaka, H., Takeuchi, T., & Ward, W. R. 2002, *ApJ*, 565, 1257

Tegler, S. C., & Romanishin, W. 2000, *Nature*, 407, 979

Teske, J. K., Shectman, S. A., Vogt, S. S., et al. 2016, *AJ*, 152, 167

Teyssandier, J., Naoz, S., Lizarraga, I., & Rasio, F. A. 2013, *ApJ*, 779, 166

Thomas, F., & Morbidelli, A. 1996, Celestial Mechanics and Dynamical Astronomy, 64, 209

Thompson, S. E., Coughlin, J. L., Hoffman, K., et al. 2018, The Astrophysical Journal Supplement Series, 235, 38

Torres, G., Andersen, J., & Giménez, A. 2010, *A&A Rev.*, 18, 67

Torres, G., Fressin, F., Batalha, N. M., et al. 2011, *ApJ*, 727, 24

Towns, J., Cockerill, T., Dahan, M., et al. 2014, Computing in Science and Engineering, 16, 62

Tremaine, S., & Dong, S. 2012, *AJ*, 143, 94

Triaud, A. H. M. J., Anderson, D. R., Collier Cameron, A., et al. 2013, *A&A*, 551, A80

Triaud, A. H. M. J., Neveu-VanMalle, M., Lendl, M., et al. 2017, *MNRAS*, 467, 1714

Trujillo, C. A., & Sheppard, S. S. 2014, *Nature*, 507, 471

Tsiganis, K., Gomes, R., Morbidelli, A., & Levison, H. F. 2005, *Nature*, 435, 459

Udalski, A., Szymanski, M., Stanek, K. Z., et al. 1994, , 44, 165

Udalski, A., Jaroszyński, M., Paczyński, B., et al. 2005, *ApJ*, 628, L109

Uehara, S., Kawahara, H., Masuda, K., Yamada, S., & Aizawa, M. 2016, *ApJ*, 822, 2

Ulanowicz, R. E. 1997, Ecology, the ascendent perspective / Robert E. Ulanowicz (Columbia University Press New York)

Vacca, W. D., Cushing, M. C., & Rayner, J. T. 2003, *PASP*, 115, 389

Valenti, J. A., & Fischer, D. A. 2005, *ApJS*, 159, 141

Valsecchi, F., Rasio, F. A., & Steffen, J. H. 2014, *ApJ*, 793, L3

Van Eylen, V., & Albrecht, S. 2015, *ApJ*, 808, 126

Van Eylen, V., Lund, M. N., Silva Aguirre, V., et al. 2014, *ApJ*, 782, 14

Van Laerhoven, C., & Greenberg, R. 2012, Celestial Mechanics and Dynamical Astronomy, 113, 215

van Saders, J. L., & Pinsonneault, M. H. 2013, *ApJ*, 776, 67

Vanderburg, A., & Johnson, J. A. 2014, *PASP*, 126, 948

Vanderburg, A., Plavchan, P., Johnson, J. A., et al. 2016a, *MNRAS*, 459, 3565

Vanderburg, A., Johnson, J. A., Rappaport, S., et al. 2015a, *Nature*, 526, 546

Vanderburg, A., Montet, B. T., Johnson, J. A., et al. 2015b, *ApJ*, 800, 59

Vanderburg, A., Becker, J. C., Kristiansen, M. H., et al. 2016b, *ApJ*, 827, L10

Vanderburg, A., Latham, D. W., Buchhave, L. A., et al. 2016c, *ApJS*, 222, 14

—. 2016d, *ApJS*, 222, 14

Vanderburg, A., Bieryla, A., Duev, D. A., et al. 2016e, *ApJ*, 829, L9

—. 2016f, *ApJ*, 829, L9

Vanderburg, A., Becker, J. C., Buchhave, L. A., et al. 2017, *AJ*, 154, 237

Vanderspek, R., Huang, C. X., Vanderburg, A., et al. 2019, *ApJ*, 871, L24

Veras, D., & Ford, E. B. 2012, *MNRAS*, 420, L23

Villanueva, Jr., S., Dragomir, D., & Gaudi, B. S. 2018, ArXiv e-prints, arXiv:1805.00956

Vogt, S. S., Butler, R. P., Marcy, G. W., et al. 2002, *ApJ*, 568, 352

Vogt, S. S., Allen, S. L., Bigelow, B. C., et al. 1994, in Society of Photo-Optical Instrumentation Engineers (SPIE) Conference Series, Vol. 2198, Instrumentation in Astronomy VIII, ed. D. L. Crawford & E. R. Craine, 362

Volk, K., & Gladman, B. 2015, *ApJ*, 806, L26

Volk, K., Murray-Clay, R. A., Gladman, B. J., et al. 2018, ArXiv e-prints, arXiv:1802.05805

Walkowicz, L. M., & Basri, G. S. 2013, *MNRAS*, 436, 1883

Wang, J., Fischer, D. A., Horch, E. P., & Huang, X. 2015a, *ApJ*, 799, 229

Wang, J., Fischer, D. A., Barclay, T., et al. 2015b, *ApJ*, 815, 127

Wang, J. J., Graham, J. R., Dawson, R., et al. 2018, *AJ*, 156, 192

Wang, S., Jones, M., Shporer, A., et al. 2019, *AJ*, 157, 51

Weiss, L. M., & Marcy, G. W. 2014a, *ApJ*, 783, L6

—. 2014b, *ApJ*, 783, L6

—. 2014c, *ApJ*, 783, L6

Weiss, L. M., Marcy, G. W., Rowe, J. F., et al. 2013, *ApJ*, 768, 14

Weiss, L. M., Deck, K., Sinukoff, E., et al. 2016a, ArXiv e-prints, arXiv:1612.04856

Weiss, L. M., Rogers, L. A., Isaacson, H. T., et al. 2016b, *ApJ*, 819, 83

Weiss, L. M., Deck, K. M., Sinukoff, E., et al. 2017, *AJ*, 153, 265

Welsh, W. F., Orosz, J. A., Carter, J. A., & Fabrycky, D. C. 2014, in IAU Symposium, Vol. 293, Formation, Detection, and Characterization of Extrasolar Habitable Planets, ed. N. Haghighipour, 125–132

Welsh, W. F., Orosz, J. A., Carter, J. A., et al. 2012, *Nature*, 481, 475

Winn, J. N. 2010, ArXiv e-prints, arXiv:1001.2010

Winn, J. N., Fabrycky, D., Albrecht, S., & Johnson, J. A. 2010a, *ApJ*, 718, L145

Winn, J. N., Johnson, J. A., Howard, A. W., et al. 2010b, *ApJ*, 718, 575

Winn, J. N., Howard, A. W., Johnson, J. A., et al. 2011, *AJ*, 141, 63

Winn, J. N., Sanchis-Ojeda, R., Rogers, L., et al. 2017a, ArXiv e-prints, arXiv:1704.00203

—. 2017b, *AJ*, 154, 60

Wittenmyer, R. A., Endl, M., Cochran, W. D., et al. 2009, *AJ*, 137, 3529

Wolfgang, A., Rogers, L. A., & Ford, E. B. 2015, arXiv preprint arXiv:1504.07557

Wolfgang, A., Rogers, L. A., & Ford, E. B. 2016, *ApJ*, 825, 19

Wöllert, M., Brandner, W., Bergfors, C., & Henning, T. 2015, *A&A*, 575, A23

Wolszczan, A., & Frail, D. A. 1992, *Nature*, 355, 145

Wright, J. T., Marcy, G. W., Howard, A. W., et al. 2012, *ApJ*, 753, 160

Wu, Y., & Lithwick, Y. 2011, *ApJ*, 735, 109

Wu, Y., & Murray, N. 2003, *ApJ*, 589, 605

Xie, J.-W., Dong, S., Zhu, Z., et al. 2016, Proceedings of the National Academy of Science, 113, 11431

Yao, X., Pepper, J., Gaudi, B. S., et al. 2018, ArXiv e-prints, arXiv:1807.11922

Yeakel, J. D., Stiefs, D., Novak, M., & Gross, T. 2011, Theoretical Ecology, 4, 179

Yi, S., Demarque, P., Kim, Y.-C., et al. 2001, *ApJS*, 136, 417

Yu, L., Rodriguez, J. E., Eastman, J. D., et al. 2018, ArXiv e-prints, arXiv:1803.02858

Zacharias, N., Finch, C., & Frouard, J. 2017, VizieR Online Data Catalog, 1340

Zeng, L., Sasselov, D. D., & Jacobsen, S. B. 2016a, *ApJ*, 819, 127

—. 2016b, *ApJ*, 819, 127

Zhou, G., Rodriguez, J. E., Collins, K. A., et al. 2016, *AJ*, 152, 136

Zhou, G., Bakos, G. Á., Hartman, J. D., et al. 2017, *AJ*, 153, 211

Zhu, W., Dai, F., & Masuda, K. 2018, Research Notes of the American Astronomical Society, 2, 160

Ziegler, C., Law, N. M., Baranec, C., et al. 2016, in Society of Photo-Optical Instrumentation Engineers (SPIE) Conference Series, Vol. 9909, Adaptive Optics Systems V, 99095U

Zuckerman, B., Koester, D., Reid, I. N., & Hünsch, M. 2003, *ApJ*, 596, 477